DISSERTATION

COMBINED MULTISPECTRAL/HYPERSPECTRAL REMOTE SENSING OF TROPOSPHERIC AEROSOLS FOR QUANTIFICATION OF THEIR DIRECT RADIATIVE EFFECT

Submitted by

Gregory R. McGarragh

Department of Atmospheric Science

In partial fulfillment of the requirements

For the Degree of Doctor of Philosophy

Colorado State University

Fort Collins, Colorado

Fall 2013

Doctoral Committee:

Advisor: Graeme Stephens

Sonia Kreidenweis
Thomas Vonder Haar
Randy Bartels

ABSTRACT

COMBINED MULTISPECTRAL/HYPERSPECTRAL
REMOTE SENSING OF TROPOSPHERIC AEROSOLS
FOR QUANTIFICATION OF THEIR DIRECT RADIATIVE EFFECT

Scattering and absorption of solar radiation by aerosols in the atmosphere has a direct radiative effect on the climate of the Earth. Unfortunately, according to the IPCC the uncertainties in aerosol properties and their effect on the climate system represent one of the largest uncertainties in climate change research. Related to aerosols, one of the largest uncertainties is the fraction of the incident radiation that is scattered rather than absorbed, or their single scattering albedo. In fact, differences in single scattering albedo have a significant impact on the magnitude of the cooling effect of aerosols (opposite to that of greenhouse gasses) which can even have a warming effect for strongly absorbing aerosols.

Satellites provide a unique opportunity to measure aerosol properties on a global scale. Traditional approaches use multispectral measurements of intensity at a single view angle to retrieve at most two aerosol parameters over land but it is being realized that more detail is required for accurate quantification of the direct effect of aerosols, in particular its anthropogenic component, and therefore more measurement information is required. One approach to more advanced measurements is to use not only intensity measurements but also polarimetric measurements and to use multiple view angles. In this work we explore another alternative: the use of hyperspectral measurements in molecular absorption bands.

Our study can be divided into three stages the first of which is the development of a fast radiative transfer model for rapid simulation of measurements. Our approach is matrix operator based and uses the Padé approximation for the matrix exponential to evaluate the homogeneous solution. It is shown that the method is two to four times faster than the standard and efficient discrete ordinate technique and is accurate to the 6th decimal place.

The second part of our study forms the core and is divided into two chapters the first of which is a rigorous sensitivity and optimal estimation based information content study that explores the

use of measurements made by a MODIS type instrument combined with measurements made by an instrument similar to GOSAT TANSO-FTS which supplies hyperspectral measurements of intensity and polarization in the O_2 A-band and the 1.61- and 2.06-μm CO_2 bands. It is found that the use of the hyperspectral bands provides a means to separate the effects of the surface and aerosol absorption from effects related to aerosol single scattering parameters. The amount of information increases significantly when the CO_2 bands are included rather than just the more traditional O_2 A-band, when polarization measurements are included, and when measurements are made at multiple view angles.

We then present a retrieval using co-located observations of MODIS and GOSAT TANSO-FTS which are both also co-located with AERONET sites for validation purposes. We introduce an optimal estimation retrieval and perform this retrieval on our co-located observations. We choose a complete state vector to maximize the use of the information in our measurements and use an a priori constraint and regularization to arrive at a stable solution. In addition to the retrieved parameters, we also calculate a self contained estimation of the retrieval error. Validation with AERONET, for retrievals using MODIS plus TANSO-FTS measurements of intensity and polarization in all three bands indicate accuracies within 15% for optical thickness, 10% for fine mode mean radius, 35% for coarse mode mean radius, 15% for the standard deviation of fine mode mean radius, 25% for the standard deviation of the coarse mode mean radius, 0.04 for the real part of the index of refraction, and 0.05 for single scattering albedo. In addition to the retrieved parameters, we also validate the estimated retrieval error and find that the estimations have distributions that are tighter and within the broader distributions of real errors relative to AERONET.

The third part of our study uses the retrieval results to calculate radiative fluxes, errors, and sensitivities at solar wavelengths along with aerosol radiative effect and effect efficiency. In addition, we outline how to propagate the errors in the retrieval through the flux calculations to provide an error estimation of the fluxes. These results are then validated against the corresponding AERONET products. It was found that the flux results were most sensitive to single scattering albedo while the size distribution and real part of the index of refraction also have significant effects. Relative to AERONET our fluxes are less accurate than an independent AERONET validation, due to uncertainties in our satellite based retrieval with accuracies within 13 Wm^{-2} for TOA upward, 9

Wm^{-2} for BOA upward, and 30 Wm^{-2} for BOA downward. The estimated errors also contained uncertainties but were in fact more conservative than the actual errors.

ACKNOWLEDGMENTS

The work presented in this thesis would not have been possible without the help of several very talented people along the way. I would like to thank my advisor Dr. Graeme Stephens for his support and helpful guidance throughout this project. I would also like the thank my other committee members Dr. Sonia Kreidenweis, Dr. Thomas Vonder Haar, and Dr. Randy Bartels for their helpful suggestions, reviewing my thesis, and their patience with scheduling delays in the end. Along with the excellent faculty members the Atmospheric Science department at CSU has an excellent research staff some of which have provided me with valuable assistance. I would like to thank Dr. Philip Gabriel for many helpful and entertaining discussions related to the details of radiative transfer modeling, Dr. Tristan L'Ecuyer for valuable insight into optimal estimation based information content analyses and retrievals, Dr. Dennis O'Brien for answering questions related to atmospheric remote sensing in the O_2 A-band, Dr. Chris O'Dell and Tommy Taylor for answering questions related to simulating measurements in the O_2 A-band and the ACOS data in general, and the rest of the Stephens research group, most of who have left, for their valuable discussion and advice. Finally, I would like to thank the O'Dell research group and CIRA for use of the OCO Cluster, without which this work would not have been computationally feasible.

A project of this magnitude not only requires support from colleagues but also support from those in one's personal life. I would like to thank my family for encouraging me to pursue a Ph.D. and for their love and support throughout the process, especially my wife Morgan who continuously supported me through thick and thin, for which I am very grateful.

This research was supported by NASA Grants 1439268 and NAS5-99237.

TABLE OF CONTENTS

LIST OF TABLES

LIST OF FIGURES

Chapter 1

Introduction

1.1 Motivation

Atmospheric aerosols affect the Earth's climate primarily by scattering and absorption of solar radiation. Scattering of solar radiation back to space results in a cooling or negative forcing of the atmosphere and surface system. This cooling impacts heating rates, atmospheric circulation patterns, evolution of the boundary layer, and precipitation [Hansen et al., 1997, Miller and Tegen, 1998, Yu et al., 2002, Dunion and Velden, 2004, Wang, 2004, Seinfeld and Pandis, 1998]. This effect is known as the direct radiative effect of aerosols. Absorption of solar radiation acts to decrease the magnitude of this direct effect. Haywood and Shine [1995] showed that the magnitude of the cooling in the presences of absorbing sulfate aerosols was significantly reduced when soot or black carbon aerosol was included in the mixture. Absorption of solar radiation by aerosols also results in what is known as a semi-direct effect, where the absorption warms the atmosphere affecting temperature and humidity profiles and, as a result, the conditions for cloud development and convection [Ackerman et al., 2000, Stephens et al., 2004, Huang et al., 2006, 2010]. In addition to the direct radiative effects, aerosols have also been shown to exhibit indirect effects wherein by acting as cloud condensation nuclei they increase cloud droplet concentration while decreasing the cloud droplet size [Lohmann and Feichter, 2005]. The effect of this is to increase the cloud albedo [Twomey, 1977, Taylor et al., 2000], known as the first indirect effect, and to decrease precipitation, increase cloud height, and increase cloud lifetime [Ramanathan et al., 2001, Tao et al., 2012, Pincus and Baker, 1994, Albrecht, 1989], know as secondary indirect effects. Figure 1.1 is a schematic diagram showing the various aerosol radiative effects.

Unfortunately, the uncertainties in aerosol properties and their effect on the climate system represents one of the largest uncertainties in climate forcing research [Mitchell et al., 1995, Hansen et al., 1997, Charlson et al., 1992, Anderson et al., 2003] and has been reported as the largest

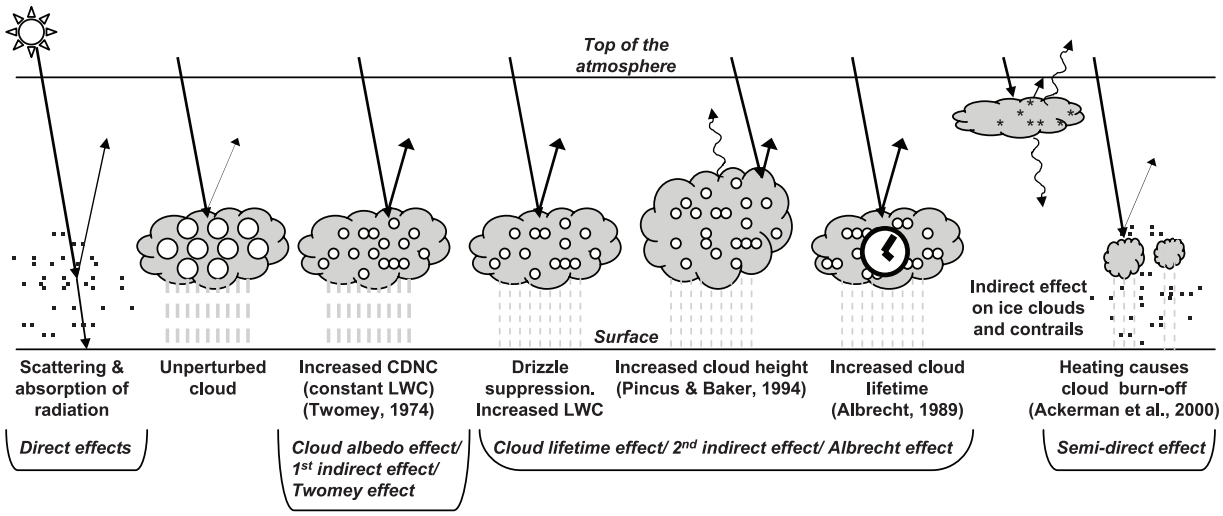

Figure 1.1: Schematic diagram showing the various aerosol radiative effects including the direct effect and indirect effects related to clouds (modified from Haywood and Boucher [2000]). The small black dots represent aerosol particles and the larger open circles cloud droplets. Straight lines represent the incident and reflected solar radiation and wavy lines represent terrestrial radiation. The filled white circles indicate cloud droplet number concentration (CDNC). The unperturbed cloud contains larger cloud drops as only natural aerosols are available as cloud condensation nuclei, while the perturbed cloud contains a greater number of smaller cloud drops as both natural and anthropogenic aerosols are available as cloud condensation nuclei (CCN). The vertical grey dashes represent rainfall, and LWC refers to the liquid water content. (Adapted from Intergovernmental Panel on Climate Change [2007a].)

uncertainty in the most recent assessment of the Intergovernmental Panel on Climate Change (IPCC) [Intergovernmental Panel on Climate Change, 2007a]. This can be seen in figure 1.2, adapted from the IPCC's most recent assessment, in which the large positive forcings of greenhouse gases have a high level of scientific understanding (LOSU) whereas the aerosol forcings are given a relatively low LOSU. The uncertainties in the direct radiative effect of aerosols is evident in the large range of estimates from individual research groups as shown in figure 1.3. Uncertainties in aerosol properties and their effects result in uncertainties in modeled predictions on the effects of greenhouse gases, making use of these model results as a basis for policy changes of some concern [Rosenzweig et al., 2008]. Indeed, Charlson et al. [1992], in a ground breaking study, showed that the total (direct plus indirect) radiative forcing by anthropogenic sulfate aerosol (non-absorbing) particles is of the same order of magnitude (but opposite in sign) as the radiative forcing by anthropogenic greenhouse gases, compensating, and in effect, masking the effect of greenhouse gases. Complicating our assessments further is the fact that aerosols typically exist as external and/or internal mixtures of multiple aerosol components, some of which are absorbing, decreasing the magnitude of the cooling [Chýlek et al., 1995, Jacobson, 2001] and also changing cloud radiative absorption [Chýlek et al., 1996, Li, 1998]. It is therefore necessary to improve our knowledge of aerosols in order to provide detailed aerosol climatologies to evaluate the chemical transport/aerosol models that are used with climate models and to improve our knowledge of the direct radiative forcing of the Earth in order to evaluate the radiative forcing component in climate change modeling [Hansen et al., 2005].

Aerosols exhibit a strong variability in distribution, due to the variability in location and magnitudes of sources, and in their atmospheric resident time of days to weeks, but also in microphysical properties such as shape, size, and chemical composition, due to a large variability in the types of sources. These microphysical properties in turn affect their optical properties such as optical thickness, single scattering albedo, and scattering phase function. These optical properties along with the aerosol's loading and the albedo of the underlying surface will determine the sign and magnitude of the radiative forcing of a particular aerosol type. This is particularly the case of the aerosol single scattering albedo, the fraction of radiation incident on a particle that is scattered rather than absorbed. In addition, the effect of the single scattering albedo depends strongly on the albedo of the surface, which can vary on a regional level at a small scale. Over dark surfaces,

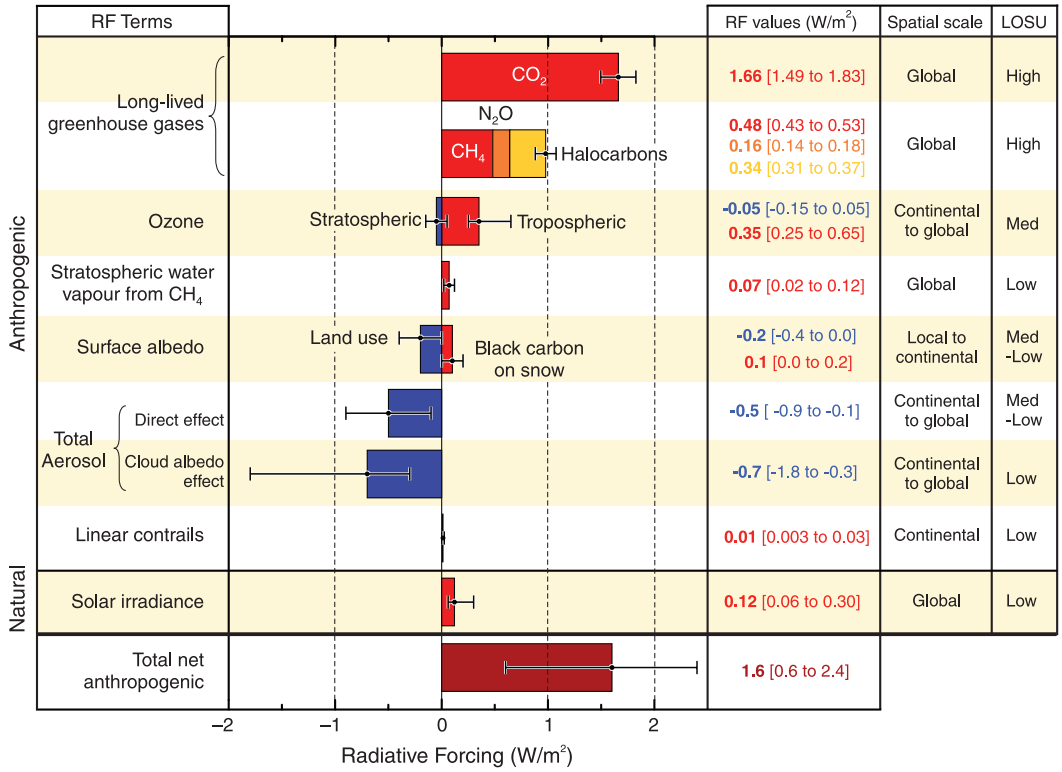

Figure 1.2: Global average radiative forcing (RF) in 2005 (best estimates and 5 to 95% uncertainty ranges) with respect to 1750 for important agents and mechanisms, together with the typical geographical extent (spatial scale) of the forcing and the assessed level of scientific understanding (LOSU). (Adapted from Intergovernmental Panel on Climate Change [2007b].)

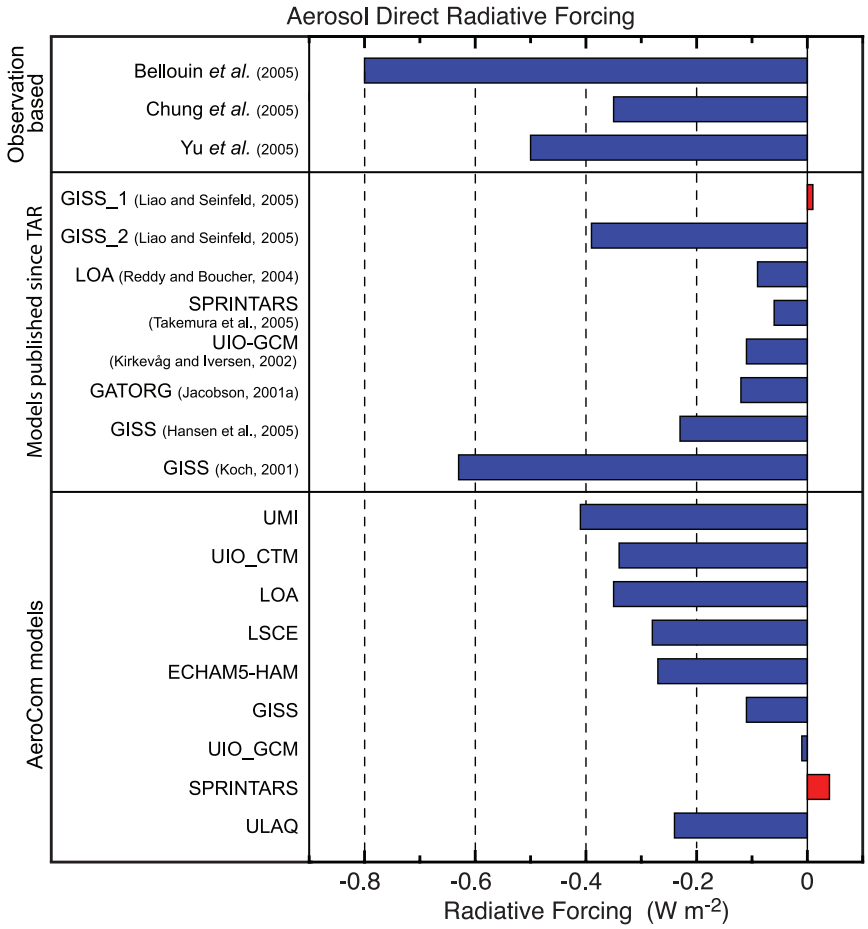

Figure 1.3: Estimates of the direct aerosol radiative forcing (RF) from observationally based studies, independent modeling studies, and AeroCom results with identical aerosol and aerosol precursor emissions. GISS_1 refers to a study employing an internal mixture of aerosol, and GISS_2 to a study employing an external mixture. (Adapted from Intergovernmental Panel on Climate Change [2007a].)

aerosols tend to have a cooling effect while over brighter surfaces, through multiple scattering with the surface, aerosols can absorb enough energy to actually have a warming effect.

Aerosols can be broadly categorized into natural and anthropogenic (man-made) aerosols [Seinfeld and Pandis, 1998]. Natural aerosols include sea-salt and mineral dust, both of which are driven into the atmosphere from wind, blowing on the ocean and the land surface, respectively. These aerosols, formed from a mechanical process, are characterized by large sizes. Sea-salt typically has low loadings, and even though land-based aerosols with large loadings can be advected over the ocean Haywood et al. [1999] showed that sea-salt is the leading aerosol contributor to the global-mean clear-sky radiation balance over oceans. Sea-salt is non-absorbing and therefore causes a negative radiative forcing. In contrast, mineral dust is characterized by larger loadings and, in addition, by non-spherical shapes. Mineral dust, with a larger mean size and single scattering albedos significantly less than unity will absorb, and, as they are typically located over bright desert surfaces, can have a significant positive radiative forcing on the climate. In addition, due to its larger size, mineral dust can have a significant effect at longwave terrestrial wavelengths, absorbing and emitting radiation contributing a heating effect depending on their vertical distribution [Tegen et al., 1996, Zhang and Christopher, 2003]. The effects of mineral dust from North Africa have been extensively studied and found to represent a significant effect on the radiation budget [Haywood et al., 2008] and tropical convection as it is advected out over the Atlantic [Stephens et al., 2004]. Other sources of natural aerosols include biogenic aerosol, typically non-absorbing, black carbon from natural fires which may have significant absorption, and organic carbon from natural fires and oxidation of biogenic gases, which generally have low absorption.

Anthropogenic aerosols are usually composed of sulfates primarily from urban and industrial fossil fuel burning, black carbon (soot) from transportation and industrial fossil fuel combustion and biomass burning, and organic carbon from biomass burning [Seinfeld and Pandis, 1998]. In contrast to natural aerosols, anthropogenic aerosols are characterized by small sizes providing a means to separate them from natural aerosols. Sulfates are generally non-absorbing and therefore have a negative climate forcing [Chuang et al., 1997, Mitchell and Johns, 1997] masking the positive climate forcing effects of greenhouse gases. Black carbon is another anthropogenic aerosol that is characteristically small in size but is usually mixed with other aerosols such as sulfates. Alone, black carbon is highly absorbing with single scattering albedos less that 0.5 and therefore will still

significantly affect the absorption of mixtures of which they are a part of. It has been shown that the presence of black carbon can actually contribute a positive radiative forcing therefore warming the climate only second to CO_2 [Jacobson, 2002, Wang, 2004, Bond et al., 2013]. Complicating the effect of black carbon is that being associated with fossil fuel combustion they are sometimes mixed with sulfate aerosols that have a comparable but opposite radiative effect [Chýlek et al., 1995, Penner et al., 1998]. Finally organic carbon based aerosols (organics) have large biomass burning sources but may also come from industrial combustion processes. They vary significantly with their source, in particular, the type of fuel and the burning conditions and their mixture with black carbon. Johnson et al. [2008] indicate that fresh biomass burning emissions in North Africa are more absorbing than those measured in southern African during the SAFARI-2000 campaign [Haywood et al., 2008].

This strong variability of tropospheric aerosols in horizontal and vertical distribution, shape, size, and chemical composition make them a difficult object of study. Many techniques exist for measuring and characterizing aerosols [Yu et al., 2006]. Ground-based in-situ measurements of aerosols from field campaigns provide accurate measurements of shape, size, and chemical composition but such detailed observations are sparse and not usually conducted operationally, with data collected for limited time periods. Ground-based remote sensing of aerosols such as that performed with AERONET [Holben et al., 1998] instruments are operational providing a more continuous data set in time but are still limited by the sparsity of the network, especially over ocean. Only with polar orbiting satellite-based measurements, with global coverage in the order of days, can aerosols be observed on scales that allow an accurate characterization of their properties with space and time, making satellite observations an indispensable source of information. Of course, even satellite observations will have spatial and temporal gaps and therefore are not sufficient alone to make an accurate global assessment of the impacts of aerosols on the current and future climate systems. The complexity of aerosol-climate interactions requires that a combination of measurements and theoretical approaches be used to accurately characterize the effect of aerosol in the climate system [Diner et al., 2004]. In this case, the role of the satellite measurements will be to provide accurate constraints for the aerosol components of climate models, validate the results from these components, and to provide a means to independently quantify aerosol radiative forcing against which the model derived aerosol direct effects can be validated [Kahn et al., 2004].

Satellite observations used for the remote sensing of aerosols typically vary in spectral range, spectral resolution, angular range, polarimetric capability, spatial resolution, global coverage, noise requirements, etc [King et al., 1999, Mishchenko et al., 2007b]. As the importance of accurately quantifying aerosol properties from space has become more recognized, the aerosol retrieval capabilities of satellite instruments have improved with some missions almost solely dedicated to the retrieval of aerosol properties. The importance of having a broad spectral range for aerosol retrievals has long been recognized as well as the advantage to measuring polarization in addition to intensity but additional passive remote sensing measurements are also valuable including measurements made a multiple view angles and hyperspectral measurements made in molecular absorption bands. A more thorough background into satellite remote sensing of aerosols is given in the next chapter and therefore we will leave more detailed discussion until then.

1.2 Theoretical primer

In this section we attempt to present a brief primer on plane-parallel radiative transfer at solar wavelengths through an atmosphere with molecular absorption and a lower aerosol layer (scattering and absorbing) bounded by a surface. For simplicity we will ignore scattering from molecules. For more detailed information look at the introductions to atmospheric radiation presented by Liou [2002] and Petty [2006]. First we will present the equations for the general case then we will look at two distinct cases: (1) the thin limit, where the aerosol layer is assumed to be optically thin, and (2) the semi-infinite limit, where the aerosol layer is assumed to be optically thick.

The general form of the plane-parallel radiative transfer equation (RTE) is given by [Chandrasekhar, 1960, Liou, 2002]

$$-\mu\frac{dI(\tau;\mu,\phi)}{d\tau} = -I(\tau;\mu,\phi) + S(\tau;\mu,\phi), \tag{1.1}$$

where $I(\tau;\mu,\phi)$ is the intensity at optical depth τ along the direction specified by the cosine of the polar angle $\mu \in [-1,1]$ (measured from the upward normal or the negative τ-direction) and the azimuthal angle $\phi \in [0,2\pi]$ (measured clockwise when looking upward). In our presentation optical depth is a vertical coordinate that may be translated to either altitude z or pressure p coordinates.

The first term on the right hand side represents a radiation sink due to extinction. The second term on the right hand represents a radiation source due to scattering which can be separated into singly scattered and multiply scattered components as

$$S(\tau;\mu,\phi) = S_s(\tau;\mu,\phi) + S_m(\tau;\mu,\phi). \tag{1.2}$$

The singly scattered source component, representing direct radiation from the sun that is scattered into direction (μ,ϕ), is given by

$$S_s(\tau;\mu,\phi) = \frac{F_0}{4\pi} e^{-\tau/\mu_0} \omega(\tau) P(\tau;\mu,\phi,-\mu_0,\phi_0), \tag{1.3}$$

where F_0 is the top of atmosphere (TOA) incident solar flux, μ_0 and ϕ_0 are the solar zenith and azimuth angles, respectively, $\omega(\tau)$ is the albedo of single scattering, and $P(\tau;\mu,\phi,\mu',\phi')$ is the scattering phase function for radiation from the direction (μ',ϕ') scattered into the direction (μ,ϕ). The multiply scattered source component, representing scattered radiation from all directions that is scattered into direction (μ,ϕ), is given by

$$S_m(\tau;\mu,\phi) = \frac{\omega(\tau)}{4\pi} \int_0^{2\pi} \int_{-1}^{1} P(\tau;\mu,\phi,\mu',\phi') I(\tau;\mu',\phi') d\mu' d\phi'. \tag{1.4}$$

It is worth discussing three important optical quantities in the above equations: the optical thickness or optical depth τ, the single scattering albedo ω, and the scattering phase function $P(\mu,\phi,\mu',\phi')$. The optical thickness (or optical depth when referenced as a vertical coordinate) is a unitless measure of attenuation which, for a plane-parallel atmosphere, is given by

$$\tau = \int_0^z \sigma_e(z) dz, \tag{1.5}$$

where z is the vertical coordinate in units of length and σ_e is the extinction coefficient of the medium in units of inverse length [Liou, 2002, Petty, 2006]. The transmission, the fraction of radiation passing through a medium with optical thickness τ, is given by

$$\mathcal{T} = e^{-\tau/\mu}, \tag{1.6}$$

where μ is the zenith angle of the propagation direction, the inverse of which acts as an adjustment factor to account for an increase in path length with zenith angle in a plane parallel atmosphere. The optical thickness component due to molecular absorption of gases is generally computed from spectroscopic information and is a function of the pressure and temperature. The optical thickness component due to scattering and absorption by aerosols is computed from the abundance and the extinction properties of the individual aerosol particles which are in turn computed from Mie theory [Mie, 1908, Liou, 2002] as a function of the aerosol size distribution and the complex index of refraction.

The single scattering albedo ω, computed from the extinction properties of the individual aerosol particles and in turn Mie theory, is the fraction of radiation that is scattered rather than absorbed when radiation interacts with a scattering medium and is given by

$$\omega = \frac{\sigma_s}{\sigma_e} = \frac{\sigma_s}{\sigma_s + \sigma_a}, \tag{1.7}$$

where σ_s is the scattering coefficient, σ_a is the absorption coefficient, and $\sigma_e = \sigma_s + \sigma_a$.

The scattering phase function $P(\mu, \phi, \mu', \phi')$ is the fraction of radiation from the direction (μ', ϕ') (incident) that is scattered by the medium into the direction (μ, ϕ) (scattered). For spherical particles it is derived by geometric transformation from the scattering phase function for individual scattering particles $P(\Theta)$ [Liou, 2002, Petty, 2006], computed from Mie theory, where Θ is the scattering angle or the angle between the incident and scattered radiation, which is normalized as

$$\frac{1}{4\pi} \int_0^{2\pi} \int_0^{\pi} P(\theta) \sin\theta d\theta d\phi = 1. \tag{1.8}$$

It is also worth noting that the asymmetry parameter $g \in [-1, 1]$ of the scattering phase function (referred to later) represents the shape of the phase function, where $g > 0$ indicates more forward scattering and $g < 0$ indicates more backscattering, with the notable values of 1 indicating all forward scattering, -1 indicating all backscattering, and 0 indicating isotropic scattering (equal in all directions). Aerosols typically have values of g with forward scattering of around 0.7.

The radiative transfer just described is subject to boundary conditions at the top and bottom of the atmosphere, where at the top downward diffuse radiation is assumed to be zero

$$I(0; -\mu, \phi) = 0 \tag{1.9}$$

and the bottom upward diffuse radiation may be separated into singly scattered and multiply scattered components with

$$I(\tau_*; +\mu, \phi) = I_s(\tau_*; +\mu, \phi) + I_m(\tau_*; +\mu, \phi). \tag{1.10}$$

where τ_* is the total optical thickness of the atmosphere. The singly scattered component, representing direct radiation from the sun that is scattered upward by the surface, is given by

$$I_s(\tau_*; +\mu, \phi) = \frac{\mu_0}{\pi} F_0 e^{-\tau_*/\mu_0} A\rho(+\mu, \phi, -\mu_0, \phi_0), \tag{1.11}$$

where A is the surface albedo or reflectance factor and $\rho(\mu, \phi, \mu', \phi')$ is the normalized surface bidirectional reflectance distribution function (BRDF) for reflectance from the direction (μ', ϕ') into the direction (μ, ϕ). For a Lambertian surface $\rho = 1$. The multiply scattered source component, representing diffuse downward radiation that is scattered upward by the surface, is given by

$$I_m(\tau_*; +\mu, \phi) = A \int_0^{2\pi} \int_0^1 \rho(+\mu, \phi, \mu', \phi') I(\tau_*; \mu', \phi') d\mu' d\phi'. \tag{1.12}$$

1.2.1 Thin limit

If we assume that the aerosol layer is optically thin then as an approximation we need only consider singly scattered radiation. In this case, the atmospheric and surface components for satellite observed observations may be separated as

$$I_{\text{obs}} = I_{\text{atm}} + I_{\text{sfc}}, \tag{1.13}$$

where I_{obs} is the total radiation observed by a satellite sensor and I_{atm} and I_{sfc} are the atmospheric and surface components, respectively. Assuming single scattering, equation 1.1 reduces to

$$-\mu\frac{dI(\tau;\mu,\phi)}{d\tau} = -I(\tau;\mu,\phi) + \frac{F_0}{4\pi}e^{-\tau/\mu_0}\omega(\tau)P(\tau;\mu,\phi,-\mu_0,\phi_0), \tag{1.14}$$

the solution of which for upward radiation represents the thin limit atmospheric term I_{atm} as

$$I_{\text{atm}}(+\mu,\phi) = \frac{F_0}{4\pi\mu}e^{-\tau(p_0)\left(\frac{1}{\mu_0}+\frac{1}{\mu}\right)}\int_{p_0}^{p_*} e^{-[\tau(p)-\tau(p_0])/\mu_0}e^{-[\tau(p)-\tau(p_0)]/\mu}\omega(p)P(p;+\mu,\phi,-\mu_0,\phi_0)dp, \tag{1.15}$$

where we have made the optical properties a function of pressure p and assume that the aerosol layer resides between p_0 and p_*. Assuming that the aerosol layer is homogeneous in ω and P integration of equation 1.15 leads to

$$I_{\text{atm}}(+\mu,\phi) = -\frac{F_0}{4\pi\mu}e^{-\tau(p_0)\left(\frac{1}{\mu_0}+\frac{1}{\mu}\right)}\omega P(+\mu,\phi,-\mu_0,\phi_0)\left(\frac{1}{\mu_0}+\frac{1}{\mu}\right)\left(e^{-[\tau(p_*)-\tau(p_0)]\left(\frac{1}{\mu_0}+\frac{1}{\mu}\right)}-1\right). \tag{1.16}$$

Then, by separating τ into molecular absorption and aerosol scattering and absorption components, τ_g and τ_a, respectively, introducing the mass path term $m = \frac{1}{\mu_0}+\frac{1}{\mu}$, setting $\tau_a = \tau_g(p_*) - \tau_g(p_0)$, and finally assuming that $\tau_a m \ll 1$, we obtain

$$I_{\text{atm}}(+\mu,\phi) = -\frac{F_0}{4\pi\mu}e^{-\tau_g(p_0)m}\omega P(+\mu,\phi,-\mu_0,\phi_0)m\left(e^{-[\tau_g(p_*)-\tau_g(p_0)]m}\tau_a m - 1\right), \tag{1.17}$$

where the total single scattering albedo may be given in terms of its molecular absorption and aerosol scattering and absorption components by

$$\omega(\tau) = \frac{\omega_a\tau_a}{\tau_g+\tau_a}. \tag{1.18}$$

The thin limit surface term is given by

$$I_{\text{sfc}}(+\mu,\phi) = \frac{\mu_0}{\pi}F_0e^{-\tau(p_*)m}A\rho(+\mu,\phi,-\mu_0,\phi_0). \tag{1.19}$$

The thin limit model just presented identifies several parameters controlling the radiative transfer in an atmosphere with molecular absorption and aerosol scattering for a particular solar and viewing geometry:

- The molecular absorption optical thickness τ_g.
- The upper level of the scattering layer p_0 that defines the molecular absorption optical thickness above the scattering layer.
- The pressure thickness of the scattering layer $p_* - p_0$ that defines the molecular absorption optical thickness of the scattering layer.
- The optical thickness of the aerosol layer τ_a.
- The single scattering albedo of the aerosols ω_a.
- The scattering phase function of the aerosols P_a.
- The surface albedo A.

1.2.2 Semi-infinite limit

When an optically thick aerosol layer is present a semi-infinite approximation with isotropic scattering may be applied. Anisotropic scattering may can be accounted for via the similarity transformation

$$\omega'_a = \frac{(1-g)\omega_a}{1-g\omega_a}, \tag{1.20}$$

where ω' is the scaled single scattering albedo for isotropic scattering and g is the asymmetry factor of the scattering phase function P. It follows that [Chandrasekhar, 1960]

$$I_{\text{obs}} = \frac{F_0}{4} e^{-\tau_{p_0} m} \omega'_a \frac{\mu_0}{\mu + \mu_0} R(\omega'_a, \mu, \mu_0), \tag{1.21}$$

where $R(\omega', \mu, \mu_0)$ is an azimuthally independent atmospheric reflection function for isotropic scattering. From this it is apparent that aerosol phase function information enters the function $R(\omega', \mu, \mu_0)$ through the scaling relationship 1.20 and then only in terms of g, the third moment in a Legendre expansion of the phase function. Therefore, in the semi-infinite limit, reflected radiances

only depend on bulk information about the phase function and more detailed characteristics described by higher Legendre moments are ignored.

So far our semi-infinite model has ignored molecular and aerosol absorption. An important effect of adding absorption will be to increase the dependence on more detailed phase function characteristics (higher phase function Legendre moments) by decreasing the degree of multiple scattering and therefore increasing the degree of single scattering. We will show in this study that this aspect along with the variation in molecular absorption across hyperspectral bands provides a unique variation in sensitivity to aerosol parameters.

1.3 Research objectives

As a preliminary step, we develop tools necessary to perform the research objectives focusing on three challenges specific to our purpose. The primary tool to develop is a forward model that simulates measurements taken by multispectral, multiangle, radiometric/polarimetric satellite-based instruments of a scene given physical atmospheric and surface properties along with solar and viewing geometry. Challenges with this include the wide range of instrument support required, the efficient computation of measurements for a wide dimensionality including multiangle, polarimetric, and hyperspectral measurements (in contrast to more traditional single angle, intensity only measurements at a small number of wavelengths), and the efficient computation of derivatives of the measurements with respect to inputs, a must have, for retrievals with a large number of microphysical parameters being retrieved. We must also develop an optimal estimation inversion system that is stable even with the large range of parameters and their magnitudes encountered in aerosol retrievals and provides not only an estimate of the retrieval parameters but also an estimate of their uncertainties. Finally, for demonstrating the use of our retrieval we must develop a model to compute radiative fluxes and aerosol direct radiative effects which takes as input not only the aerosol retrieval parameters but also the estimated uncertainties in these parameters to compute fluxes along with the uncertainties in those fluxes.

Our first objective is to explore the capabilities of satellite-based solar hyperspectral measurements in molecular absorption bands (particularly in the 0.76-μm O_2 A- and the 1.61- and 2.06-μm CO_2 bands) to contribute unique information to aerosol retrieval systems already using common

multispectral measurements in several bands from 0.4 to 2.0 μm. We will do this for hyperspectral measurements taken at nadir and multiple view angles and of intensity and polarization. We will look at the sensitivities of these measurements to the parameters of interest to provide an intuitive feel for their capabilities. We will then perform a formal information content analysis of the measurements in order to identify how many and which parameters are retrievable. Our primary objective here is to explore the use of hyperspectral measurements in molecular absorption bands as a means to obtain more information for aerosol retrievals than typically used multispectral observations. Ultimately, we hope this study will provide researchers developing aerosol inversions using hyperspectral measurements information necessary in the development and evaluation of their retrieval systems.

Second, we will develop a satellite-based retrieval using the multispectral and hyperspectral measurements explored in the first objective. Our retrieval will be based on the optimal estimation approach with which we will be able to maximize the use of the available information and provide a stable solution through iterative regularization. Another important aspect of our retrieval will be a self contained estimate of the retrieval errors independent of outside validation sources that will accompany the retrieval parameters to provide a basis for estimating uncertainties in applications using the retrieved aerosol quantities. We will also validate our retrieval and the estimated errors using independent ground-based aerosol retrievals. Our ultimate goal with this objective is to improve upon existing aerosol retrieval methods in order to improve our understanding of aerosols and their direct radiative effect for climate change studies. The quality of our retrieval will be assessed on how accurately loading and microphysical parameters are retrieved but also on the accuracy of the derived optical thickness and the more difficult to retrieve single scattering albedo, both of which are important for aerosol radiative forcing estimates.

Third, we will provide a sample application of our retrieval results with the aim of demonstrating the use of our aerosol retrieval in the computation of aerosol direct radiative flux and effect and validating these derived products. In addition, we also demonstrate the use of the retrieval uncertainties in evaluating the resulting uncertainties in the radiative flux and effect calculations. This will provide the basis of a framework that can be used in computing uncertainties of any quantity derived from our aerosol retrieval.

The problem of developing a multi-sensor aerosol retrieval system capable of retrieving aerosol properties accurately enough for use in climate change studies cannot be completely investigated by a single researcher in the course of a few years. Indeed, many aerosol retrieval systems are the work of several researchers over many years and their is no doubt that the retrieval presented in this study can be improved upon and benefit from further refinements. Rather, the work described in this thesis is meant to only modestly contribute to research on aerosol retrieval systems and to encourage the growth in the interest of using hyperspectral measurements in solar molecular absorption bands for remote sensing of aerosols and even clouds. The use of these kinds of satellite-based hyperspectral measurements for particle retrievals studies is still in its infancy and only recently with the development of the GOSAT and OCO-2 instruments has it been possible to do it in practice. We hope to provide some knowledge from which future researchers can further improve the use of satellite measurements for improving our understanding of aerosols and their impacts on climate change.

1.4 Thesis outline

In chapter 2 we present a detailed overview of the different types of measurements and techniques used for satellite remote sensing of tropospheric aerosols and include numerous references relevant to the discussion. We also discuss several techniques that focus on aerosol absorption as a retrieval parameter, due to its importance and difficulty of retrieval. Finally, an outline of the evolution of the use of measurements in solar molecular absorption bands for remote sensing of cloud and aerosols is given which gradually evolves to measurements of the hyperspectral type. In chapter 3 we discuss a scalar radiative transfer solution used in the forward model developed for this thesis based on the Padé approximation to the matrix exponential. The solution methodology is presented followed by accuracy tests and timing comparisons with the state-of-the-art discrete ordinate method based on scenarios relevant to this thesis. The tests indicate that with the new methodology accurate results are obtained with a fraction of the run time. This chapter represents the first of the two published papers that have grown from this work. In chapter 4 we present a generalized form of the radiative transfer solution given in the previous chapter that is capable of solving for the entire stokes vector, not just the first element. As with the previous chapter, accuracy and timing comparison are also

given and accurate and fast results are obtained relative to the vector discrete ordinate technique. This chapter represents the second of the two published papers that have grown from this work. Chapter 5 is one of the two core chapters that represents one of the two papers "to be submitted" that have grown from this work. In this chapter we describe measurements that will be investigated, the retrieval setup for this investigation, the measurement and state vectors and associated errors, and the forward model that has been developed to simulate the measurements. We then present a study of the sensitivity of these measurements to several atmospheric scenarios. Finally, an information content analysis framework is given and a formal information content for several measurements and atmospheric scenarios is presented. The results indicate that the hyperspectral measurements in solar molecular absorption bands provide a unique sensitivity not found in typical multispectral measurements and that by combining these hyperspectral measurements with multispectral measurements significantly more information about aerosols is obtained over that of using multispectral measurements alone. Chapter 6 is the other of the two core chapters and represents the other of the two papers "to be submitted" that have grown from this work. In this chapter we present an aerosol retrieval starting with a review of the measurement data and the validation data. We discuss the details of the strategy used for the co-location of the different measurement observations and the validation data along with filtering strategies taken. The details of the retrieval methodology are then presented followed by a validation of the results. The results indicate that indeed use of the hyperspectral measurements improves the retrieval results with accuracies for optical thickness and single scattering albedo approaching the stringent accuracy goals required for accurate quantification of the direct effect of aerosols. In chapter 7 we apply the retrieval results from the previous chapter to calculate radiative fluxes and aerosol radiative effect at each retrieval site. First, the flux and effect quantities computed are described followed by a description of the radiative transfer model used and the computation of the flux and effect uncertainties. Then we summarize the validation flux and effect quantities that our quantities will be compared against followed by a presentation of our results versus the results from the validation data. The results indicate, as expected from the previous chapter, that use of the hyperspectral measurements improves the accuracy of the flux and effect quantities compared to using retrieval results from multispectral measurements alone. Finally, in chapter 8 conclusions from our research and possibilities for future directions will be given.

Chapter 2

Background

2.1 Introduction

Satellite observations have the potential to address some of the challenges mentioned in the previous chapter involved in quantifying aerosol distribution, loading, and microphysical parameters, for climate prediction studies. In particular, it is only possible with spaceborne platforms to obtain the global spatial coverage, spatial resolution, and temporal resolution required for accurate climate modeling. Other measurement techniques, such as in situ measurements and ground-based radiometric measurements may have a high temporal resolution but are limited by spatial coverage and, as a result, are mostly of use for validation purposes. The use of a single satellite instrument, rather than a distribution of different ground-based instruments, also provides a sustained, self-consistent, and uniform accuracy to rely on, without introducing calibration differences among networks of different instruments. These two benefits make satellite measurements an indispensable systematic source of aerosol information on a global scale.

In this chapter we will review the current state of satellite-based remote sensing techniques for tropospheric aerosols using passive radiometric measurements. This will include a discussion of the different types of measurements available and their strengths and weaknesses along with a discussion of the two primary inversion approaches. Then we will walk through many of the most important instruments used for aerosol retrievals and discuss the common retrieval techniques presented in the literature that are used for aerosol inversion using these instruments. Then we will focus on techniques that have been proposed for specifically retrieving aerosol absorption information, or single scattering albedo, a particular challenge in satellite remote sensing of aerosols. Finally, we will discuss the evolution of observations in molecular absorption bands of solar wavelengths, in particular the O_2 A-band, for the remote sensing of atmospheric particles starting with clouds

and then moving on to aerosols, discussing high spectral resolution measurements of intensity and polarization.

2.2 General aerosol retrieval techniques

Satellite instruments that are used for passive remote sensing of tropospheric aerosols can be roughly divided in the four categories: (1) Instruments that perform measurements of intensity at multiple wavelengths at a single viewing direction. (2) Instruments that perform measurements of intensity at multiple wavelengths and at multiple view angles of the same field of view (FOV). (3) Instruments that perform measurements of intensity and polarization at multiple wavelengths at a single view angle. (4) Instruments that perform measurements of intensity and polarization at multiple wavelengths and at multiple view angles of the same FOV.

Inversion algorithms for the retrieval of aerosol properties from passive satellite instruments generally fall into two categories [Kokhanovsky and Leeuw, 2009]. The traditional approach uses a least squares type method to minimize the difference between the measurements and simulations based on a limited set of predefined aerosol models (a combination of size distribution and index of refraction for one or two modes) and aerosol optical thickness. The simulations are usually precomputed and stored in a look-up table (LUT) as a function of model, aerosol optical thickness (AOT), assumed surface properties, and solar and viewing geometry, which makes them efficient in operational environments. Unfortunately, due to the discrete nature of the inversion these methods are unable to utilize all the information contained in advanced observations with multispectral, multiangle, and/or polarimetric measurements. In addition, attempts to retrieve a larger number of parameters with these advanced measurements will increase the dimensionality of the LUT approach making the method unwieldy for operational use.

The other category of inversion algorithms includes optimal estimation approaches, where the best match between the measurements and the simulations, as computed with a forward model, is obtained by optimizing the forward model inputs. The methodology makes use of a continuous space of aerosol microphysical properties, and in some cases surface properties, as a continuous set of solutions maximizing the use of all the available information. Of course the aerosol retrieval problem is classically ill-posed with many possible solutions. To deal with this, optimal estimation

approaches usually employ some sort of a priori constraint and use some form of regularization to stabilize the solution.

Aerosol retrieval methods also vary in how they characterize the surface relative to the aerosols themselves. In other words, how they separate the signal due to aerosols from the signal due to the surface. Traditionally, this problem has been avoided by limiting aerosol retrievals to cases over dark surfaces only. Non-glint ocean observations are the standard in this case but since aerosol sources, other than the ocean, are land-based, these retrievals are limited to measurements of aerosols from the ocean and aerosols from land-based sources that are advected over the ocean. One strategy for dealing with this problem is to limit aerosol retrievals over land to dark surfaces only, in particular dark dense vegetation (DDV). Unfortunately, this method is limited by the retrieval sample size and excludes aerosols from important land-based sources, in particular desert dust over land. Multiangle measurements provide a means to characterize the surface and have been used in some cases as discussed below. The use of polarization measurements is another way to limit the surface characterization problem. Measurements of polarization from the surface not only have a lower overall magnitude than that from aerosols, they also have a relatively flat spectral signature compared to aerosols, providing a means to separate their effects. Finally, as discussed below, there is a class of aerosol retrieval techniques using UV wavelengths at which surface reflectance is small. Not surprisingly, this approach is limited in spectral range.

In the following we will discuss in detail the various instruments used for aerosol retrievals by category, in the order listed above, along with some of the inversion methods and surface characterization approaches used with each instrument. Relevant references for further details are also included.

2.2.1 Multispectral techniques

The first operational satellite aerosol retrieval used a single channel (0.63 μm) from the Advanced Very High Resolution Radiometer (AVHRR) to retrieve AOT over ocean [Stowe, 1991, Stowe et al., 1997]. Unfortunately, the use of a single channel provides no additional information to constrain the sensitivities to aerosol microphysical properties, such as size distribution and complex index of refraction, and to surface characteristics. This retrieval was later extended to use both the 0.63 and 0.83 μm AVHRR channels [Higurashi and Nakajima, 1999, Mishchenko et al., 1999, Geogdzhayev

et al., 2002] to retrieve, in addition to AOT, the Ångström exponent, an index for the aerosol size distribution, based on the spectral variation of AOT. Knowledge of aerosol size can give some idea of the aerosol type and is a first step to distinguishing anthropogenic aerosols, such as sulfates, black carbon, and organic carbon, which are predominately small, from natural aerosols, such as sea salt and desert dust, which contain larger particles. Mishchenko et al. [1999] found that imperfect cloud screening and calibration uncertainties were by far the largest sources of errors in the retrieved AOT and Ångström exponent. Holben et al. [1992] presented two different techniques using AVHRR for the retrieval of AOT over land for atmospheric correction. The first determines the AOT using path radiance in the 3.75-μm channel over targets with a dark surface reflectance (0.02 ± 0.01) while the other use the change in contrast between scenes to determine the change in AOT.

The MODerate Resolution Imaging Spectrometer (MODIS) [Salomonson et al., 1989], aboard both the Aqua and Terra satellites, provides multispectral measurements in 36 bands, 7 of which are used by the MODIS operational aerosol retrieval: 0.645 and 0.856 μm (250 m spatial resolution) and 0.469, 0.555, 1.24, 1.64, and 2.13 μm (500 m spatial resolution). This is a significant improvement in spectral range over that of AVHRR and provides sensitivity to a larger range of particle sizes along with the ability to distinguish more than one aerosol mode. The first MODIS operation retrieval of aerosol properties over ocean was introduced by Tanré et al. [1997] and used an LUT approach to minimize on total AOT at 0.55 μm, the fraction of the total AOT contributed by the fine mode, and one of a set of aerosol models, from which the mean particle radius of the dominate mode was considered accurate enough to be a third retrieval parameter. The current retrieval over ocean remains largely unchanged from the original with only small changes in aerosol models and the lookup table. The first operational MODIS retrieval over land, described by Kaufman et al. [1997], assumed that aerosols were transparent at 2.13 μm and used the reflectance in this band to identify dark pixels, particularly dark dense vegetation (DDV, reflectance less that 0.25) and to determine the surface reflectance at 0.47 μm and 0.66 μm using an empirical relationship. The retrieval then proceeded to use an LUT approach with the 0.47 μm and 0.66 μm reflectances to retrieve AOT at 0.55 μm and the fraction of the AOT contributed by the fine mode. The operational land algorithm was later improved by adding the 2.13-μm surface reflectance as an actual retrieval measurement, which was assumed to contain information about the coarse mode aerosols, and by actually retrieving the surface reflectance at 2.13 μm [Levy et al., 2007]. An alternative approach for

bright desert surfaces presented by Hsu et al. [2004, 2006] relies on the fact that desert surfaces are darker in the blue bands. The method identified as the Deep Blue algorithm uses an LUT approach based on the reflectance ratio between the blue and red bands as a function of AOT and single scattering albedo (SSA).

2.2.2 Multispectral multiangle techniques

The use of multiangle measurements for satellite aerosol retrievals was first investigated by Martonchik and Diner [1992] and later by Wang and Gordon [1994]. In both cases the authors concluded that multiangle observations provide a significant source of information over that of single viewing angle observations. Multiangle measurements provide a means to sample the aerosol single scattering phase function providing an additional constraint to reduce uncertainties in the aerosol microphysical properties [Kahn et al., 1997, 2001]. In addition, multiangle measurements provide a means to characterize the bidirectional reflectance distribution function (BRDF) of the surface.

The Along Track Scanning Radiometer-2 (ATSR-2) [Llewellyn-Jones and Remedios, 2012], aboard the ERS-2 satellite, provides measurements at two view angles, a forward view angle at approximately 55° and a view angle at nadir, in seven wavelengths, four of which are in the visible and near-infrared (0.555, 0.659, 0.865, and 1.60 μm), with a spatial resolution of 1 km. Both Flowerdew and Haigh [1996] and Veefkind et al. [1998] present algorithms for aerosol retrievals over land using ATSR-2 observations that rely on the assumption that the variation in surface reflectance with view angle is independent with wavelength and depends only on sun/satellite viewing geometry providing a basis to eliminate surface contribution to the measured radiance.

The Multiangle Imaging SpectroRadiometer (MISR) [Diner et al., 1998], aboard the Terra satellite, provides measurements in four spectral bands centered at 0.443, 0.555, 0.670, and 0.865 μm, at nine angles: nadir, $\pm$26.1°, $\pm$45.6°, $\pm$60.0°, and $\pm$70.5°, at a 275 m spatial resolution. The operational MISR retrieval [Martonchik et al., 1998] uses three different algorithms depending on the surface type (dark water, dense dark vegetation, and heterogeneous land) each of which employees an LUT approach to minimize a χ^2 statistic as a function of total AOT and a suite of aerosol models. The resulting AOT and the effective radius of the model are considered retrieval parameters. Due to its limited spectral resolution MISR lacks the large wavelength bands that are sensitive to large particles and are required to distinguish fine from coarse mode aerosols.

2.2.3 Multispectral polarimetric techniques

It has long been realized that measurements of polarization are more sensitive to particle microphysics than are measurements of intensity [Hansen and Hovenier, 1974]. Mishchenko and Travis [1997b] showed that retrieval algorithms using only intensity suffer from a severe uniqueness problem and that polarization measurements provide a stronger means of constraining aerosol properties relying less on assumed a priori information. In addition, there are several advantages to using polarization over land [Waquet et al., 2007]. First, the relative contribution to polarized reflectance from the surface compared to that from aerosols is less than in the case for total reflectance. Second, the polarized reflectance from land surfaces has relatively low spatial contrast as the primary source of surface polarization is single scattering from surface facets which depends on solar and viewing geometry. Finally, the polarized reflectance from land surfaces has a relatively weak spectral dependence.

The Global Ozone Monitoring Experiment-2 (GOME-2) [Callies et al., 2000], aboard the MetOp satellite, and planned for more missions in the future, is the first satellite instrument to be launched that belongs in the category of instruments that measures intensity and polarization at a single view angle. GOME-2 measures intensity in four bands covering the spectral range from 240 nm to 790 nm with a spectral resolution ranging from 0.24 nm at 249 nm to 0.53 nm at 790 nm and a spatial resolution of 40×40 km. GOME-2 also measures polarization in 12 programmable bands in the spectral range from 312 nm to 790 nm with a spectral resolution ranging from 2.8 nm at 312 nm to 40 nm at 790 nm and a spatial resolution of 40×5 km. Although GOME-2 is limited by a large FOV and therefore provides a limited number of cloud free observations it nevertheless provides a basis for evaluating single angle polarimetric aerosol retrievals. Hasekamp and Landgraf [2005] presented an optimal estimation based information content and retrieval technique using GOME-2 intensity and polarization measurements to retrieve, over ocean, a full set of aerosol parameters (loading, effective radius, and effective variance in two modes; the real and imaginary index of refraction; the height of the layer where the bulk of the aerosol is located, and ocean pigment concentration). Their method used both an a priori constraint and Phillips-Tikhonov regularization to retrieve a stable solution. They found that the addition of polarization information allowed the retrieval of significantly more information on effective variance, real part of the index of refraction, and ocean

pigment concentration than intensity measurements alone. Furthermore, they found that unlike intensity only measurements, measurements with intensity and polarization allowed the retrieval of information on the effective variance, imaginary part of the index of refraction, and aerosol height. Unfortunately, a strong dependence on viewing geometry was found and that for a well defined range of viewing geometries the polarization measurements show a much lower sensitivity to aerosol properties than for other geometries, at which the retrievals are less reliable. This leads us to multiangle polarimetric measurements.

2.2.4 Multispectral multiangle polarimetric techniques

Single angle measurements sample only a single scattering angle per observation depending on the solar and viewing geometry while measurements of polarization have a strong dependence on the single scattering phase matrix with scattering angle. The result of this is that the sensitivity of polarization measurements to aerosols and the reliability of the retrieval of aerosols is strongly dependent on the solar and viewing geometry of a particular observation. A solution to this inconsistency is to take measurements of polarization at multiple view angles for a single FOV sampling a range of single scattering angles and therefore a range of sensitivities.

The Polarization and Directionality of the Earth's Radiances (POLDER) [Deschamps et al., 1994] has been and is a part of three different satellite missions. The first two, ADEOS-I and ADEOS-II, failed prematurely. The current mission is PARASOL and the POLDER instrument aboard makes measurements of intensity at 443, 490, 565, 670, 763, 765, 865, 910, 1020 nm and polarization at 443, 670, and 865 nm, at up to 13 viewing geometries for a single orbit with a spatial resolution of 6×7 km. The current operational POLDER aerosol retrieval over ocean [Herman et al., 2005, Tanré et al., 2011] uses intensity and polarization measurements in the 670 and 865 nm bands in an LUT approach. Bimodal non-absorbing aerosol models are used, where the coarse mode model has a mixture of spherical and non-spherical aerosols, and the retrieval parameters include the total AOT, effective radius in both modes, real part of the index of refraction, Ångström exponent for total AOT, AOT of the fine mode, and AOT of the large mode non-spherical contribution. Over land, the current operational aerosol retrieval [Deuzé et al., 2001, Tanré et al., 2011] uses measurements in the 670 and 865 nm bands of only polarization as the contribution to polarization due to aerosols dominates over that due to land whereas the contribution to the intensity due to

aerosols is comparable or even less than that due to land. The retrieval uses an LUT approach with fine mode aerosol models of spherical non-absorbing aerosols to retrieve total AOT and the Ångström exponent, The coarse mode is neglected as the polarization from large particles is often small. The result is a systematic underestimation of AOT and overestimation of the Angström exponent when a significant large mode is present.

Several optimal estimation approaches using POLDER measurements have also been presented. Lebsock et al. [2007] presented an information content analysis and retrieval over ocean using the intensity and polarization at 670 and 860 nm. They found that the majority of the AOT information lies in the intensity only measurements while polarization was necessary to retrieve aerosol microphysical quantities. A total of three parameters were found to be retrievable including the logarithm of the number concentration of two modes and the real part of the index of refraction. Unfortunately, their optimal estimation method lacked an a priori constraint and a form of regularization, both required for efficient use of all the available information. Hasekamp et al. [2011] used an optimal estimation approach, over ocean, similar to that of Hasekamp and Landgraf [2005] (discussed above) using both intensity and polarization measurements at 490 and 670 nm to retrieve a full set of aerosol parameters including, in both modes, the loading, effective radius, effective variance, and complex index of refraction; the height of the layer where the bulk of the aerosol is located, ocean pigment concentration, wind speed in two directions, and white cap fraction. They excluded the 865 nm band due to effects caused by the relatively low signal at that wavelength over ocean. Finally, Dubovik et al. [2011] presented a statistically optimized inversion algorithm for enhanced retrieval of aerosol properties from multispectral, multiangle, polarimetric satellite observations. Their method is presented in the context of POLDER but made sufficiently general enough to be applied to other advanced satellite observations. It is based on the method developed for multiangle ground-based AOT and intensity measurements by Dubovik and King [2000] with additional refinements added since then. They use the complete set of POLDER intensity and polarization measurements (except those at 763, 765, and 910 nm which are dominated by gaseous absorption) to retrieve aerosol parameters including the total volume concentration, the size distribution (actual, not just parameters for an assumed model), fraction of the spherical particles, total real and imaginary parts of the index of refraction, mean height of the aerosol layer, and several surface BRDF parameters. Here we see, again, the trend toward using information in

the measurements to retrieve surface characteristics along with the aerosol parameters rather than determining these characteristics a prior.

POLDER represents the most advanced aerosol satellite observing system discussed so far. Unfortunately, POLDER is limited by its spectral range lacking the longer wavelengths and their sensitivity to larger particles. In addition, POLDER is limited by it angular resolution and is unable to resolve important features in the single scattering phase matrix related to the polarization. Finally, POLDER's insufficient noise requirements make it difficult to retrieve all the aerosols parameters required for accurate quantification of aerosol direct and indirect effects with sufficient accuracy [Mishchenko et al., 2004].

An alternative to POLDER like instruments is to trade spatial/temporal coverage for larger spectral range and angular resolution such as with the Research Scanning Polarimeter (RSP) and the Aerosol Polarimetry Sensor (APS) instruments. Although RSP is an airborne instrument it is relevant to discuss here as it has/will set a precedent for satellite instruments of similar design including APS. RSP measures the first three stokes parameters I, Q, and U in nine spectral channels at 410, 470, 550, 670, 865, 960, 1560, 1880, and 2250 nm and at 152 viewing angles along track $\pm 60^\circ$ [Cairns et al., 1999]. The measurements are made simultaneously for I, Q, and U in the nine spectral channels insuring that the spectral and polarimetric measurements view the same scene. Chowdhary et al. [2002] presented case studies of using RSP to retrieve non-absorbing aerosols over the ocean and determined that RSP could accurately retrieve aerosol number concentration, size distribution, and the real part of the index of refraction in two modes. In addition, the polarized reflectances at shorter wavelengths (410 and 550 nm) show a weak sensitivity to ocean color showing the potential to separate contributions from aerosols from that of ocean color. In addition, simulated examples of POLDER retrievals for the same cases indicate that the absence of longer wavelength measurements with POLDER limits the amount of information that can be retrieved about the coarse mode aerosol. Building on these developments Chowdhary et al. [2005] outlined a more formal retrieval algorithm and included the imaginary part of the index of refraction and aerosol height as retrieval parameters. Results from measurements taken during the CLAMS experiment were presented which confirmed that found in the previous study.

An optimal estimation retrieval for aerosols over land using RSP measurements was presented by Waquet et al. [2009]. In this case only the polarized reflectances were used so as to avoid the

aerosol/surface separation in the total reflectances. The polarized reflectance from the surface was represented using a simple model constrained with the 2.25-μm measurements. The complete set of aerosol parameters was retrieved for both fine and coarse modes along with the aerosol-top pressure. A sensitivity analysis showed the value of having the smaller wavelengths to estimate the aerosol height and absorption although at large AOTs sensitivity to aerosol height can still be problematic. The heritage of RSP lead to APS, an instrument of very similar design but built for satellite use and with a slightly different wavelength configuration, which was a part of the Glory Satellite mission [Mishchenko et al., 2007a, Peralta et al., 2007]. Unfortunately, that mission failed to achieve orbit depriving the science community of a valuable aerosol observing system.

2.3 Techniques focusing on aerosol absorption

Aerosol absorption is quantified either through the absorption cross section, or the derived absorption coefficient or absorption optical thickness. The absorption cross section can be determined with Mie theory from the aerosol microphysical size distribution and complex index of refraction assuming spherical particles. The retrieval techniques described above have focused on retrieving loading and microphysical quantities from which aerosol climatologies and models may be validated and radiative forcing estimates may be derived. Unfortunately, not all of these parameters may be retrievable but for radiative forcing studies only the total optical thickness and total single scattering albedo are required for a relatively accurate quantification. As we have seen, optical thickness is retrievable from satellite with a relatively good accuracy but the retrieval of single scattering albedo is more difficult due to the difficulty of separating the absorption and scattering extinction. This has lead investigators interested in aerosol radiative forcing studies to pursue techniques with which to improve the retrieval of single scattering albedo. As one goal of our study is to improve aerosol loading and microphysical retrievals, and the subsequently derived optical thickness and single scattering albedo, for radiative forcing studies we felt that is was necessary to discuss some of the alternatives involving the retrieval of single scattering albedo directly with which our study shares similar motivation.

The most prominent approach to retrieving aerosol absorption from space has been the use of measurements in the ultraviolet (UV) wavelengths. Unlike in the visible and near-infrared, the

relatively large amount of molecular scattering in the UV produces a "bright" background increasing the sensitivity of back scattered radiance to aerosol absorption. In addition, in the UV, the surface reflectively is usually insignificant and constant over both ocean and land. Unfortunately, due to the sensitivity of UV measurements to molecular scattering, aerosol retrieval methods using the UV are particularly sensitive to aerosol vertical distribution due to varying molecular scattering with height.

The first UV satellite instruments used for observing aerosols were the Total Ozone Mapping Spectrometers (TOMSs) [Bowman and Krueger, 1985]. TOMS instruments have flown on four different missions providing data with minimal interruption from 1978 to 2006. TOMS measures backscattered UV radiance in six 1-nm wide bands at 313, 318, 331, 340, 360, and 380 nm with a 50×50 km spatial resolution. The first techniques that used TOMS measurements for observing aerosols were based on the spectral contrast between two UV wavelengths and in particular the decrease in this spectral contrast in the presence of aerosols relative to that with only molecular scattering [Hsu et al., 1996, Seftor et al., 1997, Herman et al., 1997a]. The resulting "aerosol index" (AI), sometimes referred to as the absorbing aerosol index (AAI), increases with aerosol abundance, aerosol absorption, and aerosol height. The method is a useful way of mapping absorbing aerosols and small-sized non-absorbing aerosols but lacks a quantitative estimate of the aerosol AOT and/or SSA required for radiative forcing studies. Torres et al. [1998] proposed a method of retrieving AOT and SSA using the relationship between the 340/380 nm radiance ratio and the 380 nm radiance. This relationship varies depending on the AOT and the aerosol type of which the UV measurements are most sensitive to the aerosol type's SSA. The method is subject to errors induced by sub-pixel clouds in the large 50 x 50 km at nadir TOMS FOV and uncertainties in aerosol vertical distribution. This method was later generalized to an LUT approach by Torres et al. [2005]. Hu et al. [2007] and Hu and Sokhi [2009] presented a method that retrieves the column SSA necessary to reproduce the TOMS AI given the MODIS or MISR AOT and aerosol vertical distribution from the global chemical transport model GEOS-CHEM. Other/newer instruments with UV bands from which AAI is determined include the Global Ozone Monitoring Experiment-1 and -2 (GOME-1 and -2) [de Graaf et al., 2005], Scanning Imaging Absorption Spectrometer for Atmospheric Cartography SCIAMACHY [Tilstra et al., 2012], and the Ozone Monitoring Instrument (OMI) [Levelt et al., 2006], the replacement for TOMS.

As already mentioned, TOMS aerosol retrievals are limited by its large 50 x 50 km FOV and, as a result, the inevitable sub-pixel cloud contamination and by uncertainties in the aerosol vertical distribution. In addition, TOMS retrievals are valid for the UV with only limited validity in the radiatively more important visible and near-infrared wavelengths. Several other satellite-based retrieval methods have been proposed for the retrieve of aerosol absorption information. Conel [1991] used Landsat Thematic Mapper (TM) measurements of surface reflectance over selected targets with known surface properties so that the atmospheric contribution could be estimated. An algebraic inversion scheme was used to retrieve AOT and SSA. Kaufman et al. [2002] presented a hypothetical method that used ocean sunglint observations along with off-glint observations of the same location to derive AOT, size distribution, and refractive index along with aerosol spectral absorption. In this method it is the large signal of attenuation between the sunglint observation and the satellite that provides enough information to distinguish aerosol absorption. The use of critical reflectance to determine aerosol SSA was introduced by Kaufman [1987] and later used in a more comprehensive study by Wells [2010] and Wells et al. [2012] to retrieve SSA over desert using MODIS observations. The critical reflectance represents the top of the atmosphere (TOA) reflectance at which increased aerosol scattering due to increased aerosol loading is balanced by increased absorption of the surface contribution. Critical reflectance is derived by comparing two observations of the same FOV with different aerosol loading, assuming that each observations has similar surface reflectance and background aerosol. Satheesh and Srinivasan [2006] proposed a method that can be used to derive simple aerosol models that are optically equivalent and can simulate the observed aerosol optical properties and radiative fluxes from spectral optical depth measurements allowing for the differentiation between scattering and absorbing aerosol and thus, the determination of single scattering albedo.

2.4 Application of absorption and scattering in the O_2 A-band

Much of the earlier studies using the O_2 A-band focused on determining cloud-top pressure from space. The physical basis for this was that knowing the concentration of O_2, which is relatively constant, and its vertical variation, the observed absorption along the path to the top of the cloud could be translated into an estimate of cloud-top pressure. Hanel [1961] first proposed that the 2-μm

CO_2 band could be used for this purpose but in response to that paper Yamamoto [1962] suggested that the 0.76-μm O_2 A-band would be a better choice since in this band, there is no overlap by absorption lines, particularly of H_2O, the absorption of solar radiation is greater than in the 2-μm CO_2, the cloud reflectively is greater than in the 2-μm CO_2, and better detectors are available for the O_2 A-band. They also commented that the clouds may not be regarded as simple diffuse reflectors and therefore the absorption along the scattering paths within the cloud would have to be considered. Chapman [1962] also responded to the paper by Hanel [1961] suggesting the O_2 A-band for similar reasons as that of Yamamoto [1962] and, added that in shorter wavelengths emission need not be accounted for and that O_2 amounts in the atmosphere are relatively constant compared to that of CO_2. He also pointed out that the A-band was narrow enough that an observation outside of the band in the continuum could be used to practically eliminate the wavelength dependence on the back scattering of clouds.

The use of the O_2 A-band for cloud-top pressure retrievals was explored in the 60's and 70's by several researchers with results that consistently overestimated the cloud-top pressure due the extension of photon path lengths from multiple scattering in the clouds for which various corrections were derived [Saiedy, 1967, Grechko et al., 1973, Grechko, 1978, Dianov-Klokov et al., 1970, Dianov-Klokov and Krasnokutskaya, 1972]. Wu [1985] went further and attempted to simultaneously retrieve cloud properties using multiple channels in the O_2 A-band in order to improve the cloud-top pressure estimation. Fischer and Grassl [1991] and Fischer and Cordes [1991] presented simulation studies that showed that by using high resolution spectra (1 nm) and by reducing the noise level of the instrument (1%) cloud-top pressure retrieval errors could be reduced to below 100 m. O'Brien and Mitchell [1992] presented a theoretical study accounting for photon path length within the cloud and included the effects of molecular and aerosol scattering above the cloud. They used a linear least squares method to retrieval the cloud-top pressure and associated errors were determined as a function of instrument and modeling errors. They claimed a 5 mb accuracy assuming a spectral resolution of 1 cm^{-1} and a measurement noise level of 1%.

The cloud-top pressure studies just discussed, although focusing on cloud-top pressure retrievals, contributed significantly to the study of photon path length distributions in an absorbing and scattering atmosphere setting a precedent for the use of O_2 A-band measurements to retrieval cloud and aerosol macrophysical and microphysical properties. The study of photon path lengths was

revisited by Pfeilsticker et al. [1998] and Pfeilsticker [1999] who presented a technique to determine the photon path lengths in atmospheres with various kinds of loading using ground-based O_2 A-band measurements. They compared real results to modeled results and computed the Lévy index. Their results for cloudy sky showed a good agreement between measurements and modeled radiances for weak absorption lines but systematically larger errors for strong absorption lines indicating that the plane-parallel assumption in the RT model becomes problematic in these cases.

Stephens and Heidinger [2000] presented a study of the sensitivity of hyperspectral measurements made in the O_2 A-band to cloud properties including optical thickness, the single scattering phase function, the top pressure, the pressure thickness, and the surface albedo. The sensitivities to these parameters were found to vary according to the column O_2 optical thickness and it was concluded that this variation in sensitivity offers a way of separating the dependence of the measurements to these parameters providing a basis for their retrieval. The variation in sensitivity and the degree of separation is dependent on the spectral resolution and more specifically the ability to resolve a sufficient range of O_2 optical thicknesses. The physical basis presented by Stephens and Heidinger [2000] was applied in a theoretical cloud retrieval study by Heidinger and Stephens [2000]. They showed that: (1) the optical thickness τ_c, cloud-top pressure, cloud layer pressure, and the surface albedo could be retrieved with an accuracy 5% for low clouds except when the cloud is optically thin or over a bright surface. (2) Retrieval for high clouds is possible if the asymmetry parameter is included as a retrieval parameter with an accuracy of 10% for τ_c when $\tau_c > 0.1$. (3) Vertical profiling is possible up to five layers as long as the spectral resolution of the measurements is better than 0.5 cm^{-1} with an accuracy of 2% or better. Heidinger and Stephens [2002] analyzed the effects of the spatial heterogeneity of clouds on retrievals using the measurements in the O_2 A-band. For a marine stratocumulus field the radiance errors were on the order of 3–20% which can be to large for the retrievals to be useful. A method was developed that predicts when the errors are so large that the retrieval results are invalid.

So far our discussion has focused on clouds but O_2 A-band aerosol retrieval studies have also been performed by various researchers. Gabella et al. [1999b] showed that through a Fredholm integral equation of the first kind, aerosol kernel functions can be used to relate the variations in the radiance measured by satellites to the variations in the aerosol extinction profile which permits profile retrieval from the measurements by inversion of a set of equations for various spectral intervals.

An example of this retrieval method using airborne O_2 A- and B-band spectrometer observations over the Mediterranean was presented by Gabella et al. [1999a]. Although good agreement was obtained between the measured radiance and the simulated radiances using the retrieved profile no other validation was performed. Min and Harrison [2004] developed a quasi linear retrieval to profile moderately thin atmospheres using high spectral resolution O_2 A-band measurements. The properties of the linear inversion, examined using singular value decomposition of the kernel function, demonstrate the impacts of instrument specifications, such as resolution, out-of-band rejection, and signal-to-noise ratio, on information content. A system with 0.5 cm^{-1} resolution, signal-to-noise ratio of 100:1, and an out-of-band floor of 10^{-3} has four independent pieces of information. Tests with synthetic data show that errors are less that 10% for the integrated total optical thickness. In the context of the GOSAT and the planned OCO-2 missions Frankenberg et al. [2012a] analyzed the aerosol information content of hyperspectral measurements in the O_2 A-band and the 1.61- and 2.06-μm CO_2 bands in both nadir only mode and target mode in which measurements at up to three view angles are obtained. Specifically, four cases were considered: nadir only using the O_2 A- and 1.61-μm CO_2 bands, multiangle using the O_2 A- and 1.61-μm CO_2 bands, nadir only using all three bands, and multiangle using all three bands. The retrieval parameters considered were the aerosol column loading, effective radius, effective variance, real and imaginary parts of the refractive index, center width, and center height. As expected, the addition of the 2.06 μm CO_2 band added information by increasing the measurements spectral range. It was also found that the degrees of freedom for signal for the multiangle measurements increased by 2–3 compared to the nadir only measurements.

Several researchers have explored the use of polarization measurements in the O_2 A-band as a further source of information. In the context of aerosol retrievals this is of particular importance since, as we have already discussed, measurements of polarization exhibit a relatively large sensitivity to aerosol microphysical parameters. Stam et al. [1999] presented a theoretical study in which they investigate the behavior of the degree of linear polarization P of radiation in the O_2 A-band emerging from the top and bottom of atmospheres with and without aerosols. They found that P varies with O_2 optical thickness and that this variation depends strongly on the type and vertical distribution of the aerosol particles in the atmosphere. As molecular absorption increases multiple scattering decreases and P consists more of singly scattered radiation and is therefore more sensitive

to microphysical parameters that effect the aerosols single scattering phase matrix. In addition, since aerosols tend to polarize radiation less than molecules P depends on the amount of molecular scattering above the aerosol layer and is therefore sensitive to the aerosol layer height. Boesche et al. [2008] analyzed the influence of aerosol altitude, optical thickness, and microphysics on the degree of linear polarization P of zenith radiation in the O_2 A-band. They found that P in the absorption lines is particularly sensitive to aerosol height and that this sensitivity depends on the aerosol optical thickness and microphysics and surface albedo. It is also shown that in the case of a single aerosol layer measurement of P may be used to obtain the aerosol layer height. Boesche et al. [2009] study both the intensity and degree of linear polarization of reflected solar radiation at TOA in the O_2 A-band as well as the 1.61 (weak) and 2.06 (strong) μm CO_2 bands. They found, similarly to Boesche et al. [2008] that P in the absorption lines is particularly sensitive to aerosol height in the O_2 A-band as well the strong CO_2 band. In the weak CO_2 band P is less sensitive to aerosol height due to the stronger influence of surface reflection and multiple scattering.

2.5 Summary

In this chapter we discussed several types of instruments used for aerosol retrievals and the different inversion algorithms used. Measurements vary in complexity with multispectral, multiangle, and/or polarimetric capability. As measurements become more complex more information about aerosols in the troposphere is available allowing more parameters to be retrieved. In addition, different types of measurements provide different ways to separate the aerosol signal from the surface signal, the biggest challenge in aerosol inversions. In particular, multiangle and/or polarimetric measurements provide ways to characterize the surface so that more aerosol information may be obtained from the measurements.

We also explored several techniques specific to the retrieval of aerosol absorption. In particular, the use of measurements in the UV which have a relatively low sensitivity to the surface but a high sensitivity to aerosol absorption. Unfortunately, retrievals based on UV measurements lack results ranging in the visible and near-infrared wavelengths, important for radiation studies, and also suffer from a relatively high sensitivity to aerosol vertical distribution. Other methods for absorption retrievals were discussed, including the use of sunglint observations to improve aerosol signal and the

use of critical reflectance to retrieval SSA over bright desert surfaces by using coincident observations with different aerosol loadings. Unfortunately, these methods are limited to specific cases (sunglint observations or observations over desert surfaces) and do not provide a long term solution for climate change studies.

Finally, we discussed the evolution of observations in molecular absorption bands of solar wavelengths, in particular the O_2 A-band, for the remote sensing of atmospheric particles. The use of these kinds of measurements began with an interest in determining cloud-top height, but through studies of photon path length distributions, interest in retrieving other cloud parameters began to grow, especially with the availability of high spectral resolution measurements. The important study by Stephens and Heidinger [2000] showed that the sensitivities of high spectral resolution measurements to cloud parameters were found to vary according to the column O_2 optical thickness and it was concluded that this variation in sensitivity offers a way of separating the dependence of the measurements to these parameters providing a basis for their retrieval. Interest in the use of O_2 A-band measurements for retrieving aerosol profiles and microphysical properties also developed, in particular with the development of the GOSAT TANSO-FTS and OCO-2 spectrometers. Finally, the use of hyperspectral measurements of polarization for aerosol retrievals was discussed.

Chapter 3

Scalar radiative transfer paper[1]

3.1 Introduction

Satellites provide a unique opportunity to infer physical and chemical processes within the atmosphere and at the surface at a global scale. In particular, passive remote sensing uses measured radiances to retrieve atmospheric or surface variables by applying state estimation techniques to the radiative transfer equation (RTE). These methods require a radiative transfer model that accurately simulates radiances corresponding to a particular atmospheric and surface state. In addition, atmospheric retrieval schemes using multispectral, multiangle and/or hyperspectral measurements may require hundreds or even thousands of radiative transfer simulations for a single retrieval. This could pose computational difficulties, especially when processing data in real-time applications. To address this problem we present an accurate method for solving the RTE for multiple scattering, absorption, and/or emission in a multi-layer plane-parallel atmosphere that is particularly efficient for optically thin atmospheres containing containing gases, aerosols, and/or cirrus clouds.

The literature abounds with ways of solving the RTE [Lenoble, 1985]. In some of the most widely used methods for remote sensing applications the integro-differential equation of radiative transfer is angularly discretized by a quadrature scheme and expressed in matrix form as a set of coupled linear ordinary differential equations (ODEs). Formulated as an initial value problem the general solution involves the operator $e^{\mathbf{A}x}$, known as the fundamental solution, the transfer matrix solution, or the propagator, where the matrix $\mathbf{A}$ describes the single scattering properties of a homogeneous medium and x is the medium thickness [Aronson, 1972, Waterman, 1981, Flatau and Stephens, 1988]. In most radiative transfer studies the primary problem of interest is the two-point boundary value problem which can be related to the initial value problem through the interaction principle in terms of reflection and transmission matrices as in matrix operator methods based on

[1] Paper published: "Efficient Computation of Radiances for Optically Thin Media by Padé Approximants" [**?**]

doubling [Grant and Hunt, 1969, Plass et al., 1973, de Haan et al., 1987] or eigen decomposition [Nakajima and Tanaka, 1986, Voronovich et al., 2004, Spurr and Christi, 2007].

The method we propose in this paper is a matrix operator method that uses the Padé approximation to a matrix exponential [Ward, 1977, Arioli et al., 1996] to evaluate $e^{\mathbf{A}x}$. As a result, we shall call our method the "Padé approximation radiative transfer method" (PARTM). A review of the radiative transfer literature reveals several studies that use the Padé approximation to solve the radiative transfer problem. Cohen and Cureton [1971] used the Padé approximation to determine Chandrasekhar's classical X- and Y-functions for radiative transfer in finite atmospheres with isotropic scattering. Chandrasekhar's H-function, for the special case of semi-infinite atmospheres, was calculated with the Padé approximation by Saad et al. [1983] and Steinfelds et al. [1997]. Finally, El wakil et al. [1983], El Wakil et al. [1985], and Saad et al. [1988] used the Padé approximation to determine the diffuse reflection from a inhomogeneous isotropically scattering medium.

None of the above methods use the Padé approximation specifically for the exponential of a matrix. Aronson and Yarmush [1966] mention the use of the Taylor series to evaluate $e^{\mathbf{A}x}$ but due to poor convergence, suggest the use of diagonalization techniques instead. Waterman [1981] also mentions the Taylor series solution and suggests that it can be useful for optical depths less that unity. Flatau and Stephens [1988] discuss direct evaluation of $e^{\mathbf{A}\tau}$, including the use of the Padé approximation, but an actual implementation is not presented and no numerical results are given. Emde et al. [2004] mention the use of the Padé approximation in a polarized discrete ordinate scattering model for microwave measurements but their use is limited to finding the exponential of an extinction matrix in the case of arbitrarily oriented nonspherical particles. Doicu et al. [2005] used the Padé approximation for the exponential of a matrix in a Galerkin method to derive the cell equation for two-dimensional radiative transfer. More recently, Doicu and Trautmann [2009] show the use of both eigen decomposition and a first order Padé approximation to compute the exponential of a matrix in a technique that solves for the radiances as a system of equations similar to the classical discrete ordinate technique [Liou, 1973, Stamnes et al., 1988b, Siewert, 2000]. They show that the eigen problem may be halved in order but do not show that similarly, the evaluation of the Padé approximation may be halved in order.

In this paper we present a complete solution of the RTE based on the Padé approximation along with a performance evaluation of the model and some numerical results for realistic atmospheric

scenarios. In section 4.2 a description of the radiative transfer formulation used in this paper is given beginning with the basic equations developed in section 4.2.1, followed by the matrix formulation and the general solution for the radiances in section 4.2.2. In section 3.2.3 simple similarity transformations are introduced that transform the radiative transfer matrix equations into equations with symmetric matrices allowing for increased computational efficiency. In section 3.2.4 we introduce the Padé approximation for the exponential of a matrix and the "scaling and squaring" technique for reducing the error of the Padé approximation. In section 3.2.5 introduce a matrix transformation that allows the Padé approximation of $\mathbf{A}x$ to be halved in order and use the result to solve for global reflection and transmission operators. In addition, we introduce "scaling and doubling" by linking the "scaling and squaring" technique to the doubling method for radiative transfer. The use of PARTM in multi-layered atmospheres with a lower surface boundary through the adding technique is discussed in section 3.2.6. In section 3.2.7 some details and features of our implementation of PARTM are discussed. A performance evaluation, including accuracy and timing, of PARTM relative to the DISORT model [Stamnes et al., 1988b] is presented in section 3.3 while example results from two realistic applications will be presented in section 4.5. Finally, some concluding remarks are given in section 3.5.

An implementation of PARTM is available as one of several radiative transfer methods within the X Radiative Transfer Model (XRTM) software. XRTM is licensed under the GNU General Public License Version 3 and is available at `http://reef.atmos.colostate.edu/~gregm/xrtm`.

3.2 Radiative transfer formulation

3.2.1 Basic equations

The equation [Chandrasekhar, 1960] describing the transfer of monochromatic radiation through a single plane-parallel homogeneous layer is given as

$$\mu \frac{dI(\tau;\mu,\phi)}{d\tau} = I(\tau;\mu,\phi) - \frac{\omega}{4\pi}\int_0^{2\pi}\int_{-1}^{1} P(\mu,\phi,\mu',\phi')I(\tau;\mu',\phi')d\mu' d\phi' - \Sigma(\tau;\mu,\phi), \tag{3.1}$$

where $I(\tau;\mu,\phi)$ is the radiance at optical depth τ along the direction specified by the cosine of the polar angle μ and the azimuthal angle ϕ, $P(\mu,\phi,\mu',\phi')$ is the scattering phase function for radiation

from the direction (μ', ϕ') scattered into the direction (μ, ϕ), and ω is the albedo of single scattering. The third term on right hand side of equation 3.1 represents the source function given by

$$\Sigma(\tau; \mu, \phi) = \frac{\omega}{4\pi} F_0 P(\mu, \phi, -\mu_0, \phi_0) e^{-\tau/\mu_0} + (1 - \omega) B(T). \tag{3.2}$$

The first term on the right hand side of equation 3.2 represents the solar source, where F_0 is the top of atmosphere (TOA) incident solar flux and μ_0 and ϕ_0 are the solar zenith and azimuth angles, respectively. The second term on the right hand side of equation 3.2 is the thermal emission, where B is the Planck black body function with the single argument of layer temperature T.

By expanding the phase function in terms of $2n$ Legendre polynomials and using the addition theorem of spherical harmonics the phase function can be further developed as a Fourier cosine series in the relative azimuth $\phi - \phi'$ separating the dependencies of the phase function on μ and μ' from that on ϕ and ϕ'. The Fourier expansion of $I(\tau; \mu, \phi)$ follows from this and is written as

$$I(\tau; \mu, \phi) = \sum_{m=0}^{2n-1} I^m(\tau; \mu) \cos\left[m(\phi - \phi_0)\right], \tag{3.3}$$

where the individual azimuthal components of the transfer equation, indicated by a superscript m are given by

$$\mu \frac{dI^m(\tau; \mu)}{d\tau} = I^m(\tau; \mu) - (1 + \delta_{0,m}) \frac{\omega}{4\pi} \int_{-1}^{1} P^m(\mu, \mu') I^m(\tau; \mu') d\mu' - \Sigma^m(\tau; \mu), \tag{3.4}$$

where

$$\Sigma^m(\tau; \mu) = \frac{\omega}{4\pi} F_0 P^m(\mu, -\mu_0) e^{-\tau/\mu_0} + \delta_{0,m}(1 - \omega) B(T), \tag{3.5}$$

$$P^m(\mu, \mu') = (2 - \delta_{0,m}) \sum_{l=m}^{2n-1} \beta_l Y_l^m(\mu) Y_l^m(\mu'), \tag{3.6}$$

and $Y_l^m(\mu)$ is the re-normalized associated Legendre polynomial of order m and degree l, β_l is the Legendre expansion coefficient for degree l, and δ is the Kronecker delta.

To simplify notation, hereafter the superscript m will be suppressed with the dependence on azimuth mode assumed.

3.2.2 Matrix formulation

The integral in equation 3.4 can be replaced by a quadrature scheme in which n quadrature points μ_i and associated weights w_i are defined for the downward and upward hemispheres separately. As a result, equation 3.4 can be expressed in matrix form as

$$\pm \frac{d\mathbf{I}^{\pm}}{d\tau} = \mathbf{M}^{-1}\mathbf{I}^{\pm} - (1+\delta_{0,m})\frac{\omega}{4}(\mathbf{M}^{-1}\mathbf{P}^{\pm}\mathbf{W}\mathbf{I}^{+} + \mathbf{M}^{-1}\mathbf{P}^{\mp}\mathbf{W}\mathbf{I}^{-}) - \mathbf{\Sigma}^{\pm}, \tag{3.7}$$

where a '+' sign indicates upward values (positive values of μ) and a '−' sign indicates downward values (negative values of μ), $\mathbf{I}$ is the radiance vector, $\mathbf{M}$ is a diagonal matrix of quadrature points defined by $M_{ij} = \delta_{ij}\mu_i$, $\mathbf{W}$ is a diagonal matrix of quadrature weights defined by $W_{ij} = \delta_{ij}w_i$, and $\mathbf{P}$ is the phase function matrix defined as $\mathbf{P}^{\pm}_{ij} = P(\pm\mu_i, \mu_j)$. The the source vector $\mathbf{\Sigma}$ is written as

$$\mathbf{\Sigma}^{\pm} = \frac{\omega}{4\pi}F_0\mathbf{M}^{-1}\mathbf{P}^{\pm}_0 e^{-\tau/\mu_0} + (1-\omega)B(T)\mathbf{M}^{-1}\mathbf{U}, \tag{3.8}$$

where $\mathbf{P}_0$ is the phase function vector for single scattering of the direct beam defined as $\mathbf{P}^{\pm}_{i,0} = P(\pm\mu_i, -\mu_0)$ and $\mathbf{U}$ is a column vector with the elements equal to $\delta_{0,m}$. At this point it is convenient to introduce the *local* reflectance and transmittance matrices given as

$$\mathbf{r} = -(1+\delta_{0,m})\frac{\omega}{4}\mathbf{M}^{-1}\mathbf{P}^{-}\mathbf{W} \tag{3.9}$$

and

$$\mathbf{t} = -\mathbf{M}^{-1} + (1+\delta_{0,m})\frac{\omega}{4}\mathbf{M}^{-1}\mathbf{P}^{+}\mathbf{W}, \tag{3.10}$$

respectively, with which equation 3.7 can be written in an expanded matrix form as

$$\frac{d}{d\tau}\begin{bmatrix}\mathbf{I}^{-}\\ \mathbf{I}^{+}\end{bmatrix} = \begin{bmatrix}\mathbf{t} & -\mathbf{r}\\ \mathbf{r} & -\mathbf{t}\end{bmatrix}\begin{bmatrix}\mathbf{I}^{-}\\ \mathbf{I}^{+}\end{bmatrix} + \begin{bmatrix}\mathbf{\Sigma}^{-}\\ \mathbf{\Sigma}^{+}\end{bmatrix}. \tag{3.11}$$

Equation 3.11 constitutes a system of $2n$ coupled linear first-order differential equations for the initial value problem for which the general solution for a homogeneous layer of optical thickness τ is

$$\begin{bmatrix} \mathbf{I}^-(\tau) \\ \mathbf{I}^+(\tau) \end{bmatrix} = e^{\mathbf{A}\tau} \begin{bmatrix} \mathbf{I}^-(0) \\ \mathbf{I}^+(0) \end{bmatrix} + \int_0^\tau e^{\mathbf{A}(\tau - x)} \begin{bmatrix} \mathbf{\Sigma}^- \\ \mathbf{\Sigma}^+ \end{bmatrix} dx, \tag{3.12}$$

where the matrix exponential is the integrating factor, known as the fundamental solution, and the attenuation matrix $\mathbf{A}$ is given by

$$\mathbf{A} = \begin{bmatrix} \mathbf{t} & -\mathbf{r} \\ \mathbf{r} & -\mathbf{t} \end{bmatrix}. \tag{3.13}$$

The first term on the right hand side of equation 3.12 represents the homogeneous solution while the second term represents the particular solution.

If we consider the interaction principle, the upward radiance at the top of the layer $\mathbf{I}^+(0)$ and the downward radiance at the bottom of the layer $\mathbf{I}^-(\tau)$ can be written as the solution of the two-point boundary value problem with

$$\mathbf{I}^+(0) = \mathbf{T}\mathbf{I}^+(\tau) + \mathbf{R}\mathbf{I}^-(0) + \mathbf{S}^+, \tag{3.14}$$

$$\mathbf{I}^-(\tau) = \mathbf{R}\mathbf{I}^+(\tau) + \mathbf{T}\mathbf{I}^-(0) + \mathbf{S}^-, \tag{3.15}$$

where $\mathbf{I}^-(0)$ and $\mathbf{I}^+(\tau)$ are the boundary conditions at the top and bottom of the layer, $\mathbf{R}$ and $\mathbf{T}$ are the *global* reflection and transmission matrices, and the particular solution source vectors are

$$\mathbf{S}^+ = -\mathbf{R}\mathbf{F}^- - \mathbf{T}\mathbf{F}^+\mathcal{T} + \mathbf{F}^+, \tag{3.16}$$

$$\mathbf{S}^- = -\mathbf{T}\mathbf{F}^- - \mathbf{R}\mathbf{F}^+\mathcal{T} + \mathbf{F}^-\mathcal{T}, \tag{3.17}$$

with $\mathcal{T}$ as the layer transmittance $e^{-\tau/\mu_0}$. Now by ignoring the particular solution and using equations 3.14 and 3.15 to solve for $\mathbf{I}^+(\tau)$ and $\mathbf{I}^-(\tau)$ in terms of $\mathbf{I}^+(0)$ and $\mathbf{I}^-(0)$ we get

$$\begin{bmatrix} \mathbf{I}^-(\tau) \\ \mathbf{I}^+(\tau) \end{bmatrix} = \begin{bmatrix} \mathbf{T} - \mathbf{R}\mathbf{T}^{-1}\mathbf{R} & \mathbf{R}\mathbf{T}^{-1} \\ -\mathbf{T}^{-1}\mathbf{R} & \mathbf{T}^{-1} \end{bmatrix} \begin{bmatrix} \mathbf{I}^-(0) \\ \mathbf{I}^+(0) \end{bmatrix}. \tag{3.18}$$

By comparing equation 3.18 to the homogeneous part of equation 3.12 it is apparent that the matrix exponential is identified as

$$e^{\mathbf{A}\tau} = \begin{bmatrix} \mathbf{T} - \mathbf{R}\mathbf{T}^{-1}\mathbf{R} & \mathbf{R}\mathbf{T}^{-1} \\ -\mathbf{T}^{-1}\mathbf{R} & \mathbf{T}^{-1} \end{bmatrix}, \tag{3.19}$$

from which the global reflection and transmission matrices $\mathbf{R}$ and $\mathbf{T}$ can be computed. The use of the Padé approximation to evaluate the matrices $\mathbf{R}$ and $\mathbf{T}$ is the primary subject of this paper; this will be covered in detail in sections 3.2.4 and 3.2.5. The evaluation of the source vectors $\mathbf{F}^{\pm}$ requires the solution to a linear system of order $2n$ for which a reduction to order n is possible. This is discussed in detail in Siewert [2000] and will not be addressed further here.

3.2.3 Symmetrical matrix formulation

In this section we demonstrate how the matrices $\mathbf{r}$ and $\mathbf{t}$ can be transformed into symmetric forms allowing for a more efficient evaluation of the RTE. Several authors have also used this symmetry to reduce the eigen decomposition of $\mathbf{A}$ from a general to symmetric problem [Nakajima and Tanaka, 1986, Stamnes et al., 1988a, Voronovich et al., 2004]. Waterman [1981] used this symmetry to reduce the computation required to compute powers of $\mathbf{A}\tau$ as we will also do for our model. In addition, we will also use this symmetry to reduce the computation for matrix multiplications in the evaluation of $\mathbf{R}$ and $\mathbf{T}$.

From the principle of reciprocity [Chandrasekhar, 1960] we know that the phase matrices $\mathbf{P}^{+}$ and $\mathbf{P}^{-}$, introduced in equation 3.7 and that define $\mathbf{r}$ and $\mathbf{t}$, are symmetric. As a result, a diagonal matrix $\boldsymbol{\alpha}$ can be introduced as

$$\boldsymbol{\alpha} = \sqrt{\mathbf{W}\mathbf{M}}, \tag{3.20}$$

permitting symmetric forms of $\mathbf{r}$ and $\mathbf{t}$ to be written as

$$\mathbf{r}' = \boldsymbol{\alpha}\mathbf{r}\boldsymbol{\alpha}^{-1} \tag{3.21}$$

and

$$\mathbf{t}' = \boldsymbol{\alpha}\mathbf{t}\boldsymbol{\alpha}^{-1}, \tag{3.22}$$

respectively. From $\mathbf{r}'$ and $\mathbf{t}'$ a modified form of equation 3.13 can be written as

$$\mathbf{A}' = \begin{bmatrix} \boldsymbol{\alpha} & 0 \\ 0 & \boldsymbol{\alpha} \end{bmatrix} \mathbf{A} \begin{bmatrix} \boldsymbol{\alpha}^{-1} & 0 \\ 0 & \boldsymbol{\alpha}^{-1} \end{bmatrix} = \begin{bmatrix} \mathbf{t}' & -\mathbf{r}' \\ \mathbf{r}' & -\mathbf{t}' \end{bmatrix}, \tag{3.23}$$

from which it follows that a modified form of equation 3.19 is given by

$$e^{\mathbf{A}'\tau} = \begin{bmatrix} \mathbf{T}' - \mathbf{R}'\mathbf{T}'^{-1}\mathbf{R}' & \mathbf{R}'\mathbf{T}'^{-1} \\ -\mathbf{T}'^{-1}\mathbf{R}' & \mathbf{T}'^{-1} \end{bmatrix}. \tag{3.24}$$

After solving for the symmetric matrices $\mathbf{R}'$ and $\mathbf{T}'$ the original nonsymmetric matrices $\mathbf{R}$ and $\mathbf{T}$ can be recovered by inverting the similarity transformation provided by α with

$$\mathbf{R} = \boldsymbol{\alpha}^{-1}\mathbf{R}'\boldsymbol{\alpha} \tag{3.25}$$

and

$$\mathbf{T} = \boldsymbol{\alpha}^{-1}\mathbf{T}'\boldsymbol{\alpha}. \tag{3.26}$$

In section 3.2.5 we will demonstrate how the computation of $\mathbf{R}$ and $\mathbf{T}$ benefits from the symmetry just presented.

3.2.4 The exponential of a matrix

Several techniques exist for the computation of the exponential of a matrix [Moler and Loan, 1978]. One of the most commonly used methods is the Padé approximation which has become the standard method for evaluating the exponential of a matrix in mathematical software packages such as MATLAB [Moler and Loan, 2003]. The accuracy of the Padé approximation to the matrix exponential $e^{\mathbf{X}}$ is limited by $\|\mathbf{X}\|$, where $\|\cdot\|$ represents any subordinate matrix norm. As a result, one or more techniques are usually used to decrease the norm of $\mathbf{X}$. In the next two sections we will present the details of the Padé approximation followed by some common techniques for reducing $\|\mathbf{X}\|$.

The Padé approximation

The Padé approximation to the exponential of a matrix $\mathbf{X}$ [Ward, 1977, Moler and Loan, 1978] is a rational function approximation defined as

$$e^{\mathbf{X}} \approx \mathbf{R}_{pq}(\mathbf{X}) = \left[\mathbf{D}_{pq}^{-1}(\mathbf{X})\right] \mathbf{N}_{pq}(\mathbf{X}), \tag{3.27}$$

where the $\mathbf{N}_{pq}(\mathbf{X})$ and $\mathbf{D}_{pq}(\mathbf{X})$ are polynomials in $\mathbf{X}$ of degree p and q, respectively, given by

$$\mathbf{N}_{pq}(\mathbf{X}) = \sum_{i=0}^{p} \frac{(p+q-i)!p!}{(p+q)!i!(p-i)!}(\mathbf{X})^i = \sum_{i=0}^{p} a_i(\mathbf{X})^i \tag{3.28}$$

and

$$\mathbf{D}_{pq}(\mathbf{X}) = \sum_{i=0}^{q} \frac{(p+q-i)!q!}{(p+q)!i!(q-i)!}(-1)^i(\mathbf{X})^i = \sum_{i=0}^{q} b_i(-1)^i(\mathbf{X})^i. \tag{3.29}$$

It is preferable to use diagonal approximations ($p = q$) rather than off diagonal approximations ($p \neq q$) for two reasons [Moler and Loan, 1978]. First, suppose that $p \neq q$ and $i = \max(p, q)$, then $\mathbf{R}_{ii}(\mathbf{X})$ will be a more accurate approximation than $\mathbf{R}_{pq}(\mathbf{X})$ and since the powers of $\mathbf{X}$ are shared between the calculations of both $\mathbf{N}_{pq}(\mathbf{X})$ and $\mathbf{D}_{pq}(\mathbf{X})$, $\mathbf{R}_{ii}(\mathbf{X})$ can be obtained with the same number of matrix multiplications as $\mathbf{R}_{pq}(\mathbf{X})$. Second, compared to approximations with $p = q$, approximations with $p > q$ tend to have larger rounding errors due to cancellation while approximations with $p < q$ tend to have larger rounding errors due to an ill conditioned denominator $\mathbf{D}_{pq}(\mathbf{X})$. With this in mind, hereafter we will just use the subscript r instead of the subscripts pq to refer to the degree of Padé approximation. In addition, only one set of coefficients c_i will be required, where $a_i = b_i = c_i$. These coefficients may be calculated with the recurrence relation

$$c_i = c_{i-1}\frac{r-i-1}{(2r-i-1)i}, \tag{3.30}$$

starting with $c_0 = 1$.

By noting that $\mathbf{D}_r(\mathbf{X}) = \mathbf{N}_r(-\mathbf{X})$ an efficient scheme for evaluating $\mathbf{N}_r(\mathbf{X})$ and $\mathbf{D}_r(\mathbf{X})$ can be devised that uses only even powers of $\mathbf{X}$ [Higham, 1984]. For approximations of even degrees ($r = 2m$)

$$\mathbf{N}_{2m}(\mathbf{X}) = \mathbf{U}_{2m}(\mathbf{X}) + \mathbf{V}_{2m}(\mathbf{X}) \tag{3.31}$$

and

$$\mathbf{D}_{2m}(\mathbf{X}) = \mathbf{U}_{2m}(\mathbf{X}) - \mathbf{V}_{2m}(\mathbf{X}), \tag{3.32}$$

where

$$\mathbf{U}_{2m}(\mathbf{X}) = c_{2m}\mathbf{X}^{2m} + \cdots + c_2\mathbf{X}^2 + c_0\mathbf{E} \tag{3.33}$$

and

$$\mathbf{V}_{2m}(\mathbf{X}) = \mathbf{X}(c_{2m-1}\mathbf{X}^{2m-2} + \cdots + c_3\mathbf{X}^2 + c_1\mathbf{E}). \tag{3.34}$$

Approximations with odd degrees ($r = 2m + 1$) can be obtained in a similar way with

$$\mathbf{N}_{2m+1}(\mathbf{X}) = \mathbf{U}_{2m+1}(\mathbf{X}) + \mathbf{V}_{2m+1}(\mathbf{X}) \tag{3.35}$$

and

$$\mathbf{D}_{2m+1}(\mathbf{X}) = \mathbf{U}_{2m+1}(\mathbf{X}) - \mathbf{V}_{2m+1}(\mathbf{X}), \tag{3.36}$$

where

$$\mathbf{U}_{2m+1}(\mathbf{X}) = \mathbf{X}(c_{2m+1}\mathbf{X}^{2m} + \cdots + c_3\mathbf{X}^2 + c_1\mathbf{E}) \tag{3.37}$$

and

$$\mathbf{V}_{2m+1}(\mathbf{X}) = c_{2m}\mathbf{X}^{2m} + \cdots + c_2\mathbf{X}^2 + c_0\mathbf{E}. \tag{3.38}$$

From these equations it can be seen that evaluation of $\mathbf{N}_{2m+1}(\mathbf{X})$ and $\mathbf{D}_{2m+1}(\mathbf{X})$ can be performed at that same computational cost as that of $\mathbf{N}_{2m}(\mathbf{X})$ and $\mathbf{D}_{2m}(\mathbf{X})$. As noted by Higham [1984], these formulas can be improved when $r \geq 12$ by using modified forms of Horner's rule for even powers. For example, $\mathbf{N}_{13}(\mathbf{X})$ and $\mathbf{D}_{13}(\mathbf{X})$ can be obtained with only six matrix multiplications with

$$\mathbf{U}_{13} = \mathbf{X}^6(c_{12}\mathbf{X}^6 + c_{10}\mathbf{X}^4 + c_8\mathbf{X}^2 + c_6\mathbf{E}) + c_4\mathbf{X}^4 + c_2\mathbf{X}^2 + c_0\mathbf{E} \tag{3.39}$$

and

$$\mathbf{V}_{13} = \mathbf{X}\left[\mathbf{X}^6(c_{13}\mathbf{X}^6 + c_{11}\mathbf{X}^4 + c_9\mathbf{X}^2 + c_7\mathbf{E}) + c_5\mathbf{X}^4 + c_3\mathbf{X}^2 + c_1\mathbf{E}\right]. \tag{3.40}$$

Table 3.1: Number of matrix multiplications π_r required to calculate $\mathbf{N}_r(\mathbf{X})$ and $\mathbf{D}_r(\mathbf{X})$ as a function of the matrix polynomial order r.

r	1	2	3	4	5	6	7	8	9	10	
π_r	0	1	2	3	3	4	4	5	5	6	

r	11	12	13	14	15	16	17	18	19	20	21
π_r	6	6	6	7	7	7	7	8	8	8	8

Table 3.1 gives the number of matrix multiplications π_r required to calculate $\mathbf{N}_r(\mathbf{X})$ and $\mathbf{D}_r(\mathbf{X})$ for each degree up to 21. It is apparent that many values of r are not optimal. For example, one would not want to use $r = 4$ as $r = 5$ can be achieved at the same cost.

In sections 3.2.5 and 3.2.5 we will discuss the application of the Padé approximation to the radiative transfer formulation introduced in section 4.2.2 including how the structure of the $\mathbf{A}$ matrix allows powers of $\mathbf{A}$ to be calculated with increased efficiency.

Reducing the norm of X

The accuracy of the Padé approximation increases with the degree r but decreases with the matrix norm $\|\mathbf{X}\|$. Many of the methods in the literature involve one or more steps to reduce the norm of the matrix before evaluating the Padé approximation of the matrix exponential. For example, the method of Ward [1977], one of the most widely used, involves a three step process to reduce the matrix norm. The first step minimizes, by approximation, the matrix norm over all possible translations by subtracting the mean of the eigenvalues from the diagonal elements of the matrix. The second step attempts to minimize the norm of over all possible diagonal similarity transformations by using a method described by Parlett and Reinsch [1969]. Finally, by exploiting the matrix property given by

$$e^{\mathbf{X}} = (e^{\mathbf{X}/2^s})^{2^s}, \tag{3.41}$$

the third step, referred to as "scaling and squaring", reduces the norm of $\mathbf{X}$ by scaling it by the factor 2^{-s} resulting in a new matrix given by

$$\mathbf{X}' = \mathbf{X}/2^s. \tag{3.42}$$

With this, $e^{\mathbf{X}}$ can be evaluated by repeated squaring of the exponential of $e^{\mathbf{X}'}$:

$$e^{\mathbf{X}} = (e^{\mathbf{X}'})^{2^s}, \tag{3.43}$$

where $e^{\mathbf{X}'}$ is evaluated using the Padé approximation. The exponent s is typically chosen so that $\|\mathbf{X}\|$ is less than some prescribed threshold value although methods may vary as computational efficiency depends on an optimal combination of both r and s [Higham, 1984].

It turns out that due to the special structure of the $\mathbf{A}$ matrix the first two steps discussed above do not effect the norm of $\mathbf{A}$. In section 3.2.5 we will discuss the application of the third step, "scaling and squaring", to our radiative transfer method and we will show that in fact "scaling and squaring" is analogous to the doubling method for radiative transfer.

3.2.5 Radiative transfer using the Padé approximation

In this section we apply the Padé approximation to the radiative transfer formulation introduced in section 4.2.2 to solve for the global reflection and transmission operators $\mathbf{R}$ and $\mathbf{T}$. But rather than using the Padé approximation for the fundamental solution matrix $e^{\mathbf{A}\tau}$ the operators $\mathbf{R}$ and $\mathbf{T}$ are taken directly from the matrix functions that comprise the Padé approximation. It will also be shown that a significant computational advantage is achieved by the using the symmetry introduced in section 3.2.3 and the block symmetry within the $\mathbf{A}$ matrix. In addition, we will link the "scaling and squaring" technique to the doubling method and show that the symmetric radiative transfer formulation provides additional computational savings in the doubling method as well.

A word on operation counting

As a prerequisite to the descriptions that follow, it is helpful to describe briefly how operations are counted and the definition of a floating point operation (flop), as used in this paper. As is common for matrix algebra applications, we will only count operations of order n^3 and ignore lower order operations which have a negligible contribution for larger n. Operation counts will be given in flops which will represent the operation $ab + c$ (one scalar multiplication and one scalar addition), which is the primary operation within the inner loops of the n^3 matrix operations of interest. These operations are listed in table 3.2 along their flop count and operators that will only

Table 3.2: Approximate number of flops and the associated operator for relevant matrix operations. (Operation counts are from Golub and Van Loan [1996].)

matrix operation	flops	operator
general matrix multiplication	n^3	$\times$
symmetric matrix multiplication	$n^3/2$	$\otimes$
LU-decomposition with substitution	$n^3/3 + n^3$	$LU()$

be used when it is necessary to distinguish between different matrix multiplications. Of the three operations listed in table 3.2 two require more explanation. "Symmetric matrix multiplication" is when matrix multiplication results in a symmetric matrix so that only the elements above or below the main diagonal need to be calculated with the remaining elements following from symmetry. LU-decomposition with substitution represents the solution to a linear system of equations using LU-decomposition and forward and backward substitution, where the operator takes two arguments so that $LU(\mathbf{A}^{-1}, \mathbf{B}) = \mathbf{A}^{-1}\mathbf{B} = \mathbf{X}$ and $LU(\mathbf{B}, \mathbf{A}^{-1}) = \mathbf{B}\mathbf{A}^{-1} = \mathbf{X}$.

Evaluation of N and D

In this section we discuss the evaluation of the numerator $\mathbf{N}_r(\mathbf{X})$ and denominator $\mathbf{D}_r(\mathbf{X})$ of the Padé approximation, discussed in section 3.2.4, as applied to our radiative transfer formulation introduced in section 4.2.2. Specifically, we are interested in $\mathbf{N}_r(\mathbf{A}'\tau)$ and $\mathbf{D}_r(\mathbf{A}'\tau)$, the evaluation of which starts with calculating powers of $\mathbf{A}'\tau$. It turns out that by taking advantage of the symmetries within $\mathbf{A}'\tau$ the computational complexity of computing powers of $\mathbf{A}'\tau$ can be reduced by a factor of eight.

As described by Aronson and Yarmush [1966] and Waterman [1981], we introduce a similarity transform on $\mathbf{A}'\tau$ as

$$\mathbf{A}''\tau = \boldsymbol{\beta}^{-1}\mathbf{A}'\tau\boldsymbol{\beta}, \tag{3.44}$$

where

$$\boldsymbol{\beta} = \begin{bmatrix} \mathbf{E} & \mathbf{E} \\ \mathbf{E} & -\mathbf{E} \end{bmatrix} \quad \text{and} \quad \boldsymbol{\beta}^{-1} = \frac{1}{2}\begin{bmatrix} \mathbf{E} & \mathbf{E} \\ \mathbf{E} & -\mathbf{E} \end{bmatrix}. \tag{3.45}$$

Evaluation of equation 3.44 leads to $\mathbf{A}''\tau$ with the form

$$\mathbf{A}''\tau = \begin{bmatrix} 0 & \mathbf{x} \\ \mathbf{y} & 0 \end{bmatrix}, \tag{3.46}$$

where $\mathbf{x} = (\mathbf{t}' + \mathbf{r}')\tau$ and $\mathbf{y} = (\mathbf{t}' - \mathbf{r}')\tau$. This transformation is analogous to reducing the order of the eigenvalue problem in the discrete ordinate method for radiative transfer [Stamnes and Swanson, 1981]. At this point we are interested in calculating $\mathbf{N}_r(\mathbf{A}''\tau)$ and $\mathbf{D}_r(\mathbf{A}''\tau)$ for which we need powers of $\mathbf{A}''\tau$. Even powers of $\mathbf{A}''\tau$ are given by

$$(\mathbf{A}''\tau)^{2i} = \begin{bmatrix} (\mathbf{xy})^i & 0 \\ 0 & (\mathbf{yx})^i \end{bmatrix} \tag{3.47}$$

while odd powers are given by

$$(\mathbf{A}''\tau)^{2i+1} = \begin{bmatrix} 0 & \mathbf{x}(\mathbf{yx})^i \\ \mathbf{y}(\mathbf{xy})^i & 0 \end{bmatrix}. \tag{3.48}$$

We then substitute the even powers of $\mathbf{A}''\tau$, calculated with equation 3.47, for powers of $\mathbf{X}$ into the equations 3.31 and 3.32 or 3.35 and 3.36, depending on whether the degree of Padé approximation is even or odd. In addition, we note that the outer multiplication in $\mathbf{V}_{2m}(\mathbf{A}''\tau)$ and $\mathbf{U}_{2m+1}(\mathbf{A}''\tau)$ (equations 3.34 and 3.37) will have the same form as equation 3.48 as it results in odd powers of $\mathbf{A}''\tau$. Finally $\mathbf{N}_r(\mathbf{A}'\tau)$ and $\mathbf{D}_r(\mathbf{A}'\tau)$ may be recovered from $\mathbf{N}_r(\mathbf{A}''\tau)$ and $\mathbf{D}_r(\mathbf{A}''\tau)$ by inverting the similarity transformation provided by β as

$$\mathbf{N}_r(\mathbf{A}'\tau) = \boldsymbol{\beta}\mathbf{N}_r(\mathbf{A}''\tau)\boldsymbol{\beta}^{-1} \tag{3.49}$$

and

$$\mathbf{D}_r(\mathbf{A}'\tau) = \boldsymbol{\beta}\mathbf{D}_r(\mathbf{A}''\tau)\boldsymbol{\beta}^{-1}, \tag{3.50}$$

respectively. As with the forward transformation 3.44, due to the simple form of β, the inverse transformations 3.49 and 3.50 may be evaluated to eliminate the matrix multiplications and expressed

as

$$\mathbf{N}' = \frac{1}{2}\begin{bmatrix} \mathbf{N}''_{11} + \mathbf{N}''_{21} + \mathbf{N}''_{12} + \mathbf{N}''_{22} & \mathbf{N}''_{11} + \mathbf{N}''_{21} - \mathbf{N}''_{12} - \mathbf{N}''_{22} \\ \mathbf{N}''_{11} - \mathbf{N}''_{21} + \mathbf{N}''_{12} - \mathbf{N}''_{22} & \mathbf{N}''_{11} - \mathbf{N}''_{21} - \mathbf{N}''_{12} + \mathbf{N}''_{22} \end{bmatrix} \tag{3.51}$$

and

$$\mathbf{D}' = \frac{1}{2}\begin{bmatrix} \mathbf{D}''_{11} + \mathbf{D}''_{21} + \mathbf{D}''_{12} + \mathbf{D}''_{22} & \mathbf{D}''_{11} + \mathbf{D}''_{21} - \mathbf{D}''_{12} - \mathbf{D}''_{22} \\ \mathbf{D}''_{11} - \mathbf{D}''_{21} + \mathbf{D}''_{12} - \mathbf{D}''_{22} & \mathbf{D}''_{11} - \mathbf{D}''_{21} - \mathbf{D}''_{12} + \mathbf{D}''_{22} \end{bmatrix}, \tag{3.52}$$

where we have dropped the subscript r and replaced the arguments $(\mathbf{A}'\tau)$ and $(\mathbf{A}''\tau)$ with a $'$ and $''$, respectively, to simplify notation and have expanded $\mathbf{N}$ and $\mathbf{D}$ to expose the individual $(n \times n)$ blocks defined by

$$\mathbf{N} = \begin{bmatrix} \mathbf{N}_{11} & \mathbf{N}_{12} \\ \mathbf{N}_{21} & \mathbf{N}_{22} \end{bmatrix} \quad \text{and} \quad \mathbf{D} = \begin{bmatrix} \mathbf{D}_{11} & \mathbf{D}_{12} \\ \mathbf{D}_{21} & \mathbf{D}_{22} \end{bmatrix}, \tag{3.53}$$

respectively.

Since the $n \times n$ blocks of $\mathbf{A}''$ are symmetric, the diagonal blocks of $(\mathbf{A}''\tau)^{2i}$ are equal by transposition, that is to say $(\mathbf{xy})^i = \left[(\mathbf{yx})^i\right]^T$ [Waterman, 1981]. The result is that each even power $(\mathbf{A}''\tau)^{2i}$ can be evaluated with only one $n \times n$ matrix multiplication (n^3 flops), a reduction by a factor of eight compared to that if $\mathbf{A}''\tau$ was a general matrix. In addition, as noted above, the outer multiplication in $\mathbf{V}_{2m}(\mathbf{A}''\tau)$ and $\mathbf{U}_{2m+1}(\mathbf{A}''\tau)$ (both $2n \times 2n$) has the same form as equation 3.48 and since $\mathbf{x}$ and $\mathbf{y}$ are symmetric, and therefore $\mathbf{x}(\mathbf{yx})^i$ and $\mathbf{y}(\mathbf{xy})^i$ are symmetric, $\mathbf{V}_{2m}(\mathbf{A}''\tau)$ or $\mathbf{U}_{2m+1}(\mathbf{A}''\tau)$ may be evaluated with two symmetric $n \times n$ matrix multiplications the equivalent of only one general $n \times n$ matrix multiplication (n^3 flops). Overall, this translates to $\pi_r n^3$ flops to evaluate $\mathbf{N}(\mathbf{A}'\tau)$ and $\mathbf{D}(\mathbf{A}'\tau)$ to degree r.

Due to the special structure of $\mathbf{A}'$, the matrices $\mathbf{N}'$ and $\mathbf{D}'$ take on the symmetry relations given by

$$\begin{aligned} \mathbf{N}'_{11} &= \mathbf{D}'_{22} \qquad \mathbf{N}'_{12} = \mathbf{D}'_{21} \\ \mathbf{N}'_{22} &= \mathbf{D}'_{11} \qquad \mathbf{N}'_{21} = \mathbf{D}'_{12}. \end{aligned} \tag{3.54}$$

This symmetry provides an additional benefit in that only $\mathbf{N}'$ or $\mathbf{D}'$ needs to be evaluated, reducing the computational burden and decreasing memory usage. For example, for an even degree Padé

approximation, if we decide to evaluate only $\mathbf{N}'$, only equations 3.31 and 3.51 need to be evaluated while equations 3.32 and 3.52 can be dropped. For odd degree Padé approximations, only equations 3.35 and 3.51 need to be evaluated while equations 3.36 and 3.52 can be dropped. Later when $\mathbf{N}'$ or $\mathbf{D}'$ are required to evaluate global $\mathbf{R}'$ and $\mathbf{T}'$ we can just replace the blocks of $\mathbf{D}'$ with the appropriate blocks of $\mathbf{N}'$.

Evaluation of R and T

By using the Padé approximation on $\mathbf{A}'\tau$ we can approximate the right hand side of equation 3.24 with the right hand side of equation 3.27 and express the result with the four $n \times n$ blocks exposed as

$$\begin{bmatrix} \mathbf{T}' - \mathbf{R}'\mathbf{T}'^{-1}\mathbf{R}' & \mathbf{R}'\mathbf{T}'^{-1} \\ -\mathbf{T}'^{-1}\mathbf{R}' & \mathbf{T}'^{-1} \end{bmatrix} \approx \begin{bmatrix} \mathbf{D}_{11} & \mathbf{D}_{12} \\ \mathbf{D}_{21} & \mathbf{D}_{22} \end{bmatrix}^{-1} \begin{bmatrix} \mathbf{N}_{11} & \mathbf{N}_{12} \\ \mathbf{N}_{21} & \mathbf{N}_{22} \end{bmatrix}, \tag{3.55}$$

where to simplify notation we have dropped the subscript r and $(\mathbf{A}'\tau)$ from the $\mathbf{D}$ and $\mathbf{N}$ matrices. Since we are only interested in solving for $\mathbf{R}'$ and $\mathbf{T}'$ rather than the entire exponential of $\mathbf{A}'\tau$ we can reduce the order of the inversion from a single $2n \times 2n$ inversion to two $n \times n$ inversions operating on the $n \times n$ matrix components. With some simple algebraic manipulation the global $\mathbf{R}'$ and $\mathbf{T}'$ matrices can be expressed as

$$\mathbf{T}' = LU(\mathbf{a}^{-1}, \mathbf{b}) \tag{3.56}$$

and

$$\mathbf{R}' = \mathbf{c} \otimes \mathbf{T}' - \mathbf{d}, \tag{3.57}$$

where

$$\mathbf{a} = \mathbf{D}_{21} \times \mathbf{c} - \mathbf{N}_{22}, \tag{3.58}$$

$$\mathbf{b} = \mathbf{D}_{21} \otimes \mathbf{d} - \mathbf{D}_{22}, \tag{3.59}$$

$$\mathbf{c} = LU(\mathbf{D}_{11}^{-1}, \mathbf{N}_{12}), \tag{3.60}$$

$$\mathbf{d} = LU(\mathbf{D}_{11}^{-1}, \mathbf{D}_{12}). \tag{3.61}$$

These equations can be evaluated with a total of $(5\frac{2}{3})n^3$ flops (note that the LU decomposition of $\mathbf{D}_{11}$ is shared between equations 3.60 and 3.61). Once $\mathbf{R}'$ and $\mathbf{T}'$ are determined, $\mathbf{R}$ and $\mathbf{T}$ can be recovered from $\mathbf{R}'$ and $\mathbf{T}'$ by using the inverse transformations given by equations 3.25 and 3.26.

Scaling and doubling

In section 3.2.4 we stated that the accuracy of the Padé approximation of a matrix exponential increases with the degree r and decreases as the norm of the matrix increases. Of the three methods for reducing the matrix norm presented, only one, "scaling and squaring", is applicable to our radiative transfer formulation. "Scaling and squaring" expressed as

$$e^{\mathbf{A}'\tau} = (e^{\mathbf{A}'\tau/2^s})^{2^s}, \tag{3.62}$$

involves reducing the norm of $\mathbf{A}'\tau$ by dividing it by the scalar 2^s, evaluating the exponential of the resulting matrix using the Padé approximation, and squaring the resulting matrix exponential s times to recover the $e^{\mathbf{A}'\tau}$. This is analogous to the doubling method for radiative transfer. Indeed, many initialization procedures for doubling, such as the infinitesimal generator initialization (IGI) [Grant and Hunt, 1969] and the expanded diamond initialization (EDI) [Wiscombe, 1976], are truncated Taylor series decompositions in $\Delta\tau$, where $\Delta\tau$ is some very small optical thickness analogous to the scalar $\tau/2^s$ of "scaling and squaring".

Then, the doubling of layers is analogous to repeated squaring, where s is the number of doublings or squarings. It has even been suggested by Flatau and Stephens [1988] that the Padé approximation may itself be useful for doubling initialization. With this in mind it can be shown that in our formulation the doubling of $\mathbf{R}'$ and $\mathbf{T}'$ is equivalent to squaring $e^{\mathbf{A}'\tau}$ and in fact, is computationally more efficient than squaring $e^{\mathbf{A}'\tau}$ (see Appendix A). As a result, we have introduced the expression "scaling and doubling" to describe this modification to "scaling and squaring".

If "scaling and doubling" is desired we start by scaling $\mathbf{A}'\tau$ with $1/(2^s)$ before calculating $\mathbf{N}$ and $\mathbf{D}$ as in section 3.2.5. Then after $\mathbf{R}'$ and $\mathbf{T}'$ are calculated as in section 3.2.5 and before $\mathbf{R}$ and

$\mathbf{T}$ are recovered, $\mathbf{R}'$ and $\mathbf{T}'$ are doubled using the iterative equations

$$\mathbf{R}'_{i+1} = \mathbf{R}'_i + \mathbf{A}'_i \otimes \mathbf{R}'_i \times \mathbf{T}'_i, \tag{3.63}$$

$$\mathbf{T}'_{i+1} = \mathbf{A}'_i \otimes \mathbf{T}'_i, \tag{3.64}$$

where

$$\mathbf{P}'_i = (\mathbf{E} - \mathbf{R}'_i \otimes \mathbf{R}'_i)^{-1}, \tag{3.65}$$

$$\mathbf{A}'_i = LU(\mathbf{T}'_i, \mathbf{P}'_i), \tag{3.66}$$

and i indicates the current doubling out of a total of s doublings. The global reflection and transmission matrices are being doubled in their symmetric form, indicated by the single prime, so as a result, there is some efficiency to gain over that of the standard doubling technique. Each doubling will cost a total of $(3\frac{5}{6})n^3$ flops. This is a significant improvement over the computational burden for standard doubling, where a symmetric transformation has not been made, which consists of a total of $(5\frac{1}{3})n^3$ flops.

3.2.6 Multi-layer atmospheres with a lower surface boundary

The method just proposed is for a homogeneous, single layer medium. Its extension to a heterogeneous medium is straight forward with the adding method. By dividing an atmosphere into layers, where the optical properties in each layer can be assumed homogeneous, the reflection and transmission operators, $\mathbf{R}_k$ and $\mathbf{T}_k$, where $k = 1, \ldots, N_L$ and N_L is the number of layers, can be determined for each layer with PARTM while the source vectors for each layer, $\mathbf{S}_k^+$ and $\mathbf{S}_k^-$, can be determined with equations 3.16 and 3.17. The adding method can then be used to combine the reflection and transmission operators and the source vectors for each layer into reflection and transmission operators and source vectors for the entire multi-layer stack, where the operators for incidence from below are $\mathbf{R}_a^+$ and $\mathbf{T}_a^+$, the operators for incidence from above are $\mathbf{R}_a^-$ and $\mathbf{T}_a^-$ and the source vectors are $\mathbf{S}_a^+$ and $\mathbf{S}_a^-$. Finally, the TOA upwelling radiance $\mathbf{I}^+(0)$ and bottom of atmosphere (BOA) downwelling radiance $\mathbf{I}^-(\tau_s)$, where τ_s is the optical depth to the surface (or the total optical thickness of the stack), can be determined. If a lower surface boundary is present it may be added as a bottom layer with reflection matrix $\mathbf{R}_s$ characterized by a bidirectional distribution

function (BRDF) and source vector $\mathbf{S}_s^+$ including both the direct beam reflected from the surface and surface emission, while $\mathbf{T}_s$ and $\mathbf{S}_s^-$ vanish. Details of the adding method are presented in Spurr and Christi [2007] while a discussion of BRDFs along with the details for several common BRDF kernels is given in Spurr [2004].

There are several key points about the adding method that are noteworthy in regards to our implementation. First, it is important to understand that even though PARTM is limited by the optical thickness of a layer, this is not the case for the entire layer stack. In fact, the adding of layer reflection and transmission operators determined by PARTM results in a "scaling and squaring" effect that bounds the overall error to the error incurred in the individual layers. Second, many retrieval schemes will require repeated simulations with changes in only a subset of layers. It is therefore possible to save the solution for all other layers or save the layer stacks above and below the layers that change. This is referred to as "layer saving" and is covered in detail by Gabriel et al. [2006]. The advantage of layer saving is also apparent in the application of surface retrievals. In this case the entire atmospheric layer stack will remain constant throughout the retrieval with only the surface BRDF changing with each iteration. Finally, if only TOA upward radiances are required, as is the case for most satellite retrievals, the computational burden of the adding equations can be reduced by over a half since only the reflection matrix $\mathbf{R}_a^-$ and the source vector $\mathbf{S}_a^+$ for the stack are required. As a result, if adding is performed from the bottom up, starting with $\mathbf{R}_s$ and $\mathbf{S}_s^+$ defined by the surface, only $\mathbf{R}_a^-$ and $\mathbf{S}_a^+$ for the current stack need to be calculated with the addition of each layer. If only the BOA downward radiances are required, for example for a upward looking sensor at the surface, then the adding equations can be reduced in a similar way but adding from the top-down. In this case, if a cosmic background radiation is required it is included as the downward source from an otherwise transparent top layer.

3.2.7 Implementation details

Our implementation of PARTM includes several features that are standard in many other radiative transfer models including a choice of (standard) Gauss-Legendre, double Gauss-Legendre, or Lobatto quadrature; delta-M scaling [Wiscombe, 1977], the Nakajima-Tanaka TMS correction [Nakajima and Tanaka, 1988], and the pseudo-spherical approximation [Dahlback and Stamnes, 1991]. For the surface boundary a generalized BRDF implementation including several common

BRDF kernels has been added Spurr [2004]. Finally, radiance output at arbitrary viewing angles is implemented by the inclusion of dummy nodes in the quadrature scheme. All these features are optional and controlled by boolean input values.

In writing an efficient implementation of PARTM, two performance enhancing measures are worthy of remark. First, as much as possible, matrix computations have been isolated to BLAS [Dongarra et al., 1990] and LAPACK [Anderson et al., 1999] calls. In fact, for a typical PARTM run with $n = 16$ over 80% of the computational burden lies within BLAS and LAPACK. This results in a considerable benefit for PARTM when linked with hardware optimized BLAS libraries that are available for most platforms. Second, a full layer/stack saving feature has been implemented in PARTM as described in section 3.2.6 which allows typical retrieval iterations to be performed optimally. As this feature is a trade off between memory use and CPU use it is optional and can be turned off in the case where memory use is of concern, for example when the number of streams is relatively large.

3.3 Performance evaluation

In this section we present accuracy and timing comparisons relative to the Discrete Ordinate Radiative Transfer (DISORT) model version 2.0 [Stamnes et al., 1988b]. DISORT is a general purpose plane-parallel radiative transfer model appropriate for multiple scattering atmospheres with solar and thermal sources which is widely used as benchmark in the remote sensing community. Accuracy results are presented as fractional differences between DISORT and PARTM defined as

$$\Delta(x) = \frac{I_{\text{DISORT}} - I_{\text{PARTM}}}{I_{\text{DISORT}}} \tag{3.67}$$

where I_{DISORT} and I_{PARTM} are radiances determined by DISORT and PARTM, respectively. For all the examples presented in this section and section 4.5, for both PARTM and DISORT, double Gaussian quadrature was used and Delta-M scaling and the Nakajima-Tanaka TMS correction were turned on. A solar source was included with the solar flux F_0 set to unity while thermal emission sources were turned off.

In a general radiative transfer model, the accuracy of the computed results is set primarily by the accuracy of the model inputs and the number of quadrature points n used. In contrast, PARTM will depend also on the adjustable parameters r and s. Conversely, for a fixed r and s, the accuracy will depend not only on the accuracy of the model inputs and n but also on the magnitude of the model inputs and the model geometry. For example, the optical thickness will directly affect the norm of $\mathbf{A}\tau$ which in turn affects the accuracy for a particular r and s configuration. The view angle θ also affects the accuracy significantly, especially at high angles where the plane-parallel optical path increases rapidly. In figure 3.1 fractional differences Δ for the upwelling radiance $\mathbf{I}^+(0)$ and the downwelling radiance $\mathbf{I}^-(\tau)$ are plotted as a function of the view angle θ for a single homogeneous slab with no lower boundary, where $\tau = 1.0$, $\omega = 0.9$, P is a Henyey-Greenstein phase function with asymmetry parameter $g = 0.75$, $\theta_0 = 45°$, $\phi - \phi_0 = 45°$, and $n = 16$. The plot on the top is for $r = 9$ and $s = 0$ while the bottom left plot is for $r = 13$ and $s = 0$ and the bottom right plot is for $r = 7$ and $s = 1$. The dependence of Δ on θ is evident. If an accuracy requirement of $|\Delta| < 10^{-4}$ is chosen, shown by the dashed lines, $r = 9$ and $s = 0$ provide accurate results up to $\theta \approx 76.0°$. For larger view angles r and/or s must be increased. For $\theta < 84.0°$ $r = 13$ and $s = 0$ is sufficient while for $\theta < 85.5°$ $r = 7$ and $s = 1$ is required.

The optimal choice of r and s should be one that meets the accuracy requirement with the lowest overall computational cost which we will define in terms of n^3 flops as

$$C_I = \pi_r + 3\frac{5}{6}s, \tag{3.68}$$

where, from section 3.2.5, π_r is the number of n^3 flops required to evaluate $\mathbf{N}$ and $\mathbf{D}$ of the Padé approximation and, from section 3.2.5, the factor $3\frac{5}{6}$ is the number of n^3 flops required for a single doubling. The *constant* cost of computing $\mathbf{R}$ and $\mathbf{T}$ from $\mathbf{N}$ and $\mathbf{D}$ as in section 3.2.5 has been ignored.

For timing comparisons relative to DISORT a speed-up factor f will be used defined as

$$f = \frac{t_{\text{DISORT}}}{t_{\text{PARTM}}}, \tag{3.69}$$

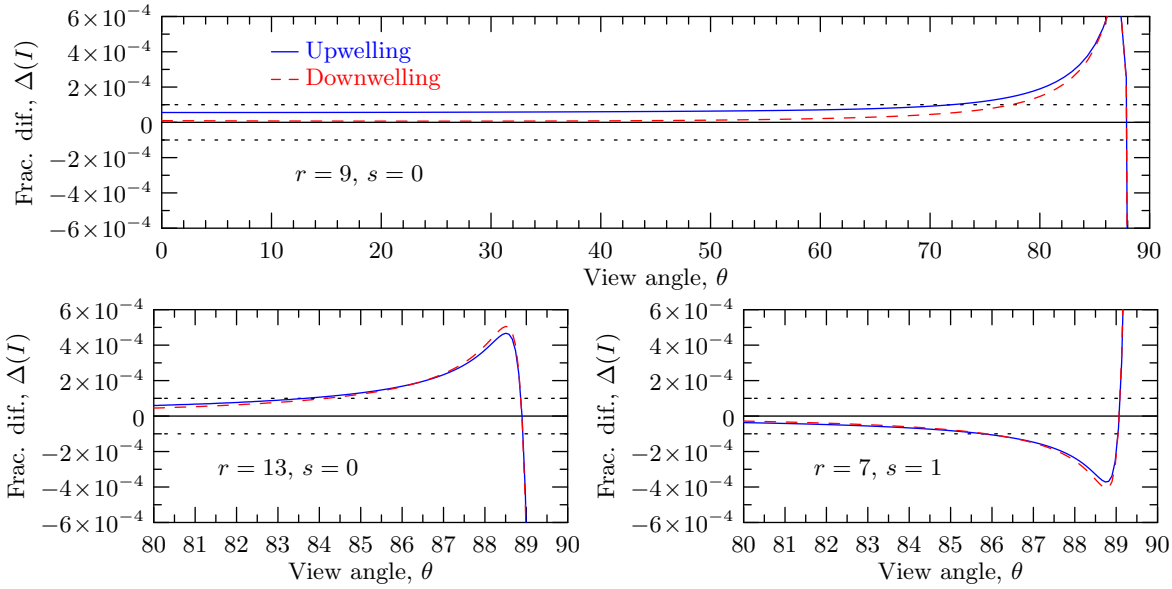

Figure 3.1: Fractional differences Δ for the TOA upwelling radiance $\mathbf{I}^+(0)$ and the BOA downwelling radiance $\mathbf{I}^-(\tau)$ as a function of θ for a single homogeneous slab with no lower boundary, where $\tau = 1.0$, $\omega = 0.9$, P is a Henyey-Greenstein phase function with $g = 0.75$, $\theta_0 = 45°$, $\phi - \phi_0 = 45°$, and $n = 16$ The upper plot is for $(r, s) = (9, 0)$ while the lower left plot is for $(r, s) = (13, 0)$ and the lower right plot is for $(r, s) = (7, 1)$. The dashed lines indicate the accuracy goal of $|\Delta| < 10^{-4}$.

where t_{DISORT} and t_{PARTM} are the times required for DISORT and PARTM, respectively. All timing tests were performed on an computer with an Intel(R) Core(TM)2 Duo CPU E8600 @ 3.33GHz running GNU/Linux (kernel version 2.6.27). The PARTM and DISORT codes were compiled with the GNU Compiler Collection (GCC) 4.4.3 and linked with reference (unoptimized) BLAS and LAPACK (version 3.2.1) libraries from http://www.netlib.org. To average out OS scheduling variations the timing tests were performed not for a single call but for a number of calls. The number chosen was the number of DISORT calls required to exceed a time of 20 s for each test.

In table 3.3 optimal r and s along with their associated speed-up factor f, presented as $(r,\ s,\ f)$, are given as a function of τ and θ for a homogeneous slab with no lower boundary, where $\omega = 1.0$, P is isotropic ($g = 0$), $\theta_0 = 65°$, $\phi - \phi_0 = 0°$, and $n = 16$. Values were computed by sorting r and s pairs by increasing cost C_I and successively running the model with r and s values from the list until $|\Delta|$ for both the upwelling radiance $\mathbf{I}^+(0)$ and downwelling radiance $\mathbf{I}^-(\tau)$ from the layer were less than 10^{-4}. For each value of τ the associated 1-norm of $\mathbf{A}\tau$ is also listed. The increasing requirements for r and s with increasing τ and therefore $\|\mathbf{A}\tau\|_1$ are easily seen. At larger values of τ the r and s requirements also tend to increase with increasing θ. It is interesting that several (r, s)

Table 3.3: Optimal r and s values along with their associated speed-up factor f for the computation of radiances only with an accuracy requirement of $|\Delta| < 10^{-4}$. Values are given as a function of τ and θ for a homogeneous slab with no lower boundary, where $\omega = 1.0$, P is isotropic, $\theta_0 = 45°$, $\phi - \phi_0 = 45°$, and $n = 16$.

τ	$\|\tau\mathbf{A}\|_1$	$\theta = 0°$	$\theta = 30°$	$\theta = 60°$	$\theta = 75°$	$\theta = 85°$	$\theta = 89°$
0.01	1.90e+00	(2, 0, 5.22)	(2, 0, 5.22)	(2, 0, 5.22)	(2, 0, 5.22)	(2, 0, 5.22)	(2, 0, 5.22)
0.02	3.80e+00	(3, 0, 4.91)	(3, 0, 4.91)	(3, 0, 4.91)	(3, 0, 4.91)	(3, 0, 4.91)	(3, 0, 4.91)
0.05	9.49e+00	(5, 0, 4.73)	(5, 0, 4.73)	(5, 0, 4.73)	(5, 0, 4.73)	(5, 0, 4.73)	(5, 0, 4.73)
0.10	1.90e+01	(5, 0, 4.73)	(5, 0, 4.73)	(5, 0, 4.73)	(5, 0, 4.73)	(5, 0, 4.73)	(5, 0, 4.73)
0.20	3.80e+01	(5, 0, 4.73)	(5, 0, 4.73)	(5, 0, 4.73)	(7, 0, 4.55)	(7, 0, 4.55)	(7, 0, 4.55)
0.50	9.49e+01	(7, 0, 4.55)	(7, 0, 4.55)	(7, 0, 4.55)	(9, 0, 4.39)	(13, 0, 4.21)	(7, 1, 3.68)
1.00	1.90e+02	(9, 0, 4.39)	(9, 0, 4.39)	(13, 0, 4.21)	(13, 0, 4.21)	(9, 1, 3.60)	(13, 1, 3.46)
2.00	3.80e+02	(7, 1, 3.68)	(7, 1, 3.68)	(9, 1, 3.60)	(13, 1, 3.46)	(13, 1, 3.46)	(5, 2, 3.17)
5.00	9.49e+02	(7, 2, 3.11)	(7, 2, 3.11)	(9, 2, 3.05)	(9, 2, 3.05)	(13, 2, 2.93)	(13, 2, 2.93)
10.0	1.90e+03	(7, 3, 2.69)	(7, 3, 2.69)	(7, 3, 2.69)	(7, 3, 2.69)	(9, 3, 2.64)	(13, 3, 2.56)
20.0	3.80e+03	(5, 4, 2.41)	(5, 4, 2.41)	(5, 4, 2.41)	(7, 4, 2.37)	(7, 4, 2.37)	(7, 4, 2.37)
50.0	9.49e+03	(5, 5, 2.15)	(5, 5, 2.15)	(5, 5, 2.15)	(5, 5, 2.15)	(5, 5, 2.15)	(7, 5, 2.12)
100.0	1.90e+04	(7, 5, 2.12)	(7, 5, 2.12)	(7, 5, 2.12)	(5, 6, 1.94)	(5, 6, 1.94)	(5, 6, 1.94)

pairs are not used and that the ones which are used tend to be pairs of higher r and lower s. This is due to the much higher cost of an increase in s compared to that of r. It is also interesting that $(1, 0)$ is never used, even down to values of $\tau = 0.001$ (not shown) which is most likely due to a loss of significance in floating point arithmetic [Higham, 1984]. From these results it is apparent that for the single layer solution with $n = 16$ PARTM is faster than DISORT with significant computational speed-ups of $f > 4.0$ for lower optical thicknesses common to atmospheres with aerosols and/or cirrus clouds.

With table 3.3 in mind we have implemented a simple yet effective method of automatically choosing optimal values for r and s in PARTM. By using $\|\mathbf{A}\tau\|_1$ and the view angle θ, r and s are looked-up in a table similar to table 3.3 but with smaller increments in $\|\mathbf{A}\tau\|_1$ and θ. The $\|\mathbf{A}\tau\|_1$ and θ values represent the maximum allowable values for their associated (r, s) pair with 1.9×10^4 and 89°, respectively, as the maximum values supported. Variations in the single scattering albedo ω and the phase function P are represented by variations in $\|\mathbf{A}\tau\|_1$. This is also the case for the quadrature scheme and the number of points n which effect the norm of $\mathbf{A}\tau$ through $\mathbf{M}^{-1}$ in $\mathbf{r}$ and $\mathbf{t}$ (equations 3.9 an 3.10). The optimal r and s values are dependent on layer properties and are therefore independently chosen for each layer. The result is that the r and s values are optimized for each layer separately.

Table 3.4: Speed-up factor f for several values of n for a homogeneous slab with no lower boundary, where $(r, s) = (5, 0)$.

n	2	4	6	8	12	16	24	32	40	48	56	64
f_I	1.36	1.59	1.70	2.74	3.80	4.77	5.57	6.16	5.81	5.43	4.55	3.54

Table 3.4 lists the speed-up factor for several values of n to compute radiances for a homogeneous slab with no lower boundary, where $\tau = 1.0$, $\omega = 0.9$, P is isotropic ($g = 0$), $\theta_0 = 45°$, $\theta = 25°$, and $\phi - \phi_0 = 45°$. In this case we have chosen $r = 5$ and $s = 0$ appropriate for a τ of around 0.1. For all values of n the speed-up factors exceed unity, indicating a computational speed-up for PARTM relative to DISORT. The speed-up factors start at a minimum for $n = 2$ and tend to increase with increasing n up to $n = 32$. In theory the computational burden for both solutions is $O(n^3)$. However, at lower values of n, program overhead, including n^2 operations, becomes more important lessening the relative differences in speed due to solution strategy alone. In contrast, for larger values of n, the n^3 operations related to the solution strategy dominate and therefore differences in the solutions themselves dominate the speed-up factors. It is interesting that the speed-up factors decrease with n after $n = 32$. The reason for this is not obvious and probably has to due with implementation details.

Speed-up factors as a function of the number of layers N_L are presented in table 3.5. The layers are identical and the optical and geometric inputs are the same as that used for table 3.4. As before, no lower boundary is included and $r = 5$ and $s = 0$ while in this case $n = 16$. Speed-up factors are given for the computation of TOA upward and BOA downward radiances (f_I) and for the computation of TOA upward radiances only ($f_{I,R}$). It is apparent that PARTM provides a significant improvement in speed for any number of layers. In theory the computational burden for both methods should increase linearly with N_L, although speed-up factor tends to decrease with N_L. As before, we assume that the cause of this discrepancy has to due with implementation details.

3.4 Numerical results

PARTM has been shown to provide a significant computational advantage for optically thin atmospheres. It is for this reason that PARTM is particularly suited for remote sensing applications of gases and aerosols. In particular, use of multispectral, multiangle and/or hyperspectral measurements

Table 3.5: Speed-up factor f as a function of the number of layers, where no lower boundary is included and $n = 16$ and $(r, s) = (5, 0)$. Values are given for two cases: to compute upward and downward radiances (f_I) and to compute upward radiances only ($f_{I,R}$).

N_L	1	2	4	8	16	32	64	128
f_I	4.77	3.58	3.20	3.04	3.04	2.99	3.01	2.42
$f_{I,R}$	4.91	4.11	3.87	3.71	3.74	3.69	3.74	3.04

may require hundreds or even thousands of simulations for which a fast RTM is critical. We have chosen two practical examples to demonstrate the use of PARTM, one for a multispectral instrument similar to the Moderate Resolution Imaging Spectrometer (MODIS) [King et al., 1992] and one for an instrument similar to the 0.76-μm O_2 A-band spectrometers on the Greenhouse gases Observing SATellite (GOSAT, http://www.gosat.nies.go.jp/index_e.html) and the Orbital Carbon Observatory (OCO) [Crisp et al., 2004].

Before we present results it is worth noting how optical properties are input to the model. The RT formulation presented takes as its input one optical thickness τ, one single scattering albedo ω, and one set of phase function expansion coefficients β_l, although in our example cases, and in most other applications, what is known are the optical properties of several individual components. In this case the optical properties of the mixture, to be input to the model, may be determined from the individual optical properties with

$$\tau_j = \sum_i \tau_{i,j}, \tag{3.70}$$

$$\omega_j = \frac{\sum_i \tau_{i,j}\omega_{i,j}}{\tau_j}, \tag{3.71}$$

and

$$\beta_{j,l} = \frac{\sum_i \tau_{i,j}\omega_{i,j}\beta_{i,j,l}}{\sum_i \tau_{i,j}\omega_{i,j}}, \tag{3.72}$$

where i represents the index of an individual component whether it is gaseous absorption, Rayleigh scattering, or a Mie scatterer, j is the layer index, and l is the expansion coefficient degree. In the special case of gaseous absorption and Rayleigh scattering $\omega = 0$ and $\omega = 1$, respectively.

Our first example involves a scenario applicable to an instrument similar to MODIS, a multispectral radiometer with 36 bands, seven of which, at wavelengths = 0.469, 0.555, 0.645, 0.858, 1.24, 1.64, and 2.13 μm, will be used here. For this example we have chosen the 33 level mid-latitude summer atmosphere from McClatchey et al. [1972]. All of the spectral bands used are free of significant molecular absorption which will therefore be ignored. The Rayleigh scattering properties were determined as in Bodhaine et al. [1999]. Aerosols were derived from d'Almeida et al. [1991] for a maritime polluted atmosphere, where Mie theory was used to calculate aerosol scattering properties. The resulting column optical depth of this atmosphere at 0.555 μm is 0.201. The surface is assumed to be ocean with a specular component modeled as in Cox and Munk [1954] with a wind speed of 10 m/s and an index of refraction from Hale and Querry [1973] or Palmer and Williams [1974], depending on wavelength. In addition, a Lambertian foam component modeled as in Koepke [1984] was also added.

In figure 3.2a TOA radiance $I^+(0)$ is plotted as a function of view angle θ for each band. The solar factor F_0 was set to unity for each wavelength while the solar zenith angle and relative azimuth were assumed to be $\theta_0 = 45^\circ$ and $\phi - \phi_0 = 45^\circ$, respectively. In this case we have chosen a moderate number of streams with $2n = 32$. In figure 3.2b the fractional differences Δ between DISORT and PARTM are shown. It is apparent that for all cases $|\Delta|$ is well below our accuracy requirement of 10^{-4} suggesting the PARTM is a viable alternative even in cases where high accuracy is required. The speed-up factors associated with this example are 3.74 for the case when both TOA and BOA radiances are required and 4.69 for the case when only TOA radiances are required both of which can be significant for moderate to high accuracy calculations.

Our second example is applicable to hyperspectral instruments such as those on board GOSAT and the expected replacement for OCO, the goal of which are to make global measurements of atmospheric CO_2, and in the case of OCO, with the precision, resolution, and coverage required to characterize CO_2 sources and sinks on regional scales. This would be achieved by incorporating measurements from three high resolution spectrometers measuring reflected sunlight in the 0.76-μm O_2 A-band and the 1.61- and 2.06-μm CO_2 bands either in nadir, target, or glint modes. For this example we have calculated radiances in the O_2 A-band as would be observed in target mode. The atmospheric model used for this example is one of many in a database that is used to generate synthetic spectra replicating those that would have been measured by GOSAT or OCO in operational

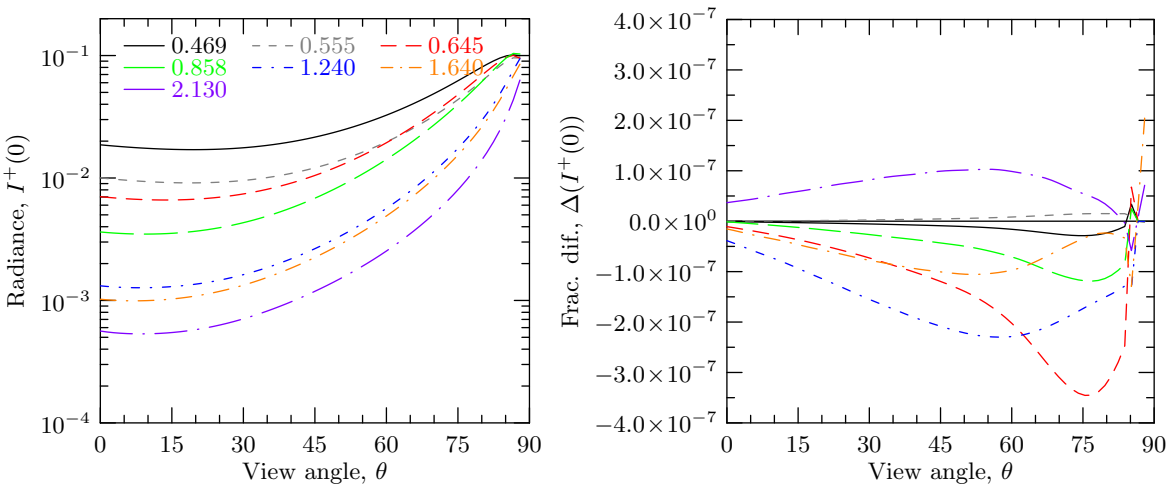

Figure 3.2: Model results for the MODIS example described in the text. TOA upwelling radiance (a) and the corresponding fractional differences Δ between DISORT and PARTM (b) are given as a function of the view angle θ while $\theta_0 = 45°$, $\phi - \phi_0 = 45°$, and $n = 16$. Seven shortwave and near-infrared bands are plotted, where the legend indicates the central wavelength in μm.

mode. In this case we have chosen an atmosphere over a snow covered region in Norway at 66.93° latitude, 16.06° longitude and an elevation of 0.73 km representing winter conditions on 2007-12-23 at 12:13 PM. The model is divided into 61 levels from the surface up to a pressure of 1 Pa. Meteorological conditions were provided by ECMWF [Chevallier et al., 2000]. Line-by-line gaseous optical thickness was derived for O_2 and H_2O at a resolution of 0.005 cm^{-1} from HITRAN 2004 [Rothman et al., 2005] using a Voigt line profile. The O_2 volume mixing ratio (VMR) is assumed to be constant at 2.0947×10^{-1} while the H_2O VMR was variable and was provided by ECMWF. The Rayleigh scattering properties were determined as in Bodhaine et al. [1999]. Atmospheric Mie scatterers include a mixture of clean continental and clean maritime aerosols between 0.0 and 11.02 km and a mixture of both water and ice cloud particles between 0.75 and 2.62 km. Mie theory was used to calculate aerosol/cloud scattering properties which were performed at the minimum and maximum wavelengths for each spectrum and assumed to vary linearly across the spectrum. The result is an atmosphere with mean aerosol and cloud column optical thicknesses of 0.0644 and 0.355, respectively, for a total aerosol/cloud optical thickness of 0.420. The snow covered surface is assumed to be Lambertian with constant albedo of 0.418 over the O_2 A-band.

In figure 3.3a TOA radiance $I^+(0)$ in the O_2 A-band is plotted as a function of wavenumber (cm^{-1}). Solar and viewing angles were chosen so that $\theta_0 = 45°$, $\theta = 25°$, and $\phi - \phi_0 = 45°$ while

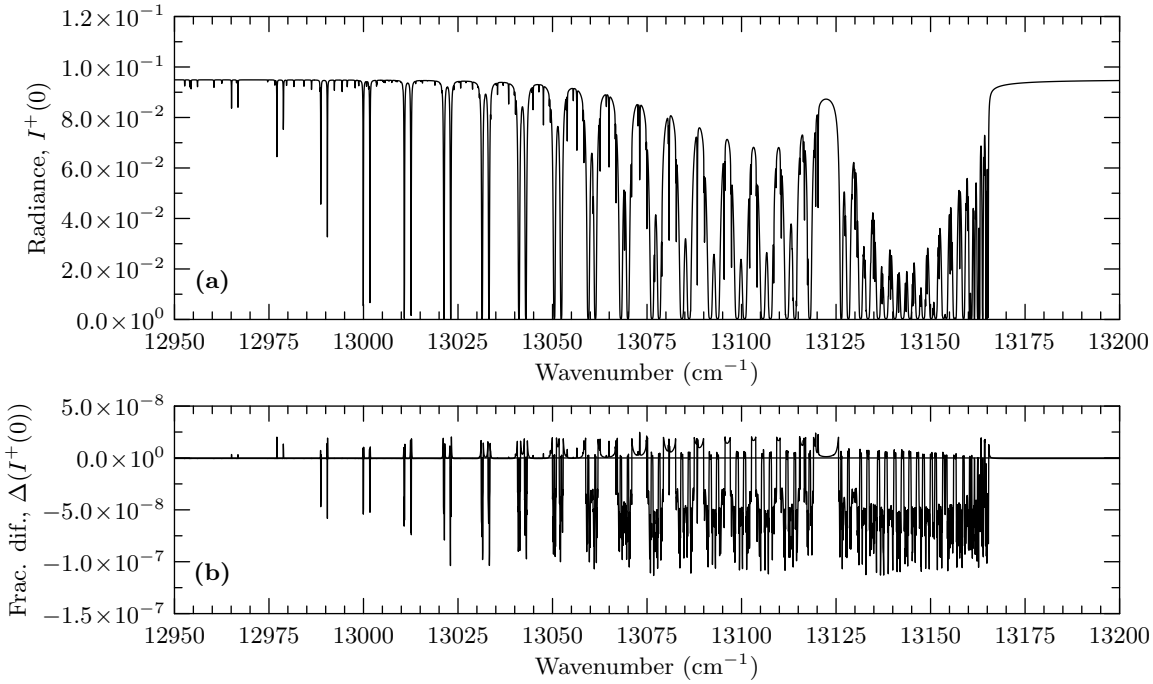

Figure 3.3: Model results for the 0.76-μm O_2 A-band for the GOSAT/OCO example described in the text. Plot (a) is the TOA upwelling radiance spectrum and plot (b) shows the corresponding fractional differences Δ between DISORT and PARTM. The geometry is $\theta_0 = 45°$, $\theta = 25°$, and $\phi - \phi_0 = 45°$ while $n = 16$.

F_0 was set to unity for the entire spectrum. As in the first example the number of streams was set to $2n = 32$. The characteristic P and R branches of the A-band are well illustrated while the narrow absorption lines occurring in singlet and doublet pairs are easily seen. It is also apparent that the continuum radiance is approximately 9.5×10^{-2} which is primarily a result of Rayleigh and Mie scattering along with surface reflection. In figure 3.3b the fractional differences Δ between DISORT and PARTM are shown. The absolute differences are lower in the continuum and higher in the center of strong absorption lines as expected. The maximum difference of $|\Delta| \approx -1.25 \times 10^{-7}$ is well below an accuracy requirement of 10^{-4}. The speed-up factors for this example are 3.23 for both TOA and BOA radiances and 3.92 for TOA radiances only. Compared to the first example the lower speed-up factors are result of the larger optical depths that occur deep within O_2 A-band absorption lines.

The results just presented are from line-by-line calculations at a resolution of 0.005 cm^{-1}. In many cases, it can be computational prohibitive to calculate the entire spectrum explicitly and a faster approach will be required to speed-up calculations, including k-distribution methods [Lacis and

Hansen, 1974, Goody et al., 1989], modified k-distribution or spectral mapping techniques [Bennartz and Fischer, 2000, Duan and Min, 2005, Hasekamp and Butz, 2008, Boesche et al., 2009], methods based on PCA analysis [Natraj et al., 2005], or spectral interpolations [O'Dell, 2010]. These techniques rely on the fact that although the gaseous absorption varies rapidly over the band of interest the effects due to Rayleigh scattering, clouds, and aerosols vary slowly. The advantage of this is that the number of high accuracy/multiple scattering calculations required may be significantly reduced. It is for such calculations that PARTM may used in these methods as an alternative to other general radiative transfer solvers.

Given the two examples just presented, it is instructive to look at table 3.6 which lists the number of times each (r, s) pair was used in the two simulations. The pairs and their associated counts are sorted by increasing cost. All cases where the count was zero for both examples have been omitted. From the table we can see that in most cases the counts decrease with increasing cost. This behavior is expected in the O_2 A-band as the lower column optical depths in the continuum and in the wings of absorption lines are more abundant than optical depths from deeper inside absorption lines. In addition, for both cases layers without aerosols are more abundant than layers with aerosols also contributing to this behavior. It is also apparent that the maximum cost required to model the O_2 A-band spectrum is considerably higher than that for MODIS due to the large O_2 A-band optical depths deep within absorption lines. The total counts are listed at the bottom of the table. The maximum values for these are 50001 spectral points $\times$ 60 layers $\times$ a maximum of $2n = 32$ Fourier terms = 96001920 for the O_2 A-band example and 7 channels $\times$ 64 angles $\times$ 32 layers $\times$ a maximum of $2n = 32$ Fourier terms = 458752 for the MODIS example. By dividing the actual total count by the maximum total count and multiplying by 32, the average number of Fourier terms used can be determined, which is 10.28 for MODIS and 10.86 for the O_2 A-band.

3.5 Summary and conclusions

In this paper we have presented a radiative transfer solution for a multi-layer, multiple-scattering plane-parallel atmosphere with solar scattering and thermal emission sources and a lower surface boundary characterized by a BRDF. The purpose of this study is to provide a radiative transfer solution that is an efficient alternative to more general solutions. The method, identified as PARTM,

Table 3.6: Number of times each (r, s) pair was used to calculate the MODIS radiances for all seven bands and to calculate O_2 A-band radiance spectrum. The rows are sorted by increasing cost C_I. All cases where the count was zero for both cases have been omitted.

(r, s)	C_I	MODIS	O_2 A-band
(2, 0)	1.00	122146	24565875
(3, 0)	2.00	13980	3833319
(5, 0)	3.00	11190	3452474
(7, 0)	4.00	64	401993
(9, 0)	5.00	0	154525
(13, 0)	6.00	0	31722
(7, 1)	7.83	0	50333
(9, 1)	8.83	0	18857
(13, 1)	9.83	0	15602
(5, 2)	10.67	0	0
(7, 2)	11.67	0	23815
(9, 2)	12.67	0	8104
(5, 3)	14.50	0	6275
(7, 3)	15.50	0	6058
(5, 4)	18.33	0	68
Total		147380	32569020

is based on the Padé approximation to the exponential of a matrix used in concert with the interaction principle. It was demonstrated how this method, when combined with the doubling method, parallels the popular "scaling and squaring" method for evaluating the exponential of a matrix. Two similarity transformations were introduced that allow for considerable computational gain, first by exploiting the symmetry inherent in the matrix form of the RTE, and then by exploiting the structure of the attenuation matrix to halve the order of the matrix solution. For multi-layer atmospheres the Padé approximation is used to obtain individual layer reflectance and transmission operators which can then be combined into a multi-layer solution using the adding method. Use of the adding method adds additional efficiency to PARTM through layer saving strategies for iterative retrieval methods and through efficient use of the adding equations when only the TOA upwelling or the BOA downwelling radiance is required.

Numerical tests were performed demonstrating the accuracy and speed of PARTM relative to DISORT. The tests show that the optimal choice for the degree of the Padé approximation r and the number of doublings s is dependent not only on layer optical thickness τ but also on the view angle θ. A brute-force technique was used to find the optimal configuration of r and s for several

values of τ and θ based on an accuracy requirement of 10^{-4}. The results of this technique were incorporated into our PARTM implementation to automate the selection of the optimal (r, s) pair.

Timing comparisons with DISORT for a homogeneous slab using these optimal configurations and $n = 16$ reveal that PARTM is faster in all cases presented with speed-up factors f ranging from approximately 5.22 at $\tau = 0.01$ to approximately 1.94 at $\tau = 100.0$. Timing tests as function of the number of streams $2n$ for $(r, s) = (5, 0)$ show that PARTM is faster than DISORT in all cases with speed-up factors ranging from 1.36 at four streams to 6.16 at 64 streams. Timing tests as function of the number of layers demonstrate that PARTM's efficiency relative to DISORT decreases with the number of layers with speed-up factors ranging from 4.77 for 1 layer to 2.42 for 128 layers. In addition, the special case of one way adding for TOA or BOA only radiances is usually 10–20% faster than when two way adding is used for both TOA and BOA radiances.

Simulations were performed for radiances as seen by a multispectral instrument similar to MODIS and an O_2 A-band spectrometer similar to those on GOSAT and OCO. Radiances were calculated using PARTM and DISORT and fractional differences and speed-up factors were presented. The results confirm that PARTM easily meets the accuracy requirement for radiances in all cases while also being computationally advantageous, suggesting that PARTM may be an efficient alternative for moderate to high accuracy requirements, especially as PARTM's relative speed-up is significant for a moderate to high number of streams.

Much of the formulation presented in this paper can be generalized to a full Stokes-vector treatment to include polarization effects. As a result, development of a vectorized implementation of PARTM is currently in progress and will be presented in a future paper.

Chapter 4

Vector radiative transfer paper[2]

4.1 Introduction

As modern remote sensing instruments have improved in sensitivity, vector radiative transfer modeling has become an increasingly important component in retrieval algorithms. It has been shown that in some cases the errors incurred from using the scalar approximation (neglecting polarization) are considerable [Mishchenko et al., 1994, Lacis et al., 1998, Natraj et al., 2007]; this can lead to significant errors in the retrieval of atmospheric and surface parameters. Vector radiative transfer models are also an important aspect in polarization correction algorithms for instruments sensitive to polarization [Hasekamp et al., 2002, Schutgens and Stammes, 2003]. Polarization measurements have also been shown to provide important information in some retrieval scenarios. When combined with observations at multiple view angles, polarization can reveal information about particle size, shape, and/or refractive index that otherwise would be difficult to retrieve from intensity only measurements [Mishchenko and Travis, 1997a, Deuzé et al., 2000, Chowdhary et al., 2005]. It has also been demonstrated that high resolution spectropolarimetry can reveal aerosol profile information [Stam et al., 1999, Boesche et al., 2009] while observations of polarized radiances are useful in separating atmospheric and surface reflectance contributions [Herman et al., 1997b].

Unfortunately vector radiative transfer has an order of up to four times greater than that of scalar radiative transfer and therefore is computationally slower. When a large number of radiative transfer calculations are required, such as with high spectral resolution measurements, an efficient radiative transfer model is needed, especially when processing data in real-time applications.

The modern treatment of polarized radiative transfer is based on the work of Chandrasekhar [1960] who formulated polarization in terms of the Stokes vector. An important contribution was

[2]Paper published: "A new vector radiative transfer solution using Padé approximants" [McGarragh and Gabriel, 2013].

provided by Kuščer and Ribarič [1959] who formulated the phase matrix decomposition in azimuth angle using the addition theorem of generalized spherical functions. This was later more conveniently reformulated by Siewert [1981] and Siewert [1982] which is the method used in most vector radiative transfer models today. With this formulation, extension of scalar radiative transfer codes to solve for the Stokes vector is relatively straight forward. Several vector methods have been developed including the discrete ordinate method [Schulz et al., 1999, Spurr, 2006], matrix operator methods based on doubling and adding [de Haan et al., 1987], the spherical harmonics method [Garcia and Siewert, 1986], the F_N method [Garcia and Siewert, 1989], and successive orders of scattering [Min and Duan, 2004, Lenoble et al., 2007].

In a previous paper [McGarragh and Gabriel, 2010], hereafter referred to as MG2010, we presented a scalar radiative transfer method based on the Padé approximation to the exponential of a matrix. It was found to be accurate and significantly faster compared to the discrete ordinate method, especially for optically thin media (optical thickness x less than one). In this study we extend this method to solve the vector radiative transfer equation and refer to this extension as the "Vector Padé approximation radiative transfer method" (VPARTM). In section 4.2 a description of the radiative transfer formulation used in this paper is given beginning with the presentation of the basic equations in section 4.2.1 followed by the matrix formulation and the general solution for the Stokes vector in section 4.2.2. In section 4.2.3 we discuss the solution methodology touching primarily on the differences required to extend the scalar solution in MG2010 to the vector case. In section 4.3 some details and features of our implementation of VPARTM are discussed. Timing comparisons relative to a reference model for several model configurations are given in section 4.4 while example results from two realistic applications are presented in section 4.5 including accuracy and timing comparisons relative to a reference model. Finally, some concluding remarks are given in section 4.6.

An implementation of VPARTM is available as one of several radiative transfer methods within the X Radiative Transfer Model (XRTM) software. XRTM is licensed under the GNU General Public License Version 3 and is available at `http://reef.atmos.colostate.edu/~gregm/xrtm`.

4.2 Radiative transfer formulation

4.2.1 Basic equations

The vector radiative transfer equation [Chandrasekhar, 1960] for a single plane-parallel homogeneous layer is given by

$$\mu \frac{d\mathbf{I}(\tau,\mu,\phi)}{d\tau} = \mathbf{I}(\tau,\mu,\phi) - \frac{\omega}{4\pi}\int_0^{2\pi}\int_{-1}^{1}\mathbf{P}(\mu,\phi,\mu',\phi')\mathbf{I}(\tau,\mu',\phi')d\mu' d\phi' - \mathbf{\Sigma}(\tau,\mu,\phi), \tag{4.1}$$

where $\mathbf{I}(\tau,\mu,\phi)$ is the Stokes vector $[I,Q,U,V]^T$ at optical depth $\tau \in [0,x]$, x is optical thickness of the layer, $\mu \in [-1,1]$ is the cosine of the polar angle of propagation (measured from the upward normal or the negative τ-direction), $\phi \in [0,2\pi]$ is the azimuthal angle of propagation (measured clockwise when looking upward), $\mathbf{P}(\mu,\phi,\mu',\phi')$ is the phase matrix for radiation from the direction (μ',ϕ') scattered into the direction (μ,ϕ), and ω is the albedo of single scattering. With this formulation positive values of μ represent upward radiation in the direction of decreasing τ and negative values of μ represent downward radiation in the direction of increasing τ. The third term on right hand side of Eq. (4.1) represents the source function given by

$$\mathbf{\Sigma}(\tau,\mu,\phi) = \frac{\omega}{4\pi}\mathbf{P}(\mu,\phi,-\mu_0,\phi_0)\mathbf{F}_0 e^{-\tau/\mu_0} + (1-\omega)\mathbf{B}(T). \tag{4.2}$$

The first term on the right hand side of Eq. (4.2) represents the solar source where $\mathbf{F}_0 = [1,0,0,0]^T$ is the top of atmosphere (TOA) incident solar flux and μ_0 and ϕ_0 are the solar zenith and azimuth angles, respectively. The second term on the right hand side of Eq. (4.2) is the thermal emission, where $\mathbf{B}(T) = [B(T),0,0,0]^T$ and $B(T)$ is the Planck black body function with the single argument of layer temperature T.

From the addition theorem for generalized spherical functions the azimuthal dependence of the Stokes vector can be separated into a Fourier decomposition in relative azimuth. This was first formulated in terms of complex parameters by Kuščer and Ribarič [1959] and then later reformulated in terms of real quantities by Siewert [1981] which can be written as

$$\mathbf{I}(\tau,\mu,\phi) = \sum_{m=0}^{M}\mathbf{\Lambda}^m(\phi-\phi_0)\mathbf{I}^m(\tau,\mu), \tag{4.3}$$

where

$$\mathbf{\Lambda}^m(\phi) = \mathrm{diag}\left[\cos m\phi, \cos m\phi, \sin m\phi, \sin m\phi\right], \tag{4.4}$$

while the azimuthal expansion of the phase matrix can be written as

$$\mathbf{P}(\mu, \phi, \mu'\phi') = \frac{1}{2}\sum_{m=0}^{M}(2-\delta_{0,m})\left[\mathbf{C}^m(\mu,\mu')\cos m(\phi-\phi_0) + \mathbf{S}^m(\mu,\mu')\sin m(\phi-\phi_0)\right], \tag{4.5}$$

where

$$\mathbf{C}^m(\mu,\mu') = \mathbf{P}^m(\mu,\mu') - \mathbf{D}\mathbf{P}^m(\mu,\mu')\mathbf{D}, \tag{4.6}$$

$$\mathbf{S}^m(\mu,\mu') = \mathbf{P}^m(\mu,\mu')\mathbf{D} - \mathbf{D}\mathbf{P}^m(\mu,\mu'), \tag{4.7}$$

$$\mathbf{P}^m(\mu,\mu') = \sum_{l=m}^{L}\mathbf{P}_l^m(\mu)\mathbf{B_l}\mathbf{P}_l^m(\mu'), \tag{4.8}$$

$$\mathbf{D} = \mathrm{diag}\left[1, 1, -1, -1\right]. \tag{4.9}$$

The azimuthal components of the phase matrix are expressed through two matrices one of which is

$$\mathbf{P}_l^m(\mu) = \begin{bmatrix} P_l^m(\mu) & 0 & 0 & 0 \\ 0 & R_l^m(\mu) & -T_l^m(\mu) & 0 \\ 0 & -T_l^m(\mu) & R_l^m(\mu) & 0 \\ 0 & 0 & 0 & P_l^m(\mu) \end{bmatrix}, \tag{4.10}$$

where $P_l^m(\mu)$ are the normalized Legendre functions and the functions $R_l^m(\mu)$ and $T_l^m(\mu)$ are related to the generalized spherical functions $P_{mn}^l(\mu)$. Computation of the matrix $\mathbf{P}_l^m(\mu)$ through convenient recursive relations is described in detail in Siewert [1982] and we refer the reader to this reference for more information. The second matrix $\mathbf{B}_l$ is written as

$$\mathbf{B}_l = \begin{bmatrix} \beta_l & \gamma_l & 0 & 0 \\ \gamma_l & \alpha_l & 0 & 0 \\ 0 & 0 & \zeta_l & -\varepsilon_l \\ 0 & 0 & \varepsilon_l & \delta_l \end{bmatrix}, \tag{4.11}$$

where the so-called "Greek constants" $\{\alpha_l, \beta_l, \gamma_l, \delta_l, \varepsilon_l, \zeta_l\}$ define the scattering law and follow from the expansion of the scattering phase matrix, valid for mediums that are macroscopically isotropic and mirror-symmetric with ensembles of randomly oriented particles having at least one plane of symmetry,

$$\mathbf{F}(\Theta) = \begin{bmatrix} a_1(\Theta) & b_1(\Theta) & 0 & 0 \\ b_1(\Theta) & a_2(\Theta) & 0 & 0 \\ 0 & 0 & a_3(\Theta) & b_2(\Theta) \\ 0 & 0 & -b_2(\Theta) & a_4(\Theta) \end{bmatrix}, \tag{4.12}$$

in terms of generalized spherical functions,

$$\beta_l = \frac{2l+1}{2} \int_0^\pi a_1(\Theta) P_{00}^l(\cos\Theta) \sin\Theta d\Theta, \tag{4.13}$$

$$\alpha_l + \zeta_l = \frac{2l+1}{2} \int_0^\pi \left[a_2(\Theta) + a_3(\Theta)\right] P_{22}^l(\cos\Theta) \sin\Theta d\Theta, \tag{4.14}$$

$$\alpha_l - \zeta_l = \frac{2l+1}{2} \int_0^\pi \left[a_2(\Theta) - a_3(\Theta)\right] P_{2-2}^l(\cos\Theta) \sin\Theta d\Theta, \tag{4.15}$$

$$\delta_l = \frac{2l+1}{2} \int_0^\pi a_4(\Theta) P_{00}^l(\cos\Theta) \sin\Theta d\Theta, \tag{4.16}$$

$$\gamma_l = -\frac{2l+1}{2} \int_0^\pi b_1(\Theta) P_{20}^l(\cos\Theta) \sin\Theta d\Theta, \tag{4.17}$$

$$\varepsilon_l = -\frac{2l+1}{2} \int_0^\pi b_2(\Theta) P_{20}^l(\cos\Theta) \sin\Theta d\Theta. \tag{4.18}$$

The phase matrix $\mathbf{P}(\mu, \phi, \mu'\phi')$ is related to the scattering phase matrix $\mathbf{F}(\Theta)$ with

$$\mathbf{P}(\mu, \phi, \mu'\phi') = \mathbf{L}(\pi - \chi_2)\mathbf{F}(\Theta)\mathbf{L}(-\chi_1), \tag{4.19}$$

where the rotation matrices are defined as

$$\mathbf{L}(\chi) = \begin{bmatrix} 1 & 0 & 0 & 0 \\ 0 & \cos 2\chi & \sin 2\chi & 0 \\ 0 & -\sin 2\chi & \cos 2\chi & 0 \\ 0 & 0 & 0 & 1 \end{bmatrix} \tag{4.20}$$

and χ_i is positive in the counter clockwise direction when looking in the direction of propagation. For definitions of the angles of rotation χ_i and more details see Hovenier et al. [2004].

The individual azimuthal components of the radiative transfer equation are given by

$$\mu \frac{d\mathbf{I}^m(\tau,\mu)}{d\tau} = \mathbf{I}^m(\tau,\mu) - (1+\delta_{0,m})\frac{\omega}{4}\int_{-1}^{1}\mathbf{P}^m(\mu,\mu')\mathbf{I}^m(\tau,\mu')d\mu' - \mathbf{\Sigma}^m(\tau,\mu), \tag{4.21}$$

where

$$\mathbf{\Sigma}^m(\tau,\mu) = \frac{\omega}{4\pi}\mathbf{P}^m(\mu,-\mu_0)\mathbf{F}_0 e^{-\tau/\mu_0} + \delta_{0,m}(1-\omega)\mathbf{B}(T). \tag{4.22}$$

To simplify notation, hereafter the superscript m will be suppressed in most cases with the dependence on azimuthal mode assumed.

4.2.2 Matrix formulation

If the integration over zenith angle is replaced by a quadrature scheme in which n quadrature points μ_i and associated weights w_i are defined for the integration interval $[0,1]$ in the downward and upward hemispheres separately then Eq. (4.21) may be written as two equations for upward and downward radiation, respectively, given by

$$+\frac{d\tilde{\mathbf{I}}^+(\tau)}{d\tau} = \tilde{\mathbf{M}}^{-1}\tilde{\mathbf{I}}^+(\tau) - (1+\delta_{0,m})\frac{\omega}{4}(\tilde{\mathbf{M}}^{-1}\tilde{\mathbf{P}}^{++}\tilde{\mathbf{W}}\tilde{\mathbf{I}}^+(\tau) + \tilde{\mathbf{M}}^{-1}\tilde{\mathbf{P}}^{+-}\tilde{\mathbf{W}}\tilde{\mathbf{I}}^-(\tau)) - \tilde{\mathbf{\Sigma}}^+(\tau), \tag{4.23}$$

$$-\frac{d\tilde{\mathbf{I}}^-(\tau)}{d\tau} = \tilde{\mathbf{M}}^{-1}\tilde{\mathbf{I}}^-(\tau) - (1+\delta_{0,m})\frac{\omega}{4}(\tilde{\mathbf{M}}^{-1}\tilde{\mathbf{P}}^{-+}\tilde{\mathbf{W}}\tilde{\mathbf{I}}^+(\tau) + \tilde{\mathbf{M}}^{-1}\tilde{\mathbf{P}}^{--}\tilde{\mathbf{W}}\tilde{\mathbf{I}}^-(\tau)) - \tilde{\mathbf{\Sigma}}^-(\tau), \tag{4.24}$$

where a '+' sign indicates upward values (positive values of μ) and a '−' sign indicates downward values (negative values of μ). To maintain a clear distinction in this equation and in the equations that follow, 4×1 vectors and 4×4 matrices are written in bold typeface while $4n\times 1$ vectors and $4n\times 4$, $4n\times 4n$, and $8n\times 8n$ matrices are written in bold typeface with a tilde symbol. The source term is given by

$$\tilde{\mathbf{\Sigma}}^{\pm}(\tau) = \frac{\omega}{4\pi}\tilde{\mathbf{M}}^{-1}\tilde{\mathbf{P}}_0^{\pm}\mathbf{F_0}e^{-\tau/\mu_0} + \delta_{0,m}(1-\omega)\tilde{\mathbf{M}}^{-1}\tilde{\mathbf{B}}(T), \tag{4.25}$$

and

$$\tilde{\mathbf{I}}^{\pm}(\tau) = \left[\mathbf{I}^{\pm}(\tau,\mu_1), \mathbf{I}^{\pm}(\tau,\mu_2), \ldots, \mathbf{I}^{\pm}(\tau,\mu_n)\right]^T, \tag{4.26}$$

$$\tilde{\mathbf{M}} = \mathrm{diag}\left[\mu_1\mathbf{E}, \mu_2\mathbf{E}, \ldots, \mu_n\mathbf{E}\right], \tag{4.27}$$

$$\tilde{\mathbf{W}} = \mathrm{diag}\left[w_1\mathbf{E}, w_2\mathbf{E}, \ldots, w_n\mathbf{E}\right], \tag{4.28}$$

$$\tilde{\mathbf{B}}(T) = \left[\mathbf{B}(T), \ldots, \mathbf{B}(T)\right]^T, \tag{4.29}$$

where $\mathbf{E}$ is the 4×4 identity matrix. The $4n \times 4n$ $\tilde{\mathbf{P}}$ matrices contain the individual 4×4 phase matrices and can be conveniently computed using a compact formulation given by

$$\tilde{\mathbf{P}}^{++} = \begin{bmatrix} \mathbf{P}(\mu_1,\mu_1) & \cdots & \mathbf{P}(\mu_1,\mu_n) \\ \vdots & & \vdots \\ \mathbf{P}(\mu_n,\mu_1) & \cdots & \mathbf{P}(\mu_n,\mu_n) \end{bmatrix} = (2-\delta_{0,m}) \sum_{l=m}^{2n-1} \tilde{\mathbf{P}}(l,m)\mathbf{B}_l\tilde{\mathbf{P}}^T(l,m), \tag{4.30}$$

$$\tilde{\mathbf{P}}^{--} = \begin{bmatrix} \mathbf{P}(-\mu_1,-\mu_1) & \cdots & \mathbf{P}(-\mu_1,-\mu_n) \\ \vdots & & \vdots \\ \mathbf{P}(-\mu_n,-\mu_1) & \cdots & \mathbf{P}(-\mu_n,-\mu_n) \end{bmatrix} = (2-\delta_{0,m}) \sum_{l=m}^{2n-1} \tilde{\mathbf{D}}\tilde{\mathbf{P}}(l,m)\mathbf{D}\mathbf{B}_l\mathbf{D}\tilde{\mathbf{P}}^T(l,m)\tilde{\mathbf{D}}, \tag{4.31}$$

$$\tilde{\mathbf{P}}^{-+} = \begin{bmatrix} \mathbf{P}(-\mu_1,\mu_1) & \cdots & \mathbf{P}(-\mu_1,\mu_n) \\ \vdots & & \vdots \\ \mathbf{P}(-\mu_n,\mu_1) & \cdots & \mathbf{P}(-\mu_n,\mu_n) \end{bmatrix} = (2-\delta_{0,m}) \sum_{l=m}^{2n-1} (-1)^{l-m}\tilde{\mathbf{D}}\tilde{\mathbf{P}}(l,m)\mathbf{D}\mathbf{B}_l\tilde{\mathbf{P}}^T(l,m), \tag{4.32}$$

$$\tilde{\mathbf{P}}^{+-} = \begin{bmatrix} \mathbf{P}(\mu_1,-\mu_1) & \cdots & \mathbf{P}(\mu_1,-\mu_n) \\ \vdots & & \vdots \\ \mathbf{P}(\mu_n,-\mu_1) & \cdots & \mathbf{P}(\mu_n,-\mu_n) \end{bmatrix} = (2-\delta_{0,m}) \sum_{l=m}^{2n-1} (-1)^{l-m}\tilde{\mathbf{P}}(l,m)\mathbf{B}_l\mathbf{D}\tilde{\mathbf{P}}^T(l,m)\tilde{\mathbf{D}}, \tag{4.33}$$

and for the solar source term by

$$\tilde{\mathbf{P}}_0^+ = \begin{bmatrix} \mathbf{P}(\mu_1, -\mu_0) \\ \vdots \\ \mathbf{P}(\mu_n, -\mu_0) \end{bmatrix} = (2 - \delta_{0,m}) \sum_{l=m}^{2n-1} \tilde{\mathbf{P}}(l,m)\mathbf{B}_l \mathbf{P}_l^m(\mu_0), \tag{4.34}$$

$$\tilde{\mathbf{P}}_0^- = \begin{bmatrix} \mathbf{P}(-\mu_1, -\mu_0) \\ \vdots \\ \mathbf{P}(-\mu_n, -\mu_0) \end{bmatrix} = (2 - \delta_{0,m}) \sum_{l=m}^{2n-1} \tilde{\mathbf{D}}\tilde{\mathbf{P}}(l,m)\mathbf{D}\mathbf{B}_l \mathbf{P}_l^m(\mu_0), \tag{4.35}$$

where

$$\tilde{\mathbf{D}} = \mathrm{diag}\left[\mathbf{D}, \ldots, \mathbf{D}\right], \tag{4.36}$$

$$\tilde{\mathbf{P}}(l,m) = \left[\mathbf{P}_l^m(\mu_1), \mathbf{P}_l^m(\mu_2), \ldots, \mathbf{P}_l^m(\mu_n)\right]^T, \tag{4.37}$$

and $\mu_1 \ldots \mu_n$ are the quadrature points. Eqs. (4.30) through (4.35) take advantage of the symmetry relation for generalized spherical functions [Gel'fand et al., 1963] given by

$$\mathbf{P}_{m,n}^l(\mu) = \mathbf{P}_{n,m}^l(\mu) = \mathbf{P}_{-m,-n}^l(\mu), \tag{4.38}$$

which leads to

$$\mathbf{P}_l^m(-\mu) = (-1)^{l-m}\mathbf{D}\mathbf{P}_l^m(\mu)\mathbf{D}, \tag{4.39}$$

and, with the fact that $\mathbf{B}_l = \mathbf{D}\mathbf{B}_l\mathbf{D}$ and $\mathbf{D}\mathbf{D} = \mathbf{E}$, leads to

$$\tilde{\mathbf{P}}(l,m,-\mu) = \tilde{\mathbf{D}}\tilde{\mathbf{P}}(l,m,+\mu)\tilde{\mathbf{D}} \tag{4.40}$$

and consequently to

$$\tilde{\mathbf{P}}^{--} = \tilde{\mathbf{D}}\tilde{\mathbf{P}}^{++}\tilde{\mathbf{D}}, \tag{4.41}$$

$$\tilde{\mathbf{P}}^{+-} = \tilde{\mathbf{D}}\tilde{\mathbf{P}}^{-+}\tilde{\mathbf{D}}. \tag{4.42}$$

The symmetry relation given in Eqs. (4.41) and(4.42) represents the third of the three basic relations introduced by Hovenier [1969]: changing the sign of μ and μ' simultaneously, given by

$$\mathbf{P}(-\mu,-\mu',\phi-\phi') = \mathbf{D}\mathbf{P}(\mu,\mu',\phi-\phi')\mathbf{D}. \tag{4.43}$$

At this point it is convenient to introduce the *local* reflectance and transmittance matrices given as

$$\tilde{\mathbf{r}}^{+} = -(1+\delta_{0,m})\frac{\omega}{4}\tilde{\mathbf{M}}^{-1}\tilde{\mathbf{P}}^{-+}\tilde{\mathbf{W}} \tag{4.44}$$

and

$$\tilde{\mathbf{t}}^{+} = -\tilde{\mathbf{M}}^{-1} + (1+\delta_{0,m})\frac{\omega}{4}\tilde{\mathbf{M}}^{-1}\tilde{\mathbf{P}}^{++}\tilde{\mathbf{W}}, \tag{4.45}$$

respectively, for incidence from below (upward radiation) while for incidence from above (downward radiation) the symmetry relations given in Eqs. (4.41) and (4.42) lead to

$$\tilde{\mathbf{r}}^{-} = \tilde{\mathbf{D}}\tilde{\mathbf{r}}^{+}\tilde{\mathbf{D}}, \tag{4.46}$$

$$\tilde{\mathbf{t}}^{-} = \tilde{\mathbf{D}}\tilde{\mathbf{t}}^{+}\tilde{\mathbf{D}}. \tag{4.47}$$

With the upward and downward *local* reflectance and transmittance matrices defined, Eqs. (4.23) and (4.24) may be combined into a single equation written as

$$\frac{d}{d\tau}\begin{bmatrix}\tilde{\mathbf{I}}^{-}\\ \tilde{\mathbf{I}}^{+}\end{bmatrix} = \begin{bmatrix}\tilde{\mathbf{t}}^{-} & -\tilde{\mathbf{r}}^{+}\\ \tilde{\mathbf{r}}^{-} & -\tilde{\mathbf{t}}^{+}\end{bmatrix}\begin{bmatrix}\tilde{\mathbf{I}}^{-}\\ \tilde{\mathbf{I}}^{+}\end{bmatrix} + \begin{bmatrix}\tilde{\mathbf{\Sigma}}^{-}\\ \tilde{\mathbf{\Sigma}}^{+}\end{bmatrix}. \tag{4.48}$$

Eq. (4.48) constitutes a system of $8n$ coupled linear first-order differential equations for the initial value problem for which the general solution for a homogeneous layer of optical thickness x is

$$\begin{bmatrix}\tilde{\mathbf{I}}^{-}(x)\\ \tilde{\mathbf{I}}^{+}(x)\end{bmatrix} = e^{\tilde{\mathbf{A}}x}\begin{bmatrix}\tilde{\mathbf{I}}^{-}(0)\\ \tilde{\mathbf{I}}^{+}(0)\end{bmatrix} + \int_0^x e^{\tilde{\mathbf{A}}(x-x')}\begin{bmatrix}\tilde{\mathbf{\Sigma}}^{-}\\ \tilde{\mathbf{\Sigma}}^{+}\end{bmatrix}dx', \tag{4.49}$$

where the matrix exponential is the integrating factor, known as the fundamental solution, and the attenuation matrix $\tilde{\mathbf{A}}$ is given by

$$\tilde{\mathbf{A}} = \begin{bmatrix} \tilde{\mathbf{t}}^{-} & -\tilde{\mathbf{r}}^{+} \\ \tilde{\mathbf{r}}^{-} & -\tilde{\mathbf{t}}^{+} \end{bmatrix}. \tag{4.50}$$

The first term on the right hand side of Eq. (4.49) represents the homogeneous solution while the second term represents the particular solution.

If we consider the interaction principle, the upward radiance at the top of the layer $\tilde{\mathbf{I}}^{+}(0)$ and the downward radiance at the bottom of the layer $\tilde{\mathbf{I}}^{-}(x)$ can be written as the solution of the two-point boundary value problem with

$$\tilde{\mathbf{I}}^{+}(0) = \tilde{\mathbf{T}}^{+}\tilde{\mathbf{I}}^{+}(x) + \tilde{\mathbf{R}}^{-}\tilde{\mathbf{I}}^{-}(0) + \tilde{\mathbf{S}}^{+}, \tag{4.51}$$

$$\tilde{\mathbf{I}}^{-}(x) = \tilde{\mathbf{R}}^{+}\mathbf{I}^{+}(x) + \mathbf{T}^{-}\tilde{\mathbf{I}}^{-}(0) + \tilde{\mathbf{S}}^{-}, \tag{4.52}$$

where $\tilde{\mathbf{I}}^{-}(0)$ and $\tilde{\mathbf{I}}^{+}(x)$ are the boundary conditions at the top and bottom of the layer, $\tilde{\mathbf{R}}^{+}$ and $\tilde{\mathbf{T}}^{+}$ are the *global* reflection and transmission matrices for incidence from below (upward radiation), $\tilde{\mathbf{R}}^{-}$ and $\tilde{\mathbf{T}}^{-}$ are for incidence from above (downward radiation), and the particular solution source vectors are

$$\tilde{\mathbf{S}}^{+} = -\tilde{\mathbf{R}}^{-}\tilde{\mathbf{F}}^{-} - \tilde{\mathbf{T}}^{+}\tilde{\mathbf{F}}^{+}\mathcal{T} + \tilde{\mathbf{F}}^{+}, \tag{4.53}$$

$$\tilde{\mathbf{S}}^{-} = -\tilde{\mathbf{T}}^{-}\tilde{\mathbf{F}}^{-} - \tilde{\mathbf{R}}^{+}\tilde{\mathbf{F}}^{+}\mathcal{T} + \tilde{\mathbf{F}}^{-}\mathcal{T}, \tag{4.54}$$

with $\mathcal{T}$ as the layer transmittance e^{-x/μ_0}. Now by ignoring the particular solution and using equations 4.51 and 4.52 to solve for $\tilde{\mathbf{I}}^{+}(x)$ and $\tilde{\mathbf{I}}^{-}(x)$ in terms of $\tilde{\mathbf{I}}^{+}(0)$ and $\tilde{\mathbf{I}}^{-}(0)$ we get

$$\begin{bmatrix} \tilde{\mathbf{I}}^{-}(x) \\ \tilde{\mathbf{I}}^{+}(x) \end{bmatrix} = \begin{bmatrix} \tilde{\mathbf{T}}^{-} - \tilde{\mathbf{R}}^{+}(\tilde{\mathbf{T}}^{+})^{-1}\tilde{\mathbf{R}}^{-} & \tilde{\mathbf{R}}^{+}(\tilde{\mathbf{T}}^{+})^{-1} \\ -(\tilde{\mathbf{T}}^{+})^{-1}\tilde{\mathbf{R}}^{-} & (\tilde{\mathbf{T}}^{+})^{-1} \end{bmatrix} \begin{bmatrix} \tilde{\mathbf{I}}^{-}(0) \\ \tilde{\mathbf{I}}^{+}(0) \end{bmatrix}. \tag{4.55}$$

By comparing Eq. (4.55) to the homogeneous part of Eq. (4.49) it is apparent that the matrix exponential is identified as

$$e^{\tilde{\mathbf{A}}x} = \begin{bmatrix} \tilde{\mathbf{T}}^- - \tilde{\mathbf{R}}^+(\tilde{\mathbf{T}}^+)^{-1}\tilde{\mathbf{R}}^- & \tilde{\mathbf{R}}^+(\tilde{\mathbf{T}}^+)^{-1} \\ -(\tilde{\mathbf{T}}^+)^{-1}\tilde{\mathbf{R}}^- & (\tilde{\mathbf{T}}^+)^{-1} \end{bmatrix}, \tag{4.56}$$

from which the global reflection and transmission matrices $\tilde{\mathbf{R}}^+$, $\tilde{\mathbf{T}}^+$, $\tilde{\mathbf{R}}^-$, and $\tilde{\mathbf{T}}^-$ can be computed. The use of the Padé approximation to evaluate these matrices is the primary subject of this paper. The evaluation of the source vectors $\tilde{\mathbf{F}}^{\pm}$ requires the solution to a linear system of order $8n$ for which a reduction to order $4n$ is possible. This is discussed in detail in Spurr [2006] and will not be addressed further here.

4.2.3 Solution methodology

In section 2.5 of MG2010 we discussed the use of the Padé approximation to solve for $\mathbf{R}$ and $\mathbf{T}$ followed by the use of scaling and doubling for solution accuracy. It turns out that with a few minor modifications the same solution methodology can be used for the vector case outlined in the previous section. Since this methodology is covered in detail in MG2010 we refer the reader to that paper for more information while here we will discuss one symmetry relation and one similarity transformation required for the vector case.

For the scalar case $\mathbf{R}$ and $\mathbf{T}$ are invariant with respect to direction of incidence (up or down). In the vector case $\mathbf{R}$ and $\mathbf{T}$ do not exhibit this invariance, however, the upward and downward operators can be related by the relations introduced in Eqs. (4.41) and (4.42). As a result, $\mathbf{R}$ and $\mathbf{T}$ for only one direction need to be computed while $\mathbf{R}$ and $\mathbf{T}$ for the other direction follow from symmetry. This is reflected in the equations presented below, where all computations are done for upward quantities only.

In MG2010 two similarity transformations were introduced that 1) transform the matrix formulation into a symmetric form (equations 21 and 22) and 2) reduce the order of the problem from $2n$ to n (equation 44). The symmetric form is used to reduce the computation required to compute powers of $\mathbf{A}x$ through "equality by transposition", specifically of the diagonal blocks of equation 47 in MG2010, that is $(\mathbf{xy})^i = \left[(\mathbf{yx})^i\right]^T$. In addition, with the symmetric form, matrix multiplication

in some cases results in a symmetric matrix in which case the number of computations required can be reduced to just over half of that required in the general case. This operation was referred to as "symmetric matrix multiplication" in MG2010. For the vector case the transformation to the symmetric form is achieved with

$$\tilde{\mathbf{r}}^{+\prime} = \tilde{\boldsymbol{\alpha}}\tilde{\mathbf{r}}^{+}\tilde{\boldsymbol{\alpha}}^{-1}, \tag{4.57}$$
$$\tilde{\mathbf{t}}^{+\prime} = \tilde{\boldsymbol{\alpha}}\tilde{\mathbf{t}}^{+}\tilde{\boldsymbol{\alpha}}^{-1},$$

and likewise for $\tilde{\mathbf{r}}^{-\prime}$ and $\tilde{\mathbf{t}}^{-\prime}$, where

$$\tilde{\boldsymbol{\alpha}} = \sqrt{\tilde{\mathbf{W}}\tilde{\mathbf{M}}}, \tag{4.58}$$

which results in a modified form of $\tilde{\mathbf{A}}$ called $\tilde{\mathbf{A}}'$. The result of the transformation is the second of the three basic symmetry relations introduced by Hovenier [1969], interchanging μ and μ', given by

$$\mathbf{P}(\mu', \mu, \phi - \phi') = \mathbf{G}\mathbf{P}(\mu, \mu', \phi - \phi')\mathbf{G}, \tag{4.59}$$

where $\mathbf{G} = \text{diag}[1, 1, -1, 1]$, which may be applied to implement "equality by transposition" and "symmetric matrix multiplication" for the vector solution. This is done by noting the following relation relevant to the two cases:

$$\tilde{\mathbf{Y}} = (\tilde{\mathbf{G}}\tilde{\mathbf{X}}\tilde{\mathbf{G}})^{T(4)}, \tag{4.60}$$

where $T(4)$ refers to 4×4 block transposition and $\tilde{\mathbf{G}} = \text{diag}[\mathbf{G}, \ldots, \mathbf{G}]$.

The second similarity transformation introduced in MG2010 (equation 44) is used to halve the order of the solution methodology from $2n$ to n. This is possible due to the block asymmetric structure of the $\mathbf{A}$ matrix in the scalar case. In the vector case, as presented in the previous section, the matrix $\tilde{\mathbf{A}}$ does not possess this symmetry but can be transformed into a matrix that allows equation 44 from MG2010 to be applied leading to a reduction in order of $8n$ to $4n$. This is possible in part by the symmetry expressed by Eqs. (4.41) and (4.42) and noting that $\tilde{\mathbf{A}}'$ can be written as

$$\tilde{\mathbf{A}}' = \begin{bmatrix} \tilde{\mathbf{D}}\tilde{\mathbf{t}}^{+\prime}\tilde{\mathbf{D}} & -\tilde{\mathbf{r}}^{+\prime} \\ \tilde{\mathbf{D}}\tilde{\mathbf{r}}^{+\prime}\tilde{\mathbf{D}} & -\tilde{\mathbf{t}}^{+\prime} \end{bmatrix}. \tag{4.61}$$

The transformation is given by

$$\tilde{\mathbf{A}}'' = \tilde{\boldsymbol{\gamma}}\tilde{\mathbf{A}}'\tilde{\boldsymbol{\gamma}}, \tag{4.62}$$

where $\tilde{\boldsymbol{\gamma}} = \text{diag}[\tilde{\mathbf{D}}, \tilde{\mathbf{E}}]$, which results in

$$\tilde{\mathbf{A}}'' = \begin{bmatrix} \tilde{\mathbf{t}}^{+\prime\prime} & -\tilde{\mathbf{D}}\tilde{\mathbf{r}}^{+\prime\prime} \\ \tilde{\mathbf{D}}\tilde{\mathbf{r}}^{+\prime\prime} & -\tilde{\mathbf{t}}^{+\prime\prime} \end{bmatrix}, \tag{4.63}$$

which has a block asymmetric form. Finally, the second similarity transformation introduced in MG2010 (equation 44) may be applied and for completeness is listed here as

$$\tilde{\mathbf{A}}''' = \tilde{\boldsymbol{\beta}}^{-1}\tilde{\mathbf{A}}''\tilde{\boldsymbol{\beta}}, \tag{4.64}$$

where

$$\boldsymbol{\beta} = \begin{bmatrix} \mathbf{E} & \mathbf{E} \\ \mathbf{E} & -\mathbf{E} \end{bmatrix} \quad \text{and} \quad \boldsymbol{\beta}^{-1} = \frac{1}{2}\begin{bmatrix} \mathbf{E} & \mathbf{E} \\ \mathbf{E} & -\mathbf{E} \end{bmatrix}. \tag{4.65}$$

At this point the solution methodology in section 2.5 of MG2010 can proceed unmodified. The accuracy of the method is determined by the order of the Padé approximation r and the number of doublings s used. A method for choosing the optimal (r, s) pair was outlined in MG2010 and will be used "as is" for VPARTM as well.

Finally, inversion of these transformations proceeds as follows

$$\tilde{\mathbf{R}}^{+\prime\prime} = \tilde{\boldsymbol{\beta}}^{-1}\tilde{\mathbf{R}}^{+\prime\prime\prime}\tilde{\boldsymbol{\beta}}, \tag{4.66}$$
$$\tilde{\mathbf{T}}^{+\prime\prime} = \tilde{\boldsymbol{\beta}}^{-1}\tilde{\mathbf{T}}^{+\prime\prime\prime}\tilde{\boldsymbol{\beta}},$$

$$\tilde{\mathbf{R}}^{+\prime} = \tilde{\boldsymbol{\gamma}}\tilde{\mathbf{R}}^{+\prime\prime}\tilde{\boldsymbol{\gamma}}, \tag{4.67}$$

$$\tilde{\mathbf{T}}^{+\prime} = \tilde{\mathbf{T}}^{+\prime\prime}, \tag{4.68}$$

$$\tilde{\mathbf{R}}^{+} = \tilde{\boldsymbol{\alpha}}^{-1}\tilde{\mathbf{R}}^{+\prime}\tilde{\boldsymbol{\alpha}}, \tag{4.69}$$

$$\tilde{\mathbf{T}}^{+} = \tilde{\boldsymbol{\alpha}}^{-1}\tilde{\mathbf{T}}^{+\prime}\tilde{\boldsymbol{\alpha}}. \tag{4.70}$$

Once $\tilde{\mathbf{R}}^{+}$, $\tilde{\mathbf{T}}^{+}$ and $\tilde{\mathbf{R}}^{-}$, $\tilde{\mathbf{T}}^{-}$ have been obtained for each layer and for an individual Fourier component the solution for the radiance emerging from the multilayer atmosphere with a lower surface boundary can obtained for the Fourier component with the adding method and the interaction principle details of which are given in MG2010 and references therein. Finally, the individual Fourier components may be combined to get the full solution using Eq. (4.3) with $M = 2n - 1$. In practice, it is common to truncate the Fourier series based on some user prescribed convergence criterion.

4.3 Implementation details

Both the scalar and vector implementations are distributed together and share as much code as possible. As a result, the same features that we listed in MG2010 for PARTM are available for VPARTM including a choice of (standard) Gauss-Legendre or double Gauss-Legendre quadrature, Wiscombe delta-M scaling [Wiscombe, 1977], the Nakajima-Tanaka TMS correction [Nakajima and Tanaka, 1988], and the pseudo-spherical approximation [Dahlback and Stamnes, 1991]. For the surface boundary a generalized BRDF implementation including several common BRDF kernels is included [Spurr, 2004]. A full layer/stack saving feature as described in Gabriel et al. [2006] is also part of the implementation. All these features are optional and controlled by boolean input values. Output is available at TOA and BOA and at the layer boundaries in between with an efficient implementation when only TOA upward or BOA downward output is required (see MG2010). Output at arbitrary view angles is implemented by the inclusion of nodes with zero weights, so called "dummy nodes", in the quadrature scheme [Chalhoub and Garcia, 2000]. The implementation makes extensive use of BLAS [Dongarra et al., 1990] and LAPACK [Anderson et al., 1999] calls providing the potential for increased performance when linked with hardware optimized BLAS libraries. Finally, the current scalar/vector implementation is fully linearized, capable of analytically computing radiance derivatives with respect to atmospheric and surface input parameters.

4.4 Timing comparisons

In this section we present timing comparisons relative to the Vector Linearized Discrete Ordinate Radiative Transfer (VLIDORT) model version 2.3 [Spurr, 2006]. VLIDORT is a general purpose plane parallel vector radiative transfer model appropriate for multiple scattering atmospheres with solar and thermal sources and is capable of computing both the vector radiance and its derivatives with respect to atmospheric and surface parameters. VLIDORT is an accurate and efficient implementation and is widely used in the remote sensing community and is therefore an appropriate general benchmark. For all the cases presented in this section and section 4.5, for both VPARTM and VLIDORT, double Gaussian quadrature was used while Delta-M scaling and the Nakajima-Tanaka TMS correction were turned on. A solar source was included with the solar flux F_0 set to unity and the computation of radiance derivatives was turned off. It is also important to mention that the Fourier convergence in our VPARTM implementation is similar to that in VLIDORT and, as a result, in all tests the number of azimuthal terms computed are the same for both VLIDORT and VPARTM.

For timing comparisons relative to VLIDORT a speed-up factor f will be used defined as

$$f = \frac{t_{\text{VLIDORT}}}{t_{\text{VPARTM}}}, \tag{4.71}$$

where t_{VLIDORT} and t_{VPARTM} are the times required for VLIDORT and VPARTM, respectively. All timing tests were performed on an computer with an Intel(R) Core(TM)2 Duo E8600 @ 3.33GHz CPU running GNU/Linux (kernel version 2.6.27). The VPARTM and VLIDORT codes were compiled with the GNU Compiler Collection (GCC) 4.6.3 and linked with reference (unoptimized) BLAS and LAPACK (version 3.4.1) libraries from http://www.netlib.org. To average out OS scheduling variations the timing tests were performed not for a single call but for a number of calls. The number chosen was the number of VLIDORT calls required to exceed a time of 20 s for each test.

It is important to note that VLIDORT uses static allocation for internal arrays, the size of which are determined at compile time. As a result, it suffers from inefficient use of cache memory when compiled to handle large sizes but is used for smaller sizes. This is especially the case for the

Table 4.1: Speed-up factor f for several values of n for a single layer with no lower boundary, where $(r, s) = (5, 0)$.

n	2	4	6	8	12	16	24	32	40	48	56	64
f_I	1.28	1.99	2.37	2.68	3.01	3.37	4.02	4.02	3.83	3.57	3.39	3.50

number of hemispherical streams and the number of layers. This is due to poor spatial locality of reference. To alleviate this problem VLIDORT was recompiled for each test case using only the minimum array size requirements.

Table 4.1 lists the speed-up factors for several values of n to compute the vector radiance from a single layer with no lower boundary and a log-normal size distribution of "accumulation mode mineral dust" aerosol [d'Almeida et al., 1991] given by

$$n(r) = Cr^{-1} \exp\left[-\frac{(\ln r - \ln r_g)^2}{2 \ln^2 \sigma_g}\right], \tag{4.72}$$

where C is a normalization constant, $r_g = 0.39\,\mu\text{m}$, and $\sigma_g = 2.0$. The ensemble averaged scattering phase matrix Greek constants and single scattering albedo ω were computed using Mie theory at a wavelength of $0.55\,\mu\text{m}$ with a complex index of refraction $m_r + im_i = 1.53 + i0.0055$. The optical thickness was set to $x = 0.1$ and the incident and viewing geometry was set to $\theta_0 = 45°$, $\theta = 25°$, and $\phi - \phi_0 = 45°$. Given these parameters, values for r and s may be chosen using the look-up table approach described in MG2010. In this case we use table 3 of MG2010 built for a fractional difference, as defined by Eq. (4.74), of no greater than 10^{-4}. For all values of n the speed-up factors exceed unity, indicating a computational speed-up for VPARTM relative to VLIDORT. The speed-up factors start at a minimum of 1.28 for $n = 2$ and tend to increase with increasing n up to 4.02 at $n = 24$ after which they decrease a bit and tend to level off to 3.50 at $n = 64$. In theory, the computational burden for both solutions is $\text{O}(n^3)$. However, at lower values of n, program overhead, including n^2 operations, become more important lessening the relative differences in speed due to solution strategy alone. In contrast, for larger values of n, the n^3 operations related to the solution strategy dominate and therefore differences in the solutions themselves dominate the speed-up factors.

Table 4.2: Speed-up factor f as a function of the number of layers N_L, where no lower boundary is included and $n = 16$ and $(r, s) = (5, 0)$. Values are given for two cases: to compute TOA upward and BOA downward radiances (f_I) and to compute TOA upward radiances only ($f_{I,R}$).

N_L	1	2	4	8	16	32	64	128
f_I	3.37	2.85	2.82	2.89	2.95	2.90	2.89	2.89
$f_{I,R}$	3.30	3.24	3.37	3.51	3.63	3.58	3.58	3.57

Table 4.3: Speed-up factor f as a function of optical thickness x and the associated optimal (r, s) for a single layer with no lower boundary, where $n = 16$.

x	0.01	0.02	0.05	0.10	0.20	0.50	1.00	2.00	5.00	10.0	20.0	50.0	100.0
(r, s)	(2, 0)	(3, 0)	(5, 0)	(5, 0)	(5, 0)	(7, 0)	(9, 0)	(7, 1)	(7, 2)	(5, 3)	(5, 4)	(5, 5)	(5, 5)
f_I	3.94	3.56	3.37	3.37	3.37	3.14	2.98	2.56	2.16	1.94	1.75	1.63	1.51

-1in-1in

Speed-up factors as a function of the number of layers N_L are presented in table 4.2. The layers are identical and the optical and geometric inputs are the same as that used for table 4.1. As with table 4.1, no lower boundary is included and $r = 5$ and $s = 0$, while in this case $n = 16$. Speed-up factors are given for the computation of TOA upward ($\theta = 25°$) and BOA downward ($\theta = -25°$) radiance (f_I) and for the computation of the TOA upward radiance only $f_{I,R}$. It is apparent that VPARTM provides a significant improvement in speed for any number of layers. In theory, the computational burden for both methods should increase linearly with N_L and this is evident in the table as the factors starting with the first multilayer configuration ($N_L = 2$) remain relatively constant with N_L for f_I with and average of 2.88 and slightly increase with N_L for $f_{I,R}$ with an average of 3.50.

Speed-up factors as a function of optical thickness x are presented for a single layer in table 4.3. Except for x the optical and geometric inputs are the same as that used for table 4.1. As with table 4.1, no lower boundary is included, $n = 16$, and parameters r and s were chosen using the method described in MG2010 for a fractional difference accuracy of at least 10^{-4}. From the table, it is evident that VPARTM provides a significant speed improvement for all values x with speed-up factors decreasing with increasing x, as expected, from 3.94 at $x = 0.01$ to 1.51 at $x = 100.0$.

4.5 Numerical results

In this section we have chosen two practical examples to demonstrate the use of VPARTM, one for a range of wavelengths typically used to retrieve aerosol properties and one for an instrument similar to the 0.76-µm O_2 A-band spectrometers on the Greenhouse gases Observing SATellite (GOSAT, http://www.gosat.nies.go.jp/ index_e.html) and the Orbital Carbon Observatory 2 (OCO-2) [Crisp et al., 2004]. Results are presented for the intensity I and for the degree of polarization given by

$$P(0,\mu,\phi) = \frac{\sqrt{Q^2(0,\mu,\phi) + U^2(0,\mu,\phi) + V^2(0,\mu,\phi)}}{I(0,\mu,\phi)}. \tag{4.73}$$

In addition, fractional differences between VLIDORT and VPARTM are presented which are given by

$$\Delta(X) = \frac{X_{\text{VLIDORT}} - X_{\text{VPARTM}}}{X_{\text{VLIDORT}}}, \tag{4.74}$$

where X_{VLIDORT} and X_{VPARTM} are either $I(0,\mu,\phi)$ or $P(0,\mu,\phi)$ determined by VLIDORT and VPARTM, respectively.

Our first example involves a range of wavelengths typically used to retrieve aerosol properties including 0.469, 0.555, 0.645, 0.858, 1.240, 1.640, and 2.130 µm. The atmospheric profile for this example is the same as that used for the first example in MG2010. As a result, we refer the reader to that paper and references therein for details. In short, the profile is a 32 level mid-latitude summer atmosphere with aerosols corresponding to maritime pollution. The wavelengths used are assumed to be free of molecular absorption while the model optical property inputs include both molecular and Mie scattering components with a total aerosol optical thickness at 0.555 µm of 0.201. The surface is assumed to be ocean with both a specular and a Lambertian foam component.

In figures 4.1a and 4.1c TOA intensity $I(0,\mu,\phi)$ and degree of polarization $P(0,\mu,\phi)$ are plotted as a function of viewing zenith angle θ for each wavelength. The solar factor F_0 was set to unity while the solar zenith and relative azimuth angles were set to $\theta_0 = 45^\circ$ and $\phi - \phi_0 = 45^\circ$, respectively. In this case we have chosen a moderate number of streams with $2n = 32$. In figures 4.1b and 4.1d the associated fractional differences Δ between VLIDORT and VPARTM are shown. It is apparent that for all channels and view angles, for both $I(0,\mu,\phi)$ and $P(0,\mu,\phi)$, $|\Delta|$ is well below our accuracy requirement of 10^{-4} specified in MG2010. This suggests that VPARTM is a viable alternative even

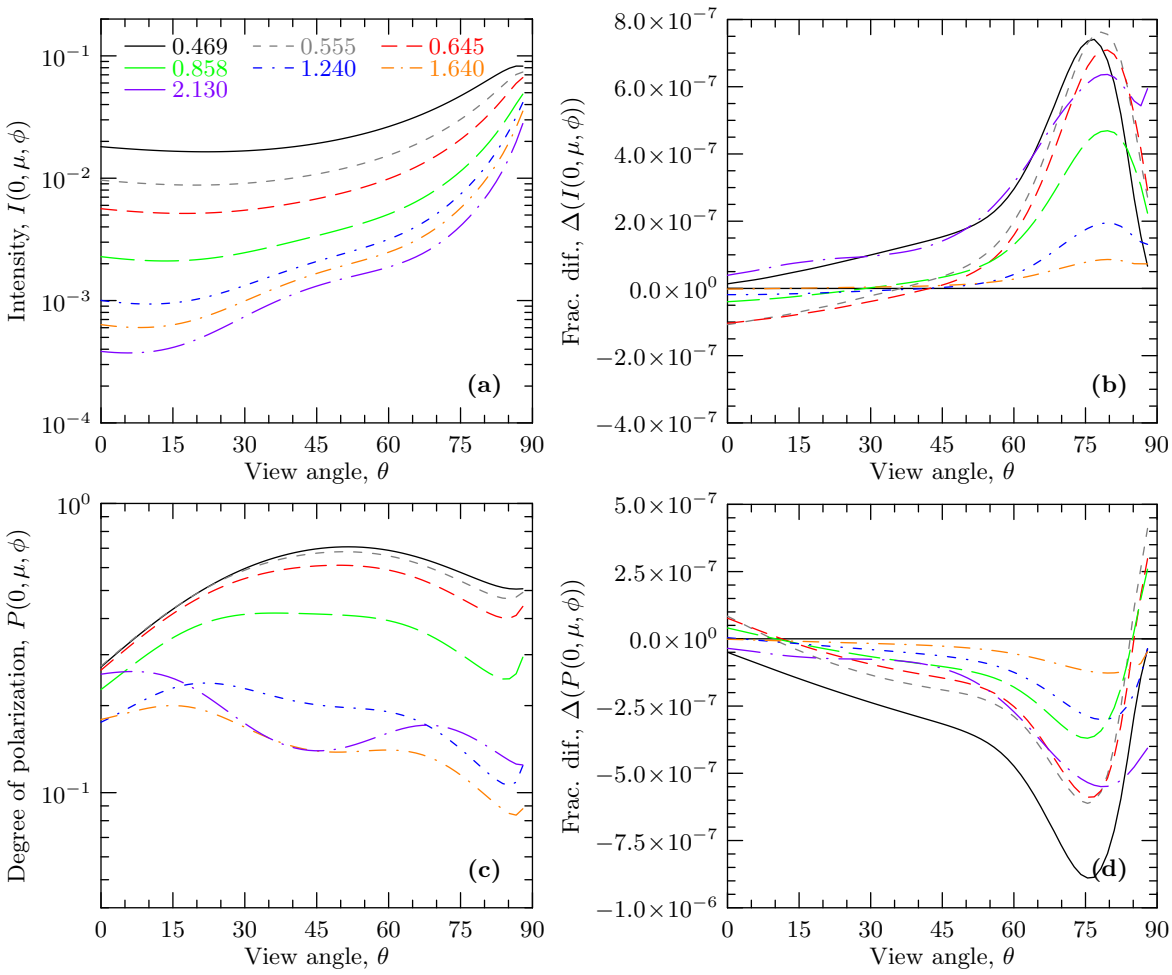

Figure 4.1: Model results for the first example described in the text. TOA upwelling intensity (a) and degree of polarization (c) and the corresponding fractional differences Δ between VLIDORT and VPARTM, (b) and (d), respectively, are given as a function of the view angle θ, where $\theta_0 = 45°$, $\phi - \phi_0 = 45°$, and $n = 16$. Seven wavelengths are plotted with the wavelength in microns (μm) indicated in the legend.

in cases where high accuracy is required. The speed-up factors associated with this example are 3.27 for the case when both TOA and BOA radiances are required and 4.16 for the case when only TOA radiances are required, both of which can be significant for moderate to high accuracy calculations. It is informative to look at table 6 in MG2010 which lists the number of times different values of (r, s) were used. It is not surprising that the majority of the calculations were performed with $(r, s) = (2, 0)$ as the majority of the layers are optically thin with only a molecular scattering component.

Our second example is applicable to hyperspectral instruments such as those on board GOSAT and OCO-2. Both satellites cover the 0.76-µm O_2 A-band and the 1.61- and 2.06-µm CO_2 bands, while additionally GOSAT covers a fourth band from 5.5 µm to 14.3 µm. For this example we will present results for the 0.76-µm O_2 A-band. GOSAT is capable of measuring polarization and while OCO-2 cannot measure polarization it is still sensitive to polarization and therefore a vector radiative transfer solution is essential for accurate retrievals.

The atmospheric profile used for this example is the same as that used for the GOSAT/OCO example in MG2010. As a result, we refer the reader to that paper and references therein for details. In short, the profile was generated using the OCO/GOSAT simulator [O'Brien et al., 2009] and is located over a forest and snow covered region in Norway at 66.93° latitude and 16.06° longitude representing winter conditions on 2007-12-23 at 12:13 PM. The profile has 61 levels with the meteorological conditions from ECMWF, clouds from CloudSat, aerosols from CALIPSO, CO_2 concentrations from PCTM, and surface proprieties from MODIS. Model optical property inputs include O_2 and CO_2 absorption, molecular scattering, and Mie scattering components while the surface is assumed to be Lambertian. The total optical thickness for clouds and aerosols in the profile is 0.42 and the surface albedo is 0.42.

In figure 4.2a and 4.2c TOA intensity $I(0, \mu, \phi)$ and degree of polarization $P(0, \mu, \phi)$ in the O_2 A-band are plotted as a function of wavenumber (cm^{-1}). Solar and viewing angles were chosen so that $\theta_0 = 45°$, $\theta = 25°$, and $\phi - \phi_0 = 45°$ while F_0 was set to unity for the entire spectrum. As in the first example the number of streams was set to $2n = 32$. In figures 4.2b and 4.2d the associated fractional differences Δ between VLIDORT and VPARTM are shown. For both $I(0, \mu, \phi)$ and $P(0, \mu, \phi)$, the absolute differences are lower in the continuum and higher in the center of strong absorption lines as expected. The maximum differences of $|\Delta[I(0, \mu, \phi)]| \approx 2.5 \times 10^{-7}$ and $|\Delta[P(0, \mu, \phi)]| \approx 2.0 \times 10^{-7}$ are well below our accuracy requirement of 10^{-4} specified in MG2010, indicating, as with the previous example, that VPARTM can be used for high accuracy calculations. The speed-up factors for this example are 3.04 for both TOA and BOA radiances and 3.93 for TOA radiances only. Compared to the first example the lower speed-up factors are primarily a result of the larger optical depths that occur deep within O_2 A-band absorption lines and indeed table 6 in MG2010 indicates that maximum values of $r = 13$ and $s = 4$ are used for some layers. This is in contrast to $(r, s) = (7, 0)$ being the most expensive layer calculation used in the first example.

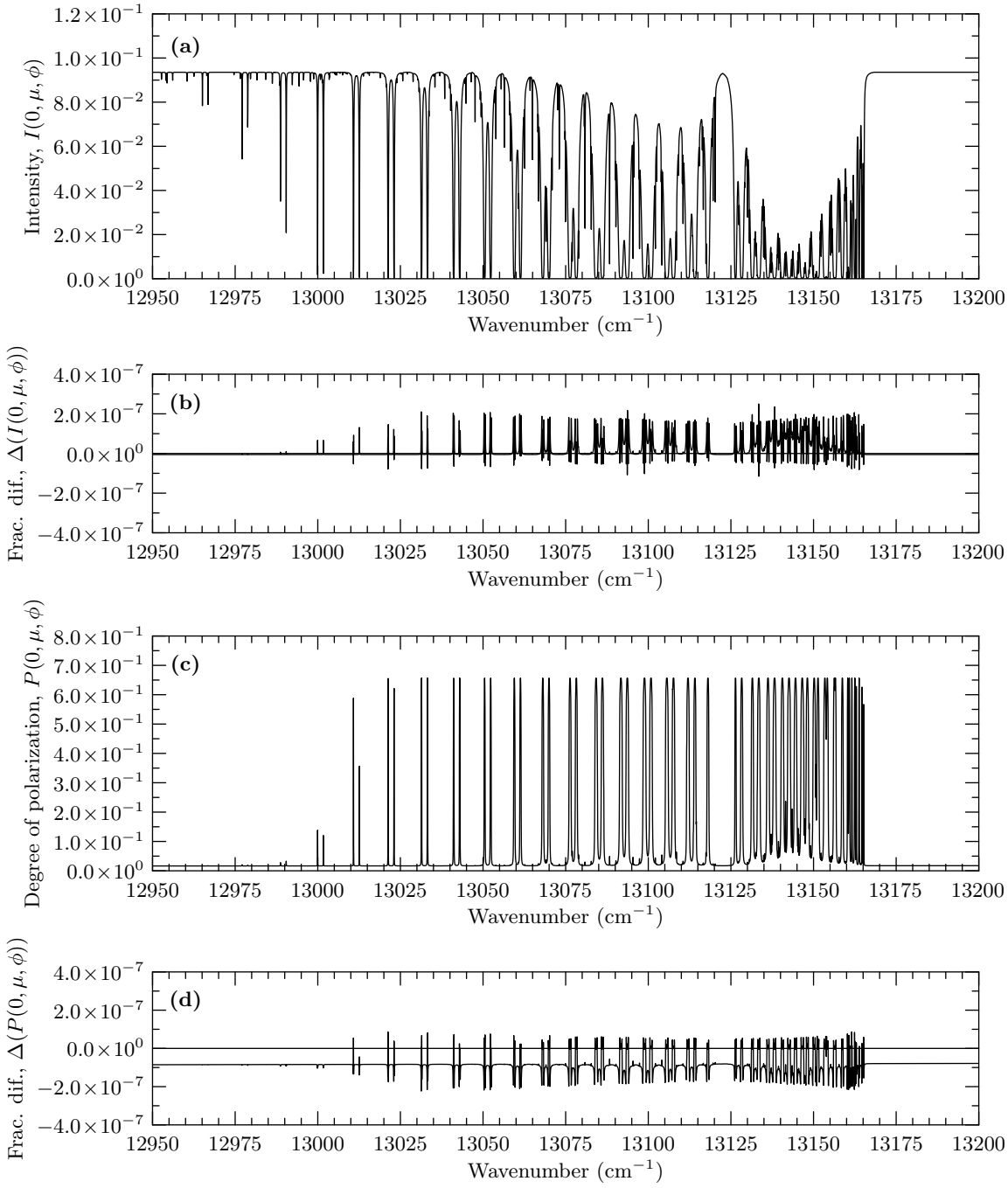

Figure 4.2: Model results for the 0.76-μm O_2 A-band for the second example described in the text. TOA upwelling intensity (a) and degree of polarization (c) and the corresponding fractional differences Δ between VLIDORT and VPARTM, (b) and (d), respectively, are given as a function of the wavenumber (cm^{-1}). The geometry is $\theta_0 = 45°$, $\theta = 25°$, and $\phi - \phi_0 = 45°$, while $n = 16$.

4.6 Concluding remarks

In this paper we have presented a vector radiative transfer solution for a multi-layer, multiple-scattering, plane-parallel atmosphere with solar scattering and thermal emission sources and a lower surface boundary characterized by a BRDF. The solution method, based on the Padé approximation, is an extension of the scalar solution outlined in MG2010 to the vector case. It is shown, that given the expansion of the phase matrix in terms of generalized spherical functions and a couple of additional matrix transformations, the solution can proceed as in MG2010, unmodified, taking advantage of the symmetric structure of the radiative transfer matrix formulation that was exploited in the scalar case.

Run time comparisons relative to the VLIDORT model as a function of the number of streams per hemisphere n for $(r, s) = (5, 0)$ show that VPARTM is faster than VLIDORT in all cases with speed-up factors f increasing from 1.28 at $n = 2$ to 4.02 at $n = 40$ and then decreasing and leveling off to 3.50 at $n = 64$. Run time comparisons as a function of the number of layers indicate a relatively stable speed up factor with an average of 2.88 when both TOA and BOA radiances are required and a slightly increasing factor with an average of 3.50 when only TOA (or analogously BOA) radiances are required. Speed-up factors as a function of layer optical thickness x start at 3.94 for $x = 0.01$ and decrease, as expected, to 1.51 for $x = 100.0$.

Simulations were performed for a range of wavelengths typically used to retrieve aerosol properties and an O_2 A-band spectrometer similar to that on GOSAT and OCO-2. Polarized radiances were calculated using VPARTM and VLIDORT and fractional differences (in intensity and the degree of polarization) and speed-up factors were presented. The results confirm that VPARTM easily meets a fractional difference accuracy of at least 10^{-4} in all cases while also being computationally advantageous with speedup factors for TOA radiances of 4.16 and 3.93 for the first and second examples, respectively, suggesting that VPARTM may be an efficient alternative for moderate to high accuracy requirements especially for optically thin media.

Finally, it should be noted that VPARTM may be used with efficient specialty methods that require a general radiative transfer solver. These include methods used to calculate high resolution radiance spectrums, such as techniques using PCA analysis [Natraj et al., 2005] or low stream interpolation [O'Dell, 2010], or methods developed for media with highly anisotropic scattering such

as the technique presented in Budak et al. [2011]. In both cases performance improvements in the general radiative transfer solution used internally will be passed on to the method as a whole.

Chapter 5

Information content analysis paper[3]

5.1 Introduction

Atmospheric aerosols effect the Earth's climate system directly by scattering and absorbing incoming solar radiation and indirectly by modifying cloud development, and as a result, cloud albedo and precipitation. Unfortunately, uncertainties in aerosol properties and their effect on the climate system represents one of the largest uncertainties in climate change research [Intergovernmental Panel on Climate Change, 2007a]. Due to the large variability of source types, strengths, and locations aerosols vary significantly in size, shape, and chemical composition as well as spatial and temporal distribution with variabilities on the order of kilometers and days, respectively. Satellite observations provide the only realistic means to resolve these variabilities while making measurements on a global scale.

The first operational satellite aerosol retrieval used a single channel (0.63 μm) from the Advanced Very High Resolution Radiometer (AVHRR) to retrieve aerosol optical thickness (AOT) over ocean [Stowe, 1991, Stowe et al., 1997]. This retrieval was later extended to use both the 0.63 and 0.83 μm AVHRR channels [Higurashi and Nakajima, 1999, Mishchenko et al., 1999] to retrieve, in addition to AOT, the Ångström exponent. The development the MODerate Resolution Imaging Spectrometer (MODIS) [Salomonson et al., 1989], aboard both the Aqua and Terra satellites, provided more bands with a larger spectral range (0.469 to 2.13 μm) from which to retrieval aerosol properties. Retrievals using MODIS and a look-up table (LUT) approach over both ocean [Tanré et al., 1997] and land [Kaufman et al., 1997, Levy et al., 2007] have been developed. The ocean algorithm retrieves AOT at 0.55 μm, fine mode AOT fraction, and mean particle radius of the fine mode. The land algorithm retrieves AOT at 0.55 μm and fine mode AOT fraction but due to the difficulty in separating the

[3]Paper to be submitted: "A Multi-Sensor Concept for Retrieving Aerosol Parameters, Part I: Sensitivity and information Content Analysis".

aerosol signal from the surface signal is limited to aerosols over dark surfaces (2.13 μm reflectance less that 0.25). An alternative for bright surfaces referred to as the Deep Blue algorithm is presented by Hsu et al. [2004, 2006].

Retrieval of aerosols in the UV have also been performed [Hsu et al., 1996, Seftor et al., 1997, Herman et al., 1997a, Torres et al., 1998, 2005] using measurements from the series of Total Ozone Mapping Spectrometers (TOMSs) [Bowman and Krueger, 1985]. Measurements in the UV have the advantage that the surface reflectively is usually insignificant and constant over both ocean and land while the relatively large amount of molecular scattering in the UV produces a "bright" background providing a unique sensitivity to aerosol absorption and a means to retrieve single scattering albedo. Unfortunately, the latter means that the aerosol retrievals using the UV are particularly sensitive to aerosol vertical distribution due to varying molecular scattering with height. In addition, UV measurements lack important information about aerosols in the visible and near-infrared.

Multispectral techniques have set the standard for aerosol retrieval techniques for the past two decades but as the importance of accurate quantification for the direct effect of aerosols has grown the requirements for accurate knowledge of aerosol distribution, loading, and microphysical parameters have become more stringent [Mishchenko et al., 2004]. This has in turn lead investigators to seek additional types of measurements to contribute more information to the aerosol retrieval problem. These additional measurements, including multiangle and/or polarimetric measurements, not only provide more sensitivity to the aerosols themselves but help distinguish aerosol signal from surface signal, a significant challenge for aerosols over land.

Multiangle measurements emerged as an additional source of information used to improve the accuracy of already commonly retrieved parameters and to retrieve additional parameters [Martonchik and Diner, 1992, Wang and Gordon, 1994]. Multiangle measurements provide a means to sample the aerosol single scattering phase function providing an additional constraint to reduce uncertainties in the aerosol microphysical properties [Kahn et al., 1997, 2001]. In addition, multiangle measurements provide a means to characterize the bidirectional reflectance distribution function (BRDF) of the surface.

The Along Track Scanning Radiometer-2 (ATSR-2) [Llewellyn-Jones and Remedios, 2012], aboard the ERS-2 satellite, provides measurements at two view angles, a forward view angle at approximately 55° and a view angle at nadir in four wavelengths used for aerosol retrievals: 0.555,

0.659, 0.865, and 1.6 μm. Both Flowerdew and Haigh [1996] and Veefkind et al. [1998] present aerosol retrieval algorithms that use the measurements at the two angles to attempt to eliminate the surface contribution from the signal. The Multiangle Imaging SpectroRadiometer (MISR) [Diner et al., 1998], aboard the Terra satellite, provides measurements in four spectral bands centered at 0.443, 0.555, 0.670, and 0.865 μm, at nine angles. The operational MISR retrieval [Martonchik et al., 1998] uses three different algorithms depending on the surface type each of which employees an LUT approach to minimize a χ^2 statistic as a function of total AOT and a suite of mono-modal aerosol models. The retrieval parameters are the total AOT and the effective radius. Unfortunately, MISR is limited in spectral range lacking information on large mode particles.

It has long been realized that measurements of polarization are more sensitive to particle microphysics than that of intensity [Hansen and Hovenier, 1974]. Mishchenko and Travis [1997b] showed that retrieval algorithms using only intensity suffer from a severe uniqueness problem and that polarization measurements provide a much greater means of constraining aerosol properties relying less on assumed a priori information. In addition, there are several advantages to using polarization over land [Waquet et al., 2007] compared to using intensity including the lower surface signal relative to that from the aerosols, the relatively low spatial contrast in polarization from the surface, and the relatively weak spectral dependence of polarization from the surface.

The Global Ozone Monitoring Experiment-2 (GOME-2) [Callies et al., 2000], aboard the MetOp satellite, measures intensity in four bands covering the spectral range from 240 nm to 790 nm and polarization in 12 bands in the spectral range from 312 nm to 790 nm. Hasekamp and Landgraf [2005] presented an optimal estimation based information content and retrieval technique using GOME-2 intensity and polarization measurements along with an a priori constraint and Phillips-Tikhonov regularization to retrieve, over ocean, a full set of aerosol parameters (loading, effective radius, and effective variance in two modes; the real and imaginary index of refraction; the height of the layer where the bulk of the aerosol is located, and ocean pigment concentration). They found that the addition of polarization information allowed the retrieval of significantly more information on effective variance, real part of the index of refraction, and ocean pigment concentration than intensity measurements alone. Furthermore, they found that unlike intensity only measurements, measurements with intensity and polarization allowed the retrieval of information on the effective variance, imaginary index of refraction, and aerosol height. Unfortunately, the sensitivity and

therefore the information content of the polarization measurements showed a strong dependence on viewing geometry.

In order to maximize the information attainable from measurements of polarization measurements of the same FOV made at multiple angles is required. The Polarization and Directionality of the Earth's Radiances (POLDER) [Deschamps et al., 1994] currently aboard the PARASOL satellite makes measurements of intensity at 443, 490, 565, 670, 763, 765, 865, 910, 1020 nm and polarization at 443, 670, and 865 nm, at up to 13 viewing geometries for a single orbit with a spatial resolution of 6×7 km. The current operational POLDER aerosol retrieval over ocean [Herman et al., 2005, Tanré et al., 2011] uses intensity and polarization measurements in the 670 and 865 nm bands in an LUT approach to retrieve AOT and effective radius in two modes, the real part of the index of refraction, and the Ångström exponent. Over land, the current operational aerosol retrieval [Deuzé et al., 2001, Tanré et al., 2011] uses measurements of only polarization in the 670 and 865 nm bands due to the larger relative contribution to polarization from aerosols compared to land relative to intensity. The retrieval uses an LUT approach with fine mode aerosol models of spherical non-absorbing aerosols to retrieve total AOT and the Ångström exponent. The coarse mode is neglected as the polarization from large particles is often small. The result is a systematic underestimation of AOT and overestimation of the Angström exponent when a significant large mode is present.

Optimal estimation based retrievals using POLDER have been presented by several researchers. Lebsock et al. [2007] presented an information content analysis and retrieval over ocean using the intensity and polarization at 670 and 860 nm. They found that the majority of the AOT information lies in the intensity only measurements while polarization was necessary to retrieve aerosol microphysical quantities. A total of three parameters were found to be retrievable including the logarithm of the number concentration of two modes and the real part of the index of refraction. Unfortunately, their optimal estimation method lacked an a priori constraint and a form of regularization, both required for efficient use of all the available information. Hasekamp et al. [2011] used an optimal estimation approach, over ocean, similar to that of Hasekamp and Landgraf [2005] (discussed above) using both intensity and polarization measurements at 490 and 670 nm to retrieve a full set of aerosol parameters including, in both modes, the loading, effective radius, effective variance, and complex index of refraction; the height of the layer where the bulk of the aerosol is located, ocean pigment concentration, wind speed in two directions, and white cap fraction. Finally, Dubovik et al. [2011]

presented a statistically optimized inversion algorithm for enhanced retrieval of aerosol properties from multispectral, multiangle, polarimetric satellite observations. Their method is presented in the context of POLDER but made sufficiently general enough to be applied to other advanced satellite observations. They use a complete set of POLDER intensity and polarization measurements to retrieve aerosol parameters including the total volume concentration, the size distribution, fraction of the spherical particles, total real and imaginary parts of the index of refraction, mean height of the aerosol layer, and several surface BRDF parameters. Although these retrievals are ill-posed and under-constrained, use of these relatively large multi-parameter retrieval vectors with advanced measurements allows one to maximize the use of the information contained within the measurements. With proper use of a priori information and regularization techniques the retrieval process can be stabilized to converge on the best possible solution given the information.

By trading spatial/temporal coverage for larger spectral range and angular resolution we arrive at an instrument such as the Research Scanning Polarimeter (RSP). RSP is designed to retrieve aerosol properties with the accuracy and detail required for accurate quantification of the direct radiative effect of aerosols [Mishchenko et al., 2004]. RSP is an airborne instrument that measures the first three stokes parameters I, Q, and U in nine spectral channels at 410, 470, 550, 670, 865, 960, 1560, 1880, and 2250 nm and at 152 viewing angles along track $\pm 60^{\circ}$ [Cairns et al., 1999]. Chowdhary et al. [2002] presented case studies of using RSP to retrieve non-absorbing aerosols over the ocean and determined that RSP could accurately retrieve aerosol number concentration, size distribution, and the real part of the index of refraction in two modes. Building on these developments Chowdhary et al. [2005] outlined a more formal retrieval algorithm and included the imaginary part of the index of refraction and aerosol height as retrieval parameters. An optimal estimation retrieval for aerosols over land using RSP measurements was presented by Waquet et al. [2009]. In this case only the polarized reflectances were used so as to avoid the aerosol/surface separation in the total reflectances. The complete set of aerosol parameters was retrieved for both fine and coarse modes along with the aerosol-top pressure. The heritage of RSP lead to the Aerosol Polarimetry Sensor (APS), an instrument of very similar design but built for satellite use and with a slightly different wavelength configuration, which was a part of the Glory Satellite mission [Mishchenko et al., 2007a, Peralta et al., 2007]. Unfortunately, that mission failed to achieve orbit depriving the science community of a valuable aerosol observing system.

The use of hyperspectral measurements in molecular absorption bands within the solar spectrum for remote sensing of atmospheric particles is relatively unexplored compared to multiangle and polarimetric measurements. Much of the early O_2 A-band research in the 60's and 70's was focused on determining cloud-top pressure [Hanel, 1961, Yamamoto, 1962, Chapman, 1962]. The physical basis for this was that knowing the concentration of O_2, which is relatively constant, and its vertical variation, the observed absorption along the path to the top of the cloud could be translated into an estimate of cloud-top pressure. Unfortunately, the results from these studies consistently overestimated the cloud-top pressure due the extension of photon path lengths from multiple scattering in the clouds. Various corrections were derived for this effect [Saiedy, 1967, Grechko et al., 1973, Grechko, 1978, Dianov-Klokov et al., 1970, Dianov-Klokov and Krasnokutskaya, 1972] while several researches found that there is enough information, especially in higher spectral resolution measurements, to retrieve not only the cloud-top but also the parameters that determine the distribution of photon path lengths within the cloud [Wu, 1985, Fischer and Grassl, 1991, O'Brien and Mitchell, 1992]. Stephens and Heidinger [2000] presented a study of the sensitivity of hyperspectral measurements made in the O_2 A-band to cloud properties including optical thickness, the single scattering phase function, the top pressure, the pressure thickness, and the surface albedo. The sensitivities to these parameters were found to vary according to the column O_2 optical thickness offering a way of separating the dependence of the measurements to these parameters providing a basis for their retrieval. The variation in sensitivity and the degree of separation is dependent on the spectral resolution and more specifically the ability to resolve a sufficient range of O_2 optical thicknesses. This physical basis was applied in a theoretical cloud retrieval study by Heidinger and Stephens [2000] who found accuracies of better that 5% for low clouds, except when they are optically thin or over bright surfaces, and 10% for high clouds.

There has also been research focused on the use hyperspectral measurements in molecular absorption bands for remote sensing of aerosols. Gabella et al. [1999b] showed that aerosol extinction profiles could be retrieved and provided an example of a real retrieval using airborne O_2 A- and B-band spectrometer observations [Gabella et al., 1999a]. Min and Harrison [2004] showed that a system with 0.5 cm^{-1} resolution, signal-to-noise ratio of 100:1, and an out-of-band floor of 10^{-3} has four independent pieces of aerosol information while tests with synthetic data show that errors are less that 10% for the integrated total optical thickness. In the context of the Greenhouse Gases

Observing Satellite (GOSAT) [Kuze et al., 2009] and the planned Orbital Carbon Observatory-2 (OCO-2) [Crisp et al., 2004] missions Frankenberg et al. [2012a] analyzed the aerosol information content of hyperspectral measurements in the O_2 A-band and the 1.61- and 2.06-μm CO_2 bands for both nadir and multiangle observations. For retrieval parameters including aerosol column loading, effective radius, effective variance, real and imaginary parts of the refractive index, center width, and center height they found that the degrees of freedom for signal for the multiangle measurements increased by 2–3 compared to the nadir only measurements.

Some research has focused on the use of polarization measurements in the O_2 A-band as a further source of information. In the context of aerosol retrievals this is of particular importance since, as we have already discussed, measurements of polarization exhibit a relatively large sensitivity to aerosol microphysical parameters. Stam et al. [1999] presented a theoretical study in which they investigate the behavior of the degree of linear polarization P of radiation in the O_2 A-band emerging from the top and bottom of atmospheres with and without aerosols. They found that P varies with O_2 optical thickness and that this variation depends strongly on the type and vertical distribution of the aerosol particles in the atmosphere due to the relative contribution to polarization from molecular scattering and aerosols. A study by Boesche et al. [2008] had similar results while also finding that this sensitivity depends on the aerosol optical thickness and microphysics and surface albedo. Boesche et al. [2009] investigate the O_2 A-band as well as the 1.61 (weak) and 2.06 (strong) μm CO_2 bands finding that the weak 1.61-μm band provides significantly less sensitivity due to the stronger influence of surface reflection and multiple scattering.

In this paper we aim to analyze the information content of a satellite-based tropospheric aerosol retrieval system that uses both common multispectral measurements along with hyperspectral measurements in molecular absorption bands within the solar spectrum. Motivated by the stringent aerosol information requirements for accurate quantification of the direct radiative effect of aerosols [Mishchenko et al., 2004] we focus on these hyperspectral measurements as a new source of information which can be used to improve satellite-based aerosol retrievals. An analysis of this kind has particular relevance now with recent launch of GOSAT and the planned launch of OCO-2. Although these missions focus on the retrieval of greenhouse gas column mixing ratios their suite of measurements include the hyperspectral measurements that are of interest to this study including observations in the 0.76-μm O_2 A-band and the 1.61- and 2.06-μm CO_2 bands. As GOSAT actually measures

polarization and is capable of making these measurements at multiple view angles, and due to the importance of these kinds of measurements to aerosol remote sensing, we will investigate nadir, multiangle, intensity, and polarimetric hyperspectral measurements.

This paper is the first of two on a combined multispectral and hyperspectral aerosol retrieval system. Whereas in this paper we focus on the theoretical aspects including the measurement sensitivity and information content, in the second paper [McGarragh and Stephens, 2013b], hereafter referred to as "Part II" we implement a real retrieval using MODIS and GOSAT observations co-located with ground-based AERONET sites for validation.

The structure of the paper is as follows: Section 5.2 describes the measurements used including the multispectral and hyperspectral measurements. Section 5.3 describes the setup of the retrieval which includes a brief description of the retrieval technique followed by detailed descriptions of the measurement vector and the state vector and a priori state. In section 5.4 the forward model, essential to the retrieval, is described broken down into components including the atmospheric, surface, solar, radiative transfer, and instrument models. In section 5.5 the atmospheric, surface, and geometric scenarios used in the rest of the paper are described. Section 5.6 presents a study of the sensitivity of the measurements to the state vector parameters and the derived optical thickness and single scattering albedo. Section 5.7 presents a formal information content study of the measurements for the state vector parameters including an description of the methodology followed by a singular value decomposition analysis and presentation of the degrees of freedom, averaging kernels, and posteriori error. Finally, in section 5.8 we summarize our findings and discuss some conclusions that may be taken from this study.

5.2 Measurements

For this study we consider two primary satellite instruments: a instrument similar to the Moderate Resolution Imaging Spectroradiometer (MODIS) [Salomonson et al., 1989] and an instrument similar to the Thermal And Near infrared Sensor for carbon Observations - Fourier Transform Spectrometer (TANSO-FTS) instrument aboard the Greenhouse gases Observing SATellite (GOSAT) [Kuze et al., 2009]. In addition, for comparison with an "ideal" aerosol observing system we also, in a few cases,

Table 5.1: The MODIS bands used in our retrieval along with their center wavelengths (nm), bandwidth (nm), SNR, and pixel size (m).

Band	Center wavelength (nm)	Bandwidth (nm)	SNR	Pixel Size (m)
1	645	620 - 670	128	250
2	858	841 - 876	201	250
3	469	459 - 479	243	500
4	555	545 - 565	228	500
5	1240	1230 - 1250	74	500
6	1640	1628 - 1652	275	500
7	2130	2105 - 2155	110	500

show results for an instrument similar to the Aerosol Polarimetry Sensor (APS) [Mishchenko et al., 2007a, Peralta et al., 2007].

MODIS instruments reside aboard both the Terra (launched May 2002) and Aqua (launched December 1999) satellites, each of which fly at a 705 km altitude, in sun-synchronous orbits at a 98° inclination, with 10:30 a.m. (descending) and 1:30 p.m. (ascending) nodal crossing times, respectively. With a cross track swath of 2330 km each instrument provides global coverage every 1–2 days. MODIS has 36 bands from 0.41 to 15 μm at 250 m (2 bands), 500 m (5 bands), and 1 km (29 bands) spatial resolutions. For this study, we will use 7 of the 36 bands, presented in table 6.1: 0.645 and 0.858 μm (250 m) and 0.469, 0.555, 1.24, 1.64, and 2.13 μm (500 m).

The TANSO-FTS instrument resides aboard GOSAT (launched January 2009) with a 666 km altitude, sun-synchronous orbit at a 98° inclination, a 12:49 p.m. nodal crossing time, and a three-day ground track repeat cycle. TANSO-FTS has four hyperspectral resolution bands of which the 0.76-μm O_2 A-band and the 1.61- and 2.06-μm CO_2 bands, presented in table 5.2, will be used for this study. The instrument views a 10 km footprint (spatial resolution at nadir) in one of three different modes: nadir, looking straight down; target, where a single surface location is targeted at up to three viewing zenith angles; and sunglint mode, where a sunglint spot over the ocean is targeted to increase signal to noise ratio. For this study we will consider both nadir and target mode.

APS was originally planned to reside aboard the Glory satellite which failed to reach orbit when launched on March 4, 2011. APS is considered the ideal satellite-based passive aerosol observing system and as such it is interesting to present some results for APS as we will present them for

Table 5.2: The GOSAT TANSO-FTS bands used in our retrieval along with their name, wavelength range (cm^{-1} and μm), and number of channels.

		Spectral range		
	Name	cm^{-1}	μm	# of channels
Band 1	O_2-A	12950–13190	0.758–0.772	1203
Band 2	Weak CO_2	6166–6286	1.59–1.62	601
Band 3	Strong CO_2	4810–4897	2.04–2.08	436

our MODIS/TANSO-FTS observing system. It was a multispectral, multiangle, polarimeter. It had 9 spectral channels at: 0.410, 0.443, 0.555, 0.670, 0.865, 0.910, 1.378, 1.610, and 2.250 μm. Observations, with a 5.6 km spatial resolution at nadir, were to be taken along track from 60° fore to 60° aft resulting in over 250 viewing angles per observation pixel. APS was to measure the first three stokes components (I, Q, and U) with radiometric and polarimetric accuracies of better than 5.0% and 0.3%, respectively.

In the rest of this paper the instruments just described will be referred to as: MODIS, TANSO-FTS, and APS, respectively.

5.3 Retrieval setup

Our retrieval algorithm is based on the optimal estimation approach in which the best match between simulated measurements computed with a forward model and real measurements is obtained by optimizing the forward model inputs [Rodgers, 2004]. The forward model inputs that are optimized are the n elements of the state vector $\mathbf{x}$ while the measurements are the m elements of vector $\mathbf{y}$. The relationship between $\mathbf{x}$ and $\mathbf{y}$, based on the forward model, may be written as

$$\mathbf{y} = \mathbf{F}(\mathbf{x}, \mathbf{b}) + \epsilon, \tag{5.1}$$

where $\mathbf{F}$ is the forward model; $\mathbf{b}$ is the set of all other assumed model parameters not in the state vector $\mathbf{x}$ such as meteorological conditions, spectroscopic parameters, solar and viewing geometry, etc.; and ϵ represents the measurement and forward model error.

The optimal estimation approach we have employed uses the forward model to minimize the cost function

$$\chi^2 = [\mathbf{F}(\mathbf{x}, \mathbf{b}) - \mathbf{y}]^T \, \mathbf{S}_\epsilon^{-1} \, [\mathbf{F}(\mathbf{x}, \mathbf{b}) - \mathbf{y}] + (\mathbf{x} - \mathbf{x}_a)^T \mathbf{S}_a^{-1} (\mathbf{x} - \mathbf{x}_a) \tag{5.2}$$

to obtain the retrieved state vector $\hat{\mathbf{x}}$, where $\mathbf{S}_\epsilon$ is the measurement and forward model error covariance matrix which accounts for errors in $\mathbf{y}$ and the errors in the forward model due to errors in $\mathbf{b}$, and $\mathbf{x}_a$ and $\mathbf{S}_a$ are the a priori state vector, representing any a priori knowledge of the state vector to be retrieved, and the corresponding error covariance matrix, respectively. From the equation we can see that the cost function is a combination of the deviations between the measurements and the forward model and the retrieved state vector and the a priori state vector, each weighted by its associated covariance matrix.

5.3.1 Measurement vector

The intensity and state of polarization of light can described by the (4×1) stokes vector [Hovenier et al., 2004]

$$\mathbf{I} = [I, Q, U, V]^T \, , \tag{5.3}$$

where the stokes parameters I, Q, U, and V have irradiance units of W m^{-2} μm^{-1} and radiance units of W m^{-2} μm^{-1} sr^{-1} and are defined with respect to a plane of reference. I describes the intensity of the radiation, Q and U describe the magnitude and orientation of linear polarization, and V describes the magnitude and helicity of circular polarization. For naturally illuminated scenes V is typically negligible and therefore will not be considered in this study. The measurements we use are the total and polarized reflectances given by

$$R = \frac{\pi I}{\mu_0 I_0} \tag{5.4}$$

and

$$P = \frac{\pi \sqrt{Q^2 + U^2}}{\mu_0 I_0}, \tag{5.5}$$

respectively, where μ_0 is the solar zenith angle and I_0 is the solar irradiance at the top of the atmosphere (TOA).

Since it is the goal of this study to assess the information content in different measurement combinations it is useful to break the measurement vectors into contiguous measurement units for each sensor. For MODIS the measurement vector will always be the same as:

$$\mathbf{y}_{\mathrm{M}} = [R_{0.47}, R_{0.55}, R_{0.66}, R_{0.86}, R_{1.24}, R_{1.64}, R_{2.13}]\,. \tag{5.6}$$

where each reflectance value R_x represented the reflectance observed at wavelength x. For TANSO-FTS, the measurement vector will be a combination of basic units given as

$$\mathbf{y}_{\mathrm{TF},b,r,v} = [y_{b,r,v,1}, \ldots, y_{b,r,v,n}]\,, \tag{5.7}$$

where $b \in \{1, 2, 3\}$ refers to the band number, $r \in \{R, P\}$ refers to reflectance or polarized reflectance measurements, $v \in \{\text{'fore'}, \text{'nadir'}, \text{'aft'}\}$ refers to the view angle, and n is the number of channels in bands b. Based on equation 5.7 several combinations of TANSO-FTS measurements can be constructed

$$\mathbf{y}_{\mathrm{TF},1,R,\mathrm{nadir}} \tag{5.8}$$

$$\mathbf{y}_{\mathrm{TF},1,R,\mathrm{M}} = [\mathbf{y}_{\mathrm{TF},1,R,\mathrm{fore}}, \mathbf{y}_{\mathrm{TF},1,R,\mathrm{nadir}}, \mathbf{y}_{\mathrm{TF},1,R,\mathrm{aft}}]\,. \tag{5.9}$$

$$\mathbf{y}_{\mathrm{TF},1\text{–}3,R,\mathrm{N}} = [\mathbf{y}_{\mathrm{TF},1,R,\mathrm{nadir}}, \mathbf{y}_{\mathrm{TF},2,R,\mathrm{nadir}}, \mathbf{y}_{\mathrm{TF},3,R,\mathrm{nadir}}]\,. \tag{5.10}$$

$$\begin{aligned} \mathbf{y}_{\mathrm{TF},1\text{–}3,R,\mathrm{M}} &= [\mathbf{y}_{\mathrm{TF},1,R,\mathrm{fore}}, \mathbf{y}_{\mathrm{TF},1,R,\mathrm{nadir}}, \mathbf{y}_{\mathrm{TF},1,R,\mathrm{aft}} \\ &= \mathbf{y}_{\mathrm{TF},2,R,\mathrm{fore}}, \mathbf{y}_{\mathrm{TF},2,R,\mathrm{nadir}}, \mathbf{y}_{\mathrm{TF},2,R,\mathrm{aft}} \\ &= \mathbf{y}_{\mathrm{TF},3,R,\mathrm{fore}}, \mathbf{y}_{\mathrm{TF},3,R,\mathrm{nadir}}, \mathbf{y}_{\mathrm{TF},3,R,\mathrm{aft}}]\,. \end{aligned} \tag{5.11}$$

$$\mathbf{y}_{\mathrm{TF},1,R+P,\mathrm{N}} = [\mathbf{y}_{\mathrm{TF},1,R,\mathrm{nadir}}, \mathbf{y}_{\mathrm{TF},1,P,\mathrm{nadir}}]\,, \tag{5.12}$$

$$\begin{aligned} \mathbf{y}_{\mathrm{TF},1,R+P,\mathrm{M}} &= [\mathbf{y}_{\mathrm{TF},1,R,\mathrm{fore}}, \mathbf{y}_{\mathrm{TF},1,R,\mathrm{nadir}}, \mathbf{y}_{\mathrm{TF},1,R,\mathrm{aft}} \\ &= \mathbf{y}_{\mathrm{TF},1,P,\mathrm{fore}}, \mathbf{y}_{\mathrm{TF},1,P,\mathrm{nadir}}, \mathbf{y}_{\mathrm{TF},1,P,\mathrm{aft}}]\,, \end{aligned} \tag{5.13}$$

$$\begin{aligned} \mathbf{y}_{\mathrm{TF},1\text{–}3,R+P,\mathrm{N}} &= [\mathbf{y}_{\mathrm{TF},1,R,\mathrm{nadir}}, \mathbf{y}_{\mathrm{TF},1,P,\mathrm{nadir}} \\ &= \mathbf{y}_{\mathrm{TF},2,R,\mathrm{nadir}}, \mathbf{y}_{\mathrm{TF},2,P,\mathrm{nadir}} \\ &= \mathbf{y}_{\mathrm{TF},3,R,\mathrm{nadir}}, \mathbf{y}_{\mathrm{TF},3,P,\mathrm{nadir}}]\,, \end{aligned} \tag{5.14}$$

$$
\begin{aligned}
\mathbf{y}_{\mathrm{TF},1,R+P,\mathrm{M}} = &[\mathbf{y}_{\mathrm{TF},1,R,\mathrm{fore}}, \mathbf{y}_{\mathrm{TF},1,R,\mathrm{nadir}}, \mathbf{y}_{\mathrm{TF},1,R,\mathrm{aft}} \\
= &\mathbf{y}_{\mathrm{TF},1,P,\mathrm{fore}}, \mathbf{y}_{\mathrm{TF},1,P,\mathrm{nadir}}, \mathbf{y}_{\mathrm{TF},1,P,\mathrm{aft}} \\
= &\mathbf{y}_{\mathrm{TF},2,R,\mathrm{fore}}, \mathbf{y}_{\mathrm{TF},2,R,\mathrm{nadir}}, \mathbf{y}_{\mathrm{TF},2,R,\mathrm{aft}} \\
= &\mathbf{y}_{\mathrm{TF},2,P,\mathrm{fore}}, \mathbf{y}_{\mathrm{TF},2,P,\mathrm{nadir}}, \mathbf{y}_{\mathrm{TF},2,P,\mathrm{aft}} \\
= &\mathbf{y}_{\mathrm{TF},3,R,\mathrm{fore}}, \mathbf{y}_{\mathrm{TF},3,R,\mathrm{nadir}}, \mathbf{y}_{\mathrm{TF},3,R,\mathrm{aft}} \\
= &\mathbf{y}_{\mathrm{TF},3,P,\mathrm{fore}}, \mathbf{y}_{\mathrm{TF},3,P,\mathrm{nadir}}, \mathbf{y}_{\mathrm{TF},3,P,\mathrm{aft}}] \,.
\end{aligned}
\tag{5.15}
$$

Measurement vectors with both MODIS and TANSO-FTS measurements will be given by

$$
\mathbf{y}_{\mathrm{M,TF},b,r,v} = [\mathbf{y}_{\mathrm{M}}, \mathbf{y}_{\mathrm{TF},b,r,v}] \,. \tag{5.16}
$$

Finally, for comparison proposes we define the APS measurement vector for each channel i as

$$
\mathbf{y}_{\mathrm{APS},i} = [R_{i,\mathrm{fore}}, \ldots, R_{i,\mathrm{aft}}, P_{i,\mathrm{fore}}, \ldots, P_{i,\mathrm{aft}}] \,, \tag{5.17}
$$

where the R and P range over the set of view angles from fore to aft. The total APS measurement vector is given by

$$
\begin{aligned}
\mathbf{y}_{\mathrm{APS}} = &[\mathbf{y}_{\mathrm{APS},0.410}, \mathbf{y}_{\mathrm{APS},0.443}, \mathbf{y}_{\mathrm{APS},0.555}, \\
&\mathbf{y}_{\mathrm{APS},0.670}, \mathbf{y}_{\mathrm{APS},0.865}, \mathbf{y}_{\mathrm{APS},0.910}, \mathbf{y}_{\mathrm{APS},1.610}, \mathbf{y}_{\mathrm{APS},2.250}] \,.
\end{aligned}
\tag{5.18}
$$

Here we will discuss $\mathbf{S}_\epsilon$, the measurement and forward model error covariance matrix. $\mathbf{S}_\epsilon$ accounts for errors in the measurement vector $\mathbf{y}$ and errors in the forward model $\mathbf{F}(\mathbf{x}, \mathbf{b})$ due to errors in $\mathbf{b}$. In this study we assume that both the errors in $\mathbf{y}$ and the errors in $\mathbf{F}(\mathbf{x}, \mathbf{b})$ are uncorrelated and therefore $\mathbf{S}_\epsilon$ is a diagonal matrix of variances. The measurement errors $\sigma_{y,j}$ are computed according to the instrument noise model discussed in section 5.4.5. The vector $\mathbf{b}$ contains several parameters of which only a few have errors large enough to justify accounting for. These are the atmospheric pressure, temperature, and humidity. Other parameters such as spectroscopic parameters; concentrations of O_2, O_3, and CO_2; instrument calibration parameters; and solar and viewing geometry; are assumed to be known to a negligible error. The errors for pressure (σ_p), temperature (σ_t), and humidity (σ_h), obtained from ECMWF, are taken from Molteni et al. [1996]

and Buizza et al. [1999]. The resulting errors in the forward model due to these parameters are obtained by running the forward model over a range of extreme base state values of $\mathbf{x}$ and $\mathbf{b}$ then computing the error with

$$\sigma_{\epsilon,b,j} = \sigma_b \frac{\partial y_j}{\partial b}, \tag{5.19}$$

where $b \in \{p, t, h\}$ and the derivative $\frac{\partial y_j}{\partial b}$ is part of the forward model output (see section 5.4). The total error may then be obtained from the maximum σ_j values obtained for the measurements y_j for each parameter b from

$$\mathbf{S}_{\epsilon,j,j} = \sigma^2_{y,j} + \sigma^2_{\epsilon,p,j} + \sigma^2_{\epsilon,t,j} + \sigma^2_{\epsilon,h,j}. \tag{5.20}$$

5.3.2 State vector and a priori state

The state vector $\mathbf{x}$ contains the parameters that are optimized so that simulated measurements match the real measurements according to the cost function χ^2 (equation 5.2). These parameters may be retrieval quantities of interest or other quantities that are sufficiently unknown and to which the retrieval is sufficiently sensitive to warrant inclusion in the state vector. The alternative of making assumptions about the values of these latter quantities may induce unnecessary constraints on the retrieval leading to errors in the retrieved quantities of interest.

The a priori state vector $\mathbf{x}_a$ represents our best guess of the state vector parameters given our a priori knowledge. Along with the a priori state vector one of the most important aspects of our optimal estimation approach is the definition of the a priori covariance matrix $\mathbf{S}_a$. The a priori covariance weights the influence that the a priori knowledge has on the retrieval. In other words, the a priori covariance constrains the a priori knowledge. When the constraint for a parameter is strong (large covariance) the retrieval relies more on the measurements to determine the parameter. When the constraint is weak (small covariance) the retrieval relies less on the measurements to determine the parameter. For our approach we use 1-sigma (σ_1) errors for the a priori parameter uncertainties, assuming Gaussian statistics. It should be noted that any non-Gaussian statistics could be utilized, however, as Rodgers [2004] notes, according to the Principle of Maximum Entropy, the Gaussian distribution is the most appropriate if only a mean and variance is known. We assume that the a priori errors for each parameter are uncorrelated with that of every other parameter and therefore our a priori covariance matrix is a diagonal matrix of variances (σ^2_1).

The state vector and a priori state vector elements along with the a priori 1-sigma values are listed in table 5.3. Below we will describes the state vector parameters in more detail followed by a brief description of our choice of a priori value and associated 1-sigma values.

Our state vector begins with a five parameter polynomial fit to spectral surface albedo $A(\lambda)$. The fit is advantageous over retrieving A for individual wavelengths separately as it induces a sort of smoothing constraint that accounts for the fact that measurements at all wavelengths contain information about an albedo at a particular wavelength. Although not a retrieval quantity of interest, albedo is never the less the quantity to which our retrieval is most sensitive to (as shown later) and therefore must be either accurately known a priori or retrieved.

The state vector also contains a value which we refer to as aerosol-top pressure P_{top} which represents the top of the aerosol layer which is defined from P_{top} down to the surface. Although simplistic, this value is appropriate in our case as we make the assumption that the aerosol profile loading is constant with height. P_{top} is another parameter to which our retrieval is sensitive enough to warrant its inclusion in the state vector. This is particularly the case for retrievals using measurements in molecular absorption bands and measurements of polarization and when allowing for the variation or retrieval of single scattering albedo. Measurement weighting functions (TOA radiance derivatives with respect to parameters as a function of their vertical location) peak at, and are therefore most sensitive to, different vertical locations in the atmosphere, depending on molecular absorption. In the hyperspectral bands used in this study variation in molecular absorption across the bands provides sensitivity at a range of vertical locations. Polarization measurements are also sensitive to aerosol vertical location [Stam et al., 1999]. Since radiance scattered from molecules has a greater degree of polarization than that from aerosols, the degree of polarization measured at TOA will depend on the amount of molecular scattering above the aerosol layer and therefore the height of the aerosol layer which acts to decrease the degree of polarization relative to that from molecular scattering alone. Finally, it is also important to consider aerosol vertical location when single scattering albedo or parameters from which it is derived are allowed to vary [Chowdhary et al., 2005]. This is because, as mentioned previously, the radiance sensitivity to single scattering albedo increases with multiple scattering and since molecular scattering contributes to the over all multiple scattering, a decreasing molecular abundance with height results in a decreasing sensitivity

Table 5.3: The state vector parameters used in our retrieval, along with a brief description and the corresponding a priori values and a priori 1-sigma values.

Parameter	Description	A priori value	A priori 1-sigma
$A_1 \dots A_n$	n fit parameters for the wavelength dependent Lambertian surface albedo	from meas.	0.5
P_{top}	The "effective" top to the aerosol layer	700.0 hPa	50.0 hPa
$N_{0,f}$	Aerosol # concentration for the fine mode	$\tau_1(0.55) = 0.1$	5 × a priori
$r_{g,f}$	Mean radius of a log-normal size distribution for the fine mode	0.15 μm	0.1 μm
σ_f	Variance of a log-normal size distribution for the fine mode	0.4	0.1
$m_{r,f,1} \dots m_{r,f,n}$	n fit parameters for the wavelength dependent real part of the index of refraction for the fine mode	1.47 (flat)	0.14
$m_{i,f,1} \dots m_{i,f,n}$	n fit parameters for the wavelength dependent imaginary part of the index of refraction for the fine mode	0.002 (flat)	0.005
$N_{0,c}$	Aerosol # concentration for the coarse mode	$\tau_2(0.55) = 0.1$	5 × a priori
$r_{g,c}$	Mean radius of a log-normal size distribution for the coarse mode	0.8 μm	0.2 μm
σ_c	Variance of a log-normal size distribution for the coarse mode	0.6	0.3
$m_{r,c,1} \dots m_{r,c,n}$	n fit parameters for the wavelength dependent real part of the index of refraction for the coarse mode	1.47 (flat)	0.14
$m_{i,c,1} \dots m_{i,c,n}$	n fit parameters for the wavelength dependent imaginary part of the index of refraction for the coarse mode	0.002 (flat)	0.005

to single scattering albedo with height. Given the sensitivities just described it is apparent that it is necessary to place the top of the aerosol layer at a location that is consistent with the measurements.

Our choice of retrieval quantities of interest is driven by the quantities that are required for accurate quantification of direct aerosol effects [Mishchenko et al., 2004], namely: aerosol spectral optical thickness $\tau_a(\lambda)$, spectral single scattering albedo $\omega_a(\lambda)$, spectral phase function $P_a(\Theta, \lambda)$, and chemical composition. To determine these quantities the aerosol parameters that must be retrieved are (for two aerosol modes): aerosol spectral optical thickness $\tau_{a,i}(\lambda)$, effective radius $r_{e,i}$, effective variance $v_{e,i}$, at least one parameter describing non-sphericity x_i, the real and imaginary parts of the spectral refractive index $m_{r,i}(\lambda)$ and $m_{i,i}(\lambda)$, and spectral single scattering albedo $\omega_{a,i}(\lambda)$, where i is f or c for the fine and coarse modes, respectively.

We derive our list of retrieval quantities of interest from the "ideal" list just presented by making several modifications. First we retrieve not the spectral optical thickness $\tau_{a,i}(\lambda)$ but instead the column number density of particles $N_{0,i}$ (μm^{-2}), a spectrally independent parameter. Then, instead of effective radius $r_{e,i}$ and effective variance $v_{e,i}$, we assume a log-normal size distribution given by

$$N(r) = \frac{N_0}{\sqrt{2\pi}\sigma r} \exp\left[-\frac{(\ln r - \ln r_g)^2}{2\sigma^2}\right], \tag{5.21}$$

and retrieve the mean radius $r_{g,i}$ (μm) and the standard deviation of the natural logs of r's σ_i, from which $r_{e,i}$ and $v_{e,i}$ may be obtained from

$$r_{e,i} = r_{g,i} \exp(\frac{5}{2}\sigma_i^2) \tag{5.22}$$

and

$$v_{e,i} = \exp(\sigma_i^2) - 1, \tag{5.23}$$

respectively. We also assume for simplicity that aerosols are spherical and therefore leave the non-sphericity parameter $x_{a,i}$, to be added to the state vector in a future study. Finally, instead of retrieving $m_{r,i}(\lambda)$ and $m_{i,i}(\lambda)$ as a function of wavelength, for reasons already presented above for the retrieval of spectral surface albedo $A(\lambda)$, we retrieve, n parameter polynomial fits to these spectral quantities. The resulting state vector is written as

$$\begin{aligned}\mathbf{x}^T = [&A_1 \ldots A_n, P_{\text{top}}, \\ &N_{0,f}, r_{g,f}, \sigma_f, m_{r,f,1} \ldots m_{r,f,n}, m_{i,f,1} \ldots m_{i,f,n}, \\ &N_{0,c}, r_{g,c}, \sigma_c, m_{r,c,1} \ldots m_{r,c,n}, m_{i,c,1} \ldots m_{i,c,n}] .\end{aligned} \tag{5.24}$$

The a priori state vector has the same form as the state vector shown in equation 5.24. It begins with a five parameter polynomial fit to a priori spectral surface albedo $A(\lambda)$. The fit is determined from a surface albedo that is retrieved from the measurements for each band, where the rest of the state vector parameters presented above are assumed to be constant and equal to their corresponding a priori values presented below. For the a priori 1-sigma values (identical for each fit parameter) we use the relatively loose value of 0.5. For aerosol-top pressure we use a a priori value of 700 hPa with a 1-sigma value of 50 hPa based on the study of aerosol vertical distributions presented by Yu et al. [2010]. For each aerosol mode the a priori value for $N_{0,i}$ is determined for an a priori optical thickness $\tau_{a,i}(0.55) = 0.1$. Since $\tau_{a,i}(0.55)$ can vary over several orders magnitude its 1-sigma value is set to 5 times that of the a priori value, a relatively loose value allowing the measurements to have a large influence on the retrieval of $N_{0,i}$. The a priori values of the aerosol microphysical parameters $r_{g,i}$, σ_i, $m_{r,i,j}$, and $m_{i,i,j}$ along with their associated 1-sigma values are taken from Waquet et al. [2009] and are based on the aerosol climatology of Dubovik et al. [2002b]. For $m_{r,i,j}$ and $m_{i,i,j}$ the spectral dependence is considered flat so the first polynomial fit parameter is equal to the a priori value while the other four parameters are set to zero. The a priori 1-sigma values for the fits are identical for each fit parameter.

Results in the following sections will be presented for not only the state vector elements but also the two radiatively important derived quantities, $\tau_{a,i}(\lambda)$ and $\omega_{a,i}(\lambda)$. These quantities may be obtained from the state vector elements $r_{g,i}$, σ_i, $m_{r,i}(\lambda)$, and $m_{i,i}(\lambda)$ using Mie theory and the following relations:

$$\tau_{a,i}(\lambda) = N_{0,i} C_{e,i}(\lambda) \tag{5.25}$$

and

$$\omega_{a,i}(\lambda) = \frac{C_{s,i}(\lambda)}{C_{e,i}(\lambda)}, \tag{5.26}$$

where $C_{e,i}(\lambda)$ and $C_{s,i}(\lambda)$ are the extinction and scattering cross sections (μm), respectively, derived from the Mie computations.

5.4 Forward model

The forward model takes as input the state vector $\mathbf{x}$ and the vector $\mathbf{b}$ and simulates measurements, the elements of $\mathbf{y}$, produced by an instrument along with derivatives of these measurements with respect to the model inputs of which derivatives with respect to the state vector elements form the elements of $\mathbf{K}$. The vector $\mathbf{b}$ contains atmospheric and surface parameters that are assumed to be known, solar and viewing geometry parameters, and instrument parameters. The forward model consists of atmospheric and surface models that define the physical parameters required to simulate measurements, a spectroscopic module from which molecular absorption parameters are obtained, a molecular scattering module that computes molecular scattering parameters, a particle scattering module that computes aerosol scattering parameters, a radiative transfer model (RTM), a solar spectral model defining solar spectral irradiance, and instrument models for each instrument that define both the instrument response function and the instrument noise levels. Each of these will be described below. The forward model is diagrammed as a fin figure 5.1.

5.4.1 Atmospheric model

The atmospheric model takes as input physical quantities including profiles of temperature, pressure, gas concentration, and aerosol properties, for any number of modes, including number concentration, top pressure, size distribution, and complex index of refraction and produces profiles of optical properties including optical thickness, single scattering albedo, and scattering phase matrix expansion coefficients, along with derivatives of these optical quantities with respect to the model inputs, both of which are used as input into the RTM. This model accounts for molecular absorption and scattering and absorption and scattering by aerosols, Other sources of emission, absorption, and scattering such as thermal emission, air glow, and Raman scattering are negligible in the wavelength regions considered in this study and are therefore ignored. Currently fluorescence from chlorophyll is ignored although there is evidence that it can contribute significantly to the

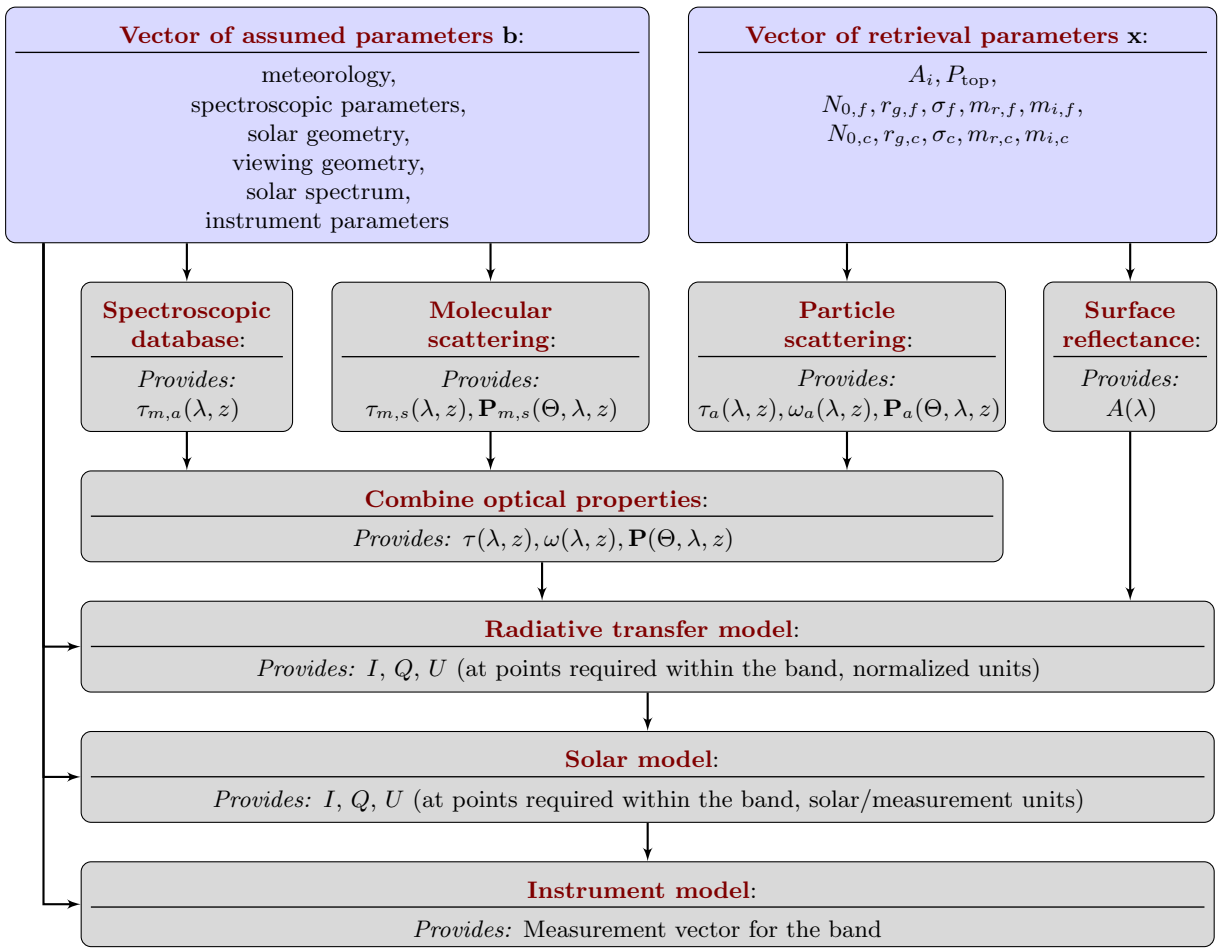

Figure 5.1: Flow chart showing the forward model components and input and output variables. Light blue represents inputs and light gray represents computations. The names for each node (in red) link to the appropriate description in this document if clicked.

measurements made in the O_2 A-band [Frankenberg et al., 2012b] and may be considered in the future.

The RTM takes optical property inputs for an atmosphere discretized into homogeneous layers. As such, our atmospheric model consists of multiple layers, where in each layer the physical quantities are assumed to be constant. The values for temperature, pressure, and gas concentrations are defined as the mean of the upper and lower levels of the layer while the aerosol number concentrations and microphysical properties must be supplied as means for the layer. Below we describe computations that are applied on a layer by layer basis.

The molecular absorption optical thickness $\tau_{m,a}(\lambda)$ is required for the 0.76-μm O_2 A-band and 1.61- and 2.06-μm CO_2 bands and is computed from the mixing ratios of CO_2, H_2O, and O_2 along with a three-dimensional lookup table of gas absorption coefficients in pressure, temperature, and wavelength. The table, described in Crisp et al. [2010], includes the state-of-the-art spectroscopic data for CO_2 and O_2 including non-Voigt line shapes, speed dependence, line mixing, and collision-induced absorption. HITRAN-2008 [Rothman et al., 2009] is used for all other absorbers within the required bands.

The molecular scattering optical thickness for dry air $\tau_{m,s}(\lambda)$ is computed with the standard formulation using the methods recommended by Bodhaine et al. [1999], where the refractive index of dry air for a CO_2 concentration of 300 ppm is computed according to Peck and Reeder [1972] which is then scaled to the actual CO_2 concentration and the King factor for dry air is computed for O_2, N_2, Ar, and CO_2 according to Bates [1984]. The molecular scattering phase matrix expansion coefficients $\beta_{m,s,i,j,k}$ are computed from the depolarization ratio which may be determined from the King factor for dry air [Peck and Reeder, 1972].

Aerosol scattering properties for each mode including the extinction $[C_{e,i}(\lambda)]$ and scattering $[C_{s,i}(\lambda)]$ cross sections (μm) and the scattering phase matrix expansion coefficients are computed with the LMie linearized Mie scattering code [McGarragh, 2013a] using as input the state vector elements: $r_{g,i}$, σ_i, $m_{r,i}(\lambda)$, and $m_{i,i}(\lambda)$. Then aerosol optical thickness $\tau_a(\lambda)$ and single scattering albedo $\omega_a(\lambda)$, required along with the scattering phase matrix expansion coefficients for input to the RTM, are computed from $C_{e,i}(\lambda)$, $C_{s,i}(\lambda)$, and $N_{0,i}$ using equations 5.25 and 5.26.

The RTM requires single total values for optical thickness, single scattering albedo, and scattering phase matrix expansion coefficients so it is necessary to compute these values from the corresponding

values for molecular absorption, molecular scattering, and aerosol effects. This is done with the following relations based on averages weighted by optical thickness and single scattering albedo

$$\tau = \tau_{m,a} + \tau_{m,s} + \tau_{a,f} + \tau_{a,f}, \tag{5.27}$$

$$\omega = \frac{\tau_{m,s} + \tau_{a,f}\omega_{a,f} + \tau_{a,f}\omega_{a,c}}{\tau_{m,a} + \tau_{m,s} + \tau_{a,f} + \tau_{a,c}}, \tag{5.28}$$

$$\beta_{i,j,k} = \frac{\tau_{m,s}\beta_{m,s,i,j,k} + \tau_{a,f}\omega_{a,f}\beta_{a,f,i,j,k} + \tau_{a,c}\omega_{a,c}\beta_{a,c,i,j,k}}{\tau_{m,s} + \tau_{a,f}\omega_{a,f} + \tau_{a,c}\omega_{a,c}}, \tag{5.29}$$

where wavelength dependence is implied and the single scattering albedo for molecular absorption $\omega_{m,a}$ is zero and for molecular scattering $\omega_{m,s}$ is unity.

Finally, since the aerosol-top pressure P_{top} does not in general coincide with the layer boundaries defined by the input meteorological profiles an additional level is inserted into the layer containing the aerosol-top.

Linearization of all the computations in the atmospheric model discussed above to compute derivatives of the outputs with respect to their inputs is straight forward and will not be discussed here.

5.4.2 Surface model

The surface model used in this study is just a simple Lambertian surface characterized by Lambertian surface albedo. In the future more complex surface BRDF kernels will be considered. This is especially important for multiangle measurements and/or polarimetric measurements.

5.4.3 Radiative transfer model

With the atmospheric optical properties for each layer and surface optical properties determined along with their associated derivatives with respect to physical inputs, the TOA Stokes parameters I, Q, and U, and their associated derivatives with respect to physical inputs are calculated using a radiative transfer model (RTM). As is common, the Stokes parameter V is ignored as it is typically negligible and most instruments are insensitive to it. This reduces the order of the scattering phase matrix from four to three resulting in faster radiative transfer calculations. The RTM Stokes output is unit normalized and are either converted directly to reflectance units consistent with the MODIS

or APS instruments or are first multiplied by the solar spectrum computed from the solar model to obtain physical units consistent with the hyperspectral measurements which are then converted to reflectance units.

The radiative transfer calculations are all performed using the XRTM radiative transfer model [McGarragh, 2013b]. XRTM is a linearized plane-parallel vector radiative transfer model that includes emission, absorption, and multiple scattering and supports both solar and thermal sources. It includes several different RT solvers and many standard features. Of the features supported, in the calculations for this study we use Delta-M scaling for scattering phase matrix truncation [Wiscombe, 1977, Chami et al., 2001], the TMS single scattering correction [Nakajima and Tanaka, 1988], and the pseudo spherical approximation, where the solar beam is modeled through a spherical atmosphere [Dahlback and Stamnes, 1991].

The radiative transfer calculations are performed differently depending on whether monochromatic or hyperspectral measurements are being simulated. In the case of the MODIS and APS measurements used in this study it is assumed that that a particular channel measures at a single wavelength and therefore a single monochromatic calculation is appropriate in this case. For this we use the discrete ordinates solver in XRTM which is capable of efficiently computing multiangle measurements simultaneously. For these calculations we set the number of streams to 32 which therefore truncates the scattering phase matrix expansion to 32 terms. In the case of hyperspectral measurements each of the three spectrums must be simulated at a spectral resolution of 0.01 cm^{-1} resulting in tens of thousands of individual monochromatic calculations. This is computationally prohibitive and therefore we adopt an approximation referred to as "Low Stream Interpolation" (LSI) described by O'Dell [2010]. With LSI, fast low accuracy calculations are performed using XRTM's dedicated two-stream solution at each of the monochromatic points required while slower more accurate monochromatic calculations, using XRTM's Padé approximation solver [McGarragh and Gabriel, 2010, 2013] at 32 streams, are performed for a small number (a few tens) of select profiles representing a range of scattering conditions. The high accuracy calculations are then used to correct the full resolution low accuracy calculations under the assumption that the scattering properties remain constant across the spectrum. Linearization of LSI to compute, in addition to the hyperspectral measurements, derivatives of these measurements, is straight forward.

5.4.4 Solar model

The solar model consists of a solar absorption spectrum and a solar continuum. The absorption spectrum is derived from an empirical list of over 20,000 lines that includes line frequency, line strength, and Doppler and $1/e$-folding widths. The use of a model allows for the computation of solar spectra with an arbitrary resolution without resampling. The solar line list covers the range from 550 to 15,000 cm^{-1} and is derived from FTS solar spectra: Atmospheric Trace Molecule Spectroscopy (ATMOS) exoatmospheric and MkIV balloon spectra for 550–5650 cm^{-1} [Geller, 1992, 1995] and Kitt Peak ground-based spectra for 5000–15,000 cm^{-1} [Wallace et al., 1993, Livingston and Wallace, 1991]. The solar continuum is a ninth-order polynomial fit to the near-infrared part of the solar spectrum measured by the SOLSPEC instrument [Thuillier et al., 2003]. It is modulated by the sun-earth distance while sunspots and other solar activity are ignored. The solar spectrum is the product of the solar absorption spectrum and the solar continuum. A doppler shift is also applied to transform the spectrum to the frame of reference of a particular FOV.

5.4.5 Instrument models

The instrument models consists of two components: (1) An instrument radiance model which takes as input the radiances and associated derivatives simulated by the RTM and produces radiances and associated derivatives consistent with that actually measured by the instrument and used in the measurement vector $\mathbf{y}$ and the matrix $\mathbf{K}$. This is first done by application of the instrument's Mueller matrix to each point within a band and then use of the instrument's spectral response function (SRF) to convolve the points to channels within a band. (2) An instrument noise model that determines the noise levels for the measurements $\sigma_{y,i}$ which are used, in addition to other forward model errors, to construct the forward model error covariance matrix $\mathbf{S}_\epsilon$.

In the case of MODIS and APS the instruments measure I (MODIS) or I, Q, and U (APS) directly so application of a Mueller matrix is not necessary. In addition, we assume that the bands are monochromatic so that the actual measurement may be set equal to the radiances computed for the center point of each band. As a result, and instrument radiance model is not necessary and the last two nodes given in figure 5.1 may be skipped. For the MODIS noise we use the signal-to-noise ratios (SNRs) specified by the instrument requirements [Xiong and Barnes, 2006]. These are 243,

228, 128, 201, 74, 275, and 110, for the 0.469, 0.555, 0.645, 0.856 1.24, 1.64, and 2.13 μm bands respectively. For the APS measurements we use the model for the Research Scanning Polarimeter (RSP), an instrument very similar to APS, given in Waquet et al. [2009].

For TANSO-FTS measurements the instrument radiance model takes as input monochromatic Stokes vectors (and associated derivatives) computed at the "full" resolution of 0.01 cm^{-1} (enough resolution to resolve the centers of individual lines) and produces radiances (and associated derivatives) as would be measured by the instrument with the following relation:

$$I_{b,i,p} = \int_0^\infty \left(m_{I,p} I(\lambda) + m_{Q,p} Q(\lambda) + m_{U,p} U(\lambda)\right) \mathrm{SRF}_{b,p}(\lambda) d\lambda, \tag{5.30}$$

where $I_{b,i,p}$ is the measured radiance (or an associated derivative) in band b and channel i at polarization $p \in \{P, S\}$, λ represents the monochromatic wavelength, the $m_{S,p}$ coefficients are elements of the instrument Mueller matrix, and $\mathrm{SRF}_{b,p}$ is the spectral response function for band b and polarization p. In this study our target hyperspectral instrument is the GOSAT TANSO-FTS for which the channel wavelengths for each band and the SRF for each band and polarization are provided with the data. The integration is performed over a 100 cm^{-1} range centered on each channel.

For the TANSO-FTS instrument noise model we use a model presented by O'Dell et al. [2012], where the actual noise from the TANSO-FTS instrument was characterized by analyzing over a year's worth of high-gain spectra. It was found that the instrument noise is roughly constant across each band and is broadly consistent with the following parameterization:

$$N_{b,p} = \sqrt{A_{b,p} + B_{b,p} I_{c,b,p}}, \tag{5.31}$$

where $I_{c,b,p}$ is the continuum signal level in band b and polarization p and $A_{b,p}$ and $B_{b,p}$ are parameters listed in table 5.4 for each band and polarization.

5.5 Atmospheric, surface, and geometry scenarios

Rigorous sensitivity and information content studies must include a full range of atmospheric parameters related to pressure, temperature, humidity, O_2, O_3, CO_2, aerosols, and the surface. In

Table 5.4: Coefficients of the TANSO-FTS noise model assuming standard GOSAT intensity units (W cm^{-1} cm^{1} sr^{-1}).

	A		B	
	P	S	P	S
Band 1	0.0	0.0	0.0	0.0
Band 2	0.0	0.0	0.0	0.0
Band 3	0.0	0.0	0.0	0.0

addition, a full range of possible solar and instrument geometries must be accounted for. Unfortunately, due to the large dimensionality of our parameter space we must make some simplifications in order to keep the presentation to a reasonable length. Below we describe the set of atmospheric parameters and assumptions about these parameters used in the studies that follow. In these studies given parameters are varied, with others remaining constant at a "standard". The "standard" is identified for each parameter. Note, that we have assumed that observations have been screened for clouds and that the cloud screening process performs well enough and is strict enough to assume that clouds are not present and need not be considered.

For pressure, temperature, humidity, and O_3 we use a mean of the mid-latitude summer and winter profiles given by McClatchey et al. [1972] for all cases. As discussed in section 5.3.1 a rigorous error characterization is preformed for these parameters and as such we believe that errors incurred in our assumptions here will be accounted for in our information content results. These profiles are provided at 33 levels which will define our vertical atmospheric discretization to 32 layers. For O_2 and CO_2 volume fractions taken from Seinfeld and Pandis [1998] were used. For the aerosols we use three of the five key aerosol types presented by Dubovik et al. [2002b] based on AERONET [Holben et al., 1998] observations at several locations worldwide: "urban-industrial", "biomass burning", and "desert dust". The properties of these aerosol models are presented in table 5.5. These are bimodal aerosol types with both a fine and coarse mode although, unlike our state vector, the real and imaginary parts of the index of refraction are identical for each mode. In Dubovik et al. [2002b] the models are given for a log-normal volume distribution but, as already discussed, we consider a log-normal size distribution. As a result, the mean radius of the volume distribution r_V must be

Table 5.5: The three fundamental aerosol models used in this study along with their relevant microphysical parameters.

type	$r_{g,f}$	$r_{e,f}$	σ_f	$v_{e,f}$	$r_{g,c}$	$r_{e,c}$	σ_c	$v_{e,c}$	m_r	m_i
urban-industrial	0.071	0.113	0.43	0.20	0.845	2.280	0.63	0.49	1.47	0.01400
biomass burning	0.087	0.138	0.43	0.20	0.451	2.327	0.81	0.93	1.50	0.00940
desert dust	0.088	0.137	0.42	0.19	0.832	2.109	0.61	0.45	1.55	0.00250 (440)
										0.00140 (670)
										0.00100 (870)
										0.00100 (1020)

converted to a mean radius for a size distribution r_g with

$$r_g = r_V \exp(-3\sigma^2). \tag{5.32}$$

The real and imaginary indices of refraction are considered constant with wavelength for all cases except the imaginary index for desert dust. In this case, the index is given for the four primary AERONET inversion wavelengths of 0.440, 0.670, 0.870, and 1.020 μm. Linear interpolation/extrapolation were used to obtain the imaginary index at the wavelengths required for this study. The other land-based key aerosol type presented by Dubovik et al. [2002b], "mixed" was not considered in this study as it was assumed that the three other types represented components of the "mixed" aerosol. In our presentation the aerosol model used varies depending on the case. In cases requiring a standard aerosol model we used the "biomass burning" model since, as shown in the sensitivity study, the optical properties of this model fall between that of the "urban/industrial" and "desert dust" models. For aerosol loading we use optical thickness at 0.55 μm $\tau_a(0.55)$ which may be converted to the required number concentration N_0 given the aerosol model. In cases requiring a standard value of $\tau_a(0.55)$ we use $\tau_{a,i}(0.55) = 0.1$ for each mode. In cases requiring a large range of $\tau_a(0.55)$ values we use values of 0.01, 0.1, and 1.0 for each mode. In some cases $\tau_a(0.55)$ varies at a finer resolution from a total of 0.1 to 2.0. The aerosol layers were assumed to exist homogeneously from a particular top pressure P_{top} to the surface, where three values of P_{top} were used, depending on the case: 400, 600, and 800 hPa, with 600 hPa as the standard. For the spectral surface albedo $A(\lambda)$ we assumed it was constant with wavelength and used, depending on the case: 0.0, 0.2, and 0.4, with 0.2 as the standard.

For the solar geometry we use a standard zenith angle θ_0 of 35° and in some cases vary the angle from 0° to 90°. For the solar azimuth angle ϕ_0 we use a standard angle of 180° and in some cases vary the angle from 90° to 270°. For the instrument viewing geometry we have to consider the types of instruments used. For simplicity will assume that all the instruments are on a polar orbiting descending platform inclined 0° from north. For MODIS we use a standard viewing zenith angle θ of 0° (nadir) and in some cases vary the angle from 0° to 70°. For the viewing azimuth angle MODIS observations are viewed to the left or to the right (looking into the flight direction) which, with a 0° inclination, results in viewing azimuth angles of 270 and 90° respectively. Since for the radiative transfer calculations it is the relative azimuth angle $(\phi - \phi_0)$ that is important it is sufficient to just relay on the variation in the solar azimuth angle ϕ_0 and use one viewing azimuth angle for which we choose right looking at 90°. For the nadir viewing TANSO-FTS observations the viewing zenith angle is 0° and the relative azimuth angle is irrelevant from a radiative transfer perspective so that variation in solar azimuth angle is not required in our range of test scenarios. For the multiangle observations the viewing zenith angle variation is a part of the measurement and therefore does not need to be considered in our range of test scenarios. For the viewing azimuth angle, since the observations are performed on track and the inclination is 0° the azimuth angle is fixed at 0 and 180° for aft and fore viewing directions, respectively.

5.6 Sensitivity study

Before attempting a formal information content analysis it is informative to look at the sensitivities for individual state vector parameters under different conditions involving the state vector parameters in $\mathbf{x}$ themselves and the vector of assumed parameters $\mathbf{b}$. This will provide insight in to which parameters are more sensitive to a particular measurement and if and how the variation in the measurement space provides sensitivity to a variation in parameters. An ideal measurement space would be one where each retrieval parameter produces sensitivity in one or more particular measurements in which all other parameters in both $\mathbf{x}$ and $\mathbf{b}$ have negligible effect. In reality this is almost never the case, but as we shall show, a significant variation in different types of measurements in wavelength, molecular absorption, Stokes vector, and view angle is a significant step in the right direction. Note, that instead of showing sensitivities to $N_{0,i}$ we show sensitivities to the derived

aerosol optical thickness $\tau_{a,i}(\lambda)$. In addition, we also show sensitivities to derived single scattering albedo $\omega_{a,i}(\lambda)$ as this parameter provides an intuitive perspective of the measurement sensitivities.

To show the sensitivities it is convenient to introduce a sensitivity normalized by the absolute value of the parameter and the measurement. In this way sensitivities between different measurements and between different parameters may be compared on a similar basis. For this we introduce our sensitivity for total reflectance R and polarized reflectance P to a particular parameter as

$$S_m(x) = \frac{\partial m}{\partial x}\frac{x}{m}, \tag{5.33}$$

where $m \in \{R, P\}$, x is the parameter, and $\frac{\partial m}{\partial x}$ is the derivative of the measurement with respect to the parameter x as calculated by the forward model.

5.6.1 MODIS measurements

We begin by showing total reflectance sensitivities $S_R(x)$ for the MODIS bands as a function of view angle θ for the three different aerosol models, urban-industrial, biomass burning, and desert dust, in figures 5.2, 5.3, and 5.4, respectively. In this case, we use the already defined standard of $\tau_{a,i}(0.55) = 0.1$, $P_{\text{top}} = 600$ hPa, $A = 0.2$, $\theta_0 = 35°$, $\phi_0 = 180°$, and $\phi = 90°$. For perspective, the absolute total reflectance values are given in the upper left corner. The sensitivities are given in a separate plot for each channel ranging row-wise starting from the upper right corner. Several aspects are of note here. First, sensitivity to surface albedo A dominates in almost all cases. This is not surprising and illuminates why characterization of the surface is of the utmost importance in aerosol retrievals without which large retrieval biases would result. It is also worth noting that although not as consistent as A, sensitivity to single scattering albedo ω_a is usually second to that of A indicating again that retrievals that incorrectly characterize ω_a will suffer from biases. Second, sensitivity almost always increases with view angle and in a few cases even surpasses that with respect to A. This is due to the increased optical path at large view angles and therefore and an increase in the opportunity for photon aerosol interaction. This suggests that, in general, multiangle measurements may provide more information than single angle measurements alone. Third, the sensitivity to the fine mode aerosols tends to decrease with wavelength. This is a result of a decrease in the size parameter $a = \frac{2\pi r}{\lambda}$ for the fine mode and a move away from the optically active region

of $a > 1$. This shows the importance of having measurements made at wavelengths of less than or equal to around 0.6 μm to retrieve fine mode aerosol properties. Fourth, from the first aerosol model to the third aerosol model there is an increase in sensitivities to the fine mode and a decrease in sensitivities to the coarse mode, with exception to the coarse mode single scattering albedo $\omega_{a,c}$ which also increases. This effect is more difficult to explain due to the multitude of parameters in an aerosol model although it is likely that both effects are due to the steady increase in both the real part of the index of refraction m_r and the single scattering albedo ω_a with model in both modes.

5.6.2 TANSO-FTS measurements

Next, we show sensitivities of the TANSO-FTS measurements with respect to the state vector parameters for the standard of model two, $\tau_{a,i}(0.55) = 0.1$, $P_{\text{top}} = 600$ hPa, $A = 0.2$, $\theta_0 = 35°$, and $\phi_0 = 180°$. There are several dimensions of measurements for which to show sensitivities including band, channel, total or polarized reflectance, and angle. In figures 5.5 through 5.7 and figures 5.8 through 5.10 we show sensitivities for the total reflectances R and the polarized reflectances P, respectively. Each figure contains three columns, where the first, second, and third, columns are for bands 1, 2, and 3 respectively. In figures 5.5 and 5.8 the absolute value of the R and P are shown in the first row for reference, respectively, while the sensitivities to A and P_{top} are shown in the second and third rows. Sensitivities to τ_a, ω_a, r_g, σ, m_r, and m_i, are shown for R, for the fine and coarse modes, in figures 5.6 and 5.7, respectively, and for P, for the fine and coarse modes, in figures 5.9 and 5.10, respectively. In each plot, the spectrum for each view angle, nadir (red), fore (green), and aft (blue), are given as a function of wavenumber. It is important to note the scales for $S_R(x)$ and $S_P(x)$ have been set identically for all sensitivities and all bands. The result is that the sensitivities may be compared visually with ease with the consequence that spectral variations across the spectrum in some of the plots is not easily apparent.

It turns out, as we shall see, that it is useful to present the sensitivities as a function of the molecular absorption optical thickness [Stephens and Heidinger, 2000]. Figure 5.11 shows for the standard of model two, $\tau_{a,i}(0.55) = 0.1$, $P_{\text{top}} = 600$ hPa, $A = 0.2$, $\theta_0 = 35°$, and $\phi_0 = 180°$, the total reflectance R (column 1) and polarized reflectance P (column 2) in the O_2 A-band as a function of τ_{O_2} along with their associated sensitivities with respect to the state vector parameters for nadir, fore, and aft in the second, third, and fourth rows respectively. Using the same standard figure 5.12

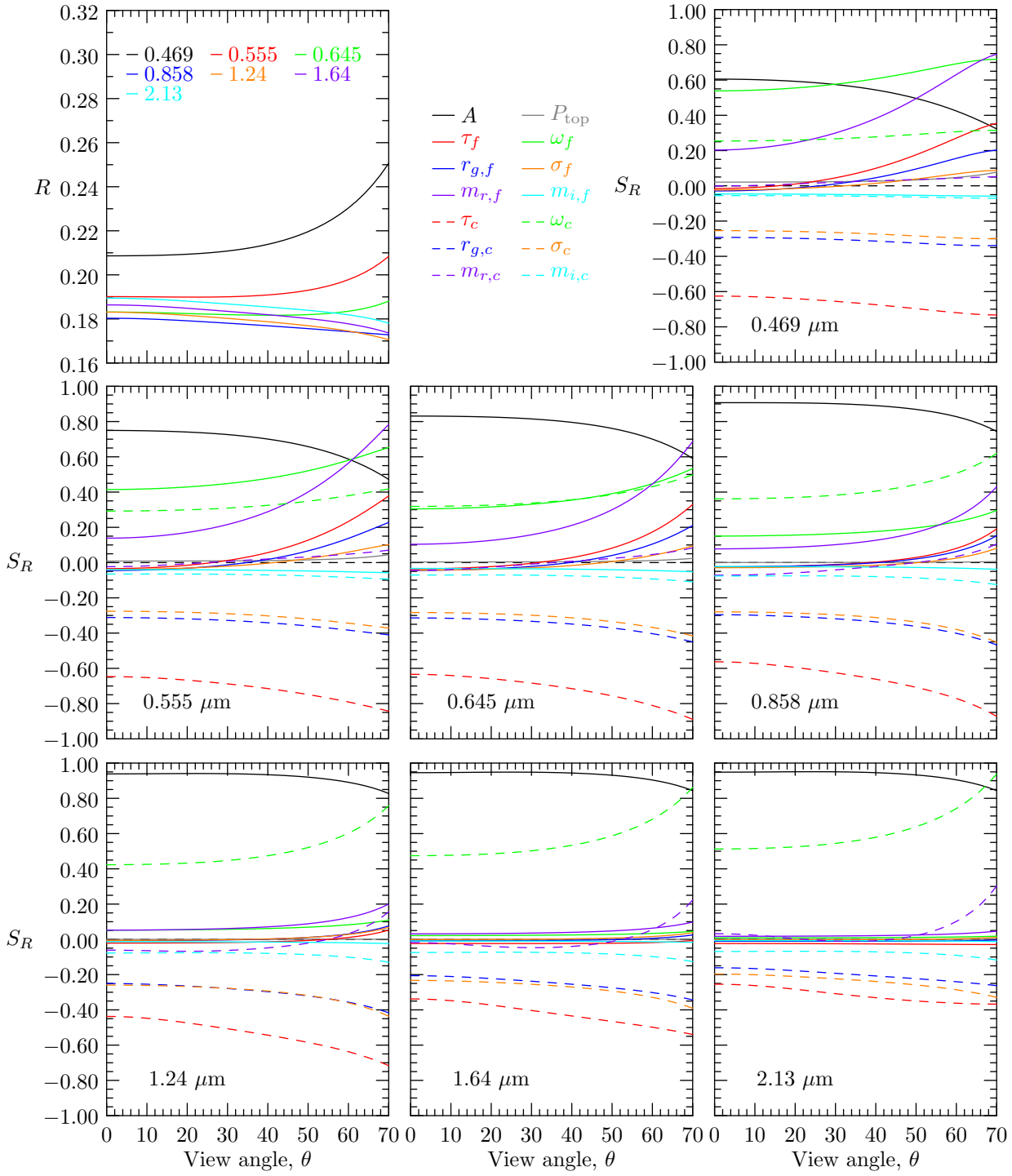

Figure 5.2: MODIS reflectance R and sensitivities S_R for model one (urban-industrial), $\tau_{a,i}(0.55) = 0.1$, $P_{\text{top}} = 600$ hPa, $A = 0.2$, $\theta_0 = 35°$, $\phi_0 = 180°$, and $\phi = 90°$.

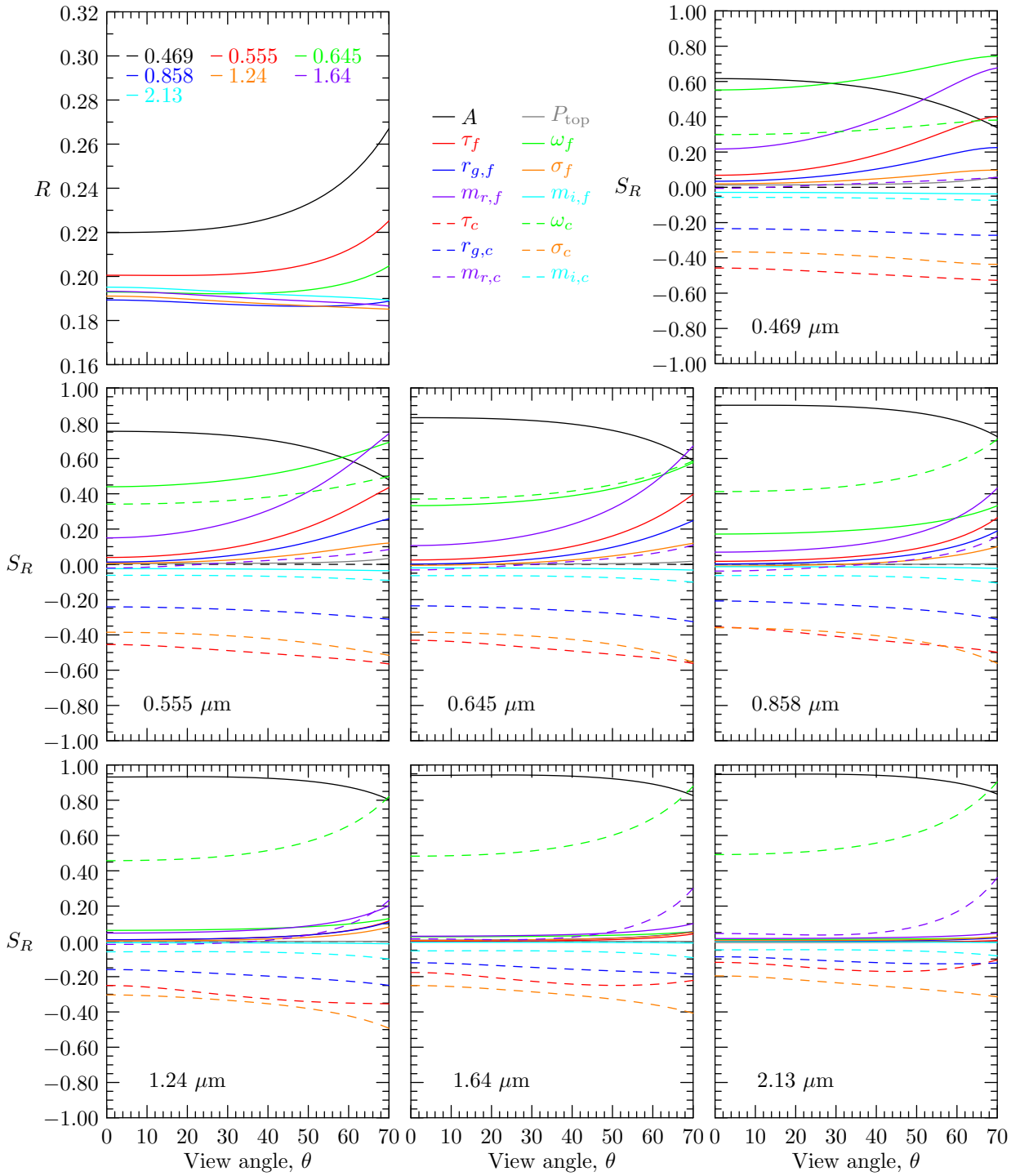

Figure 5.3: Same as figure 5.2 but for model two (biomass burning).

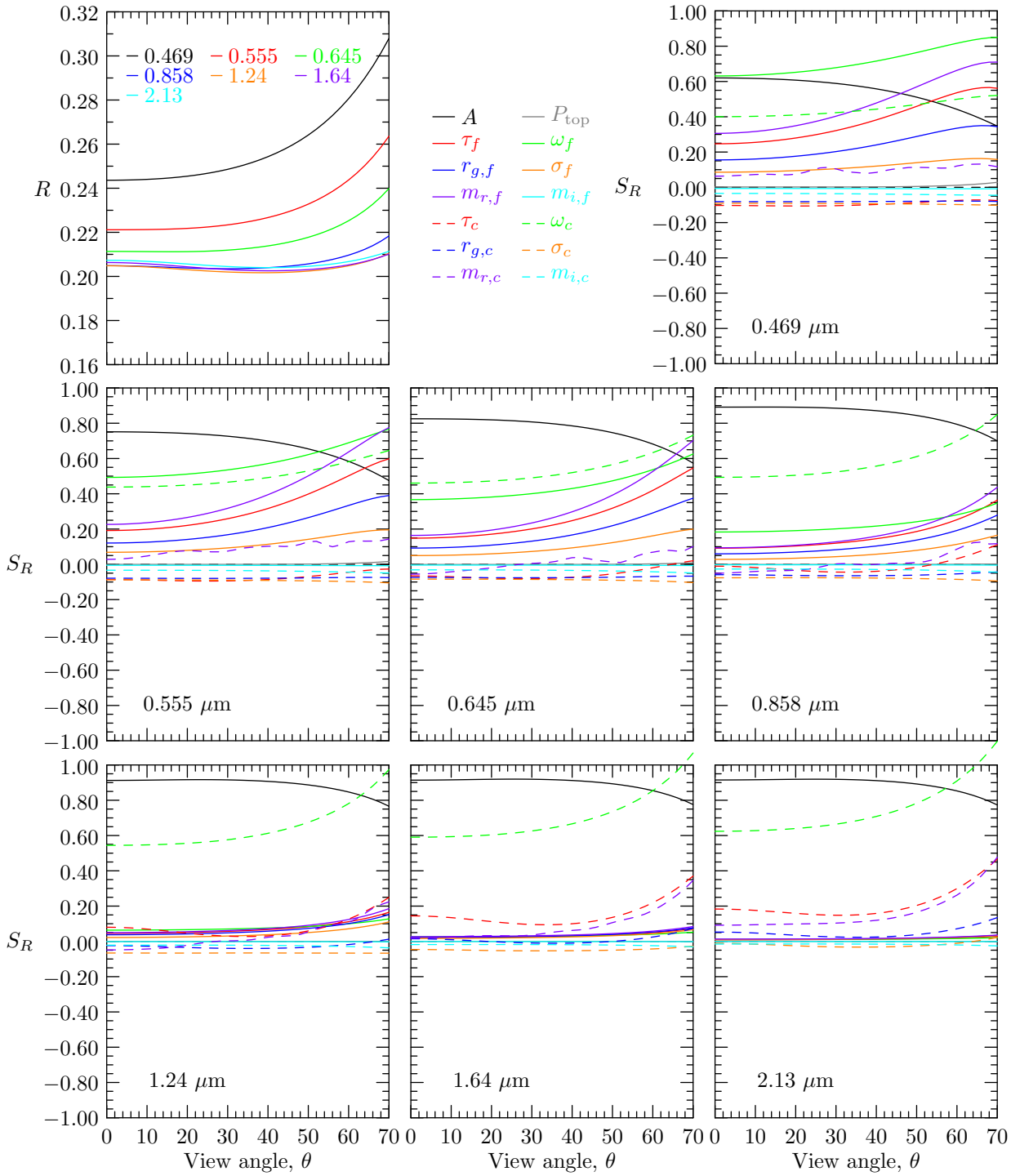

Figure 5.4: Same as figure 5.2 but for model three (desert dust).

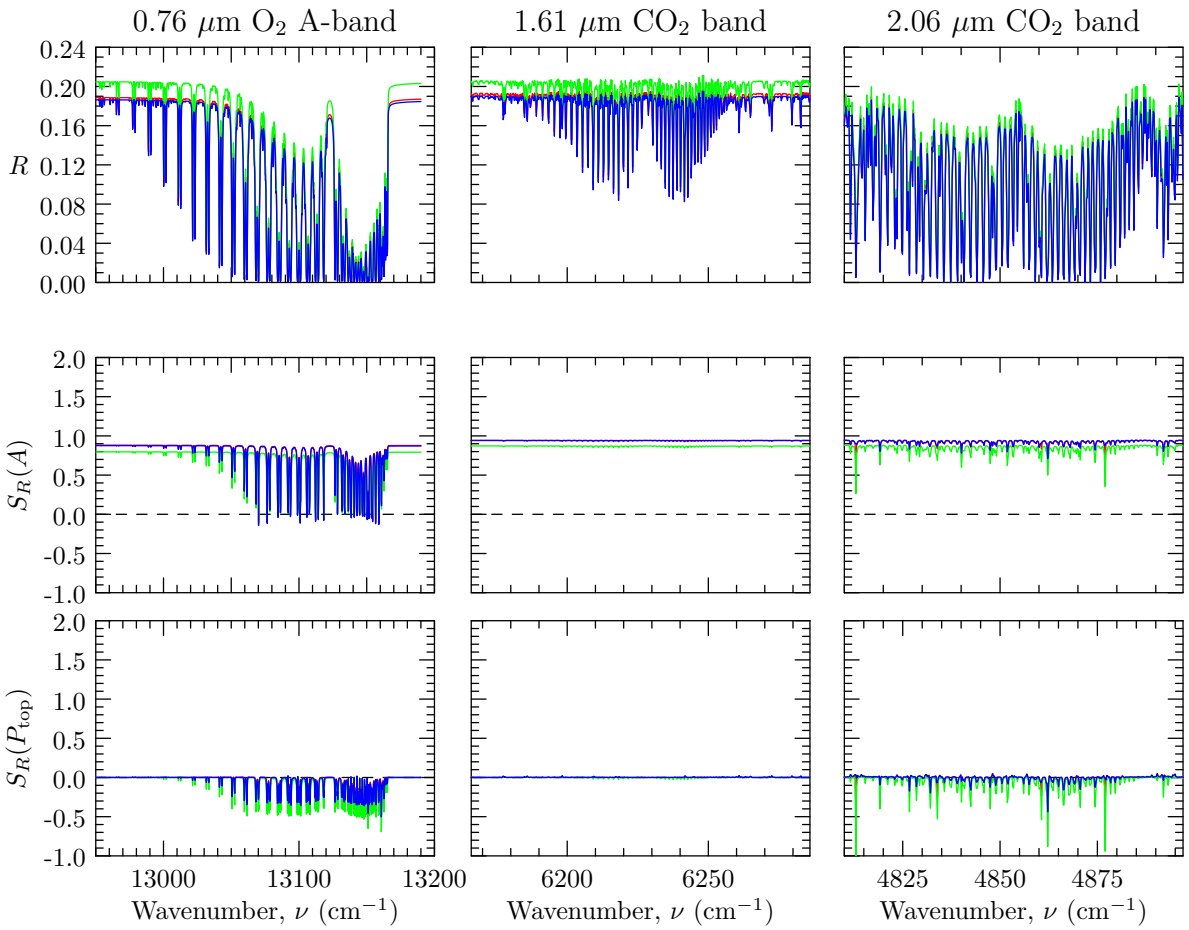

Figure 5.5: Reflectance R and sensitivities S_R for model two (biomass burning), $\tau_{a,i}(0.55) = 0.1$, $P_{\text{top}} = 600$ hPa, $A = 0.2$, $\theta_0 = 35°$, $\phi_0 = 180°$, and $\phi = 90°$, in the three TANSO-FTS bands for the nadir (red), fore (green), and aft (blue) viewing directions. Reflectances and sensitivities for A and P_{top} are in the current figure and sensitivities to optical and microphysical parameters are in figure 5.6 for the fine mode and figure 5.7 for the coarse mode.

shows the sensitivities for the three different aerosol models in the first, second, and third rows, respectively. Similarly figures 5.13, 5.14, and 5.15 show the sensitivities for modal aerosol optical thicknesses $\tau_{a,i}$ of 0.01, 0.1, and 1.0; aerosol-top pressures P_{top} of 400.0, 600.0, and 800.0 hPa; and surface albedos A of 0.0, 0.2, and 0.4; respectively.

There is wealth of information in these plots which we will discuss in the following three sections starting first with information related to the nadir total reflectance R, then information related to the nadir polarized reflectance P, and finally additional information related to multiangle measurements of both R and P.

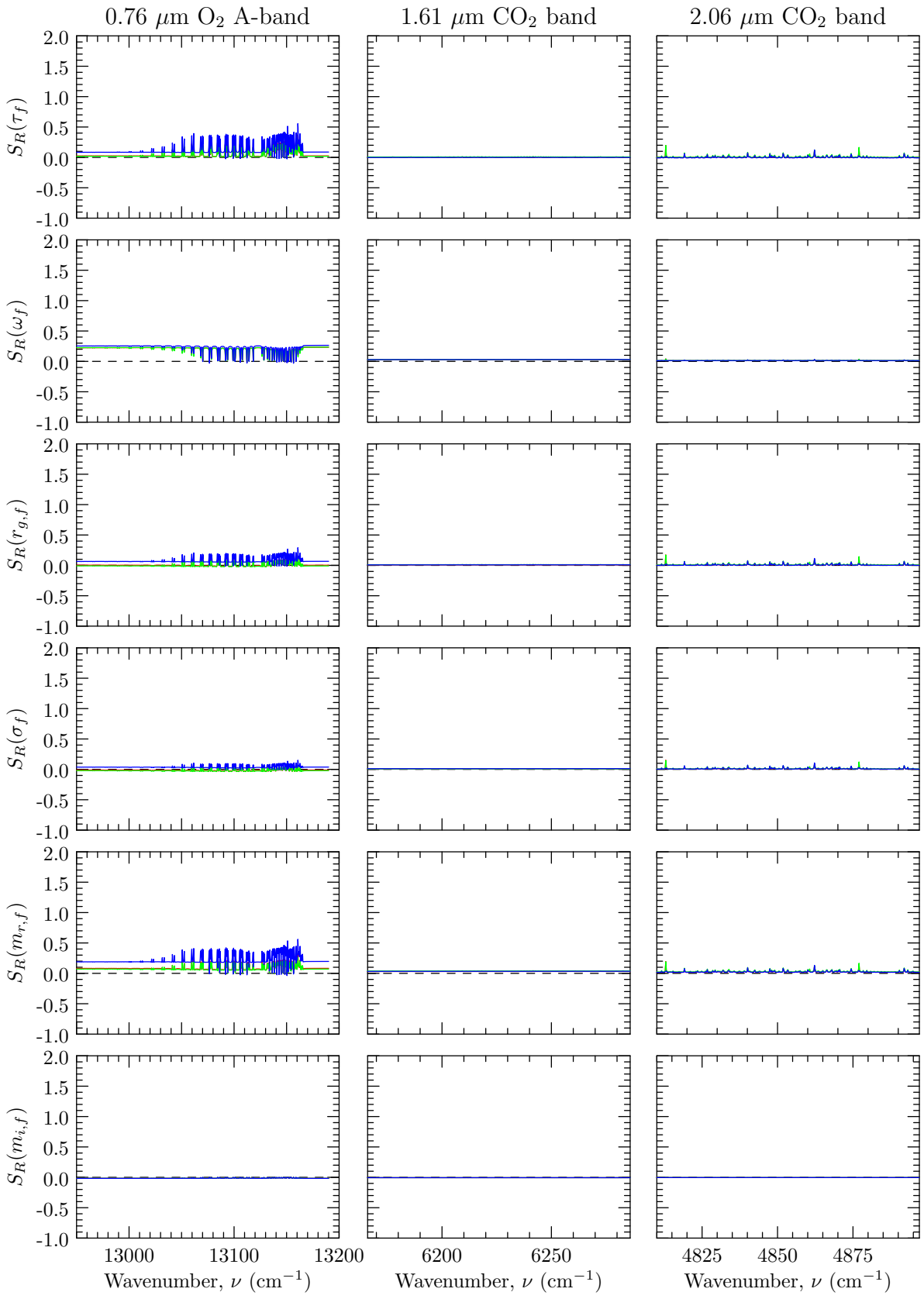

Figure 5.6: See caption for figure 5.5.

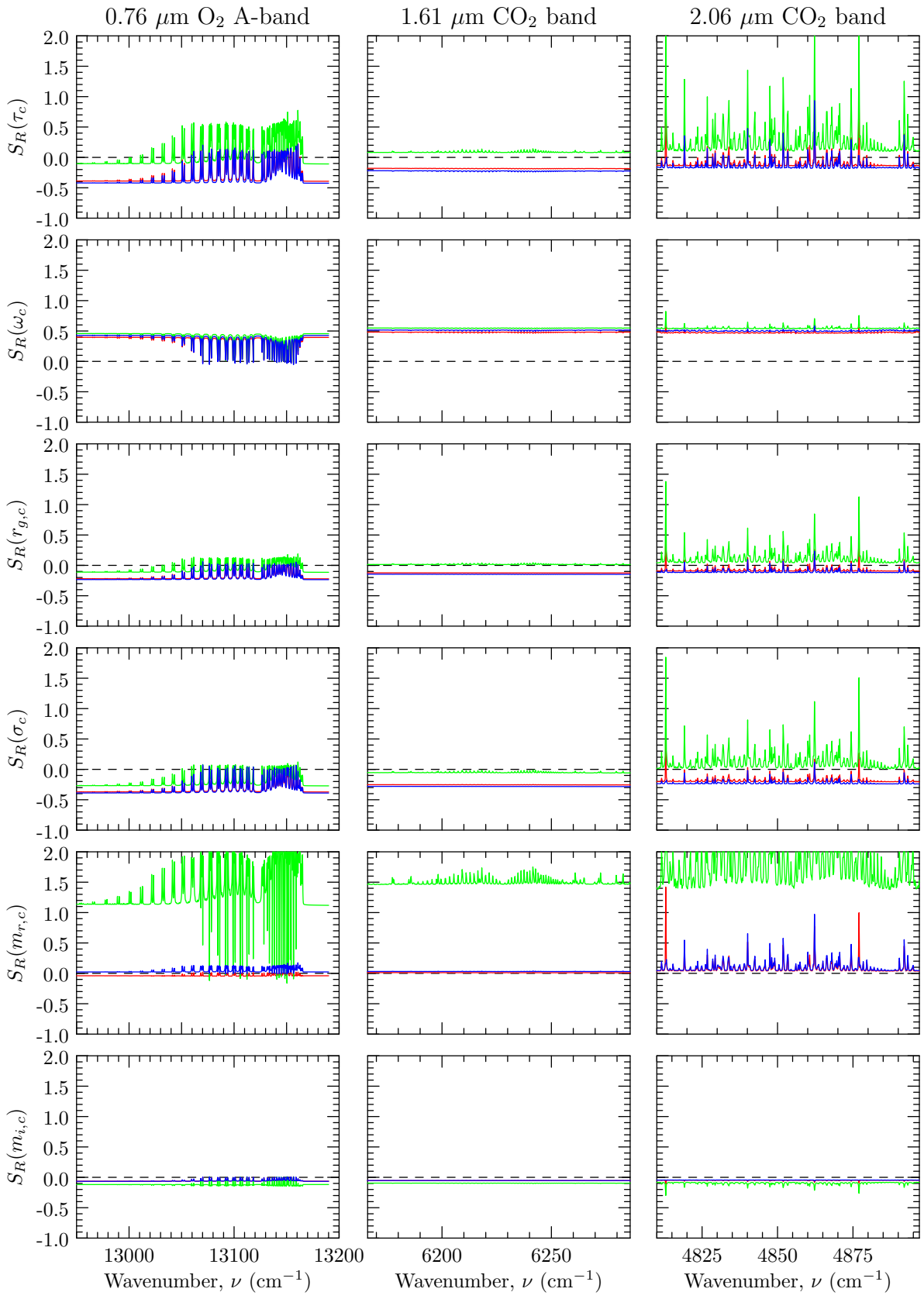

Figure 5.7: See caption for figure 5.5.

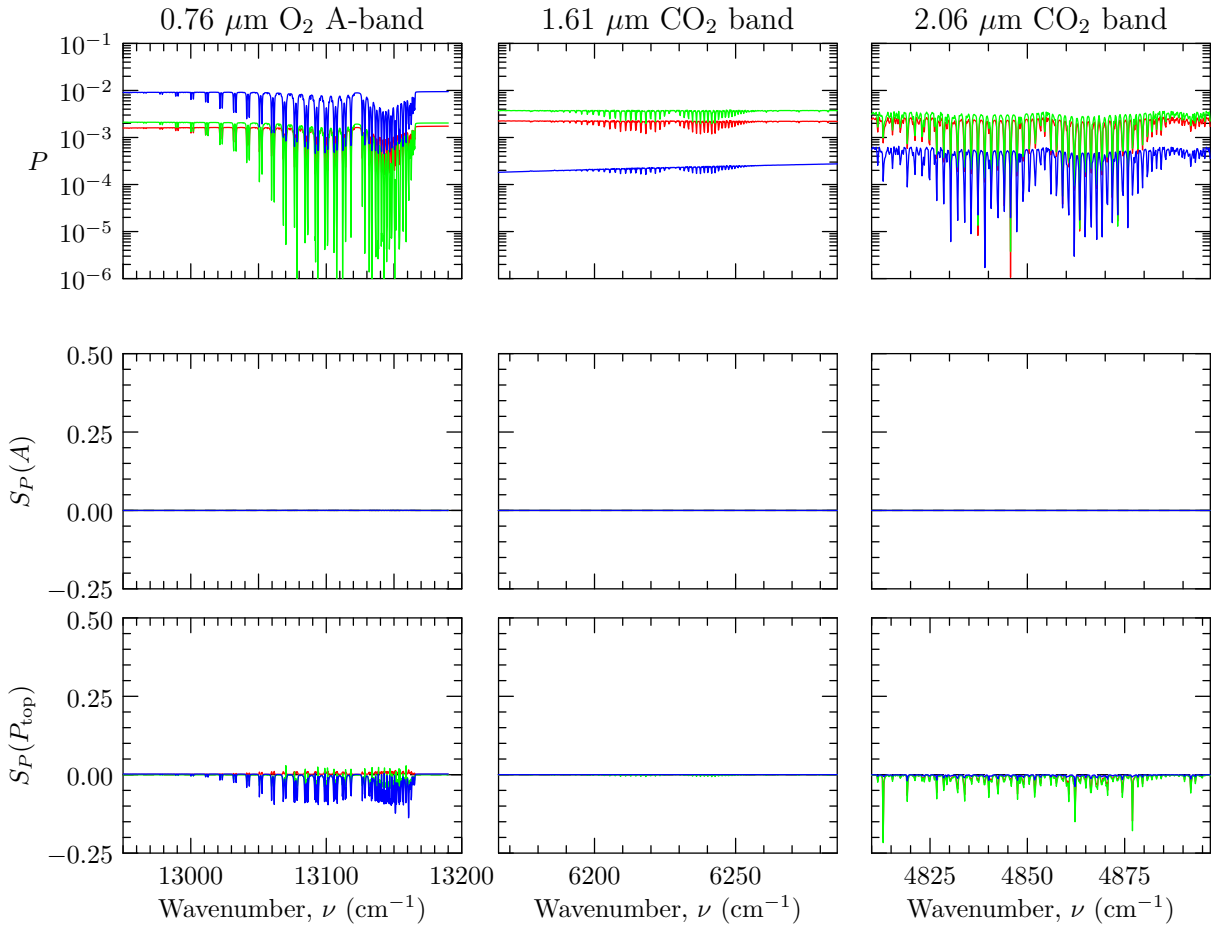

Figure 5.8: Same as figure 5.5 but for polarized reflectance P and associated sensitivity S_P.

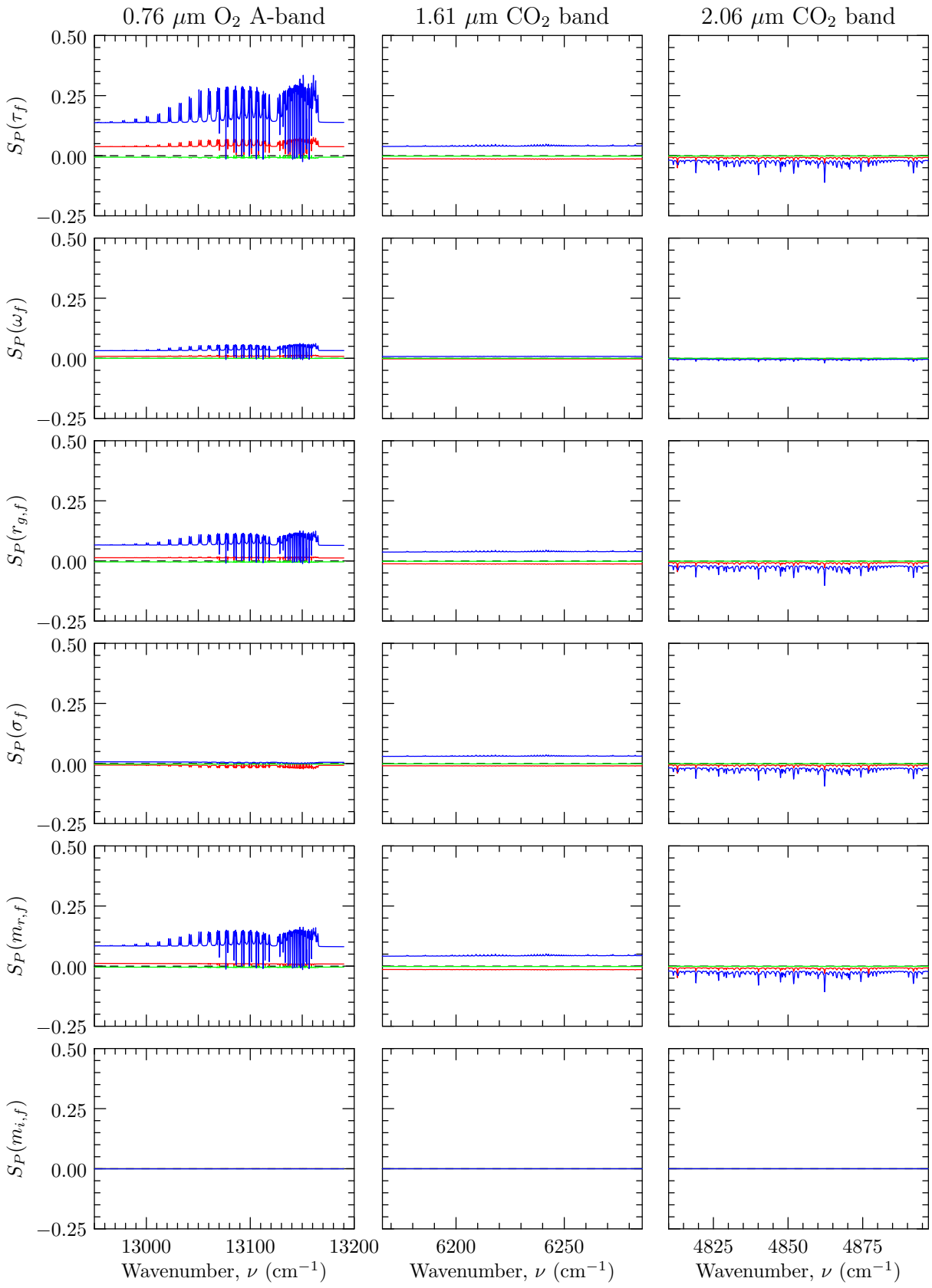

Figure 5.9: See caption for figure 5.8.

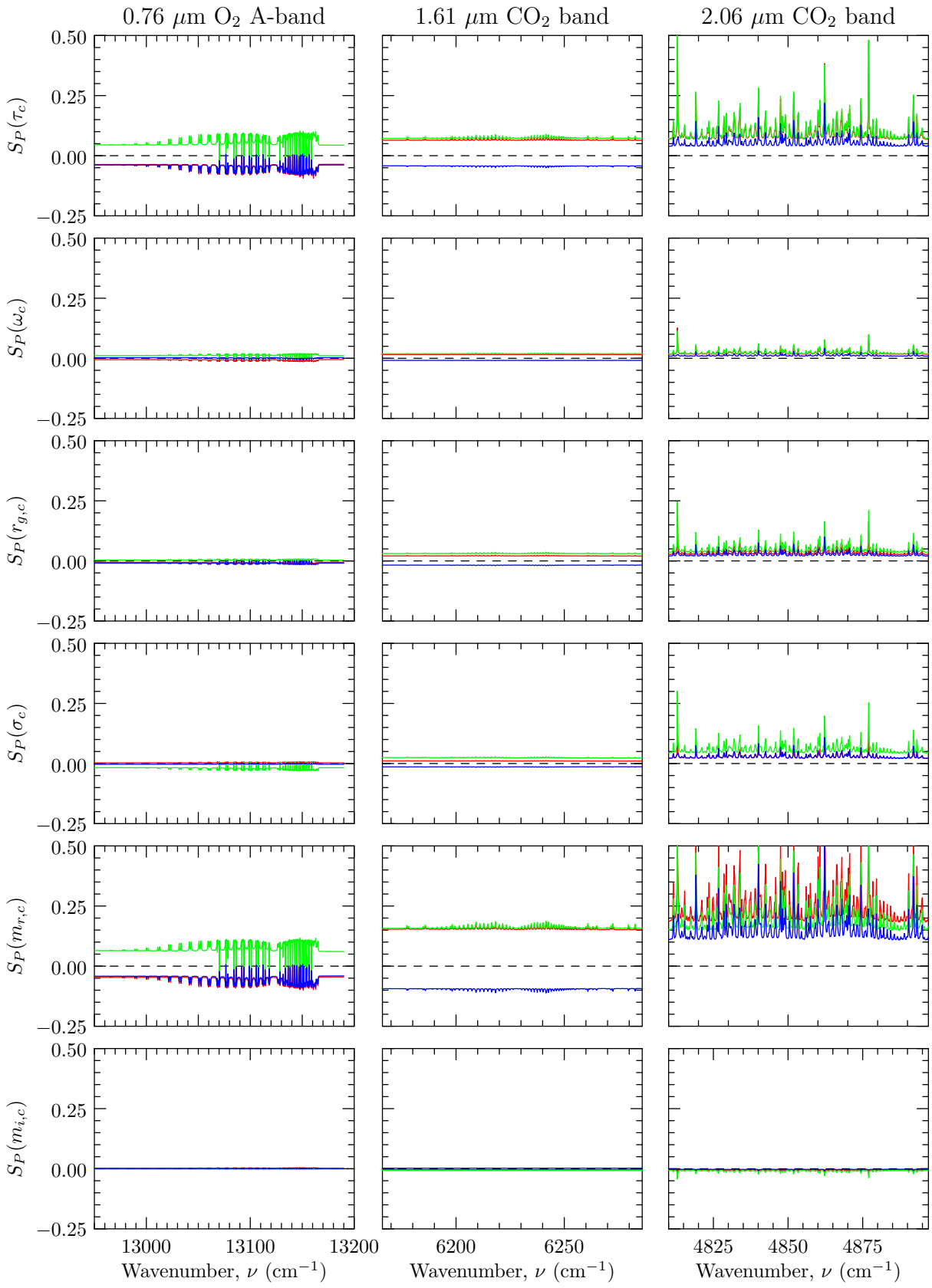

Figure 5.10: See caption for figure 5.8.

Total reflectance

In figures 5.5 through 5.7 the so called "continuum", where molecular absorption is negligible is apparent in most of the plots and is useful for comparison to the MODIS sensitivities of similar wavelengths as those bands also have negligible molecular absorption. The centers of absorption lines are also apparent with decreasing reflectance, especially in the O_2 A-band where the singlet and doublet pairs along with the P and R branches of the O_2 A-band are visible. In all cases (for nadir measurements) the sensitivity to surface albedo A in the continuum dominates over other sensitivities in the continuum which is not surprising considering what we have shown for the MODIS bands. It is in the absorption lines that the O_2 A-band provides new information. As molecular absorption increases the sensitivity to surface albedo A and single scattering albedo ω_a both decrease in magnitude whereas the sensitivity to all other parameters increases in magnitude (sometimes after crossing zero).

As we can see it is the variation in molecular absorption across each band that provides the variation in sensitivity which is why it useful to reorder the sensitivities as already discussed. In figure 5.11 it is clear that in the continuum, the values are much like that which are seen by the 0.645 and 0.856 μm MODIS bands but as mentioned above the sensitivities change as τ_{O_2} increases. The sensitivities with respect to surface albedo A and single scattering albedo ω_a decrease in magnitude with τ_{O_2}. The sensitivities with respect to the other aerosol parameters vary in magnitude with τ_{O_2} but the variation is more complicated than can be seen in the figures 5.5 through 5.7. The sensitivities first increase in magnitude with τ_{O_2} and then start to decrease, where in some cases, particularly for the coarse mode parameters, the sensitivities must decrease and cross zero before increasing. In some cases the sensitivity to the non-albedo parameters surpasses that of the albedo parameters.

The observations presented above can be explained in several ways. First, the decrease in sensitivity to surface albedo A is a result of the O_2 absorption obscuring the effect of the surface. That is, as the O_2 absorption increases a decreasing portion of the photons reaching the instrument have paths that encounter the surface. Second, the decrease in sensitivity to single scattering albedo ω_a with τ_{O_2} is a result of the fact that the sensitivity increases with multiple scattering since the radiance scattered n times is proportional to ω_a^n. As O_2 absorption increases photons are more likely

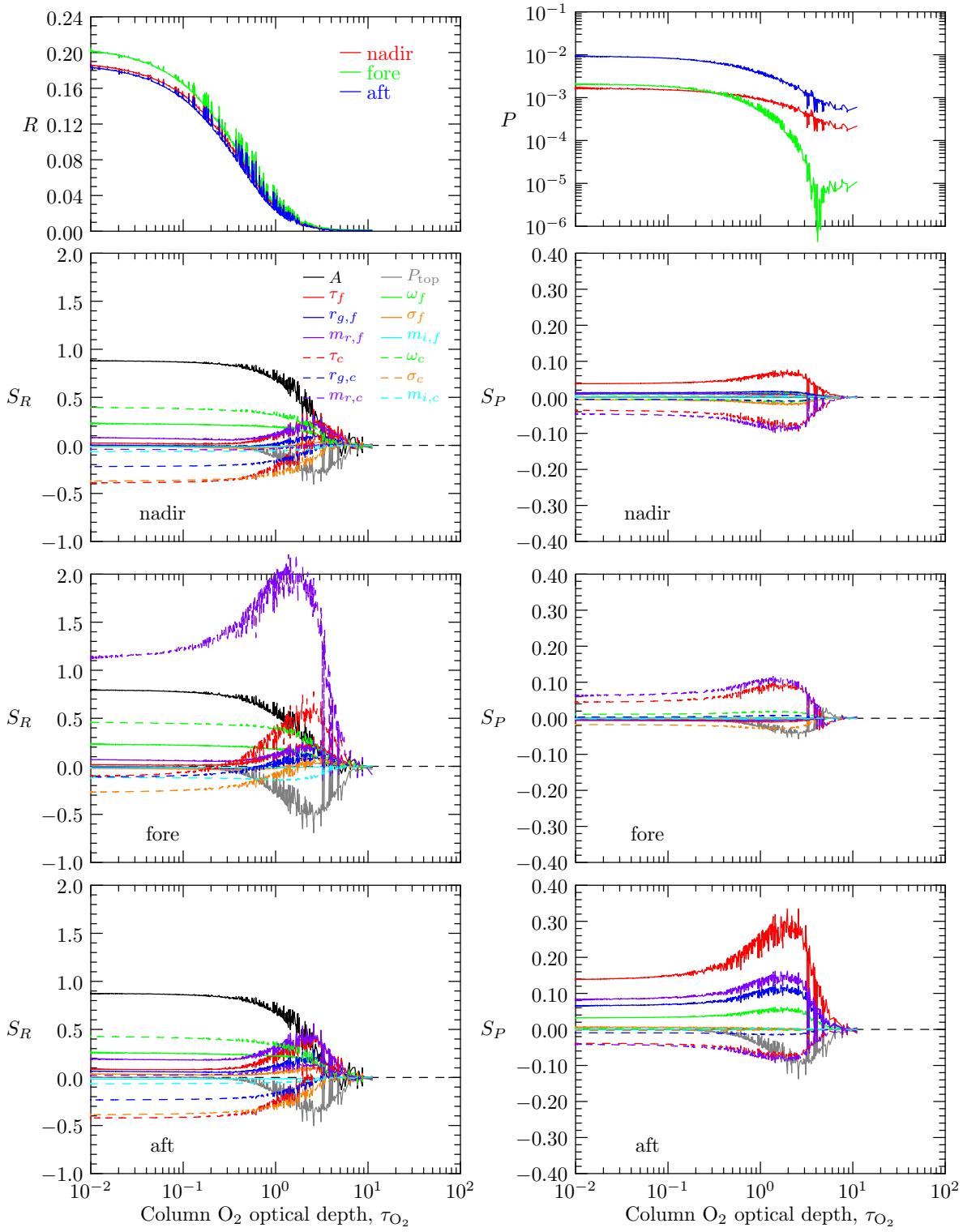

Figure 5.11: Nadir reflectance R and polarized reflectance P and corresponding multiangle sensitivities S_R and S_P for model two (biomass burning), $\tau_{a,i}(0.55) = 0.1$, $P_{\rm top} = 600$ hPa, $A = 0.2$, $\theta_0 = 35°$, $\phi_0 = 180°$, and $\phi = 90°$. R is in the left column while P is in the right column and S_R and S_P for the nadir, fore, and aft viewing directions are in the second, third, and forth rows respectively.

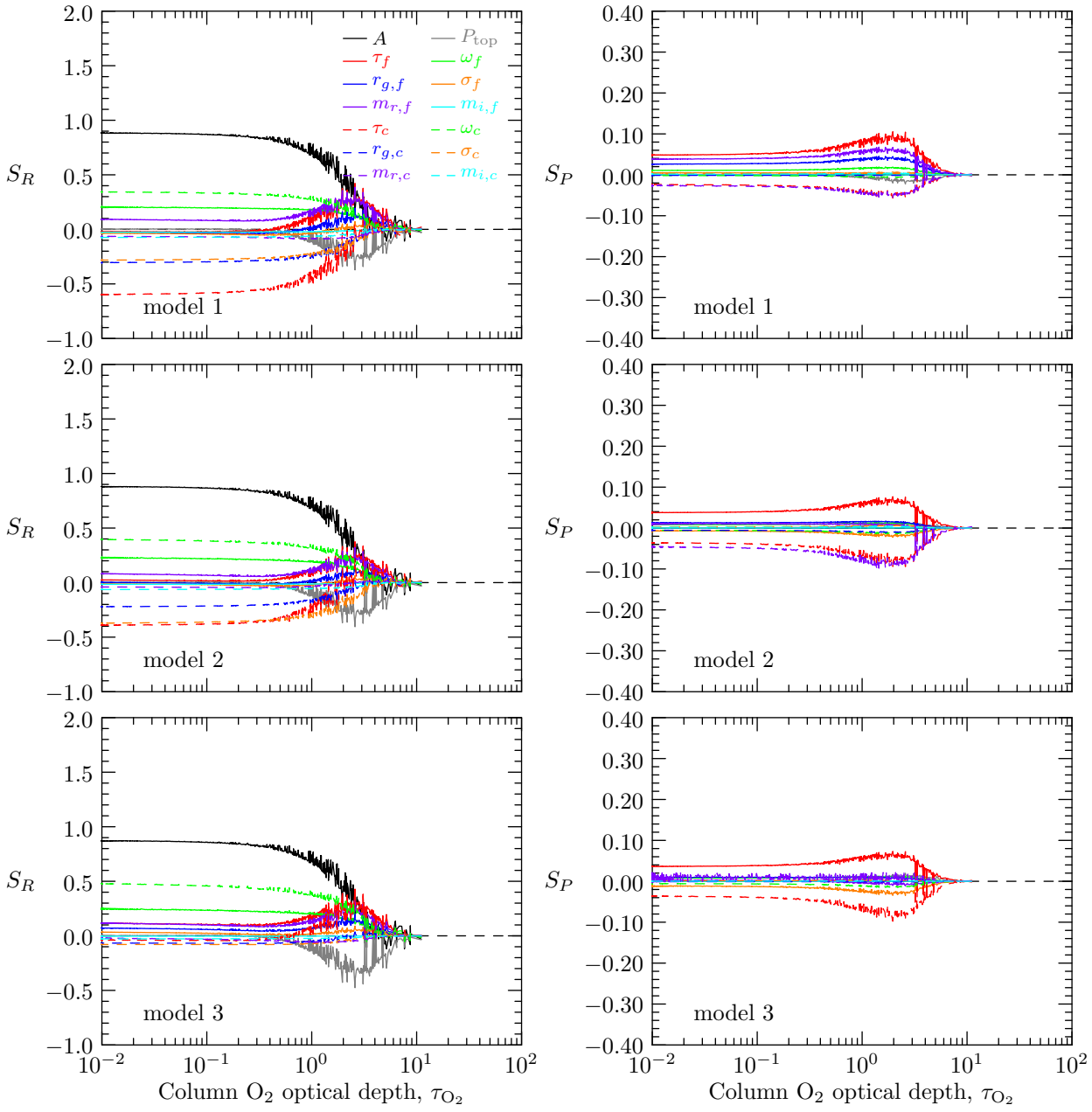

Figure 5.12: Same as the sensitivities S_R and S_P in figure 5.11 but for models one, two, and three in the first, second, and third rows, respectively.

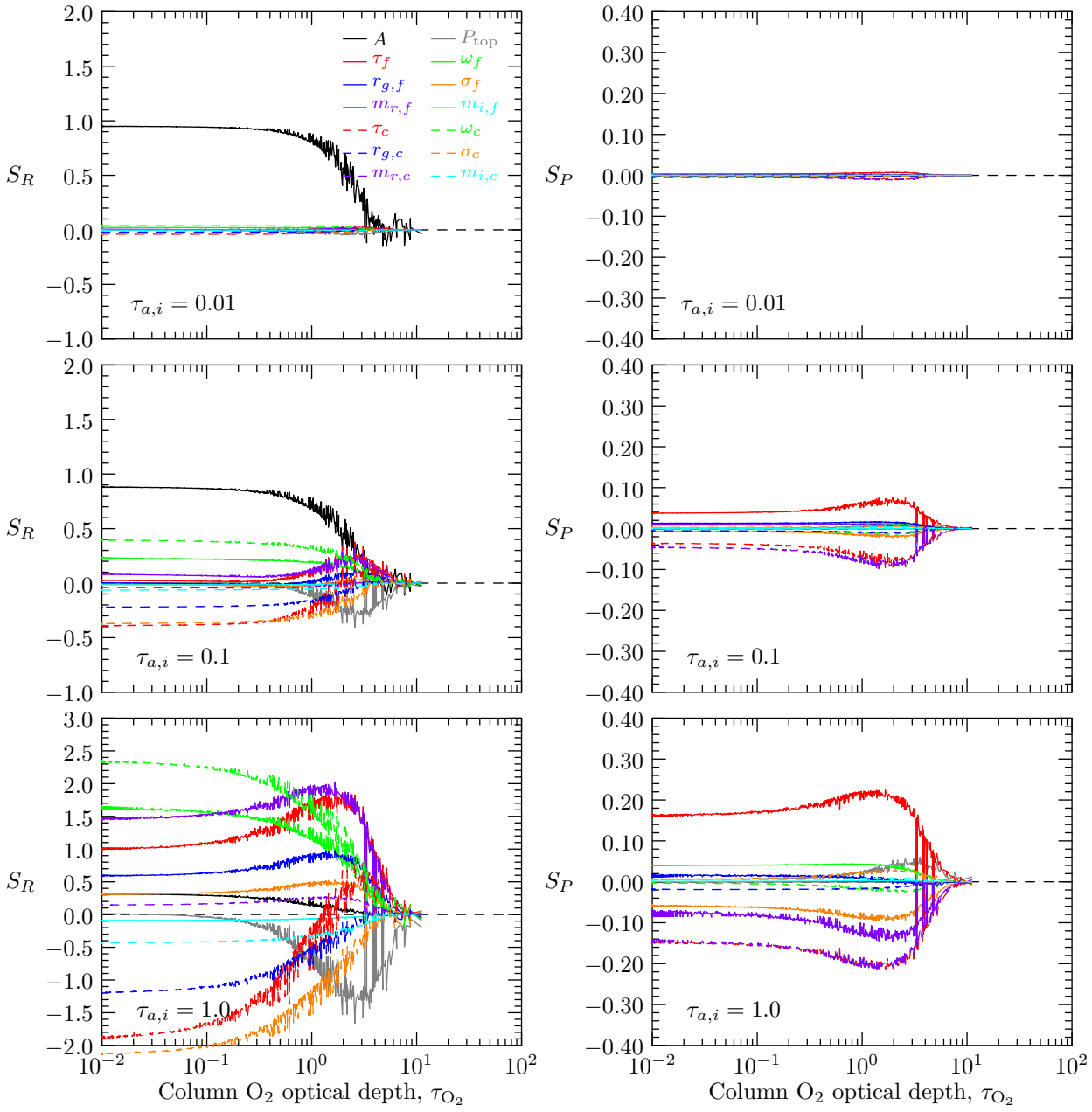

Figure 5.13: Same as the sensitivities S_R and S_P in figure 5.11 but for modal optical thicknesses $\tau_{a,i}(0.55) = 0.01$, 0.1, and 1.0 in the first, second, and third rows, respectively.

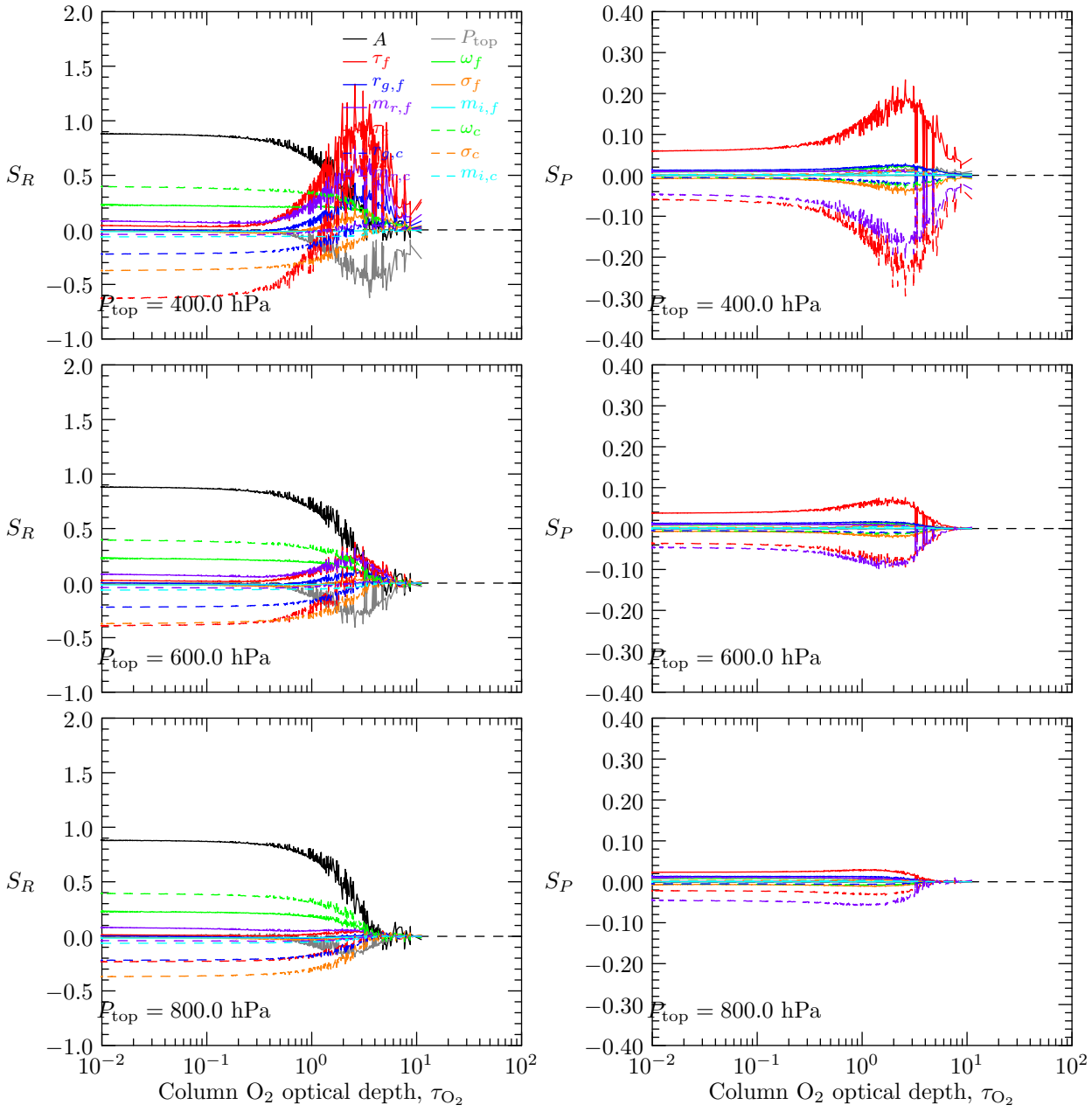

Figure 5.14: Same as the sensitivities S_R and S_P in figure 5.11 but for aerosol-top pressure values $P_{\rm top} = 400$ hPa, 600 hPa, and 800 hPa in the first, second, and third rows, respectively.

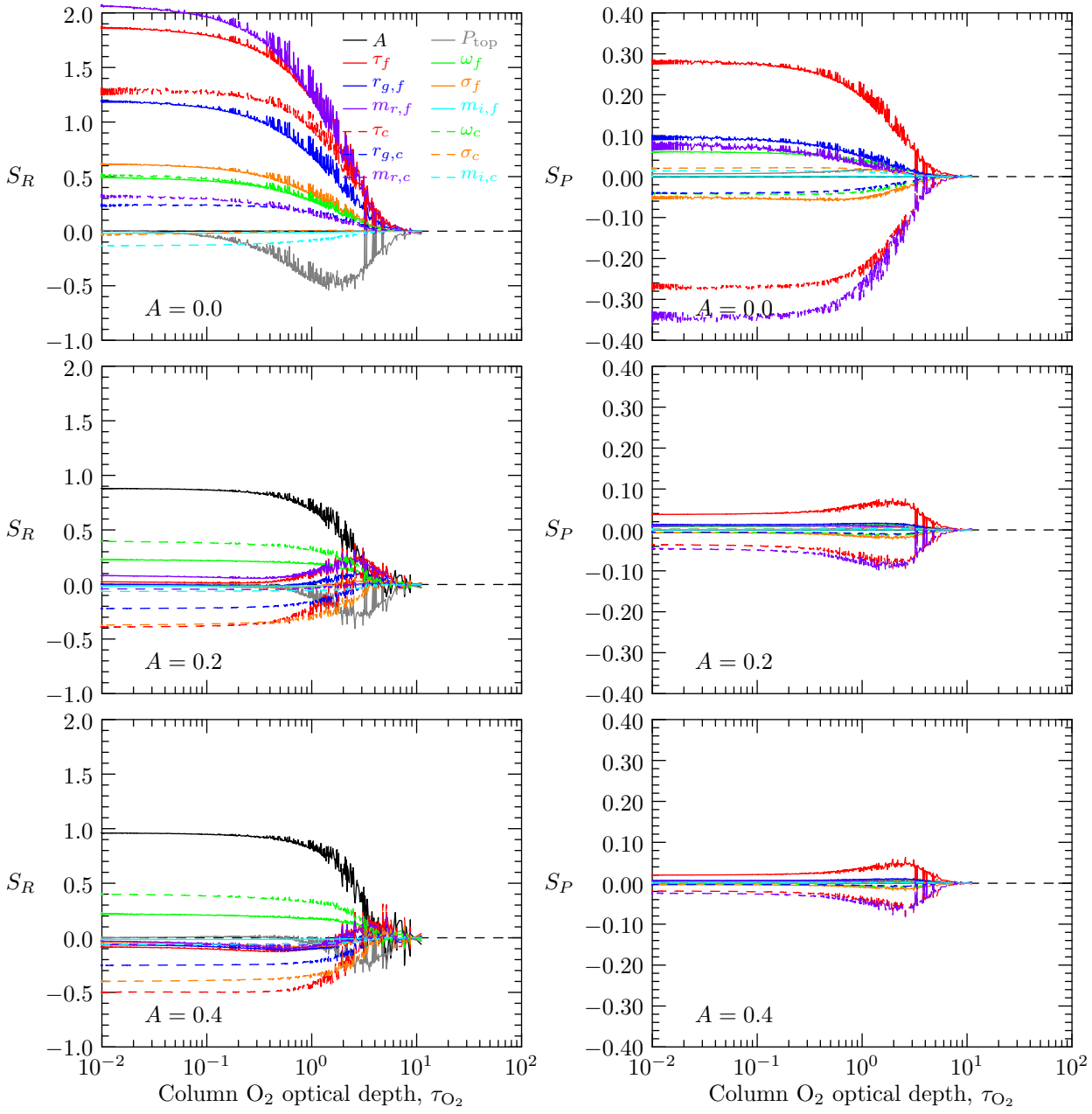

Figure 5.15: Same as the sensitivities S_R and S_P in figure 5.11 but for surface albedos $A = 0.0$, 0.2, and 0.4 in the first, second, and third rows, respectively.

to get absorbed before the next scattering event and as a result the degree of multiple scattering, and therefore the sensitivity to ω_a, decreases with τ_{O_2}. Third, the increase in sensitivity to aerosol properties other than ω_a is due not only to a relative increase in their effect compared to surface albedo A but also due to an increasing portion of single scattered photons reaching the sensor. This effect, where the sensitivity increases inversely with multiple scattering, is opposite to that of ω_a. The result is more photons scattered once which contain a more direct relationship to the single scattering properties of aerosols. Forth, the reason the coarse mode aerosol properties other than $\omega_{a,c}$ decrease with τ_{O_2} before increasing again is do to the more prevalent relationship between these properties and single scattering albedo with particle size. Finally, the peak in sensitivity to pressure top P_{top} corresponds with the values of τ_{O_2} for which the weighting functions in the vertical peak at around the aerosol-top.

In figure 5.12 sensitivities for each of the three models are shown. The difference between the sensitivities with model are similar to that shown in figures 5.2 through 5.4 for MODIS measurements, where from the first aerosol model to the third aerosol model there is in general an increase in sensitivities to the fine mode and a decrease in sensitivities to the coarse mode, except to the coarse mode single scattering albedo $\omega_{a,c}$ which also increases. The variation in sensitivity with modal optical thickness $\tau_{a,i}$ shown in figure 5.13 is dramatic. It is clear that there is little sensitivity to the aerosol at $\tau_{a,i}(0.55) = 0.01$ and a large sensitivity to the aerosol at $\tau_{a,i}(0.55) = 1.0$. In fact, at $\tau_{a,i}(0.55) = 1.0$, the sensitivities to almost all the parameters exceed that to the surface albedo A even in the continuum and the sensitivities to a number of the parameters exceed that to single scattering albedo ω_a in the absorption lines. The variation in sensitivity with aerosol-top pressure P_{top} shown in figure 5.14 show larger sensitivities at higher top pressures both in the continuum and in the absorption lines. The decrease in sensitivity in the continuum is due to the large contribution to the measurements from molecular scattering and due to the increased interaction with the surface. In the absorption lines the sensitivity to P_{top}, τ_f, $r_{g,f}$, and $m_{r,f}$ exceeds that to A and both $\omega_{a,f}$ and $\omega_{a,c}$ for $P_{\text{top}} = 400$ hPa. At $P_{\text{top}} = 800$ hPa the sensitivity decreases with absorption for all parameters limiting the extra information provided in the presence of molecular absorption. Finally, the variation in sensitivity with surface albedo A is shown in figure 5.15. For $A = 0.0$ the sensitivities to almost all the aerosols parameters in the continuum are relatively large since the surface does not contribute to the measurements. In fact, the sensitivities to τ_f, $r_{g,f}$, σ_f, $m_{r,f}$, and τ_c, exceed that to

$\omega_{a,f}$ and $\omega_{a,c}$. An increase in the sensitivities to aerosol parameters (except ω_a) typically observed in the absorption lines is not apparent in the plot for $A = 0.0$ as the continuum sensitivities are already at a maximum sensitivity. As A increases the continuum sensitivities decrease, as expected, and the increased sensitivity in the absorption lines becomes apparent.

So far our discussion has been focused on common aspects for all the TANSO-FTS bands and a few characteristics relating to variation between the bands themselves should be discussed. Most importantly, it is apparent that the 1.61-μm CO_2 band provides significantly less variation in sensitivity to aerosol properties across the spectrum than the other two bands. In the context of the GOSAT and OCO-2 missions this band was chosen to provide sensitivity to CO_2 at the surface and therefore has relatively weak absorption. In contrast, the 2.06-μm CO_2 band, with relatively strong absorption was chosen for the ability to derive more aerosol properties than with the O_2 A-band alone, especially wavelength dependent properties, and properties of coarse mode aerosols. Indeed, looking at the plots in figure 5.6 compared to 5.7 it is apparent that the 2.06-μm CO_2 band shows much more sensitivity to the coarse mode aerosols than to the fine mode aerosols.

Polarized reflectance

The polarized reflectances P exhibit significantly different characteristics than the total reflectances R. Of particular importance is the relative difference between the albedo parameters and the non-albedo parameters. In contrast to the total reflectances the sensitivity of the polarized reflectances to the albedo parameters does not dominate over that of the non-albedo parameters. In fact, sensitivities to τ_a, r_g, and m_r tend to be greater than that to the albedo parameters for both modes. Relative to total reflectances the polarized sensitivities to the albedo parameters is generally lower and the sensitivity to non-albedo parameters is larger. These results are not surprising. It is well know that intensity measurements tend to be more sensitive to parameters characterizing absorption such as surface and single scattering albedo and to some extent particle size whereas measurements of polarization are more sensitive to single scattering parameters such as particle size distribution and complex index of refraction [Chowdhary et al., 2005]. In addition, whereas the contribution to the total reflectance signal is usually greater for the surface than for aerosols, the contribution to the polarized reflectance signal is usually smaller for the surface than for aerosols [Waquet et al., 2007].

Moving into the absorption lines the sensitivities to all the parameters tend to increase in magnitude even to the albedo parameters that decreased in magnitude for the total reflectance measurements. This is to be expected for the non-albedo parameters since as discussed previously in relation to total reflectance, the increase in τ_{O_2} will increase the portion of single scattering in the measurements and therefore the sensitivity to particle single scattering properties. For the albedo parameters it is, again, the decreased sensitivity to extinction (surface albedo and single scattering albedo) and the increased sensitivity to single scattering properties (single scattering albedo) of polarized reflectances relative to total reflectances that is significant here.

The variation with model of the polarized reflectance sensitivities is complicated but there is some change in the sensitivities in the fine mode $r_{g,f}$ and $m_{r,f}$ and the coarse mode $\tau_{a,c}$ and $m_{r,c}$ most likely due to changes in both the real part of the index of refraction m_r and the single scattering albedo ω_a with model in both modes. As with the total reflectance, the changes in sensitivity of the polarized reflectance with $\tau_{a,i}(0.55)$ are dramatic. As expected, the sensitivity increases with $\tau_{a,i}(0.55)$ while being almost negligible at $\tau_{a,i}(0.55) = 0.01$. Interestingly, the sensitivity to A increases in the absorption lines at $\tau_{a,i}(0.55) = 0.01$. This is a result of the variation from the non-polarizing surface compared to that from highly polarizing molecular scattering. The variations in sensitivity with top pressure P_{top} are also significant. In the continuum, larger sensitivities at higher altitudes are a result of less surface interaction and more sensitivity to the interaction between highly polarizing molecular scattering and less polarizing aerosol scattering. Masking of the surface in the absorption lines increases this effect particularly to P_{top}, τ_a, and m_r. The variation in sensitivities with surface albedo A are less dramatic for the polarized reflectances compared to the total reflectances. This is due to the lower overall sensitivity of the polarized reflectances to A relative to the other parameters.

Spectrally, the polarized reflectances show some of the same characteristics as total reflectance, including the fact that the 1.61-μm CO_2 band provides significantly less variation in sensitivity to aerosol properties across the spectrum than the other two bands. In addition, the 2.06-μm CO_2 band shows much more sensitivity to the coarse mode aerosols than to the fine mode aerosols. One apparent difference in the spectral variation between the total reflectance and polarized reflectance is that the magnitude of the sensitivities in the 2.06-μm CO_2 band relative to the O_2 A-band are larger in the polarized reflectance than in the total reflectances. There are two reasons for this

including a larger sensitivity to size parameter $a = \frac{2\pi r}{\lambda}$ for the polarization and a larger decrease in the influence of molecular scattering with wavelength in the polarization measurements compared to the intensity measurements.

Multiangle measurements

Measurements at multiple view angles θ can provide additional information than to that of measurements taken at a single angle (nadir for TANSO-FTS) in two ways. First, the increase in optical path with θ increases the path length through the aerosols especially before surface interaction. This increases the aerosol signal and in particular the portion of the signal that has not been influenced by the surface. The variation in sensitivity itself between view angle to varying path length is also a unique source of information. Second, multiangle measurements provide a means to obtain information related to the scattering phase matrix (a function of scattering angle Θ) at more than one scattering angle. This is particularly the case with polarization measurements, where the scattering phase matrix exhibits significant micro-physically dependent features at scattering angles commonly encountered in solar-satellite viewing geometries.

From looking at figures 5.5 through 5.7 it is apparent that the variation in the sensitivity of total reflectance R with view angle is well below the variation with molecular absorption for A, P_{top}, and the fine mode aerosol parameters but becomes significant for some of the coarse mode aerosol parameters, in particular $\tau_{a,c}$ and $m_{r,c}$. In these cases the variation comes from the fore viewing angle whereas the nadir and aft viewing angles are similar. If the difference was a result of longer optical paths we would expect that that both the fore and aft directions would be different from nadir which is not the case. Instead, it is the near backscattering ($\Theta = 175^\circ$) single scattering angle in the fore direction that provides information related to the relatively large sensitivity of the scattering phase function to microphysical parameters at large scattering angles. This effect can also be seen in the sorted sensitivities of figure 5.11, where the sensitivities to, in particular, $\tau_{a,c}$ and $m_{r,c}$ peak much higher for the fore viewing direction.

For the polarized reflectance P the variation in sensitivity with view angle becomes important for P_{top} and some of the fine mode parameters in the case of the CO_2 bands, where the variation is continuum based for the 1.61-μm band but is dependent on molecular absorption in the 2.06-μm band. As with the total reflectance, angular variation is greater for the coarse mode compared to

the fine mode with separation apparent for all the view angles. The greater overall variation for the polarized reflectance is due to the greater sensitivity of the scattering phase matrix as a whole to microphysical parameters, than the scattering phase function alone [element (1,1) of the scattering phase matrix]. The greater variation for the CO_2 bands is due to a larger size parameter for this mode and therefore a larger variation in the scattering phase function with respect to scattering angle.

5.7 Information content study

5.7.1 Methodology

The sensitivity study just presented provides some insight into the response of the measurements to each parameter indicating, for example, which measurements are more suited for retrieving a particular parameter, but because of measurement correlations and uncertainties it is not always obvious how many and which parameters are retrievable. To quantify the information content of different instrument combinations it is necessary to consider the response of all the measurements together. This will account not only for the individual measurement sensitivities but also for correlations between different measurements. The measurement and a priori error covariances must also be incorporated to accurately quantify the amount of independent information the measurements provide relative to the measurement noise and the a priori state. In the following we will briefly define several information content quantities that address these goals and are useful for assessing the capabilities of a particular measurement combination. The reader is referred to Rodgers [2004] for a more thorough description.

To quantify the number of retrievable parameters and to provide some insight into which parameters are accurately retrievable a singular value decomposition (SVD) is employed. The matrix to be decomposed is a transformation of $\mathbf{K}$ given by

$$\tilde{\mathbf{K}} = \mathbf{S}_\epsilon^{-1/2}\mathbf{K}\mathbf{S}_a^{1/2}, \tag{5.34}$$

where $\mathbf{K}$ $(m \times n)$, refereed to as the Jacobian, contains derivatives of the forward model $\mathbf{F}$ with respect to the elements of the state vector $\mathbf{x}$:

$$K_{ij} = \frac{\partial F_i(\mathbf{x})}{\partial x_j}. \tag{5.35}$$

As noted by Rodgers [2004], $\tilde{\mathbf{K}}$ provides a basis, where the measurement error and a priori errors are uncorrelated and, in fact, both the measurement and a priori covariances are unit matrices. The SVD of $\tilde{\mathbf{K}}$ is given by

$$\tilde{\mathbf{K}} = \mathbf{U}\mathbf{\Lambda}\mathbf{V}^T, \tag{5.36}$$

where $\mathbf{\Lambda}$ $(p \times p)$ is a diagonal matrix of singular values λ_i, $\mathbf{U}$ is a matrix of left singular vector, $\mathbf{V}$ is a matrix of right singular vectors, and p is the rank of $\tilde{\mathbf{K}}$. Rodgers [2004] indicates that the number of singular values greater than unity is the number of independent measurements made to better than measurement error, the effective rank of the problem N, which can be interpreted as the number of independent quantities that can be retrieved from the measurements with a significant accuracy.

From the singular values two additional quantities may be defined: the Shannon information content (SIC) H and the number of degrees of freedom (DOF) for signal d_s. The SIC, given as

$$H = \frac{1}{2}\sum_{i=1}^{n} \ln(1 + \lambda_i^2), \tag{5.37}$$

measures the reduction in disorder of the retrieval state space with the addition of a measurement, i.e. the reduction in entropy of our a priori knowledge. Defined using a logarithm of base two, H may interpreted as bits of information indicating that 2^H different atmospheric states can be distinguished from the measurements. DOF for signal given by

$$d_s = \sum_{i=1}^{n} \frac{\lambda_i^2}{1 + \lambda_i^2} = \mathrm{tr}(\mathbf{A}), \tag{5.38}$$

describes the number of useful independent quantities there are in a measurement, i.e. the amount of independent pieces of information. Note that whereas N applies to measurement space, d_s applies to retrieval space.

Another useful quantity is the averaging kernel matrix given by

$$\mathbf{A} = \frac{\partial \hat{\mathbf{x}}}{\partial \mathbf{x}} = \mathbf{GK} = (\mathbf{K}^T \mathbf{S}_\epsilon^{-1} \mathbf{K} + \mathbf{S}_a^{-1})^{-1} \mathbf{K}^T \mathbf{S}_\epsilon^{-1} \mathbf{K}, \tag{5.39}$$

where $\mathbf{G}$ is referred to as the gain matrix. $\mathbf{A}$ quantifies the response of the retrieval to changes in the true state vector about the linearization point or in this case the true state vector. The diagonal elements of $\mathbf{A}$ range from zero to one, where for a perfect retrieval $\mathbf{A}$ would be an identity matrix indicating that changes in each state vector element are perfectly represented by the retrieval. In other words, the closer $\mathbf{A}$ is to the identity matrix the higher the information content of the measurements. Information not included in the measurements is taken from the a priori information so that the retrieved state vector can be written as

$$\hat{\mathbf{x}} = \mathbf{Ax} + (\mathbf{I} - \mathbf{A})\mathbf{x}_a. \tag{5.40}$$

Essentially, the a priori represents an estimate of the part of the retrieved state vector that cannot be retrieved from the measurements. Note that $\mathbf{A}$ may be linked to the SIC H and the DOF for signal d_s with

$$H = -\frac{1}{2} \ln(\mathbf{I} - \mathbf{A}) \tag{5.41}$$

and

$$d_s = \mathrm{tr}(\mathbf{A}), \tag{5.42}$$

respectively.

The error covariance matrix of the posteriori state $\hat{\mathbf{S}}$ describes the error in the retrieved state $\hat{\mathbf{x}}$ due to both measurement and forward model error as well as error in the a priori state each weighted by their associated error covariances:

$$\hat{\mathbf{S}} = (\mathbf{K}^T \mathbf{S}_\epsilon^{-1} \mathbf{K} + \mathbf{S}_a^{-1})^{-1}. \tag{5.43}$$

$\hat{\mathbf{S}}$ may be regarded as a measure of the overall accuracy of the retrieval when suitable convergence has been obtained. The diagonal elements of $\hat{\mathbf{S}}$ are the variances for each retrieved stater vector parameter.

Even though we briefly presented the retrieval methodology at the beginning of section 5.3 it is important to understand that the characterization of information content as described above does not require an actual retrieval but is evaluated at the linearization point for a particular base state of interest.

5.7.2 Singular value decomposition

In this section the singular value decomposition is presented in figures showing the normalized values χ_i of all the singular values λ_i greater than unity along with their associated right singular vectors of $\mathbf{V}$. The singular values are normalized according to

$$\chi_i = \frac{\lambda_i}{\sum_{j=1}^{p} \lambda_j}. \tag{5.44}$$

Presentation of the normalized singular values provides a means to compare singular values from different measurement combinations. The values can be interpreted as the fraction of the variance in their retrieval space explained by a particular singular vector. The singular vectors indicate linear combinations of retrieval parameters that correspond to each singular value. For brevity we combine the contributions from spectral fit parameters into a single value representative of the entire fit. Multiple singular peaks indicate the presence of non-unique sensitivities in the measurements and that the combination of state vector elements required to reproduce the measurements is not unique. An ideal retrieval would be one where the number of singular vectors greater than unity is equal to the number of retrieval parameters and where each associated singular vector peaks at a single parameter at which no other singular vector peaks.

In all the SVD cases that follow, we use the defined standard of model two, $\tau_{a,i}(0.55) = 0.1$, $P_{\text{top}} = 600$ hPa, $A = 0.2$, $\theta_0 = 35°$, $\phi_0 = 180°$, and $\phi = 90°$.

Figure 5.16 shows the SVD results for the MODIS only measurement vector $\mathbf{y}_{\text{M}}$. Three singular values are greater unity indicating that there are at most three retrievable parameters from the MODIS data. The first singular value explains 83% of the variance and, not surprisingly, has its strongest peak at A but also contributes to $N_{0,c}$, $r_{g,c}$, and σ_c. The second explains 15% of the variance and contributes to the same parameters as the first vector in addition to $N_{0,f}$. The dominate parameter in this case is for $N_{0,c}$. Finally, the third explains 1% of the variance and is

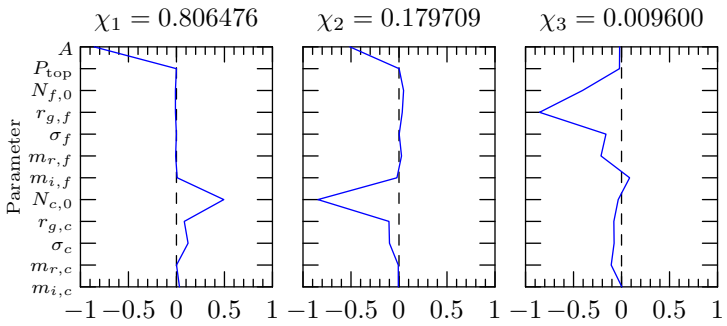

Figure 5.16: Normalized singular values and corresponding singular vectors for all singular values greater than one for a retrieval of the standard model two, $\tau_{a,i}(0.55) = 0.1$, $P_{\text{top}} = 600$ hPa, $A = 0.2$, $\theta_0 = 35°$, $\phi_0 = 180°$, and $\phi = 90°$ using the measurement vector $\mathbf{y}_{\text{M}}$.

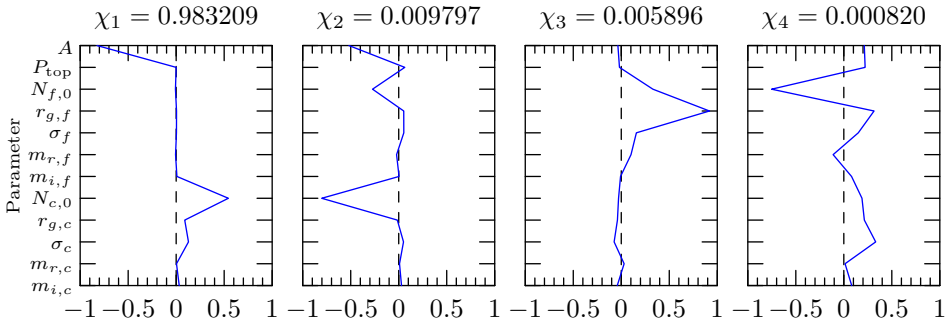

Figure 5.17: Same as figure 5.16 but for the measurement vector $\mathbf{y}_{\text{TF},1,R,\text{N}}$

dominated by a peak at $N_{0,f}$ and $r_{g,c}$. This information, suggests that A, $N_{0,c}$, and $N_{0,f}$ should be the retrieval parameters. If the surface is known a priori then either $r_{g,f}$ or $r_{g,c}$ may also be retrievable. Determining the surface albedo a priori was the approach used by the MODIS operational retrieval product [Kaufman et al., 1997] but it has since moved on to actually retrieving the albedo [Levy et al., 2007].

Figure 5.17 shows the SVD results for the measurement vector $\mathbf{y}_{\text{TF},1,R,\text{N}}$ with TANSO-FTS O_2 A-band nadir total reflectance measurements. In this case at most four parameters are retrievable. The first singular vector explains 88% of the variance to which A is the dominate contribution as in the MODIS only case. The second vector has contributions primarily from both $N_{0,f}$ and $N_{0,c}$, while in addition to these, the last two vectors contain contributions from the fine and coarse mode size distribution parameters with $r_{g,f}$ dominating over $r_{g,c}$. This information suggests that A, $N_{0,f}$, $N_{0,c}$, and $r_{g,f}$ would be a good choice for the retrieval parameters but that the results for $r_{g,f}$ should be treated with caution.

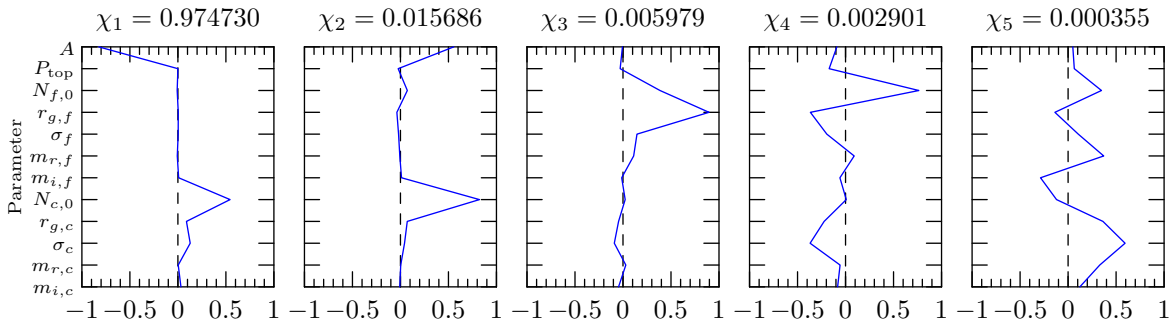

Figure 5.18: Same as figure 5.16 but for the measurement vector $\mathbf{y}_{\text{M,TF},1,R,\text{N}}$

Figure 5.18 shows the SVD results for the measurement vector $\mathbf{y}_{M,\text{TF},1,R,\text{N}}$ with both the MODIS and TANSO-FTS O_2 A-band nadir total reflectance measurements. This combined case brings two more retrievable parameters relative to the MODIS only case and one more relative to the TANSO-FTS O_2 A-band nadir total reflectance only case. In addition, the second and third singular vectors have a larger portion of the contributions going to a single parameter than the previous case indicating a larger degree of uniqueness. For this case we suggest that the set of retrieval parameters be A, $N_{0,f}$, $N_{0,c}$, $r_{g,f}$, and $r_{g,c}$.

Figure 5.19 shows the SVD results for the measurement vector $\mathbf{y}_{\text{M,TF},1,R,\text{M}}$ with both the MODIS and TANSO-FTS O_2 A-band multiangle total reflectance measurements. At most seven parameters are retrievable in this case. Of particular interest is that the second through the fifth singular vectors contain information on $m_{r,c}$ which is consistent with the sensitivities discussed in section 5.6.2. In addition, this is the first case, where in the last two singular vectors, there is some constraint on P_{top}, σ_c, and m_i. A good set of retrieval parameters in this case would be A, $N_{0,f}$, $N_{0,c}$, $r_{g,f}$, $r_{g,c}$, and $m_{r,c}$ with either P_{top} or σ_c as an additional parameter.

Figure 5.20 shows the SVD results for the measurement vector $\mathbf{y}_{\text{M,TF},1\text{–}3,R,\text{N}}$ with both the MODIS and TANSO-FTS nadir total reflectance measurements in all bands. As in the last case at most seven parameters are retrievable. In this case the singular vectors show large contributions to single parameters indicating an improvement in the non-uniqueness problem. In addition, there is more information on σ_c (fifth singular vector) mostly due to the additional spectral information at large wavelengths. A good set of retrieval parameters in this case would be A, $N_{0,f}$, $N_{0,c}$, $r_{g,f}$, $r_{g,c}$, σ_c, and $m_{r,c}$.

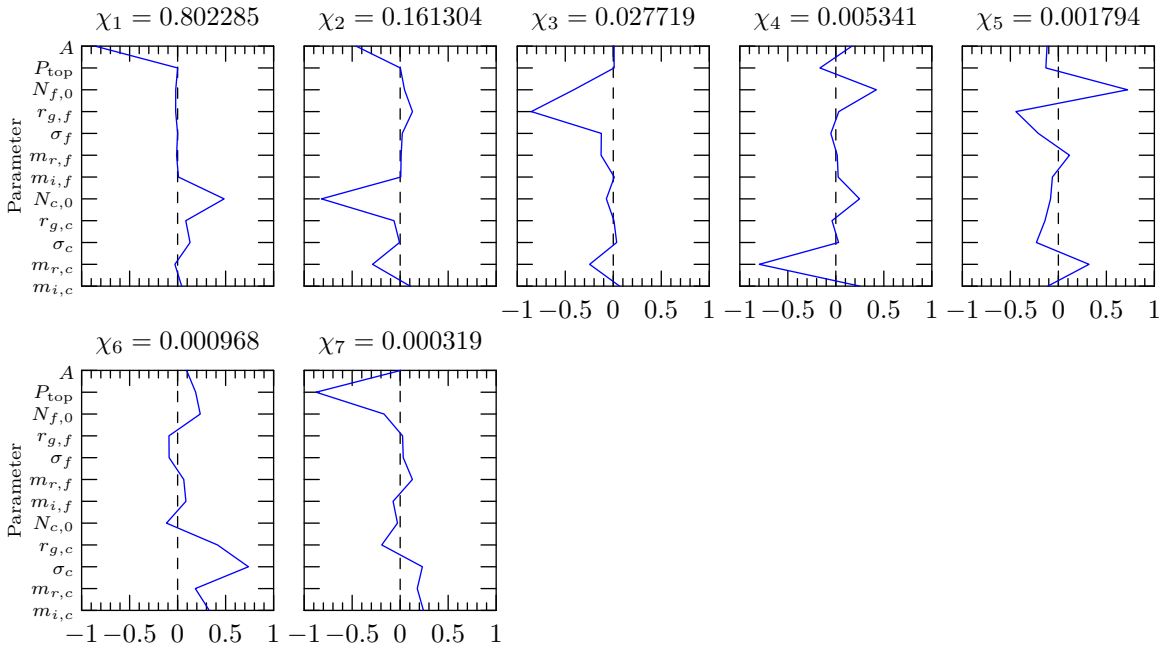

Figure 5.19: Same as figure 5.16 but for the measurement vector $\mathbf{y}_{\text{M,TF},1,R,\text{M}}$

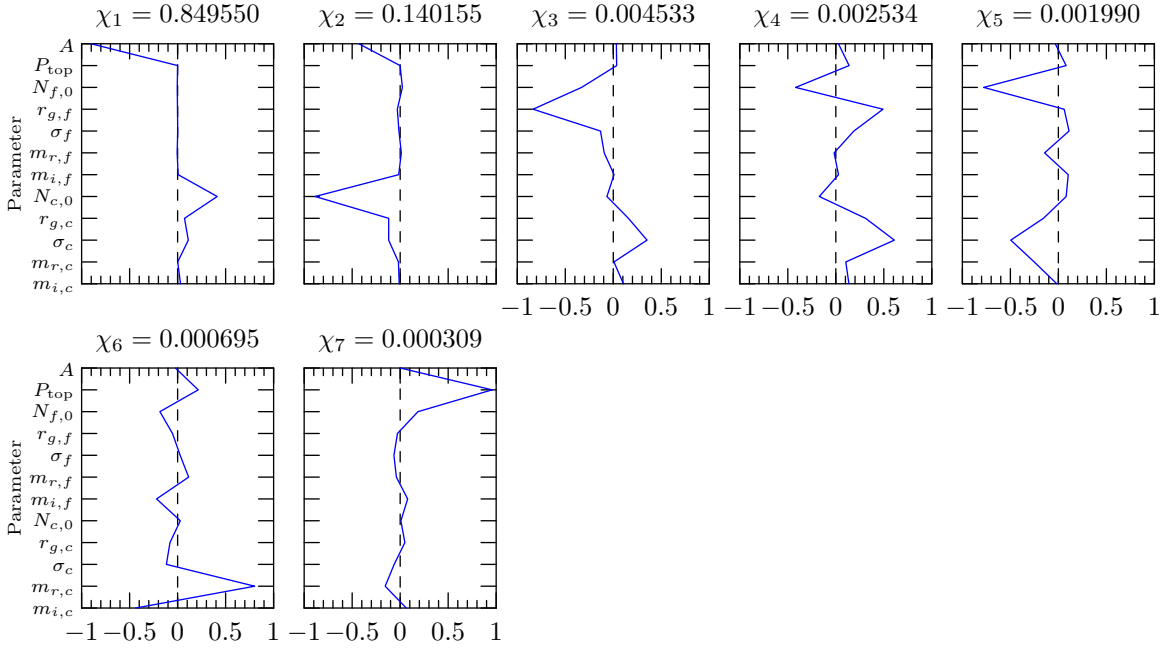

Figure 5.20: Same as figure 5.16 but for the measurement vector $\mathbf{y}_{\text{M,TF},1\text{–}3,R,\text{N}}$

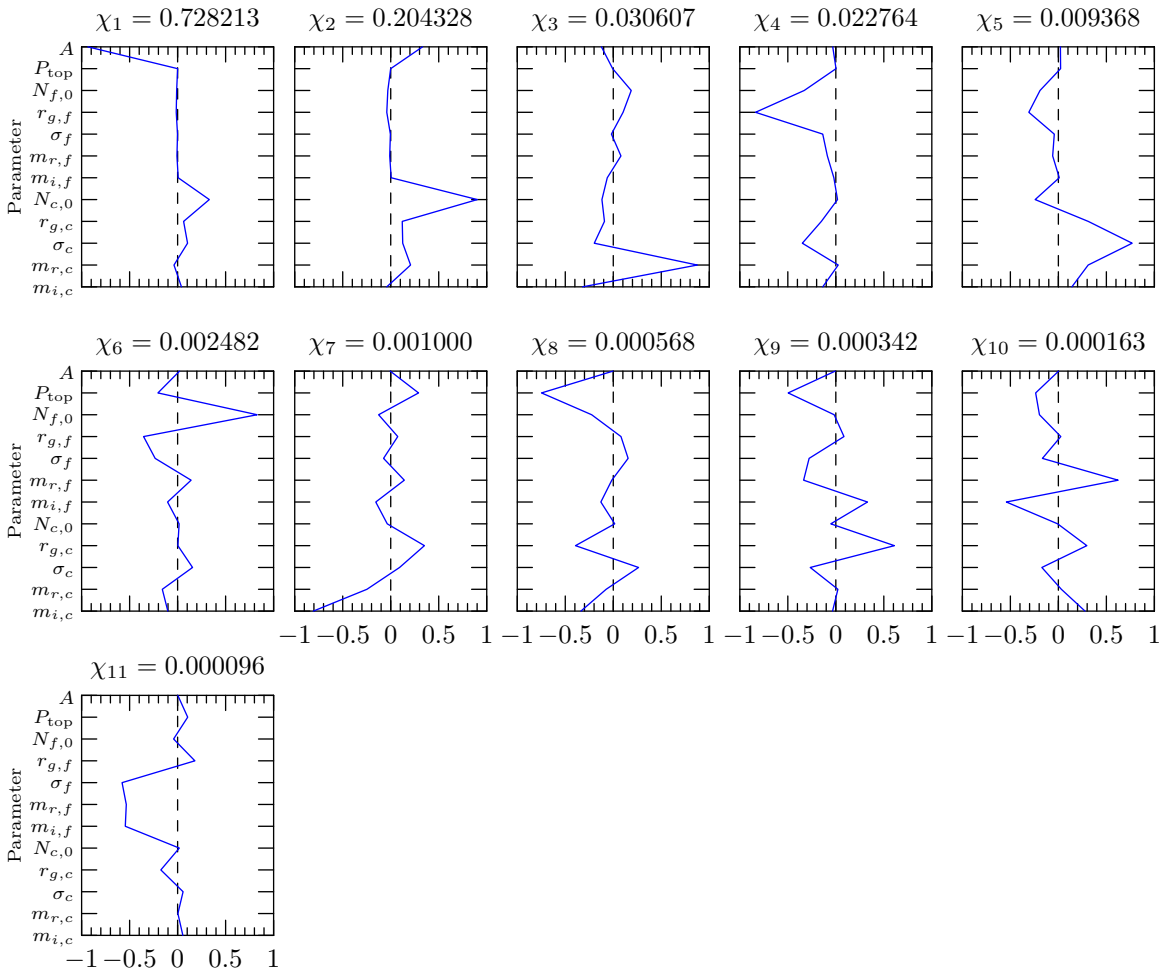

Figure 5.21: Same as figure 5.16 but for the measurement vector $\mathbf{y}_{\text{M,TF,1–3,}R\text{,M}}$

Figure 5.21 shows the SVD results for the measurement vector $\mathbf{y}_{\text{M,TF,1–3,}R\text{,M}}$ with both the MODIS and TANSO-FTS multiangle total reflectance measurements in all bands. In this case at most 11 parameters are retrievable. This is one less parameter than our full spectrally condensed state vector of 12 parameters. We would suggest in this case that either $m_{i,f}$ or $m_{i,c}$ be the unretrieved parameter.

The next four cases, which are briefly discussed, are the same as the previous four cases but with both total and polarized reflectance. Figure 5.22 shows the SVD results for the measurement vector $\mathbf{y}_{\text{M,TF,1,}R+P\text{,N}}$ with both the MODIS and TANSO-FTS nadir total and polarized reflectance measurements in the O_2 A-band. In this case at most six parameters are retrievable. This is one more than the same case but with only total reflectance. Figure 5.23 shows the SVD results for the measurement vector $\mathbf{y}_{\text{M,TF,1,}R+P\text{,M}}$ with both the MODIS and TANSO-FTS multiangle total

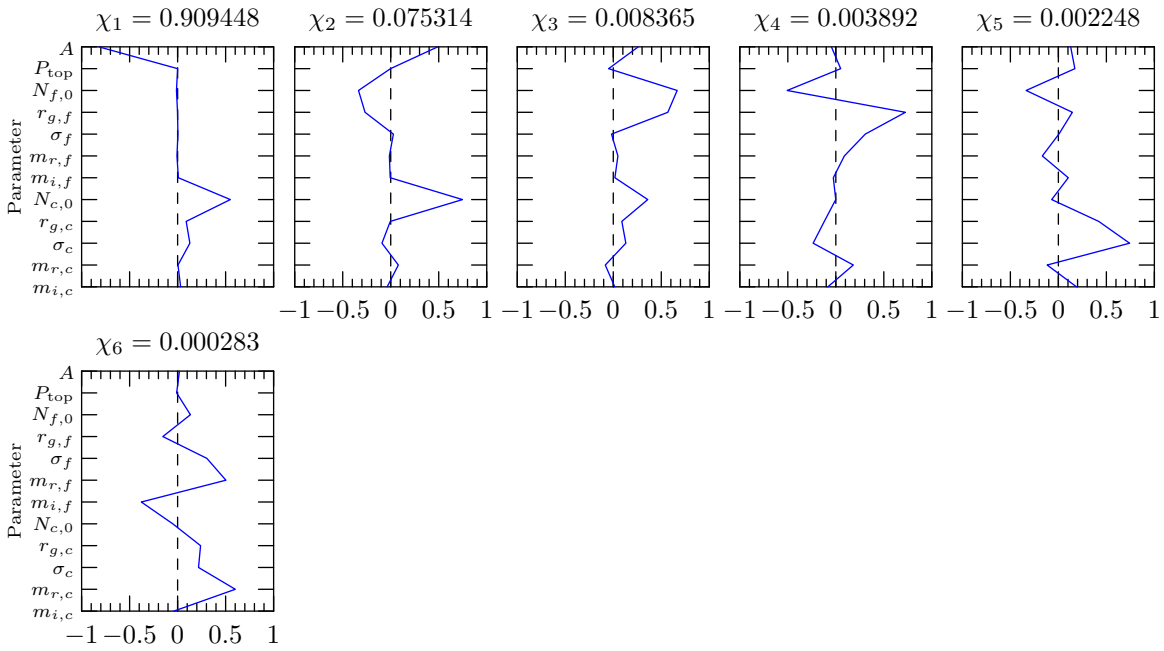

Figure 5.22: Same as figure 5.16 but for the measurement vector $\mathbf{y}_{\text{M,TF,1},R+P,\text{N}}$

and polarized reflectance measurements in the O_2 A-band. In this case at most ten parameters are retrievable. This is three more than the same case but with only total reflectance. Compared to the nadir case, where the polarized reflectance only added one more retrievable parameter this result is expected and is consistent with that discussed in section 5.6.2.

Figure 5.24 shows the SVD results for the measurement vector $\mathbf{y}_{\text{M,TF,1–3},R+P,\text{N}}$ with both the MODIS and TANSO-FTS nadir total and polarized reflectance measurements in all bands. In this case at most nine parameters are retrievable. Finally, we end with figure 5.25 for measurement vector $\mathbf{y}_{\text{M,TF,1–3},R+P,\text{M}}$ with both the MODIS and TANSO-FTS multiangle total and polarized reflectance measurements in all bands. In this case all 12 parameters are retrievable.

To gain some idea on the variation of the SVD results with a range of state vector parameters we have plotted the normalized singular values χ_i, for all singular values greater than unity, for each measurement case presented, and for the ideal aerosol measurement instrument, a multispectral, multiangle, polarimeter such as APS described in section 5.2. In figure 5.26 singular values are plotted for models one, two, and three on the left and for modal optical thicknesses ($\tau_{a,f}$ and $\tau_{a,c}$) of 0.01, 0.1, and 1.0 (for total optical thicknesses of 0.02, 0.2, and 2.0) on the right. In figure 5.27 singular values are plotted for top pressures $P_{\text{top}} = 400$ hPa, 600 hPa, and 800 hPa on the left and

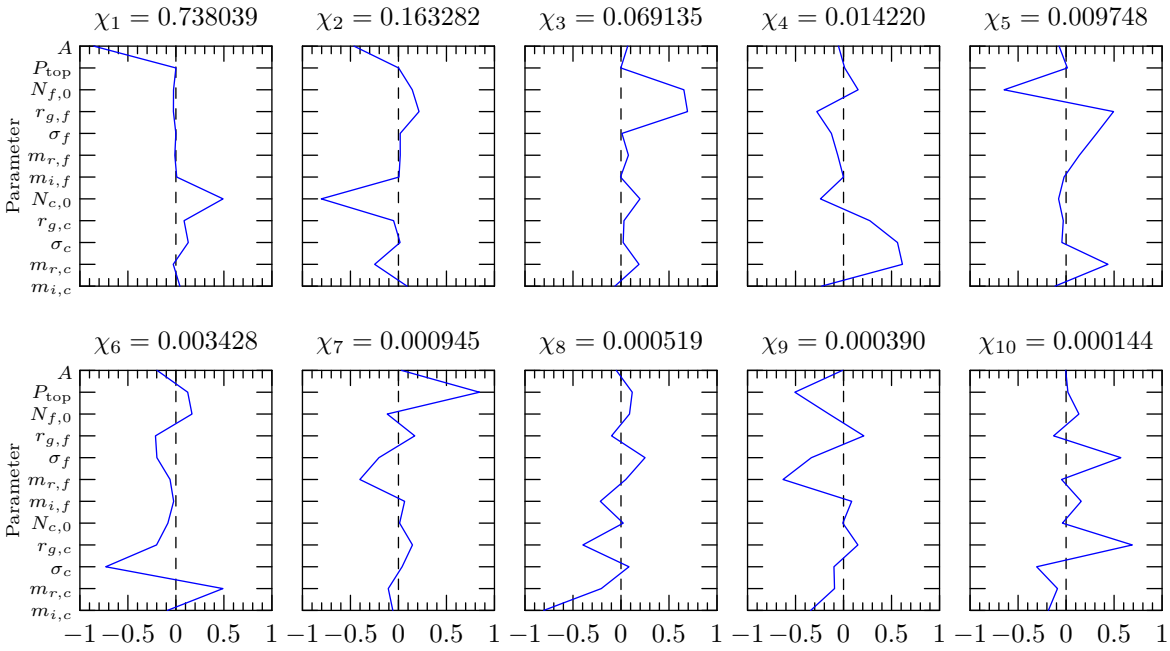

Figure 5.23: Same as figure 5.16 but for the measurement vector $\mathbf{y}_{\text{M,TF},1,R+P,\text{M}}$

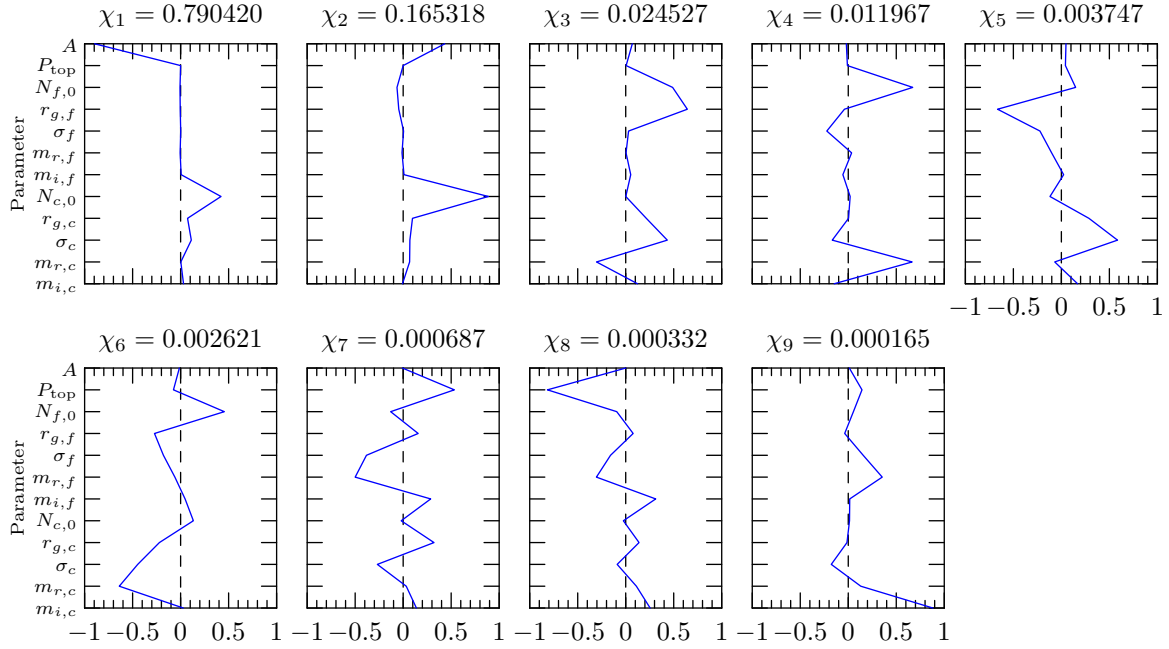

Figure 5.24: Same as figure 5.16 but for the measurement vector $\mathbf{y}_{\text{M,TF},1\text{–}3,R+P,\text{N}}$

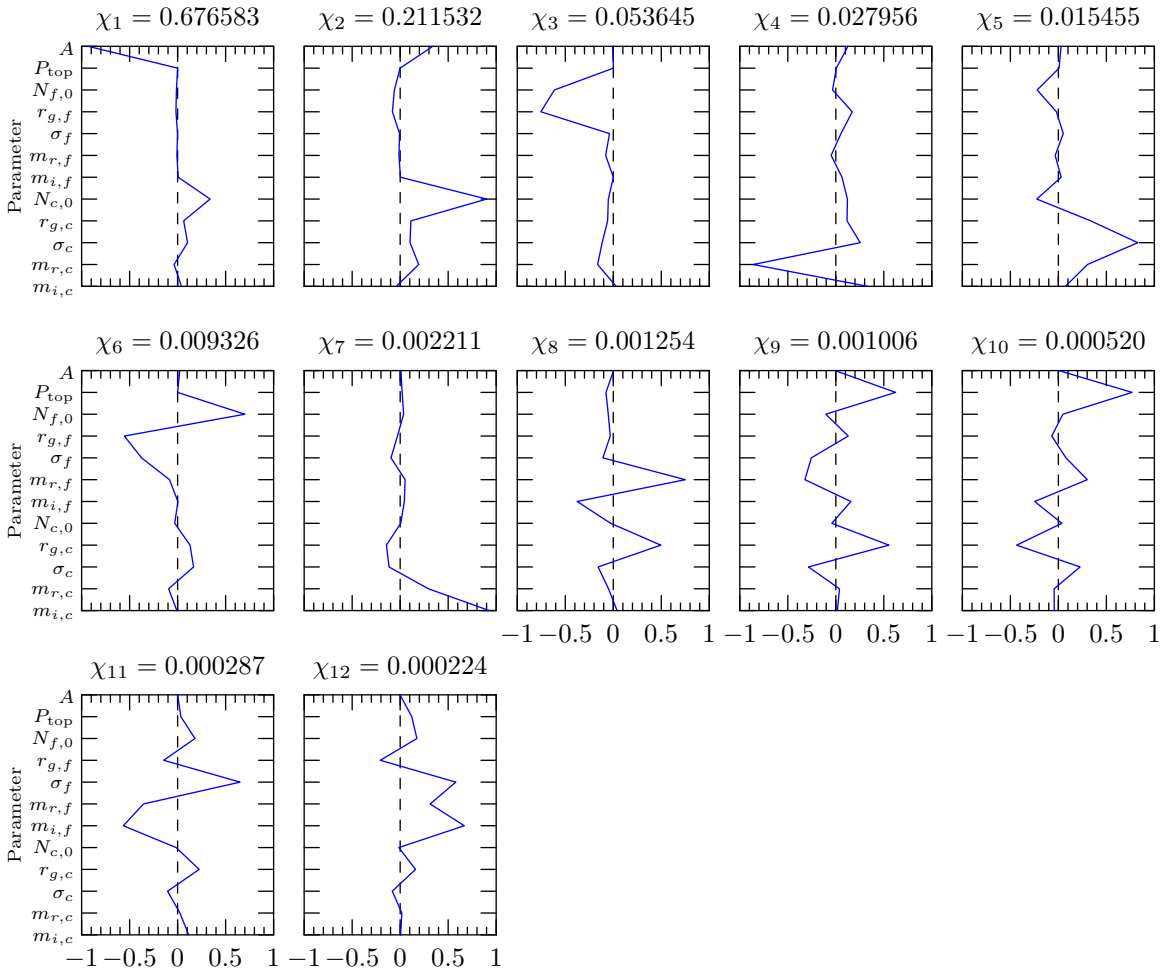

Figure 5.25: Same as figure 5.16 but for the measurement vector $\mathbf{y}_{\mathrm{M,TF,1\text{–}3},R+P,\mathrm{M}}$

for surface albedos $A = 0.0$, 0.2, and 0.4 on the right. It is apparent in all the plots that APS measurements provide significantly more information than even our most complete measurement system M,TF,1–3,R+P,M. With APS a minimum of 20 and a maximum of 30 parameters are retrievable whereas for M,TF,1–3,R+P,M a minimum of 16 and a maximum of 22 parameters are retrievable. With MODIS only a maximum of four parameters are retrievable whereas the maximum number of retrievable parameters for the MODIS + TANSO-FTS cases increases as expected with more bands, polarization, and more angles.

The variability with model is small with the number of retrievable quantities changing only by one or two for the more complex measurements systems. There is a slight decrease in the actual values of the singular values from model one to model three especially to the third model most likely due to a decrease in information content for desert dust due to the larger average particle size and the presence of non-spherical particles. As expected from our sensitivity results, in particular the increase in measurement sensitivity to aerosol parameters with optical thickness, the number of retrievable parameters increases with optical thickness. It is also apparent that the magnitude of this increases is greater for the more complex measurement scenarios containing more information, and therefore more possibility for variability. Whereas the MODIS only scenario varies from only two to four retrievable parameters the APS scenario varies from 20 to 30 parameters. The variation with top pressure is small with only a slight decrease in the number of retrievable parameters with pressure as expected from the sensitivity study. The variation with surface albedo is also as expected, with a small decrease in the number of retrievable parameters with increasing albedo. It is important to keep in mind that although the number of retrievable quantities overall, with a few exceptions, is relatively constant this does not mean that all the parameters will be retrieved with a high accuracy. In fact, the exponential decrease in the singular values indicates that the number of accurately retrieved parameters will be considerably less than the number of retrievable parameters indicated by the SVD analysis. We will investigate the range of retrieval errors in a later section.

5.7.3 Degrees of freedom

In this section we look at how the degrees of freedom for signal d_s changes with measurement scenario and with total optical thickness $\tau_a(0.55)$, top pressure P_{top}, surface albedo A, solar zenith angle θ_0, and solar azimuth angle ϕ_0. Figure 5.28 shows d_s as a function of $\tau_a(0.55)$, otherwise

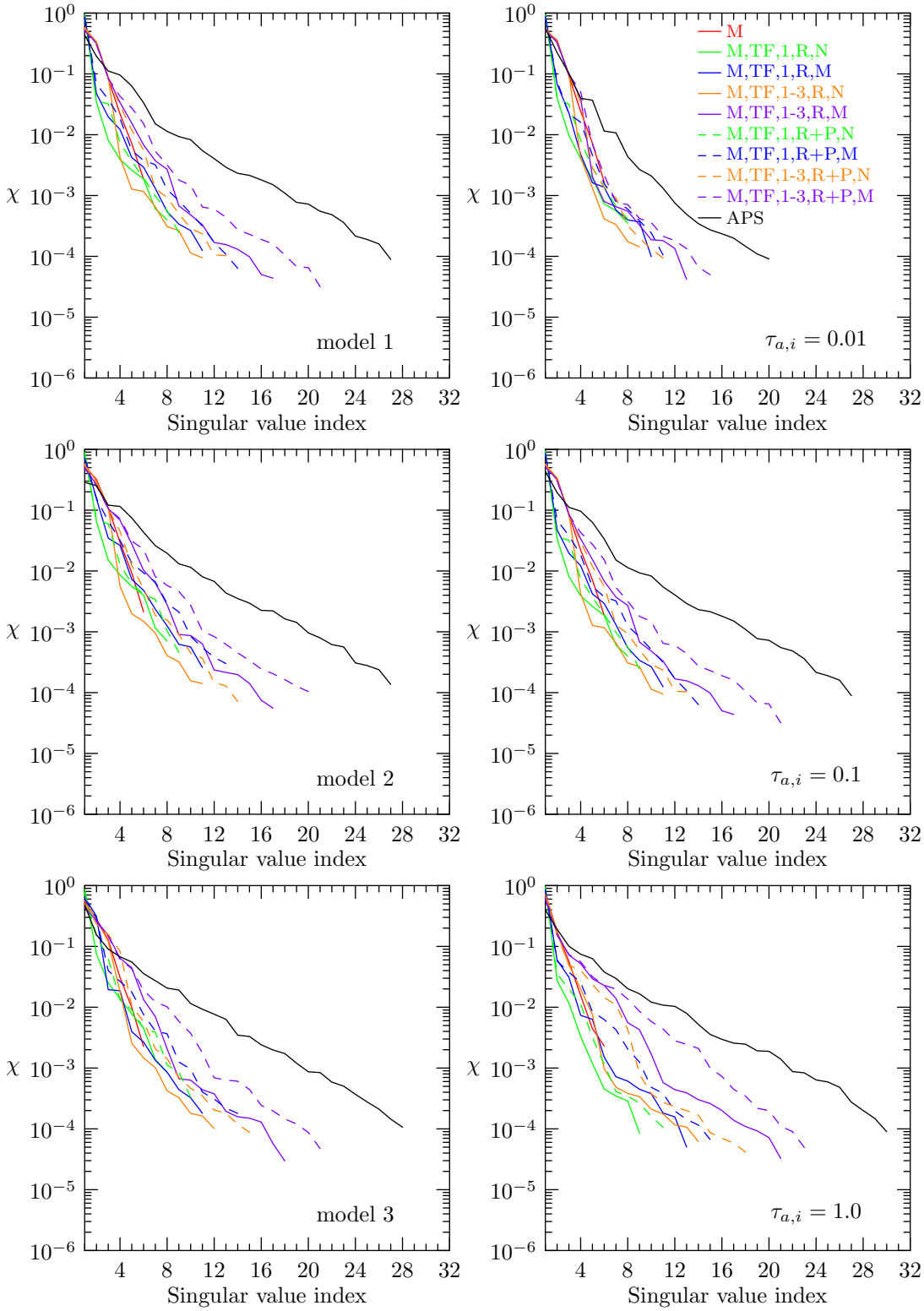

Figure 5.26: Normalized singular values for all the measurement scenarios considered in this study for a standard of model two, $\tau_{a,i}(0.55) = 0.1$, $P_{\text{top}} = 600$ hPa, $A = 0.2$, $\theta_0 = 35°$, $\phi_0 = 180°$, and $\phi = 90°$. The left column is for models one, two, and three and the right column is for modal optical thicknesses $\tau_{a,i}(0.55) = 0.01$, 0.1, and 1.0.

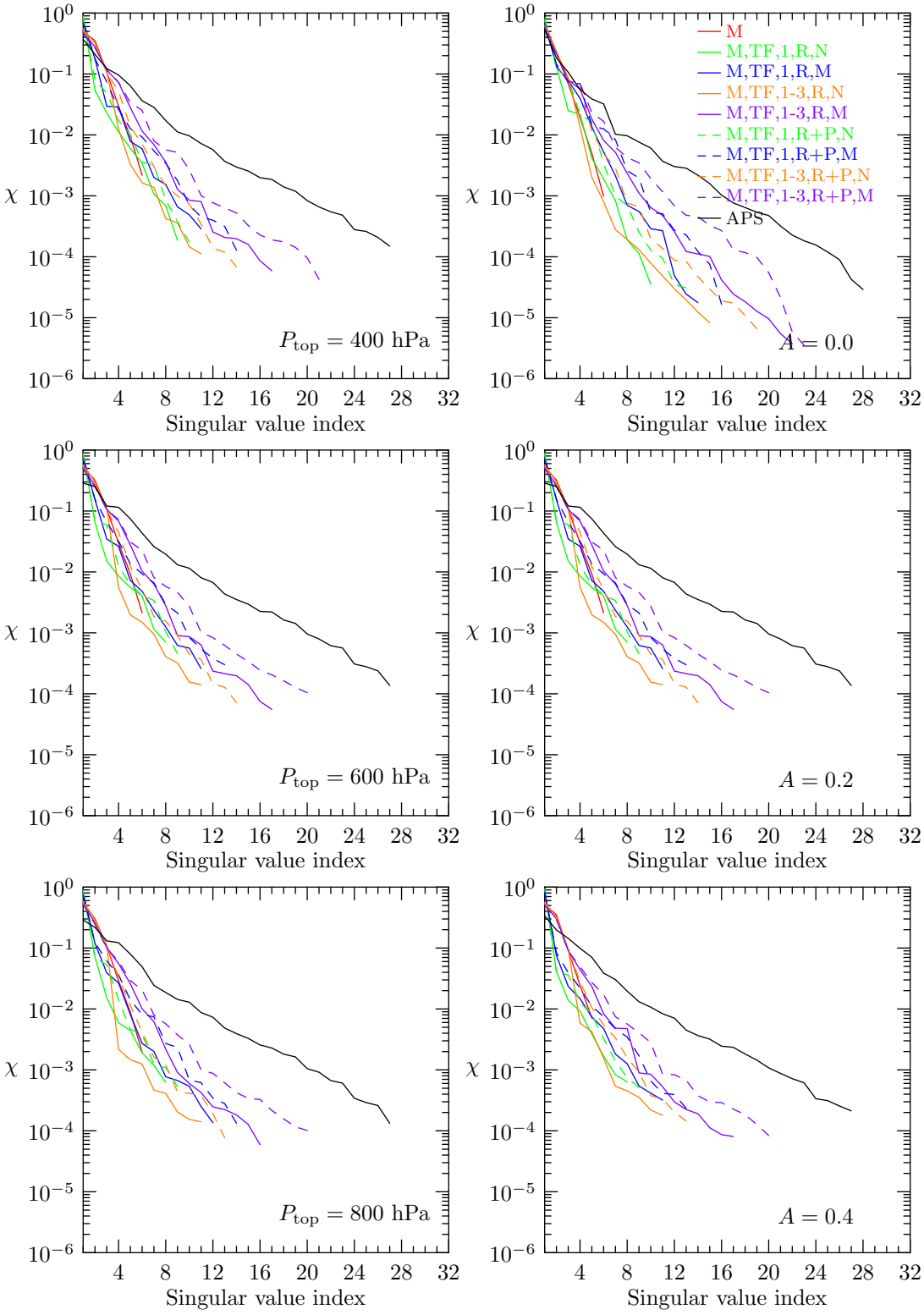

Figure 5.27: Same as figure 5.26 but for aerosol-top pressure $P = 400$ hPa, 600 hPa, and 800 hPa in the left column and surface albedo $A = 0.0$, 0.2, and 0.4 in the right column.

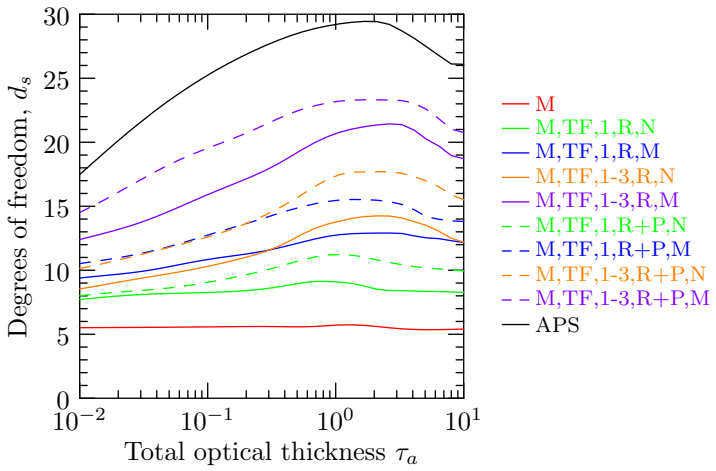

Figure 5.28: Degrees of freedom for signal d_s as a function of total optical thickness $\tau_a(0.55)$ for all the measurement scenarios considered in this study for a standard of model two, $P_{\text{top}} = 600$ hPa, $A = 0.2$, $\theta_0 = 35°$, $\phi_0 = 180°$, and $\phi = 90°$.

using the standard parameters of model two, $P_{\text{top}} = 600$ hPa, $A = 0.2$, $\theta_0 = 35°$, $\phi_0 = 180°$, and $\phi = 90°$, for our full set of measurement scenarios. As expected the MODIS only scenario has the smallest number of degrees of freedom while the APS scenario has the largest. For the TANSO-FTS measurements the addition of the multiangle measurements provides a greater increase in d_s than the addition of polarization measurements. The use of all three bands instead of just the O_2 A-band provides a slightly smaller increase than multiangle measurements at low optical thicknesses and a larger increase at large optical thicknesses. An increase in d_s with optical thickness is also apparent, particularly for the more complex measurement systems up to around $\tau_a(0.55) = 2$ to 8 after which the d_s decreases again. The increase is due to an increase in aerosol signal with larger $\tau_a(0.55)$ (loading). The eventual decrease is due to a decrease in single scattering offset by an increase in multiple scattering and therefore a decrease in sensitivity to aerosol single scattering properties such as the aerosol scattering phase matrix.

Figure 5.29 shows d_s as a function of P_{top} (upper left), A (upper right), θ_0 (lower left), and ϕ_0 (lower right). The variation with P_{top} is small with a slight decrease particularly for the measurement scenarios including the TANSO-FTS measurements. A rapid decrease after around 900 hPa are due to the molecular absorption above the aerosol layer being large enough to significantly limit the effects of the aerosols on the measurements. d_s decreases with A with rapid decrease from $A = 0.0$ to 0.1, again for the measurement scenarios including the TANSO-FTS measurements.

With θ_0, d_s increases primarily for the scenarios including the TANSO-FTS nadir measurements at all bands. The reason for this is that the 1.61 μm CO_2 band with its relatively weak molecular absorption begins to contribute information at larger solar zenith angles therefore larger optical paths. At lower values of θ_0 variations are also apparent for the measurements including multiangle observations due to features in the scattering phase matrix encountered at these single scattering angles. With ϕ_0 variation is primarily seen in the measurements including multiangle observations with a peak at $\phi_0 = 180.0°$ and minimums at $\phi_0 = 90.0°$ and 270.0°. Since our TANSO-FTS and APS multiangle measurements are taken along track in a single plane and we designated these instruments to platforms with a 0.0° orbital inclination, at $\phi_0 = 180.0°$ the scattering plane for all the observations lies on the same plane formed by the multiangle measurements maximizing the range of possible single scattering angles while minimizing single scattering angle redundancy.

5.7.4 Averaging kernels

In this section we investigate the diagonal elements of the averaging kernel matrix **A** for a select number of cases and for several different measurement scenarios. As discussed previously the elements A_{ii} quantify how well changes in the state vector elements x_i are represented by the retrieval. A_{ii} ranges from zero to one, where zero indicates the retrieval has no response to x_i and one indicates a perfect response. First we look at our standard case (model one, $\tau_{a,f}(0.55) + \tau_{a,c}(0.55) = \tau_a(0.55) = 0.2$, $P_{\text{top}} = 600$ hPa, and $A = 0.2$) including all the state vector elements, even the higher order spectral fit parameters. For this case we look at all the measurement scenarios. Then we look at cases that deviate from our standard case combining the spectral fit parameters into a single parameter as was done for the presentation of the SVD results. For this case we exclude the measurement scenarios including multiangle observations, as in Part II where we present a real retrieval, we will not be using multiangle measurements, due to their limited availability.

Figure 5.30 shows all the diagonal elements A_{ii} of **A** for our standard cases of model two, $\tau_{a,i} = 0.1$, $P_{\text{top}} = 600$ hPa, $A = 0.2$, $\theta_0 = 35°$, $\phi_0 = 180°$, and $\phi = 90°$ and for all our measurement scenarios. First we notice that all the spectral fit parameters for A have large retrieval responses for all the measurement scenarios. The is expected and underscores why surface characterization is so important for aerosol retrievals. Although already very large for the MODIS only measurements,

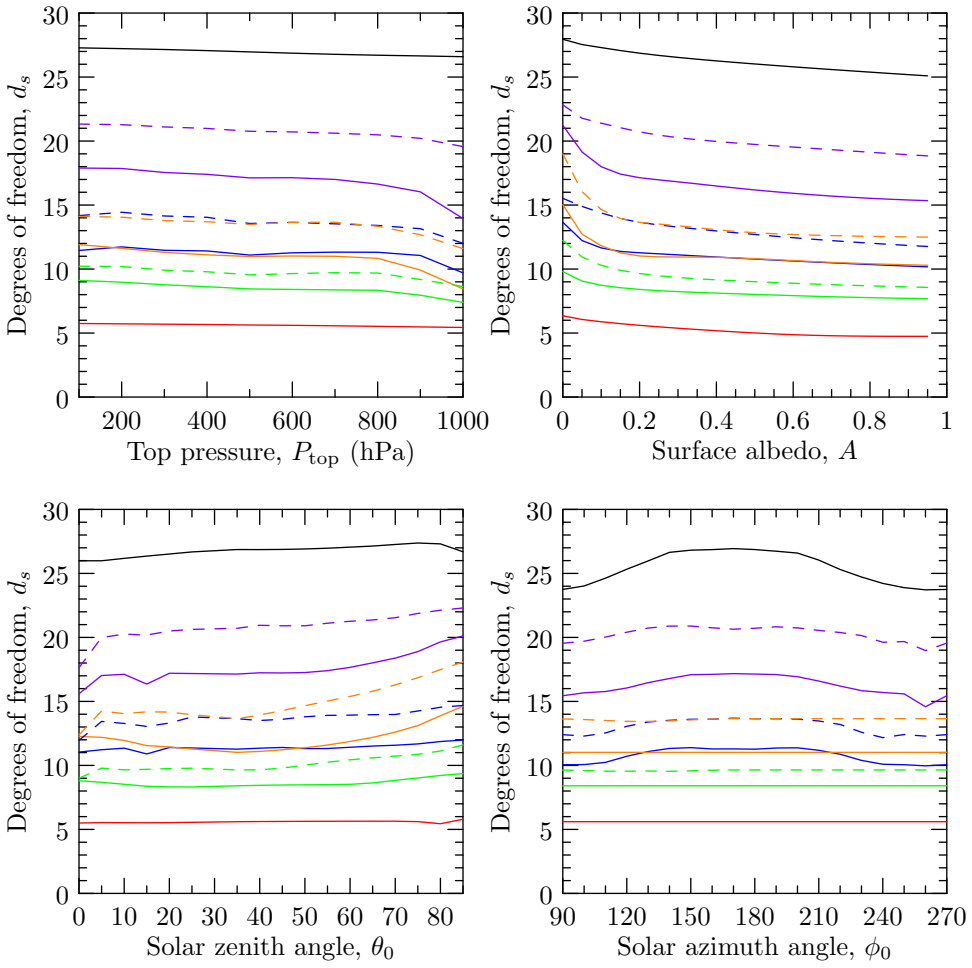

Figure 5.29: Degrees of freedom for signal d_s as a function of aerosol-top pressure P_{top} (upper left), surface albedo A (upper right), solar zenith angle θ_0 (lower left), and solar azimuth angle ϕ_0 (lower right) for all the measurement scenarios considered in this study for a standard of model two, $\tau_{a,i}(0.55) = 0.1$, $P_{\text{top}} = 600$ hPa, $A = 0.2$, $\theta_0 = 35°$, $\phi_0 = 180°$, and $\phi = 90°$.

the response for A_i increases when the TANSO-FTS measurements are included approximately reaching unity in most cases. For P_{top}, the response for the MODIS only scenario is approximately zero but increases dramatically for the cases including the TANSO-FTS measurements. This is as expected since, as discussed earlier, it is variability in molecular absorption and/or measurements of polarization that provide aerosol height information which the MODIS only measurements do not have. The responses to N_f and $r_{g,f}$ also increases significantly when the TANSO-FTS measurements are added reaching close to unity in all cases whereas they are below 0.3 for the MODIS only measurements. The responses to σ_f is essentially zero for MODIS only but increases for the cases with the TANSO-FTS measurements particularly for the cases including polarization and multiangle observations. For $m_{r,f,i}$ MODIS provides essentially no response while the addition of nadir only O_2 A-band reflectance measurements provides a little response. It is only when including additional information such as polarization or multiangle measurements that the response for $m_{r,f,i}$ becomes significant. In addition, the use of all three TANSO-FTS bands contributes significantly to the response to higher order spectral fit terms due to the increase in measurement spectral range. The situation for $m_{i,f,i}$ is similar to that of $m_{r,f,i}$ but with significantly smaller responses. This is expected as our sensitivity study has shown that our measurements have only a small sensitivity to $m_{i,f,i}$.

Moving to the coarse mode we see that for N_c MODIS provides a larger response than for N_f while the response to N_c is similar to that of N_f for the scenarios including the TANSO-FTS bands. To $r_{g,c}$ the MODIS measurements provide almost no response while the addition of nadir only O_2 A-band reflectance measurements provides a little improvement. The response increases to unity as more information is added for the most complete measurement scenario M,TF,1–3,R+P,M. The situation for σ_c is similar to that of $r_{g,c}$ except that, in contrast to the fine mode, the responses to σ_c are in general larger than to $r_{g,c}$. Our sensitivity study does indicate larger sensitivities to σ_c than to $r_{g,c}$ so this result is consistent. For $m_{r,c,i}$, the situation is similar to that for the fine mode but with larger overall responses reaching unity for the first and second fit parameters for M,TF,1–3,R+P,M. Finally, the response to $m_{i,c,i}$ actually becomes significant for the scenarios including the TANSO-FTS bands reaching almost unity for the first fit parameter for M,TF,1–3,R+P,M. The larger overall response to the coarse mode, which is consistent with the sensitivity study, is

primarily due to the spectral proximity of the TANSO-FTS bands which reside at larger wavelengths providing a larger sensitivity to the coarse mode.

Figure 5.31 shows the diagonal elements of $\mathbf{A}$, with the spectral fit parameters combined, for the standard case but using model one and model three. The primary difference between these cases is the larger response to the coarse mode for model three (desert dust). This is primarily due to the large overall size of the coarse mode particles in the desert dust model. Figure 5.32 shows the diagonal elements of $\mathbf{A}$ for the standard case but using a modal optical thicknesses $\tau_{a,i}(0.55)$ of 0.01 and 1.0. For the MODIS only scenario the response in the case of $\tau_{a,i}(0.55) = 0.01$ is limited almost entirely to the surface albedo A since in this case with the relatively low optical thickness the aerosol provides almost no signal relative to that of the surface. As discussed earlier, the use of the hyperspectral bands provides a means to discriminate the aerosol signal from the surface signal. This is evident in the cases including the TANSO-FTS measurements, where the response to many of the other parameters is significant in the case of $\tau_{a,i}(0.55) = 0.01$. In the case of $\tau_{a,i}(0.55) = 1.0$ the response to A in the MODIS only case is significantly lower and in fact is lower than that for several other parameters including N_f, $r_{g,f}$, N_c, and σ_c. In this case the aerosol signal is comparable or exceeds that of the surface signal which is the ideal situation for retrievals only using MODIS measurements. Interestingly, in the cases using the TANSO-FTS measurements at $\tau_{a,i}(0.55) = 1.0$ the response to A is in general less but is more comparable to that of the other parameters, in contrast to using MODIS only, indicating more ability to retrieve A even under large aerosol loadings. It is also worth pointing out the increase in responses to m_r and m_i at $\tau_{a,i}(0.55) = 1.0$ compared to $\tau_{a,i}(0.55) = 0.1$ even for the coarse mode in the case of using MODIS only. Figure 5.33 shows the diagonal elements of $\mathbf{A}$ for the standard case but using top pressures P_{top} of 400 hPa and 800 hPa. Compared to optical thickness the variation in the responses is smaller. In fact, the only note worthy change in response with P_{top} is the decrease in the response to N_c in the MODIS only case which is most likely due to an increase in multiple scattering with the surface and coarse mode absorption. Figure 5.34 shows the diagonal elements of $\mathbf{A}$ for the standard case but using surface albedos A of 0.0 and 0.4. In general there is a decrease in the response with A and this decrease is noticeably less for the cases including the TANSO-FTS measurements. The exception is an increase in the response to N_c for the MODIS only case most likely, again, having to do with multiple scattering with the surface and coarse mode absorption.

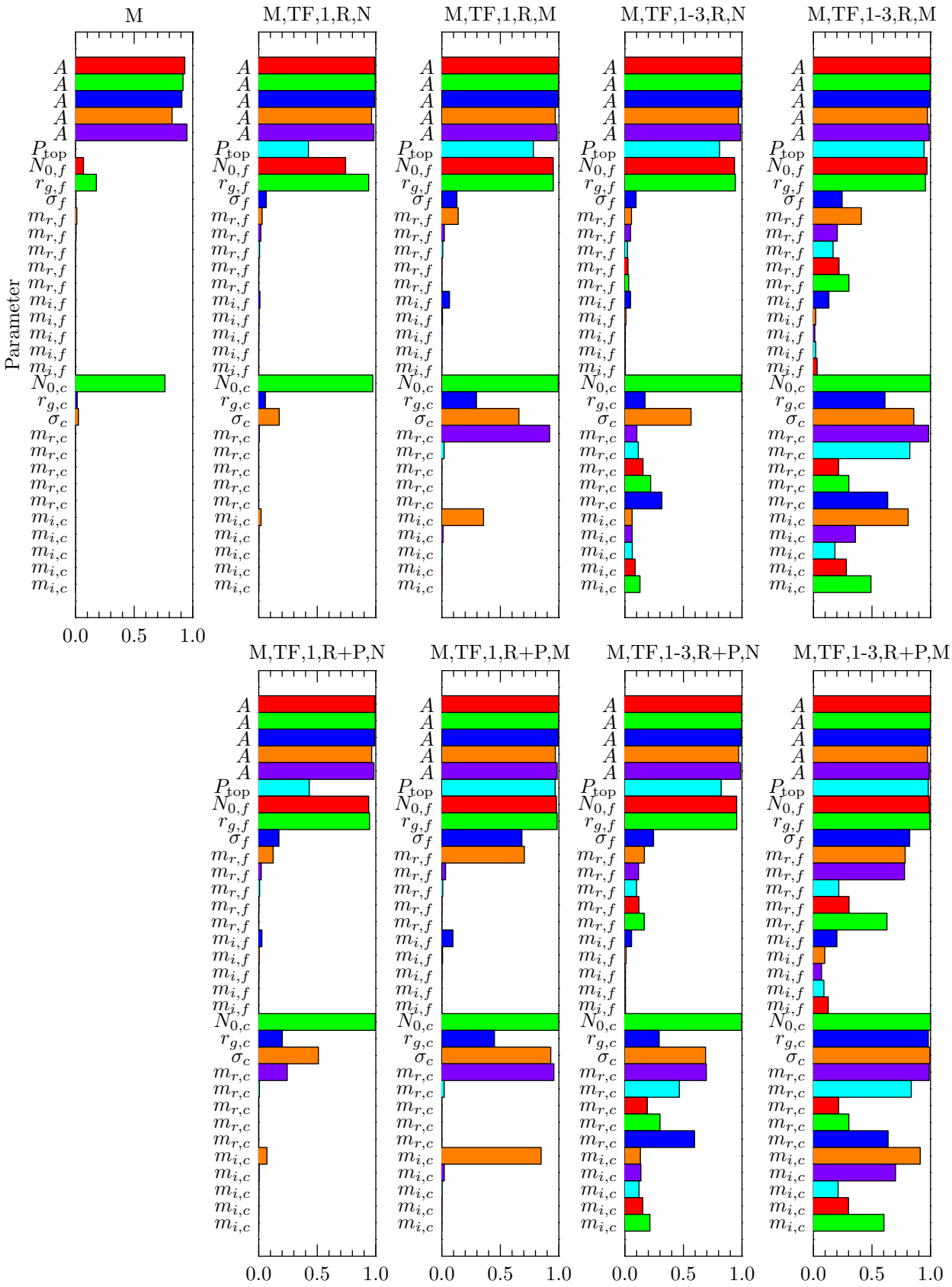

Figure 5.30: Diagonal elements of the averaging kernel matrix for the standard setup.

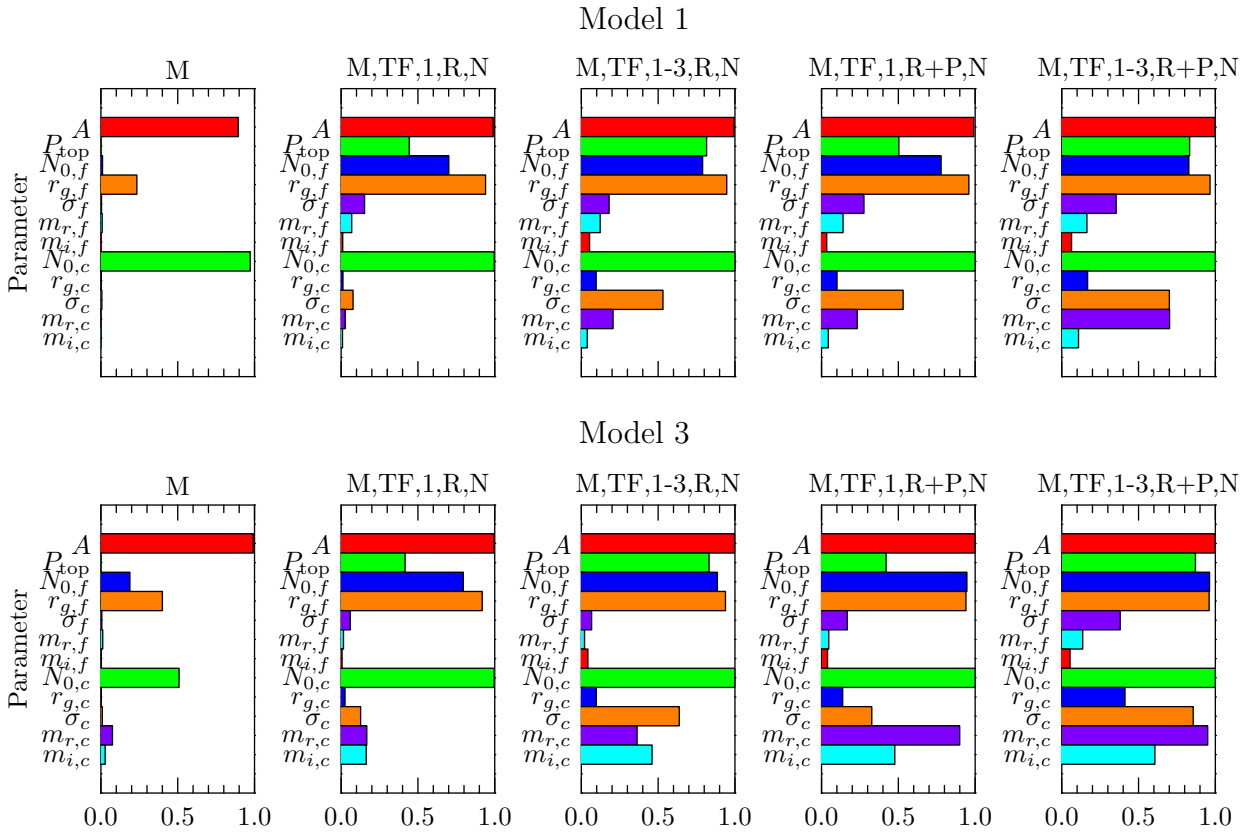

Figure 5.31: Diagonal elements of the averaging kernel matrix for the standard setup except for model one (top) and model 3 (bottom). Values for the spectral fit parameters have been linearly combined to a single representative value.

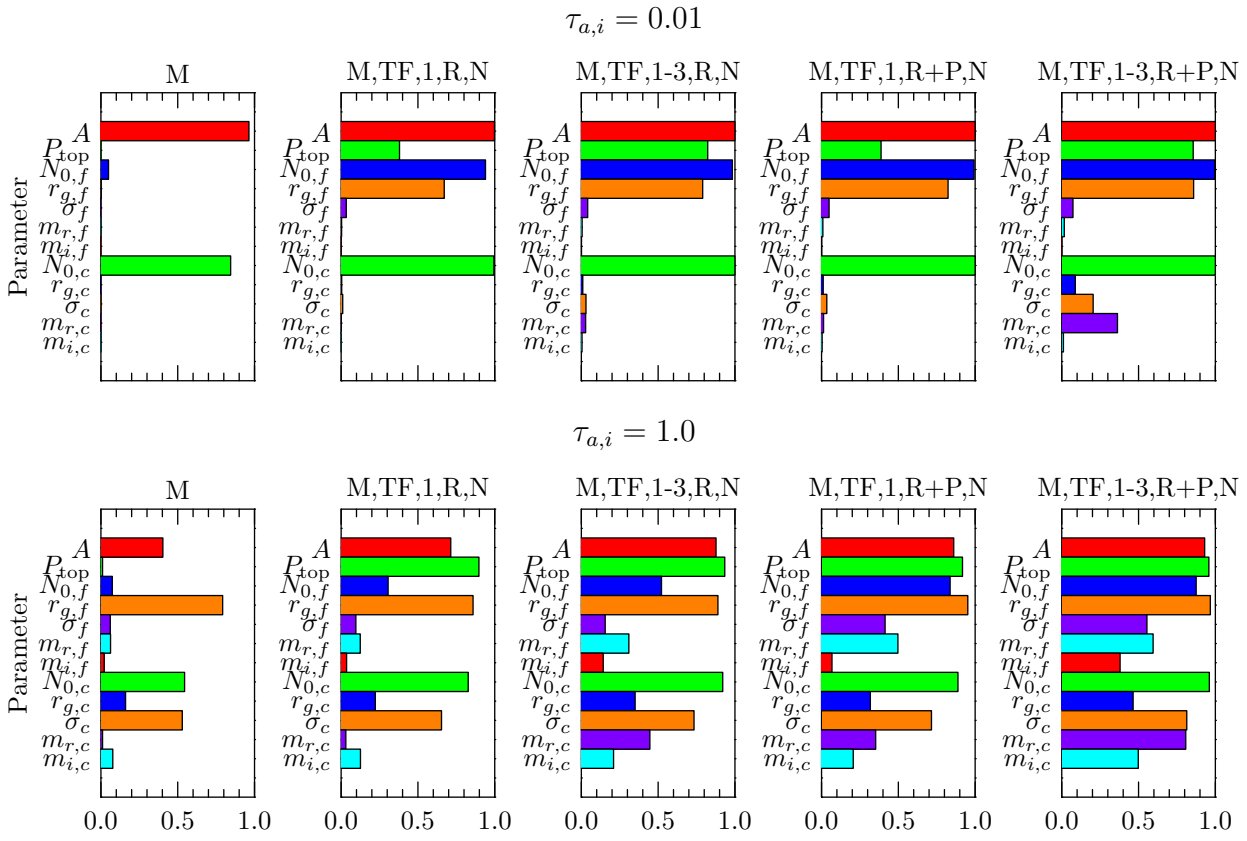

Figure 5.32: Same as figure 5.31 but for modal optical thickness $\tau_{a,i}(0.55) = 0.01$ (top) and 1.0 (bottom).

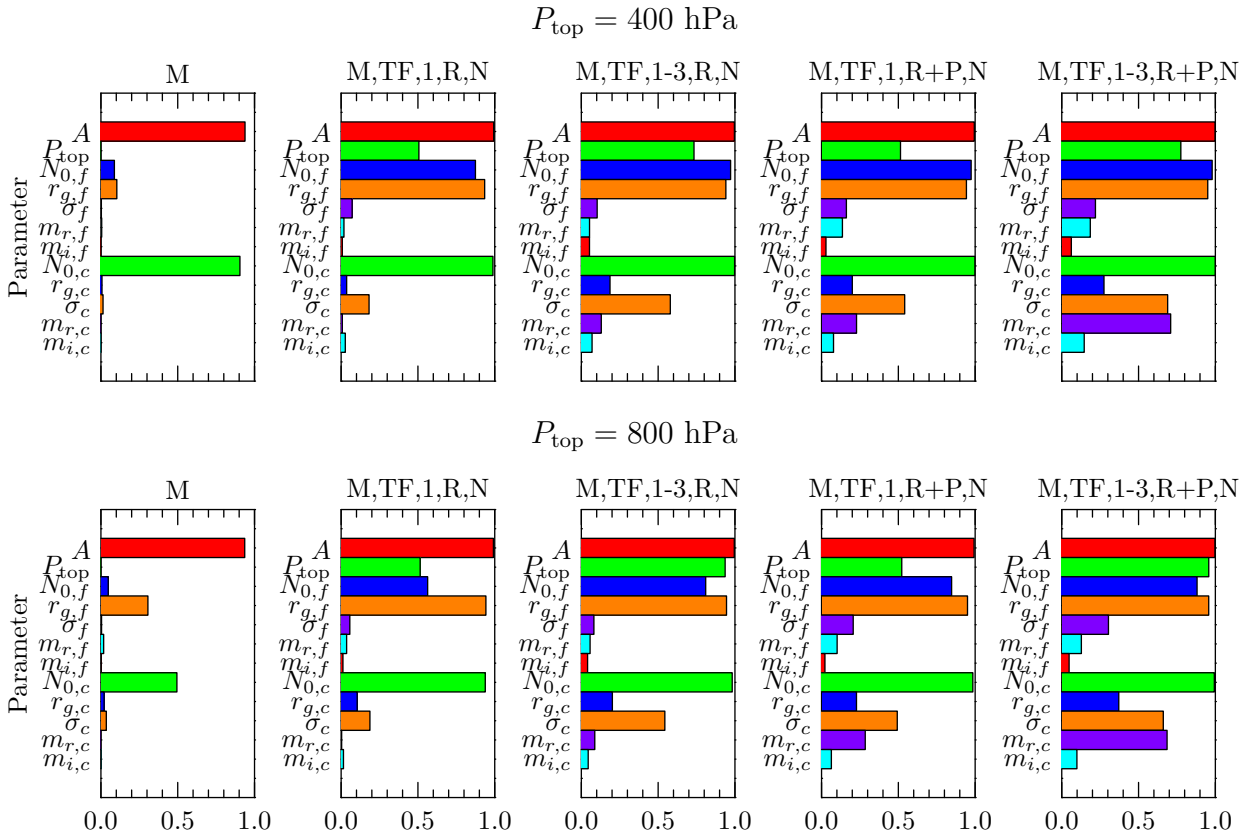

Figure 5.33: Same as figure 5.31 but for aerosol-top pressure $P_{\rm top}$ = 400 hPa (top) and 800 hPa (bottom).

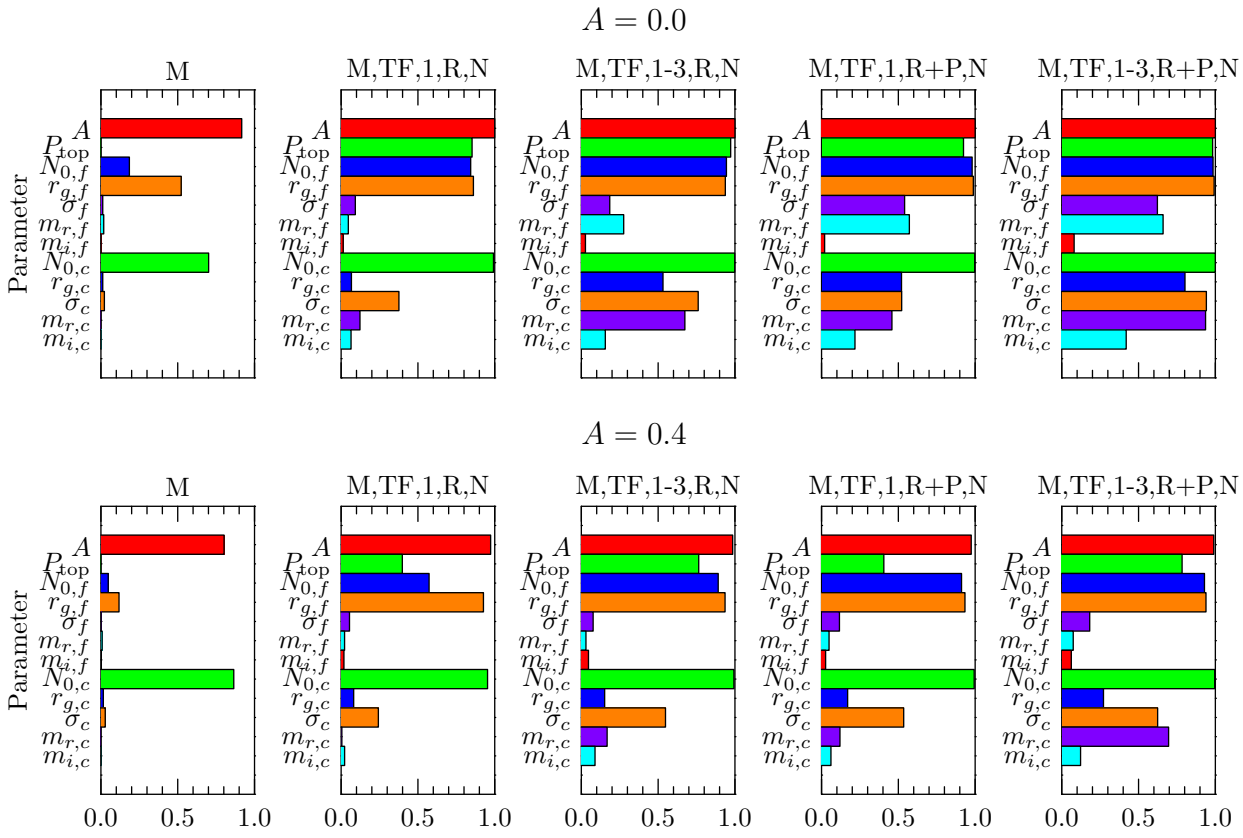

Figure 5.34: Same as figure 5.31 but for surface albedo $A = 0.0$ (top) and 0.4 (bottom).

5.7.5 Posteriori error

In this section we look at the diagonal elements of the posteriori error covariance matrix $\hat{\mathbf{S}}$. $\hat{\mathbf{S}}$ is an "estimate" of the error in the retrieved state $\hat{\mathbf{x}}$ due to errors in the measurements, forward model, and a priori knowledge. For our results here $\hat{\mathbf{S}}$ represents the retrieval error for a case in which the true state vector is that of our base state. A rigorous error characterization that is independent of outside validation sources is an important part of any retrieval but it should only be considered as an estimate of the retrieval error and like the retrieval results themselves validation of the posteriori error is necessary as we will do in Part II. In the following, rather than showing the absolute magnitudes of the diagonal elements of $\hat{\mathbf{S}}$, we show the normalized error fraction given by

$$\varepsilon(\hat{x}_i) = \frac{\sqrt{\hat{S}_{ii}}}{\hat{x}_i}. \tag{5.45}$$

All the results shown are for our standard case (model 2, $\tau_{a,i}(0.55) = 0.1$, $P_{\text{top}} = 600$ hPa, $A = 0.2$, $\theta_0 = 35°$, $\phi_0 = 180°$, and $\phi = 90°$) as a function of one of the parameters. In the interest of brevity, for the spectral fits we will show errors for a combination of the fit parameters.

In the following we show $\varepsilon(\hat{x}_i)$ as a function of total optical thickness $\tau_a(0.55)$, aerosol-top pressure P_{top}, surface albedo A, solar zenith angle θ_0, and solar azimuth angle ϕ_0, in figures 5.35, 5.36, 5.37, 5.38, and 5.39, respectively. In each case, the errors for all parameters except, A, N_f, and N_c are bounded by the error determined by the a priori 1-sigma value divided by the base state value. In almost all cases for the MODIS only retrieval the error is at this bound except for the size distribution parameters at large values of $\tau_a(0.55)$. It is also apparent that the error improves with the complexity of the measurement scenario as expected. This is especially the case for σ, m_r, and m_i for which the multiangle and/or polarimetric measurements provide significantly more information than the nadir and/or intensity only measurements.

Figure 5.35 shows values of $\varepsilon(x_i)$ as a function of the total optical thickness $\tau_a(0.55)$. The errors for A increase with $\tau_a(0.55)$ as the surface signal decreases relative to the aerosol signal. The errors in P_{top} decrease with $\tau_a(0.55)$ for all the cases including TANSO-FTS and the case for APS. It is interesting that at lower values of $\tau_a(0.55)$ the errors in P_{top} are lower for the cases including TANSO-FTS measurements compared to the APS retrieval while for larger optical thicknesses the

APS retrieval improves to be comparable to the retrievals including TANSO-FTS measurements. This contrast is due to the different sources of sensitivity to aerosol height. The TANSO-FTS measurements are sensitive to P_{top} due to the variation in molecular absorption across the bands. The APS measurements and the TANSO-FTS polarization measurements are sensitive to P_{top} due to the variation in polarizing molecular scattering with height. It is apparent that the polarization based sensitivity is more affected by the lower aerosol signal at low values of $\tau_a(0.55)$. For the rest of the parameters the error decreases with $\tau_a(0.55)$ up to approximately $\tau_a(0.55) = 1.0$. This is as expected from the previous analyses and is due to the larger aerosol signal overall and relative to the surface with $\tau_a(0.55)$. Except for m_i the errors tend level off and sometimes increase, for the single scattering related parameters, after $\tau_a(0.55) > 1.0$. The reason for the increase is due to a decrease in single scattering and an increase in multiple scattering and therefore a signal that is more indirectly related to the single scattering related parameters.

Figure 5.36 shows values of $\varepsilon(x_i)$ as a function of the aerosol-top pressure P_{top}. The errors for A remain relatively constant with P_{top} indicating that the surface signal is relatively invariant with the aerosol vertical distribution even in the TANSO-FTS cases, where lower aerosol layers should have more multiple scattering interaction with the surface. The errors for P_{top} decrease with P_{top} which is probably related to an increase in the influence of molecular absorption and scattering with P_{top}. Errors in both $N_{0,f}$ and $N_{0,c}$ increase with P_{top} for the cases with the TANSO-FTS measurements most likely do to molecular absorption above the aerosol layer decreasing the aerosol signal. For the case of MODIS only the error remains constant for $N_{0,f}$ as we would expect as the MODIS channels should be free of molecular absorption but they increase for $N_{0,c}$ which is probably due the influence of large particles on aerosol absorption and the increasing aerosol/surface interaction with P_{top}. For the rest of the parameters that are not significantly affected by the a priori the error remains relatively stable with P_{top}. This suggests that the amount of single scattering, from which much of the sensitivity to aerosols comes from, relative to multiple scattering remains relatively stable with P_{top}. There is some increase with P_{top} in the cases including polarimetric multiangle measurements for $m_{r,f}$ and $m_{i,c}$ although the explanation for this is not entirely obvious.

Figure 5.37 shows values of $\varepsilon(x_i)$ as a function of the surface albedo A. In general, the errors increase with A, as the aerosol signal decreases relative to that from the surface, mostly at lower values and then tend to level off. There is a spike in the error in A for MODIS at around $A = 0.05$

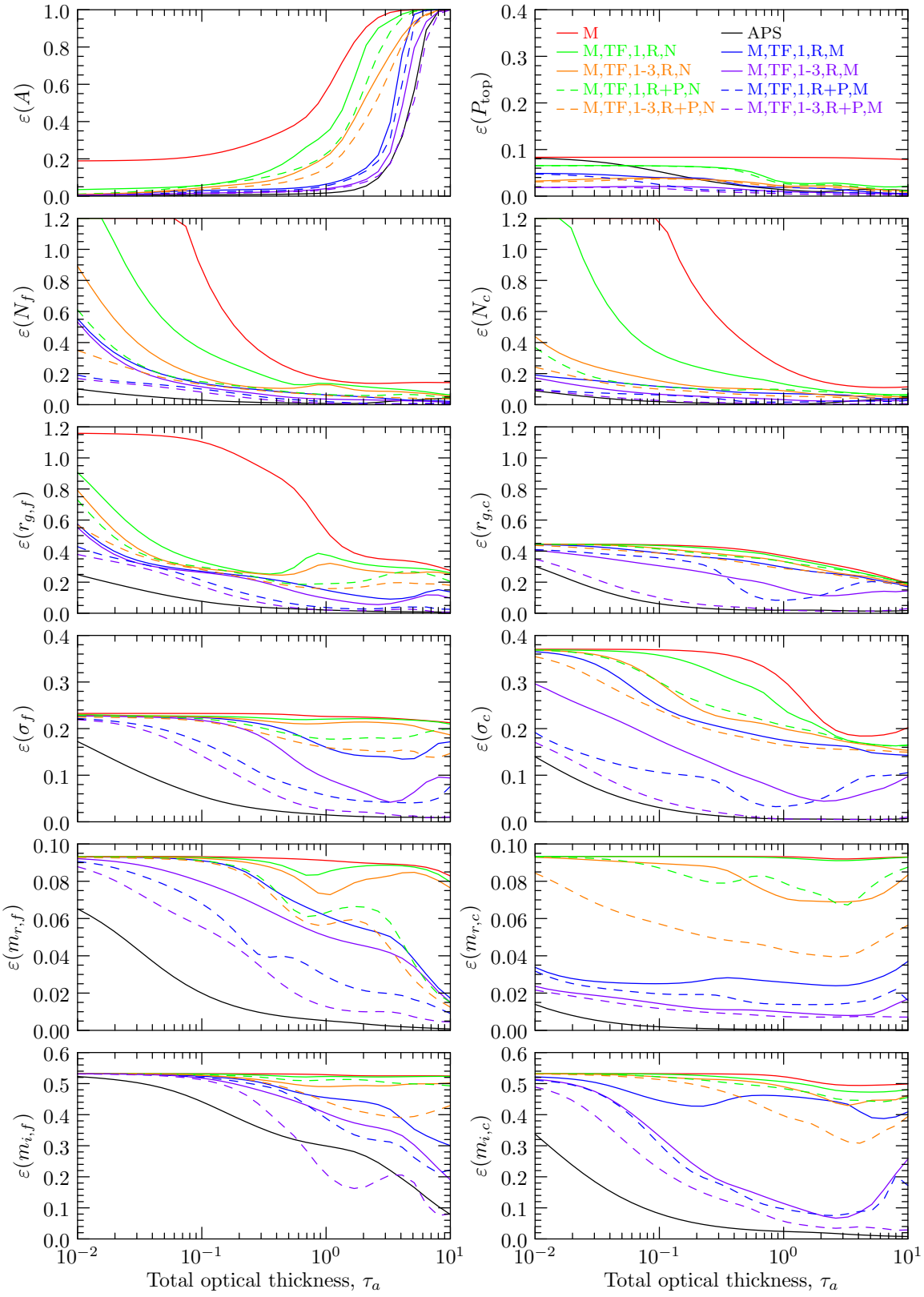

Figure 5.35: Posteriori error fraction $\varepsilon(\hat{x}_i)$ of each retrieval parameter for a retrieval of the standard setup as a function of the total optical thickness $\tau_a(0.55)$.

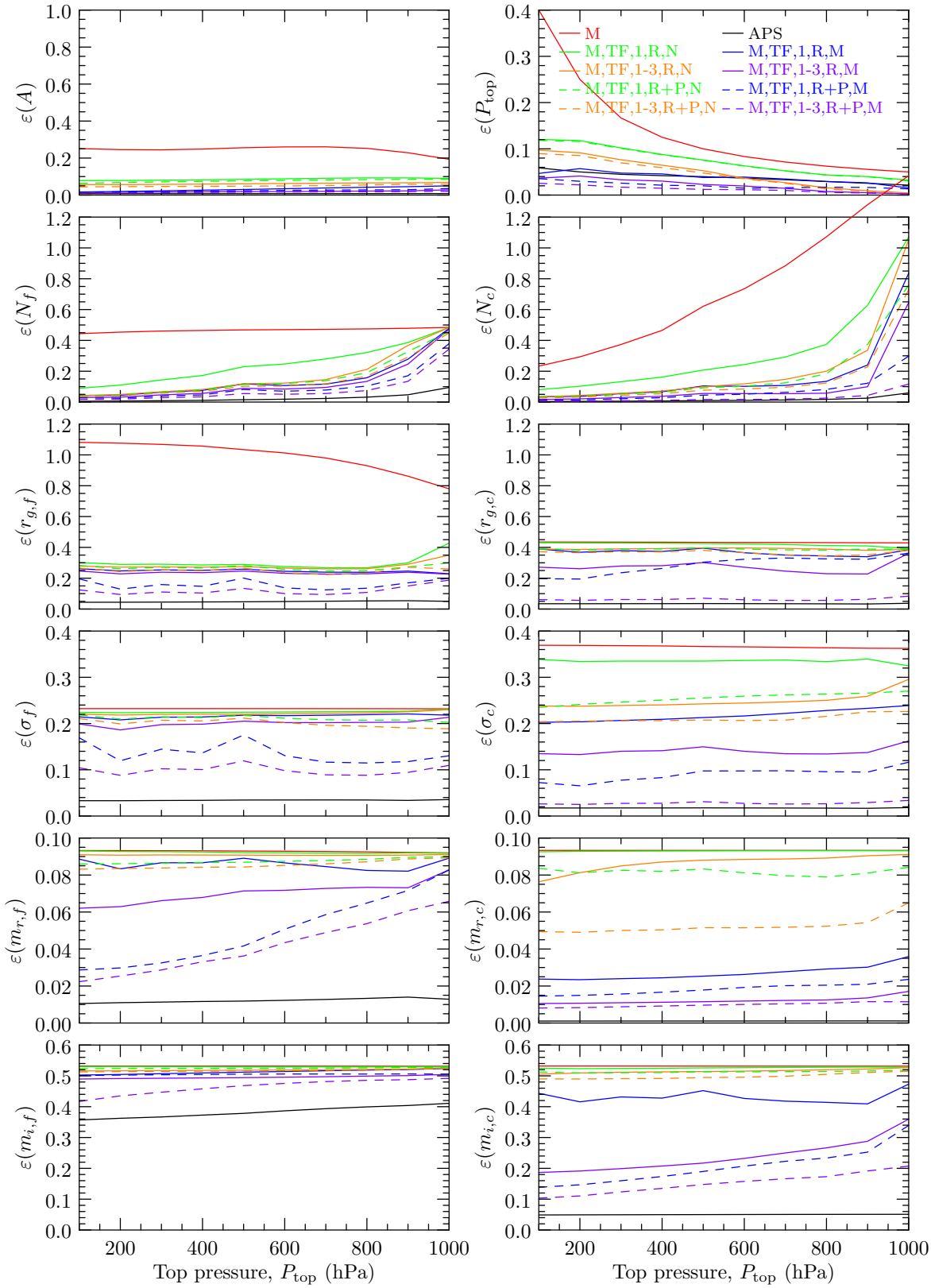

Figure 5.36: Same as figure 5.35 but as a function of aerosol-top pressure $P_{\rm top}$.

which is probably due to large changes in the measurement sensitivities to other parameters around that region. In addition, the errors for MODIS, in cases not determined entirely by the a priori, actually decrease eventually due to the limited amount of information available.

Figure 5.38 shows values of $\varepsilon(x_i)$ as a function of the solar zenith angle θ_0. Significant features are the rather large variation/increase in the errors for A for the MODIS retrieval which is probably due to the increase in optical path and, as a result, and decrease in signal from the surface. The scenarios with TANSO-FTS measurements, with more information, have flatter errors as they are not as susceptible to the effects. The errors for P_{top} vary little with θ_0 while the errors for $N_{0,f}$ and $N_{0,c}$ vary with θ_0 for the simpler measurement scenarios and are relatively flat for the more complex scenarios. For the more single scattering related parameters even the more complex scenarios have significant variation as the aerosol phase matrix provides significant, geometry dependent, sensitivity to these parameters.

Figure 5.39 shows values of $\varepsilon(x_i)$ as a function of the solar azimuth angle ϕ_0. Notable features are the fact that A, P_{top}, and N_0 show little sensitivity to the ϕ_0 due to their lack of sensitivity to the single scattering phase matrix and therefore geometry. For the rest of the parameters, nadir measurement show little sensitivity to ϕ_0 as the scattering angle is invariant with ϕ_0 for nadir viewing. In contrast, the multiangle measurements show significant sensitivity to ϕ_0 due to both variations in the phase matrix with scattering angle and the variation in the range of sampled scattering angles with ϕ_0.

5.8 Summary and conclusions

We have presented a sensitivity and information content study to investigate the capability of hyperspectral measurements in solar molecular absorption bands combined with more common multispectral measurements to retrieve tropospheric aerosol properties. For the hyperspectral observations we use measurements of the type made by the GOSAT TANSO-FTS instrument including measurements in the 0.76-μm O_2 A-band and the 1.61- and 2.06-μm CO_2 bands. In addition, as TANSO-FTS actually takes measurements in two polarizations and is capable of taking observations at multiple view angles (target mode) we investigate the use of polarization and multiangle observations as additional sources of information. For the multispectral observations we use the first seven

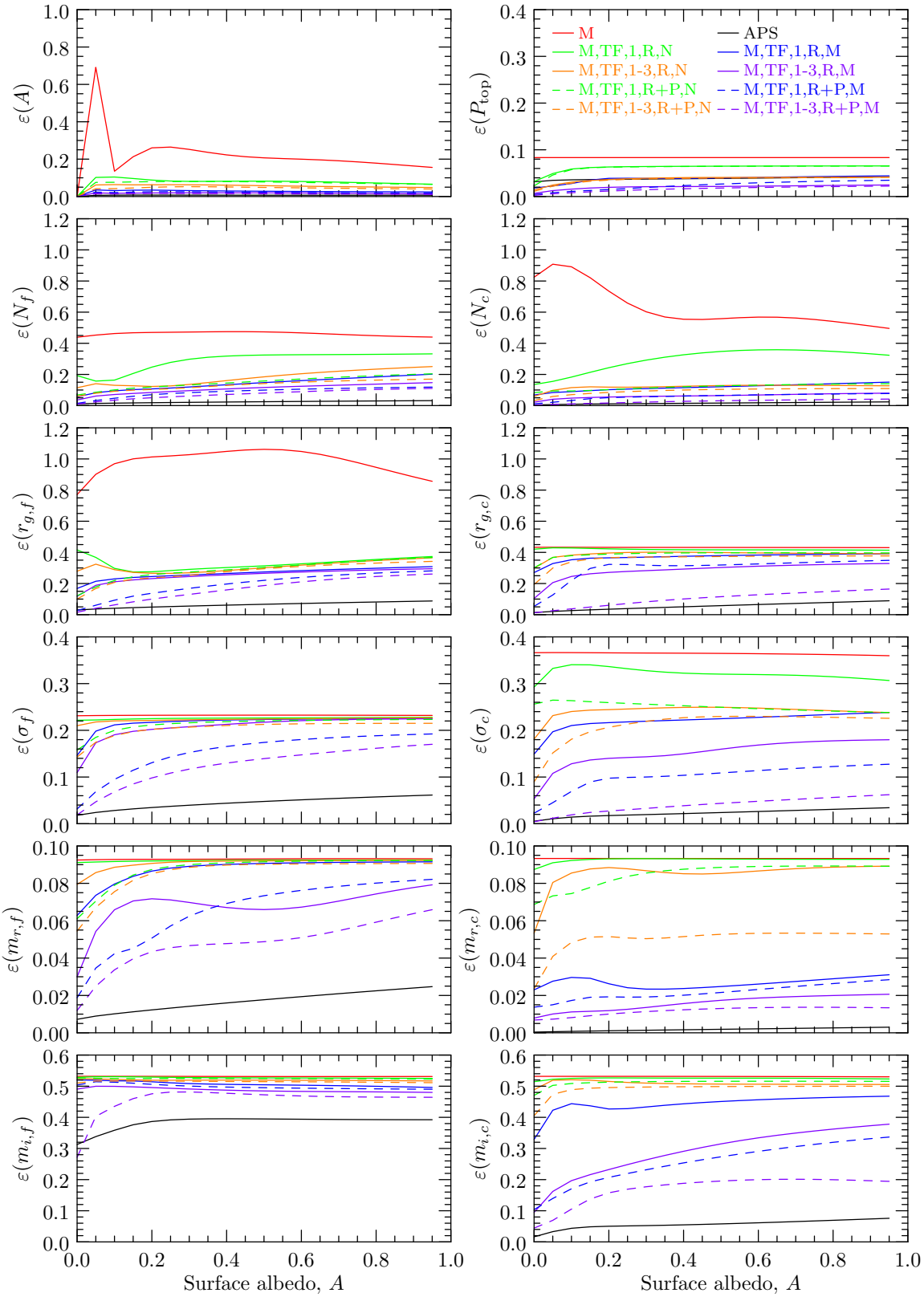

Figure 5.37: Same as figure 5.35 but as a function of surface albedo A.

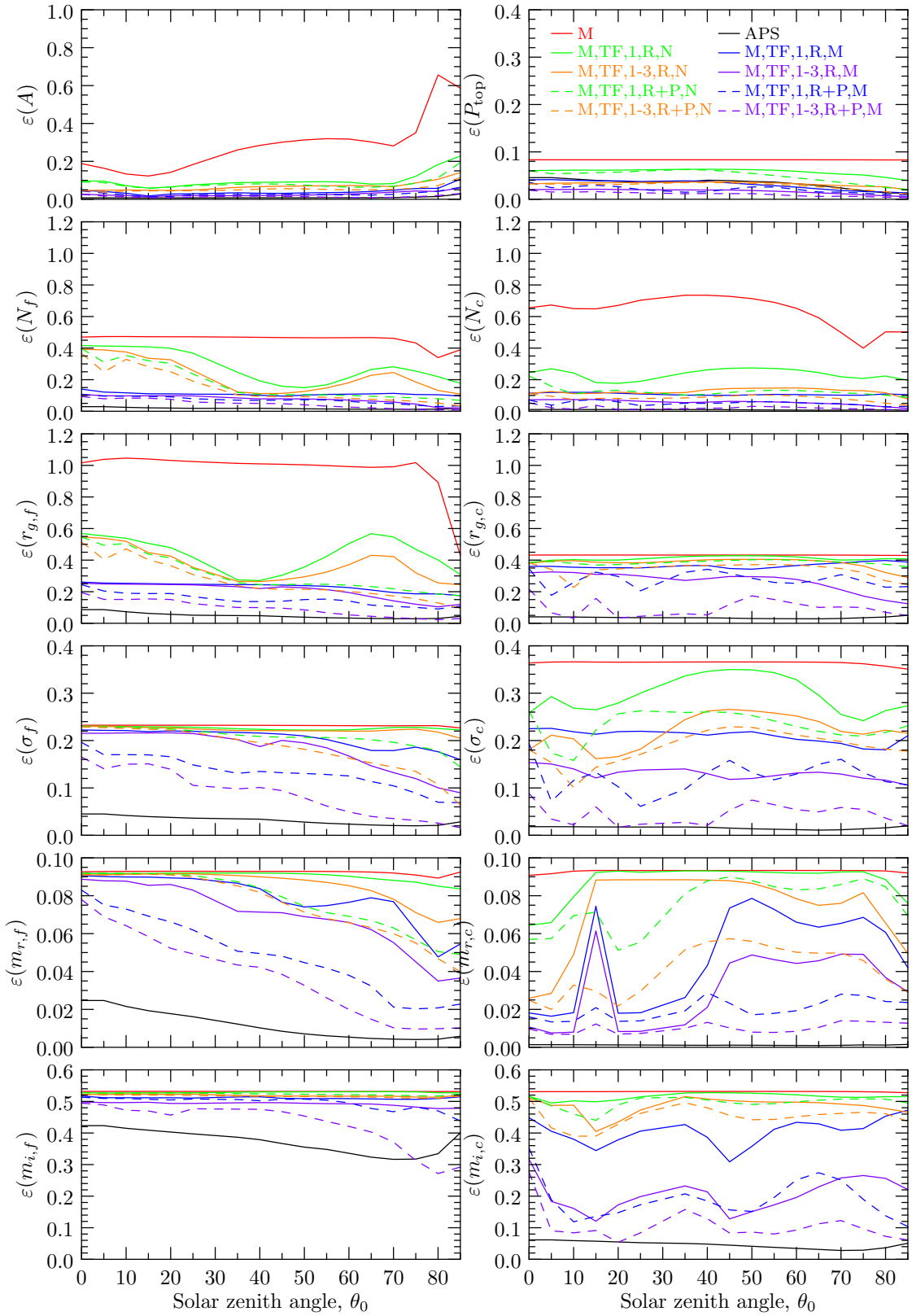

Figure 5.38: Same as figure 5.35 but as a function of solar zenith angle θ_0.

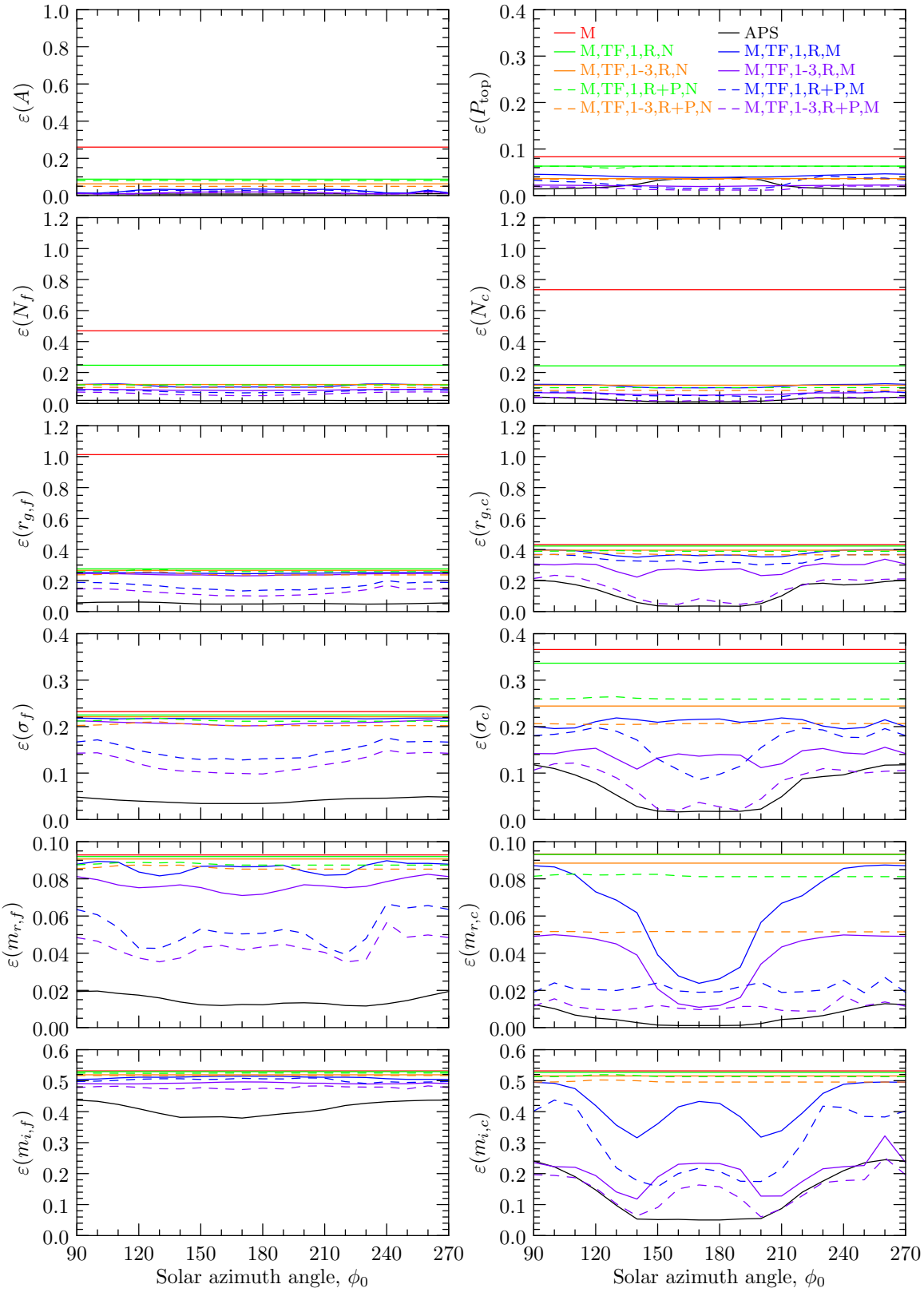

Figure 5.39: Same as figure 5.35 but as a function of solar azimuth angle ϕ_0.

bands of MODIS which are commonly used for aerosol retrievals. Several measurement scenarios are investigated including the case of using MODIS only and MODIS + TANSO-FTS, where all possible combinations of O_2 A-band only/all three bands, total reflectance/total + polarized reflectance, and nadir/multiangle are investigated.

Our retrieval parameters include the spectral surface albedo $A(\lambda)$, aerosol-top pressure P_{top}, and the aerosol number concentration, mean radius and variance of a log-normal size distribution, and the spectral real and imaginary parts of the index of refraction for a fine mode ($N_{0,f}$, $r_{g,f}$, σ_f, $m_{r,f}(\lambda)$, $m_{i,f}(\lambda)$) and a coarse mode ($N_{0,c}$, $r_{g,c}$, σ_c, $m_{r,c}(\lambda)$, $m_{i,c}(\lambda)$). The spectral parameters are derived from retrieved parameters for a polynomial fit in wavelength.

We describe in moderate detail our forward model for simulation of measurements and the derivatives of those measurements with respect to input parameters. The model components described include the atmospheric, surface, solar, radiative transfer, instrument, and noise models. References are given for readers that require more detailed information.

We outline several atmospheric, surface, and geometric scenarios investigated. The types of aerosols investigated include urban-industrial, biomass burning, and desert dust. In addition, aerosol 0.55-μm optical thicknesses from 0.01 to 1.0, aerosol-top pressures from 400 to 800 hPa, and surface albedos from 0.0 to 0.4 were investigated. Ranges in solar and viewing geometry account for the most common ranges appropriate for the particular measurement scenario.

The relevant conclusions that can be taken from the sensitivity study are the following:

1. The sensitivity of total reflectance to surface albedo A dominates the sensitivities in the continuum.

2. The sensitivity of total reflectance to single scattering albedo ω_a is usually second to that of A.

3. The sensitivity of total reflectance and polarized reflectance to the fine and coarse modes is dependent on wavelength. Smaller wavelengths are more sensitive to the fine mode whereas larger wavelengths are more sensitive to the coarse mode.

4. In general, in the absorption bands, as molecular absorption increases the sensitivity of total reflectance to A and ω_a decreases whereas the sensitivity to all the other parameters increases up to a point and then decreases. The decrease in sensitivity to A is due to the

increased molecular absorption masking the surface influence. The decrease in sensitivity to ω_a is due to the decrease in multiple scattering with increased molecular absorption. The increase in sensitivity to aerosol-top pressure P_{top} is a result of the variation in the vertical weighting function with molecular absorption. The increase in the sensitivity to the other aerosol parameters is due to both a decrease in the effects from the surface and an increase in only singly scattered photons with increased molecular absorption which contain a more direct relationship with the single scattering properties of the aerosol than multiply scattered photons.

5. The sensitivity of total reflectance to P_{top} and the aerosol parameters both in the continuum and in the molecular absorption lines increases with a aerosol optical thickness $\tau_a(0.55)$ while the sensitivity to A decreases. The sensitivity to several parameters in the molecular absorption lines decreases with aerosol-top pressure P_{top} due to the masking of the effects of aerosols at low altitudes. The sensitivity to aerosol parameters decreases with surface albedo A in the continuum but remains relatively constant within the absorption lines — an important advantage to using these hyperspectral observations for aerosol retrievals over dark surfaces.

6. The 1.61-μm CO_2 band with it's relatively weak absorption provides little variation in sensitivity across it's spectrum whereas the 2.06-μm CO_2 band provides valuable sensitivity variations to the coarse mode but contributes less information on the fine mode than the O_2 A-band.

7. In contrast to total reflectance, the sensitivity of the polarized reflectances to A and ω_a do not dominate over that to the non-albedo parameters and are in general lower than that to the non-albedo parameters.

8. As with total reflectance, the sensitivity of the polarized reflectances to P_{top} and the non-albedo aerosol parameters, in general, increases in the absorption lines. In contrast to total reflectance, the sensitivity of the polarized reflectances to A and ω_a also increases in the absorption lines.

9. The variation in sensitivity with view angle, in relation to multiangle measurements, is greater for the polarized reflectance than for the total reflectance, as expected, and is greater for the coarse mode than for the fine mode.

With the sensitivity study presented we outline our information content methodology and use the same set of atmospheric/surface/geometry scenarios used for the sensitivity analysis to evaluate the information content of the different measurement scenarios. The relevant conclusions that can be taken from the information content study are the following:

1. From the SVD analysis using the spectrally reduced state vector we find that with the use of MODIS only up to three parameters are retrievable, which should be A, $N_{0,f}$, and $N_{0,c}$ or if the surface reflectance is known a priori $N_{0,f}$, $N_{0,c}$, and $r_{g,f}$.

2. From the SVD analysis using the spectrally reduced state vector we find that with the addition of the TANSO-FTS measurements five parameters are retrievable and the degree of non-uniqueness is reduced. The use of all three bands instead of just the O_2 A-band, the use of multiangle measurements, and/or polarization measurements provides more information increasing the number of retrievable parameters and decreasing the degree of non-uniqueness. In the case of the most complex measurement scenario up to all 12 of the state vector parameters are retrievable.

3. The degrees of freedom for signal d_s at $\tau_a(0.55) = 0.1$ varies from around five for MODIS up to around 21 for the case of the ideal APS like measurement scenario. With the TANSO-FTS measurements included d_s at $\tau_a(0.55) = 0.1$ varies from approximately seven for the simplest measurement scenario of just MODIS + the O_2 A-band total reflectance at nadir to approximately 17 for the most complex MODIS + TANSO-FTS case including total and polarized reflectance at multiple view angles in all three bands. The variation of d_s with $\tau_a(0.55)$ is in general an increase up to approximately $\tau_a(0.55) = 2.0$, where the magnitude of the increase is more for the more complex scenarios with a maximum range of 17 to 23 for APS. d_s also decreases slightly with aerosol-top pressure P_{top} and surface albedo A. Finally, d_s shows some dependence on geometry, particularly for the cases using measurements at multiple view angles.

4. As expected, the averaging kernels indicate an almost complete retrieval response to the surface albedo A for all measurement scenarios. The MODIS only retrieval shows some response to $N_{0,f}$, $r_{g,f}$, and $N_{0,c}$ which increase significantly when adding the TANSO-FTS measurements. In addition, the TANSO-FTS measurements provide response to P_{top} and

to other parameters especially in the coarse mode. The use of all three bands increases the response to the higher order spectral fit parameters and the use of polarized reflectance and/or multiangle observations provides response to the real part, and to a lesser degree the imaginary part, of the index of refraction. The response decreases with the total aerosol optical thickness $\tau_a(0.55)$ but this effect is significantly less for scenarios including TANSO-FTS compared to the MODIS only scenario.

5. Posteriori error estimates indicate the surface albedo A is retrieved within an accuracy of 50% for the MODIS only scenario when $\tau_a(0.55) < 1.0$. The errors when the TANSO-FTS measurements are added are less that 20%. In all cases the errors rapidly increase fir $\tau_a(0.55) > 1.0$. The error in aerosol-top pressure P_{top} is determined entirely by the a priori error for MODIS whereas with TANSO-FTS the errors are mostly within 10% and decrease with $\tau_a(0.55)$ and P_{top}. The errors in $N_{0,f}$ and $N_{0,c}$ decrease significantly with $\tau_a(0.55)$. They also vary significantly with measurement scenario with errors at $\tau_a(0.55) = 0.1$ ranging from greater than 100% for MODIS only to less than 10% for the most complex TANSO-FTS scenario. It is important to understand that it is actually the optical thickness, derived from $N_{0,f}$ and $N_{0,c}$, that is radiatively more important, and will show significantly less error at low values of $\tau_a(0.55)$. The errors for $r_{g,f}$ at $\tau_a(0.55) = 0.1$ vary from the a priori error of approximately 110% for MODIS only to approximately 15% for the most complex TANSO-FTS scenario and generally decrease with $\tau_a(0.55)$. For $r_{g,c}$ the errors at $\tau_a(0.55) = 0.1$ for MODIS only and the simpler scenarios including TANSO-FTS are determined by a priori error at approximately 40% decreasing down to approximately 10% for the more complex scenarios including TANSO-FTS. For both modes the errors decrease with $\tau_a(0.55)$. For σ_f the errors at $\tau_a(0.55) = 0.1$ range from the a priori determined bound of approximately 23% to 15% for the more complex scenarios including TANSO-FTS. For σ_c at $\tau_a(0.55) = 0.1$ the errors are bounded by the a priori at approximately 37% but improve with more complex measurements to 5% and increase with $\tau_a(0.55)$. For both modes the errors decrease significantly with $\tau_a(0.55)$. Errors for $m_{r,f}$ and $m_{r,c}$ at $\tau_a(0.55) = 0.1$ are bounded by the a priori (approximately 9%) at low values of $\tau_a(0.55)$ ranging down to 6% and 1%, respectively, for the more complex measurement scenarios. For both modes the errors decrease with $\tau_a(0.55)$. Finally, errors for

$m_{i,f}$ and $m_{i,c}$ at $\tau_a(0.55) = 0.1$ are bounded by the a priori (approximately 55%) with little improvement with measurement scenario for the fine mode but ranging down to 20% for the coarse mode. For both modes the errors decrease with $\tau_a(0.55)$.

6. With the P_{top} the errors in P_{top} decrease while the errors in $N_{0,f}$ and $N_{0,c}$ increase. The errors for all other parameters remain relatively constant with P_{top}.

7. With A the errors in all parameters increase rapidly at low values of A but level off after approximately $A = 0.2$.

8. The Posteriori error values also vary with solar zenith angle θ_0 especially for the size distribution and index of refraction parameters that are more directly related to the single scattering phase matrix and therefore geometry. With the solar azimuth angle ϕ_0 the errors in A, P_{top}, and N_0 are almost perfectly flat. For the size distribution and index of refraction parameters the errors show little variation with ϕ_0 as the scattering angle is invariant with ϕ_0 for nadir viewing while the multiangle measurements show significant sensitivity to ϕ_0 due to variations in the single scattering phase matrix.

Chapter 6

Retrieval Method, Results, and Validation[4]

6.1 Introduction

Atmospheric aerosols effect the Earth's climate system directly by scattering and absorbing incoming solar radiation and indirectly by modifying cloud development, and as a result, cloud albedo and precipitation. Unfortunately, uncertainties in aerosol properties and their effect on the climate system represents one of the largest uncertainties in climate change research [Intergovernmental Panel on Climate Change, 2007a]. Due to the large variability of source types, strengths, and locations aerosols vary significantly in size, shape, and chemical composition as well as spatial and temporal distribution with variabilities on the order of kilometers and days, respectively. Satellite observations provide the only realistic means to resolve these variabilities while making measurements on a global scale.

Multispectral measurements of intensity have been used for decades but more recently, motivated by more stringent requirements for the retrieval of aerosol parameters [Mishchenko et al., 2004], multispectral, multiangle, and/or polarimetric satellite instruments are being put into orbit. A review of different types of passive satellite measurements used for the remote sensing of tropospheric aerosols along with references is presented in the first part of this study [McGarragh and Stephens, 2013a] hereafter refereed to as "Part I".

In addition to these more common types of observations, high spectral resolution measurements within molecular absorption bands at solar wavelengths, in particular the 0.76-μm O_2 A-band and the 1.61- and 2.06-μm CO_2 bands, show a promising amount of information on atmospheric

[4]Paper to be submitted: "A Multi-Sensor Concept for Retrieving Aerosol Parameters, Part II: Retrieval Method, Results, and Validation".

particulates [Stephens and Heidinger, 2000]. A review of the research related to the use of these kinds of measurements for remote sensing of clouds and aerosols is given in Part I. In short, it is the broad photon path length distribution within these bands and the variation in the multiple scattering that provides variations in sensitivities to aerosol parameters with molecular absorption optical thickness that provides a basis for the retrieval of these parameters. In addition, the variation in molecular absorption results in variation in the peak location of vertical weighting functions making it possible to retrieval aerosol layer height information. Finally, the molecular absorption provides a means to mask the effects of the surface, in order to separate the aerosol signal from the surface signal, a particular challenge in aerosol remote sensing. It is only recently that these kinds of observations have been made available from satellite with the recent launch of the Greenhouse Gases Observing Satellite (GOSAT) [Kuze et al., 2009] and will be also be available with the planned launch of the Orbital Carbon Observatory-2 (OCO-2) [Crisp et al., 2004].

In Part I we present a sensitivity and information content analysis for a retrieval system that combines common multispectral observation, as would be measured with the MODerate Resolution Imaging Spectrometer (MODIS), with hyperspectral observations in the 0.76-μm O_2 A-band and the 1.61- and 2.06-μm CO_2 bands as would be measured from the GOSAT Thermal And Near infrared Sensor for carbon Observations - Fourier Transform Spectrometer (TANSO-FTS) instrument. Since TANSO-FTS actually takes measurements at two polarizations and is capable of viewing the same scene at multiple angles we explored not only the use of intensity at nadir but the use of polarization and/or multiangle measurements. It was found that the use of the TANSO-FTS hyperspectral bands added a significant amount of information to the retrieval system and that the use of polarization and/or multiangle measurements added even more information. The study in Part I, with its encouraging results, set a precedent for the development of a real retrieval system using MODIS and TANSO-FTS measurements which will be the topic of this paper. Although the retrieval is general enough to be used over land or ocean we focus on land since it is over land that the hyperspectral measurements will bring the greatest benefit with their unique ability to separate the aerosol and surface effects and also since most of the AERONET observations used for validation are land-based.

Inversion algorithms for the retrieval of aerosol properties from passive satellite instruments generally fall into two categories [Kokhanovsky and Leeuw, 2009]. The traditional approach uses a least squares type method to minimize the difference between the measurements and simulations

based on a limited set of predefined aerosol models and aerosol optical thickness. The simulations are usually precomputed and stored in a look-up table (LUT) as a function of aerosol model, aerosol optical thickness (AOT), assumed surface properties, and solar and viewing geometry, which makes them efficient in operational environments. Retrievals using the LUT approach include the operational MODIS [Tanré et al., 1997, Kaufman et al., 1997, Levy et al., 2007], Multiangle Imaging SpectroRadiometer (MISR) [Martonchik et al., 1998], and Polarization and Directionality of the Earth's Radiances (POLDER) [Herman et al., 2005, Tanré et al., 2011, Deuzé et al., 2001, Tanré et al., 2011] retrievals. (See the review in Part I for more details on these retrievals.) Unfortunately, due to the discrete nature of the inversion these methods are unable to utilize all the information contained in advanced observations with multispectral, hyperspectral, multiangle, and/or polarimetric measurements [Dubovik et al., 2011]. In addition, attempts to retrieve a larger number of parameters with these advanced measurements will increase the dimensionality of the LUT approach making the method unwieldy for operational use.

The other category of inversion algorithms includes optimal estimation approaches, where the best match between the measurements and the simulations, as computed with a forward model, is obtained by optimizing the forward model inputs [Rodgers, 2004]. The methodology makes use of a continuous space of aerosol microphysical properties, and in some cases surface properties, as a continuous set of solutions maximizing the use of all the available information. Of course the aerosol retrieval problem is ill-posed with many possible solutions. To deal with this optimal estimation approaches usually employ some sort of a priori constraint and use some form of regularization to stabilize the solution.

The use of optimal estimation for aerosol retrievals is relatively new but growing due to the availability of more advanced measurements and increased computing power. Hasekamp and Landgraf [2005] presented an optimal estimation based information content and retrieval technique using GOME-2 intensity and polarization measurements to retrieve, over ocean, a full set of aerosol parameters. Their method used both an a priori constraint and a Phillips-Tikhonov regularization to retrieve a stable solution. Lebsock et al. [2007] presented an information content analysis and optimal estimation retrieval over ocean using the POLDER intensity and polarization at 670 and 860 nm. Unfortunately, they did not use an a priori constraint or a form of regularization limiting the number of retrieval parameters and the inversion stability. Both Hasekamp et al. [2011]

and Dubovik et al. [2011] present optimal estimation type approaches that retrieve a full set of aerosol parameters using POLDER intensity and polarization measurements. Similar to Hasekamp and Landgraf [2005], Hasekamp et al. [2011] use an a priori constraint and Phillips-Tikhonov regularization. The algorithm of Dubovik et al. [2011] uses the principals of statistical estimation in a generalized multi-term least squares formulation that allows for an a priori constraint and unites the advantages of many of the common inversion approaches such as Phillips-Tikhonov-Twomey inversion, Kalman filter, Newton-Gauss iteration, and Levenberg-Marquardt iteration. The retrieval algorithm presented in this paper is of the optimal estimation type and uses an a priori constraint as well as Levenberg-Marquardt regularization.

The structure of the paper is as follows: Section 6.2 describes the data used including the MODIS and TANSO-FTS measurements and the AERONET aerosol retrieval used for validation. In section 6.3 we describe our MODIS/TANSO-FTS/AERONET co-location strategy as well as the filters used to remove unwanted data. Section 6.4 describes our retrieval setup including methodology and the measurement, state, and a priori state vectors. In section 6.5 we present our retrieval result in the form of a validation against the AERONET retrieval. The presentation includes scatter plots, timeseries plots, spectral comparisons, and retrieval error histograms. Finally, in section 6.6 we summarize our findings and discuss some conclusions that may be taken from this study.

6.2 Data

6.2.1 Retrieval measurements

For this study we use data from two satellite instruments: the Moderate Resolution Imaging Spectroradiometer (MODIS) [Salomonson et al., 1989] and the Thermal And Near infrared Sensor for carbon Observations - Fourier Transform Spectrometer (TANSO-FTS) instrument aboard the Greenhouse gases Observing SATellite (GOSAT) [Kuze et al., 2009].

MODIS instruments reside aboard both the Terra (launched May 2002) and Aqua (launched December 1999) satellites, each of which fly at a 705 km altitude, in sun-synchronous orbits at a 98° inclination, with 10:30 a.m. (descending) and 1:30 p.m. (ascending) nodal crossing times, respectively. With a cross track swath of 2330 km each instrument provides global coverage every 1–2 days. MODIS has 36 bands from 0.41 to 15 μm at 250 m (2 bands), 500 m (5 bands), and

Table 6.1: The MODIS bands used in our retrieval along with their, center wavelengths (nm), bandwidth (nm), SNR, and pixel size (m). (Reproduced from Part I.)

Band	Center wavelength (nm)	Bandwidth (nm)	SNR	Pixel Size (m)
1	645	620 - 670	128	250
2	858	841 - 876	201	250
3	469	459 - 479	243	500
4	555	545 - 565	228	500
5	1240	1230 - 1250	74	500
6	1640	1628 - 1652	275	500
7	2130	2105 - 2155	110	500

Table 6.2: The GOSAT TANSO-FTS bands used in our retrieval along with their name, wavelength range (cm^{-1} and μm), and number of channels. (Reproduced from Part I.)

		Spectral range		
	Name	cm^{-1}	μm	# of channels
Band 1	O_2-A	12950–13190	0.758–0.772	1203
Band 2	Weak CO_2	6166–6286	1.59–1.62	601
Band 3	Strong CO_2	4810–4897	2.04–2.08	436

1 km (29 bands) spatial resolutions. For this study, we will use 7 of the 36 bands, presented in table 6.1: 0.645 and 0.858 μm (250 m) and 0.469, 0.555, 1.24, 1.64 (not for Aqua), and 2.13 μm (500 m). In addition to the MODIS measurement data product, we also make use of the land/sea mask available in the MODIS geolocation product and the operational MODIS aerosol retrieval product [Kaufman et al., 1997, Remer et al., 2005, Levy et al., 2007].

The TANSO-FTS instrument resides aboard GOSAT (launched January 2009) with a 666 km altitude, sun-synchronous orbit at a 98° inclination, a 12:49 p.m. nodal crossing time, and a three-day ground track repeat cycle. TANSO-FTS has four hyperspectral resolution bands of which the 0.76-μm O_2 A-band, band one, and the 1.61- and 2.06-μm CO_2 bands, bands two and three, respectively, presented in table 6.2, will be used for this study. The instrument views a 10 km footprint (spatial resolution at nadir) in one of three different modes: nadir, looking straight down; target, where a single surface location is targeted at up to three viewing zenith angles; and sunglint mode, where a sunglint spot over the ocean is targeted to increase signal to noise ratio. For this study we use only the nadir mode.

MODIS data is readily available for almost the entire period of its operation aboard both Aqua and Terra. For this study we are limited by the data availability of GOSAT which at the time of this study was April 5, 2009 through Dec 5 2011. Therefore the time range for this study will be between these dates. Spatially we are restricting our retrieval to co-locations between MODIS, GOSAT, and our ground-based validation data AERONET which is discussed in the next section.

In addition to the measurement data, our retrieval also requires meteorological profiles of pressure, temperature, water vapor, and ozone contrition. This data is provided from ECMWF along with the GOSAT measurement data.

6.2.2 AERONET validation data

AERONET was started as a NASA EOS and expanded into a federation including many non-NASA institutions [Holben et al., 1998]. AERONET consists of over 100 permanent sites world wide (see figure 6.1) each operating in periods ranging from 1992 to the present. An important aspect of the AERONET network is that it uses identical fully automated instruments at each site. The instruments make two different measurements at 15 minute intervals: direct sun measurements and sky (diffuse scattering) measurements. Both measurements are made in several bands including the standard bands at 0.440, 0.670, 0.870, and 1.020 μm. The direct sun measurements are used to compute aerosol optical thickness (AOT) directly using the Beer-Lambert-Bouguer law. The sky measurements are made in the "almucantar" and in the "principle plane". The almucantar consists of a series of measurements taken at the zenith angle of the sun for a series of azimuth angles. The standard principal plane consists of series of zenith angles taken in the solar principle plane. The goal with these two sky measurements is to efficiently maximize the number of single scattering measurements taken for the aerosol retrieval inversions.

All instruments are routinely calibrated, with the radiometric precision assessed with a 2-m integrating sphere at least twice per year while the reference instruments are calibrated approximately monthly. In addition, the precision is assessed by examining the dark current values taken during sky radiance measurements and by using the variability of the measurements taken at the Mauna Loa Observatory to evaluate the sun channels. Typically, the uncertainty in AOT measurements from a newly calibrated instrument under cloud-free conditions is $< \pm 0.01$ while the uncertainty for the sky radiance measurements is $< \pm 5\%$.

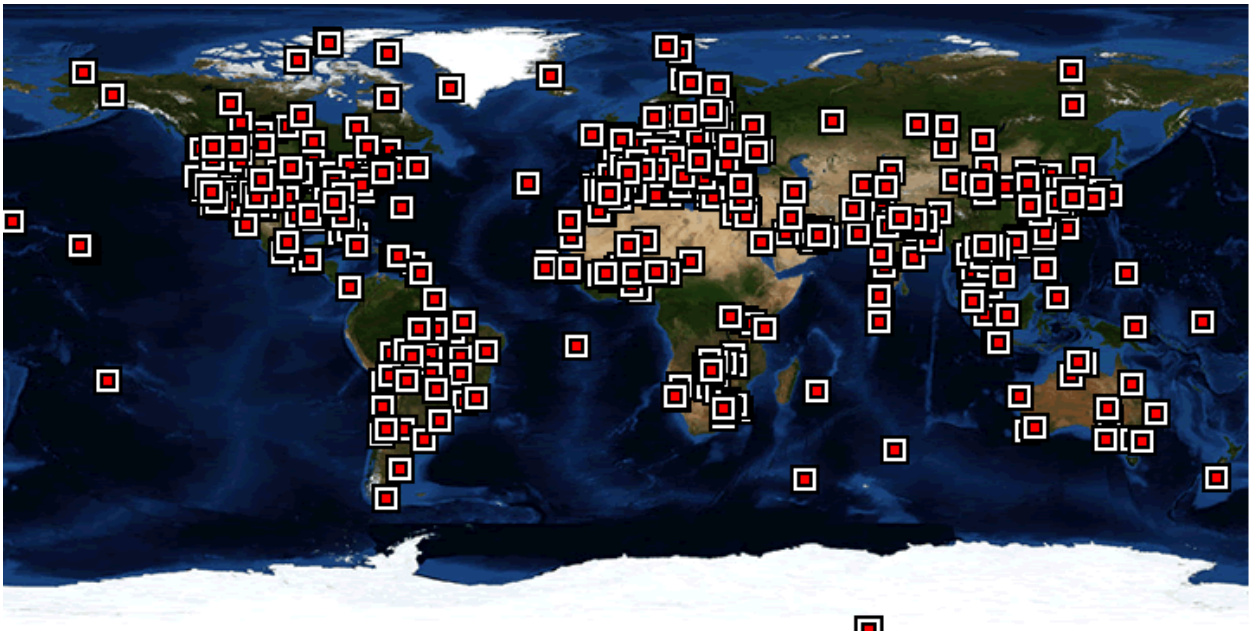

Figure 6.1: Geographic distribution of all the AERONET sites. (Obtained from the AERONET website: http://aeronet.gsfc.nasa.gov)

Using the spectral AOT and angular sky radiance measurements a flexible inversion algorithm is used for the retrieval of aerosol optical properties including size distribution and the complex index of refraction [Dubovik and King, 2000]. The accuracy of these retrieval parameters and in the derived single scattering albedo was assessed by Dubovik et al. [2000] in the presence of both random and systematic errors. It was found that the random error due to sources other than the measurements themselves (retrieval algorithm and forward model approximations, for example) were $< 1\%$, well below the random measurement error of $< 5\%$ indicated above. The systematic errors (or offset errors) analyzed included instrument miscalibration errors or calibration drifts, inaccuracies in the automated pointing mechanism ($< 0.05^\circ$ for a well tuned instrument and 0.25° for a degraded or improperly aligned instrument), and assumptions made about ground reflectance. The overall results of the inversion accuracy assessment in the presence of systematic errors is present in table 6.3. Since the retrieval uncertainties due to systematic errors dominate over that due to random errors the uncertainties presented in table 6.3 should be considered the overall inversion uncertainties.

AERONET measurements are distributed at levels 1.0 (raw), 1.5 (cloud screened), and 2.0 (quality assured). The raw level 1.0 data is not screened for clouds, may not have the final

Table 6.3: Errors in the size distribution, complex index of refraction, and single scattering albedo of the AERONET inversion algorithm. (Reproduced from Table 4 of Dubovik et al. [2000].)

Parameter	Range	Water-soluble	Dust	Biomass burning
$dV/(d\ln r)$ (%)	$r \leq 0.1$ μm	15	35	25
	$r > 0.1$ μm	15–100	35–100	25–100
	$r \geq 7.0$ μm	15	35	25
$m_r(\lambda)$	$\tau_a(440) \leq 0.2$	0.05		
	$\tau_a(440) > 0.2$	0.025		
	$\tau_a(440) \geq 0.5$		0.4	0.4
$m_i(\lambda)$ (%)	$\tau_a(440) \leq 0.2$	80–100		
	$\tau_a(440) > 0.2$	50		
	$\tau_a(440) \geq 0.5$		50	30
$\omega_a(\lambda)$	$\tau_a(440) \leq 0.2$	0.05–0.07		
	$\tau_a(440) > 0.2$	0.03		
	$\tau_a(440) \geq 0.5$		0.03	0.03

calibration applied, and is not quality assured. The cloud screened level 1.5 data may not have the final calibration applied, and is not quality assured. The quality assured level 2.0 data has the final calibration applied and is manually inspected. The cloud screening method used is based on temporal variability of the AOT measurements and is presented, along with the quality control algorithms, in more detail in Smirnov et al. [2000]. The inversion data is distributed at either level 1.5 or level 2.0. The level 1.5 inversions are determined with level 1.5 measurements or level 2.0 if available. The level 2.0 inversions are additionally screened to include only cases with a large number and range of scattering angles and minimal sky radiance errors. Due to the limited number of inversions available in the level 2.0 products we chose to use the level 1.5 products and the corresponding level 1.5 AOT measurements for our validation study.

6.3 Co-location and filtering

Our retrieval methodology requires co-located MODIS and GOSAT observations while for comparisons with AERONET we must co-locate these observations with AERONET sites as well. There are several aspects to consider here including spatial and temporal differences that must be constrained in order to minimize systematic errors from viewing different surface and/or atmospheric conditions. Observations from different sensors must have field-of-views (FOVs) with centers that are close enough with similar surface characteristics so as not to introduce biases in

the retrieved properties. The size of each sensor's FOV must also be accounted for. Even if two sensors with significantly different spatial resolutions have FOVs centered at the same place over a heterogeneous surface the high resolution sensor may be viewing a portion of the surface with an extreme surface reflectance while the low resolution sensor may be viewing an average. Atmospheric properties, especially those of aerosols and clouds, also vary on scales small enough to consider here. To complicate the process further, the atmosphere is constantly changing, so that even with spatially perfectly coincident observations the difference in acquisition time must be limited so each observation views similar conditions.

Since AERONET observations have fixed locations the goal is to find for each site cases when both MODIS and GOSAT observations are both within a certain distance from an AERONET site and when the MODIS and GOSAT observations are acquired within a certain period of time from each other. The two primary thresholds we have chosen here are a maximum 5 km difference between an observation center and the AERONET site and a maximum 30 min difference between acquisition times. MODIS, with a swath width of 2330 km, has complete daytime global coverage in 1-2 days, and therefore views solar reflectance for each AERONET location at least every other day. The limiting factor here are the nadir viewing only GOSAT observations. Figure 6.2 shows a co-location case with a 20×20 km block of MODIS pixels over an AERONET site (the solid red circle) and a GOSAT FOV (colored in green) at a maximum distance from the AERONET site for co-location. All the MODIS pixels within 5 km of the AERONET site (colored in blue) are averaged to produce a single co-located observation. Although in this case the measurements view a significantly large portion of surface independently, this case is actually the "worst case" and is illustrated to show our compromise between obtaining better co-locations and obtaining more co-locations.

Once co-located, observations are subject to two primary filters. First, even though the retrieval presented in this paper is sufficiently general enough to be applied to observations over land or ocean this particular study focuses on retrieval over land. As such, we filter out all co-locations that contain ocean within our 5 km threshold around the AERONET site. Since AERONET sites are land-based the majority of the co-locations pass this filter although coastal sites and sites on small islands will be filtered out.

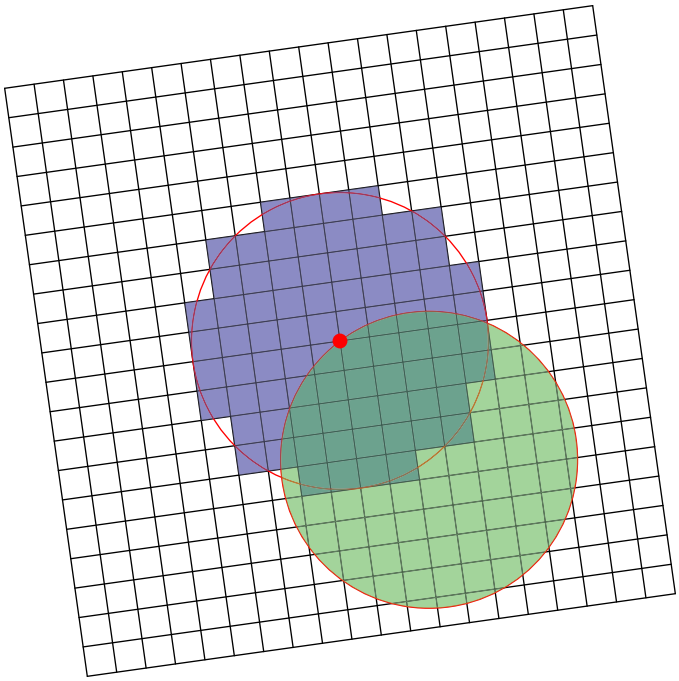

Figure 6.2: Schematic depicting the spatial aspects of our co-location strategy. The grid represents MODIS imagery with each cell a 1 km MODIS pixel. The red dot is the AERONET site, the green circle is an TANSO-FTS footprint at a maximum allowable distance from the AERONET site, and the purple cells represent the MODIS pixels that are averaged to make the MODIS measurements.

Cloud filtering is an important part of any aerosol retrieval system. The presence of clouds can significantly bias retrieval results and therefore observations with clouds must be filtered out. Both the MODIS and GOSAT data products have corresponding cloud mask products available but both are inappropriate for our purposes. On the one hand, the MODIS cloud mask [Ackerman et al., 1998] uses a combination of reflectance in the visible bands and brightness temperature in the IR bands to identify clouds. Unfortunately, the visible tests mistake thick aerosols layers as cloudy while relaying on the IR bands only allows low altitude warm clouds to go unmasked [Remer et al., 2005]. On the other hand, the GOSAT cloud mask [Taylor et al., 2012] is focused on masking for clouds and thick aerosols, both of which are undesirable for GOSAT's primary application of gas retrievals. Therefore, using the GOSAT cloud mask would result in our retrieval missing cases with thick aerosols layers.

For our retrieval we chose to use a cloud masking strategy similar to that use for the official MODIS aerosol product [Martins et al., 2002]. Two MODIS bands are used, the 0.47 and 1.38 μm reflectances, and for each channel two threshold tests are performed, a spatial variability test and

a reflectance test. For the 0.47 μm reflectances the tests are performed on the 500 m data while for the 1.38 μm reflectances the tests are performed on the 1 km data. The spatial variability test uses the standard deviation for 3×3 blocks of pixels. For the 0.47 μm reflectances if the standard deviation is greater than 0.0025 all 9 pixels are flagged as cloudy. For the 1.38 μm reflectances the standard deviation threshold is 0.003. The reflectance test uses the absolute value of reflectance on a pixel by pixel basis. For the 0.47 μm reflectances if the reflectance is greater than 0.4 the pixel is flagged as cloudy. For the 1.38 μm reflectances the reflectance threshold is 0.025.

Overall, we believe that our co-location and filtering procedure is "strict". 5 km is a small threshold radius in comparison to other Satellite/AERONET co-location projects including the Multi-sensor Aerosol Products Sampling System (MAPSS) [Petrenko et al., 2012] which uses a radius of 25 km. Part of our choice is dictated by the fact that a with GOSAT only a single FOV will fall close to the AERONET site and therefore averaging of multiple GOSAT observations is not possible. Considering aerosols alone we could likely increase our temporal threshold from 30 min. Unfortunately, cloud properties can vary at time scales much less than aerosols and since our cloud mask is from the MODIS observations we believe that 30 min is conservative in most cases for the MODIS cloud masking to be representative for the co-location overall.

The steps of our co-location and filtering strategy are:

1. For each GOSAT observation check if its center is within 5 km of a AERONET site otherwise loop to the next GOSAT observation.

2. For GOSAT observations from step 1 check for a MODIS overpass in which the AERONET site is at least 5 km from the edge and the difference between the acquisition times for the GOSAT observation and the MODIS pixel closest to the AERONET site is no more that 30 min. If no MODIS overpass is found meeting these requirements then loop back to 1.

3. Inspect the MODIS land/sea mask for all the pixels within 5 km of the AERONET site. If any of the pixels are identified as "sea" loop back to 1.

4. Run the cloud screening algorithm on all the MODIS pixels within a 5 km radius of the AERONET site. If any of the pixels are found to be cloudy loop back to 1.

5. Average all MODIS pixels within a 5 km radius of the AERONET site. This includes acquisition time, viewing zenith and azimuth angles, and reflectances in the seven bands used for our retrieval. It is these averages that are used in the retrieval as the MODIS measurements.

6. Linear interpolate the AERONET data to a time equal to the mean acquisition time of the GOSAT and MODIS observations. It is the interpolated AERONET data that is used for validation.

The results of our co-location filtering procedure ran for the period from April 1, 2009 through Dec 5 2011 is presented in table 6.4 by AERONET sites that have at least 10 successfully co-located and filtered instances. Listed for each site is the typical aerosol type encountered at the site, the latitude and longitude of the site, the number of successfully co-located and filtered instances associated with the site, and the number of MODIS operational retrievals associated with the site. The aerosol type associated with each site, determined by a survey of select AERONET related literature [García et al., 2008, 2011, Giles et al., 2012], is in some cases well representative but in other case is a rough estimate. This is particularly the case for the "mixed" aerosol type. The number of MODIS operational retrievals associated with each site is relevant for comparisons to our retrieval as the MODIS operational retrieval is performed for a dark surface only (2.13 μm reflectance less that 0.25) whereas our retrieval is performed for all surface conditions. It is apparent from the co-location results that the MODIS dark 2.13 μm reflectance requirement is not consistent with site indicating a significant change in surface type with season or with distance within our co-location requirements.

Table 6.4: The AERONET sites for which co-locations have been found along with the estimate of the predominate aerosol type at that site, the latitude and longitude of the site, the number of co-locations (count), and the number of co-locations with an MODIS operational retrieval.

Name	Type	Latitude	Longitude	Count	MODIS AOT count
Birdsville	desert dust	-25.90	139.35	74	6
Gual_Pahari	urban-industrial	28.43	77.15	52	33
New_Delhi	mixed	28.63	77.17	17	12
Kanpur	mixed	26.51	80.23	113	73
IFT-Leipzig	urban-industrial	51.35	12.44	57	25
Ersa	urban-industrial	43.00	9.36	31	24
La_Parguera	biomass burning	17.97	-67.05	17	11

Table 6.4: (continued)

Name	Type	Latitude	Longitude	Count	MODIS AOT count
Jaipur	mixed	26.91	75.81	28	12
Wits_University	urban-industrial	-26.19	28.03	22	11
Oostende	urban-industrial	51.23	2.92	43	31
Ispra	urban-industrial	45.80	8.63	76	49
Songkhla_Met_Sta	biomass burning	7.18	100.61	19	13
Tomsk	biomass burning	56.48	85.05	11	4
IER_Cinzana	mixed	13.28	-5.93	81	19
Kuwait_University	desert dust	29.32	47.97	88	7
Bonanza_Creek	biomass burning	64.74	-148.32	73	14
Railroad_Valley	mixed	38.50	-115.96	116	28
Chen-Kung_Univ	urban-industrial	23.00	120.22	90	57
Thessaloniki	urban-industrial	40.63	22.96	61	37
Camaguey	urban-industrial	21.42	-77.85	66	37
Kelowna	mixed	49.95	-119.37	36	13
Karachi	desert dust	24.87	67.03	81	50
DMN_Maine_Soroa	mixed	13.22	12.02	82	7
Zinder_Airport	mixed	13.78	8.99	67	0
Saturn_Island	mixed	48.78	-123.13	40	20
Osaka	urban-industrial	34.65	135.59	120	46
Nainital	mixed	29.36	79.46	18	18
Barrow	biomass burning	71.31	-156.66	36	2
EPA-NCU	urban-industrial	24.97	121.19	26	19
Moscow_MSU_MO	urban-industrial	55.70	37.51	92	37
Cart_Site	mixed	36.61	-97.49	154	18
Darwin	biomass burning	-12.42	130.89	45	34
Laegeren	urban-industrial	47.48	8.35	29	22
Campo_Grande_SONDA	biomass burning	-20.44	-54.54	26	22
Sao_Martinho_SONDA	biomass burning	-29.44	-53.08	22	18
London-UCL-UAO	urban-industrial	51.52	-0.13	30	11
OHP_OBSERVATOIRE	urban-industrial	43.94	5.71	32	21
Singapore	urban-industrial	1.30	103.78	58	15
Mexico_City	urban-industrial	19.33	-99.18	22	9
Halifax	urban-industrial	44.64	-63.59	41	30
Seysses	urban-industrial	43.50	1.26	14	10
Hong_Kong_PolyU	urban-industrial	22.30	114.18	35	18
Key_Biscayne	urban-industrial	25.73	-80.16	42	14
SACOL	mixed	35.95	104.14	33	11
Munich_University	urban-industrial	48.15	11.57	48	21
ATHENS-NOA	urban-industrial	37.99	23.77	73	41
Creteil	urban-industrial	48.79	2.44	18	5
Paris	urban-industrial	48.87	2.33	68	27
CCNY	urban-industrial	40.82	-73.95	49	29
Univ_of_Houston	urban-industrial	29.72	-95.34	47	11
Canberra	mixed	-35.27	149.11	68	48
Mezaira	desert dust	23.14	53.78	52	0
Banizoumbou	mixed	13.54	2.67	79	0
Silpakorn_Univ	mixed	13.82	100.04	59	52
Kelowna_UAS	mixed	49.94	-119.40	29	8
Ubon_Ratchathani	biomass burning	15.25	104.87	24	14
Kyiv	urban-industrial	50.36	30.50	53	23

Table 6.4: (continued)

Name	Type	Latitude	Longitude	Count	MODIS AOT count
Dongsha_Island	urban-industrial	20.71	116.72	18	10
Beijing	urban-industrial	39.98	116.38	99	33
Manila_Observatory	biomass burning	14.63	121.08	35	23
Lahore	mixed	31.54	74.33	56	51
Evora	urban-industrial	38.57	-7.91	17	9
Nes_Ziona	mixed	31.92	34.79	34	27
Palaiseau	urban-industrial	48.70	2.21	64	30
IASBS	mixed	36.70	48.51	23	17
Appledore_Island	urban-industrial	42.99	-70.61	30	26
CEILAP-BA	mixed	-34.57	-58.50	51	30
NCU_Taiwan	urban-industrial	24.97	121.19	22	10
Rome_Tor_Vergata	urban-industrial	41.84	12.65	61	52
Fort_McMurray	mixed	56.75	-111.48	57	26
Elandsfontein	mixed	-26.25	29.42	33	23
Zvenigorod	urban-industrial	55.70	36.77	15	6
El_Segundo	urban-industrial	33.91	-118.38	43	36
BONDVILLE	mixed	40.05	-88.37	11	5
CalTech	urban-industrial	34.14	-118.13	42	30
Sao_Paulo	biomass burning	-23.56	-46.73	13	7
Univ_of_Lethbridge	mixed	49.68	-112.87	37	12
Alta_Floresta	biomass burning	-9.87	-56.10	18	10
SAGRES	urban-industrial	37.05	-8.87	16	16
Granada	urban-industrial	37.16	-3.60	37	28
Yekaterinburg	biomass burning	57.04	59.55	21	15
Cabo_da_Roca	urban-industrial	38.78	-9.50	20	15
Baengnyeong	urban-industrial	37.97	124.63	16	12
Bratts_Lake	mixed	50.28	-104.70	14	10
ETNA	mixed	37.61	15.02	59	53
FORTH_CRETE	mixed	35.33	25.28	30	27
Eilat	desert dust	29.50	34.92	22	0
Urban-industrial				1895	1026
Biomass burning				1425	620
Desert dust				360	187
Mixed				317	63
Total				3997	1896

6.4 Retrieval setup

6.4.1 Methodology

Our retrieval algorithm is based on the optimal estimation approach in which the best match between simulated measurements computed with a forward model and real measurements is obtained

by optimizing the forward model inputs [Rodgers, 2004]. The forward model inputs that are optimized are the n elements of the state vector $\mathbf{x}$ while the measurements are the m elements of vector $\mathbf{y}$. The relationship between $\mathbf{x}$ and $\mathbf{y}$ based on the forward model may be written as

$$\mathbf{y} = \mathbf{F}(\mathbf{x}, \mathbf{b}) + \epsilon, \tag{6.1}$$

where $\mathbf{F}$ is the forward model; $\mathbf{b}$ is the set of all other assumed model parameters not in the state vector $\mathbf{x}$ such as meteorological conditions, spectroscopic parameters, solar and viewing geometry, etc.; and ϵ represents the measurement and forward model error.

The optimal estimation approach we have employed uses the forward model to minimize the cost function

$$\chi^2 = [\mathbf{F}(\mathbf{x}) - \mathbf{y}]^T \mathbf{S}_\epsilon^{-1} [\mathbf{F}(\mathbf{x}) - \mathbf{y}] + (\mathbf{x} - \mathbf{x}_a)^T \mathbf{S}_a^{-1} (\mathbf{x} - \mathbf{x}_a) \tag{6.2}$$

to obtain the retrieved state vector $\hat{\mathbf{x}}$, where $\mathbf{S}_\epsilon$ is the measurement and forward model error covariance matrix and $\mathbf{x}_a$ and $\mathbf{S}_a$ are the a priori state vector, representing any a priori knowledge of the state vector to be retrieved, and the corresponding error covariance matrix, respectively. From the equation we can see that the cost function is a combination of the deviations between the measurements and the forward model and the retrieved state vector and the a priori state vector, each weighted by its associated covariance matrix.

Due to the non-linear nature of our inverse problem an iterative solution is required for which a Gauss-Newton method based on our cost function is used:

$$\mathbf{x}_{i+1} = \mathbf{x}_i + \left[\mathbf{S}_a^{-1} + \mathbf{K}_i^T \mathbf{S}_\epsilon^{-1} \mathbf{K}_i\right]^{-1} \left\{\mathbf{K}_i^T \mathbf{S}_\epsilon^{-1} [\mathbf{y} - \mathbf{F}(\mathbf{x}_i)] - \mathbf{S}_a^{-1} [\mathbf{x}_i - \mathbf{x}_a]\right\}, \tag{6.3}$$

where $\mathbf{K}$ $(m \times n)$, referred to as the Jacobian, contains derivatives of the forward model $\mathbf{F}$ with respect to the state vector $\mathbf{x}$ elements:

$$K_{ij} = \frac{\partial F_i(\mathbf{x})}{\partial x_j}. \tag{6.4}$$

For this iteration it is typical to start with $\mathbf{x}_0 = \mathbf{x}_a$.

In general, the measurements used for our retrieval do not contain enough information to retrieve all the parameters included in the state vector and thus the inverse problem is ill-posed. In other words, there are many different combinations of the state vector parameters that will fit the measurements equally as well within the instrument noise constraints. Regardless, it is beneficial to include all the parameters of interest in the state vector in order to maximize the use of the available information, where information that is lacking will be taken from the a priori information. In other words, the a priori is an estimate of what cannot be retrieved from the state vector. Unfortunately, solving the ill-posed problem will be overwhelmed by retrieval noise and must be stabilized so that convergence can be obtained in an efficient manor. Several regularization methods exist for this purpose. For our retrieval we use a Levenberg-Marquardt method [Fletcher, 1987], where a side constraint is introduced into the minimization procedure now given by

$$\mathbf{x}_{i+1} = \mathbf{x}_i + \left[\mathbf{S}_a^{-1} + \mathbf{K}_i^T \mathbf{S}_\epsilon^{-1} \mathbf{K}_i + \gamma \mathbf{D}\right]^{-1} \left\{\mathbf{K}_i^T \mathbf{S}_\epsilon^{-1} \left[\mathbf{y} - \mathbf{F}(\mathbf{x}_i)\right] - \mathbf{S}_a^{-1} \left[\mathbf{x}_i - \mathbf{x}_a\right]\right\}, \tag{6.5}$$

where γ is referred to as the Levenberg-Marquardt parameter and $\mathbf{D}$ is a scaling matrix. In our case we take the simplest approach for choosing $\mathbf{D}$ as suggested by Rodgers [2004] and set $\mathbf{D} = \mathbf{S}_a^{-1}$. In this case our minimization procedure reduces to

$$\mathbf{x}_{i+1} = \mathbf{x}_i + \left[(1+\gamma)\mathbf{S}_a^{-1} + \mathbf{K}_i^T \mathbf{S}_\epsilon^{-1} \mathbf{K}_i\right]^{-1} \left\{\mathbf{K}_i^T \mathbf{S}_\epsilon^{-1} \left[\mathbf{y} - \mathbf{F}(\mathbf{x}_i)\right] - \mathbf{S}_a^{-1} \left[\mathbf{x}_i - \mathbf{x}_a\right]\right\}. \tag{6.6}$$

Our retrieval algorithm starts with $\gamma = 10.0$ and $\mathbf{x}_0 = \mathbf{x}_a$. After each iteration, convergence is tested for with the following criterion

$$\left[\mathbf{x}_{i+1} - \mathbf{x}_i\right]^T \hat{\mathbf{S}}_i^{-1} \left[\mathbf{x}_{i+1} - \mathbf{x}_{i-1}\right] \ll n, \tag{6.7}$$

where $\hat{\mathbf{S}}_i$ is the covariance matrix of the current state i given by

$$\hat{\mathbf{S}}_i = (\mathbf{K}_i^T \mathbf{S}_\epsilon^{-1} \mathbf{K}_i + \mathbf{S}_a^{-1})^{-1}, \tag{6.8}$$

and n is the number of state vector elements. After each iteration, if convergence has not been obtained, γ must be updated. This is done based on the ratio R of the change in χ^2 computed

properly (equation 6.2) to the change in the cost function computed with the linear approximation to the forward model:

$$R = \frac{\chi^2 - \chi^2_{i+1}}{\chi^2 - \chi^2_{i+1,L}}, \tag{6.9}$$

where $\chi^2_{i+1,L}$ is given by

$$\chi^2_{i+1,L} = \left[\mathbf{K}_i \mathbf{x}_{i+1} - \mathbf{y}\right]^T \mathbf{S}_\epsilon^{-1} \left[\mathbf{K}_i \mathbf{x}_{i+1} - \mathbf{y}\right] + (\mathbf{x}_{i+1} - \mathbf{x}_a)^T \mathbf{S}_a^{-1} (\mathbf{x}_{i+1} - \mathbf{x}_a). \tag{6.10}$$

If $R > 0.75$, γ is reduced by a factor of two. If $R < 0.25$, γ is increased by a factor of two. Otherwise, no change is made to γ. Once convergence has been obtained the information content quantities described in Part I are computed including the final error covariance matrix $\hat{\mathbf{S}}$.

6.4.2 Measurement vectors and errors

We now discuss the retrieval measurement vector $\mathbf{y}$. We use the same notation as described in Part I, and perform the retrieval using five of the measurement vectors analyzed in that paper:

$$\mathbf{y}_{\mathrm{M}}, \tag{6.11}$$

$$\left[\mathbf{y}_{\mathrm{M}}, \mathbf{y}_{\mathrm{TF},1,R,\mathrm{N}}\right], \tag{6.12}$$

$$\left[\mathbf{y}_{\mathrm{M}}, \mathbf{y}_{\mathrm{TF},1\text{–}3,R,\mathrm{N}}\right], \tag{6.13}$$

$$\left[\mathbf{y}_{\mathrm{M}}, \mathbf{y}_{\mathrm{TF},1,R+P,\mathrm{N}}\right], \tag{6.14}$$

$$\left[\mathbf{y}_{\mathrm{M}}, \mathbf{y}_{\mathrm{TF},1\text{–}3,R+P,\mathrm{N}}\right], \tag{6.15}$$

where $\mathbf{y}_{\mathrm{M}}$ contains the seven MODIS reflectances and the other four vectors contain the seven MODIS reflectances and TANSO-FTS measurements (TF) of band one reflectances $(1, R)$, total reflectances from all three bands $(1\text{–}3, R)$, band one total reflectances and polarized reflectances $(1, R + P)$, and total reflectances and polarized reflectances from all three bands $(1\text{–}3, R + P)$, respectively. As described in Part I in greater detail the definitions of total and polarized reflectances are

$$R = \frac{\pi I}{\mu_0 I_0} \tag{6.16}$$

and

$$P = \frac{\pi\sqrt{Q^2 + U^2}}{\mu_0 I_0}, \tag{6.17}$$

respectively, where I, Q, and U are the first three components of the stokes vector, respectively, as defined by Hovenier et al. [2004], μ_0 is the solar zenith angle, and I_0 is the solar irradiance at the top of the atmosphere (TOA).

In addition to the above measurement vectors, Part I also considered measurement vectors containing, instead of TANSO-FTS measurement made at nadir (N) in nadir mode, TANSO-FTS measurements made at multiple angles (M) in target mode. Since the TANSO-FTS measurements made in target mode are sparse and since we are already restricted to cases of coincident AERONET, MODIS, and TANSO-FTS observations, we elected to neglect target mode and therefore multiangle measurements in the current retrieval study. In addition, the purpose of the multiangle measurements for the GOSAT and OCO-2 missions is for validation proposes and as such these measurements are not likely to be made often and as a result are not appropriate for an operational aerosol retrieval.

The measurement and forward model error covariance matrix $\mathbf{S}_\epsilon$ is described in detail in Part I and we use the same method to build the matrix as in that paper. Briefly, the matrix contains errors in the measurements in $\mathbf{y}$ and errors in the forward model $\mathbf{F}(\mathbf{x}, \mathbf{b})$ due primarily to errors in the vector of assumed model parameters $\mathbf{b}$. The instruments are assumed to be well calibrated and therefore free of bias error while the measurement noise for each instrument is obtained from the appropriate noise model integrated in the forward model as described in Part I for both MODIS and TANSO-FTS. The errors due to the parameters in $\mathbf{b}$ are constructed by running the forward model over a range of base states and using the linearized outputs along with the errors in $\mathbf{b}$ to construct the forward model output error.

6.4.3 State vector and errors

The state vector $\mathbf{x}$ is thoroughly described and justified in Part I and therefore we will only briefly describe it here. The state vector $\mathbf{x}$ may be written as

$$\begin{aligned}\mathbf{x}^T = [&A_1 \dots A_n, P, \\ &N_{0,f}, r_{g,f}, \sigma_f, m_{r,f,1} \dots m_{r,f,n}, m_{i,f,1} \dots m_{i,f,n}, \\ &N_{0,c}, r_{g,c}, \sigma_c, m_{r,c,1} \dots m_{r,c,n}, m_{i,c,1} \dots m_{i,c,n}] ,\end{aligned} \tag{6.18}$$

where $A_1 \dots A_n$ are n fit parameters for spectrally dependent Lambertian surface albedo, P_{top} is the "effective" or "radiative" top pressure of the aerosol layer, $N_{0,i}$ is the number concentration (m^{-2}) for mode i, $r_{g,i}$ is the mean radius (μm) of a log-normal size distribution for mode i, σ_i is the variance of a log-normal size distribution for mode i, $m_{r,i,1} \dots m_{r,i,n}$ are n polynomial fit parameters for the real part of the spectrally dependent index of refraction for mode i, $m_{i,i,1} \dots m_{i,i,n}$ are n polynomial fit parameters for the spectrally dependent imaginary part of the index of refraction for mode i, and i is either f or c for the fine mode and coarse modes, respectively.

It is important to understand that, even though the measurements may not contain enough information to retrieve all the parameters accurately, they are all included in the state vector in order to maximize the use of the available information. As mentioned above, in a properly implemented optimal estimation retrieval any information that is lacking will be taken from the a priori. This is an important aspect as more traditional aerosol retrieval approaches differentiate between retrievable and non-retrievable parameters discretizing the retrieval space resulting in unused information.

The state vector parameters along with their corresponding a priori values of $\mathbf{x}_a$ and subsequently their corresponding a priori 1-sigma errors, the squares of which are the diagonal elements of $\mathbf{S}_a$, are given in table 6.5.

As described in Part I, inclusion of the surface albedo A in the state vector prevents the retrieval from being too constrained by an a priori estimate of A and it is shown that there is enough information when the TANSO-FTS measurements are included in the measurement vector to retrieve A along with the aerosol parameters. The aerosol-top pressure P_{top} is also included for similar reasons and should be considered not as a physical top to the retrieved aerosol layer but as a "effective" or "radiative" top pressure. Use of both these parameters should be limited to the

Table 6.5: The state vector parameters used in our retrieval, along with a brief description and the corresponding a priori values and a priori 1-sigma values. (Reproduced from Part I.)

Parameter	Description	A priori value	A priori 1-sigma
$A_1 \dots A_n$	n fit parameters for the wavelength dependent Lambertian surface albedo	from meas.	0.5
P_{top}	The "effective" top to the aerosol layer	700.0 hPa	50.0 hPa
$N_{0,f}$	Aerosol # concentration for the fine mode	$\tau_1(0.55) = 0.1$	5 × a priori
$r_{g,f}$	Mean radius of a log-normal size distribution for the fine mode	0.15 μm	0.1 μm
σ_f	Variance of a log-normal size distribution for the fine mode	0.4	0.1
$m_{r,f,1} \dots m_{r,f,n}$	n fit parameters for the wavelength dependent real part of the index of refraction for the fine mode	1.47 (flat)	0.14
$m_{i,f,1} \dots m_{i,f,n}$	n fit parameters for the wavelength dependent imaginary part of the index of refraction for the fine mode	0.002 (flat)	0.005
$N_{0,c}$	Aerosol # concentration for the coarse mode	$\tau_2(0.55) = 0.1$	5 × a priori
$r_{g,c}$	Mean radius of a log-normal size distribution for the coarse mode	0.8 μm	0.2 μm
σ_c	Variance of a log-normal size distribution for the coarse mode	0.6	0.3
$m_{r,c,1} \dots m_{r,c,n}$	n fit parameters for the wavelength dependent real part of the index of refraction for the coarse mode	1.47 (flat)	0.14
$m_{i,c,1} \dots m_{i,c,n}$	n fit parameters for the wavelength dependent imaginary part of the index of refraction for the coarse mode	0.002 (flat)	0.005

computation of the radiative effect of the retrieved aerosols as their radiative consistency with the retrieved aerosol parameters will manifest themselves in the radiative flux calculations.

Our validation source, AERONET, provides a slightly different set of parameters, to which we elect to derive comparable parameters from our parameters. In particular AERONET, does not provide number concentration $N_{0,i}$ but instead provides optical thicknesses $\tau_{a,i}(\lambda)$

$$\tau_{a,i}(\lambda) = N_{0,i} C_{e,i}(\lambda), \tag{6.19}$$

where $C_{e,i}(\lambda)$ and $C_{s,i}(\lambda)$ (μm) are the extinction and scattering cross sections derived from Mie scattering theory with the size distribution and index of refraction state vector parameters. It is also important to validate the total optical thickness $\tau_a(\lambda)$ given by

$$\tau_a(\lambda) = \tau_{a,f}(\lambda) + \tau_{a,c}(\lambda) \tag{6.20}$$

as this quantity is what is ultimately radiatively important and may be more accurately determined than the individual optical thicknesses for each mode. AERONET also provides the radiatively important derived quantity total single scattering albedo $\omega_a(\lambda)$ to which we compare a single scattering albedo derived from our results. As with the total optical thickness $\tau_a(\lambda)$ this is an important quantity to validate as it is a fundamental radiative transfer model input and is derived from the retrieval parameters so that its errors depend on a combination of the errors of the quantities from which it is derived. The modal single scattering albedo $\omega_{a,i}(\lambda)$ is given by

$$\omega_{a,i}(\lambda) = \frac{C_{s,i}(\lambda)}{C_{e,i}(\lambda)} \tag{6.21}$$

and the total single scattering albedo $\omega_a(\lambda)$ is given by

$$\omega_a(\lambda) = \frac{\omega_{a,f}(\lambda)\tau_{a,f}(\lambda) + \omega_{a,c}(\lambda)\tau_{a,c}(\lambda)}{\tau_a(\lambda)}. \tag{6.22}$$

Finally, since AERONET does not provide modal real and imaginary parts of the index of refraction but only values that are averages of both modes we must combine our retrieval for each mode into single average values. For this we use the combinations weighted by modal optical thickness given

by

$$m_{r,i}(\lambda) = \frac{m_{r,f}(\lambda)\tau_{a,f}(\lambda) + m_{r,c}(\lambda)\tau_{a,c}(\lambda)}{\tau_a(\lambda)} \tag{6.23}$$

and

$$m_{i,i}(\lambda) = \frac{m_{i,f}(\lambda)\tau_{a,f}(\lambda) + m_{i,c}(\lambda)\tau_{a,c}(\lambda)}{\tau_a(\lambda)}. \tag{6.24}$$

Of course, since an important aspect of our retrieval system is a self contained estimate of the retrieval error, we must also provide an estimate of the error in these derived quantities as well. For this we use the general formulation given by

$$\sigma(x_d) = \sqrt{\sum_{i=1}^{n}\sum_{j=1}^{n} \hat{S}_{i,j}\frac{\partial x_d}{\partial x_i}\frac{\partial x_d}{\partial x_j}}, \tag{6.25}$$

where x_d is the derived parameter and $\frac{\partial x_d}{\partial x_i}$ is the derivative of the derived parameter with respect to state vector parameter i obtained through chain rule combination of the derivatives from the forward model and linearization of equations 6.19 through 6.24. This formulation may be used for other radiatively important quantities derived from the retrieval quantities including the asymmetry parameter and scattering phase matrix, both derived from Mie theory.

6.5 Retrieval validation

In this section we present results of our retrieval compared to AERONET retrievals. This is first done with scatter plots for all the retrievals and then for retrievals grouped by the four land-based aerosol types described by Dubovik et al. [2002b]: mixed, urban industrial, biomass burning, and desert dust, for the retrieval quantities τ_a, $\tau_{a,f}$, $\tau_{a,c}$, $r_{g,f}$, $r_{g,c}$, σ_f, σ_c, m_r, m_i, and ω_a. Whereas we retrieve and report for aerosol loading the aerosol number concentration $N_{0,i}$ for each mode i, AERONET reports the corresponding optical thickness $\tau_{a,i}$. In addition, AERONET reports single values of the real and imaginary part of the index of refraction m_r and m_i whereas we report modal specific values $m_{r,i}$ and $m_{i,i}$. For validation purposes we convert our values to derived values of $\tau_{a,i}$ from $N_{0,i}$ and our other retrieval results and combine our indices of refraction weighted according to modal optical thickness as discussed in the previous section. In addition, the AERONET results for the modal mean size distribution radius are reported for a size distribution in volume r_V whereas

our results are for a size distribution in radius r_g. In this case, for our validation, we elect to convert the AERONET values to our corresponding value with

$$r_g = r_V \exp(-3\sigma^2). \tag{6.26}$$

Unless otherwise stated, results for spectrally dependent parameters are presented at 0.55 μm calculated for our retrieval from the retrieved polynomial fit parameters and interpolated for AERONET from corresponding retrieved values at 0.440 and 0.670.

We also present for the same parameters timeseries comparisons for a set of four AERONET sites: Kanpur (mixed aerosol), Beijing (urban industrial aerosol), Sao Paulo (biomass burning aerosol, and Kuwait University (desert dust aerosol) (section 6.5.2). Since calculations of the direct radiative effect of aerosols requires spectrally dependent aerosol parameters in a range of wavelengths we must also validate our retrieved polynomial fits (section 6.5.3). To do this we present for each spectral parameter comparisons between the AERONET values at 0.440, 0.670, 0.870, and 1.020 μm and corresponding values derived from our retrieved spectral fit parameters. Each of the three comparison types are presented for results using different measurement vectors as described in each of the corresponding sections. Finally, in order to validate our retrieval error estimate we present histograms of our error estimate with histograms of the actual error superimposed on the same plots (section 6.5.4). This is done for all the previously validated quantities and for all the sites together and for retrievals grouped by the four land-based aerosol types.

Mishchenko et al. [2004] presents the accuracy requirements of aerosol retrievals to determine their direct radiative effect. The values relevant to this study are presented in table 6.6. It is these requirements that we will use to judge the effectiveness of our retrieval. Although, there is one important caveat that must be discussed. Our validation is performed relative to AERONET measurements of τ_a and AERONET retrievals of all other parameters. The accuracy of the measurements of τ_a is $< \pm 0.01$, well below that of the accuracy requirements presented in table 6.6. Unfortunately, the accuracies of the AERONET retrievals, as shown in table 6.3 are not below that of the requirements in all cases. To this end, we can only hope to evaluate our results to that of the AERONET accuracies but for our presentation will assume the AERONET results are truth and gauge the accuracy of our retrieval relative to the requirements presented in table 6.6.

Table 6.6: Accuracy requirements for accurate determination of aerosol direct radiative effects [Mishchenko et al., 2004].

Parameter	Range	Accuracy	(%)
τ_a, $\tau_{a,f}$, $\tau_{a,c}$	0.0 – 5.0	0.04	10%
$r_{g,f}$, $r_{g,c}$	0.1 – 5.0	0.1 μm	10%
$\sigma_{g,f}$, $\sigma_{g,c}$	0.0 – 3.0	0.3	50%
$m_{r,f}$ $m_{r,c}$	1.3 – 1.7	0.02	-
$\omega_{a,f}$, $\omega_{a,c}$	0.0 – 1.0	0.03	-

In addition, we will also compare our results to results from two retrieval studies similar to ours — similar in that they use advanced measurements and optimal estimation to retrieve a relatively complete aerosol state vector and that they compare their results to the AERONET retrieval. The first is the study by Hasekamp et al. [2011] who used POLDER multispectral/multiangle/polarimetric measurements at 0.490 and 0.670 μm with an optimal estimation procedure using Phillips-Tikhonov regularization to retrieve, over ocean, in two modes, aerosol loading, effective radius, effective variance, and complex index of refraction; the height of the layer where the bulk of the aerosol is located, ocean pigment concentration, wind speed in two directions, and white cap fraction. Even though this retrieval study is over ocean it is still useful as a comparison if we keep the ocean surface in mind. Validation results from this study are presented for total optical thickness τ_a, single scattering albedo ω_a, and the real part of the index of refraction m_r and are summarized in table 6.7 as the mean of the deviations $\delta_i(x) = x_{\text{AERONET},i} - x_{\text{retrieval},i}$ identified as $\mu_\delta(x)$ (also called the mean bias), the standard deviation of the deviations identified as $\sigma_\delta(x)$, and the linear regression correlation coefficient identified as $r(x)$. The second study we compare with is that of Dubovik et al. [2011] who also used POLDER measurements but at all available wavelengths free of molecular absorption in a statistically optimized inversion scheme to retrieve, over land, the total volume concentration, the size distribution, fraction of the spherical particles, total real and imaginary parts of the index of refraction, mean height of the aerosol layer, and several surface BRDF parameters. They only performed a preliminary sample retrieval using two AERONET sites and reported a correlation coefficient for total optical thickness τ_a and a range of mean deviations for single scattering albedo ω_a which are given in table 6.7.

Table 6.7: Retrieval validation results presented by Hasekamp et al. [2011] and Dubovik et al. [2011]. The m_r values are sampled by AERONET site.

Study	Parameter	R(+P)	λ (μm)	μ_δ	σ_δ	r
Hasekamp et al. [2011]	τ_a	R	0.490	0.040	0.083	0.091
			0.670	0.023	0.053	0.093
		R+P	0.490	0.015	0.053	0.096
			0.670	0.013	0.038	0.097
	ω_a	R+P	0.670	0.010	0.036	
	m_r	P+P	0.670	0.01, 0.02, 0.06, 0.02, 0.04, 0.01	0.100, 0.098, 0.037, 0.045, 0.057, 0.076	
Dubovik et al. [2011]	τ_a	R+P	0.440			0.885
	ω_a	R+P	0.440	0.03–0.05 ($\tau_a > 0.5$)		

6.5.1 Scatter plots

In this section we present scatter plots of retrieval results for various retrieval parameters (y axis) plotted vs. the corresponding parameters from the AERONET retrieval (x axis). The parameters τ_a, $\tau_{a,f}$, $\tau_{a,c}$, σ_f, σ_c, $m_{r,f}$, $m_{r,c}$, $\omega_{a,f}$, and $\omega_{a,c}$ are plotted in linear space and the parameters $r_{g,f}$, $r_{g,c}$, $m_{i,f}$, and $m_{i,c}$ are plotted in log space. The scatter points are colored from blue to red for surface albedo from 0.0 to 0.25 (purple is 0.125). In addition to the scatter plot, several statistical parameters are calculated for the data including the mean of the deviations $\delta_i(x) = x_{\text{AERONET},i} - x_{\text{retrieval},i}$ identified as $\mu_\delta(x)$ (also called the mean bias), the standard deviation of the deviations identified as $\sigma_\delta(x)$, and the linear regression correlation coefficient identified as $r(x)$.

Results are shown for various measurement vectors. For τ_a we will show the case for MODIS only ($\mathbf{y}_\text{M}$) and for MODIS plus four different TANSO-FTS based vectors including band 1 total reflectance ($[\mathbf{y}_\text{M}, \mathbf{y}_{\text{TF},1,R,\text{N}}]$), all bands total reflectance ($[\mathbf{y}_\text{M}, \mathbf{y}_{\text{TF},1\text{–}3,R,\text{N}}]$), band 1 total and polarized reflectance($[\mathbf{y}_\text{M}, \mathbf{y}_{\text{TF},1,R+P,\text{N}}]$), and all bands total and polarized reflectance ($[\mathbf{y}_\text{M}, \mathbf{y}_{\text{TF},1\text{–}3,R+P,\text{N}}]$). For the remaining parameters we make the assumption that if all bands are available then all bands will be used. This narrows our possible TANSO-FTS measurement vectors to $\mathbf{y}_{\text{TF},1\text{–}3,R,\text{N}}$, a vector possible for GOSAT, OCO-2, or a similar instrument that only measures total reflectance, and $\mathbf{y}_{\text{TF},1\text{–}3,R+P,\text{N}}$, a vector possible for GOSAT or a similar instrument that measures both total and polarized reflectance. For $\tau_{a,f}$ and $\tau_{a,c}$ we present results for MODIS only and for MODIS

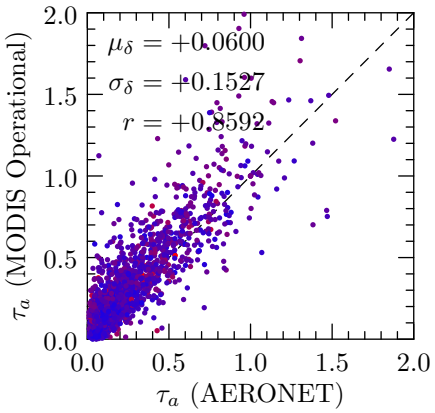

Figure 6.3: Scatter plot of retrieval results for aerosol optical thickness $\tau_a(0.55)$ for the MODIS operational retrieval vs. the AERONET retrieval for all the AERONET sites.

plus the two TANSO-FTS vectors mentioned above, $\mathbf{y}_{\mathrm{M}}$, $[\mathbf{y}_{\mathrm{M}}, \mathbf{y}_{\mathrm{TF},1\text{–}3,R,\mathrm{N}}]$, and $[\mathbf{y}_{\mathrm{M}}, \mathbf{y}_{\mathrm{TF},1\text{–}3,R+P,\mathrm{N}}]$, respectively. For the remaining parameters, results for MODIS only are not presented due to its limited information content and only results for $[\mathbf{y}_{\mathrm{M}}, \mathbf{y}_{\mathrm{TF},1\text{–}3,R,\mathrm{N}}]$, and $[\mathbf{y}_{\mathrm{M}}, \mathbf{y}_{\mathrm{TF},1\text{–}3,R+P,\mathrm{N}}]$ will be presented.

All sites

As a baseline we first compare retrieval results from the MODIS operational aerosol retrieval product [Levy et al., 2007]. The algorithm uses three bands (0.47, 0.66, and 2.13 μm) to retrieve over dark surfaces only (2.13 μm reflectance less that 0.25) three parameters, including the total optical thickness at 0.55 μm ($\tau_{a,0.55}$), the fraction of $\tau_{a,0.55}$ attributed to the fine model ($\eta_{0.55}$), and the surface reflectance at 2.13 μm ($\rho^s_{2.13}$). It finds the best match to precomputed radiative transfer calculations over a range of aerosol models, surface reflectances, and solar and viewing geometries. Figure 6.3 shows a scatter plot of the MODIS retrievals for $\tau_{a,0.55}$ vs. the AERONET measurements of $\tau_{a,0.55}$. The standard deviation of the deviations σ_δ is clearly not within the accuracy requirements given in table 6.6. A positive bias is also visible for the low optical thicknesses in which aerosol signal decreases. This result is consistent with the MODIS aerosol product validation presented by Remer et al. [2005]. Possible reasons for this bias include both instrument noise/calibration issues and/or incorrect surface characterization.

Figure 6.4 shows scatter plots for the total optical thickness τ_a from our retrieval for several different measurement vectors. For the MODIS only retrieval ($\mathbf{y}_{\mathrm{M}}$) the results have a smaller

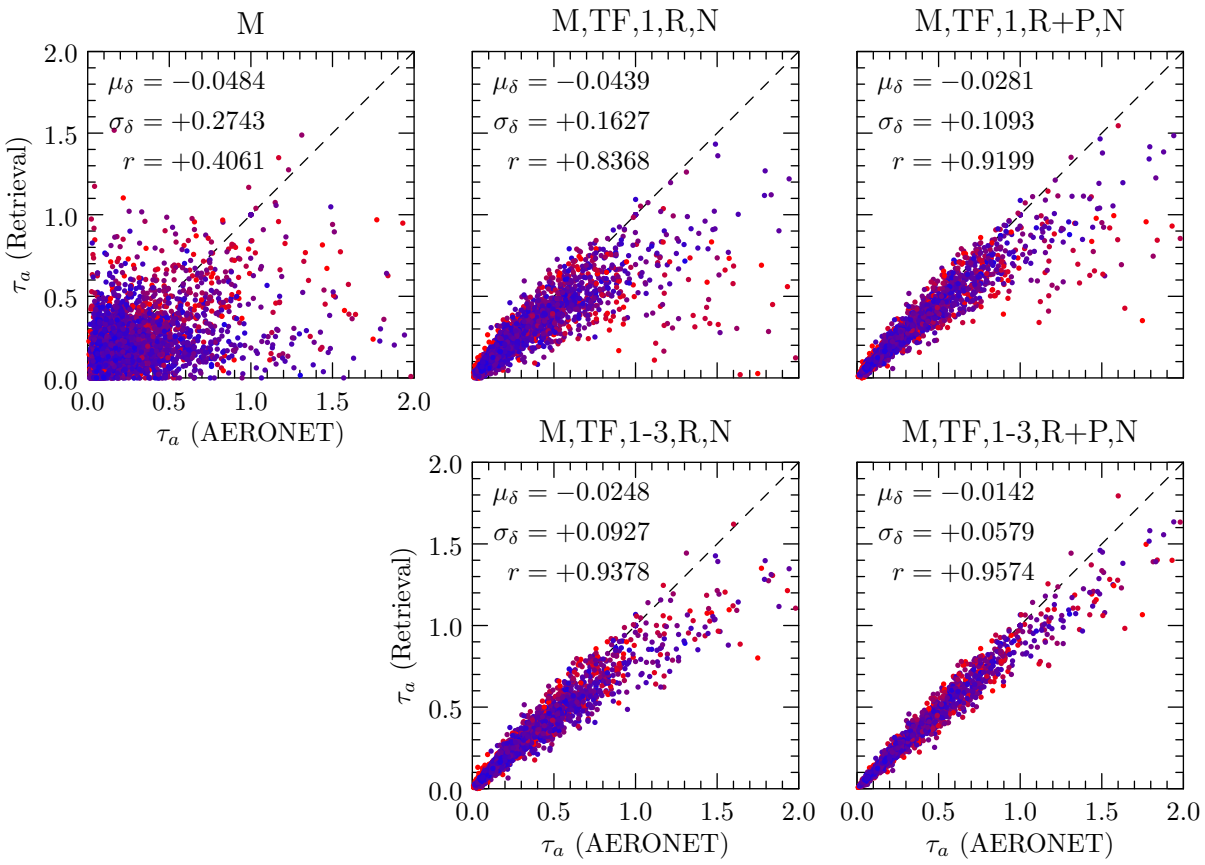

Figure 6.4: Scatter plots of results from all sites for aerosol optical thickness $\tau_a(0.55)$ for our retrieval vs. the AERONET retrieval.

mean bias μ_δ, a larger standard deviation of the deviations σ_δ, and a lower correlation coefficient r than that of the MODIS operational retrievals. The retrieval is similar to the MODIS operational retrieval in that it exhibits larger positive biases for lower optical thicknesses indicating similar issues related to lower relative aerosol signal. Although, there is also a negative bias for the larger optical thicknesses offsetting the positive bias at lower optical thicknesses resulting in a lower overall bias. This tilt in the scatter is a result of the retrievals tendency toward the a priori optical thickness of 0.1. It should be emphasized that the MODIS operational retrieval is performed for dark targets only and, as such, the statistics calculated from this subset of possible retrievals are expected to be better than that from our results computed from all possible retrievals. In addition, the MODIS operational retrieval has been tuned over many years to provide results that are as accurate as possible.

The τ_a scatter results for the measurement vectors that include the TANSO-FTS measurements show considerable improvement over the MODIS only results. For $[\mathbf{y}_{\mathrm{M}}, \mathbf{y}_{\mathrm{TF},1,R,\mathrm{N}}]$ μ_δ is under the accuracy requirement presented in table 6.6 and σ_δ is comparable to that of the MODIS operational retrieval. The significant improvement is in the scatter and in r indicating a significant reduction in individual biases caused by problems with surface/aerosol distinction in the MODIS only retrievals. As expected from the information content analysis given in Part I the retrieval results also improve when all the TANSO-FTS bands are used ($\mathbf{y}_{\mathrm{TF},1\text{–}3,R,\mathrm{N}}$) or when the polarized reflectance is used ($\mathbf{y}_{\mathrm{TF},1,R+P,\mathrm{N}}$), while the best results are obtained when both cases are true ($\mathbf{y}_{\mathrm{TF},1\text{–}3,R+P,\mathrm{N}}$). In the latter case $\sigma_\delta = 0.0579$ comes close to our accuracy requirement presented in table 6.6.

The reason for the improvement in the results using the TANSO-FTS measurements is discussed in detail in Part I. Briefly, it is increased sensitivity to τ_a relative to that of surface albedo A and single scattering albedo ω_a that improves the retrieval results. Indeed, it is the inability of the MODIS only measurements to distinguish bright surfaces from aerosols that restricts the MODIS operational retrieval to dark targets only, limiting the number of retrievals that can be made. Although the retrievals including TANSO-FTS measurements are significantly less affected by the surface reflectance, it is worth pointing out that the extreme points in the scatter have redder colors for larger surface albedos indicating that theses retrievals are still influenced by surface effects.

Compared to the results of Hasekamp et al. [2011] in table 6.7 our results for our most complex measurement scenario compare well with their results using intensity and polarization with a value for μ_δ between their corresponding values at 0.490 and 0.670, a value for σ_δ slightly larger than their corresponding value for 0.490 μm, and a value for r slightly smaller than their corresponding value for 0.490 μm. Since their results are for over ocean only and ours is over land these good comparisons highlight the unique ability of the hyperspectral measurements to separate the aerosol and surface signal. In addition, they only used measurements at 0.490 and 0.670 μm, whereas our retrieval uses a much broader spectral range.

In figure 6.5 we present scatter plots for $\tau_{a,f}$ and $\tau_{a,c}$ for measurement vectors $\mathbf{y}_{\mathrm{M}}$, $[\mathbf{y}_{\mathrm{M}}, \mathbf{y}_{\mathrm{TF},1\text{–}3,R,\mathrm{N}}]$, and $[\mathbf{y}_{\mathrm{M}}, \mathbf{y}_{\mathrm{TF},1\text{–}3,R+P,\mathrm{N}}]$. As with the total optical thickness τ_a there is significant scatter in the MODIS only results while the addition of the TANSO-FTS bands improves the results and the addition of the polarized reflectance improves the results even further. Overall, the statistics for the modal optical thicknesses are better than for the total optical thicknesses as

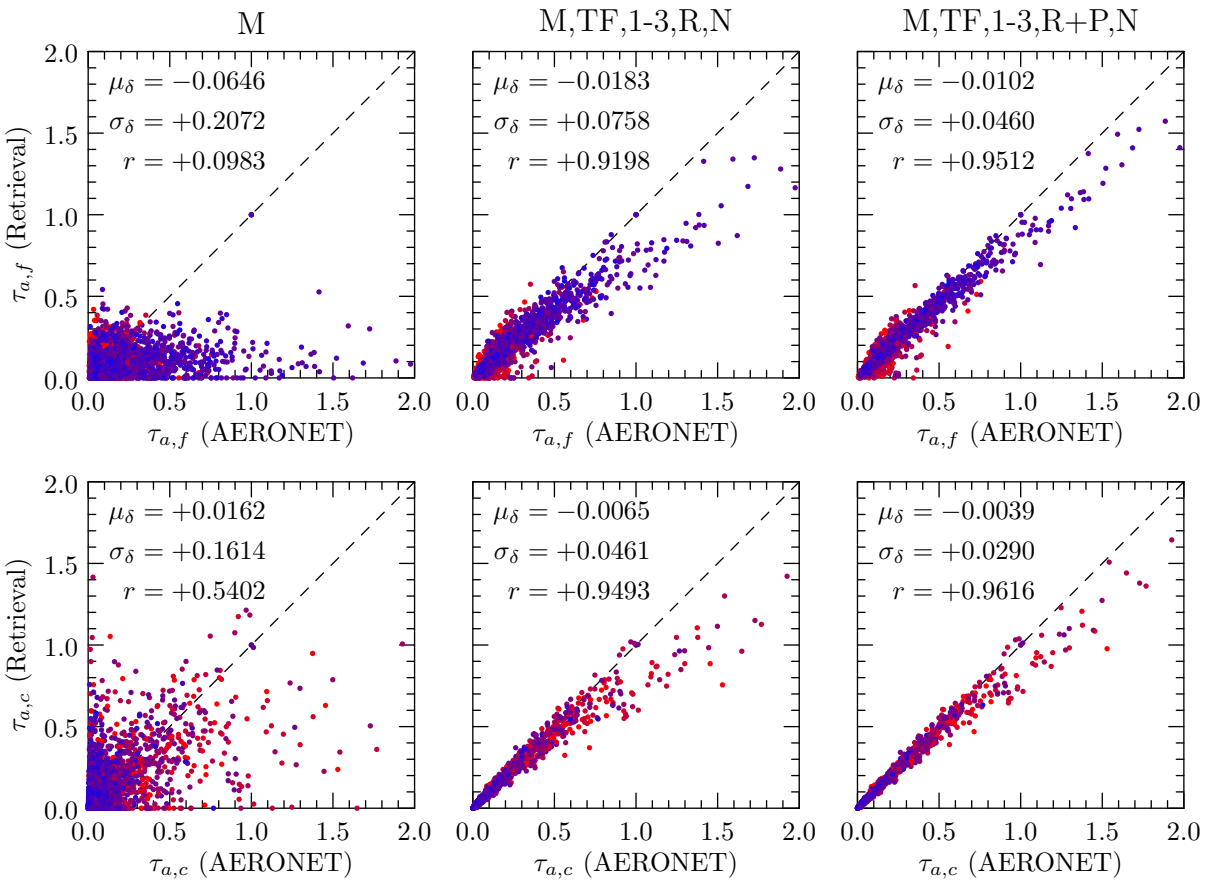

Figure 6.5: Scatter plots of retrieval results from all sites for fine and coarse mode aerosol optical thicknesses, $\tau_{a,f}(0.55)$ and $\tau_{a,c}(0.55)$, for our retrieval vs. the AERONET retrieval.

each mode occupies a distinct regime, where the combination of both produces a wider spread. In fact, the modal results for all but $\tau_{a,f}$ using $[\mathbf{y}_{\mathrm{M}}, \mathbf{y}_{\mathrm{TF},1\text{–}3,R,\mathrm{N}}]$ come close to or exceed our accuracy requirement for total optical thickness but keep in mind that it is the total optical thickness that is ultimately used for radiative flux calculations. The statistics are notably better for the coarse mode but this is due only to the lower optical thicknesses characteristic of the coarse mode. A notable feature in these scatter plots is the dominance of large surface albedos (redder colors) in the coarse mode at large optical thicknesses. This is most likely due to the predominance of desert dust particles which are characteristically larger and occur over bright desert surfaces.

Scatter plots for $r_{g,f}$, $r_{g,c}$, σ_f, and σ_c are shown in figure 6.6 for measurement vectors $[\mathbf{y}_{\mathrm{M}}, \mathbf{y}_{\mathrm{TF},1\text{–}3,R,\mathrm{N}}]$ and $[\mathbf{y}_{\mathrm{M}}, \mathbf{y}_{\mathrm{TF},1\text{–}3,R+P,\mathrm{N}}]$. For $r_{g,f}$ the mean bias μ_δ is relatively small but there is negative bias for smaller particle sizes and a positive bias for larger particle sizes evident in the plot. Both μ_δ and the standard deviation of the deviations σ_δ meet the accuracy requirement

in table 6.6 for both measurement scenarios by almost an order of magnitude. The correlation coefficient is considerably lower than seen for the optical thickness results due to the upward tilt mentioned above. For $r_{g,c}$ there is clearly an opposite effect to that of $r_{g,f}$ with positive biases for smaller particle sizes and negative biases for larger particle sizes and while μ_δ meets our accuracy requirement σ_δ is more than three times that of the accuracy requirement in either measurement scenario. It worth discussing the biases in a bit more detail. In the fine mode the small size/large size negative/positive bias is most likely due to non-uniqueness with other parameters particularly $N_{0,c}$ which exhibits larger over all sensitivities than $r_{g,f}$. The downward tilt for the $r_{g,c}$ results is a tendency of the retrieval results toward the a priori value of 0.8 μm. This is not surprising as the information content analysis in Part I reveals some lack of information on the coarse mode size distribution in the measurements giving more weight to the a priori knowledge. It is worth discussing the differences in information between our measurements and AERONET's measurements in this case. On the one hand, important in this case are larger wavelengths that are more sensitive to larger particles. AERONET's largest wavelength is 1.020 μm whereas our largest wavelengths are the 2.13-μm MODIS band and the 2.06-μm CO_2 TANSO-FTS band, and as shown in Part I, the measurements at these larger wavelengths provide significant and unique sensitivity to large particles. On the other hand, AERONET takes measurements at multiple angles which as shown in Part I also provides more information on larger particles.

The scatter plots for σ_f, and σ_c in figure 6.6 have values for μ_δ and σ_δ that meet the relatively weak accuracy requirement of 0.3. The negative biases, especially in the small mode, may be related to the assumption of a log-normal size distribution. The correlation coefficients r are small with the largest value not exceeding 0.35. There is a large scatter in the coarse mode results along the "Retrieval" axis. As shown in Part I the amount of information on σ_f is significantly less than that of $r_{g,f}$ whereas for the coarse mode there is more information on σ_c than $r_{g,c}$. It is possible, due to the lack of larger wavelength measurements available to the AERONET retrieval, that the scatter in σ_c is due to an AERONET tendency toward an a priori value and that the larger wavelengths available to our retrieval provide a more accurate result.

Figure 6.7 shows scatter plots for m_r, m_i, and ω_a for the same two measurement vectors shown in the previous figure. The results for m_r show a relatively small mean bias μ_δ and a relatively good correlation coefficient r. The scatter is large in the plot for total reflectance but improves

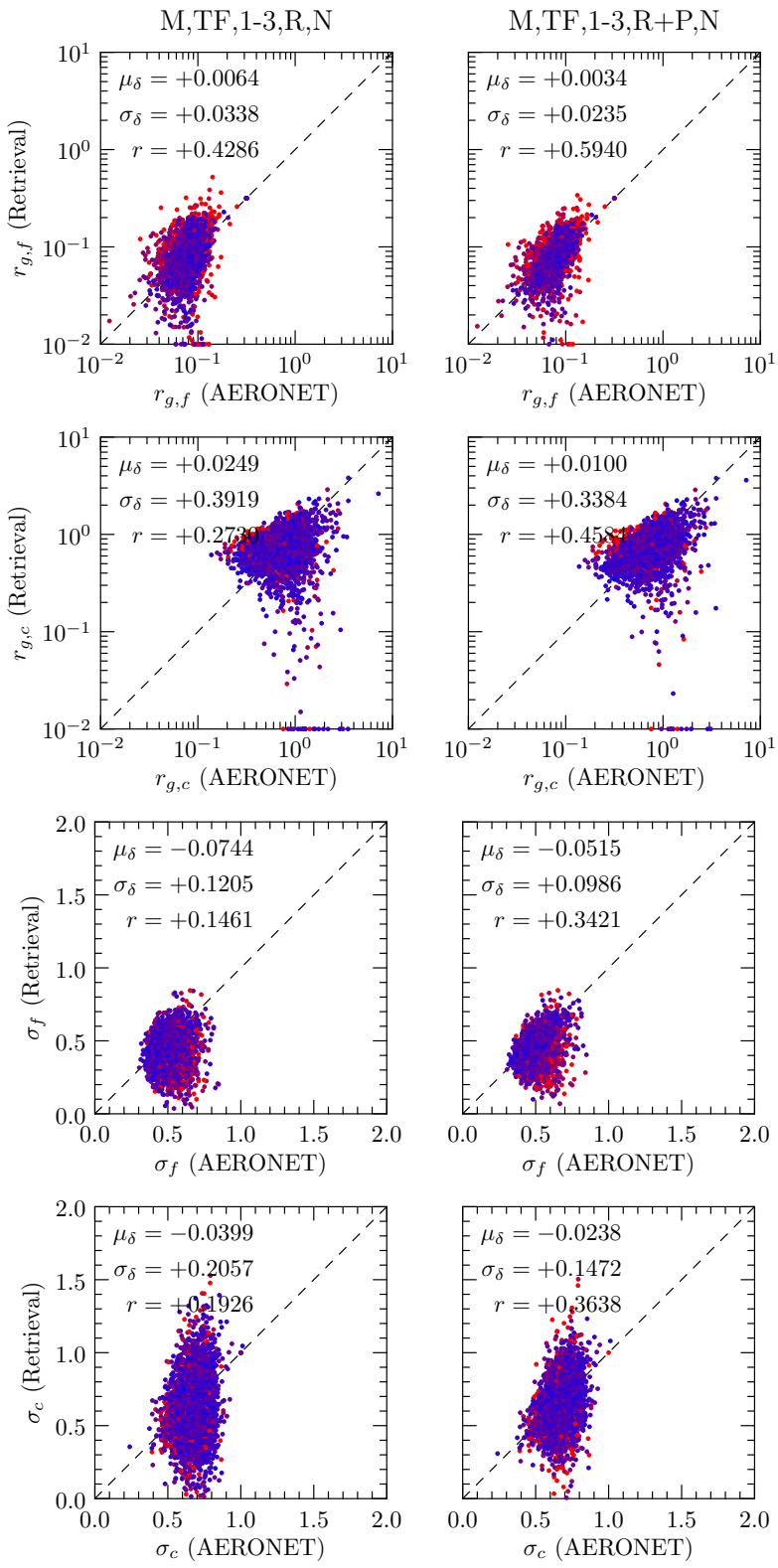

Figure 6.6: Scatter plots of retrieval results from all sites for fine and coarse mode mean particle radius, $r_{g,f}$ and $r_{g,c}$, and for fine and coarse mode particle standard deviations, σ_f and σ_c, for our retrieval vs. the AERONET retrieval.

significantly in the plot that includes polarized reflectance due to the larger overall sensitivity of polarized reflectances to m_r compared to total reflectances. In addition, minimum and maximum retrieval values of 1.32 and 1.60, respectively, are clearly evident in the AERONET results. In both cases the accuracy requirement is not met by the standard deviation of the deviations σ_δ and, as discussed in Part I, multiangle measurements of polarized reflectance may be required to accurately retrieve m_r. One must also consider that the lack of polarization measurements available to the AERONET retrieval affects its accuracy and that, as a result, for m_r AERONET may not be as accurate a validation as it is for optical thickness and size distribution. Compared to the results of Hasekamp et al. [2011] our results compare well considering that their results are made over ocean only and use multiangle measurements but on the other hand we use hyperspectral observations and a larger spectral range.

Not surprisingly, the retrieval of m_i also suffers from inaccuracies. This is to be expected as our study from Part I has shown that most of the measurements lack any real sensitivity to m_i. One should also keep in mind that, as given in table 6.3 the accuracies in the AERONET retrievals of m_i are at best 30%. In addition, a minimum retrieval value of 0.0003 is clearly evident in the AERONET results. As discussed above m_i is included in the retrieval vector in case there is any available information that can influence the values away from the a priori if need be. The retrieval results for m_i show a clear trend of positive biases at low values and negative biases a large values most likely due to a tendency toward the a priori value of 0.002.

Radiatively more important than m_i is the single scattering albedo ω_a for which μ_δ meets the accuracy requirement of 0.3 in both measurement scenarios but the σ_δ results do not meet the accuracy requirement in either case. There is some improvement in μ_δ and σ_δ when the polarized reflectance is used. Although μ_δ is negative, the biases at low values tend to be positive and at high values tend to be negative. Similar to that of m_i the source of this is most likely due to a tendency toward the priori value, derived to be approximately 0.9, but may also be due to non-uniqueness issues between $r_{g,c}$, σ_c, and m_i relating to each value's influence on aerosol absorption. Compared to the results of Hasekamp et al. [2011] in table 6.7 our results are a bit better for μ_δ but are not as good for σ_δ and r although we must keep in mind that their results are for over ocean and reported at 0.670 μm. Also given in table 6.7, Dubovik et al. [2011] reported differences in ω_a that do not exceed between 0.3–0.5 which our σ_δ results using both R and P measurements fall

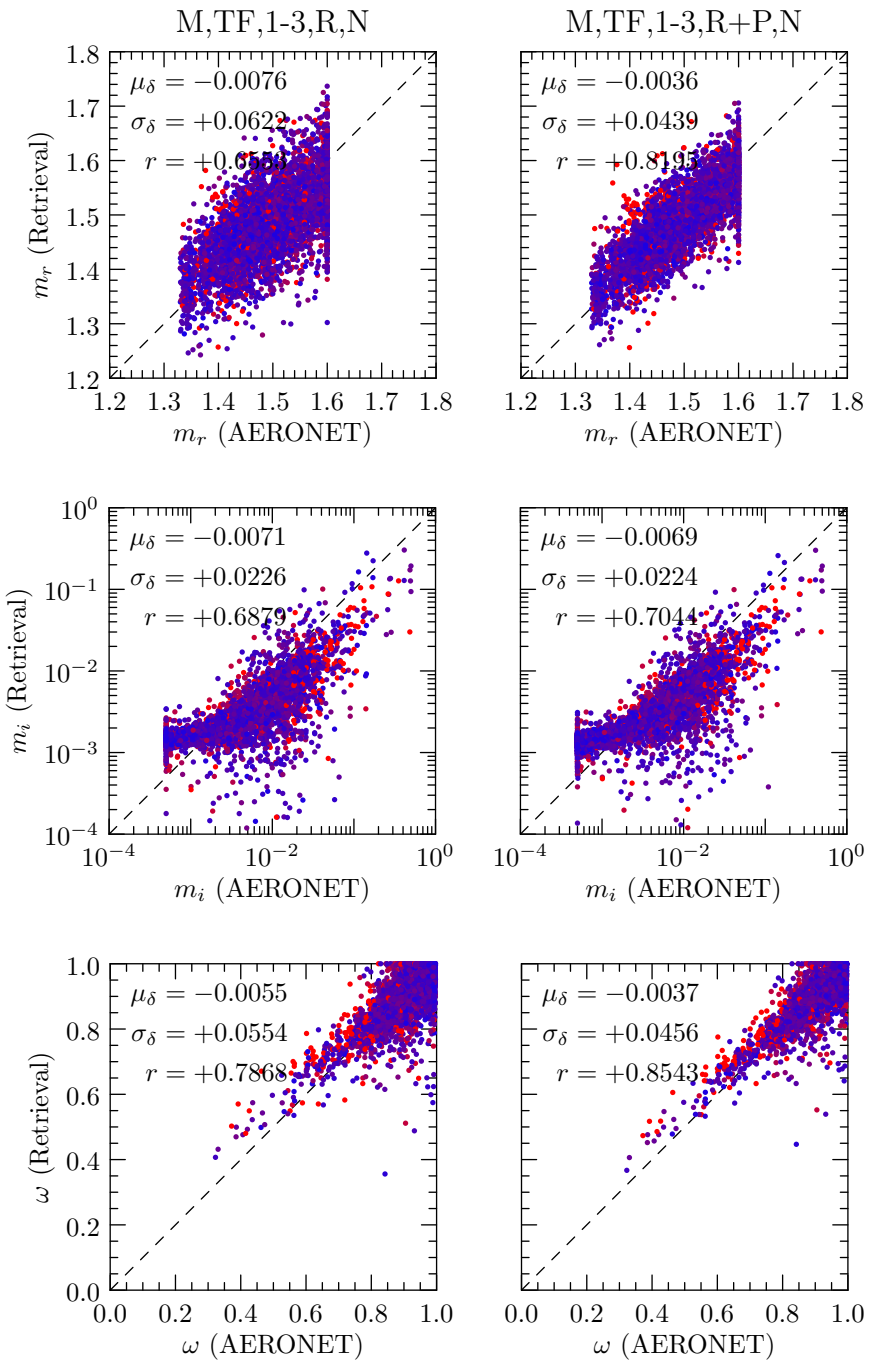

Figure 6.7: Scatter plots of retrieval results from all sites for modally averaged $m_r(0.55)$, $m_i(0.55)$, and $\omega_a(0.55)$ for our retrieval vs. the AERONET retrieval.

within. Of course, σ_δ is a standard deviation and many of the results will exceed this range. Due to the increased sensitivity to m_r, and to a lesser degree m_i, of multiangle measurements we expect that the full approach of multispectral, multiangle, and polarimetric measurements will be able to retrieval single scattering albedo to the accuracy prescribed in table 6.6. Nevertheless, the σ_δ values of 0.055 and 0.046, for each scenario, respectively, are relatively good compared to the accuracy requirement, given the difficulty of retrieving single scattering albedo, especially over land.

Mixed aerosol

In this section we present scatter plots for retrievals at sites in which we have classified as having predominately mixed aerosol. From figure 6.8 mixed aerosols are aerosols that are difficult to classify into any single class and are assumed to contain aerosols of all types including urban-industrial, biomass burning, desert dust, and oceanic. Figures 6.9 through 6.12 show results for the same parameters and same measurement scenarios as figures 6.4 through 6.7 did for all sites, respectively. The results for τ_a show significantly larger mean biases μ_δ and standard deviations of the deviations σ_δ than the results for all sites indicating that the mixed aerosol type is on the average more difficult to retrieve than the average case. Also, similarly to the results for all sites, the results improve significantly when adding TANSO-FTS measurements, improve more when using all three TANSO-FTS bands instead of band 1, and improve more when using the polarized reflectance instead of just the total reflectance. The cases when using all three bands and/or polarized reflectance have μ_δ values that meet the accuracy requirement for τ_a but fall short for σ_δ. The results for $\tau_{a,f}$ and $\tau_{a,c}$ (figures 6.10) show that the fine mode has similar results to that for all sites and that it is the coarse mode that contributes to the relative decrease in the accuracy of the mixed aerosol results. The is most likely (further supported later) due to the difficulty of retrieving desert dust, which is predominately large, over bright desert surfaces. The results for $r_{g,f}$, $r_{g,c}$, σ_f, and σ_c (figure 6.11) show similar results as that for all sites with no differences distinct enough to discuss. In figure 6.12 for m_r results are similar to that for all sites but significantly worse for m_i and better for $\omega_{a,i}$. For m_i this is primarily due to a stronger tendency toward the a priori value for the more difficult to retrieve mixed aerosol type. For $\omega_{a,i}$ the improvement is difficult to explain but may be due to less influence by desert dust in the mixed aerosol type.

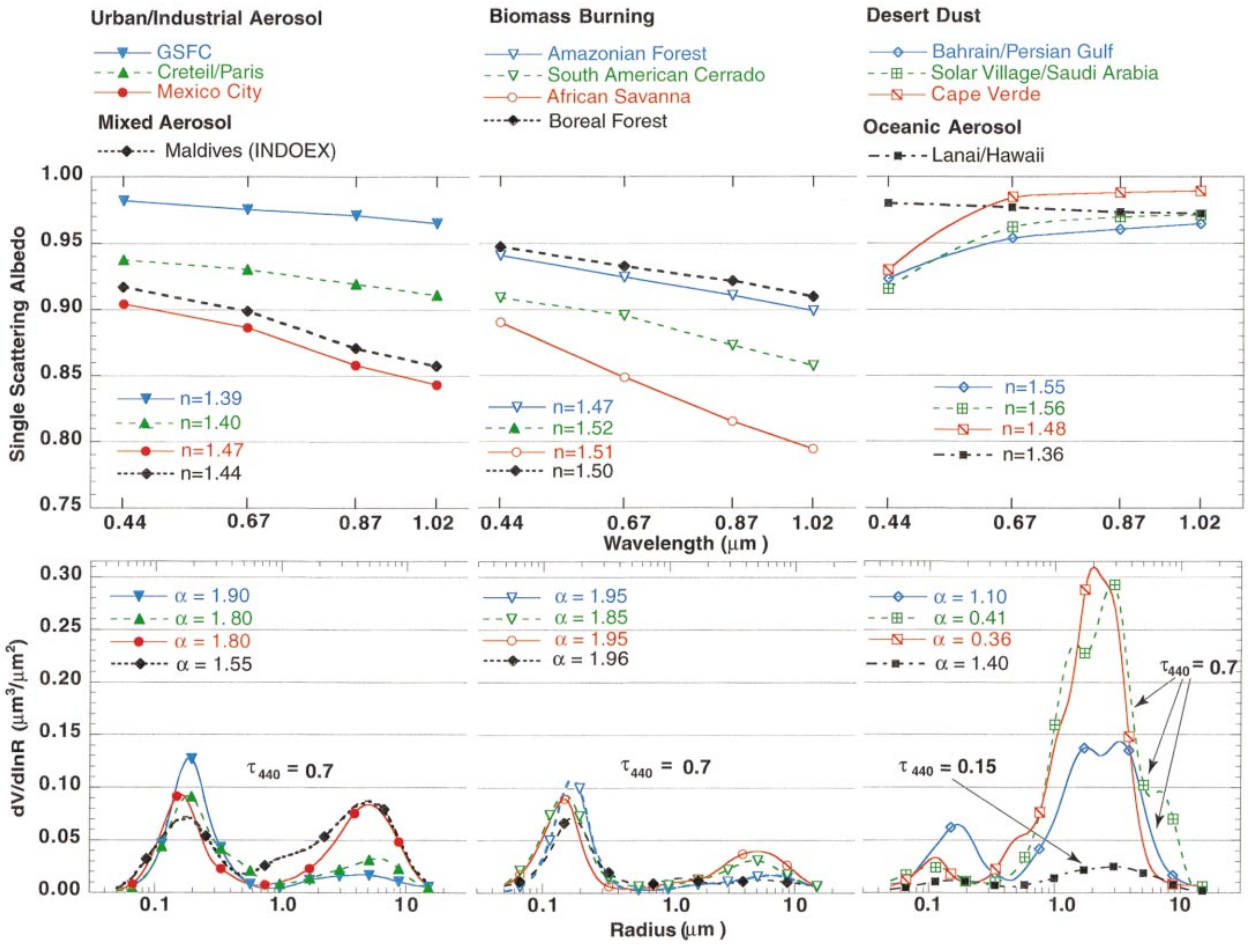

Figure 6.8: Microphysical and optical properties of the different aerosol types considered in this study for several locations. (Adapted from Dubovik et al. [2002b].)

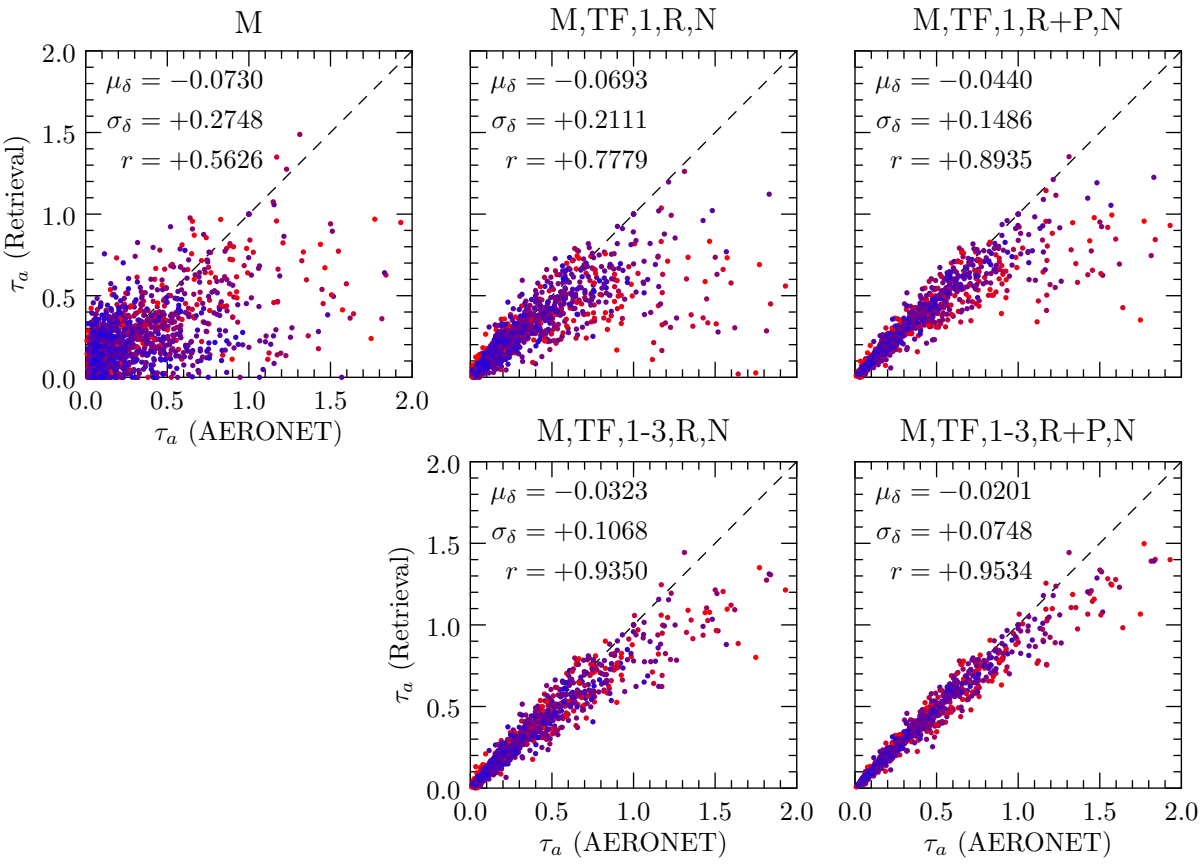

Figure 6.9: Same as figure 6.4 but for mixed aerosol sites only.

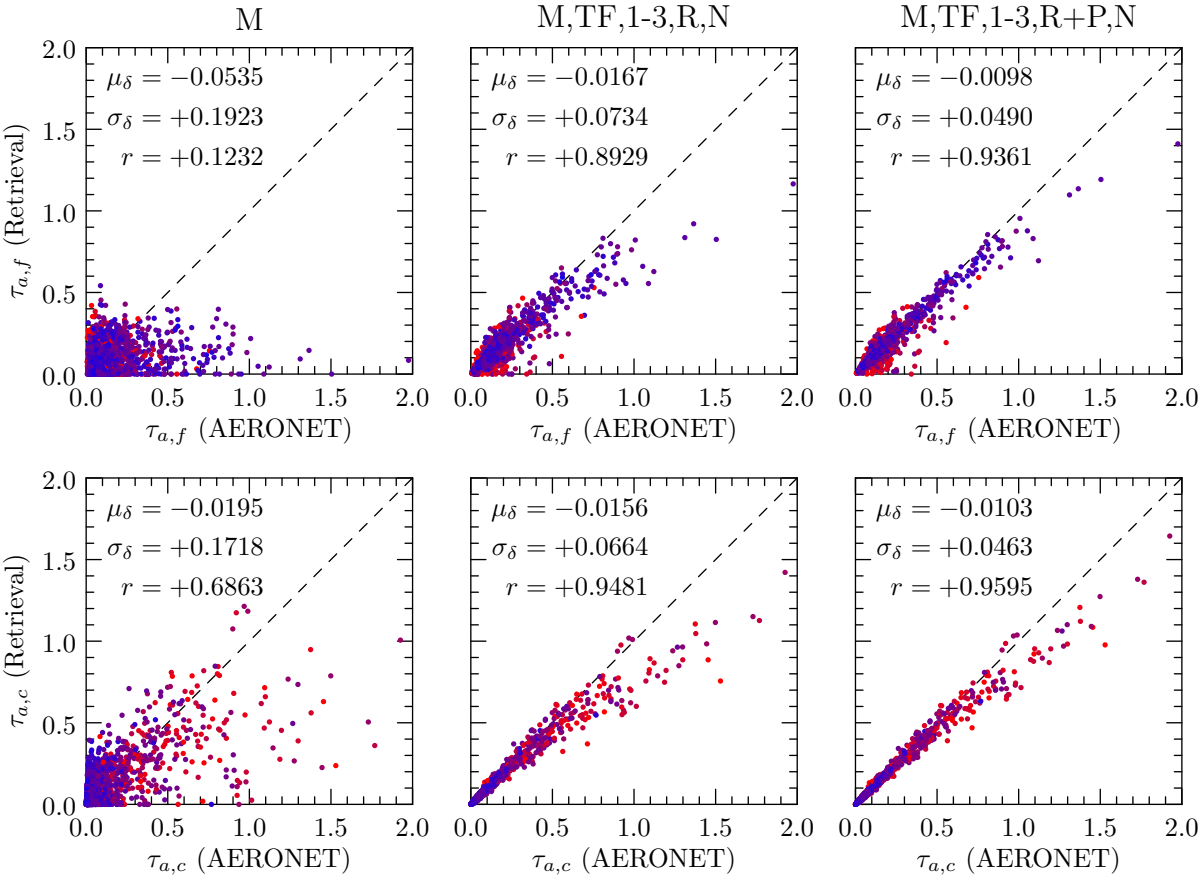

Figure 6.10: Same as figure 6.5 but for mixed aerosol sites only.

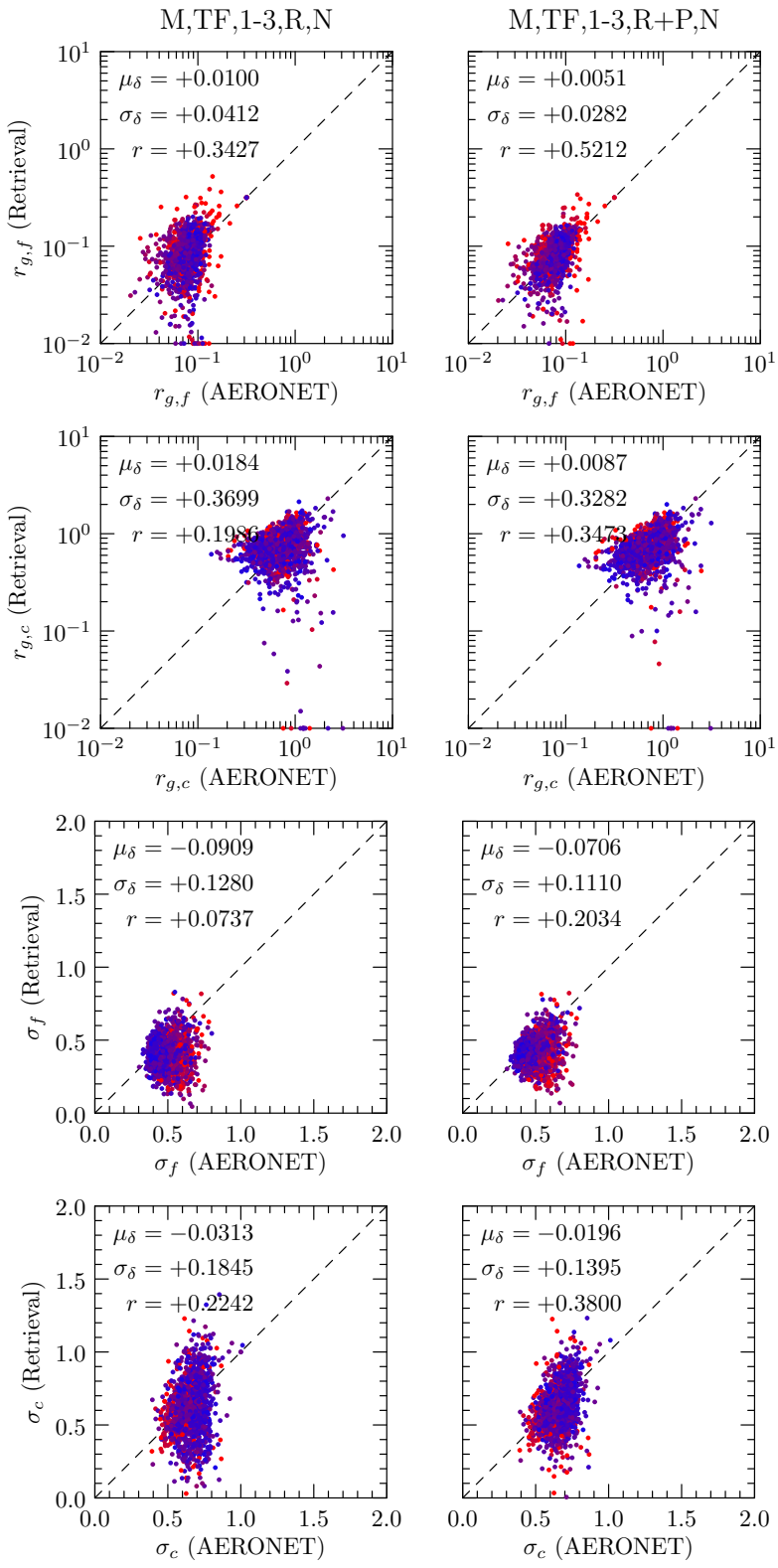

Figure 6.11: Same as figure 6.6 but for mixed aerosol sites only.

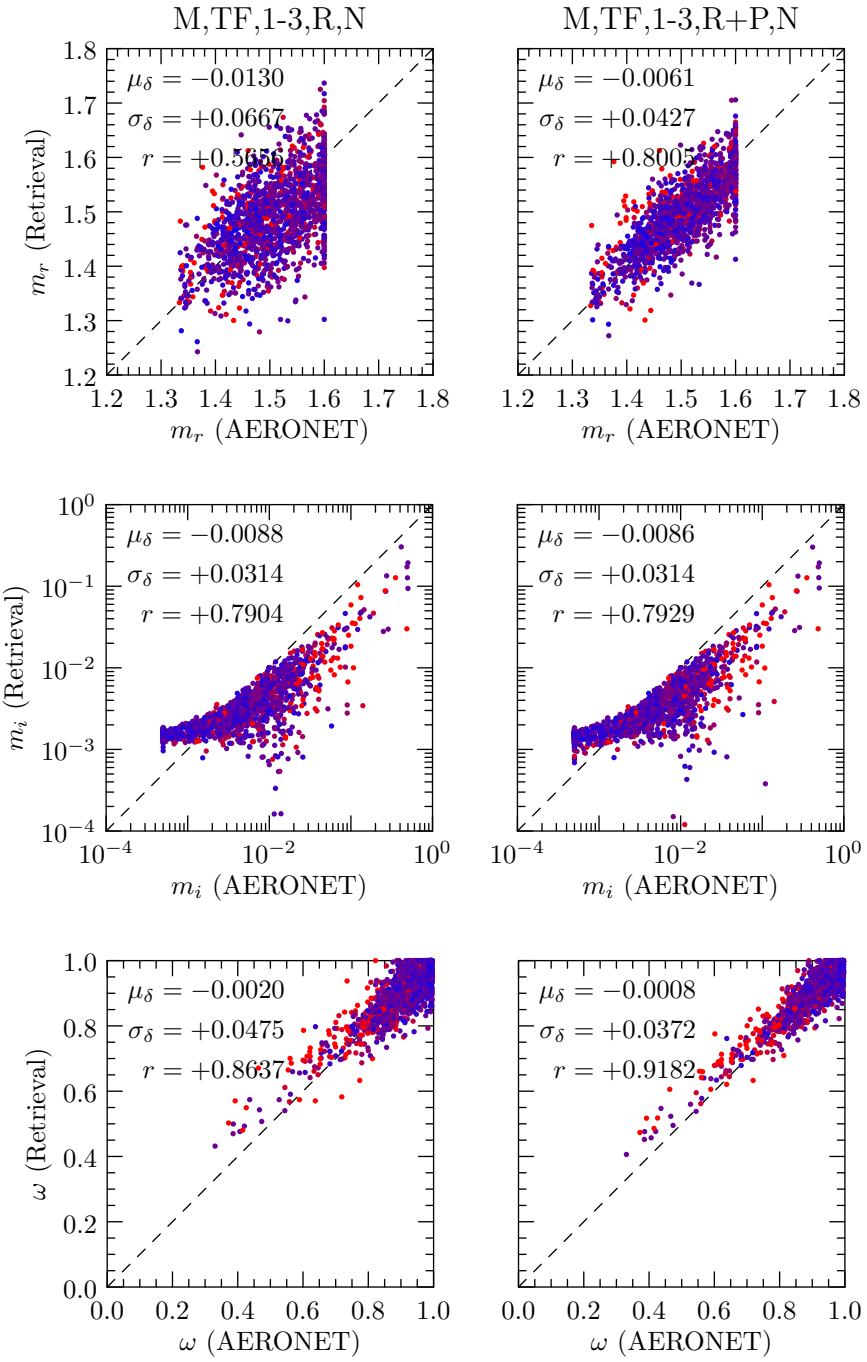

Figure 6.12: Same as figure 6.7 but for mixed aerosol sites only.

Urban-industrial aerosol

In this section we present scatter plots for retrievals at sites in which we have classified as having predominately urban-industrial aerosol. From figure 6.8 urban-industrial aerosols are characterized by similar values of $\tau_{a,f}$ and $\tau_{a,c}$ depending on the proximity of sources, values of $m_r < 1.47$, and a range of values for ω_a from 0.85 to 0.98. Figures 6.13 through 6.16 show results for the same parameters and same measurement scenarios as figures 6.4 through 6.7 did for all sites, respectively. The results for τ_a for the MODIS only retrieval are similar to that for all sites but the results for the scenarios including TANSO-FTS measurements are significantly better indicating that the urban-industrial type is on the average easier to retrieve than the average case. One reason for this is apparent from the lack of redder points in the scatter indicating that the surface at urban-industrial aerosol sites is darker increasing the aerosol signal relative to the surface. Another reason for this may be due to the larger proportion of small aerosols relative to mixed and desert dust aerosol types and, as shown in Part I, the large information content in our measurements for small mode aerosols compared to coarse mode aerosols. In this case the accuracy requirement is met by μ_δ for all TANSO-FTS cases and almost by σ_δ for the most complex TANSO-FTS cases. The results for the $\tau_{a,f}$ and $\tau_{a,c}$ in figure 6.14 show rather comparable results for $\tau_{a,f}$ compared to all sites but significantly better results for $\tau_{a,c}$. This is most likely due to the lack of desert dust at the urban-industrial sites, which as we are starting to see, may be more difficult to retrieve. As with all sites, in figure 6.15 the results for $r_{g,f}$ easily meet the accuracy requirement whereas results for $r_{g,c}$ do not. The results for $r_{g,f}$ are better compared to all sites and the results for $r_{g,c}$ are worse most likely due to a relatively larger and lower aerosol signals, respectively. The results for σ_f are better than that for all sites, most likely due to a more log-normal type size distribution, and the results for σ_c are almost identical. In figure 6.16 the results for m_r, m_i, and ω_a are moderately better than that for all sites. As with total optical thickness τ_a these values are combinations of the corresponding retrieved fine and coarse mode values and as a result are benefiting from the smaller contribution from the coarse mode in the urban-industrial aerosol.

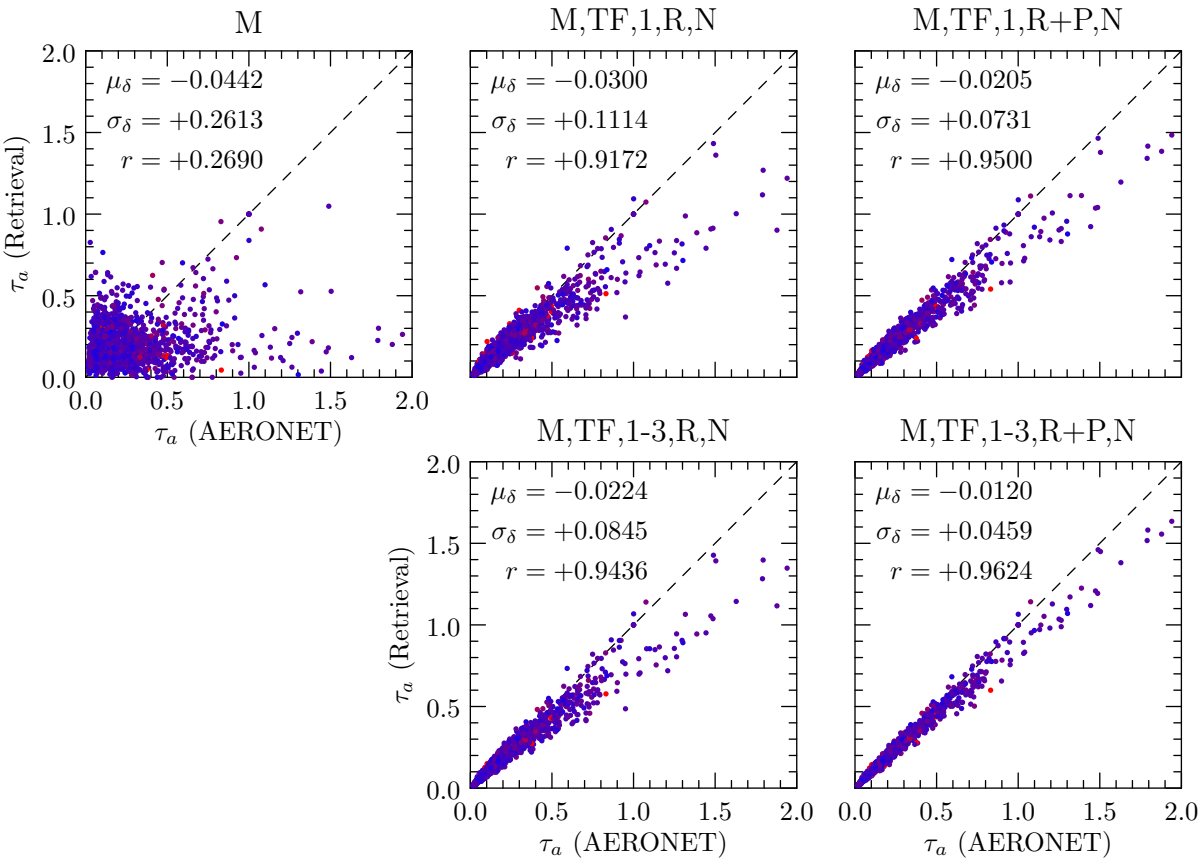

Figure 6.13: Same as figure 6.4 but for urban-industrial aerosol sites only.

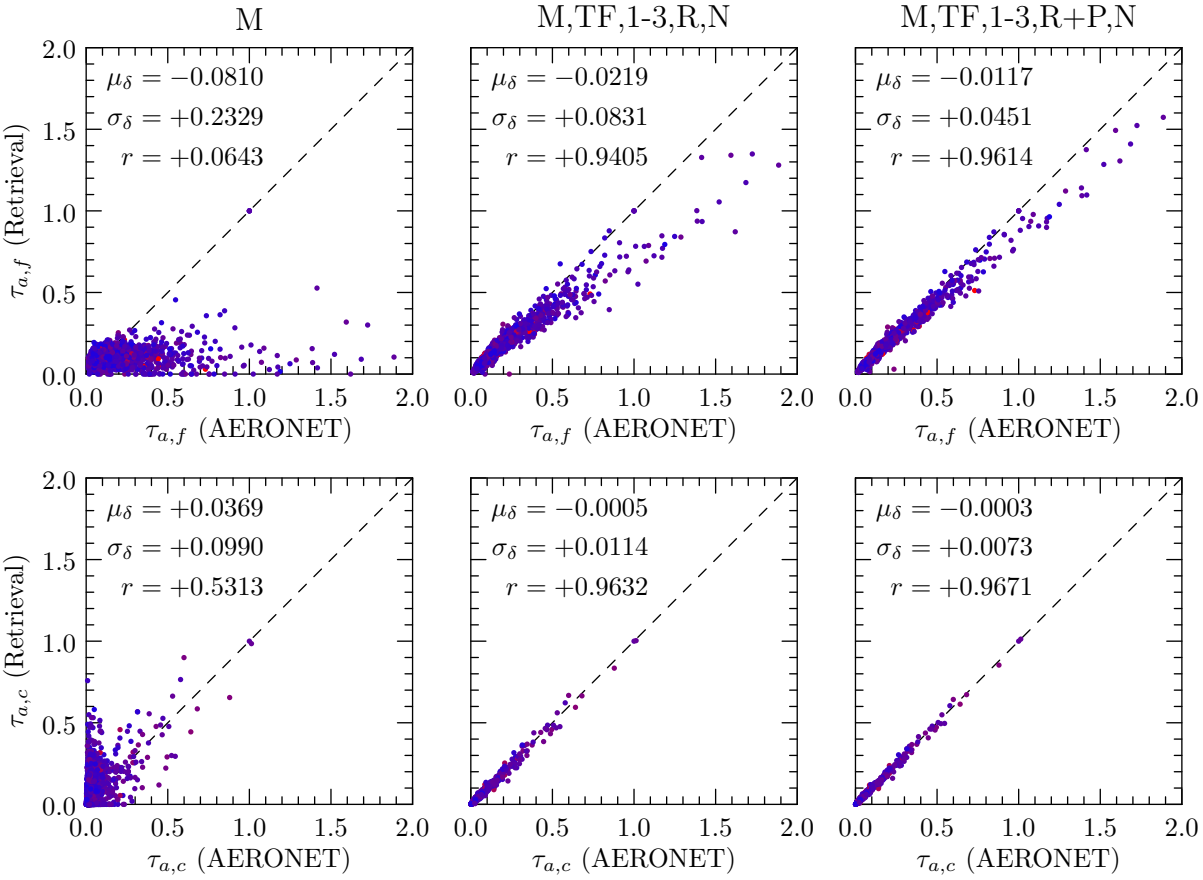

Figure 6.14: Same as figure 6.5 but for urban-industrial aerosol sites only.

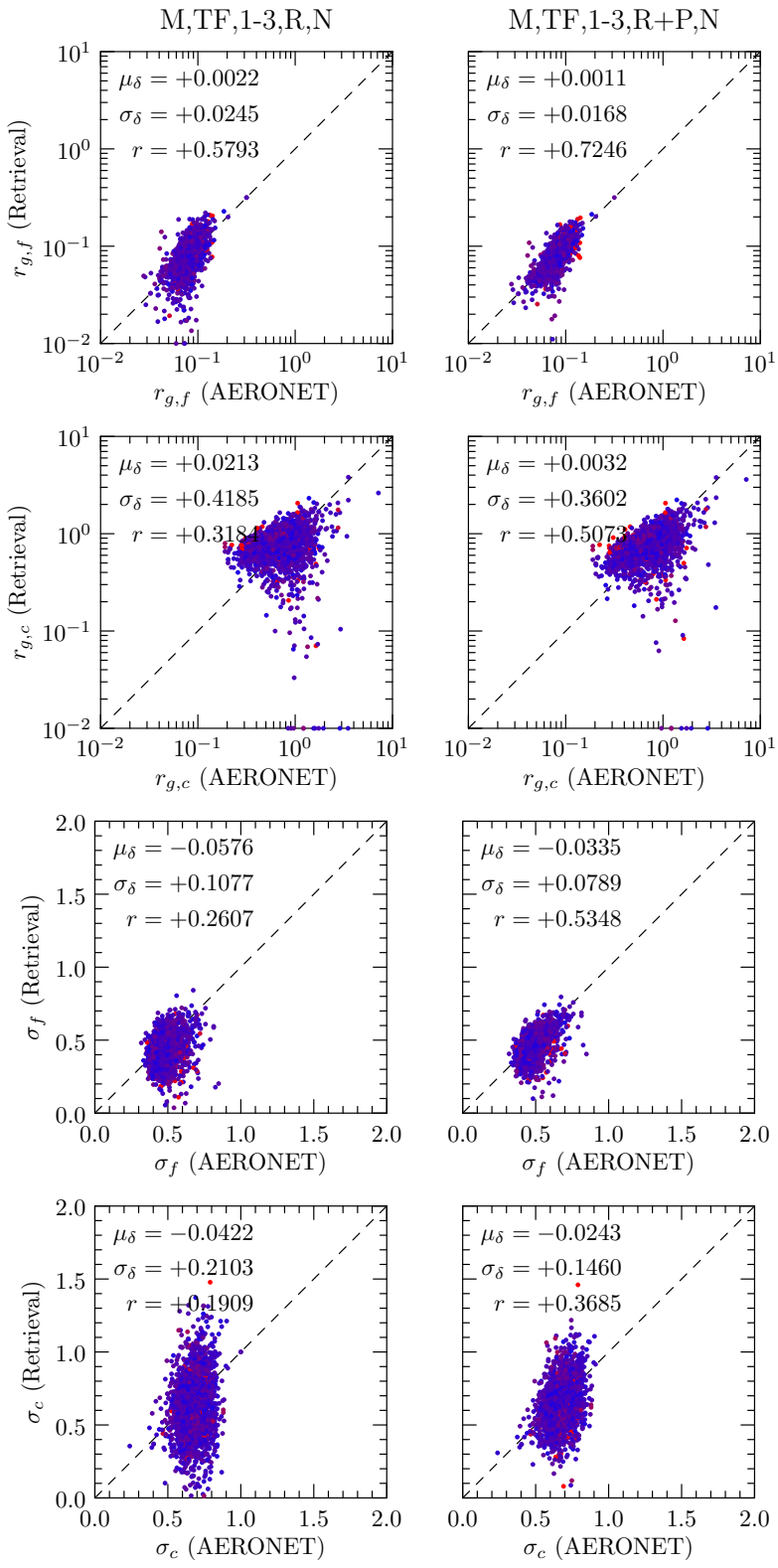

Figure 6.15: Same as figure 6.6 but for urban-industrial aerosol sites only.

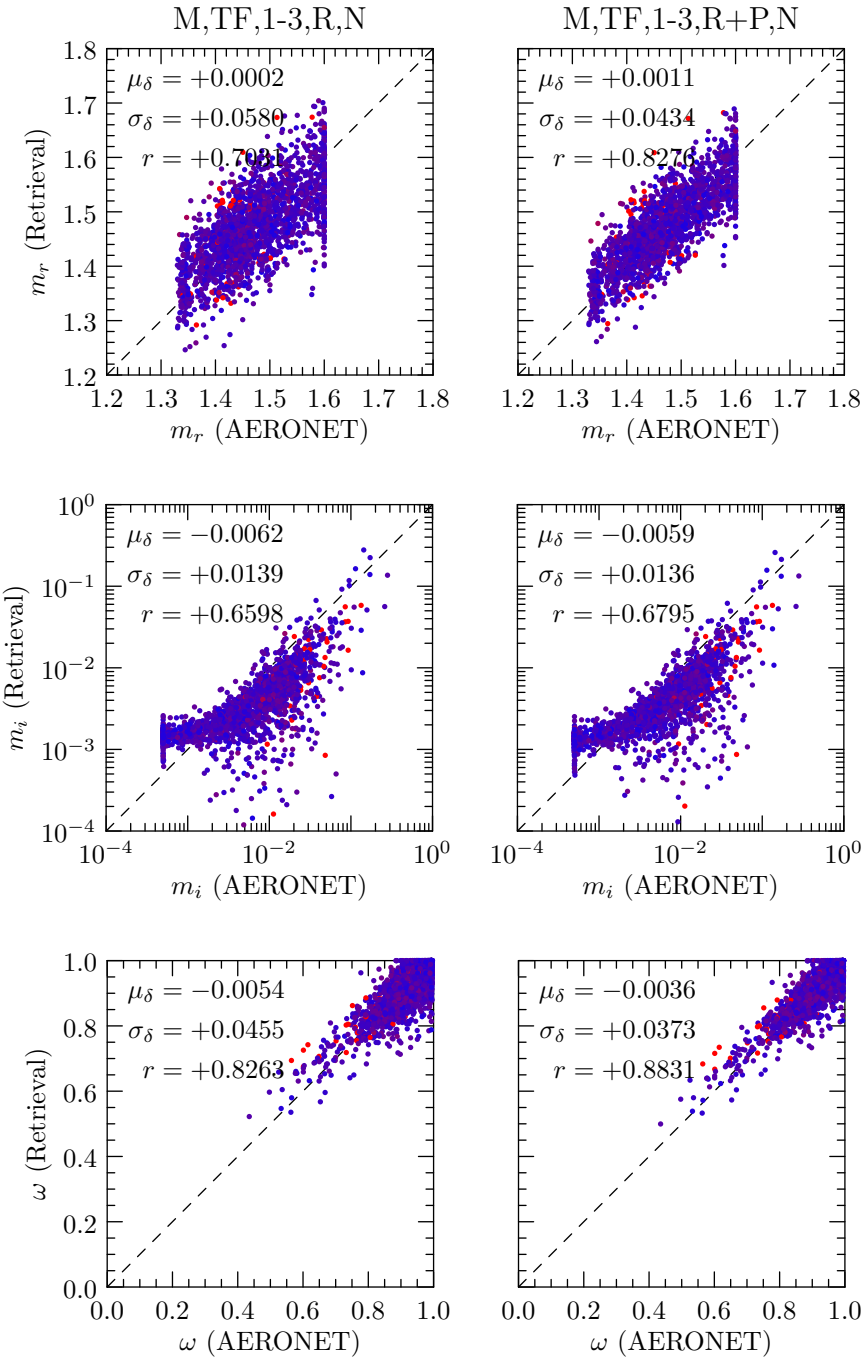

Figure 6.16: Same as figure 6.7 but for urban-industrial aerosol sites only.

Biomass burning aerosol

In this section we present scatter plots for retrievals at sites in which we have classified as having predominately biomass burning aerosol. From figure 6.8 biomass burning aerosols are characterized by larger values of $\tau_{a,f}$ compared to $\tau_{a,c}$ depending on the proximity of sources, values of $m_r > 1.47$, and a range of values for ω_a from 0.80 to 0.95. Figures 6.17 through 6.20 show results for the same parameters and same measurement scenarios as figures 6.4 through 6.7 did for all sites, respectively. The results for τ_a are significantly better than for all sites, even more so than for urban-industrial aerosol, most likely due to the larger proportion of small mode aerosols in the biomass burning type. In this case the accuracy requirement is met by μ_δ for all TANSO-FTS cases and by σ_δ for the most complex TANSO-FTS cases. The results for $\tau_{a,f}$ and $\tau_{a,c}$ in figure 6.18 are better than that for all sites for both modes. For the small mode the source of the improvement is most likely due to the darker over all surfaces and to the larger optical thicknesses. For the coarse mode the improvement is similar to that of urban-industrial but comparably there are more redder points in the scatter, an indication that some of these biomass-burning sites are savanna with brighter surfaces. As with all sites, in figure 6.19 the results for $r_{g,f}$ easily meet the accuracy requirement whereas results for $r_{g,c}$ do not. The results for $r_{g,f}$ are better compared to all sites and the results for $r_{g,c}$ are worse most likely due to a relatively larger and lower aerosol signals, respectively. The results for σ_f are better than that for all sites, most likely due to a more log-normal type size distribution, and the results for σ_c are slightly worse probably due to a small coarse mode signal. In figure 6.20 the results for m_r and m_i are similar to that of all-sites while the results for ω_a are moderately worse indicating some difficulty in retrieving aerosol absorption features of biomass burning aerosols.

Desert dust aerosol

In this section we present scatter plots for retrievals at sites in which we have classified as having predominately desert dust aerosol. From figure 6.8 desert dust aerosols are characterized by significantly larger values of $\tau_{a,c}$ compared to $\tau_{a,f}$ depending on the proximity of sources, values of $m_r > 1.50$, and a range of values for ω_a from 0.90 to 0.98. In addition, the coarse mode of desert dust aerosols has a significantly larger mean radius $r_{g,c}$ than other aerosols while the particles can be significantly non-spherical causing biases in retrievals such as ours that assume that all

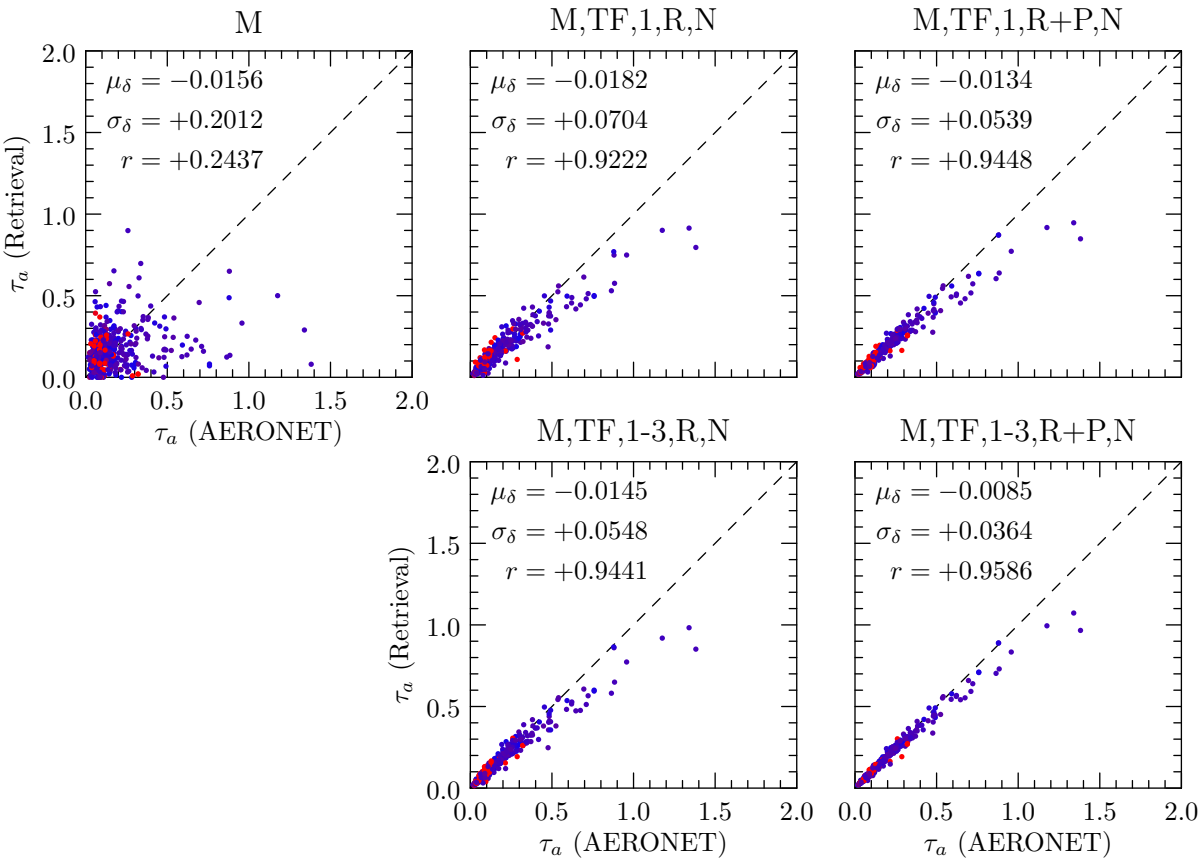

Figure 6.17: Same as figure 6.4 but for biomass burning aerosol sites only.

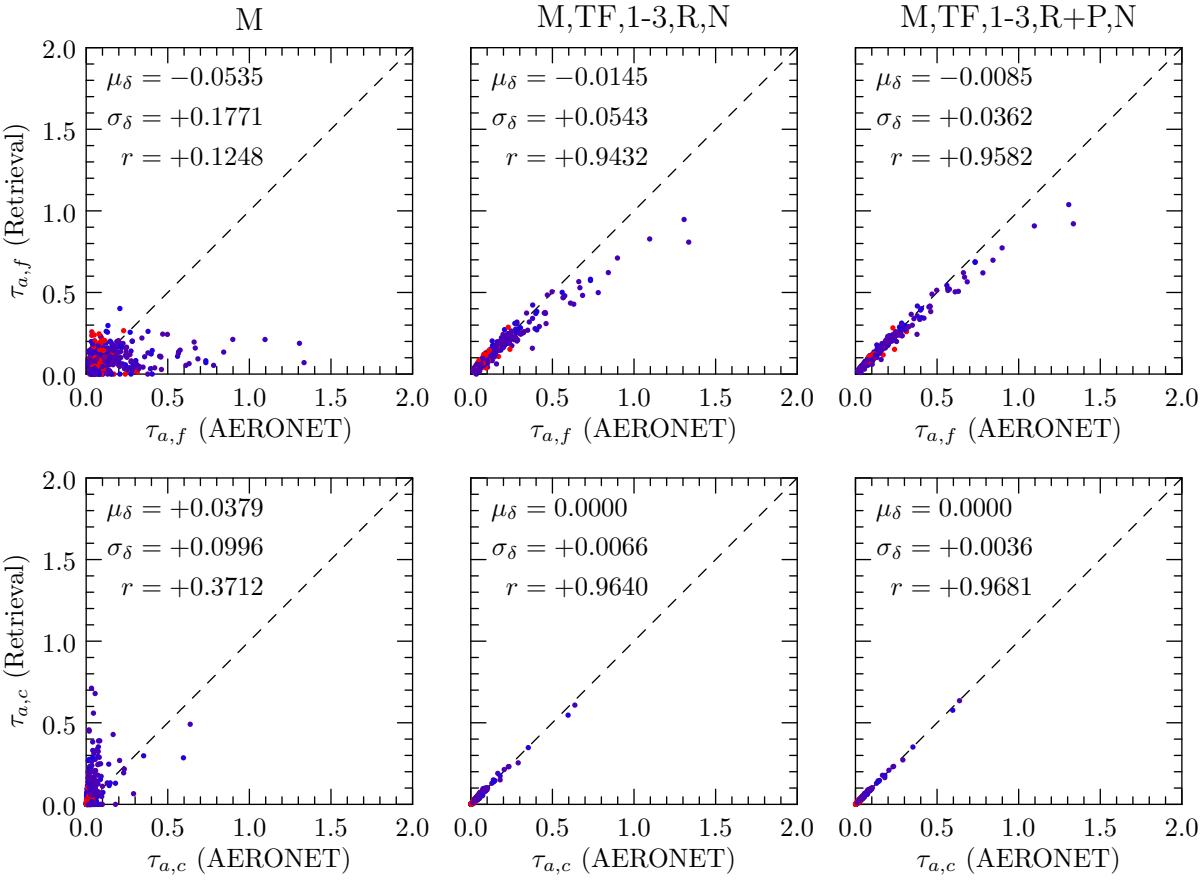

Figure 6.18: Same as figure 6.5 but for biomass burning aerosol sites only.

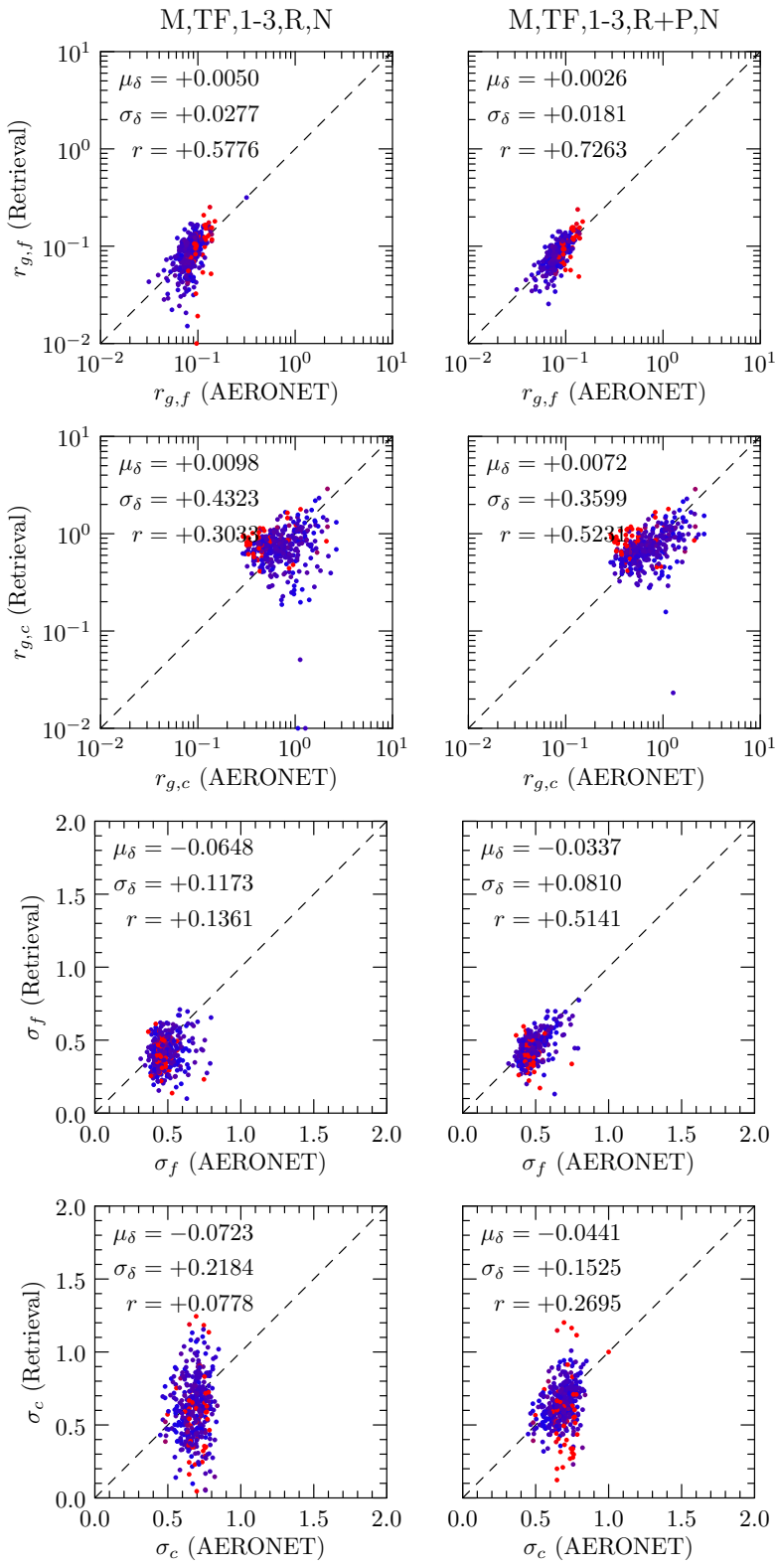

Figure 6.19: Same as figure 6.6 but for biomass burning aerosol sites only.

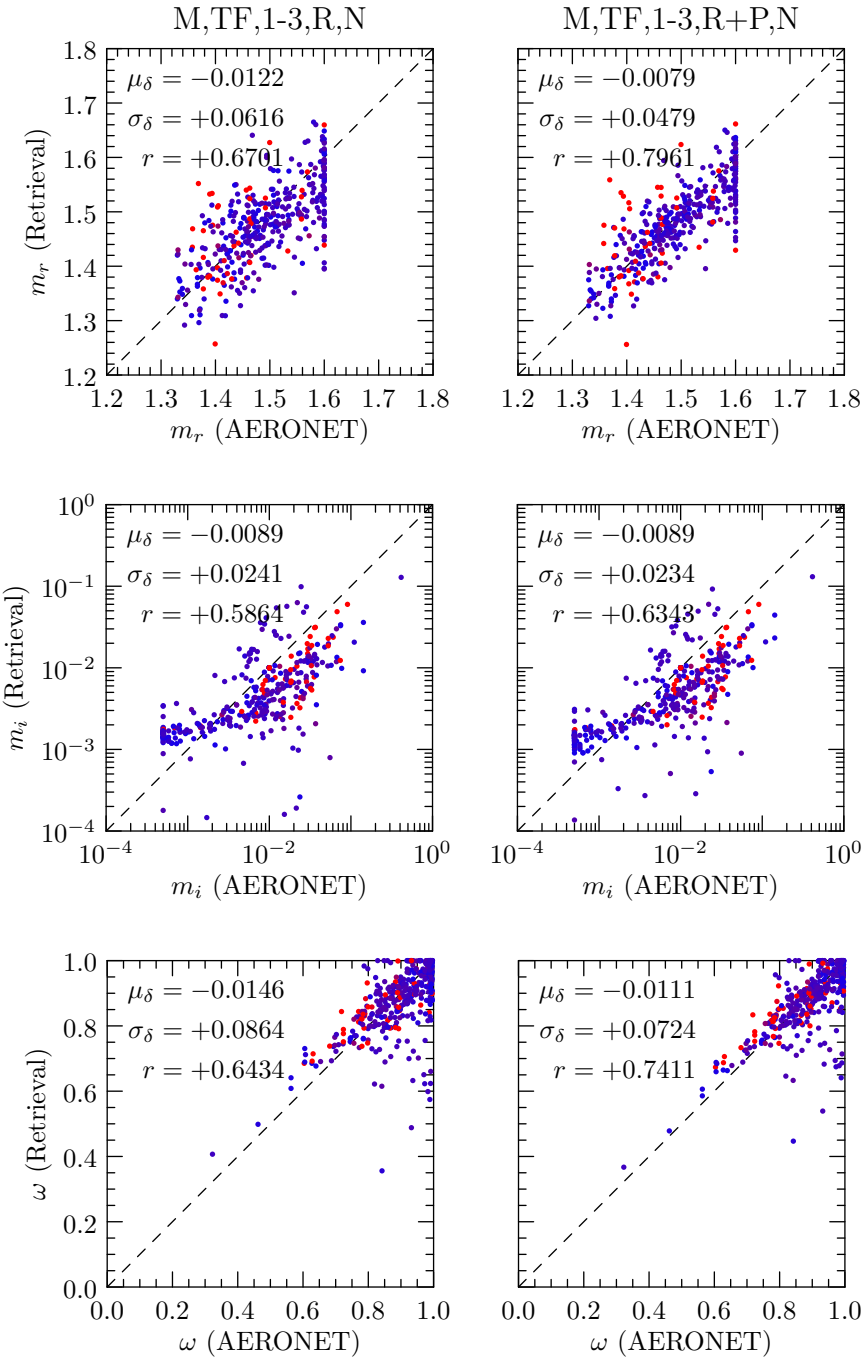

Figure 6.20: Same as figure 6.7 but for biomass burning aerosol sites only.

aerosols are spherical. Figures 6.21 through 6.24 show results for the same parameters and same measurement scenarios as figures 6.4 through 6.7 did for all sites, respectively. Compared to all sites, the results for τ_a are overall worse for $\mathbf{y}_{\mathrm{M}}$ and $[\mathbf{y}_{\mathrm{M}}, \mathbf{y}_{\mathrm{TF},1,R,\mathrm{N}}]$ but similar for the rest of the TANSO-FTS scenarios. This is as expected as our previous analysis has shown that desert dust retrievals are probably the limiting factor in the accuracy of the all site comparisons. Almost all the scatter points are red indicating that our rough aerosol site classification scheme is working as expected, at least for desert dust. In this case the accuracy requirement is met by μ_δ for all but the simplest TANSO-FTS case whereas σ_δ does not meet the accuracy requirement in any case.

Previously we have mentioned the correlation of desert dust to bright desert surfaces as a source of difficulty in desert dust retrievals. There are two other possible reasons for lower accuracy seen in desert dust retrievals. First, the coarse mode is characterized by relatively large particles for which our measurements contain less information and for which the limited spectral range of AERONET is a problem. Second, desert dust particles may be significantly non-spherical whereas our retrieval assumes spherical particles. The AERONET inversion has more recently been improved to account for non-spherical particles by Dubovik et al. [2002a]. They found, that by using a model of a shape mixture of randomly oriented spheroids, significant improvements are obtained in the retrieval of size distribution, real and imaginary parts of the index of refraction, and phase function.

The results for $\tau_{a,f}$ and $\tau_{a,c}$ shown in figure 6.22 show a much larger scatter for the fine mode compared to the coarse mode most likely due to the relatively low signal from the fine mode compared to coarse mode. In figure 6.23 the results for $r_{g,f}$ are slightly worse than for the other sites, although μ_δ and σ_δ still meet the accuracy requirement for both measurement scenarios. For $r_{g,c}$ σ_δ is significantly better than for the other sites but still does not meet the accuracy requirement while the results for μ_δ are significantly worse but still meet the accuracy requirement. We attribute these results to the fact that in the case of desert dust the small mode signal is typically less than that for other aerosol types while the coarse mode signal is significantly larger. In addition, the larger bias for the coarse mode is most likely due the assumption of spherical particles. In figure 6.24 the results for m_r are slightly worse than that for all sites due to the relatively large distance between the a priori and the large values (approximately 1.55) for desert dust. Inversely the better results for m_i are due to the small distance from the a priori and the typical value of approximately 0.005 for desert dust. The results for ω_a are the least accurate out of all the other types. This is most

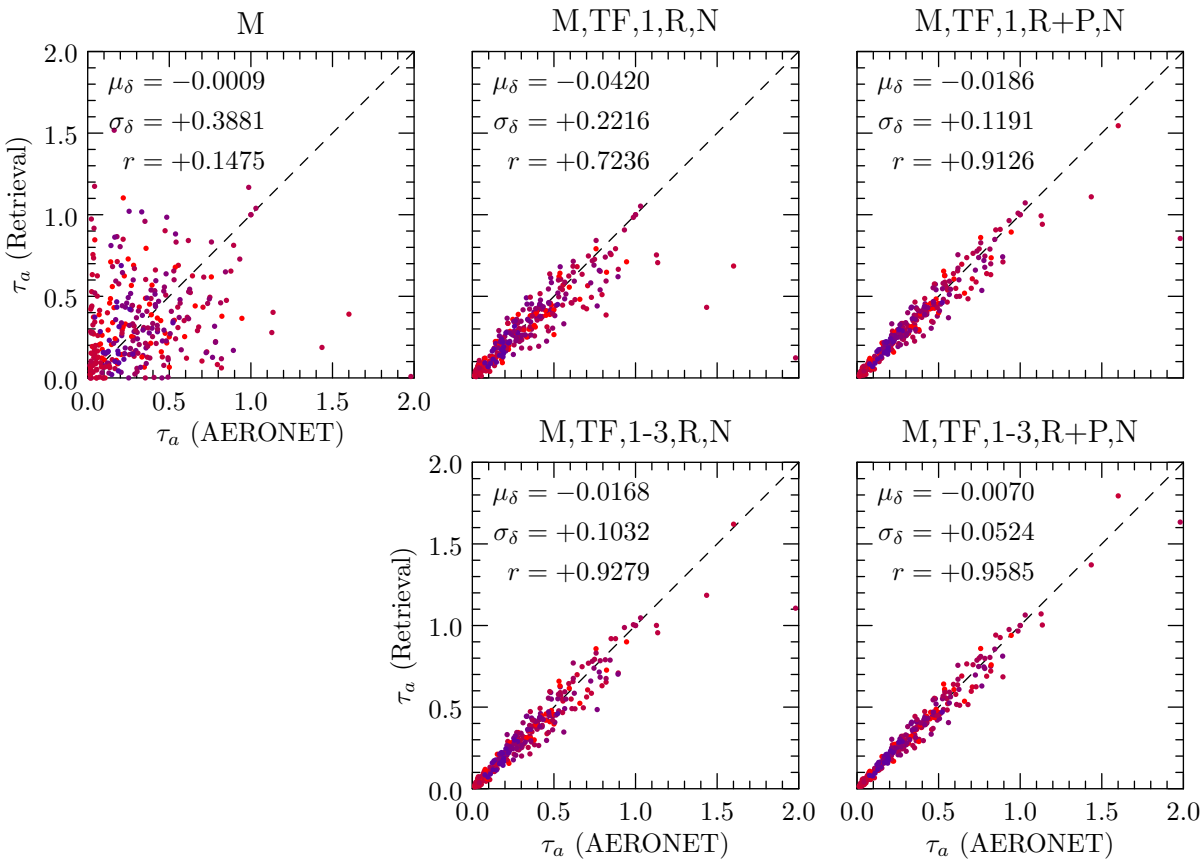

Figure 6.21: Same as figure 6.4 but for desert dust aerosol sites only.

likely due to non-uniqueness issues arising through non-sphericity and absorption of the coarse mode aerosols.

6.5.2 Timeseries

In this section and the next section we focus on four specific AERONET sites one for each aerosol type: Kanpur, India (mixed); Beijing, China (urban-industrial); Sao Paulo, Brazil (biomass burning); and Kuwait University, Kuwait City, Kuwait (desert dust). In this section we present timeseries plots of each of our validation parameters, for our two primary TANSO-FTS measurement scenarios (M,TF,1-3,R,N and M,TF,1-3,R+P,N), and for both AERONET and our retrieval. The plots are organized into figures for each parameter, where each figure contains four rows, one for each site, and two columns, one for each measurement scenario. Each plot contains timeseries for both AERONET (red) and our retrieval (blue). In addition, a seven-point Laplacian smoothing was performed on the AERONET timeseries which is plotted in black. The timeseries range from

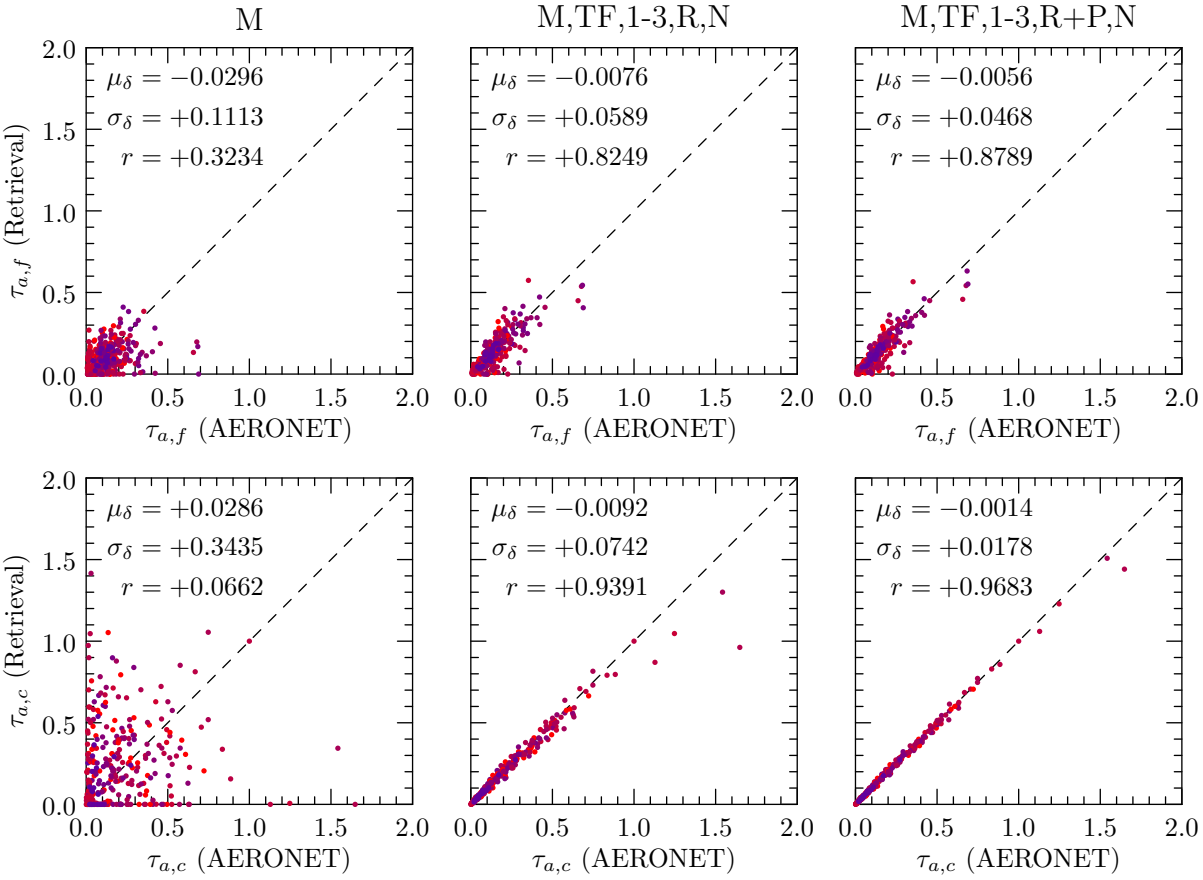

Figure 6.22: Same as figure 6.5 but for desert dust aerosol sites only.

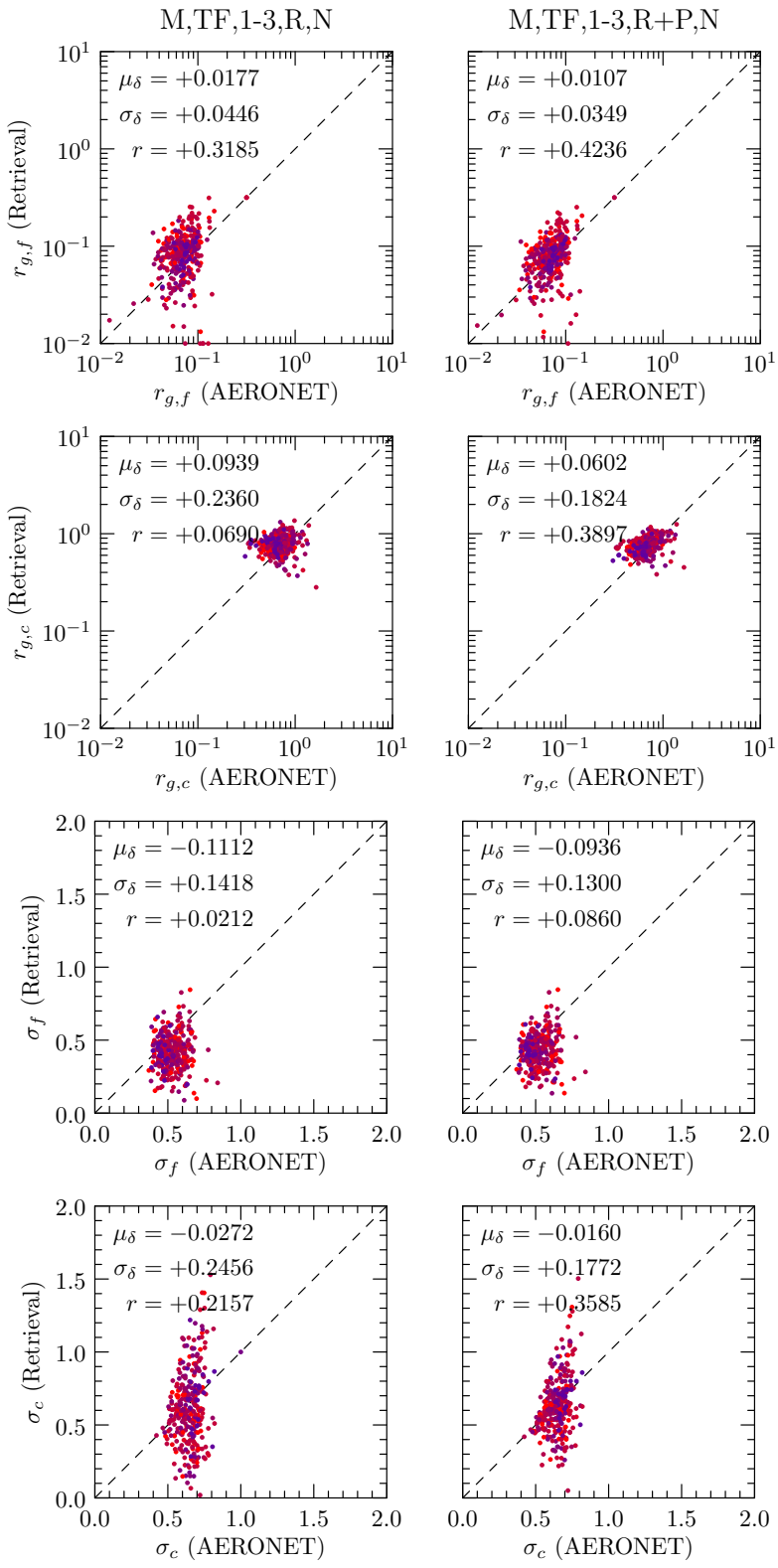

Figure 6.23: Same as figure 6.6 but for desert dust aerosol sites only.

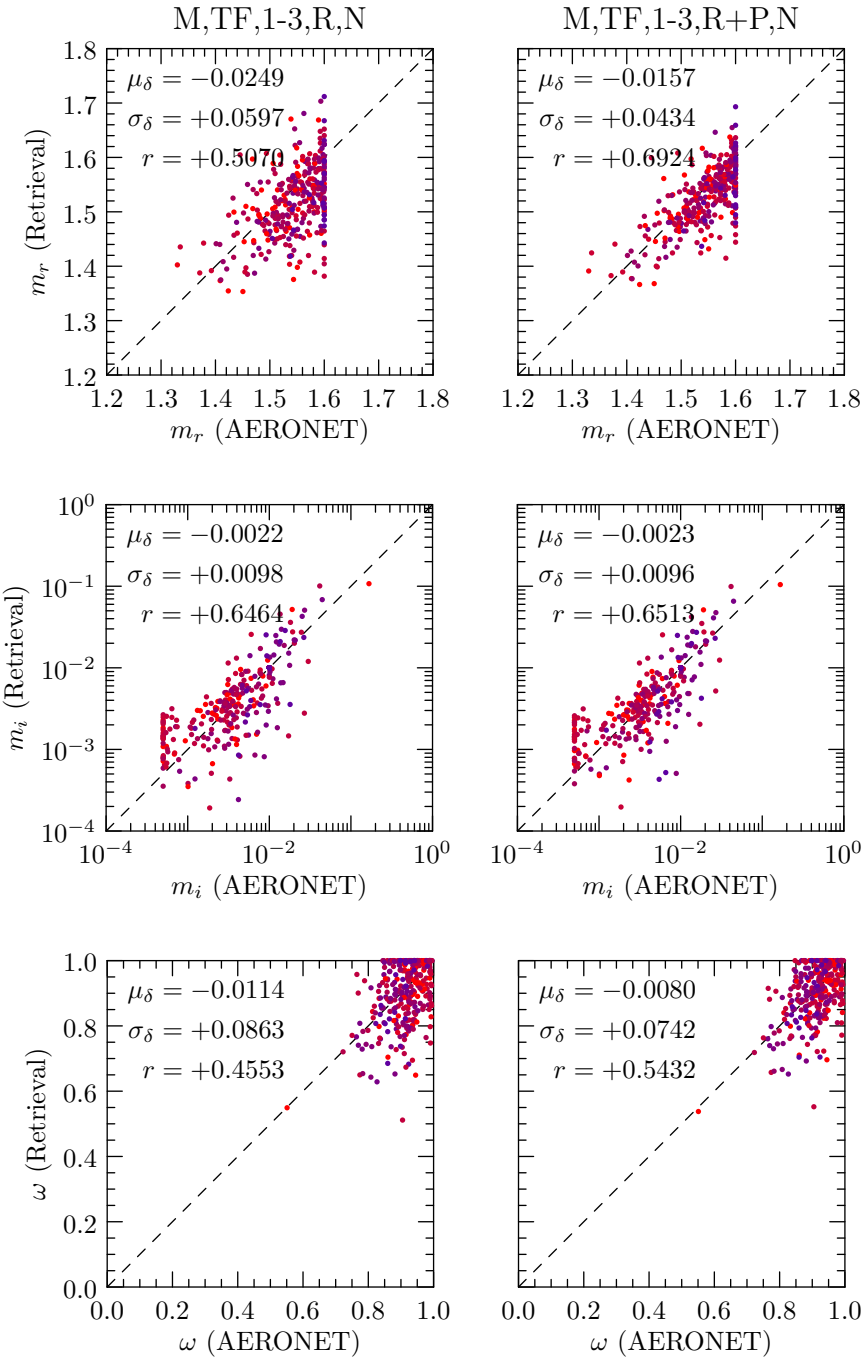

Figure 6.24: Same as figure 6.7 but for desert dust aerosol sites only.

April 5, 2009 through Dec 5 2011 but for some aerosol types (biomass burning and desert dust) co-locations were not available over the entire period. In addition, rather than just choosing the site that covers the longest time range or has the greatest number of co-locations we also choose sites based on there representativeness of their associated aerosol type.

Figure 6.25 shows timeseries of total optical thickness τ_a. As expected from our scatter plot results our τ_a retrieval results track the AERONET results well. A slight improvement relative to AERONET is apparent in the retrieval results that use measurements of polarization. Similarly, the results for the fine and coarse modes in figures 6.26 and 6.27, respectively, track well with AERONET. For Kanpur, seasonal variations are apparent in the timeseries for $\tau_{a,f}$ and $\tau_{a,c}$ and these variations partially cancel leaving the timeseries for τ_a without a significant season variation. Being of the mixed aerosol type aerosols at the Kanpur site are a mixture of different aerosol types which suggests that the different seasonal variation between the fine and coarse modes is a result of different aerosol types. For Kanpur these types would be fine mode pollution aerosols in the winter and coarse mode desert dust aerosols in the pre-monsoon months due to seasonal variation in soil moisture and winds that result from the monsoon circulation cycle [Eck et al., 2010]. In Beijing the fine mode aerosols whose primary source is pollution tend to dominate in fine mode optical thickness $\tau_{a,f}$ compared to the coarse mode $\tau_{a,c}$ for most of the year. The dust season months in Beijing are March, April, and May [Huebert et al., 2003], where dust is advected from the arid regions of western China and Mongolia which is evident in the timeseries of $\tau_{a,c}$, where the coarse mode peaks during these months, although, the fine mode optical thickness during these coarse mode peaks is still comparable justifying our classification of Beijing as urban-industrial. The number of co-locations over Sao Paulo, and for biomass burning aerosols overall in our study, is significantly less than that for the mixed and urban-industrial sites. Yet, from our small timeseries for Sao Paulo a couple of aspects are notable. First, the fine mode optical thickness $\tau_{a,f}$ dominates over the coarse mode $\tau_{a,c}$ which is characteristic of small biomass burning aerosols. Second, the peaks in the small mode appear to be during the months of August to October, the dry season when biomass burning is at its greatest. Finally, for our desert dust site, Kuwait University, also limited in temporal coverage, we see that the spring-summer months are dominated by the coarse mode optical thickness $\tau_{a,c}$ when dust outbreaks are common. This site will also have urban-industrial aerosols from Kuwait City and possibly oceanic aerosols from the Persian Gulf which is apparent from the small mode

optical thickness $\tau_{a,f}$ that seems to have a mean of around 0.2 (urban-industrial) and a large mode minimum of around 0.1 (oceanic). Unfortunately there were only a limited number of co-locations with desert dust sites away from populated areas.

Figures 6.28 and 6.29 show timeseries of fine mode mean radius $r_{g,f}$ and coarse mode mean radius $r_{g,c}$. Consistent with our scatter plots, the fine mode differences between AERONET and our retrieval are small for all the aerosol types except desert dust. Our retrieval results track the AERONET results well but spurious differences are indicative of the scatter observed in the corresponding scatter plots. The coarse mode differences are larger but as in the corresponding scatter plots the results for desert dust are better due to the larger coarse mode signal. This can also be seen in the coarse mode differences for Kanpur which are smaller during the pre-monsoon dust outbreaks. Larger fine mode sizes at Beijing correlate with larger fine mode optical thickness values due to increases in local urban-industrial emissions and therefore newer and larger aerosols. This is also apparent for the coarse mode indicating that during heavy emission periods urban-industrial emissions contribute more to the coarse mode. For Sao Paulo (biomass burning) peaks in the fine mode size correlate with peaks in the fine mode optical thickness (burning season), again, because of increased local emissions, resulting in newer aerosols with a larger mean radius. At Kuwait University (desert dust) a peak in the fine mode corresponds to a minimum in the large mode optical thickness and therefore periods of minimum dust loading which may be indicative to an increase in urban-industrial emissions during this period.

Figure 6.30 shows timeseries of the real part of the index of refraction m_r. As with the scatter plots it is apparent that m_r is not retrieved with the same accuracy as the τ_a and r_g. A small negative bias, especially for desert dust is visible which is a result of our retrieval tending toward the a priori value of 1.47. Note that the maximum possible value of 1.6 for AERONET is clearly visible in the plots for mixed and urban-industrial aerosols. In the plots for Kanpur, Beijing, and Kuwait University larger values of m_r correspond with the larger values of the $\tau_{a,c}$ and therefore to desert dust outbreaks. As already discussed, the larger errors in our retrieval results are due to lack of information in our measurements about m_r whereas AERONET's multiangle measurement provide significantly more information, in particular about the aerosol single scattering phase function, to more accurately retrieve m_r.

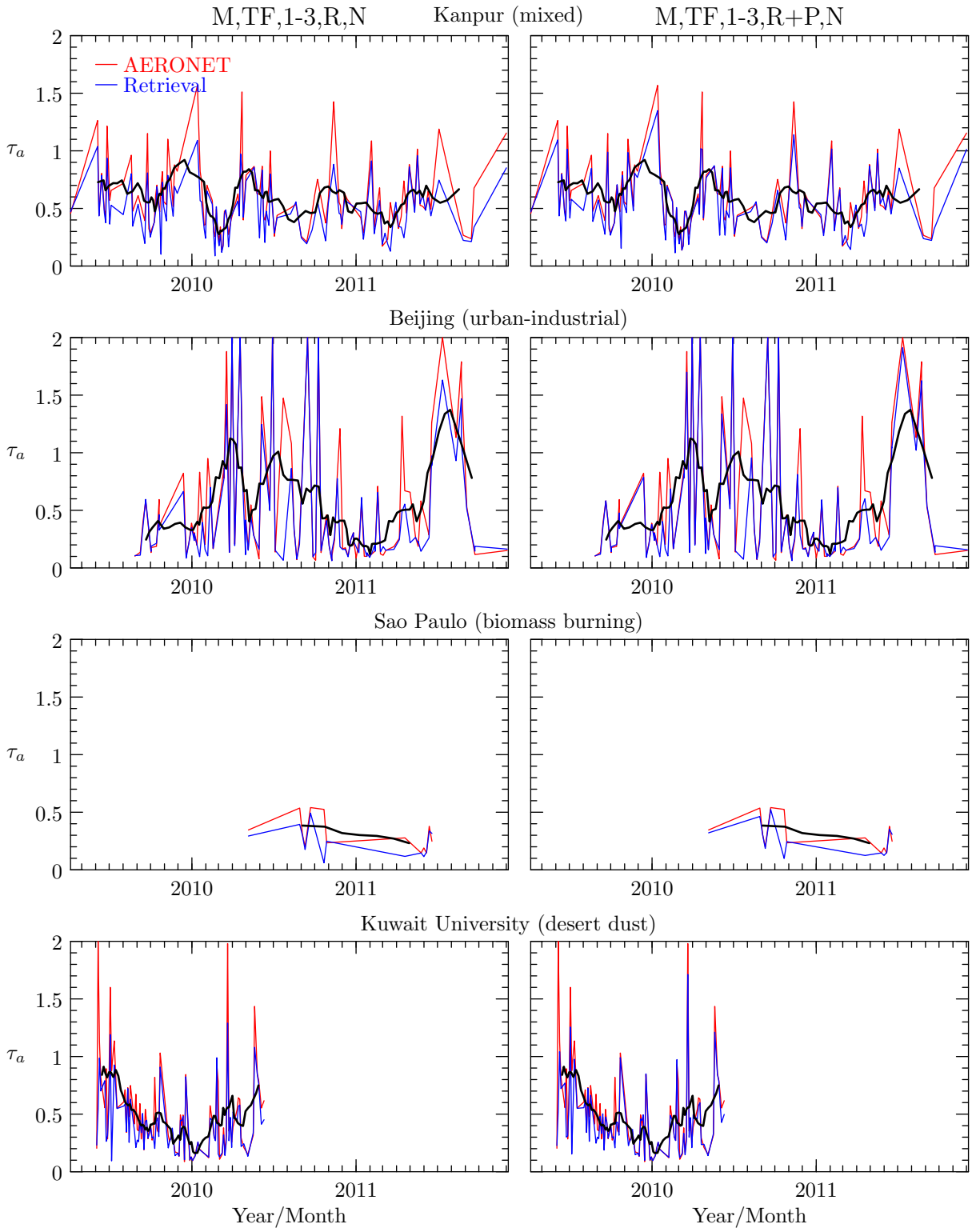

Figure 6.25: Timeseries of total optical thickness $\tau_a(0.55)$ for the AERONET retrieval (red), our retrieval (blue), and seven-point Laplacian smoothing of the AERONET timeseries (black), for our four aerosol type specific example sites (row-wise), and for our two measurement scenarios including TANSO-FTS measurements (column-wise).

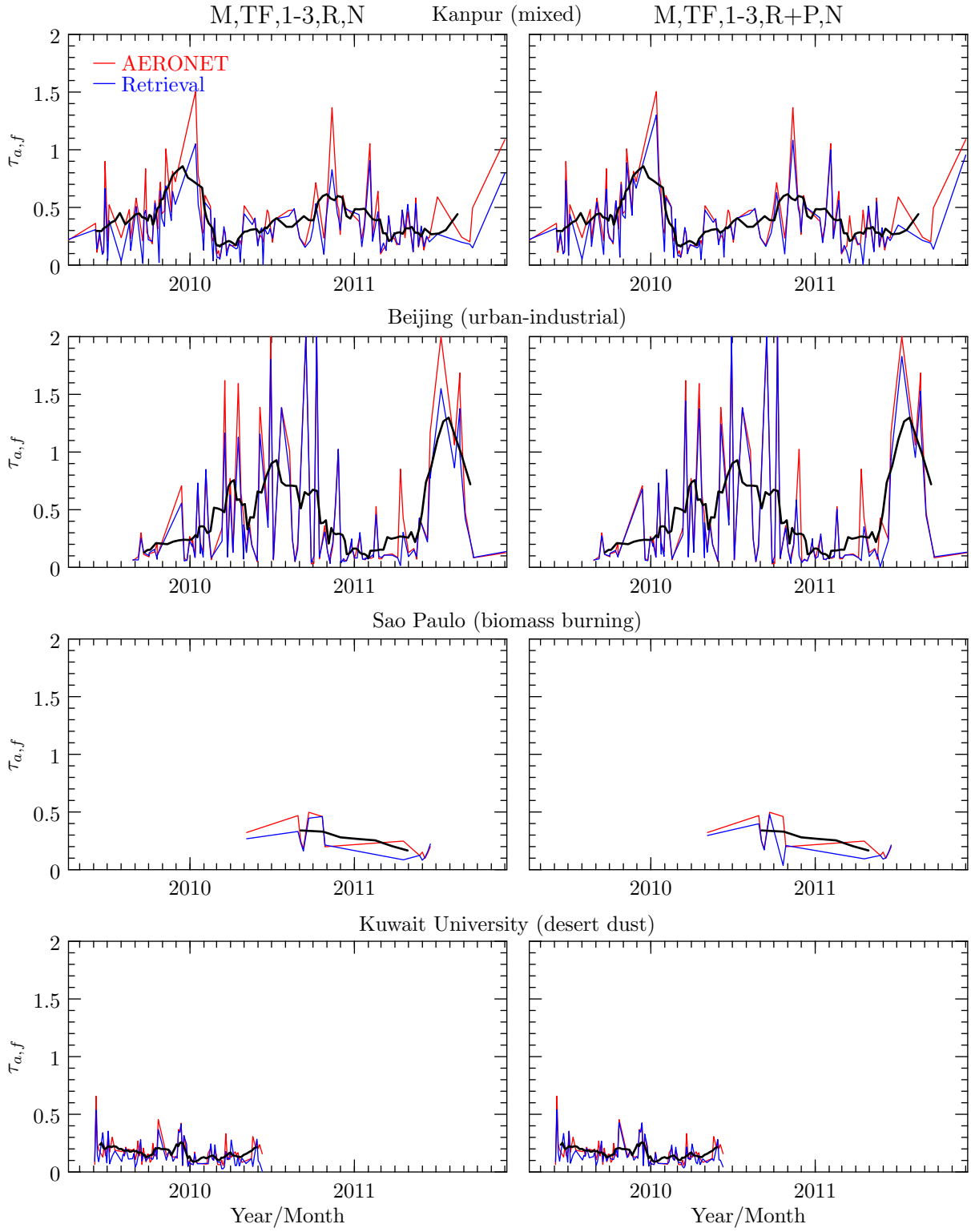

Figure 6.26: Same as figure 6.25 but for the fine mode optical thickness $\tau_{a,f}(0.55)$.

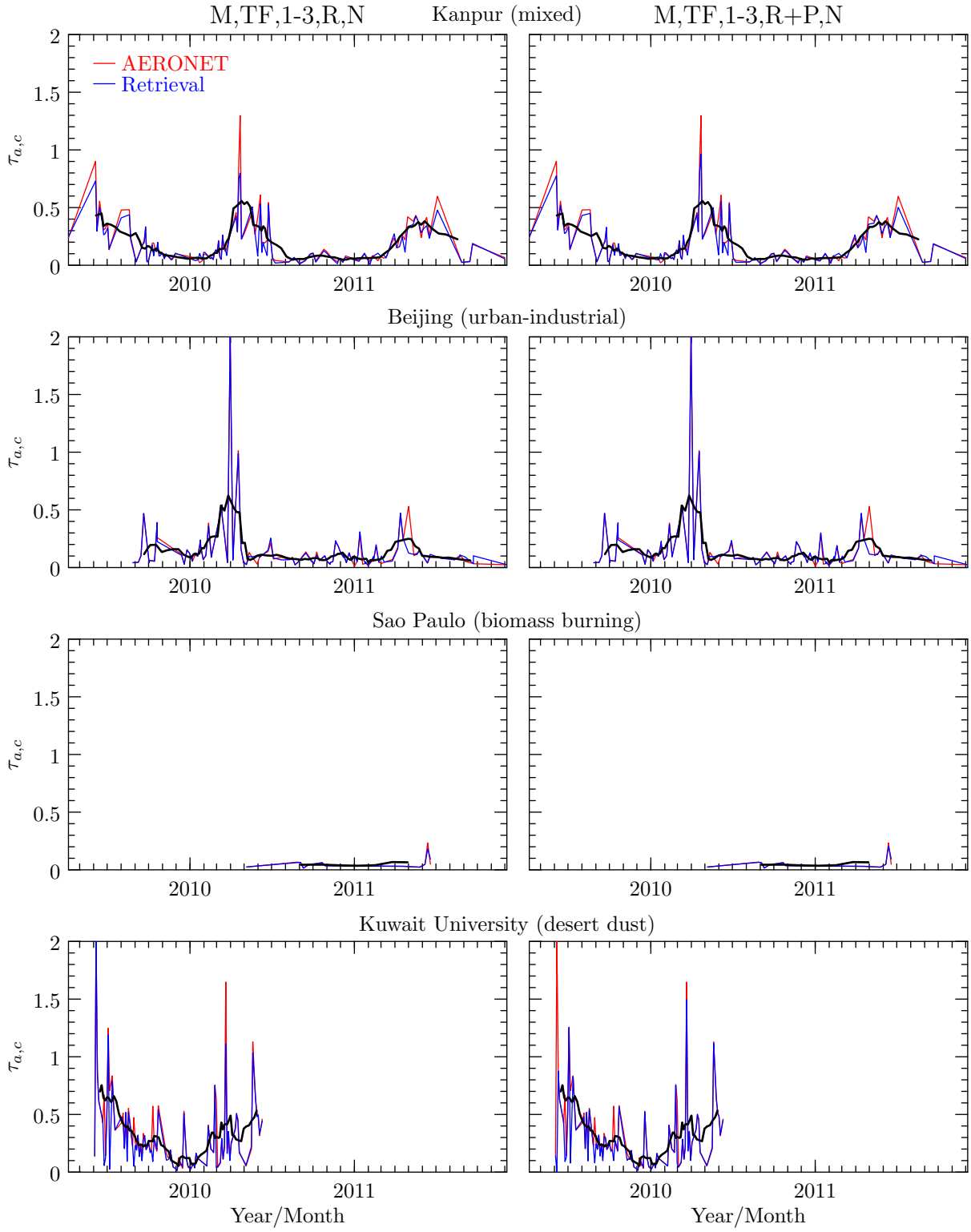

Figure 6.27: Same as figure 6.25 but for the coarse mode optical thickness $\tau_{a,c}(0.55)$.

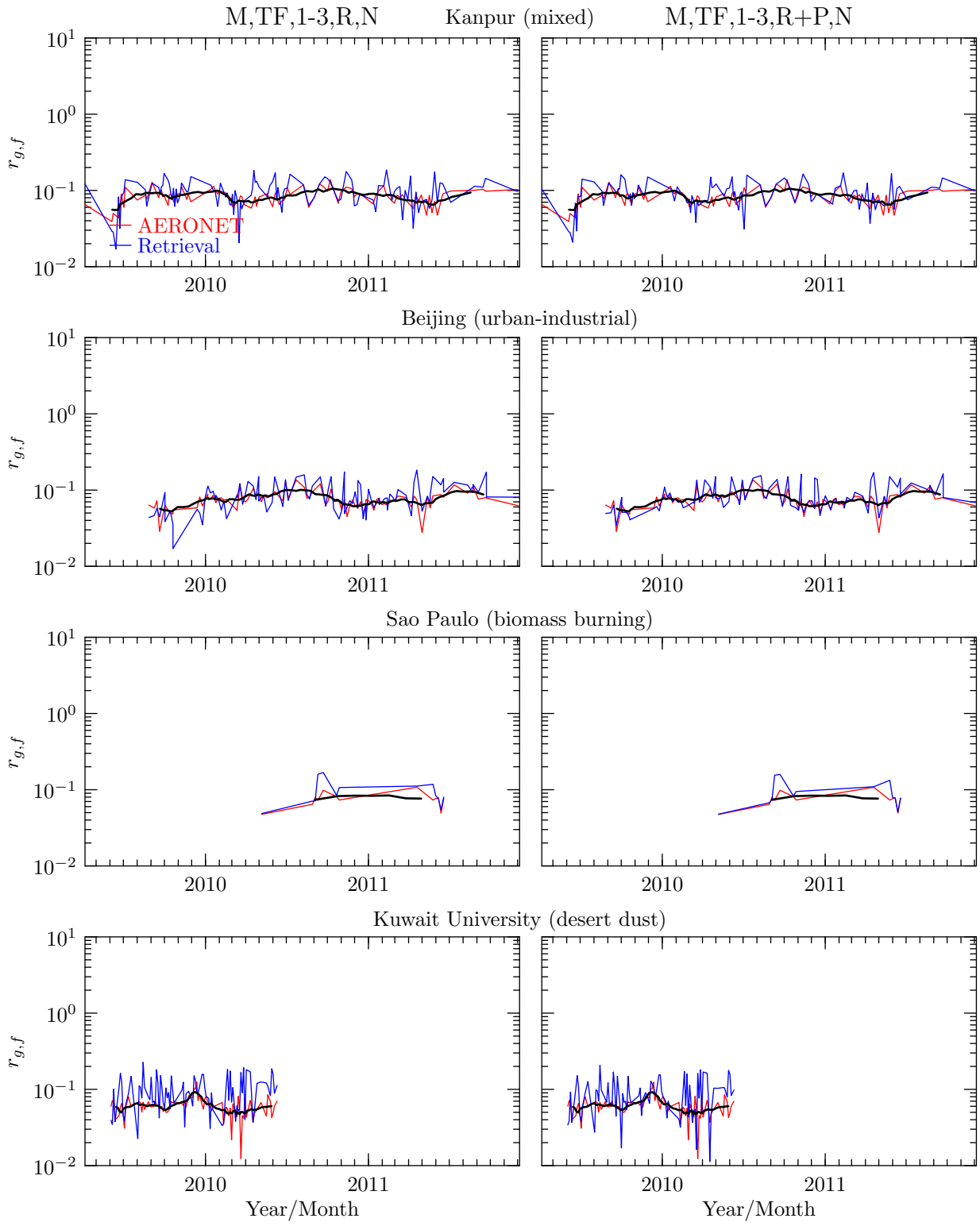

Figure 6.28: Same as figure 6.25 but for the fine mode mean particle radius $r_{g,f}$.

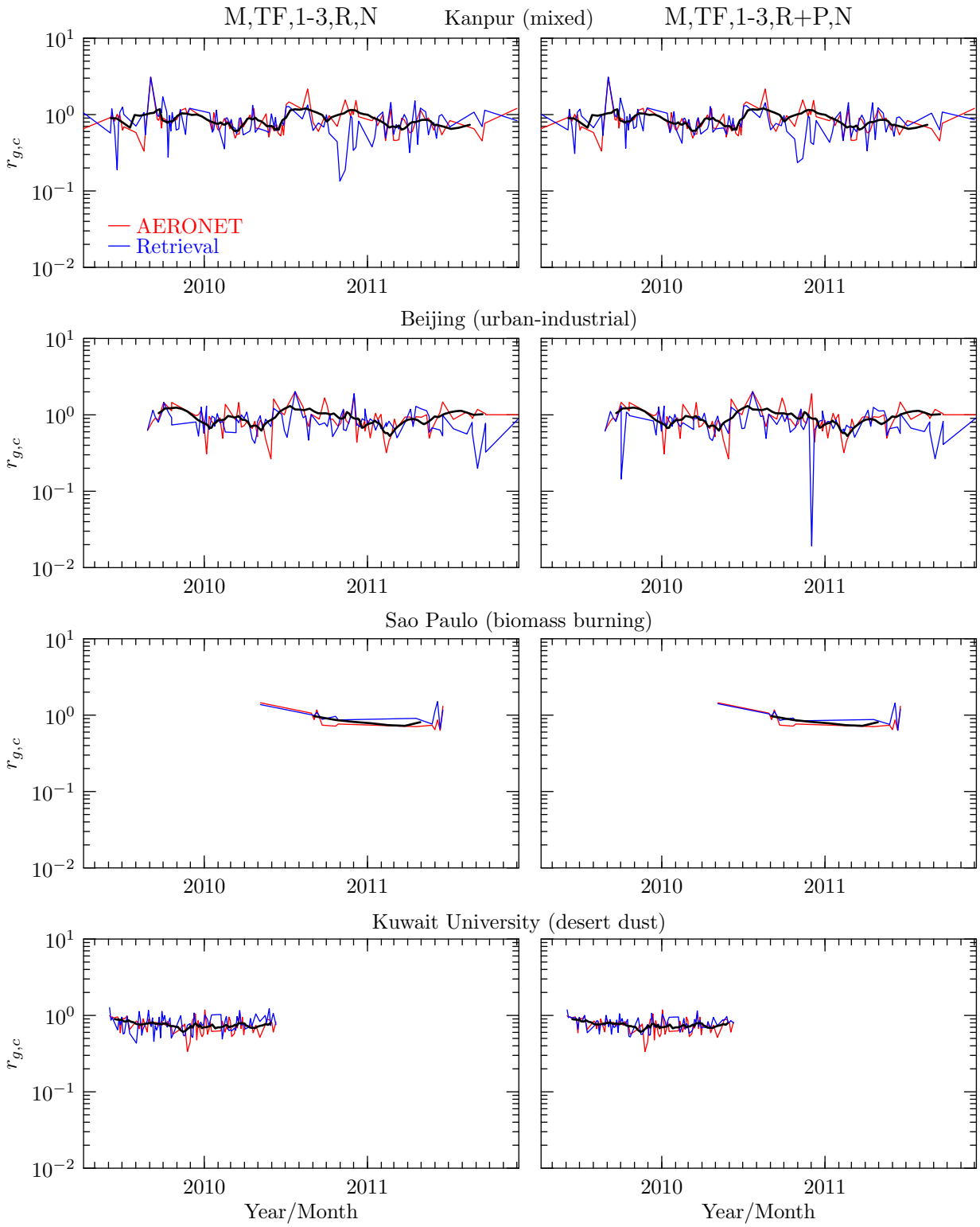

Figure 6.29: Same as figure 6.25 but for the coarse mode mean particle radius $r_{g,c}$.

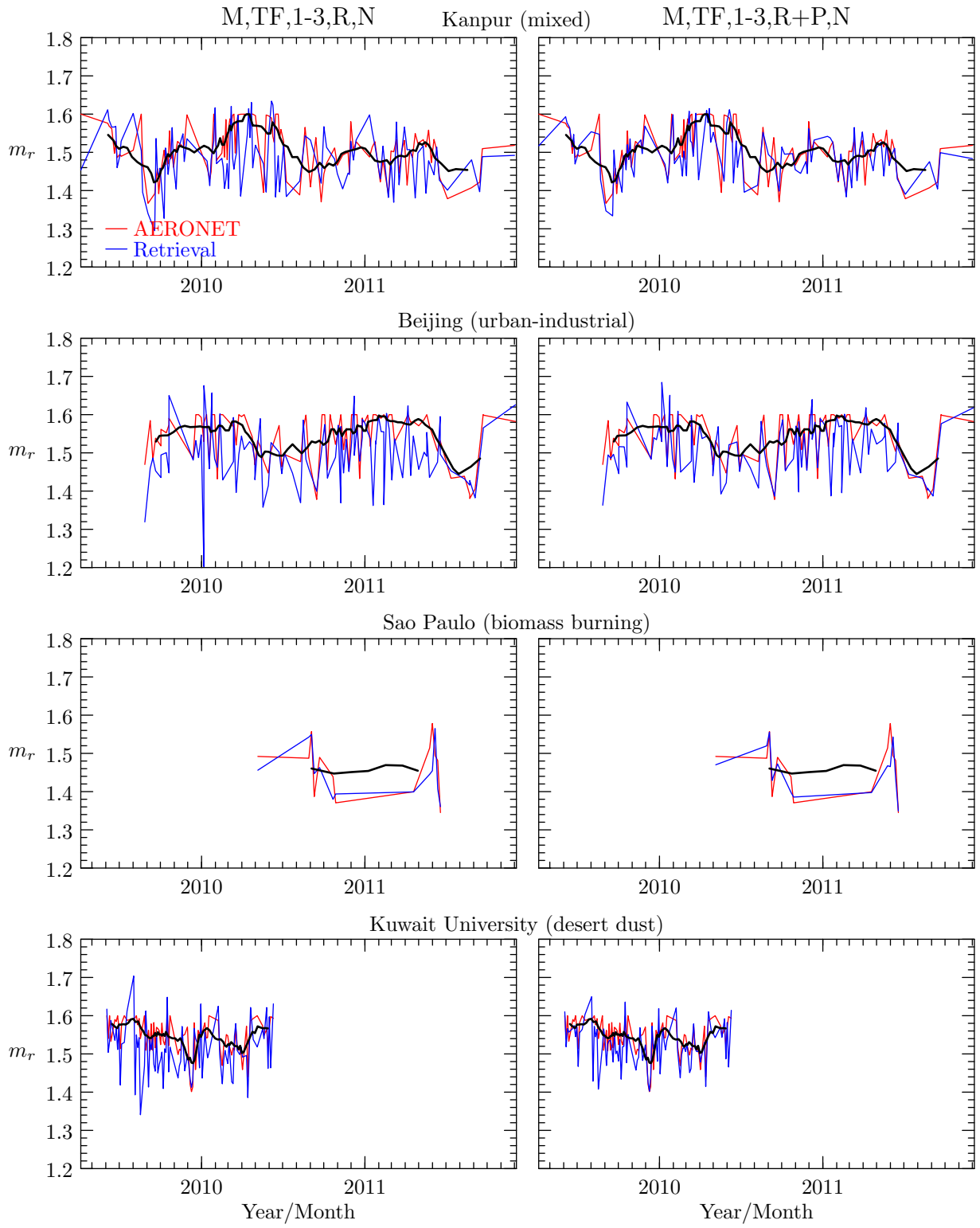

Figure 6.30: Same as figure 6.25 but for the modally averaged real part of the index of refraction $m_r(0.55)$.

Figure 6.31 shows timeseries of the imaginary part of the index of refraction m_i. The retrieval of m_i seems remarkably good in these cases but one must remember that the y-axis is in log space. There is a clear negative bias in all but the desert dust timeseries due to the tendency toward the a priori value of 0.002. Overall, the peaks in m_i tend to correlate with peaks in all three aerosol types studied, including urban-industrial aerosol (Kanpur and Beijing), desert dust aerosol (Kanpur, Beijing, and Kuwait University), and biomass burning aerosol (Sao Paulo). This indicates that these aerosols have larger values of m_i than the background aerosols typical of the locations studied.

Figure 6.32 shows timeseries of the single scattering albedo ω_a. Peaks in ω_a in both the plots for Kanpur and Beijing correspond with the peaks in urban-industrial aerosol loading indicating that for these particular cases non-absorbing sulfates dominate over more absorbing black carbon. For biomass burning aerosols smaller values of ω_a are associated with the biomass burning season as expected due again to the larger presence of black carbon and organic carbon components. For desert dust, ω_a peaks between the loading minimums and maximums. As already mentioned the loading minimum may be characterized mostly by urban-industrial aerosols which, in general, have lower values of ω_a than desert dust. The peaks are most likely due to an increasing in the less absorbing desert dust before loading increases to the point where aerosol/surface interaction begins to increase absorption again.

6.5.3 Spectral comparisons

In this section we demonstrate how well our spectral fits match the multispectral parameters retrieved by AERONET. We do this by computing the values of our spectrally dependent parameters at the four standard AERONET wavelengths of 0.440, 0.670, 0.870, and 1.020 μm, the wavelengths at which the AERONET inversion results are reported. This is done for each spectral parameter: τ_a, $\tau_{a,f}$, $\tau_{a,c}$, m_r, m_i, and ω_a; for each of the same four specific AERONET sites presented in the last section: Kanpur, India (mixed); Beijing, China (urban-industrial); Sao Paulo, Brazil (biomass burning); and Kuwait University, Kuwait City, Kuwait (desert dust); and for each of our two primary measurement scenarios (M,TF,1-3,R,N and M,TF,1-3,R+P,N). The plots are organized into parameter specific figures as in the last section. Within each plot three retrieval cases are presented: the retrieval with an optical thickness $\tau_a(0.55)$ closest to the mean $\tau_a(0.55)$ (green) for all retrievals for that site, the retrieval with a $\tau_a(0.55)$ closest to half the mean $\tau_a(0.55)$ (red), and

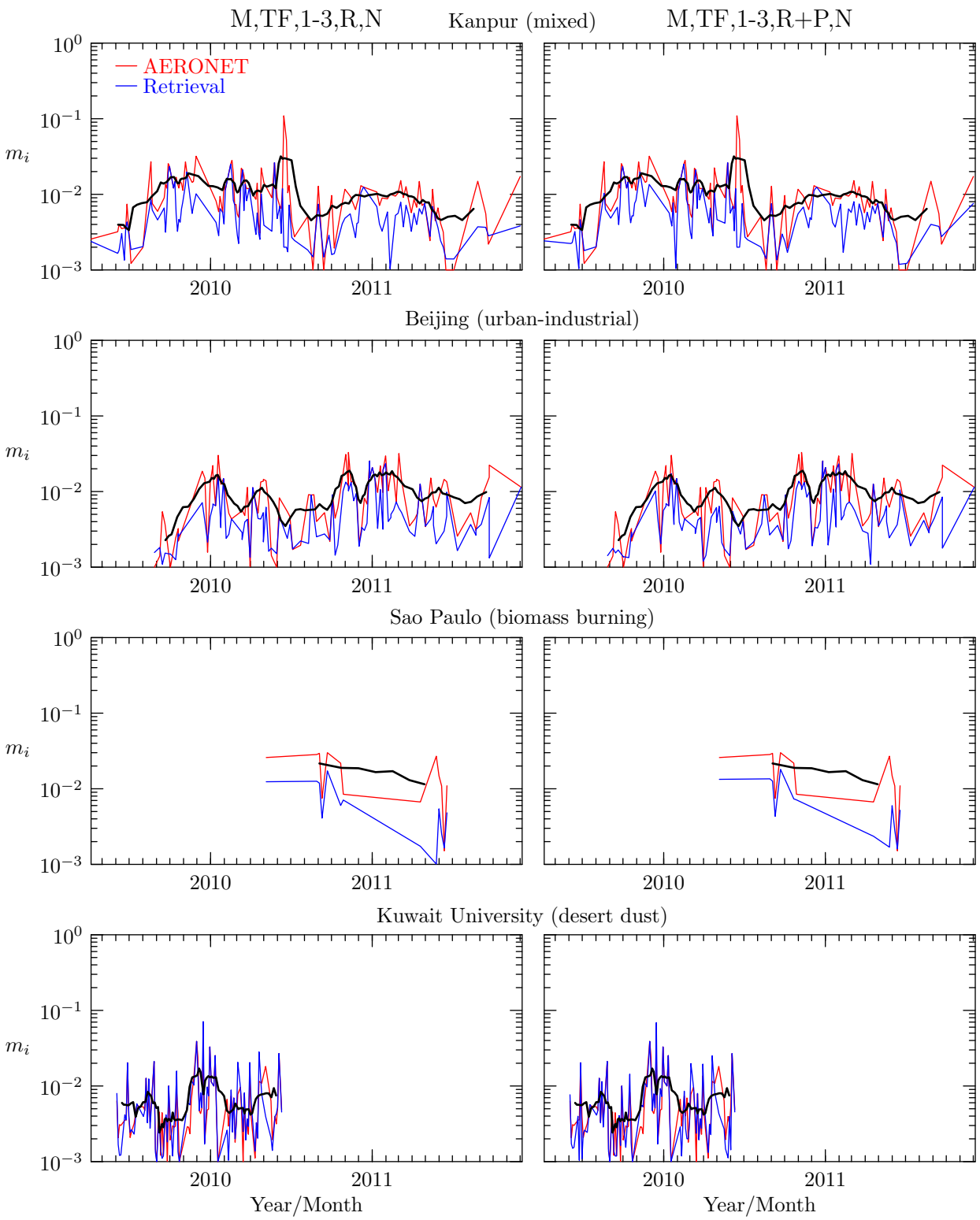

Figure 6.31: Same as figure 6.25 but for the modally averaged imaginary part of the index of refraction $m_i(0.55)$.

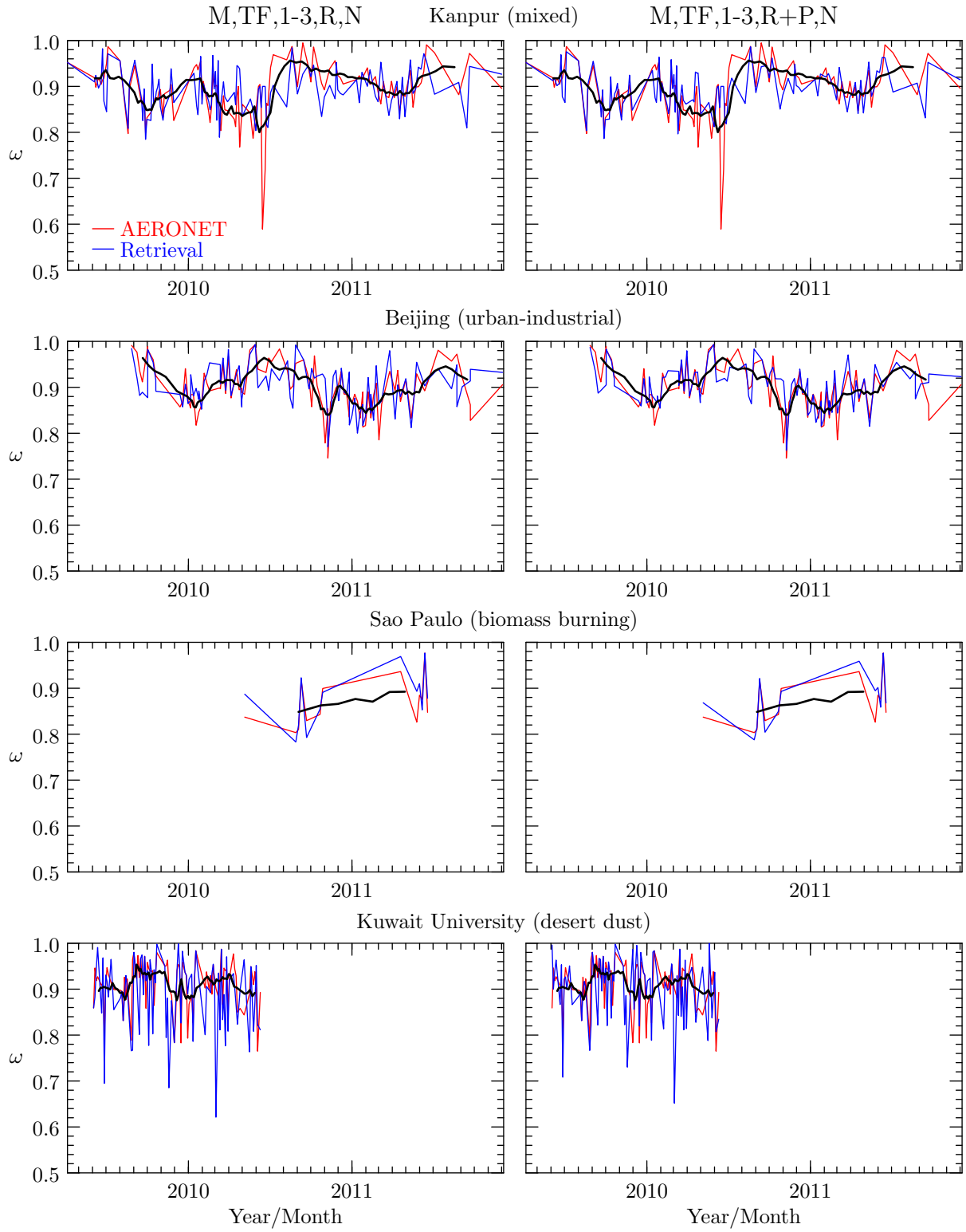

Figure 6.32: Same as figure 6.25 but for the modally averaged single scattering albedo $\omega_a(0.55)$.

the retrieval with a $\tau_a(0.55)$ closest to twice the mean $\tau_a(0.55)$ (blue). For each of these cases both the AERONET (solid line) and our retrieval (dashed line) results are plotted. In this way, variation in the quantity of the retrieved spectral fit parameters with $\tau_a(0.55)$ and therefore aerosol signal can be assessed.

Figures 6.33 to 6.35 show values for τ_a, $\tau_{a,f}$, and $\tau_{a,c}$, respectively. Remember that optical thickness is a derived quantity and therefore depends on the spectral fits of both the real and imaginary index of refraction. It is clear that our retrieval results spectrally track the AERONET results well. The spectral variations are relatively smooth indicating that linear interpolation would be appropriate for other wavelengths and that extrapolation may work for the entire solar wavelength range. The difference between AERONET and our retrieval for the total optical thickness is somewhat dependent on the optical thickness itself with larger deviations at larger optical thicknesses. Figures 6.36 and 6.37 show values for m_r and m_i, respectively. The differences in the spectral variation between AERONET and our retrieval for these parameters is more variable than for τ_a. Since τ_a is derived from these values and other values it is apparent that these variations are smoothed out in the derived computations. This can also be seen in the results for ω_a in figure 6.38. Like τ_a, ω_a is derived from, among other quantities, m_r and m_i, and like τ_a the spectral deviations of the retrieval from AERONET are smoother than those of m_r and m_i.

6.5.4 Retrieval error

In this section we present histograms of both the estimated error (the square root of the diagonal elements of the posteriori error covariance matrix $\hat{\mathbf{S}}$) and the actual error from the validation. Every retrieval system should have a self contained estimation of the retrieval error independent of any outside validation data. This means that when the retrieval is validated like we have done in the past three sections we must also validate the estimated error which is what we do in this section. The presentation is done for all sites and for each of the four different aerosol types, for our two MODIS + TANSO-FTS measurement scenarios (M,TF,1-3,R,N and M,TF,1-3,R+P,N), and for the parameters $\tau_{a,f}$, $\tau_{a,c}$, $r_{g,f}$, $r_{g,c}$, σ_f, σ_c, m_r, m_i, and ω_a. We present not the absolute magnitudes of the errors but the normalized error fractions given by

$$\varepsilon_\sigma(x) = \frac{\sigma(x)}{x} \tag{6.27}$$

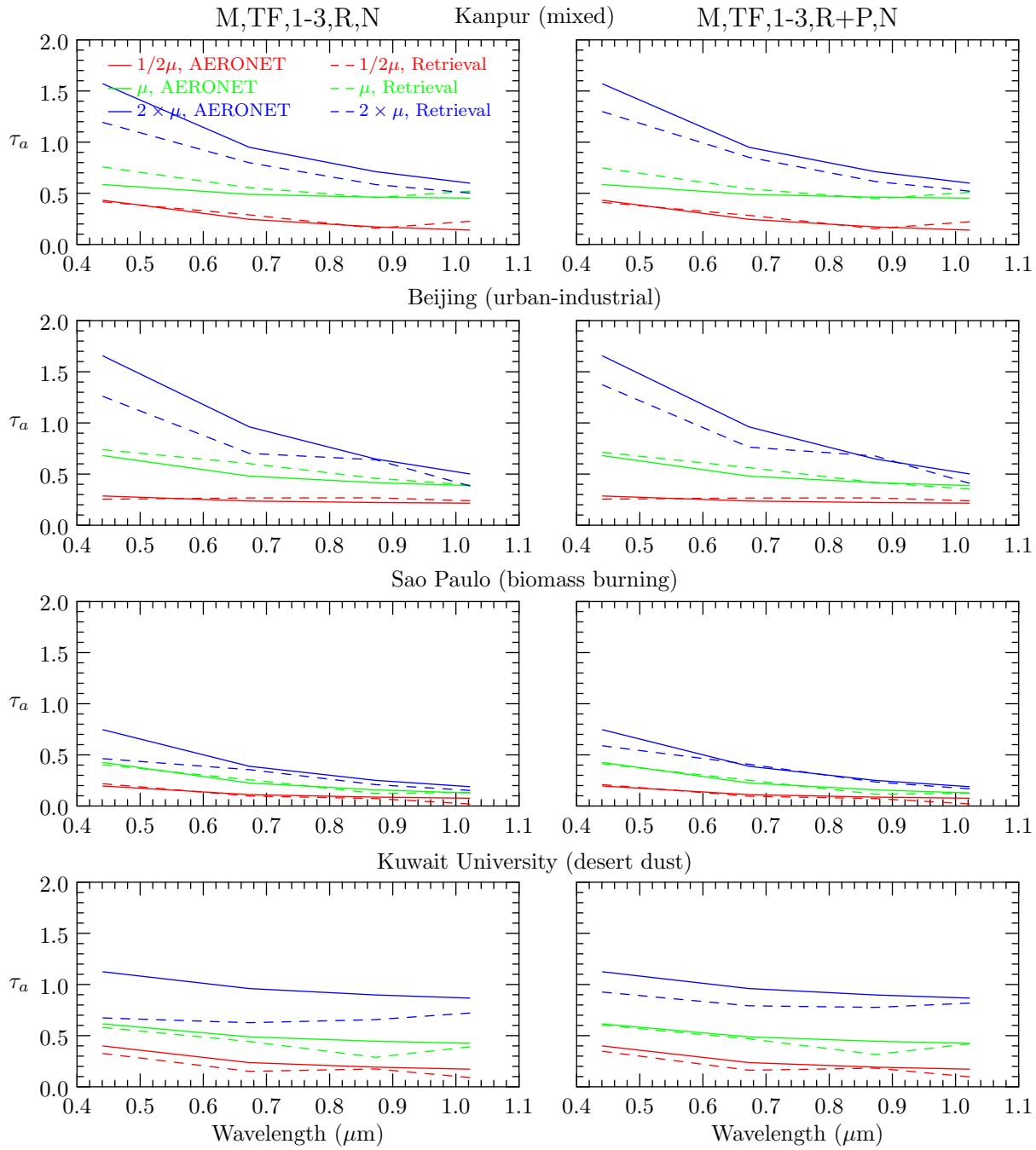

Figure 6.33: Total optical thickness $\tau_a(\lambda)$ as a function of wavelength for the AERONET retrieval (solid) and our retrieval (dashed), for our two measurement scenarios including TANSO-FTS measurements, and for our four aerosol type specific example sites. Values are given for three cases: the retrieval with an optical thickness $\tau_a(0.55)$ closest to the mean $\tau_a(0.55)$ (green) for all retrievals for that site, the retrieval with a $\tau_a(0.55)$ closest to half the mean $\tau_a(0.55)$ (red), and the retrieval with a $\tau_a(0.55)$ closest to twice the mean $\tau_a(0.55)$ (blue).

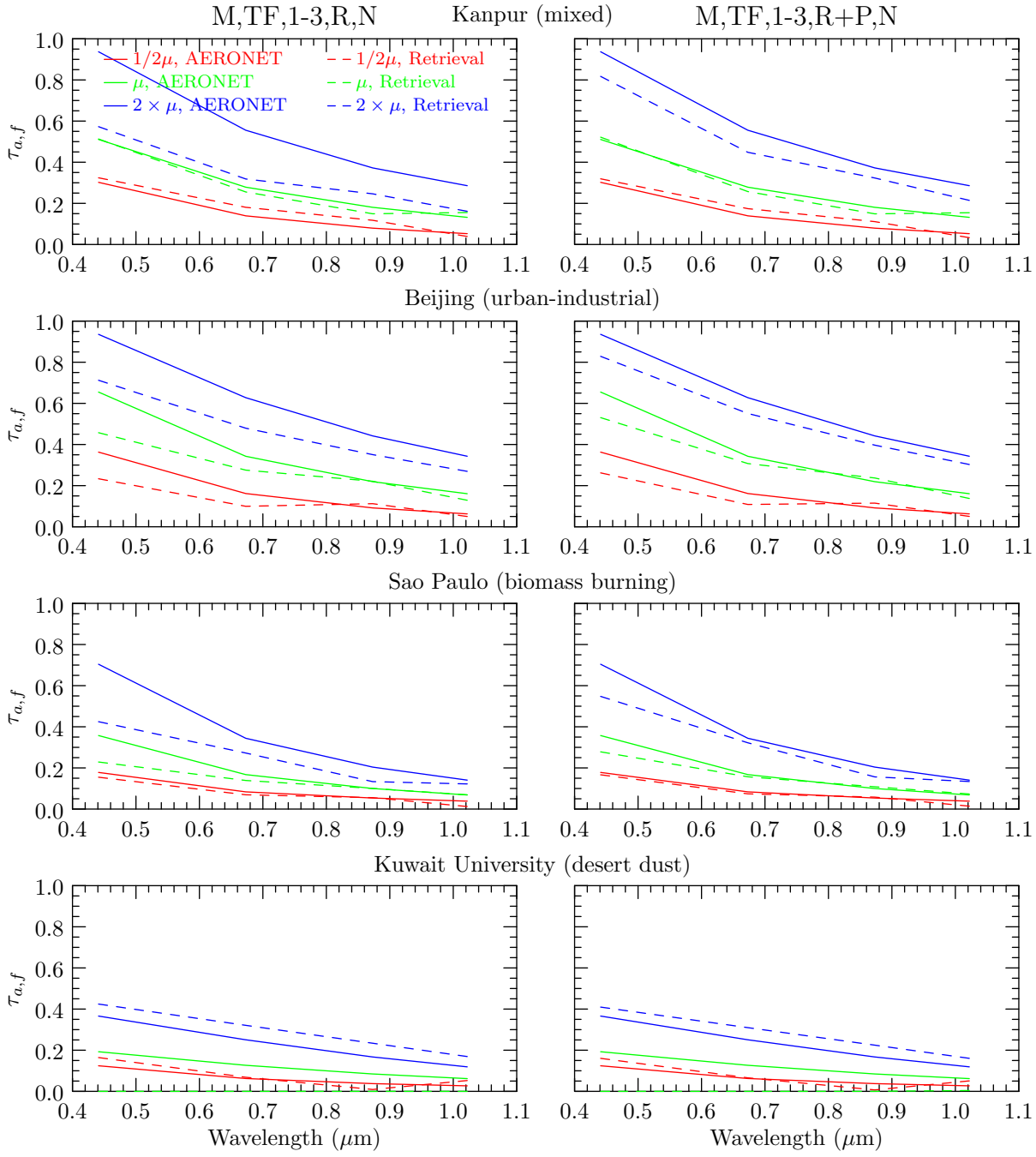

Figure 6.34: Same as figure 6.33 but for the fine mode optical thickness $\tau_{a,f}(\lambda)$.

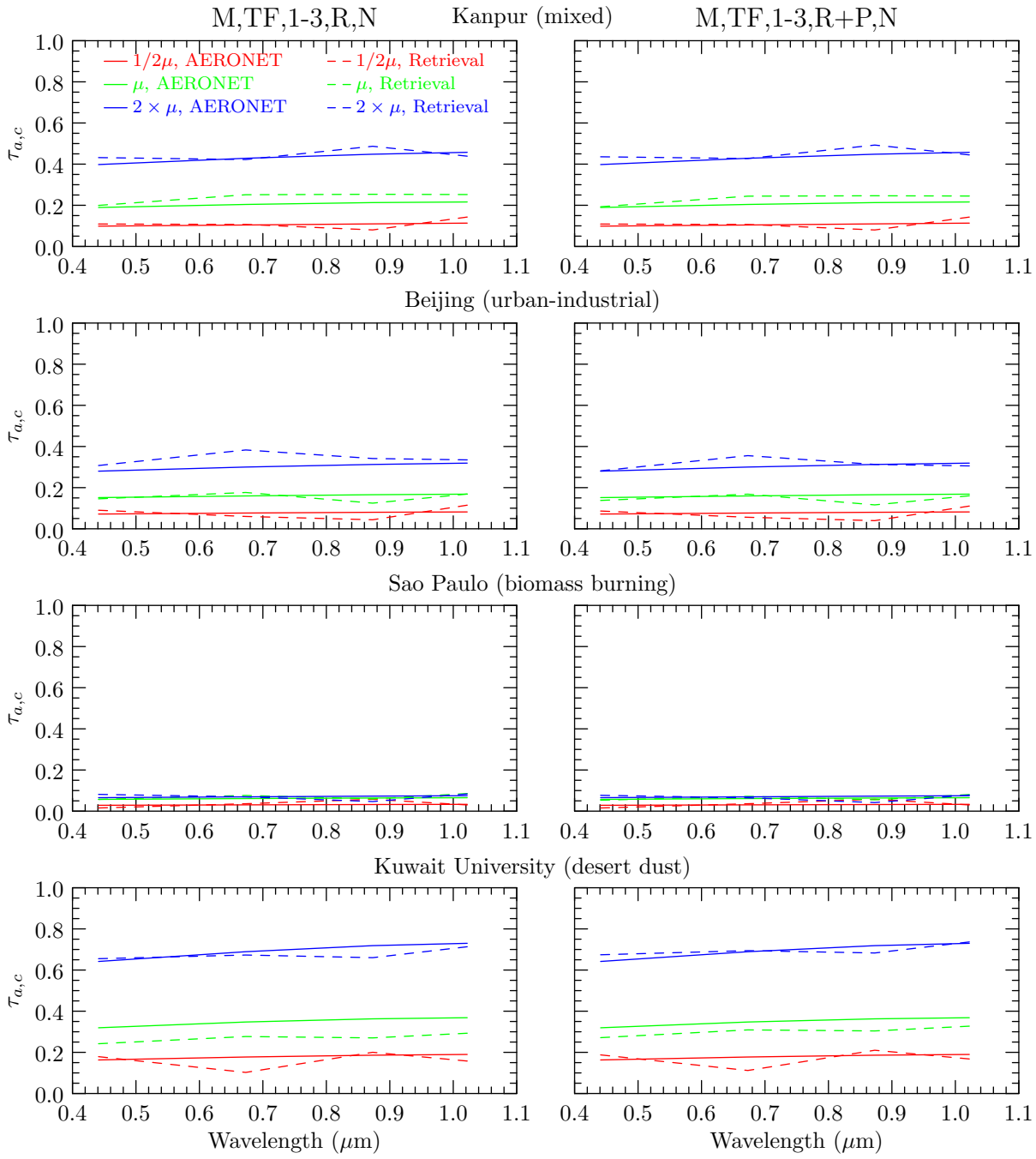

Figure 6.35: Same as figure 6.33 but for the coarse mode optical thickness $\tau_{a,c}(\lambda)$.

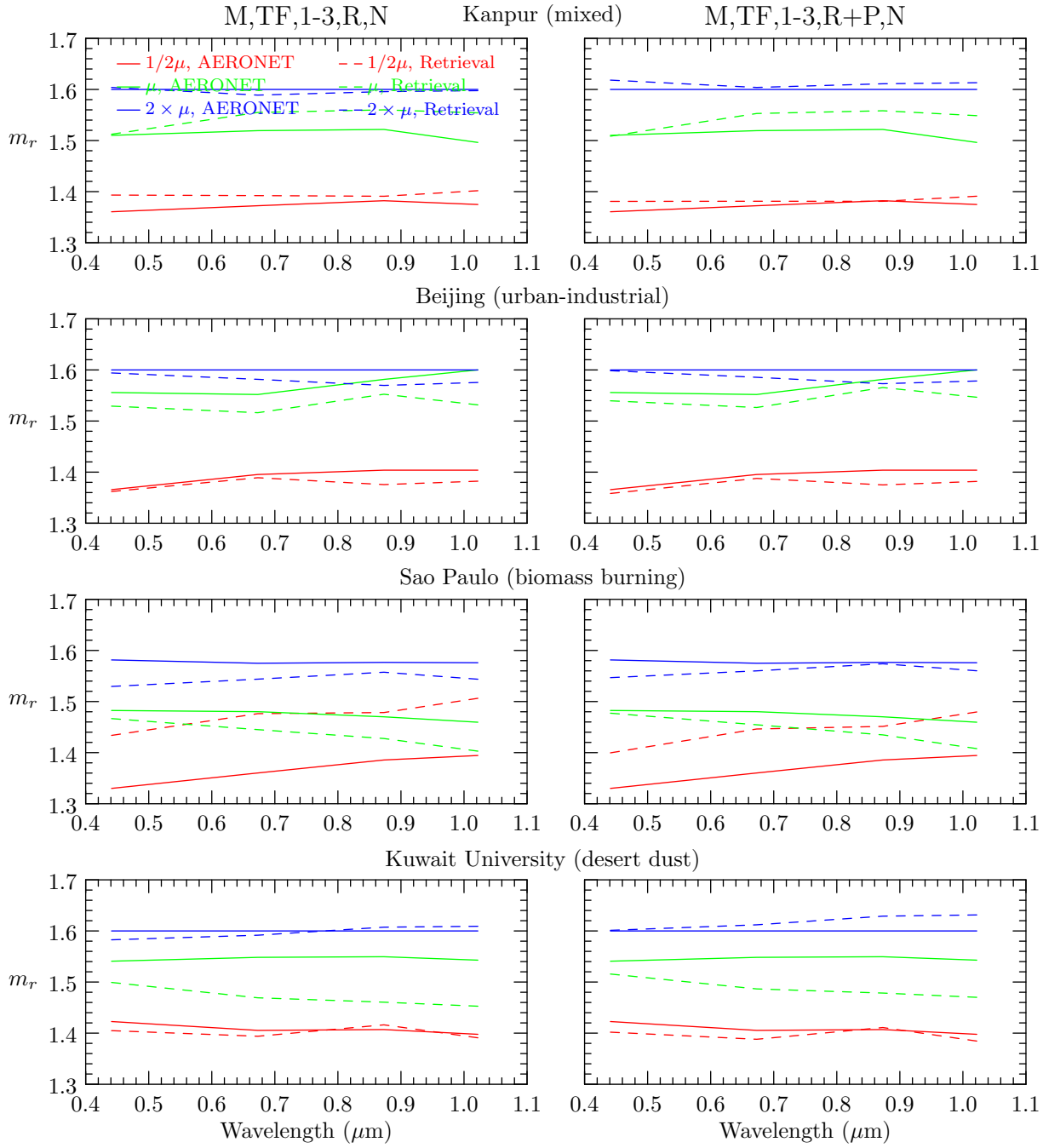

Figure 6.36: Same as figure 6.33 but for the modally averaged real part of the index of refraction $m_r(\lambda)$.

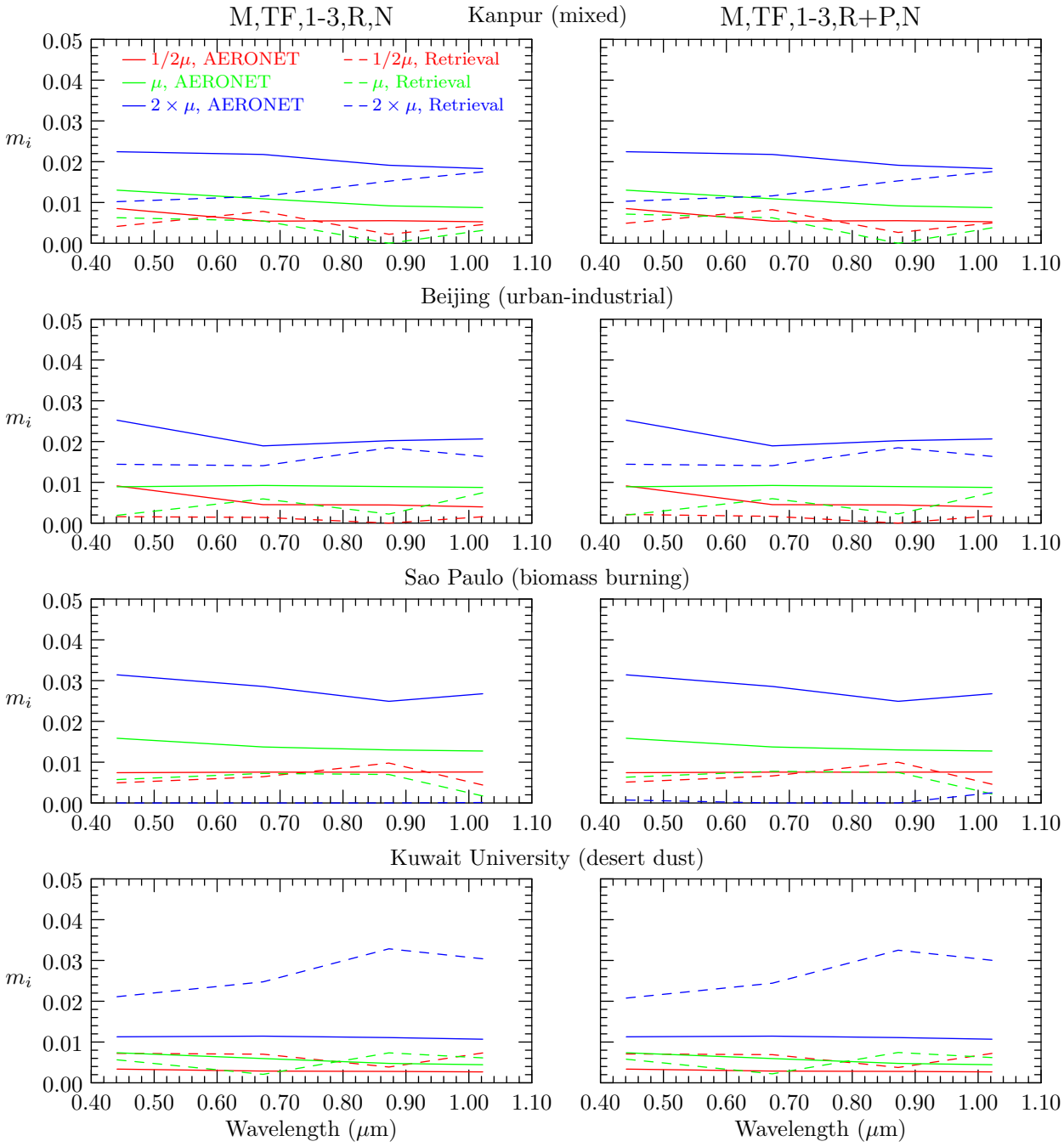

Figure 6.37: Same as figure 6.33 but for the modally averaged imaginary part of the index of refraction $m_i(\lambda)$.

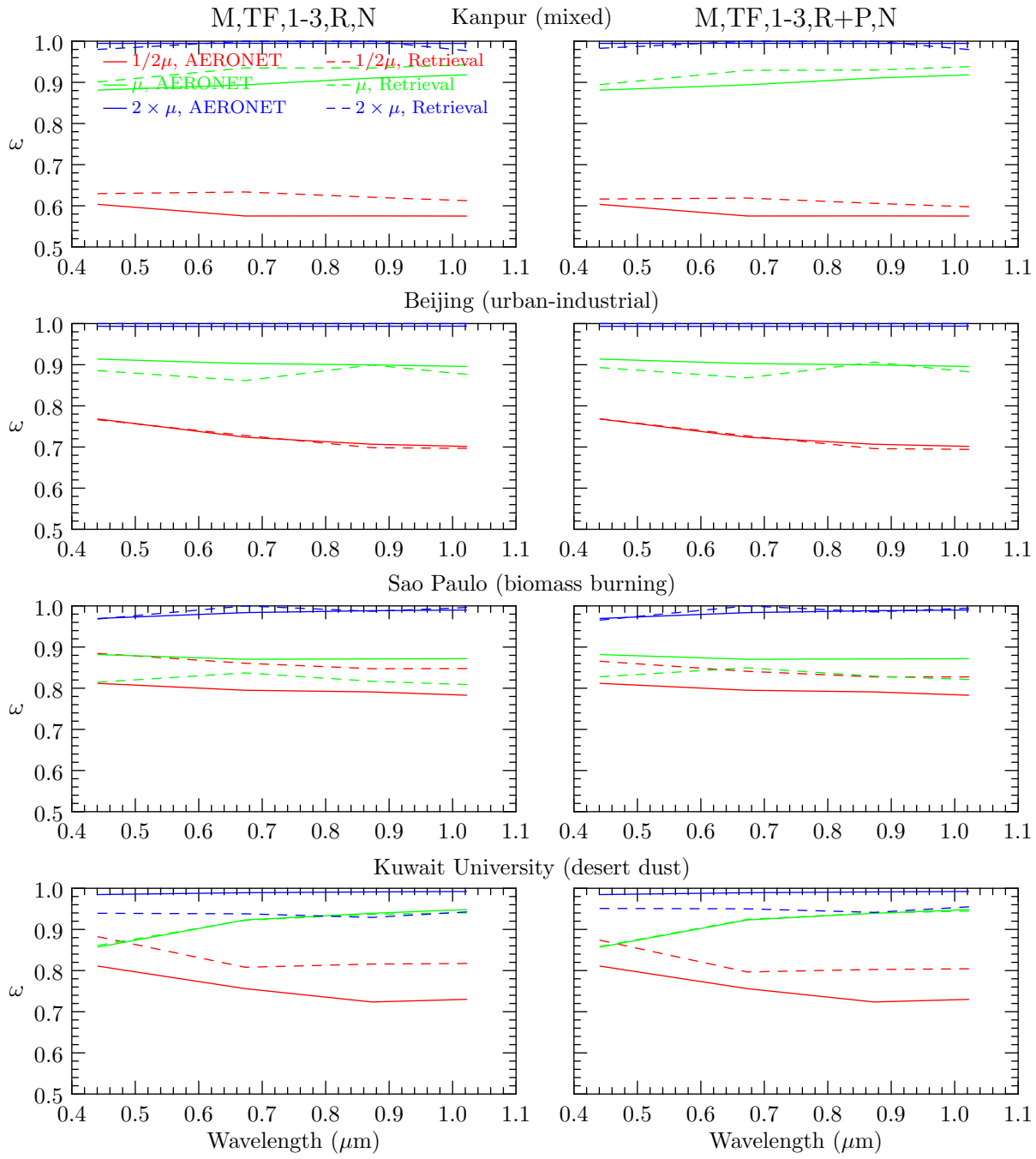

Figure 6.38: Same as figure 6.33 but for the modally averaged single scattering albedo $\omega_a(\lambda)$.

and

$$\varepsilon_\delta(x) = \frac{\delta(x)}{x}, \tag{6.28}$$

where $\sigma(x)$ is the estimated standard deviation of parameter x obtained either directly from square roots of the diagonal elements of $\hat{\mathbf{S}}$ or derived from equation 6.25 and $\delta(x)$ is the actual error in parameter x from x(Retrieval) $-$ x(AERONET).

Figure 6.39 shows histograms of estimated error (light red) and actual error (light blue) for all the retrievals at all sites while figures 6.40 through 6.43 show histograms for retrievals at sites classified as mixed, urban-industrial, biomass burning, and desert dust, respectively. Histograms are presented in pairs, where the histogram on the left is for M,TF,1-3,R,N and the histogram on the right is for M,TF,1-3,R+P,N.

It is apparent that the estimated error distributions are tighter than the actual error distributions while in some cases there is a significant offset between the distributions. This broadening in the actual error distribution and the offset between distributions indicates any of several issues including: (1) some random errors in the inputs are not accounted for in the retrieval algorithm, (2) systematic bias errors exist in the inputs that are significant enough to influence the retrieval error, (3) significant errors in the retrieval process exist, such as errors due to non-uniqueness and lack of regularization, and/or (4) errors in the AERONET retrieval due to the first three reasons just given. It is also interesting that the error distributions match up better for cases that we know are well retrieved including $\tau_{a,f}$, $\tau_{a,c}$, and $r_{g,f}$. The reason for this is that the estimated error is calculated around linearization of the retrieved state and as such will diverge in representativeness with divergence from the true state resulting in a degradation in the accuracy of the error estimation. The actual error distributions for m_i and ω_a are both bimodal indicating that a particular aerosol type is subject to a larger error. This characteristic will be explored further as we look at the errors for the individual aerosol types.

The errors for the mixed aerosol type in figure 6.40 are very similar to that for all sites as we would expect as the mixed aerosol type contains aerosols of all types. The errors for the urban-industrial aerosol type in figure 6.41 for the well retrieved parameters ($\tau_{a,f}$, $\tau_{a,c}$, and $r_{g,f}$) are in general tighter than that for mixed aerosol. This result is not surprising after our analysis of the scatter plots. The exception to this is that of $r_{g,c}$, where the distribution of the estimated error is

broader (the distribution of the actual error is already rather broad), which is due to the relatively small coarse mode loadings in urban-industrial aerosol. The bimodality seen in the estimated error distributions of m_i and ω_a for all sites is apparent in the distributions for urban-industrial sites. The reason for this bimodality is the same as above, where in some cases the coarse mode produces a relatively small signal and therefore large errors. m_i and ω_a are both optical thickness weighted means of small and coarse mode quantities and therefore cases with significant coarse mode errors produce an isolated error distribution mode. For the biomass burning aerosol type in figure 6.42 the estimated error distributions are tighter than that for all sites, for the well retrieved parameters, as with the urban-industrial type, while the actual error distributions for the coarse mode parameters and m_i are much broader. Similar to urban-industrial aerosol, but to a greater degree, biomass burning aerosol has a relatively uninfluential coarse mode, and with this, large coarse mode errors develop. Our retrieval's inability to accurately estimate these large errors is due to the four reasons already discussed. For the desert dust aerosol type in figure 6.43 the actual errors have much broader distributions than that of all the other aerosol types and, as we have seen, for the well retrieved parameters, the estimated error distributions track these actual error distributions well. In contrast, as we have also seen, for the other parameters, that are not so well retrieved, the estimated errors remain relatively tight compared to the actual error.

6.6 Summary and conclusions

We present a satellite-based tropospheric aerosol retrieval system using common multispectral measurements of total reflectance in the visible and near-infrared combined with hyperspectral measurements of total and polarized reflectance in solar molecular absorption bands. Although general enough for use over any surface we focus on the more challenging case of over land. We then present results from this retrieval by validating them against an independent ground-based retrieval.

For the multispectral observations we use the first seven bands of MODIS which are commonly used for aerosol retrievals. For the hyperspectral observations we use measurements made by the GOSAT TANSO-FTS instrument including measurements in the 0.76-μm O_2 A-band and the 1.61- and 2.06-μm CO_2 bands. Several measurement scenarios are investigated including the case of using MODIS only, MODIS + TANSO-FTS O_2 A-band total reflectance, MODIS + TANSO-FTS total

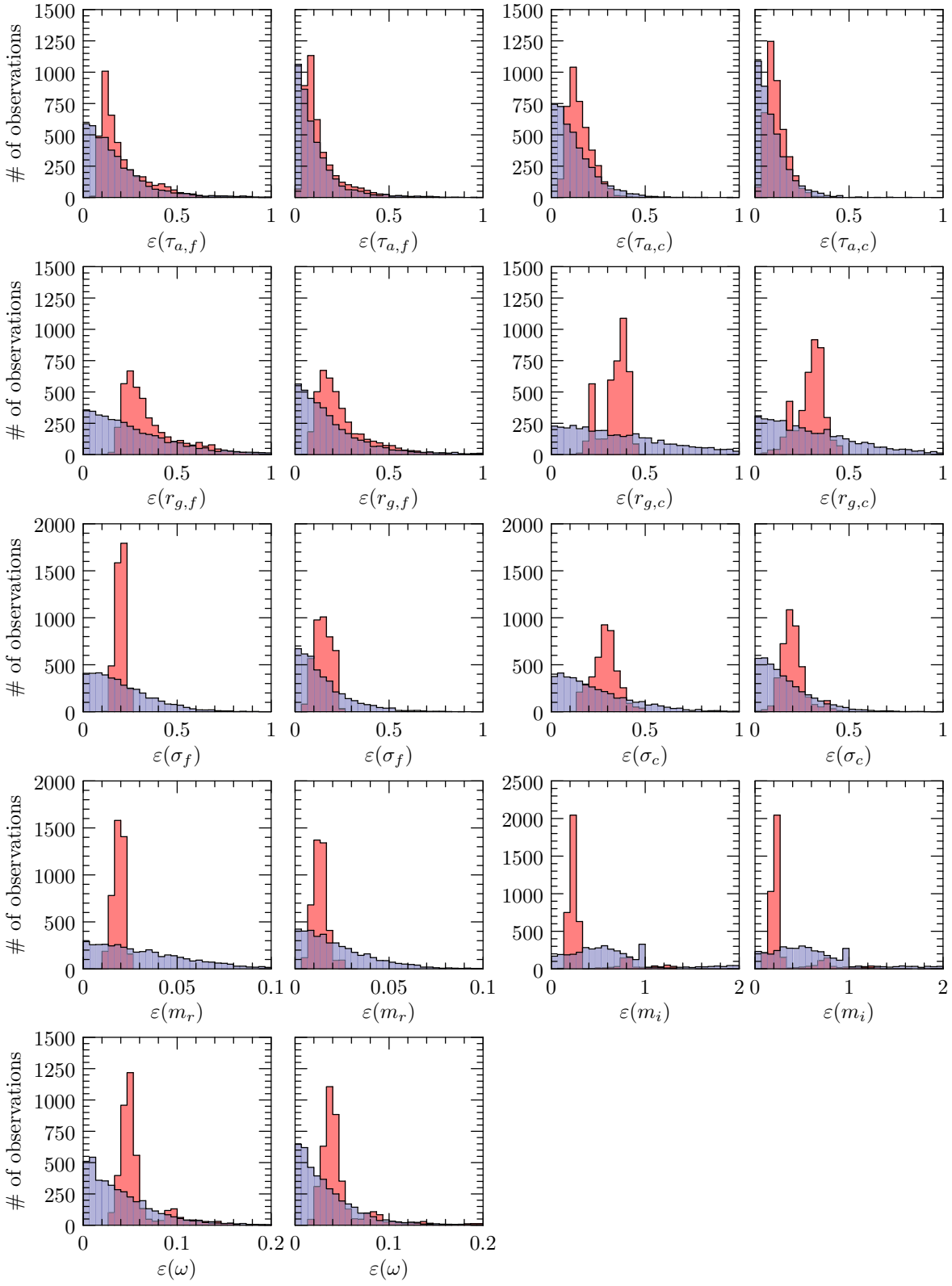

Figure 6.39: Histograms of the normalized error fractions $\varepsilon(x)$ from all sites for the posteriori error from our retrieval $\varepsilon_\sigma(x)$ (light red) and for the actual difference between our retrieval and AERONET $\varepsilon_\delta(x)$ (light blue).

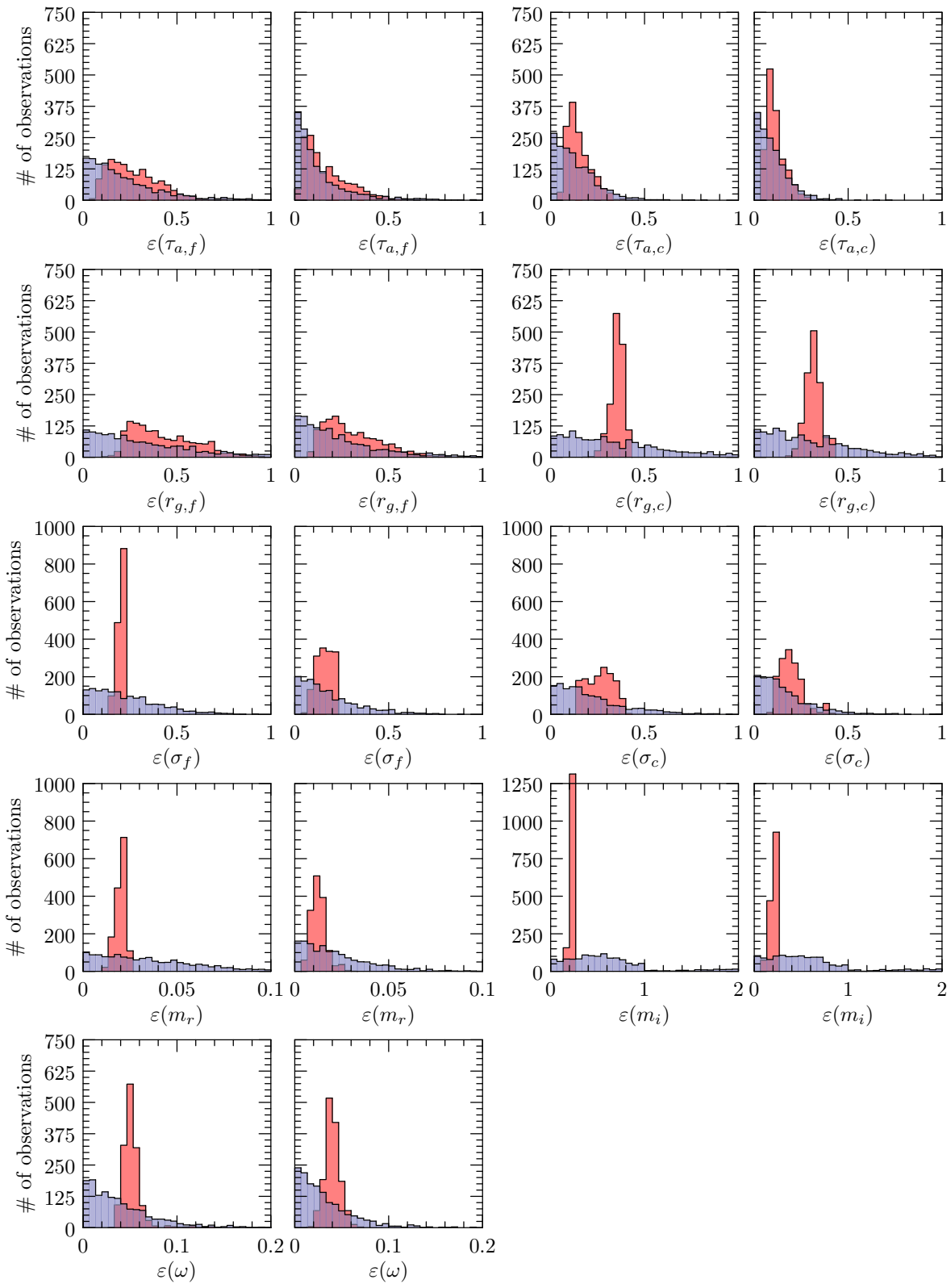

Figure 6.40: Same as figure 6.39 but for mixed aerosol sites only.

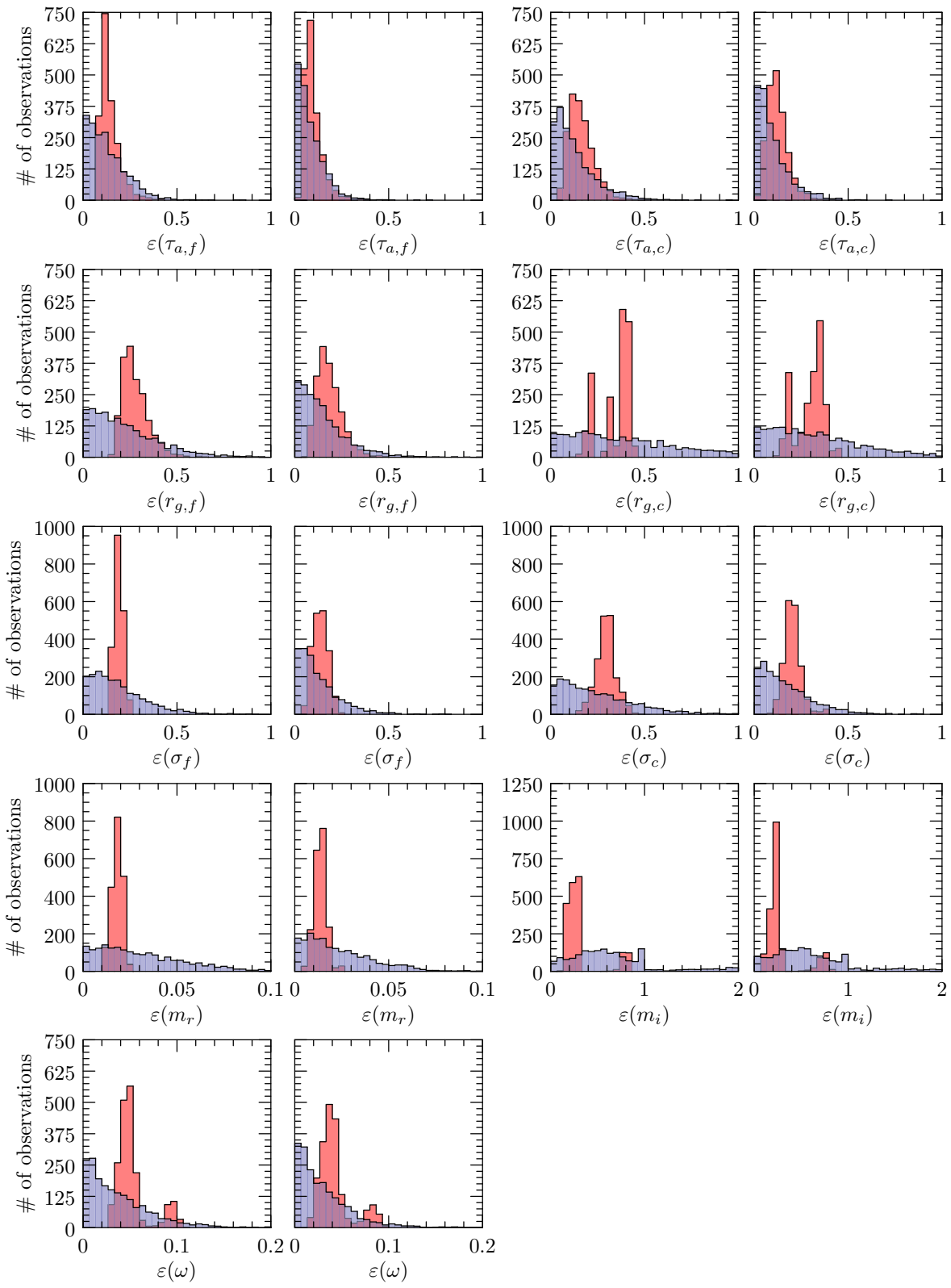

Figure 6.41: Same as figure 6.39 but for urban-industrial aerosol sites only.

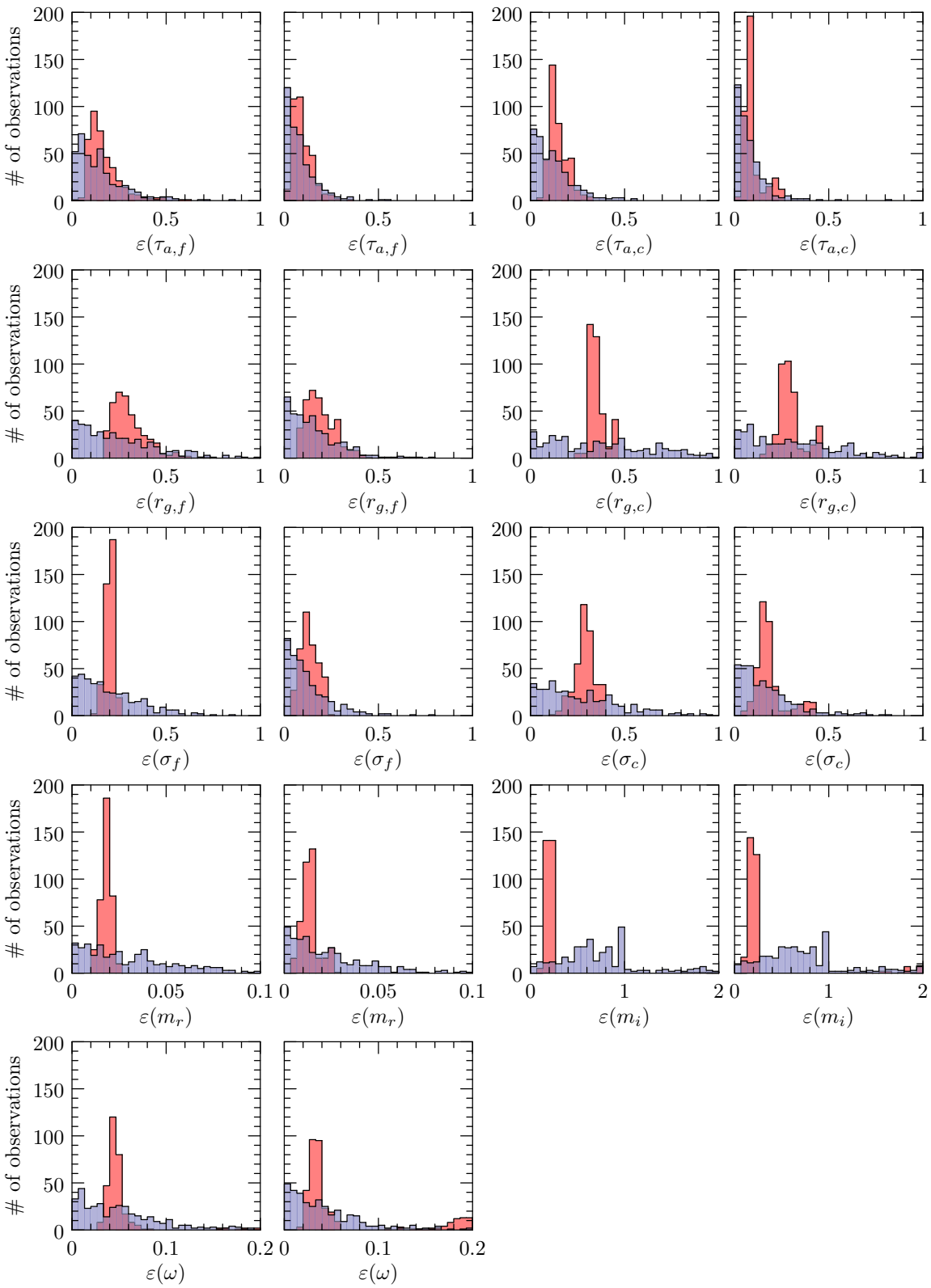

Figure 6.42: Same as figure 6.39 but for biomass burning aerosol sites only.

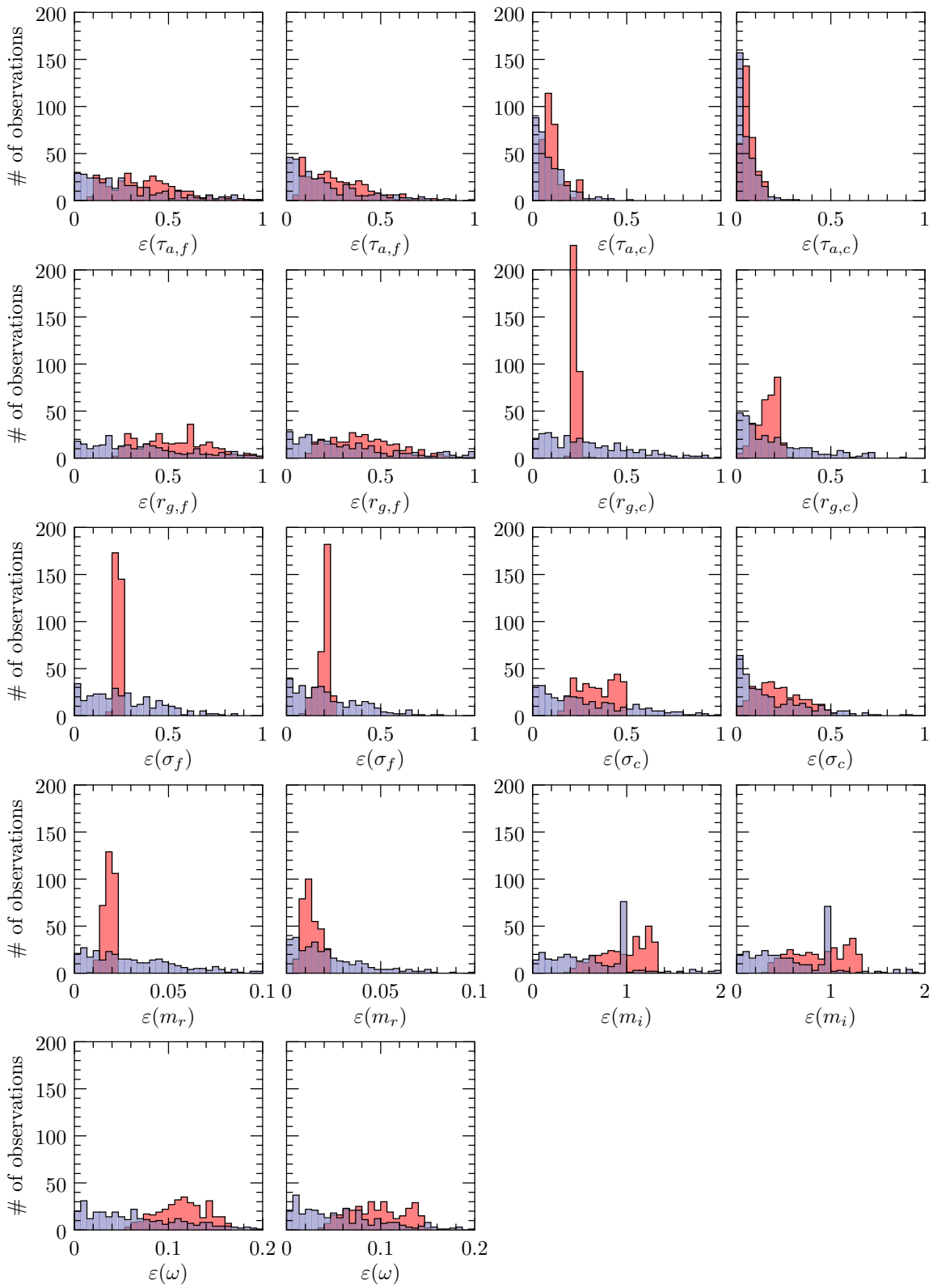

Figure 6.43: Same as figure 6.39 but for desert dust aerosol sites only.

reflectance in all three bands, MODIS + TANSO-FTS O_2 A-band total and polarized reflectance, and MODIS + TANSO-FTS total and polarized reflectance in all three bands. Measurements from these two sources must be co-located in both time and space to each other and to the ground-based validation data for which we use the AERONET inversion product. We discuss the co-location strategy along with surface type and cloud filtering. For a data set spanning April 5, 2009 through Dec 5 2011 with global coverage our co-location and filtering resulted in almost 4000 co-locations.

Our retrieval parameters include the spectral surface albedo $A(\lambda)$, aerosol-top pressure P_{top}, and the aerosol number concentration, mean radius and variance of a log-normal size distribution, and the spectral real and imaginary parts of the index of refraction for a fine mode ($N_{0,f}$, $r_{g,f}$, σ_f, $m_{r,f}(\lambda)$, $m_{i,f}(\lambda)$) and a coarse mode ($N_{0,c}$, $r_{g,c}$, σ_c, $m_{r,c}(\lambda)$, $m_{i,c}(\lambda)$). The spectral parameters are derived from retrieved parameters for a polynomial fit in wavelength. The total optical thickness $\tau_a(\lambda)$, modal optical thicknesses $\tau_{a,f}(\lambda)$ and $\tau_{a,c}(\lambda)$, and the single scattering albedos $\omega_a(\lambda)$, $\omega_{a,f}(\lambda)$ and $\omega_{a,c}(\lambda)$ may be derived from the retrieval parameters.

Our retrieval methodology is based on the optimal estimation approach. Our state vector, as presented above, includes a relatively complete set of aerosol parameters and as a result, our retrieval problem is ill-posed, with many possible solutions. In order to account for missing information we use an a priori constraint and to achieve a stable solution we use Levenberg-Marquardt regularization. Our choice of approaching the problem in this way is to generalize the retrieval to any source and quantity of measurements and to maximize the use of the available measurements. An important aspect of the our retrieval approach is that not only does it retrieve an estimate of the state vector but also a self contained estimate of the retrieval error. This provides a basis from which to estimate the error of calculations based on the retrieval product.

To validate our retrieval we first show scatter plots of the retrieved parameters vs. the corresponding AERONET results for all the sites and then for sites divided into one of four predominate aerosol types: mixed, urban-industrial, biomass burning, and desert dust. For each scatter plot we calculate the mean deviation μ_δ, the standard deviation of the deviations σ_δ, and the correlation coefficient r. We compare the results to accuracy requirements established by Mishchenko et al. [2004] for accurate quantification of the direct radiative effect of aerosols. In addition, we compare our results with two other similar aerosol retrievals [Hasekamp et al., 2011, Dubovik et al., 2011] that use advanced measurements and optimal estimation type inversions. After the scatter plots

we show timeseries for several parameters retrieved by our algorithm compared to that retrieved by AERONET for a specific site in each aerosol type category, including Kanpur, India (mixed); Beijing, China (urban-industrial); Sao Paulo, Brazil (biomass burning); and Kuwait University, Kuwait City, Kuwait (desert dust). Then we show some comparisons of the spectrally dependent parameters for our four specific AERONET sites as function of wavelength in order to show our retrieval's ability to retrieve spectral dependence. Finally, we present histograms of estimated and actual errors for all sites and then for the four specific aerosol types.

The relevant conclusions that can be taken from this study are the following:

1. The mean deviations μ_δ are always lower than the standard deviations of the deviations indicating that random error dominates over systematic bias errors. This is a good sign that the inversion process is working well and dealing with non-uniqueness issues appropriately. Similar results are were reported by Hasekamp et al. [2011].

2. Our results for all sites for total optical thickness $\tau_a(0.55)$ when using MODIS only ($\mu_\delta = -0.048$, $\sigma_\delta = 0.274$, and $r = 0.406$) show a considerable amount of error relative to the MODIS operational retrieval product ($\mu_\delta = -0.060$, $\sigma_\delta = 0.153$, and $r = 0.850$). There are two reasons for this. First, the operational retrieval is restricted to dark targets only whereas we have no such restriction for our retrieval. Second, even though ideally a retrieval system should be general without special case tuning, the MODIS operational retrieval has been tuned over several years and benefits from these special case adjustments.

3. Results for all sites for total optical thickness $\tau_a(0.55)$ improve drastically when including the TANSO-FTS measurements ($\mu_\delta = -0.044$, $\sigma_\delta = 0.163$, and $r = 0.837$), with further improvement when including all three TANSO-FTS bands (rather than just the O_2 A-band) and/or including the polarized reflectance rather than just total reflectance. With all three TANSO-FTS bands ($\mu_\delta = -0.025$, $\sigma_\delta = 0.093$, and $r = 0.938$) or including the polarized reflectance ($\mu_\delta = -0.028$, $\sigma_\delta = 0.109$, and $r = 0.920$) the results become comparable to that of the other advanced retrievals that we mentioned and with both ($\mu_\delta = -0.014$, $\sigma_\delta = 0.058$, and $r = 0.957$) they even become comparable and come close to our accuracy requirements. This suggests that improvements in our retrieval processes such as using more complex surface

models or accounting for non-spherical particles may provide results that are sufficient for accurate quantification of aerosol radiative effects.

4. Retrieval of individual optical thicknesses for each mode ($\tau_{a,f}(0.55)$ and $\tau_{a,c}(0.55)$) is typically more accurate than that of $\tau_{a,f}(0.55)$. Retrieval of small mode is typically less accurate than that of the large mode with results of $\mu_\delta = -0.010$, $\sigma_\delta = 0.046$, and $r = 0.951$ and $\mu_\delta = -0.004$, $\sigma_\delta = 0.029$, and $r = 0.962$, respectively, for the most advanced measurement scenario. The results for the fine mode mean radius $r_{g,f}$ usually fall within our accuracy requirements with $\mu_\delta = 0.003$, $\sigma_\delta = 0.024$, and $r = 0.594$ for while the results for the large mode mean radius $r_{g,c}$ are considerably less accurate with $\mu_\delta = 0.010$, $\sigma_\delta = 0.338$, and $r = 0.458$. The results for the real and imaginary index of refraction ($m_r(0.55)$ and $m_i(0.55)$) are generally not well retrieved with $\mu_\delta = -0.004$, $\sigma_\delta = 0.044$, and $r = 0.820$ and $\mu_\delta = -0.007$, $\sigma_\delta = 0.022$, and $r = 0.704$, respectively. It is expected from Part I, that use of multiangle measurements will significantly improve at least the accuracies for $m_r(0.55)$. Single scattering albedo $\omega_a(0.55)$ is retrieved with relatively good accuracy ($\mu_\delta = -0.004$, $\sigma_\delta = 0.046$, and $r = 0.854$) but does not quite meet the accuracy requirement but compares well with other retrievals using advanced measurements.

5. Overall, some of results may not achieve the strict accuracy requirements presented by Mishchenko et al. [2004] but they are a significant improvement over those from typical operational retrievals these days and compare well with other optimal estimation retrieval strategies using advanced measurements.

6. Separated by aerosol type the retrievals for urban-industrial and biomass burning aerosol, relative to the other types, typically have better accuracies for $\tau_a(0.55)$, $\tau_{a,f}(0.55)$, and $\tau_{a,c}(0.55)$ and better accuracies for $r_{g,f}$ and worse accuracies for $r_{g,c}$ as these aerosols are typically dominated by the fine mode. For desert dust the trend is opposite with worse accuracies for the optical thicknesses and $r_{g,f}$ but better accuracies for $r_{g,c}$ due to the dominate large mode. For $m_r(0.55)$ and $m_i(0.55)$ the results between aerosol types vary less as they are more influenced by the a priori knowledge. Results for the above quantities for mixed aerosols are, in general, slightly worse than those of urban-industrial or biomass burning most likely due to the presence of desert dust aerosol. For $\omega_a(0.55)$ the results for mixed and urban-industrial

aerosols are on the better side whereas the results for biomass-burning and desert dust are on the worse side.

7. Use of all three hyperspectral bands and of polarization improves the retrieval significantly. In the case of an OCO-2 type instrument all three bands should be used and in the case of a GOSAT TANSO-FTS type instrument all three bands and the polarization should be used. When computational ability is limited one can weight the benefits on not including some measurements. From Part I it is obvious that eliminating the 1.61 μm CO_2 band would be one's first choice. Eliminating either polarized reflectance or the 2.06 μm CO_2 band is possible for further efficiency and the retrieval validation indicates that eliminating polarized reflectance for τ_a retrievals is the best choice but may not be if information on m_r is desired.

8. Comparisons of the spectral dependence between the AERONET retrieval results and our retrieval results indicate that the spectral dependence is well retrieved for the derived parameters $\tau_{a,f}$, and $\tau_{a,c}$ (and as a result τ_a) and ω_a. While the spectral dependence of m_r and m_i is not as well retrieved, general trends are still resolved with some accuracy.

9. Histograms of the estimated error and the actual error show that the estimated error distribution is usually within that of the actual error. For the well retrieved parameters ($\tau_{a,f}(0.55)$, $\tau_{a,c}(0.55)$, $r_{g,f}$) the estimated distribution matches up with the actual distribution well whereas for the parameters that are not as well retrieved the estimated distributions tend to be less broad than the actual error distributions with some offset in some cases.

Chapter 7

Retrieval application: Radiative flux calculations

7.1 Introduction

The direct radiative forcing of aerosols is one of the largest uncertainties in understanding and estimating climate change [Intergovernmental Panel on Climate Change, 2007a]. On a global scale the direct radiative forcing has been estimated to be 0.0 ± 0.0 Wm^{-2}. The forcing by individual constituents is even more uncertain with -0.40 ± 0.20 Wm^{-2} for sulfates, -0.05 ± 0.05 Wm^{-2} for organic carbon, $+0.20 \pm 0.15$ Wm^{-2} for black carbon or soot, $+0.03 \pm 0.12$ Wm^{-2} for biomass burning, and -0.10 ± 0.20 Wm^{-2} for mineral dust, although local effects can be far greater reaching to over 100 Wm^{-2} in regions close to emission sources [García et al., 2011, 2012].

In the past, chemical transport and/or general circulation models have dominated the role of providing estimates of the effects of aerosols on climate while observations had been relegated to the role of validating model results, such as aerosol type and distribution relative to sources and sinks [Satheesh et al., 1999, Penner et al., 2002, Weaver et al., 2002, Kinne et al., 2003] or aerosol direct radiative forcing [Haywood et al., 1999]. Unfortunately, due the complexity of aerosol-climate interactions there is a wide range of discrepancies in model results. To reduce these uncertainties approaches with more integration between observation and models have been proposed [Diner et al., 2004, Anderson et al., 2005]. The observations may include either measurements of aerosol microphysical properties integrated as constraints into chemical transport modules or measurement-based estimates of aerosol radiative effects integrated as constraints into radiation modules. This chapter focuses on measurement-based estimates of aerosol radiative effects.

Measurement-based assessments of aerosol direct radiative effects generally fall into two categories [Yu et al., 2006]: (1) Methods that use surface- or satellite-based narrowband remote sensing measurements of aerosol properties as input to a broadband radiative transfer model. (2) Methods that measure the radiative effects more directly with broadband radiometric measurements. Methods in the first category that use surface-based measurements include, among others, the AERONET based-assessments made by García et al. [2008, 2011, 2012]. As far as assessments-based on satellite aerosol retrievals many studies have been published using the numerous aerosol retrieval methods reviewed in chapter 2. Some of those include the use of aerosol retrievals from GOES-8 [Christopher and Zhang, 2002a], SeaWiFS [Chou et al., 2002], MODIS [Ichoku et al., 2003, Remer and Kaufman, 2006], and POLDER [Boucher and Tanré, 2000].

One limitation of the first method is that the spectral aerosol properties are only valid for the narrowband channels used to retrieve them and empirical techniques for models must be used to obtain these properties as a function of wavelength across the entire broadband of interest. The use of broadband measurements from instruments such as the Earth Radiation Budget Experiment (ERBE) [Barkstrom, 1984] or the Clouds and Earth's Radiant Energy System (CERES) [Wielicki et al., 1996] eliminates this problem and early studies taking this approach include those of Minnis et al. [1993] and Haywood et al. [1999]. Unfortunately, the use of these kinds of broadband measurements is limited by the fact that the instruments have a coarse spatial resolution (ERBE at 40 km and CERES at 10 km) making it difficult to screen for sub-footprint-scale clouds. To account for this several researchers have made use of co-located high spatial resolution image measurements to screen for clouds including the use of AVHRR with ERBE [Christopher et al., 1996], VIRS with CERES [Christopher et al., 2000, Li et al., 2002, Loeb and Kato, 2002], and MODIS with CERES [Christopher and Zhang, 2002b, Loeb and Manalo-Smith, 2005]. In addition, the broadband radiance, acquired at a single angle during normal operation, must be converted to fluxes using angular distribution models [Li et al., 2002, Loeb et al., 2003b,a].

In this chapter we use the results from chapter 6 to perform a sample study using the first method presented above. Fluxes, radiative effects, and radiative effect efficiencies are calculated for each retrieval performed in chapter 6 and the results are validated against the AERONET flux and aerosol radiative forcing product. As with the retrieval presented in chapter 6 we pay particular attention to evaluating not only flux estimates but also estimates of their uncertainty.

The structure of this chapter is as follows. In section 7.2 we describe the flux quantities that are computed and the broadband radiative transfer model that is used to compute them. Section 7.3 describes how the error for our flux calculations is characterized and how one would integrate these errors into derived products. In section 7.4 we describe the AERONET flux and aerosol radiative forcing product that is used to validate our computed flux quantities. In section 7.5 we present the computed quantities and validation results. Finally, in section 7.6 we summarize our findings and discuss some conclusions that may be taken from this study.

7.2 Flux quantities and their calculation

Several radiative flux quantities are analyzed in this chapter including the upward and downward shortwave spectral flux $F^{\uparrow\downarrow}(\lambda, z)$, where λ ranges from 0.2 to 4.0 μm and z is the altitude (km) that ranges from the bottom of the atmosphere (BOA) to the top of the atmosphere (TOA), the upward and downward broadband shortwave flux $F^{\uparrow\downarrow}(z)$, the TOA and BOA aerosol radiative effect ΔF_{TOA} and ΔF_{BOA}, and the corresponding radiative effect efficiencies $\Delta F^{\mathrm{eff}}_{\mathrm{TOA}}$ and $\Delta F^{\mathrm{eff}}_{\mathrm{BOA}}$. The aerosol radiative effect is given by

$$\Delta F_{\mathrm{TOA}} = -\left[F^{\uparrow}(\mathrm{TOA}) - F^{0\uparrow}(\mathrm{TOA})\right] \tag{7.1}$$

and

$$\Delta F_{\mathrm{BOA}} = F^{\downarrow}(\mathrm{BOA}) - F^{0\downarrow}(\mathrm{BOA}), \tag{7.2}$$

where $F^{0\uparrow\downarrow}(z)$ is the upward and downward broadband shortwave flux for an atmosphere free of aerosols. The sign criterion implies that negative values of ΔF are associated with aerosol cooling and positive values are associated with aerosol warming either at TOA or BOA. The aerosol radiative effect efficiency ΔF^{eff} is defined as the rate at which the atmosphere is forced per unit of aerosol optical thickness τ_a at 0.55 μm which is given by

$$\Delta F^{\mathrm{eff}}_{\mathrm{TOA}} = \Delta F_{\mathrm{TOA}}/\tau_a(0.55) \tag{7.3}$$

and

$$\Delta F_{\mathrm{BOA}}^{\mathrm{eff}} = \Delta F_{\mathrm{BOA}} / \tau_a(0.55). \tag{7.4}$$

This quantity allows the evaluation of the aerosol radiative effect of each type of aerosol since the influence of aerosol load has been normalized.

The flux quantities were calculated from 0.2 to 4.0 μm in intervals of 0.01 μm. Within each spectral interval a correlated k-distribution [Fu and Liou, 1992] approach was used, where each monochromatic calculation was performed using the X Radiative Transfer Model's (XRTM) dedicated linearized 4-stream solver [McGarragh, 2013b] with which upward and downward fluxes at each atmospheric level are solved for simultaneously. In addition, along with the absolute values, the derivatives of the fluxes with respect to the model input quantities were also calculated. Broadband fluxes and their associated derivatives were then determined for each level by integrating over the spectral intervals from 0.2 to 4.0 μm.

Within each spectral interval the RTM input quantities for each k-distribution point are for each atmospheric layer the total optical thickness $\tau(\lambda)$, the total single scattering albedo $\omega(\lambda)$, and the total phase function $P(\Theta)$, along with the surface albedo A. These quantities are obtained from the individual quantities for molecular absorption ($\tau_{m,a}(\lambda)$), molecular scattering ($\tau_{m,s}(\lambda)$ and $P_{m,s}(\Theta)$), and aerosols ($\tau_{a,i}(\lambda)$, $\omega_{a,i}(\lambda)$, and $P_{a,i}(\Theta)$), where i is either f or c for fine and coarse modes, respectively, using the method of combination described in section 5.4.1. The molecular absorption optical thickness $\tau_{m,a}(\lambda)$ is obtained from the LOWTRAN 7 model [Kneizys et al., 1988] and the molecular scattering optical thickness $\tau_{m,s}(\lambda)$ and phase function $P_{m,s}(\Theta)$ are obtained as described in section 5.4.1. The required meteorological profiles are the ECMWF profiles used for the corresponding retrieval as described in section 6.2.1 while ozone concentration is taken from monthly climatological values based on Total Ozone Mapping Spectrometer (TOMS) and Ozone Monitoring Instrument (OMI) retrievals (http://ozoneaq.gsfc.nasa.gov/) and all other gas concentrations are taken as constant from LOWTRAN 7.

The aerosol optical properties are assumed to be constant within each interval and are interpolated from optical properties computed at several points from 0.2 to 4.0 μm. At each point λ the retrieved microphysical quantities $r_{g,i}$, σ_i, $m_{r,i}(\lambda)$, and $m_{i,i}(\lambda)$ are used as input to the Linearized Mie scattering implementation (LMie) [McGarragh, 2013a] to compute the aerosol optical properties

$C_{e,i}(\lambda)$, $C_{s,i}(\lambda)$, and $P_{a,i}(\lambda)$, and their associated derivatives with respect to the input microphysical quantities. From $C_{e,i}(\lambda)$ and $C_{s,i}(\lambda)$ and the retrieved aerosol number concentration $N_{0,i}$ the optical quantities $\tau_{a,i}(\lambda)$ and $\omega_{a,i}(\lambda)$ may be obtained from equations 5.25 and 5.26.

The RTM requires vertically discretized profiles of optical properties with homogeneous layers. Vertical discretization is defined by the 91 level ECMWF profiles, where the meteorological quantities in each layer are taken to be the mean of the values for the upper and lower level for a total of 90 layers. The TOMS/OMI ozone profiles are interrelated to the 90 layers. The molecular absorption and molecular scattering optical properties are calculated for each for the homogeneous layers while the retrieved aerosol number concentration $N_{0,i}$ is assumed to be constant between the retrieved aerosol-top pressure P_{top} and the surface. Since P_{top} does not in general coincide with the ECMWF layer boundaries an additional level is inserted into the layer containing the aerosol-top.

The surface is assumed to be Lambertian, characterized by a spectral albedo $A(\lambda)$, assumed to be constant within each spectral interval, calculated from the retrieved polynomial fit parameters in wavelength A_i.

The TOA solar irradiance spectrum is taken from LOWTRAN 7 which provides irradiance at a 20 cm^{-1} resolution. The TOA irradiance is corrected to account for the seasonal variations of the earth-sun distance. Normally the solar zenith angle θ_0 would be taken at the time of the MODIS and TANSO-FTS co-location but in order to compare fluxes with that of AERONET we choose the value of θ_0 given in the AERONET inversion product which is the value used in the AERONET flux calculations. The reason is that small differences in θ_0 result in significant flux differences and since θ_0 is known exactly these differences will only serve to hide the more important differences from our retrieval results.

In addition to the optical quantities discussed, in some cases the RTM requires derivatives of these quantities, with respect to the physical quantities of interest, which are obtained through straight forward linearization of the discussed computations.

7.3 Error characterization

As with any measurement or modeled quantity a rigorous error characterization is necessary for the modeled fluxes to be useful in scientific applications. In addition, knowledge of the error sources

is a useful starting point for improving the accuracy of model results. Accessing the error of modeled results using a specific validation study is useful as a source of independent information but is not a stable self contained solution. Rather, error characterization that is inherent in the modeling methodology itself is a better alternative. This is the approach taken in our optimal estimation strategy discussed in chapters 5 and 6, where the retrieval errors are characterized based on the errors in assumed quantities, a priori knowledge of retrieval quantities, and the measurements. In fact, in this case, validation with independent measurements or modeled results not only serves to validate the results but also the error characterization of the results.

As with the aerosol retrieval presented in the previous chapter our flux modeling approach presented in this chapter will produce not only the absolute quantities of interest but also errors in those quantities due to errors in the model inputs and the modeling approach. Since flux calculations in the chapter depend on the aerosol retrieval results presented in the last chapter the errors computed for those retrieval results will propagate into our flux calculations. In fact, one can look at the combined retrieval and flux calculations as a single system, where the errors in the flux calculations ultimately come from: (1) The retrieval measurement and forward model errors, including the radiance measurement error and the errors in the assumed parameters such as meteorological, spectroscopic, and instrument parameters. (2) The error in the retrieval a priori state vector knowledge. (3) The errors in the flux model including errors in the assumed inputs including meteorological and spectroscopic parameters. Again, outside validation, as performed in the next section, is useful in validating our error characterization and pointing to sources of error that may have been neglected.

In the following we assume $\sigma(x)$ represents the 1-sigma error for a parameter x. Values of $\sigma(x)$ must be supplied for each assumed parameter b_i that does not come from the retrieval, given by $\sigma(b_i)$, and for each of the retrieved parameters $\hat{x}_i$, given by $\sigma(\hat{x}_i)$. The values of σ for the assumed parameters are given by the user and for the retrieved parameters are simply the square roots of the diagonal elements of the retrieval error covariance matrix $\hat{\mathbf{S}}$

$$\sigma(\hat{x}_i) = \sqrt{\hat{S}_{ii}}. \tag{7.5}$$

Then by running our broadband flux model which includes all the computations discussed in section 7.2 the derivatives of flux quantity F with respect a parameter x may be computed and used to estimate the error in F due to the parameter x with

$$\sigma(F,x) = \sigma(x)\frac{\partial F}{\partial x}. \tag{7.6}$$

Finally, the total error in the flux quantity F may be determined with

$$\sigma(F) = \sqrt{\sum_i [\sigma(F,b_i)]^2 + \sum_i [\sigma(F,x_i)]^2}. \tag{7.7}$$

Later our estimated error σ_F will be compared to actual error $\delta(x) = x(\text{Retrieval}) - x(\text{AERONET})$.

7.4 AERONET radiative fluxes

To validate our results we use the TOA/BOA upward/downward broadband fluxes $F^{\uparrow\downarrow}$(TOA) and $F^{\uparrow\downarrow}$(BOA), TOA and BOA aerosol radiative forcing ΔF_{TOA} and ΔF_{BOA}, and TOA and BOA aerosol radiative forcing efficiency $\Delta F^{\text{eff}}_{\text{TOA}}$ and $\Delta F^{\text{eff}}_{\text{TOA}}$, provided with the AERONET inversion product [García et al., 2008]. The fluxes are calculated using the same spectral interval used for our calculations of 0.2 to 4.0 μm with over 200 spectral sub-intervals. The monochromatic calculations where performed with the discrete ordinate implementation DISORT [Stamnes et al., 1988b]. Molecular absorption and scattering properties where obtained from the correlated k-distributions used in the Global Atmospheric ModEl (GAME) code [Dubuisson et al., 1996]. Required gas concentration profiles for the GAME code are that of water vapor and ozone which were obtained by scaling the US standard 1976 atmospheric model to the total water vapor content retrieved by AERONET, provided with the inversion product, and the total ozone content from the TOMS/OMI monthly climatology similar to our calculations. The aerosol optical properties were calculated from Mie theory using AERONET retrieval quantities as input including the continuous size distribution and the complex index of refraction at 0.440, 0.670, 0.870, and 1.020 μm, where the real and imaginary parts of the index of refraction are interpolated and extrapolated to the required wavelengths. In addition, the spectral surface albedo is interpolated/extrapolated from the surface

albedo assumed in the AERONET inversion scheme which is provided with the inversion product at 0.440, 0.670, 0.870, and 1.020 μm.

The AERONET BOA downward fluxes have been validated by García et al. [2008] against ground-based downward flux observations including that of BSRN [Ohmura et al., 1998] and SolRad-Net (http://solrad-net.gsfc.nasa.gov/index.html). In addition, comparison between AERONET measured and modeled downward fluxes at BOA was used to characterize the uncertainties in the modeled fluxes. Globally, a small uncertainty of 9 ± 12 Wm^{-1} was found that is within the uncertainty of the BSRN and SolRad-Net observations. The differences between AERONET measured and modeled flues are within 15 Wm^{-1} for all the stations included in the study. Broken down by aerosol type the uncertainties are 14 ± 10 Wm^{-1} for urban-industrial, 6 ± 13 Wm^{-1} for biomass burning, and 16 ± 10 Wm^{-1} for desert dust. Under clear atmospheric conditions a dispersion of 10 Wm^{-1} was apparent.

7.5 Results

7.5.1 Spectral and vertical flux profiles

In this section we show plots of fluxes, flux errors, and flux sensitivities for the four sample AERONET sites used in the last chapter: Kanpur, Beijing, Sao Paulo, and Kuwait University, that represent mixed, urban-industrial, biomass burning, and desert dust aerosol, respectively. In each case we choose the M,TF,1-3,R+P,N retrieval with a total optical thickness $\tau_a(0.55)$ closest to the mean. Relevant parameters for the chosen retrieval for each site are given in table 7.1.

First we plot quantities as a function of wavelength in figures 7.1 through 7.4 for each aerosol type, respectively. In each of these figures quantities related to the upward flux at TOA ($F^{\uparrow}(\lambda, \text{TOA})$) are in the first row, quantities related to the upward flux at BOA ($F^{\uparrow}(\lambda, \text{BOA})$) are in the second row, and quantities related to the downward flux at BOA ($F^{\downarrow}(\lambda, \text{BOA})$) are in the last row. The absolute value of the flux along with flux errors are plotted in the left column while the flux sensitivities to a number of aerosol parameters are plotted in the right column. The flux errors are given for a MODIS (M) only retrieval (red) and for the retrievals including the TANSO-FTS measurements, where green is for using intensity only measurements (M,TF,1-3,R,N) and blue is for using intensity and polarization measurements (M,TF,1-3,R+P,N).

Table 7.1: Parameters for the four specific sample retrievals used in the section.

Parameter	Kanpur	Beijing	Sao Paulo	Kuwait University
τ_a	0.49	0.57	0.31	0.55
$\tau_{a,f}$	0.13	0.28	0.24	0.20
$r_{g,f}$	0.032	0.055	0.077	0.047
σ_f	0.49	0.53	0.37	0.36
$\tau_{a,c}$	0.36	0.29	0.07	0.35
$r_{g,c}$	0.679	0.935	0.574	0.955
σ_c	0.61	0.60	0.61	0.59
m_r	1.52	1.50	1.52	1.52
m_i	0.00446	0.00404	0.00726	0.00508
ω_a	0.92	0.87	0.80	0.92
A_a	0.13	0.07	0.08	0.17
θ_0	55.20	65.36	47.85	42.01

The flux values track the incoming solar spectrum well as they should. The $F^{\downarrow}(\lambda, \mathrm{BOA})$ values dominate over the other values as they include mostly direct and singly scattered radiation neither of which has interacted with the surface. The $F^{\uparrow}(\lambda, \mathrm{BOA})$ are the least of the three since it is affected mostly by the surface albedo which for our cases varies between 0.07 and 0.17, 93% and 83% reductions compared to $F^{\downarrow}(\lambda, \mathrm{BOA})$. The values for $F^{\uparrow}(\lambda, \mathrm{TOA})$ fall in between and contain not only radiation scattered from the surface but also radiation scattered from the aerosols in the atmosphere. With aerosol type, the fluxes tend to increase with surface albedo A and single scattering albedo ω_a which will be further explored when we look at the sensitivities. The flux errors vary as expected with retrieval scenario with the MODIS only retrieval having the largest errors and significant improvement with the TANSO-FTS intensity measurements and a further improvement with both the intensity and polarization.

The flux sensitivity to surface albedo A dominates for the upward fluxes. This is as expected and underscores the importance of having an accurate characterization of the surface for shortwave radiative flux calculations. The sensitivity to A in the downward flux is significantly less since this quantity is only affected by radiation multiply scattered between the surface and the aerosols rather than the more direct single scattering from the surface. Second to A for the upward fluxes is single scattering albedo ω_a which, due to the smaller sensitivity to A, dominates most of the cases for downward flux. The reason for this is that ω_a regulates the amount for shortwave radiation absorbed by the aerosols rather than scattered and therefore the amount of shortwave radiation

lost. In general, the sensitivity is larger for the cases with larger values of ω_a due to the exponential nature of attenuation and therefore the decreasing impact of increasing absorption. The third most important parameter in regards to flux sensitivity tends to be the real part of the index of refraction m_r. Due to the sensitivity of the single scattering phase function $P_a(\Theta)$ this indicates that the radiative flux calculations have a significant sensitivity to $P_a(\Theta)$ and that making assumptions about this quantity, such as using the asymmetry parameter, could result in some biases in the flux results.

Interestingly, the sensitivities to A and ω_a tend to always be positive whereas the sensitivities to the single scattering parameters r_g, σ, m_r, and m_i tend to be either positive or negative for $F^{\uparrow}(\lambda, \mathrm{TOA})$ and negative for $F^{\uparrow}(\lambda, \mathrm{BOA})$ and $F^{\downarrow}(\lambda, \mathrm{BOA})$. The reason that the sensitivities to A and ω_a are always positive is because each parameter is inversely related to the amount of shortwave radiation absorbed by the aerosol/surface system and therefore an increase in either parameter results in less shortwave flux lost. The reason that the sensitivities to the single scattering parameters are negative for the BOA fluxes is that an increase in their values tends to lead to either an increase in the amount of radiation absorbed (r_g, σ, and m_i) or an increase in the amount of radiation scattered back upward (m_r) from the aerosol layer, both cases of which lead to less radiation reaching the surface. The magnitude of these sensitivities and that of ω_a is considerably less for BOA upward as this value is predominately affected by the surface. Finally, the reason that the sensitivities to the single scattering parameters are both positive and negative at TOA is due to the change in sign for the scattering component of the sensitivity at TOA relative to BOA, that is, an increase in scattering results in more radiation back to TOA and less reaching the surface.

It might be surprising at first that the sensitivity to optical thickness τ_a is so small but it is the offsetting effect between aerosol absorption and aerosol scattering that results in the low sensitivities. On the one hand, as τ_a increases the aerosol absorption will increase and the multiple scattering between the surface and the aerosol will increase further increasing absorption. On the other hand, an increase in τ_a also results in more scattering of radiation back to space. The fact that the sensitivity to τ_a is positive at TOA but negative at BOA is due both to the relative importance of increased aerosol absorption at BOA relative to TOA and the change in sign of the scattering component of the sensitivity, as already mentioned above. This relatively small sensitivity to τ_a

compared to other parameters underscores the importance of accurate retrievals of these other parameters and not just of τ_a as is the standard for operational retrievals these days.

Comparing the results for different cases we can see that the mode to which the flux results are most sensitive to tends to be the mode with the larger optical thickness, as expected. In particular, mixed aerosol at Kanpur and desert dust aerosol at Kuwait University both have a relatively dominate coarse mode whereas biomass-burning aerosol at Sao Paulo has a dominate fine mode. The large mode sensitivities also have spectral dependencies that tend to peak at larger wavelengths than that of the small mode keeping the dominate size parameter constant. It is also interesting that for $F^{\uparrow}(\lambda, \text{TOA})$ ω_a is the dominate aerosol parameter for mixed and desert dust whereas for urban-industrial and biomass burning m_r is the dominate aerosol parameter. This is due the lower surface albedo for the sites associated with the latter aerosols and therefore a larger component of the TOA upward flux coming from the aerosol only instead of multiple aerosol-surface interactions.

In the next four figures we show upward and downward broadband flux $F^{\uparrow\downarrow}(z)$ as a function of altitude z in figures 7.5 through 7.8 for each aerosol type, respectively. In each figure the first and third plots are the absolute values of $F^{\uparrow}(z)$ and $F^{\downarrow}(z)$, respectively, along with their errors for a MODIS (M) only retrieval (red) and for the retrievals including the TANSO-FTS measurements, where green is for using intensity only measurements (M,TF,1-3,R,N) and blue is for using intensity and polarization measurements (M,TF,1-3,R+P,N). In the second and fourth plots are the flux sensitivities to the same set of parameters as in figures 7.1 through 7.4 for $F^{\uparrow}(z)$ and $F^{\downarrow}(z)$, respectively.

The upward fluxes $F^{\uparrow}$ increase with z as the effects of the surface decrease and the flux contribution from the atmosphere increases. The downward fluxes $F^{\downarrow}$ also increase with altitude as the backscattering effects of the atmosphere decrease with altitude particularly that of the aerosol layer. The sensitivity of $F^{\uparrow}$ to surface albedo A tends to decrease with altitude as the effects from the surface diminish. In contrast, the sensitivity of $F^{\uparrow}$ to aerosol parameters tends to increase with altitude as the effects from the aerosol becomes more significant relative to that of A. The sensitivity of $F^{\downarrow}$ to all parameters tends to decrease with altitude as the effects from the surface and the aerosol layer diminish with altitude.

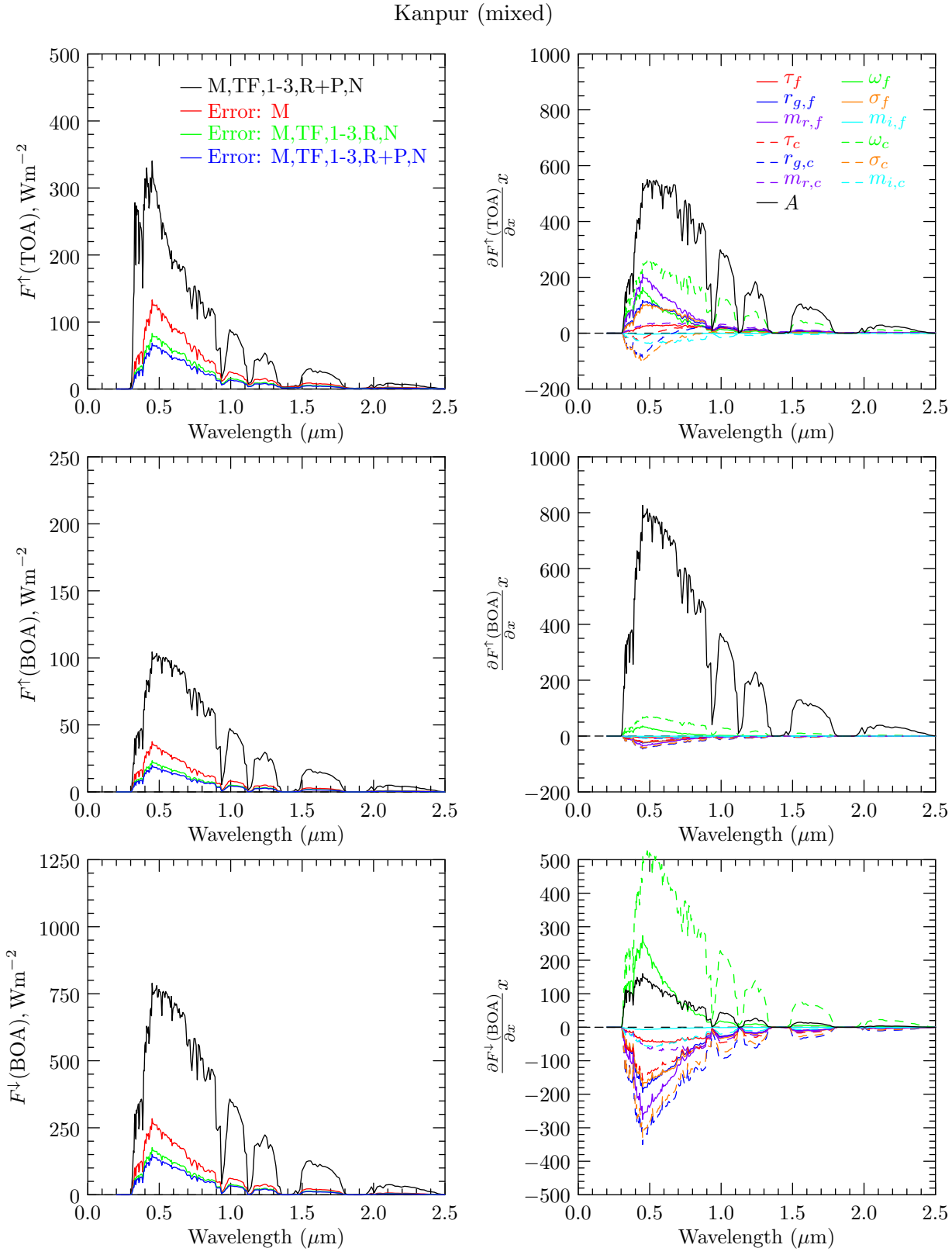

Figure 7.1: Fluxes, flux errors, and flux sensitivities as a function of wavelength λ for the Kanpur AERONET site (mixed aerosol) calculated using parameters as listed in table 7.1.

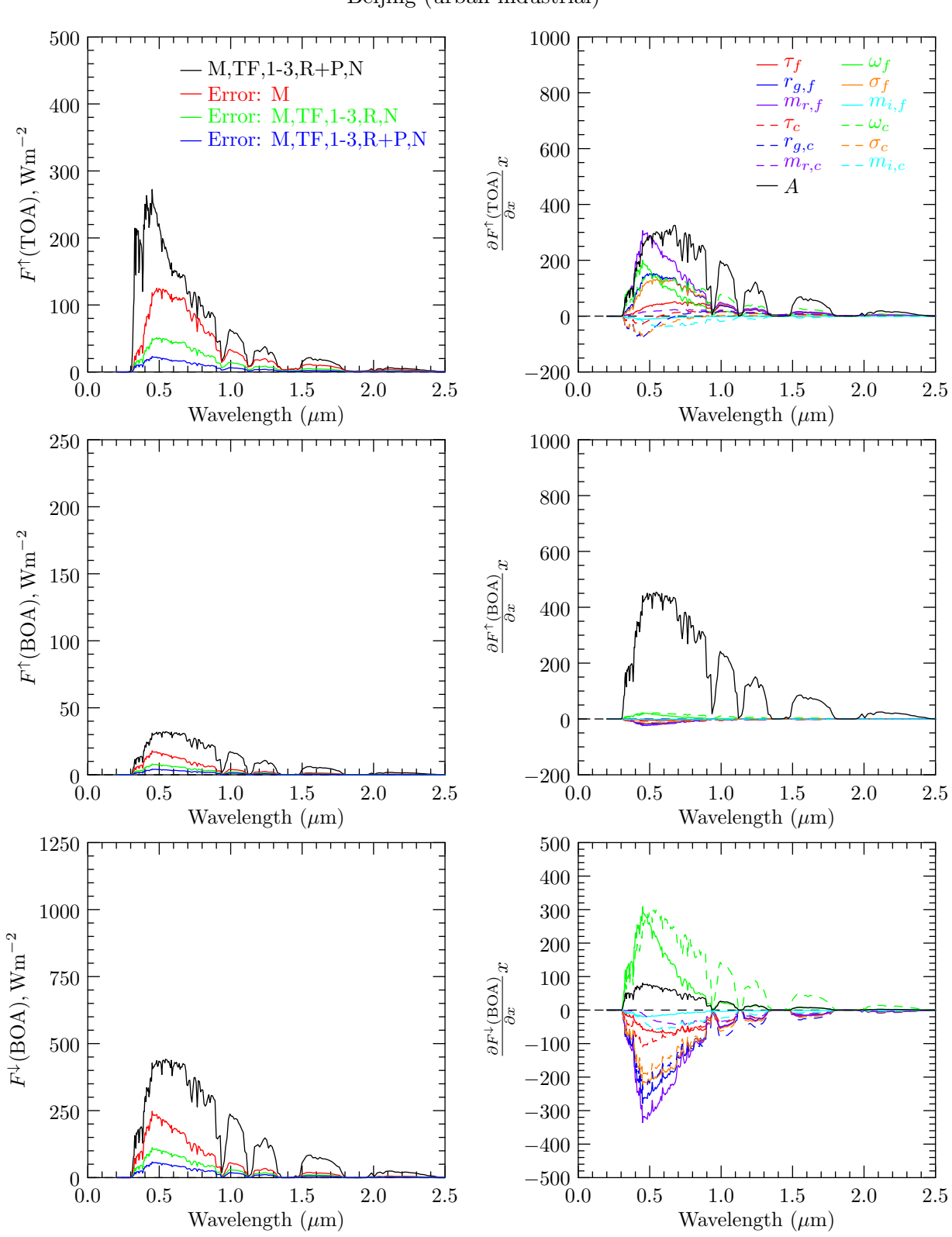

Figure 7.2: Same as figure 7.1 but for the Beijing AERONET site (urban-industrial aerosol).

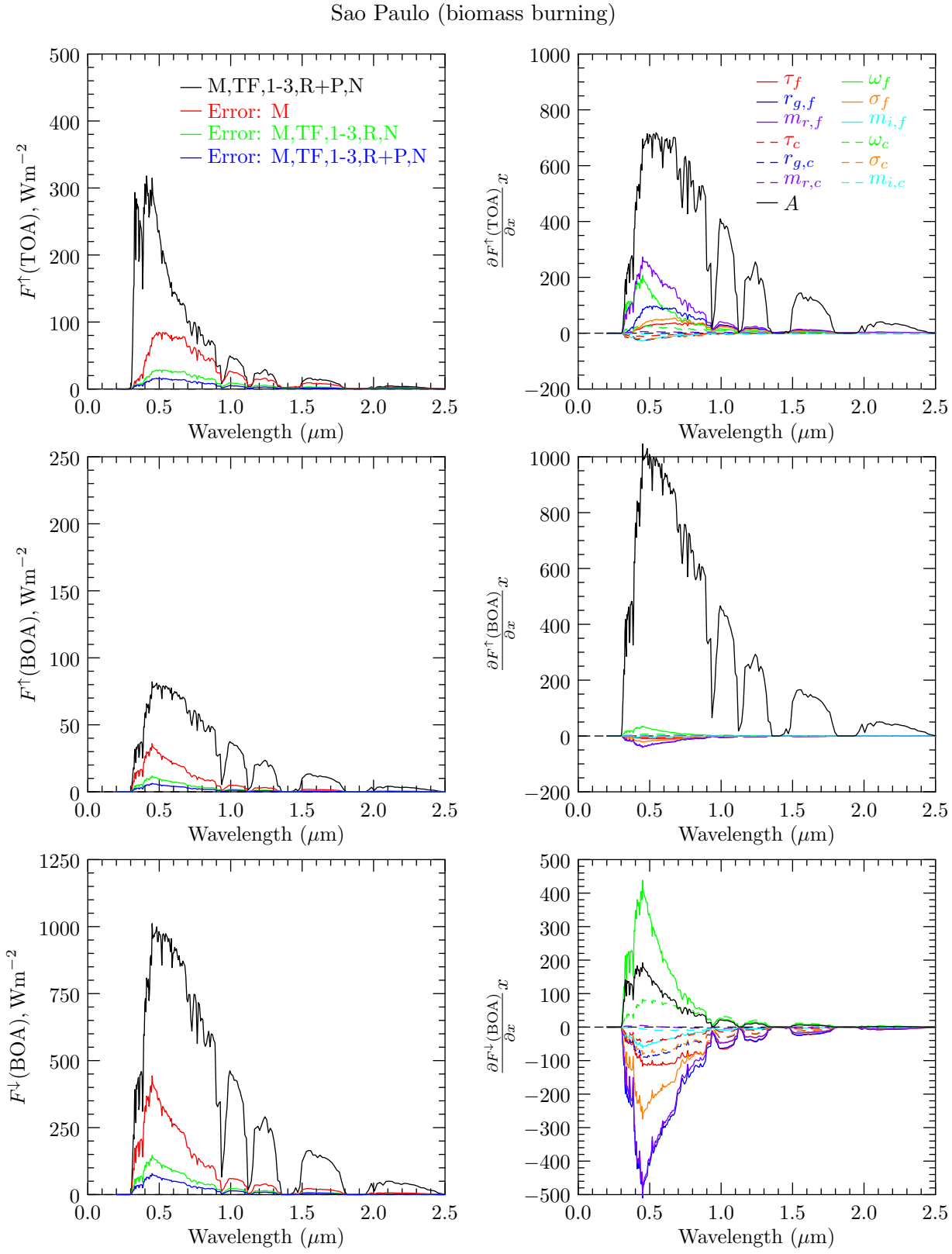

Figure 7.3: Same as figure 7.1 but for the Sao Paulo AERONET site (biomass burning aerosol).

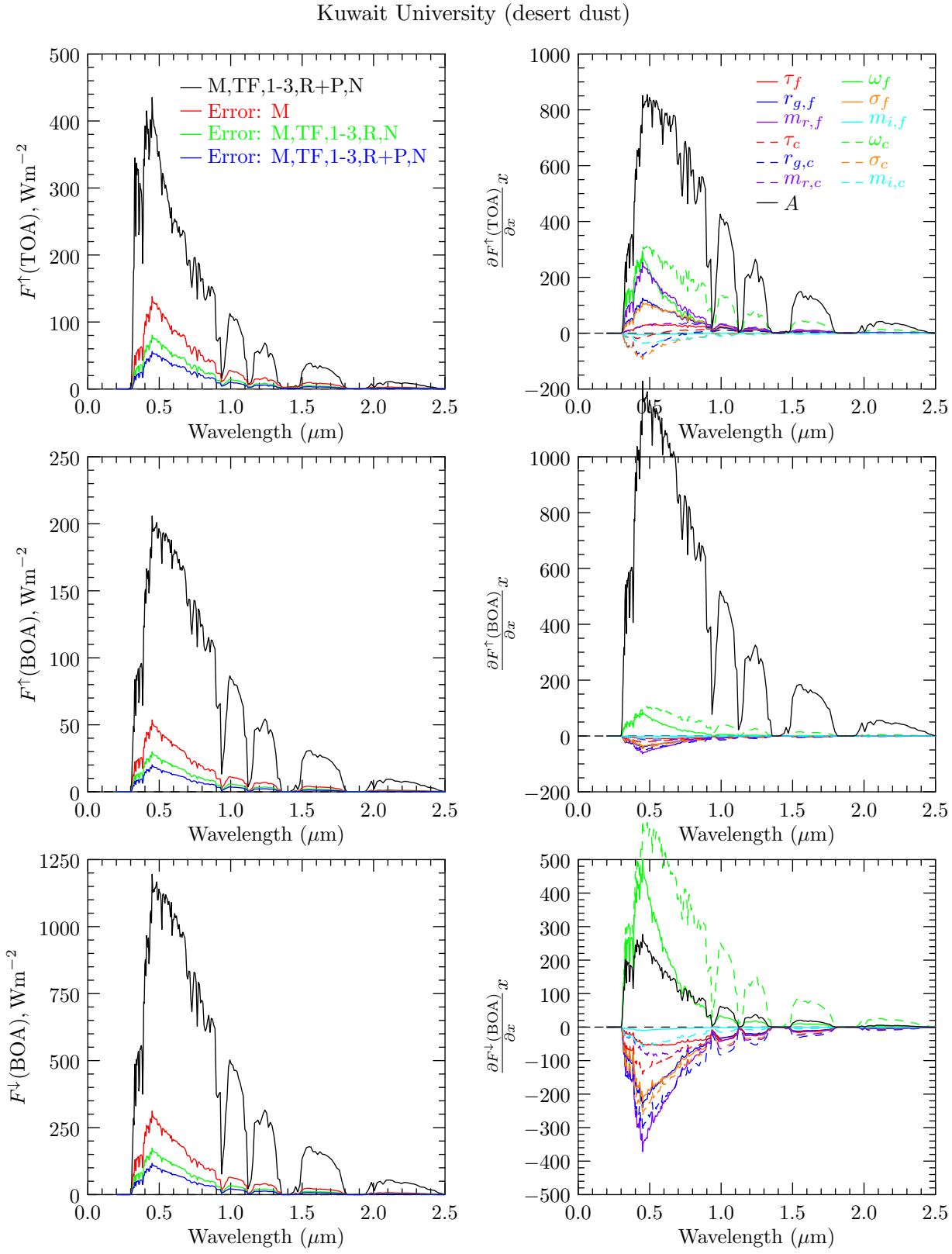

Figure 7.4: Same as figure 7.1 but for the Kuwait University AERONET site (desert dust aerosol).

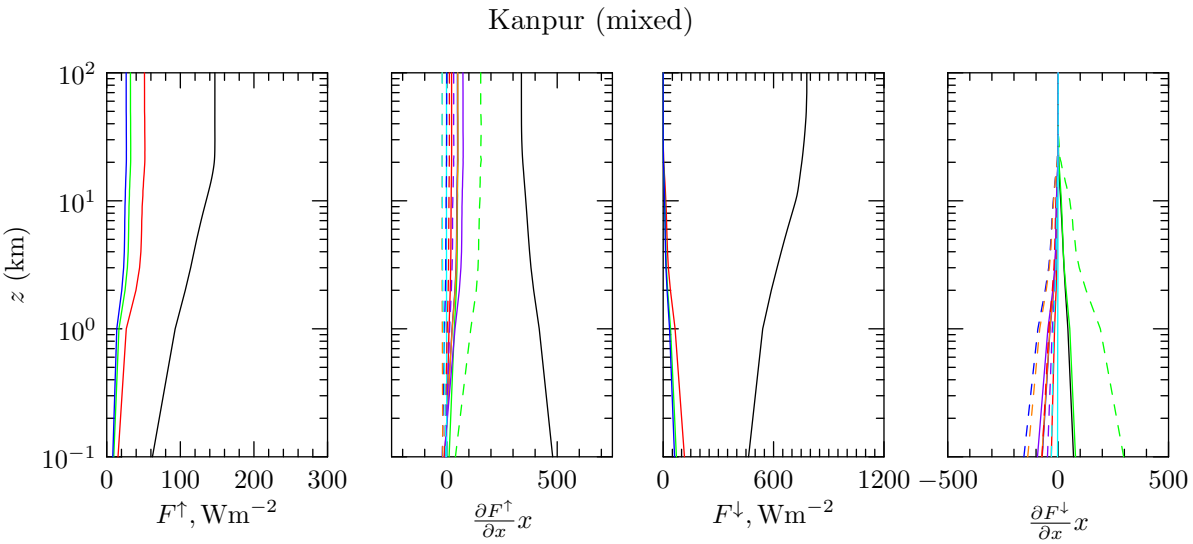

Figure 7.5: Fluxes and sensitivities as a function of altitude z for the Kanpur AERONET site (mixed aerosol) calculated using parameters as listed in table 7.1. The legends (not shown) are identical to that of figure 7.1.

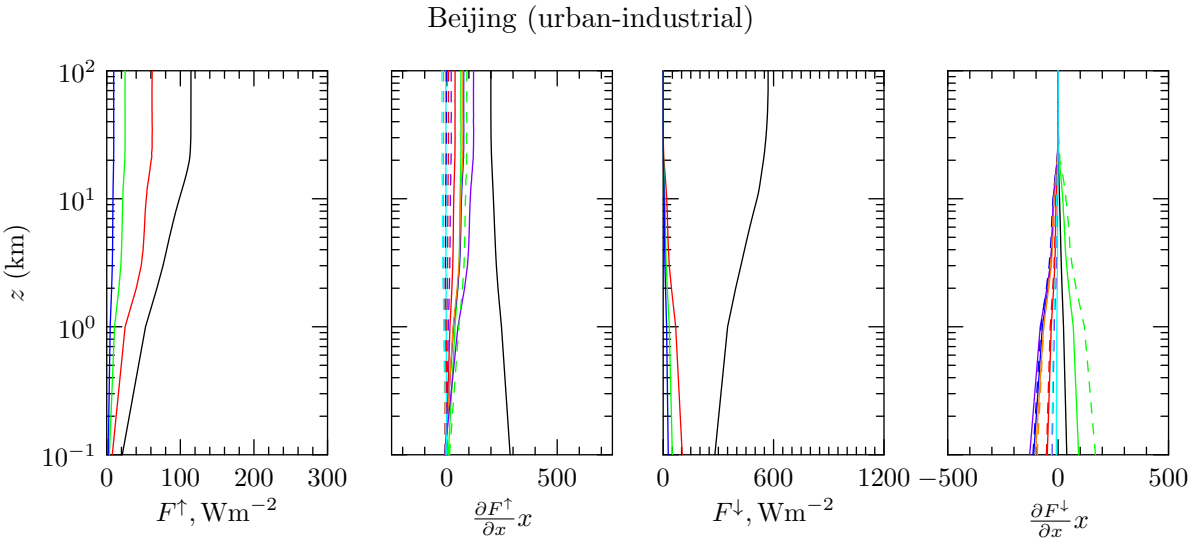

Figure 7.6: Same as figure 7.5 but for the Beijing AERONET site (urban-industrial aerosol).

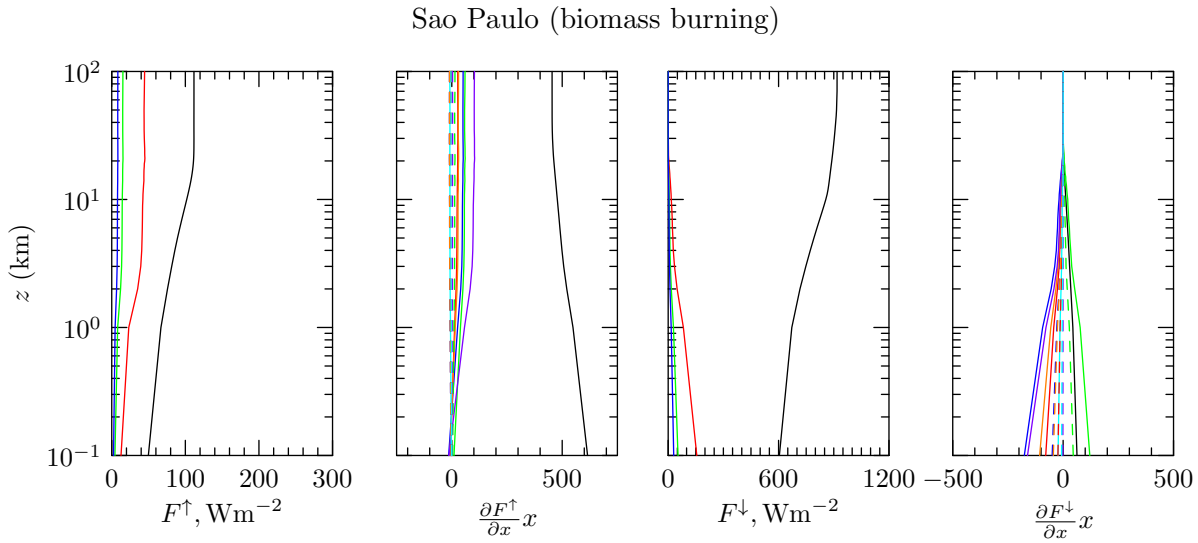

Figure 7.7: Same as figure 7.5 but for the Sao Paulo AERONET site (biomass burning aerosol).

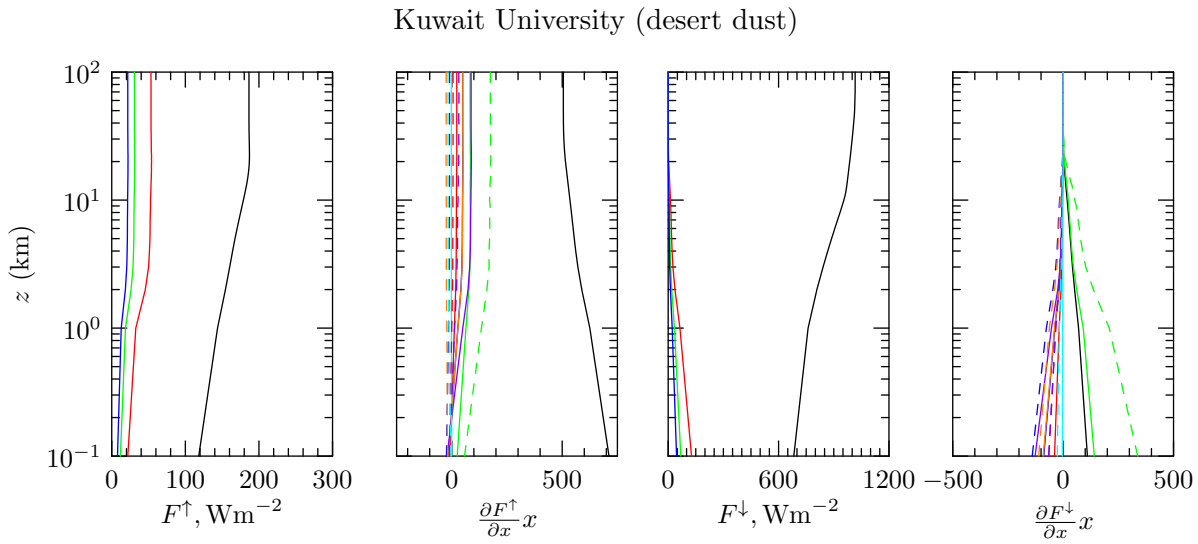

Figure 7.8: Same as figure 7.5 but for the Kuwait University AERONET site (desert dust aerosol).

7.5.2 Scatter plots

In this section we show scatter plots for broadband upward and downward fluxes at TOA $\Delta F^{\uparrow\downarrow}$(TOA) and BOA $\Delta F^{\uparrow\downarrow}$(BOA) computed from our aerosol retrieval results vs. the same fluxes provided from the AERONET retrieval product. Figure 7.9 shows results for all sites while figures 7.10 through 7.13 show results for the mixed, urban-industrial, biomass burning, and desert dust aerosol types only, respectively. For each figure the first row is for upward flux at TOA $F^{\uparrow}$(TOA), the second row is for upward flux at BOA $F^{\uparrow}$(BOA), and the third row is for downward flux at BOA $F^{\downarrow}$(BOA). The downward flux at TOA is not plotted as it is unaffected by the Earth's atmosphere and differences between AERONET's value and ours are less than 4 Wm^{-2} most likely due to the use of different solar spectral irradiance sources. The first column is for aerosol properties from the MODIS (M) only retrieval whereas the second and third columns are for the retrievals including the TANSO-FTS measurements, where the first is using intensity only measurements (M,TF,1-3,R,N) and the second is using intensity and polarization measurements (M,TF,1-3,R+P,N). In each case, the mean of the deviations $\delta_i(x) = x_{\mathrm{AERONET},i} - x_{\mathrm{retrieval},i}$ $\mu_\delta(x)$ (also called the mean bias), the standard deviation of the deviations $\sigma_\delta(x)$, and the linear regression correlation coefficient $r(x)$ are computed.

The values for $\Delta F^{\downarrow}$(BOA) are larger than that for the upward fluxes as they have not been affected directly by surface absorption. They also have a larger range due to the variation in solar zenith angle which is lost in the upward fluxes by reflection from a Lambertian surface that scatters evenly in all directions.

It is apparent from the plots that our results improve as we use the more accurate retrievals including the TANSO-FTS measurements of intensity and improve further when we use the retrievals that include TANSO-FTS measurements of intensity and polarization. The results for the upward fluxes are clearly better than for the downward fluxes. This is due to absorption of direct solar radiation by the surface lowering the overall magnitudes of the upward fluxes and the relative importance of aerosol effects relative to surface effects. Looking at the upward fluxes only, the errors are larger for the TOA than for BOA as it contains a larger aerosol component due to the aerosol layer between the surface and TOA.

The mean biases μ_δ are small for the upward fluxes but much larger for $\Delta F^{\downarrow}$(BOA) with values of -26, -18, and -17 Wm^{-2} for the three different measurement scenarios from left to right. These values are considerably more than the value of 9 ± 12 Wm^{-2} obtained by García et al. [2008] who compared the AERONET fluxes with ground-based flux measurements. The primary source of biases in our results is the uncertainty in our satellite-based retrievals. Since the upward fluxes contain a direct component from the surface, the albedo of which is relatively well retrieved, they are less affected by the aerosol layer relative to the surface and as a result have smaller biases than that of $\Delta F^{\downarrow}$(BOA). Although, as discussed above, the bias for $\Delta F^{\uparrow}$(TOA) is greater than that for $\Delta F^{\uparrow}$(BOA) as it contains an additional direct component from the aerosol layer.

The strong negative bias in the $\Delta F^{\uparrow}$(BOA) results implies that either more radiation is being scattered back to space by the aerosol layer or that more radiation is being absorbed by the aerosol layer. Before discussing the reason for this we must first note that the bias found by García et al. [2008], who compared AERONET derived $\Delta F^{\downarrow}$(BOA) to ground-based measurements of $\Delta F^{\downarrow}$(BOA), for all sites is positive at 9 ± 12 Wm^{-2} indicating that relative to their validation measurements our strong negative biases may be significantly less (by ~ 9 Wm^{-2}). Looking at the sensitivity results from the last section and noting that the albedo is relatively well retrieved and ω_a is only a derived parameter and not an input to our broadband model (ω_a is computed internally from the size distribution and index of refraction) we can make the assumption that the source of our bias is a positive bias in N_0 (related to τ_a), r_g, σ_g, m_r, or m_i. From the last chapter the biases for τ_a are small so we rule out N_0. The biases for $r_{g,f}$, $\sigma_{g,f}$, and $\sigma_{g,c}$ are also small so we can rule them out as well. The biases for m_r are m_i are not as small but negative which would result in a positive bias in $\Delta F^{\uparrow}$(BOA). The biases for $r_{g,c}$ are large and positive and as such could be responsible for the large negative biases in $\Delta F^{\uparrow}$(BOA). This is further supported by the fact that the $\Delta F^{\uparrow}$(BOA) biases are significantly smaller for urban-industrial and biomass burning aerosols which typically have a relatively uninfluential coarse mode.

The values of $\sigma_\delta(x)$ show the same trends as the values of μ_δ in that the values improve with more advanced measurements and that the values for $\Delta F^{\uparrow}$(BOA) dominate over that of the upward fluxes. The results for $\Delta F^{\uparrow}$(BOA) fall outside of the accuracy range given by García et al. [2008] of 9 ± 12 Wm^{-2}. Again, the reason for our greater uncertainty is primarily due to the uncertainty in our satellite-based retrievals whereas differences in our modeling results contribute a much smaller

uncertainty. As with μ_δ, the $\sigma_\delta(x)$ values are much better for the urban-industrial and biomass burning aerosols indicating that the primary source of the error is the coarse mode mean radius $r_{g,c}$ although the errors in both m_r are m_i will also have a significant effect, especially that of m_r given the large sensitivities to this value presented in the last section.

Not surprisingly, given our retrieval results from last chapter, the flux results for desert dust are the least accurate relative to the AERONET derived fluxes. Not only are the retrieval results over desert less accurate, the large albedos of bright desert surfaces increase the sensitivities to aerosol absorption and as a result increase the influence of errors in retrieved aerosol microphysical parameters.

7.5.3 Error histograms

In this section we present histograms of the estimated error in our flux computations computed as shown in section 7.3 and the actual error from the difference between our fluxes and the fluxes provided with the AERONET inversion product. As the last section served to validate the magnitudes of our derived fluxes this section will serve to validate the estimated errors of our derived fluxes. Figure 7.14 shows results for all sites while figures 7.15 through 7.18 show results for the mixed, urban-industrial, biomass burning, and desert dust aerosol types only, respectively. For each figure the first row is for upward flux at TOA $F^{\uparrow}$(TOA), the second row is for upward flux at BOA $F^{\uparrow}$(BOA), and the third row is for downward flux at BOA $F^{\downarrow}$(BOA). The downward flux at TOA is not plotted as it is unaffected by the Earth's atmosphere. The first column is for fluxes computed with aerosol properties from the MODIS (M) only retrieval whereas the second and third columns are for the retrievals including the TANSO-FTS measurements, where the first is using intensity only measurements (M,TF,1-3,R,N) and the second is using intensity and polarization measurements (M,TF,1-3,R+P,N). We present not the absolute magnitudes of the errors but the normalized error fractions for flux quantity F given by

$$\varepsilon_\sigma(F) = \frac{\sigma(F)}{F} \tag{7.8}$$

and

$$\varepsilon_\delta(F) = \frac{\delta(F)}{F}, \tag{7.9}$$

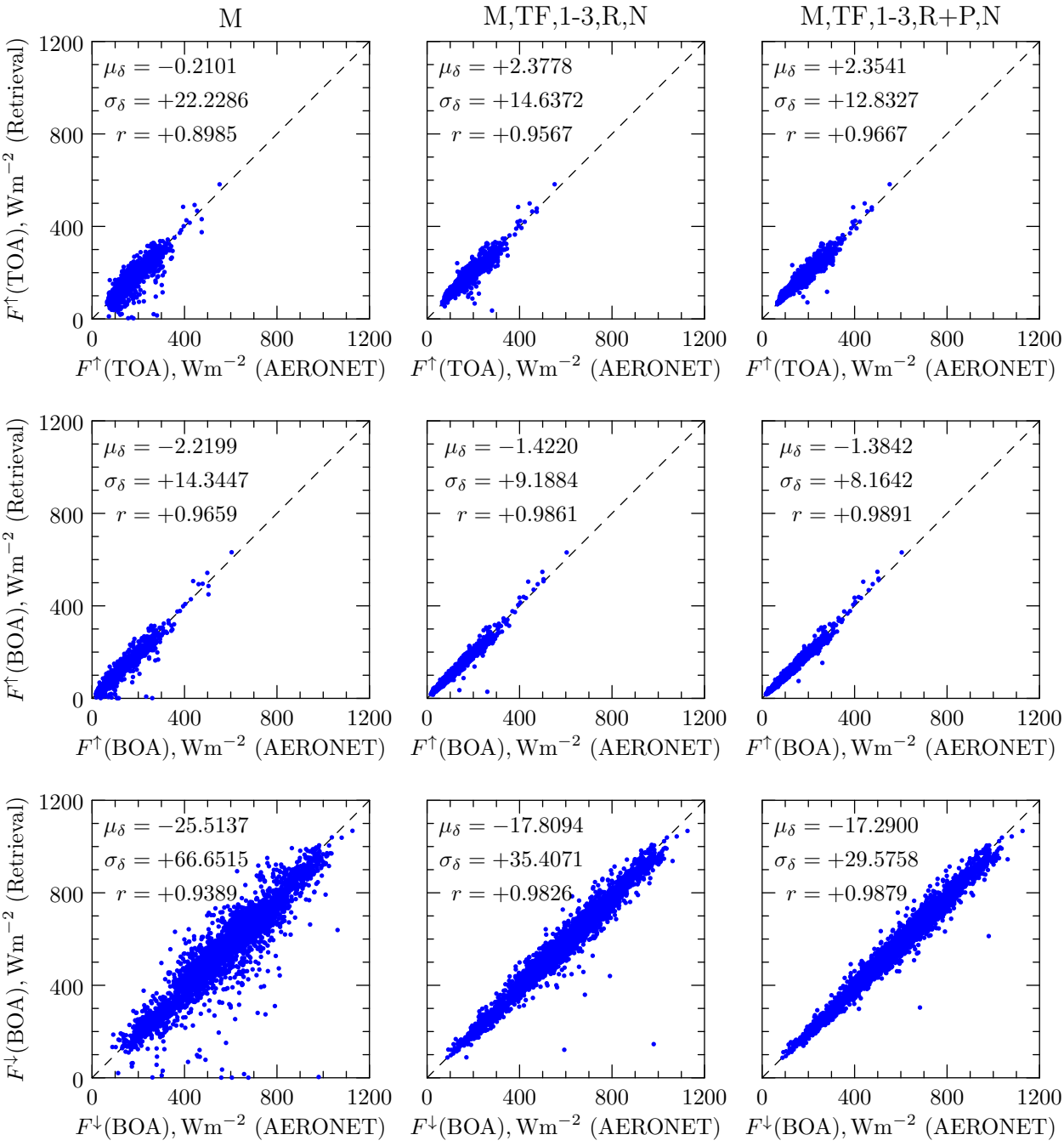

Figure 7.9: Scatter plots of fluxes computed from our retrieval results vs. fluxes from the AERONET inversion product. All retrieval sites are included.

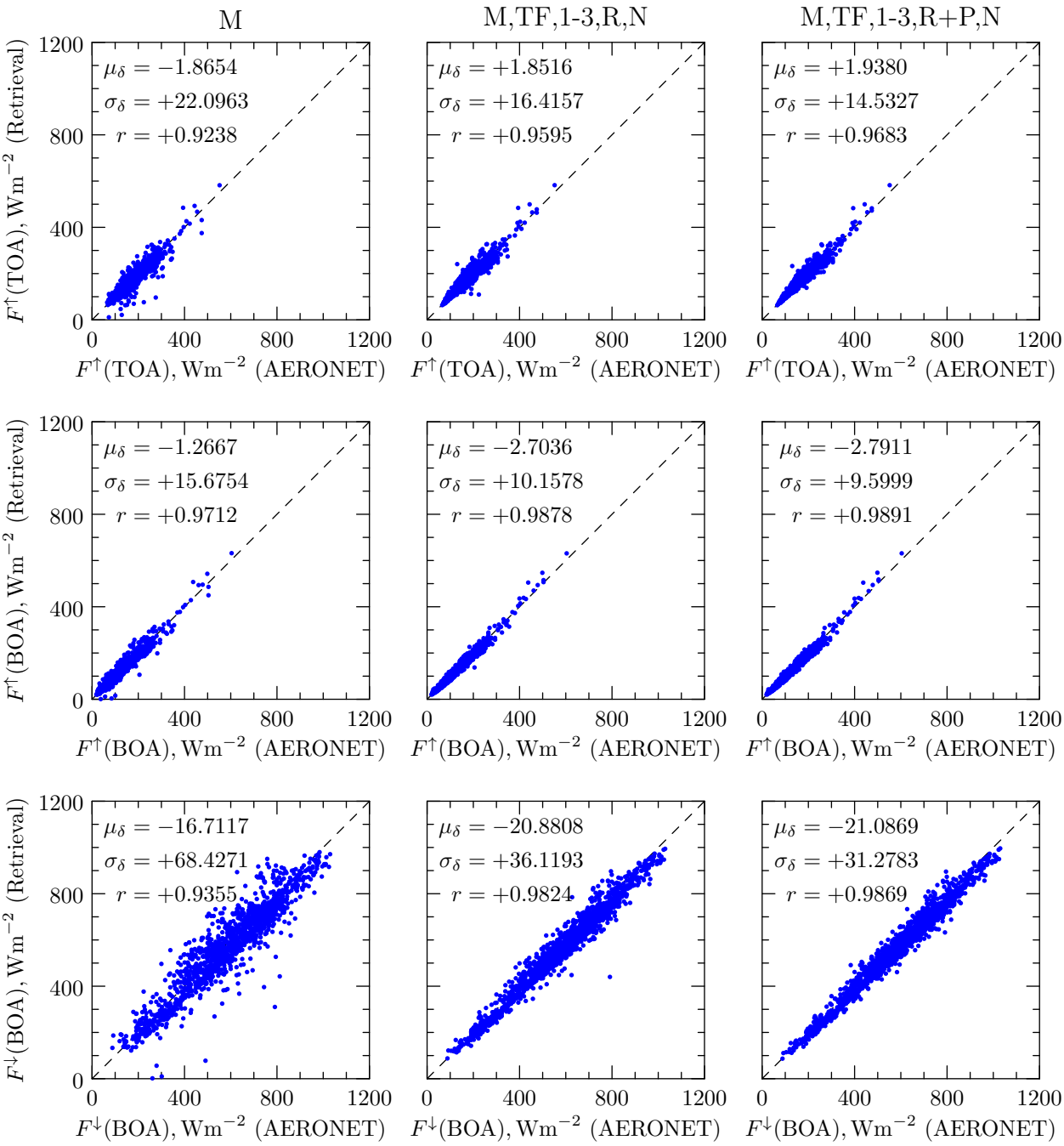

Figure 7.10: Same as figure 7.9 but only sites classified as mixed aerosol are included.

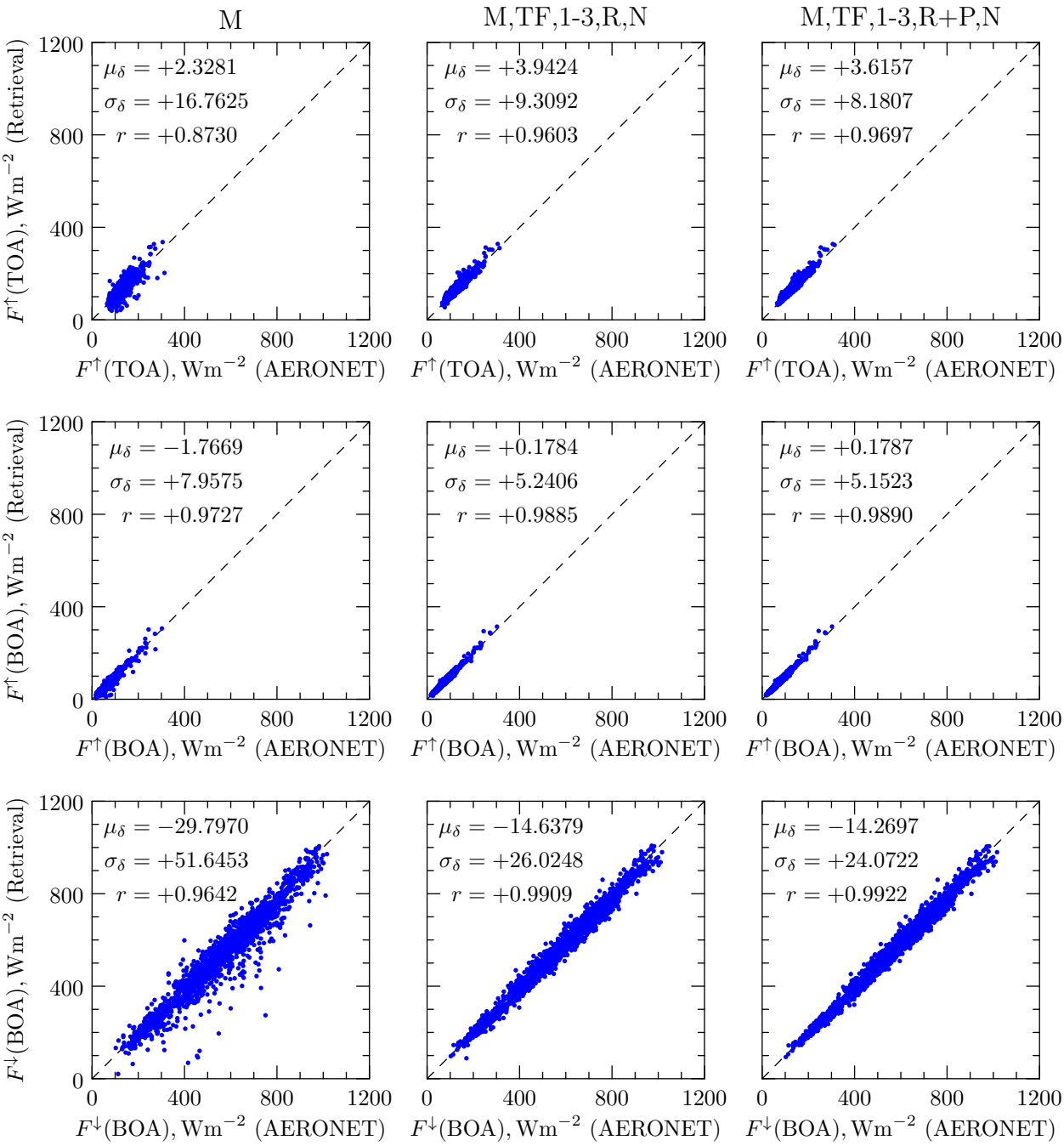

Figure 7.11: Same as figure 7.9 but only sites classified as urban-industrial aerosol are included.

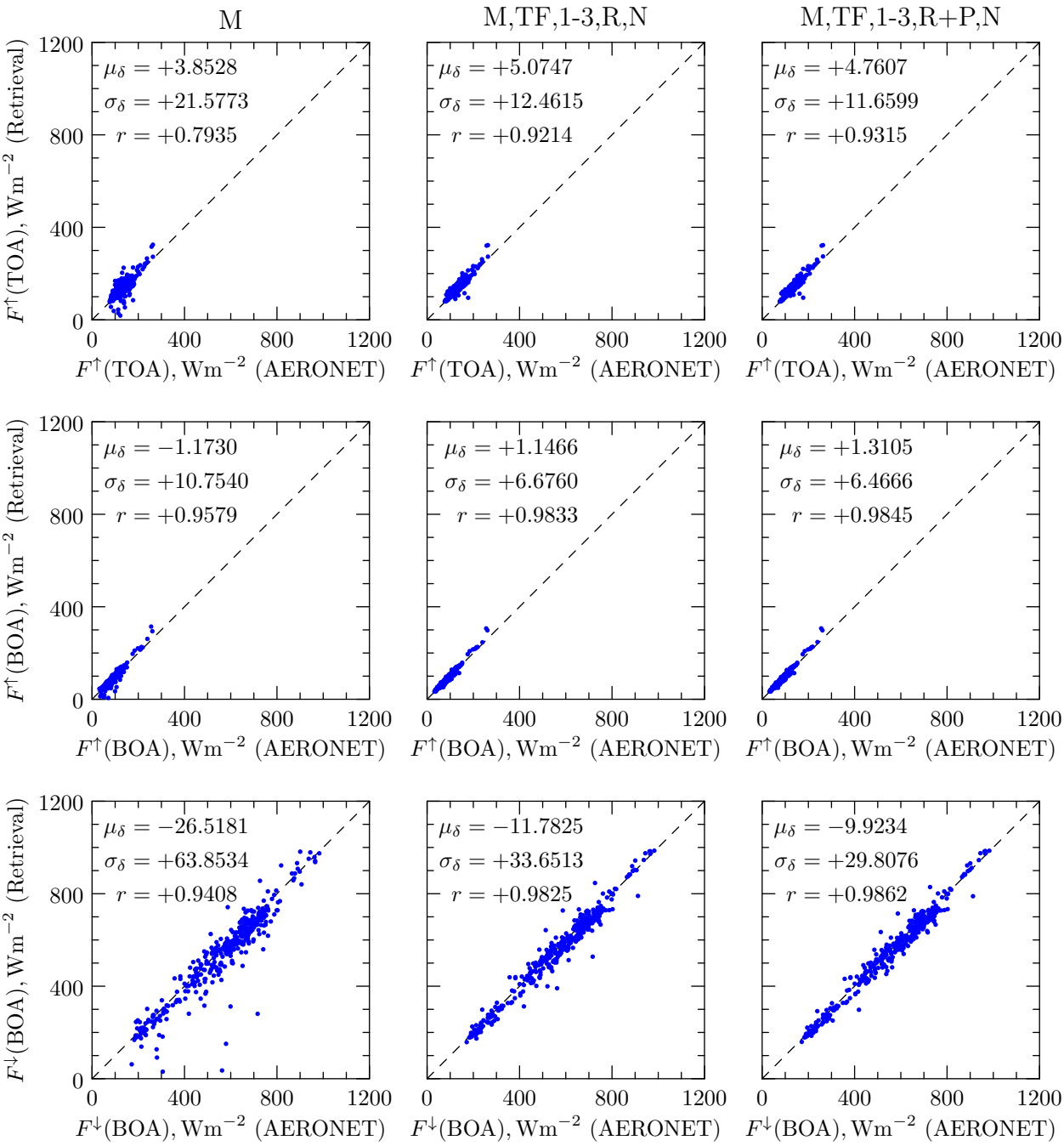

Figure 7.12: Same as figure 7.9 but only sites classified as biomass burning aerosol are included.

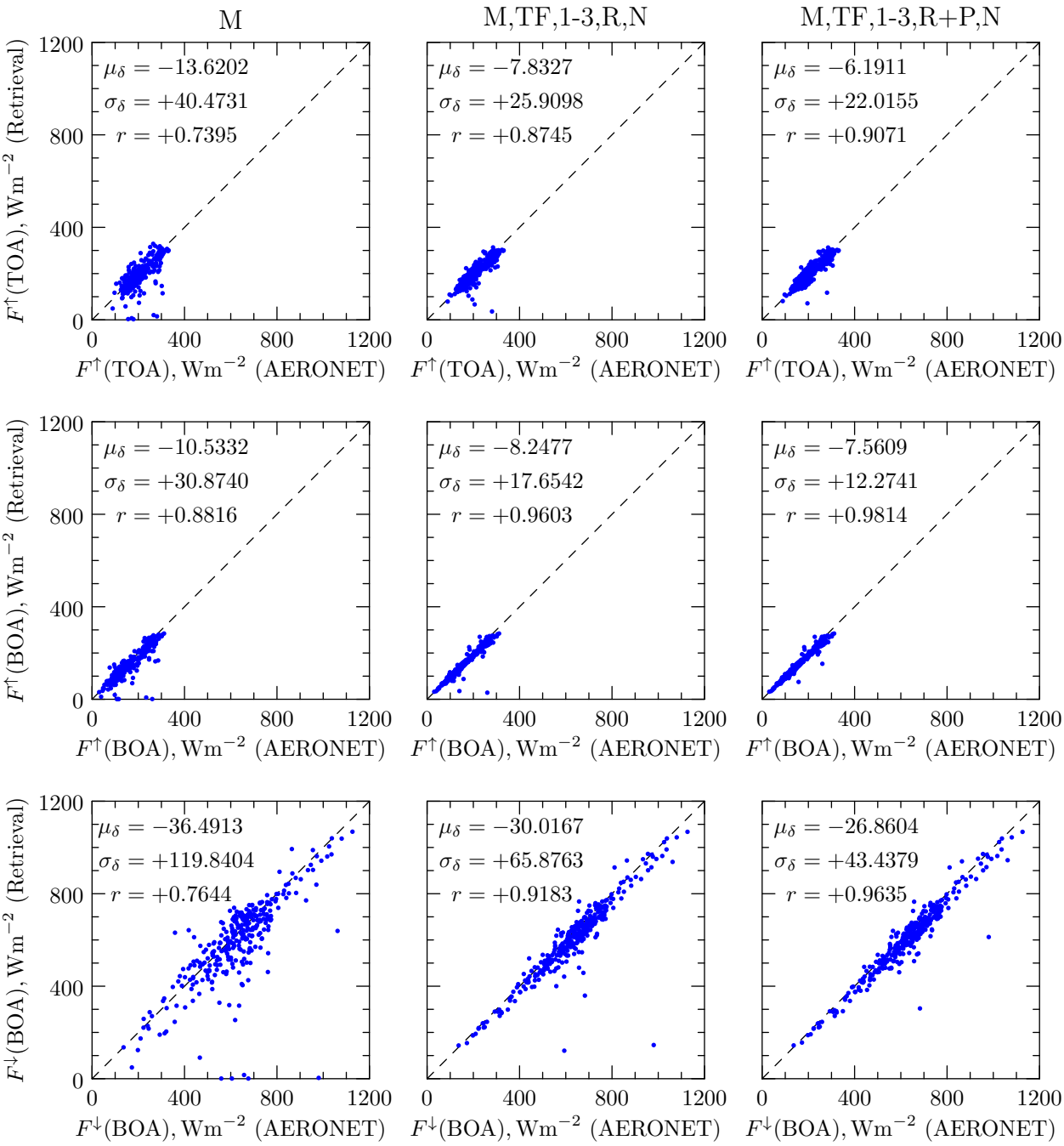

Figure 7.13: Same as figure 7.9 but only sites classified as desert dust aerosol are included.

where $\sigma(F)$ is the estimated standard deviation for flux quantity F computed as shown in section 7.3 and $\delta(F)$ is the actual error in the flux quantity F relative to AERONET from F(Retrieval) − F(AERONET).

The error distributions for the different flux quantities are all on the same order of magnitude and as expected, while the errors decrease with the more advanced measurement systems. Keep in mind, that these errors are normalized and the absolute values of the errors will differ as we have seen with the scatter plots, where the differences for $F^{\downarrow}$(BOA) are considerably larger than that of the other fluxes. The estimated errors are on the average larger than the actual errors, typically by $\sim 100\%$. This is in contrast to our estimation of the aerosol retrieval errors which mostly fell within the actual retrieval error. The reason our estimated errors for the fluxes are in general larger that the actual error is most likely do to non-linearities in our broadband flux model not accounted for in our error estimate which is based on linearization at the base state. It is also apparent that the error estimation gets better with the more advanced measurement systems. This comes from the estimated retrieval errors which were also better with the more advanced measurement systems as seen in the last chapter. As discussed, the accuracy of the estimated retrieval error depends on the information content of the measurements similar to the retrieved quantities themselves.

With aerosol type the error distributions are consistent with what we have seen in the scatter plots. For example, the error distributions for desert dust are some what flatter than for the other aerosol types due to the larger overall errors in our retrieved aerosol parameters for desert dust.

7.5.4 Radiative effect and effect efficiency

In this section we show timeseries plots of TOA and BOA radiative effect ΔF and radiative effect efficiency ΔF^{eff} from both the AERONET flux product and our derived fluxes for the four sample sites representing each aerosol type. Figure 7.19 shows radiative effects ΔF_{TOA} (left column) and ΔF_{BOA} (right column) and figure 7.20 shows radiative effect efficiencies $\Delta F^{\text{eff}}_{\text{TOA}}$ (left column) and $\Delta F^{\text{eff}}_{\text{BOA}}$ (right column). In each figure the results for mixed, urban-industrial, biomass burning, and desert dust aerosol types are given in the first, second, third, and fourth rows, respectively. Each plot contains timeseries for both AERONET (red) and our retrieval (blue). In addition, a seven-point Laplacian smoothing was performed on the AERONET timeseries which is plotted in black. Finally, the mean values for each timeseries are also given in each plot. The timeseries range

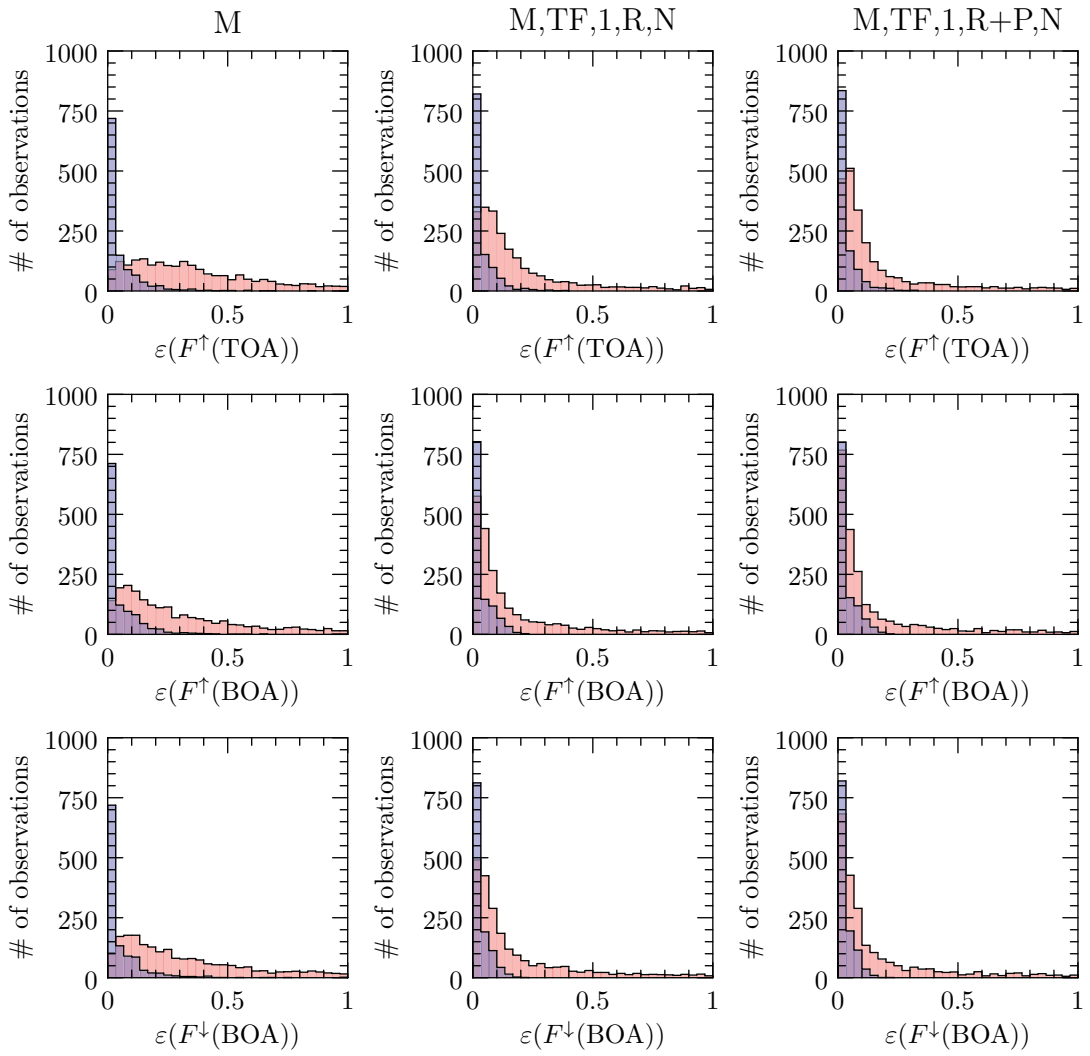

Figure 7.14: Histograms of the normalized error fractions $\varepsilon(x)$ from all sites for the estimated flux error $\varepsilon_\sigma(F)$ (light red) and for the actual difference between fluxes computed with our retrieval results and fluxes from the AERONET inversion product $\varepsilon_\delta(F)$ (light blue).

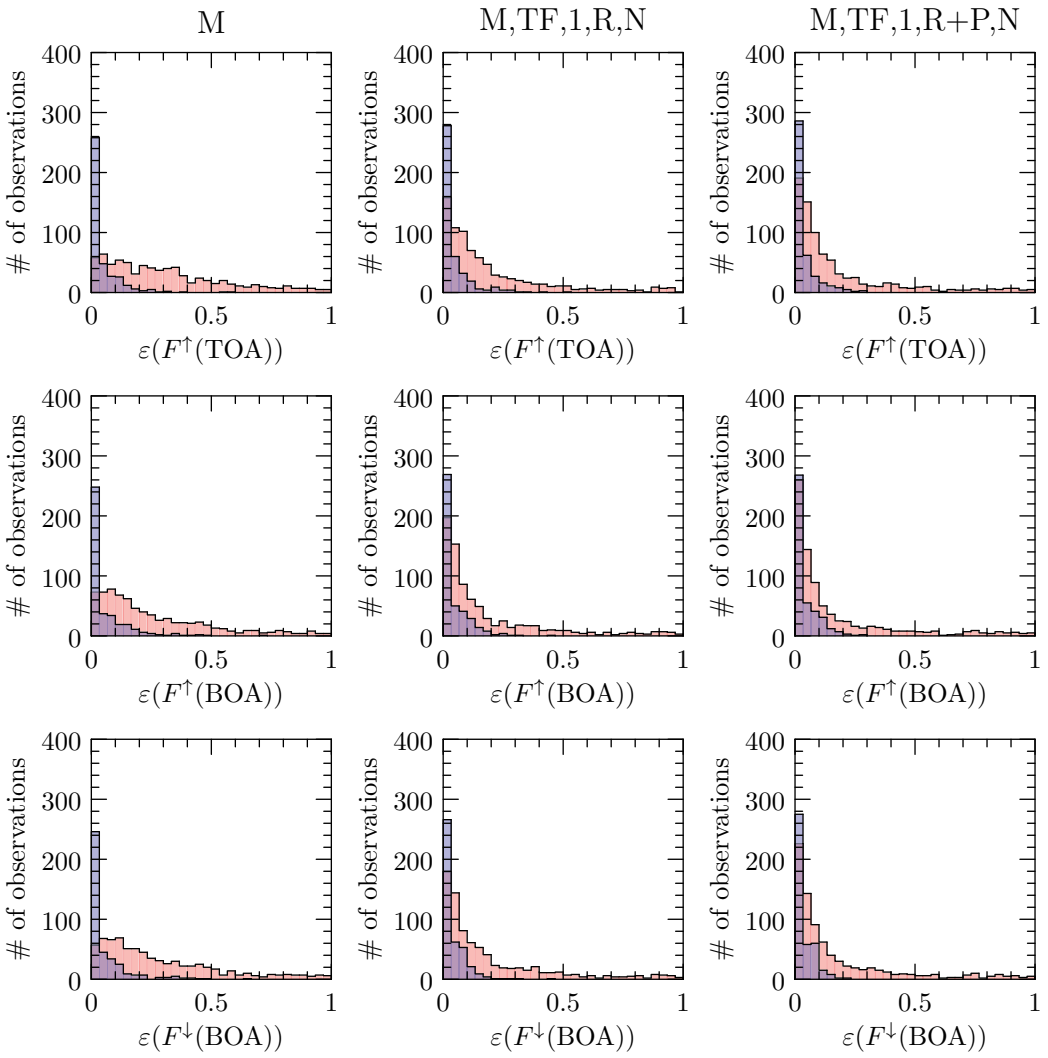

Figure 7.15: Same as figure 7.14 but only sites classified as mixed aerosol are included.

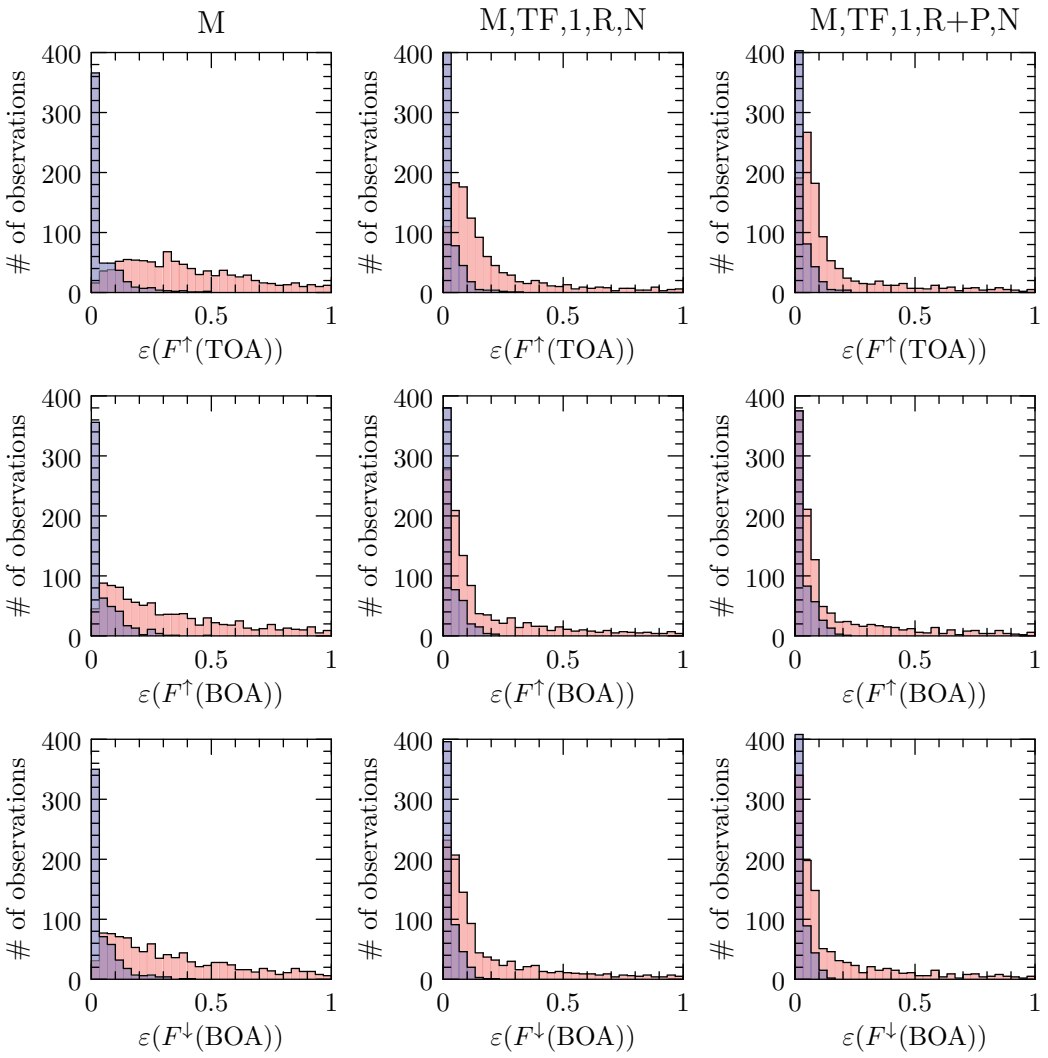

Figure 7.16: Same as figure 7.14 but only sites classified as urban-industrial aerosol are included.

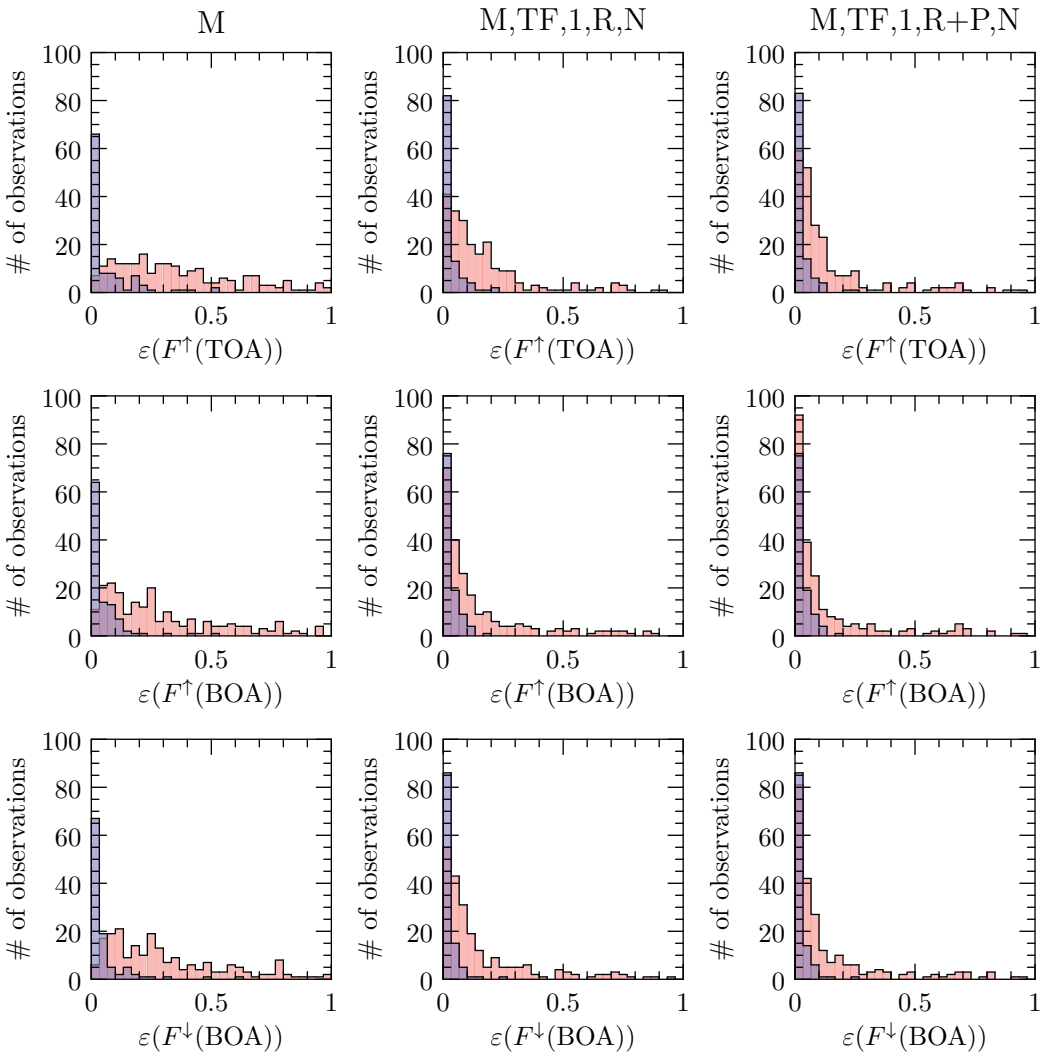

Figure 7.17: Same as figure 7.14 but only sites classified as biomass burning aerosol are included.

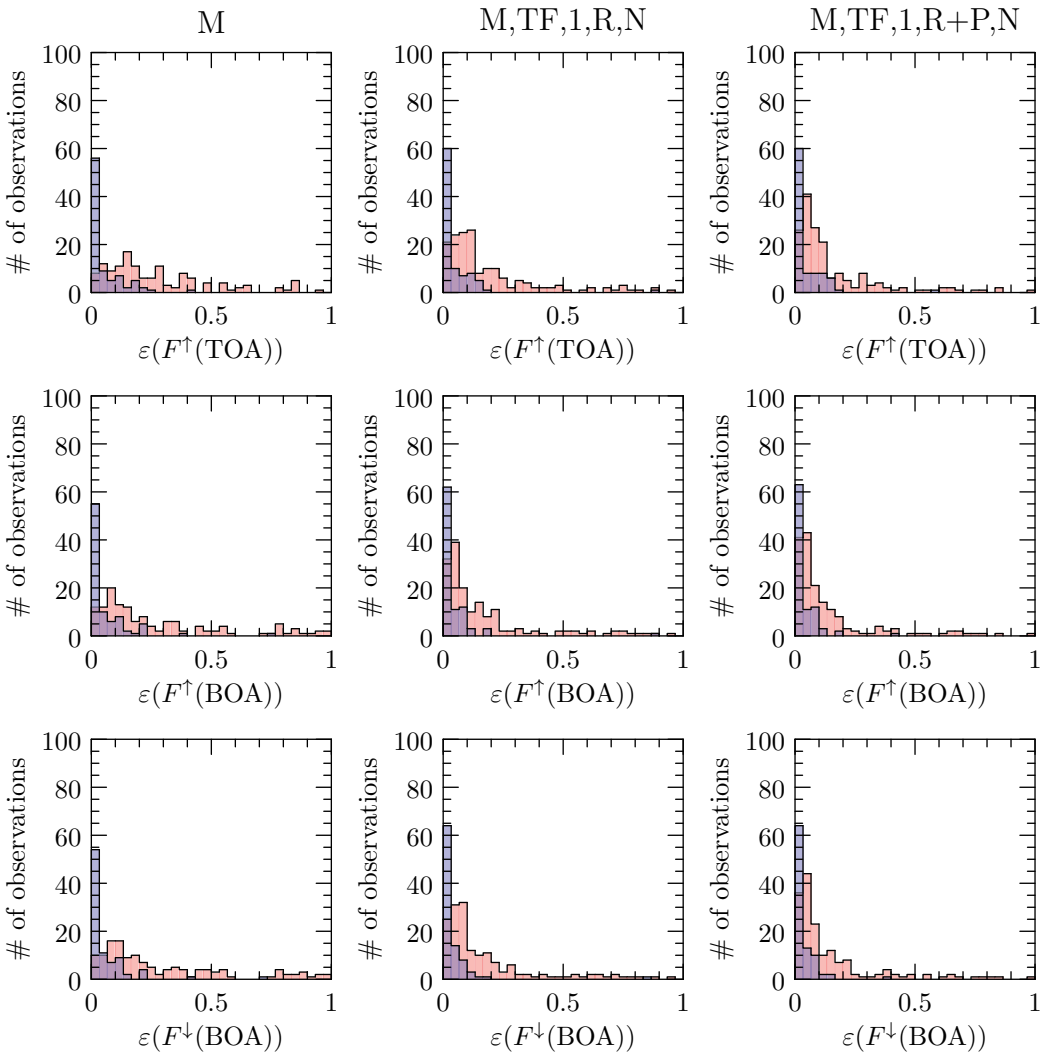

Figure 7.18: Same as figure 7.14 but only sites classified as desert dust aerosol are included.

from April 5, 2009 through Dec 5 2011 but for some aerosol types (biomass burning and desert dust) co-locations were not available over the entire period. In the following we discuss first some aspects related to the results overall then look at the effects for each aerosol type individually. In the discussion we will refer to the aerosol retrieval timeseries in chapter 6.

From the ΔF timeseries it is apparent that a negative effect or cooling predominates as expected. At TOA, the urban-industrial aerosol at Beijing is responsible for the lowest mean effect (largest cooling) of -29 Wm^{-2} whereas the biomass burning aerosols at Sao Paulo are responsible for the highest mean effect (smallest cooling) of -14 Wm^{-2}. In each case significant fluctuations in the TOA effect ΔF_{TOA} exist, where in some cases the effects at TOA reach and exceed zero to be positive (warming). At BOA, the mixed aerosol at Kanpur is responsible for the lowest mean effect (largest cooling) of -82 Wm^{-2} whereas the biomass burning aerosols at Sao Paulo are responsible for the highest mean effect (smallest cooling) of -62 Wm^{-2}. Overall the TOA coolings are less than that of BOA since at TOA cooling is due to aerosol scattering and decreases with aerosol absorption whereas at BOA cooling is caused by any attenuation of the downward radiation (backscattering and absorption) and therefore aerosols will almost always cause a cooling in the shortwave. Indeed, from the plots of BOA effect we can see that ΔF_{BOA} never exceeds zero.

From the ΔF^{eff} timeseries we can get a better idea about the mean effects of each aerosol type itself. For example, for TOA the mean effect efficiencies are -32, -62, -51, and -36 Wm^{-2} and for BOA are -171, -174, -192, and -165 Wm^{-2}, for mixed, urban-industrial, biomass burning, and desert dust, respectively. At TOA the aerosols with the least cooling are mixed and desert dust most likely due to the desert dust (a component of the mixed aerosol) absorption. Biomass burning aerosol induces a little more cooling but is still absorbing (black and organic carbon) and urban-industrial aerosol induces the largest cooling indicating the predominance of non-absorbing sulfates. Note that in some cases urban-industrial aerosol can be more absorbing due to a significant black carbon component. At BOA the aerosol with the least cooling is desert dust most likely due to strong forward scattering of large dust particles while the aerosol with the largest cooling is biomass burning due to the predominance of small particles and a relatively strong absorption.

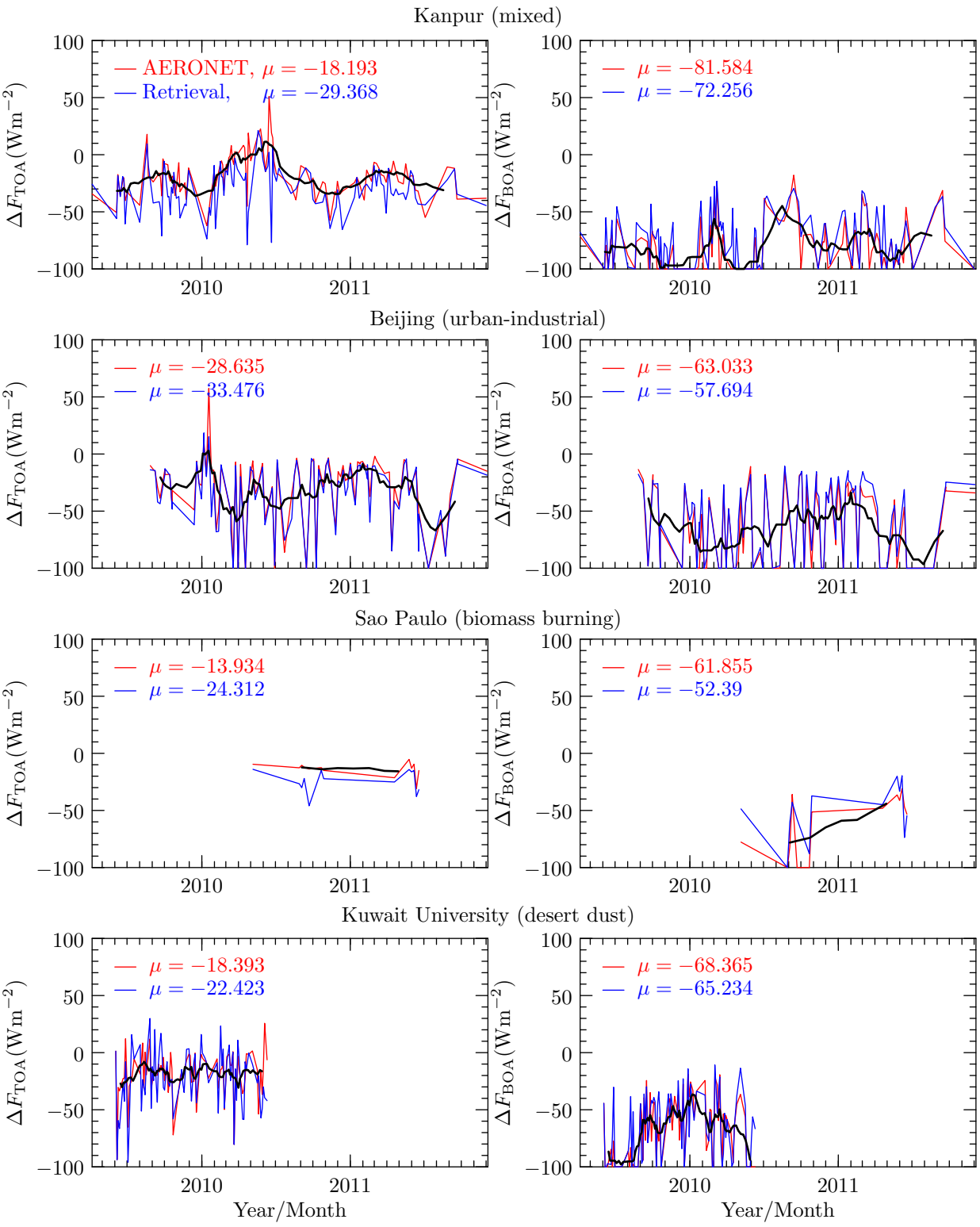

Figure 7.19: Timeseries of aerosol radiative effect ΔF from the AERONET inversion product (red), computed with our retrieval results (blue), and seven-point Laplacian smoothing of the AERONET timeseries (black), from our most advanced measurement scenario (M,TF,1-3,R+P,N). Each row is for one of our four aerosol type specific example sites and the left column is for ΔF_{TOA} and the right column is for ΔF_{BOA}.

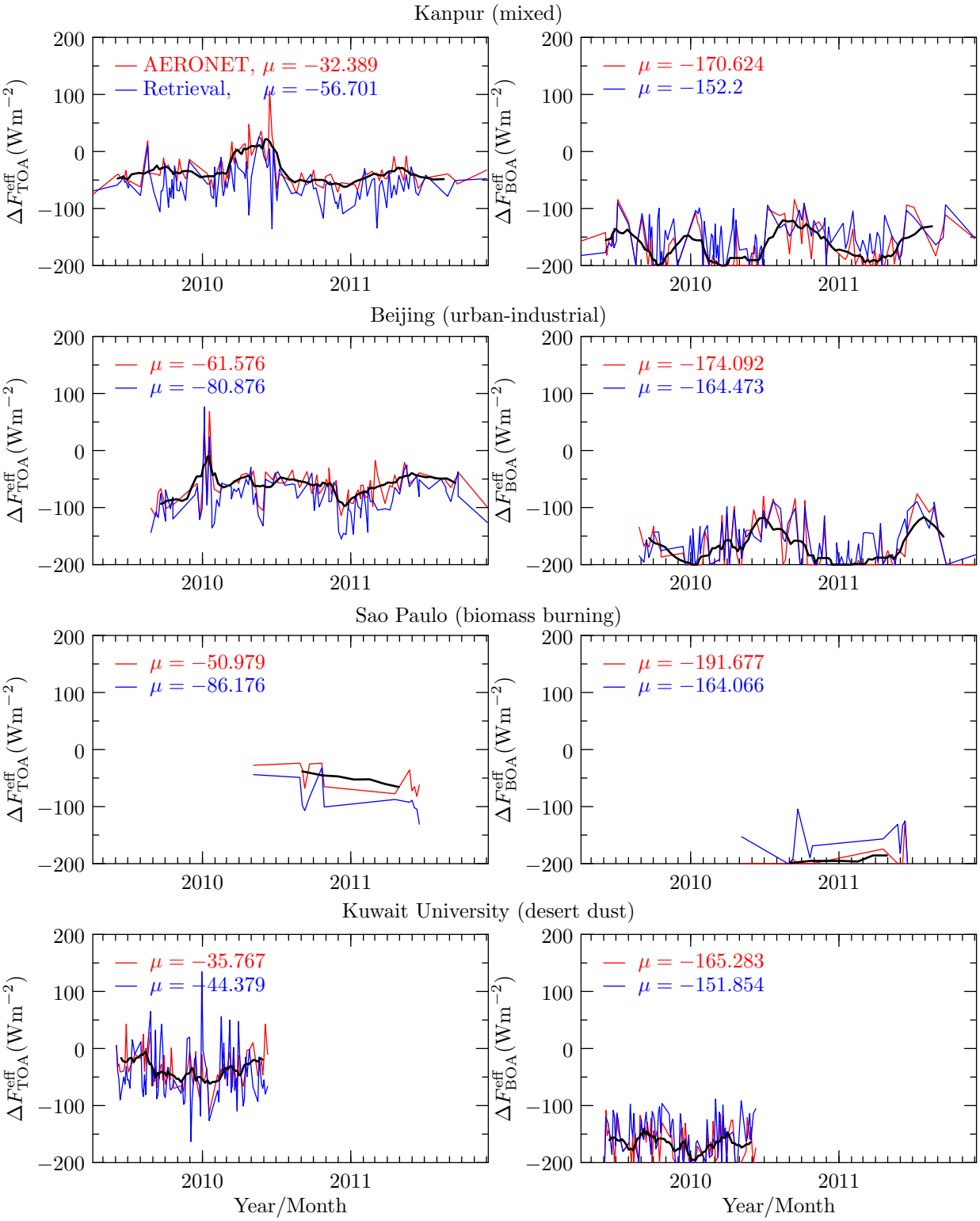

Figure 7.20: Same as figure 7.19 but for ΔF^{eff}.

Kanpur (mixed)

For Kanpur, characterized by mixed aerosol, lower TOA radiative effects (larger coolings) are associated with higher urban-industrial aerosol loadings whereas higher TOA radiative effects (smaller coolings and warmings) are associated with desert dust outbreaks (see chapter 7.5.4). For BOA radiative effect the inverse of this is true. These effects are also seen in the plots for the effect efficiency indicating that these fluctuations are not entirely driven by different loadings for each type. Looking at the corresponding timeseries for single scattering albedo $\omega_a(0.55)$ in chapter 6 we can see that larger TOA coolings of urban-industrial aerosol is associated with larger values of $\omega_a(0.55)$ whereas the lower TOA coolings and warmings of desert dust aerosol is associated with smaller values of $\omega_a(0.55)$. Again, for BOA the inverse of this is true. This is as we expect, where more absorption leads to less radiation scattered back to space increasing TOA radiative effect (a warming effect) and less radiation propagating through the aerosol layer to the surface decreasing the BOA radiative effect (a cooling effect).

Beijing (urban-industrial)

For Beijing, characterized by urban-industrial aerosol, the TOA radiative effect tends to inversely track the fine mode aerosol optical thickness $\tau_{a,f}(0.55)$ timeseries in chapter 6, that is, more cooling with larger values of $\tau_{a,f}(0.55)$ associated with larger urban-industrial aerosol loadings. In support of this the single scattering albedo $\omega_a(0.55)$ timeseries in chapter 6 shows peaks, and therefore more scattering back to space, that are associated with these larger coolings and larger fine mode optical thicknesses. As discussed previously, there is also a seasonal desert dust component in the aerosols over Beijing in March, April, and May, where dust is advected from the arid regions of western China and Mongolia. This is somewhat evident in the TOA effect plot with less cooling corresponding to larger values of coarse mode aerosol optical thickness $\tau_{a,c}(0.55)$ and smaller values of $\omega_a(0.55)$. When we look at the effect efficiency plot the timeseries tends to flatten to values associated with the troughs of urban-industrial aerosol radiative effect (~ 50 Wm^{-2}) at which $\tau_{a,f}(0.55)$ is close to unity. The desert dust component, associated with higher radiative effect, is associated with lower optical thicknesses ($\tau_{a,c}(0.55)$) and therefore have lower values of effect efficiency than actual effect

that are comparable to that of urban-industrial aerosol indicating that in this case at equal optical thicknesses the two aerosol types have similar TOA effects.

The BOA radiative effect for Beijing has similar trends to that of the TOA effect. This is unlike that of Kanpur, where TOA and BOA effects have opposite trends. The reason is the larger over all single scattering albedo for the urban-industrial aerosol and the much smaller loading of the more absorbing desert dust aerosol at Beijing. In this case, the aerosols mainly scatter radiation back to space the amount of which is dependent on the fine mode optical thickness with larger effect values for larger optical thicknesses. Looking at the BOA effect efficiencies for Beijing we see that desert dust aerosol has larger cooling values than urban-industrial aerosol indicating that in this case at equal optical thicknesses desert dust aerosol induces a larger BOA cooling than urban-industrial aerosol.

Sao Paulo (biomass burning)

For Sao Paulo, characterized by biomass burning aerosol, the number of co-locations is small, nevertheless, as discussed in chapter 6, larger values of the fine optical thickness $\tau_{a,f}(0.55)$ are associated with the burning season (August through October). Corresponding features are not discernible in the TOA radiative effect plot but the effect efficiency plot indicates smaller coolings almost reaching zero during the burning season. This is supported by looking at the timeseries for single scattering albedo $\omega_a(0.55)$ in chapter 6, where smaller values, and therefore less scattering back to space, are associated with the burning season. At BOA, there is a significantly larger cooling during the burning season which, as already discussed for desert dust, is a result of downward radiation either being scattered back to space or absorbed by the biomass burning aerosol and therefore not reaching the surface. The corresponding efficiency indicates that in this case at equal optical thicknesses the aerosols occurring both inside and outside of the burning season have comparable coolings suggesting that biomass burning aerosol also occurs outside of the burning season but with smaller loadings.

Kuwait University (desert dust)

For Kuwait University, characterized by desert dust aerosol, the TOA radiative effect is somewhat higher (warmer) for the desert dust outbreaks and lower (cooler) when urban-industrial aerosol

from Kuwait City are predominate. This is as expected and looking at the corresponding effect efficiencies indicates that in this case at equal optical thicknesses urban-industrial aerosol induces a larger TOA cooling than desert dust aerosol. AT BOA there is a much larger cooling during desert dust outbreaks compared to the beginning of the year when the desert dust aerosol has a minimum loading and urban-industrial aerosol becomes influential. As with the Beijing case, the corresponding effect efficiency indicated that in this case at equal optical thicknesses desert dust aerosol induces a larger BOA cooling than urban-industrial aerosol.

7.6 Summary and conclusions

In this chapter we use the results from chapter 6 as input to a broadband radiative flux model to compute shortwave atmospheric radiative fluxes including the upward and downward flux $F^{\uparrow\downarrow}(\lambda, z)$, upward and downward broadband flux $F^{\uparrow\downarrow}(z)$, the TOA and BOA aerosol radiative effect ΔF_{TOA} and ΔF_{BOA}, and the corresponding effect efficiencies $\Delta F^{\mathrm{eff}}_{\mathrm{TOA}}$ and $\Delta F^{\mathrm{eff}}_{\mathrm{BOA}}$. In addition to the absolute values, we compute an estimate of the uncertainties in these quantities using a rigorous error characterization of the inputs and linearization of the radiative transfer model. We then present computations for the same four case studies used for the retrieval results in chapter 6 of spectral flux as a function of wavelength and broadband flux as a function altitude along with their estimated errors for our three primary retrieval scenarios. In addition, we present sensitivities of these flux quantities with respect to the retrieved aerosol input quantities. Then we validate the results of absolute values relative to the AERONET flux product with scatter plots and corresponding statistics. In addition, we validate the estimated error with the actual error relative to the AERONET fluxes with the use of histograms. Finally, we present timeseries of the TOA and BOA aerosol radiative effect and corresponding effect efficiencies for our four case studies.

The relevant conclusions that can be taken from this study are the following:

1. For the upward fluxes at TOA $F^{\uparrow}$(TOA) and BOA $F^{\uparrow}$(BOA) the sensitivities are almost all positive with sensitivity to surface albedo dominating over that to all other retrieved parameters and the sensitivity to single scattering albedo being the second largest. For the downward flux at BOA $F^{\downarrow}$(BOA) the sensitivity to single scattering albedo dominates and is

positive along with that to surface albedo. Sensitivities to all the other aerosol parameters are negative.

2. Compared to the use of the MODIS only retrieval the flux errors improve significantly when the TANSO-FTS intensity measurements are added and improve even more when the TANSO-FTS intensity and polarization measurements are added. For the latter case, for all sites combined, the flux errors relative the AERONET fluxes are 2 ± 13 for $F^{\uparrow}$(TOA), -1 ± 8 for $F^{\uparrow}$(BOA), and -17 ± 30 for $F^{\downarrow}$(BOA). The absolute values of these errors fall outside of the absolute error for $F^{\downarrow}$(BOA) of $+9 \pm 12$ found by García et al. [2008] for AERONET compared to ground-based measurements but are opposite in sign. The larger errors for $F^{\downarrow}$(BOA) are due to larger overall values compared to upward fluxes and due to a more direct effect from aerosols. The larger errors relative to García et al. [2008] are primarily due to uncertainties in our satellite based retrieval.

3. In general, the flux errors are significantly larger for the desert dust aerosol type which is consistent with the larger retrieval errors for desert dust. Sources of retrieval errors for desert dust were discussed in the last chapter and include brighter surfaces characteristic of deserts and the presence of non-spherical particles with a retrieval that assumes spherical particles.

4. The estimated errors are in general larger than the actual errors, typically by $\sim 100\%$, most likely due to strong non-linearities in the broadband flux model. The error estimation gets better with the more advanced measurement scenarios since the estimated retrieval errors are more accurate for the more advanced measurement scenarios.

5. Timeseries of the radiative effect ΔF and the corresponding effect efficiencies ΔF^{eff} at TOA and BOA track the corresponding timeseries from the AERONET flux product well and show features that are consistent with physical understanding such as smaller cooling and even warming associated with desert dust and biomass burning aerosol and larger cooling associated with urban-industrial aerosol with a predominate sulfate component.

Chapter 8

Summary and Conclusions

This thesis explores the use of satellite-based multispectral measurements combined with hyperspectral measurements in molecular absorption bands at solar wavelengths for the remote sensing of tropospheric aerosols. The current state-of-the-art in satellite-based remote sensing of tropospheric aerosols is the use multispectral, multiangle, and/or polarimetric measurements. Unfortunately, no single instrument exists that provides quality measurements with all three characteristics. MODIS provides a large spectral range with a low noise requirement but only total reflectance at a single angle. MISR provides measurements at multiple angles but only total reflectance and a limited spectral range. POLDER provides multiangle polarimetric measurements but has poor noise characteristics and a limited spectral range. The ideal instrument APS was to fill these gaps but failed to achieve orbit. Our goal with this thesis is to explore a very different measurement approach that has largely been unexplored and provides a unique source of information and the opportunity to improve upon existing operational retrievals and hopefully fill the gap left by the failure of the Glory mission.

Below we will briefly summarize our presentation which can be roughly divided into three parts: (1) tool development, (2) core retrieval development, and (3) a sample application of retrieval results. For more detailed summaries the reader is referred to the summary and conclusions sections of each chapter. Then we discuss some key points that should be taken from the study followed by a discussion of the many possibilities for continuation of this research.

As with any numerically based science, computational tools are extremely important, the development of which is driven by both accuracy and speed requirements. Our research builds on many tools that have been developed by previous researchers. In addition, we make our own contribution, driven by the need for speed when simulating hyperspectral measurements. We present two radiative transfer models, a scalar model and vector model, that are matrix operator based and use the Padé approximation to the matrix exponential to solve the homogeneous solution for

each layer. In general, the models are 2-4 times faster than the standard discrete ordinate technique and are accurate to approximately the 6th decimal place. These RT models form the core of our instrument simulator used to simulate multispectral, multiangle, polarimetric, and/or hyperspectral measurements.

Our retrieval development falls into two phases: (1) A sensitivity and information content study and (2) a real retrieval and validation using real measurements. To start out the first phase we discuss in detail the retrieval setup, the measurement vector, the state vector and a priori, the forward model, and the case study scenarios. The sensitivity study explores all the measurement types considered including multispectral MODIS measurements and hyperspectral multiangle measurements of intensity and polarization from GOSAT. Detailed discussions of the of the sensitivity results were presented providing a physical insight into the capability of each type of measurement. Following the sensitivity study a rigorous information content analysis was presented including an SVD analysis and analysis of the degrees of freedom, averaging kernels, and the posteriori error. This was performed for several measurement scenarios including that using MODIS only and those using MODIS and the TANSO-FTS hyperspectral measurements, including the use of reflectance at nadir in the O_2 A-band, the use of reflectance at nadir in all three bands, the use of multiangle reflectance in the O_2 A-band only, the use of multiangle reflectance in all three bands, and finally the use of total and polarized reflectance in the previous four cases. The sensitivity study and information content analysis equip the researcher with an quantitative understanding of the capabilities of the retrieval system and knowledge to better understand the real retrieval results presented in the next chapter.

For our retrieval demonstration we start out by discussing the measurement data (MODIS and TANSO-FTS) and the ground based validation data (AERONET). This data must be co-located in time and space our strategy for which we discuss in detail. We then present the retrieval methodology, in particular the iterative inversion procedure. Retrieval results are then presented in the form of a comparison/validation relative to the AERONET retrieval product. We focus on the use of MODIS only and the use of MODIS along with nadir TANSO-FTS measurements, in the O_2 A-band only and in all three bands, and the total reflectance only and the use of total and polarized reflectance. The retrieval cases are divided into predominate aerosol types and each type is analyzed separately with scatter plots of our retrieval vs AERONET. One site for each aerosol type is then chosen

for which timeseries plots of each parameter are presented along with spectral comparisons for a single retrieval case. Finally, since the estimated retrieval error is just as important as the retrieved absolute values we present histograms of the actual retrieval errors and our estimated posteriori error superimposed onto a single plot.

Although our retrieval results are sufficiently general for other uses we have focused on the goal of improving our understanding of the direct radiative effect of aerosols and as such provide a sample study of the use of our retrieval results to compute radiative fluxes and aerosol radiative effects. We start out by describing the flux and radiative effect quantities computed and the radiative transfer model used to compute them. The model is fully linearized so that sensitivities of the flux quantities to input parameters and estimated errors may also be computed. The computed flux quantities are also validated against corresponding AERONET quantities so we briefly describe the AERONET flux and aerosol radiative forcing product. Finally, we present some flux spectrums and vertical profiles along with sensitivities and estimated errors followed by a validation with respect to AERONET in the form of scatter plots, timeseries, and error histograms.

8.1 Key findings

1. Surface albedo dominates the reflectance sensitivities in the continuum (free of molecular absorption) and as a result information on which dominates the information content of MODIS only retrievals that only use reflectance in bands free of molecular absorption. In contrast, molecular absorption masks the surface decreasing the relative contribution of the surface signal relative to the aerosol signal making measurements within molecular absorption bands advantageous over bright surfaces. With TANSO-FTS measurements the sensitivity to the surface decreases with molecular absorption optical thickness.

2. Second to the surface albedo the reflectance in the continuum is in general more sensitive to single scattering albedo than to any other aerosol parameter over bright surfaces. Like to surface albedo, the sensitivity of reflectance measurements to single scattering albedo decreases with molecular absorption optical thickness. This provides the opportunity to separate the effects of single scattering albedo from the other aerosol parameters within

molecular absorption bands increasing the information content relative to continuum only measurements.

3. In contrast to the surface albedo and the single scattering albedo the sensitivity to the other aerosol parameters including number concentration, mean and variance of the size distribution, and the real and imaginary parts of the index of refraction, increases with molecular absorption, in some cases surpassing the sensitivity to surface albedo and single scattering albedo.

4. Traditionally it has been the O_2 A-band that is used for atmospheric particle retrievals as the concentration and distribution of O_2 is well known. The additional use of the 1.61- and 2.06-μm CO_2 bands, available on current and future instruments along with the O_2 A-band, is also possible. Use of the 1.61-μm CO_2 band provides little additional information over that from the continuum due to the relatively weak CO_2 absorption in this band. When combined with MODIS, which also measures in the continuum at 1.61-μm this band serves mostly as redundancy. Use of the 2.06-μm CO_2 band provides a significant amount of additional information due to the relatively strong CO_2 absorption and larger wavelength with the ability to separate the effects of the fine and coarse modes and improve the retrieval of spectral dependence.

5. Measurements of polarized reflectance are more sensitive to the aerosols than to the surface providing another alternative to the standard continuum total reflectance measurements over bright surfaces. In addition, the sensitivity of polarized reflectance to single scattering albedo is, in general less than that to the other aerosol parameters. Finally, in general, the sensitivity of the polarized reflectance to all the parameters investigated, has a similar behavior with molecular absorption as that of total reflectance, where the sensitivity to the albedo parameters decreases and the sensitivity to the non-albedo parameters increases.

6. Multiangle measurements provide additional information about the aerosol single scattering phase function and therefore the size distribution and especially the complex index of refraction. This sensitivity is enhanced when polarimetric measurements are added due to the relatively large variation in the single scattering phase matrix with scattering angle.

7. As expected the number of retrievable parameters increases as more advanced measurements are added. The number ranges from three parameters when only MODIS reflectance is used,

to five parameters when TANSO-FTS O_2 A-band total reflectance is added, seven when total reflectance from all three TANSO-FTS bands are added, six when TANSO-FTS O_2 A-band total reflectance and polarized reflectance are added, and 10 when total reflectance and polarized reflectance from all three TANSO-FTS bands are added. These numbers increase by one or two when multiangle measurements are added. These numbers are also relatively stable when conditions such as aerosol type, aerosol optical thickness, aerosol-top height, and surface albedo vary. The largest variations in the number of retrievable parameters are for aerosol optical thickness $\tau_a(0.55)$. For $\tau_a(0.55) = 0.02$ to $\tau_a(0.55) = 2.0$ the case of using MODIS plus the TANSO-FTS O_2 A-band total reflectance at nadir varies by one parameter and the case of the most advanced measurement scenario varies by eight parameters.

8. Overall, as we have discussed, the amount of retrievable parameters increases with more advanced measurements. In general, the trend is that surface albedo is always the most retrievable, followed by aerosol number concentration in the coarse mode, then fine mode mean radius, then fine mode number concentration. After this, the parameters most likely to be retrieved depends more on the type of measurements, and include aerosol-top pressure, with the TANSO-FTS measurements, the coarse mode size distribution parameters with the addition of the TANSO-FTS 2.06-μm CO_2 band, and then finally spectral index of refractions when the TANSO-FTS 2.06-μm CO_2 band, the polarized reflectance, and/or multiangle measurements are added.

9. Estimates of retrieval errors vary significantly with aerosol optical thickness $\tau_a(0.55)$ with the errors in retrieved albedo increasing with $\tau_a(0.55)$ and the error in the retrieved aerosol parameters decreasing with $\tau_a(0.55)$. Errors are relatively unaffected by aerosol-top height. With surface albedo A errors increase rapidly from $A = 0.0$ to $A = 0.2$ but level off after $A = 0.2$. With the solar zenith and azimuth angles the errors vary significantly more for parameters that affect the aerosol scattering phase matrix such as size distribution and complex index of refraction especially for the cases including polarimetric and multiangle measurements.

10. Our retrieval results for all sites for total optical thickness $\tau_a(0.55)$ when using MODIS only (-0.048 ± 0.274) show a considerable amount of error relative to the MODIS operational retrieval product (-0.060 ± 0.153), primarily because the MODIS operational retrieval includes

only retrievals over dark surfaces and has been well tuned over many years. When the TANSO-FTS measurements are added the results improve significantly up to the results for the most advanced measurement scenario used (MODIS plus TANSO-FTS intensity and polarimetric measurements in all three bands) of -0.014 ± 0.058 that are comparable to our accuracy goals given by 7.5.4.

11. Our retrieval results for all sites for fine mode mean radius are typically bellow the accuracy goal of 0.1 μm whereas the results for the large mode mean radius for the most advanced measurement scenario fall short of this goal at 0.010 ± 0.338 μm. Results for the fine and coarse mode variance always fall within the rather lenient accuracy goals as a result of our relatively large spectral range. Results for the real part of the index of refraction (-0.004 ± 0.044 for the most advanced measurement scenario) do not meet our accuracy goal of 0.02 and our results for the imaginary part are even more uncertain at -0.007 ± 0.022. In the case of the index of refraction, multiangle measurements, not used for our actual retrieval study, should significantly improve results. Results for the derived and radiatively important single scattering albedo do not quite meet our accuracy goals but are close at -0.004 ± 0.0456 for the most advanced measurement scenario.

12. Distributions of the estimated retrieval error in general fall within the actual retrieval error distributions matching up better with the actual distributions when the more advanced measurements scenarios are used indicating that more information is not only important for more accurate retrieval of the quantities themselves but also for the uncertainties in those quantities.

13. Out of the retrieved parameters, positive sensitivities of TOA and BOA fluxes to surface albedo and single scattering albedo predominate. Second to these, are the sensitivities to the other aerosol parameters which are mostly positive at TOA and mostly negative at BOA with the sensitivity to mean particle radius and real part of the index of refraction for the dominate mode being predominant.

14. Fluxes calculated using our aerosol retrieval results improve with the more advanced measurement scenarios with errors for all sites combined of 2 ± 13 for $F^{\uparrow}$(TOA), -1 ± 8 for $F^{\uparrow}$(BOA), and -17 ± 30 for $F^{\downarrow}$(BOA). The absolute values of these errors fall outside of the absolute

error for $F^{\downarrow}$(BOA) of $+9 \pm 12$ found by García et al. [2008] for AERONET compared to ground-based measurements but are opposite in sign. Our larger errors are primarily due to uncertainties in our satellite based retrieval.

15. In general, the retrieval errors and the subsequent flux errors are significantly larger when desert dust aerosol are predominant. Sources of retrieval errors for desert dust include brighter surfaces characteristic of deserts and the presence of non-spherical particles with a retrieval that assumes spherical particles.

16. Distributions of the estimated flux errors are in general larger than the actual errors, typically by $\sim 100\%$, most likely due to strong non-linearities in the broadband flux model. As with estimated errors for the retrievals, the error estimation gets better with the more advanced measurement scenarios.

8.2 Future work

Although the work in this thesis is encouraging, there is definitely room for improvement. It is important to understand that the retrieval concept developed in this thesis is still at its infancy and as the literature shows it takes many years for retrieval systems to develop to maturity picking up improvements along the way. Along with GOSAT, the NASA EOS OCO-2 mission, at the implementation stage, and OCO-3 mission, at the formulation stage, ensure that the hyperspectral measurements used for our retrieval methodology will be available for several years into the future. This will allow our research to continue in order to improve and evolve the retrieval methodology. Below we list several possibilities for direct improvements that should be explored and some more evolutionary type changes that can be pursued.

1. In the current study the surface was assumed to be Lambertian while many surfaces exhibit non-Lambertian features and are better characterized with a linear combination of more representative BRDF kernels. For intensity measurements possibilities include: (1) the Roujean kernel [Roujean et al., 1992], derived by considering reflectance of a random arrangement of rectangular blocks on a flat surface, (2) the Li-sparse or Li-dense kernels [Wanner et al., 1995], derived by considering reflectance from the proportional areas of sunlit tree crowns and sunlit ground for randomly distributed cover, (3) the Ross-thin or Ross-thick kernels

[Wanner et al., 1995], based on volume-scattering empirical models, in which a radiative transfer model is applied to randomly oriented scattering facets (leaves) over a flat surface, or (4) the Rahman kernel [Rahman et al., 1993], which includes an explicit form for the phase function of the surface distribution of scatterers in the form of a Henyey-Greenstein function. For measurements of polarization a popular choice are the models of [Bréon et al., 1995] and [Nadal and Bréon, 1999]. Over the ocean the Cox and Munk kernel [Cox and Munk, 1954] for glitter reflectance, which assumes a Gaussian distribution of the slopes of the wave facets, should be used and has both intensity and polarized versions. In addition, a Lambertian foam component should also be added in the case of an ocean surface [Koepke, 1984, Monahan and Muircheartaigh, 1980, Whitlock et al., 1982].

2. It is well know that dust particles are, in general, non-spherical. Making the assumption that they are spherical can lead to significant biases in the retrieval results [Dubovik et al., 2002a, Herman et al., 2005]. The use of the t-matrix method [Mishchenko et al., 2002] to compute properties for an ensemble of oblate and prolate spheroids should be investigated. A shape parameter (ratio of the horizontal to rotational axis) can be added to the state vector introducing the possibility of retrieving information about non-sphericity.

3. The aerosol retrieval problem is both ill-posed and highly non-linear. Proper regularization is required to stabilize the inversion. In this study we use the rather simple Levenberg-Marquardt regularization. Alternative, techniques that should be explored include Philips-Tikhonov regularization [Tikhonov, 1963, Phillips, 1962] and the statistically optimized retrieval presented by Dubovik et al. [2011]. The addition of smoothing constraints can also improve the retrieval especially when spectrally dependent parameters are being retrieved as redundancy between measurements is utilized more effectively.

4. The possibility of the retrieving aerosol properties in more that one atmospheric layer was not discussed in this study even though the hyperspectral measurements in molecular absorption bands may contain enough information to do this [Heidinger and Stephens, 2000] in at least two layers. This should be explored, particularly for the retrieval of aerosol loading.

5. The use of coincident lidar observations can also improve the retrieval [Heidinger and Stephens, 2000] by providing accurate a priori information of aerosol layer boundaries introducing the

possibility of retrieving multiple aerosol layers. This should be explored, depending on the availability of CALIPSO observations in the future, particularly when OCO-2 is introduced to the A-train.

6. Extending the retrieval to use measurements from other instruments would also be an interesting research project, particularly the multiangle polarimetric measurements from POLDER, which along with MODIS, is in the A-train and will be joined by OCO-2 providing a wealth of coincident multispectral/multiangle/polarimetric/hyperspectral measurements.

7. Finally, the multi-pixel retrieval concept introduced by Dubovik et al. [2011] has the potential to significantly improve retrieval results and would in itself be a good Master's thesis or part of a Doctoral dissertation. The idea is that the spatial and temporal variations from pixel to pixel are enforced to be smooth by additional a priori constraints so that information from neighboring pixels, in space and time, contribute information to a each pixel's retrieval.

Bibliography

Ackerman, A. S., Toon, O. B., Stevens, D. E., Heymsfield, A. J., Ramanathan, V., and Welton, E. J. Reduction of tropical cloudiness by soot. *Science*, 288:1042–1047, May 2000. doi:10.1126/science.288.5468.1042.

Ackerman, S. A., Strabala, K. I., Menzel, W. P., Frey, R. A., Moeller, C. C., and Gumley, L. E. Discriminating clear sky from clouds with MODIS. *Journal of Geophysical Research*, 103(D24): 32141–32157, December 1998. doi:10.1029/1998JD200032.

Albrecht, B. A. Aerosols, cloud microphysics, and fractional cloudiness. *Science*, 245(4923): 1227–1230, September 1989. doi:10.1126/science.245.4923.1227.

Anderson, E., Bai, Z., Bischof, C., Blackford, S., Demmel, J., Dongarra, J., Croz, J. D., Greenbaum, A., Hammarling, S., McKenney, A., and Sorensen, D. *LAPACK User's Guide, Third Edition*. Society for Industrial and Applied Mathematics, Philadelphia, 1999. ISBN 0898714478. doi:10.1137/1.9780898719604.

Anderson, T. L., Charlson, R. J., Schwartz, S. E., Knutti, R., Boucher, O., Rodhe, H., and Heintzenberg, J. Climate forcing by aerosols a hazy picture. *Science*, 300:1103–1104, May 2003. doi:10.1126/science.1084777.

Anderson, T. L., Charlson, R. J., Bellouin, N., Boucher, O., Chin, M., Christopher, S. A., Haywood, J., Kaufman, Y. J., Kinne, S., Ogren, J. A., Remer, L. A., Takemura, T., Tanré, D., Torres, O., Trepte, C. R., Wielicki, B. A., Winker, D. M., and Yu, H. An "A-train" strategy for quantifying direct climate forcing by anthropogenic aerosols. *Bulletin of the American Meteorological Society*, 86(12):1795–1809, December 2005. doi:10.1175/BAMS-86-12-1795.

Arioli, M., Codenotti, B., and Fassino, C. The Padé method for computing the matrix exponential. *Linear Algebra and its Applications*, 240:111–130, 1996. doi:10.1016/0024-3795(94)00190-1.

Aronson, R. General solution for polarized radiation in a homogeneous-slab atmosphere. *The Astrophysical Journal*, 177:411–421, October 1972. doi:10.1086/151718.

Aronson, R. and Yarmush, D. L. Transfer-matrix method for gamma-ray and neutron penetration. *Journal of Mathematical Physics*, 7(2):221–237, February 1966. doi:10.1063/1.1704923.

Barkstrom, B. R. The Earth Radiation Budget Experiment (ERBE). *Bulletin of the American Meteorological Society*, 65(11):1170–1185, November 1984. doi:10.1175/1520-0477(1984)065%3C1170:TERBE%3E2.0.CO;2.

Bates, D. R. Rayleigh scattering by air. *Planetary and Space Science*, 32(6):785–790, 1984. doi:10.1016/0032-0633(84)90102-8.

Bennartz, R. and Fischer, J. A modified k-distribution approach applied to narrow band water vapour and oxygen absorption estimates in the near infrared. *Journal of Quantitative Spectroscopy and Radiative Transfer*, 66:539–553, 2000. doi:10.1016/S0022-4073(99)00184-3.

Bodhaine, B. A., Wood, N. B., Dutton, E. G., and Slusser, J. R. On rayleigh optical depth calculations. *Journal of Atmospheric and Oceanic Technology*, 16:1854–1861, November 1999. doi:10.1175/1520-0426(1999)016%3C1854:ORODC%3E2.0.CO;2.

Boesche, E., Stammes, P., Preusker, R., Bennartz, R., Knap, W., and Fischer, J. Polarization of skylight in the O_2 A band: Effects of aerosol properties. *Applied Optics*, 47(19):3467–3480, July 2008. doi:10.1364/AO.47.003467.

Boesche, E., Stammes, P., and Bennartz, R. Aerosol influence on polarization and intensity in near-infrared O_2 and CO_2 absorption bands observed from space. *Journal of Quantitative Spectroscopy and Radiative Transfer*, 110:223–239, 2009. doi:10.1016/j.jqsrt.2008.09.019.

Bond, T. C., Doherty, S. J., Fahey, D. W., Forster, P. M., Berntsen, T., DeAngelo, B. J., Flanner, M. G., Ghan, S., Kärcher, B., Koch, D., Kinne, S., Kondo, Y., Quinn, P. K., Sarofim, M. C., Schultz, M. G., Schulz, M., Venkataraman, C., Zhang, H., Zhang, S., Bellouin, N., Guttikunda, S. K., Hopke, P. K., Jacobson, M. Z., Kaiser, J. W., Klimont, Z., Lohmann, U., Schwarz, J. P., Shindell, D., Storelvmo, T., Warren, S. G., and Zender, C. S. Bounding the role of black carbon in the climate system: A scientific assessment. *Journal of Geophysical Research*, 2013. doi:10.1002/jgrd.50171. Accepted.

Boucher, O. and Tanré, D. Estimation of the aerosol perturbation to the Earth's radiative budget over oceans using POLDER satellite aerosol retrievals. *Geophysical Research Letters*, 27(8): 1103–1106, April 2000. doi:10.1029/1999GL010963.

Bowman, K. P. and Krueger, A. J. A global climatology of total ozone from the Nimbus 7 Total Ozone Mapping Spectrometer. *Journal of Geophysical Research*, 90(D5):32141–32157, August 1985. doi:10.1029/JD090iD05p07967.

Bréon, F.-M., Tanré, D., Lecomte, P., and Herman, M. Polarized reflectance of bare soils and vegetation: Measurements and models. *IEEE Transactions on Geoscience and Remote Sensing*, 33(2):487–499, March 1995. doi:10.1109/36.377949.

Budak, V. P., Klyuykov, D. A., and Korkin, S. V. Complete matrix solution of radiative transfer equation for PILE of horizontally homogeneous slabs. *Journal of Quantitative Spectroscopy and Radiative Transfer*, 112:1141–1148, 2011. doi:10.1016/j.jqsrt.2010.08.028.

Buizza, R., Miller, M., and Palmer, T. N. Stochastic representation of model uncertainties in the ecmwf ensemble prediction system. *Quarterly Journal of the Royal Meteorological Society*, 125: 2887–2908, 1999. doi:10.1002/qj.49712556006.

Cairns, B., Russell, E. E., and Travis, L. D. The research scanning polarimeter: Calibration and ground-based measurements. *SPIE*, 3754:186–196, 1999. doi:10.1117/12.366329.

Callies, J., Corpaccioli, E., Eisinger, M., Hahne, A., and Lefebvre, A. GOME-2 metop's second-generation sensor for operational ozone monitoring. *ESA Bulletin*, (102):28–36, May 2000.

Chalhoub, E. S. and Garcia, R. D. M. The equivalence between two techniques of angular interpolation for the discrete-ordinates method. *Journal of Quantitative Spectroscopy and Radiative Transfer*, 64:517–535, 2000. doi:10.1016/S0022-4073(99)00134-X.

Chami, M., Santer, R., and Dilligeard, E. Radiative transfer model for the computation of radiance and polarization in an ocean-atmosphere system: Polarization properties of suspended matter for remote sensing. *Applied Optics*, 40(15):2398–2416, May 2001. doi:10.1364/AO.40.002398.

Chandrasekhar, S. *Radiative Transfer*. Dover Publications, Inc., Mineola, New York, USA, 1960. ISBN 0486605906.

Chapman, R. M. Cloud distributions and altitude profiles from a satellite. *Planetary and Space Science*, 9:70–71, 1962. doi:10.1016/0032-0633(62)90074-0.

Charlson, R. J., Schwartz, S. E., Hales, J. M., Cess, R. D., Jr., J. A. C., Hansen, J. E., and Hofmann, D. J. Climate forcing by anthropogenic aerosols. *Science*, 255:423–430, January 1992. doi:10.1126/science.255.5043.423.

Chevallier, F., Chédin, A., Chéruy, F., and Morcrette, J.-J. TIGR-like atmospheric-profile databases for accurate radiative-flux computation. *Quarterly Journal of the Royal Meteorological Society*, 126:777–785, 2000. doi:10.1002/qj.49712656319.

Chou, M.-D., Chan, P.-K., and Wang, M. Aerosol radiative forcing derived from SeaWiFS-retrieved aerosol optical properties. *Journal of the Atmospheric Sciences*, 59:748–757, February 2002. doi:10.1175/1520-0469(2002)059%3C0748:ARFDFS%3E2.0.CO;2.

Chowdhary, J., Cairns, B., and Travis, L. Case studies of aerosol retrievals over the ocean from multi-angle, multispectral photopolarimetric remote sensing data. *Journal of the Atmospheric Sciences*, 59:383–397, February 2002. doi:10.1175/1520-0469(2002)059%3C0383:CSOARO%3E2.0.CO;2.

Chowdhary, J., , Cairns, B., Mishchenko, M. I., Hobbs, P. V., Cota, G. F., Redemann, J., Rutledge, K., Holben, B. N., and Russell, E. Retrieval of aerosol scattering and absorption properties from photopolarimetric observations over the ocean during the CLAMS experiment. *Journal of the Atmospheric Sciences*, 62:1093–1117, April 2005. doi:10.1175/JAS3389.1.

Christopher, S. A. and Zhang, J. Daytime variation of shortwave direct radiative forcing of biomass burning aerosols from GOES-8 imager. *Journal of the Atmospheric Sciences*, 59:681–691, February 2002a. doi:10.1175/1520-0469(2002)059%3C0681:DVOSDR%3E2.0.CO;2.

Christopher, S. A. and Zhang, J. Shortwave aerosol radiative forcing from MODIS and CERES observations over the oceans. *Geophysical Research Letters*, 29(18):1859, 2002b. doi:10.1029/2002GL014803.

Christopher, S. A., Kliche, D. V., Chou, J., and Welch, R. M. First estimates of the radiative forcing of aerosols generated from biomass burning using satellite data. *Journal of Geophysical Research*, 101(D16):21265–21273, September 1996. doi:10.1029/96JD02161.

Christopher, S. A., Chou, J., Zhang, J., Li, X., Berendes, T. A., and Welch, R. M. Shortwave direct radiative forcing of biomass burning aerosols estimated using VIRS and CERES data. *Geophysical Research Letters*, 27(15):2197–2200, August 2000. doi:10.1029/1999GL010923.

Chuang, C. C., Penner, J. E., Taylor, K. E., Grossman, A. S., and Walton, J. J. An assessment of the radiative effects of anthropogenic sulfate. *Journal of Geophysical Research*, 102(D3):3761–3778, February 1997. doi:10.1029/96JD03087.

Chýlek, P., Videen, G., Ngo, D., Pinnick, R. G., and Klett, J. D. Effect of black carbon on the optical properties and climate forcing of sulfate aerosols. *Journal of Geophysical Research*, 100 (D8):16325–16332, August 1995. doi:10.1029/95JD01465.

Chýlek, P., Lesins, G. B., Videen, G., Wong, J. G. D., Pinnick, R. G., Ngo, D., and Klett, J. D. Black carbon and absorption of solar radiation by clouds. *Journal of Geophysical Research*, 101 (D18):23365–23371, October 1996. doi:10.1029/96JD01901.

Cohen, H. and Cureton, K. Padé approximates and the X and Y functions of radiative transfer theory. *Journal of Quantitative Spectroscopy and Radiative Transfer*, 11:1279–1283, 1971. doi:10.1016/0022-4073(71)90102-6.

Conel, J. E. Determination of surface reflectance and estimates of atmospheric optical depth and single scattering albedo from landsat thematic mapper data. *International Journal of Remote Sensing*, 11(5):783–828, 1991. doi:10.1080/01431169008955057.

Cox, C. and Munk, W. Measurement of the roughness of the sea surface from photographs of the sun's glitter. *Journal of the Optical Society of America*, 44(11):838–850, November 1954. doi:10.1364/JOSA.44.000838.

Crisp, D., Atlas, R. M., Breon, F.-M., Brown, L. R., Burrows, J. P., Ciais, P., Connor, B. J., Doney, S. C., Fung, I. Y., Jacob, D. J., Miller, C. E., O'Brien, D., Pawson, S., Randerson, J. T., Rayner, P., Salawitch, R. J., Sander, S. P., Sen, B., Stephens, G. L., Tans, P. P., Toon, G. C., Wennberg, P. O., et al. The Orbiting Carbon Observatory (OCO) mission. *Advances in Space Research*, 34: 700–709, 2004. doi:10.1016/j.asr.2003.08.062.

Crisp, D., Boesch, H., Brown, L., Castano, R., Christi, M., Connor, B., Frankenberg, C., McDuffie, J., Miller, C., Natraj, V., O'Dell, C., O'Brien, D., Polonski, I., Oyafuso, F., Thompson, D., Toon, G., and Spurr, R. OCO (Orbiting Carbon Observatory) - 2 level 2 full physics retrieval algorithm theoretical basis. Technical Report OCO D-65488, National Aeronautics and Space Administration (NASA) Jet Propulsion Laboratory (JPL), California Institute of Technology, Pasadena, California, 2010.

Dahlback, A. and Stamnes, K. A new spherical model for computing the radiation field available for photolysis and heating at twilight. *Planetary and Space Science*, 39(5):671–683, 1991. doi:10.1016/0032-0633(91)90061-E.

d'Almeida, G. A., Koepke, P., and Shettle, E. P. *Atmospheric Aerosols: Global Climatology and Radiative Characteristics*. A. Deepak Publishing, Hampton, Virginia, USA, 1991. ISBN 093719-4220.

de Graaf, M., Stammes, P., Torres, O., and Koelemeijer, R. B. A. Absorbing aerosol index: Sensitivity analysis, application to GOME and comparison with TOMS. *Journal of Geophysical Research*, 110:D01201, 2005. doi:10.1029/2004JD005178.

de Haan, J. F., Bosma, P. B., and Hovenier, J. W. The adding method for multiple scattering calculations of polarized light. *Astronomy and Astrophysics*, 183:371–391, 1987.

Deschamps, P.-Y., Bréon, F.-M., Leroy, M., Podaire, A., Bricaud, A., Buriez, J.-C., and Séze, G. The POLDER mission: Instrument characteristics and scientific objectives. *IEEE Transactions on Geoscience and Remote Sensing*, 32(3):598–88, May 1994. doi:10.1109/36.297978.

Deuzé, J. L., Goloub, P., Herman, M., Marchand, A., Perry, G., Susana, S., and Tanré, D. Estimate of the aerosol properties over the ocean with POLDER. *Journal of Geophysical Research*, 105 (D12):15329–15346, June 2000. doi:10.1029/2000JD900148.

Deuzé, J. L., Bréon, F. M., Devaux, C., Goloub, P., Herman, M., LaFrance, B., Maignan, F., Marchand, A., Nadal, F., Perry, G., and Tanré, D. Remote sensing of aerosols over land surfaces from POLDER-ADEOS-1 polarized measurements. *Journal of Geophysical Research*, 106(D5): 4913–4926, March 2001. doi:10.1029/2000JD900364.

Dianov-Klokov, V. I. and Krasnokutskaya, L. D. Comparision of observed and calculated effective photon path-length in clouds. *Izv. Acad. Sci. USSR Atmos. Oceanic Phys.*, 8:487–492, 1972.

Dianov-Klokov, V. I., Kropotkina, E. P., Malkov, I. P., and Matveyeva, O. A. Absorption band deformation and the effective path-length of light in clouds. *Izv. Acad. Sci. USSR Atmos. Oceanic Phys.*, 6:458–463, 1970.

Diner, D. J., Beckert, J. C., Reilly, T. H., Bruegge, C. J., Conel, J. E., Kahn, R. A., Martonchik, J. V., Ackerman, T. P., Davies, R., Gerstl, S. A. W., Gordon, H. R., Muller, J.-P., Myneni, R. B., Sellers, P. J., Pinty, B., and Verstraete, M. M. Multiangle imaging spectroradiometer (MISR) instrument description and experiment overview. *IEEE Transactions on Geoscience and Remote Sensing*, 36(4):1072–1087, July 1998. doi:10.1109/36.700992.

Diner, D. J., Ackerman, T. P., Anderson, T. L., Bösenberg, J., Braverman, A. J., Charlson, R. J., Collins, W. D., Davies, R., Holben, B. N., Hostetler, C. A., Kahn, R. A., Martonchik, J. V., Menzies, R. T., Miller, M. A., Ogren, J. A., Penner, J. E., Rasch, P. J., Schwartz, S. E., Seinfeld, J. H., Stephens, G. L., Torres, O., Travis, L. D., Wielicki, B. A., and Yu, B. PARAGON: An integrated approach for characterizing aerosol climate impacts and environmental interactions. *Bulletin of the American Meteorological Society*, 85(10):1491–1501, October 2004. doi:10.1175/BAMS-85-10-1491.

Doicu, A. and Trautmann, T. Discrete-ordinate method with matrix exponential for a pseudo-spherical atmosphere: Scalar case. *Journal of Quantitative Spectroscopy and Radiative Transfer*, 110:146–158, 2009. doi:10.1016/j.jqsrt.2008.09.014.

Doicu, A., Trautmann, T., Schreier, F., and Hess, M. Finite element method for the two-dimensional atmospheric radiative transfer. *Journal of Quantitative Spectroscopy and Radiative Transfer*, 91: 347–361, 2005. doi:10.1016/j.jqsrt.2004.07.003.

Dongarra, J. J., Croz, J. D., Hammarling, S., and Duff, I. A set of level 3 Basic Linear Algebra Subprograms. *ACM Transactions on Mathematical Software*, 16(1):1–17, March 1990. doi:10.1145/77626.79170.

Duan, M. and Min, Q. A fast radiative transfer model for simulating high-resolution absorption bands. *Journal of Geophysical Research*, 110:D15201, 2005. doi:10.1029/2004JD005590.

Dubovik, O., Smirnov, A., Holben, B. N., D., M., King, Kaufman, Y. J., Eck, T. F., and Slutsker, I. Accuracy assessments of aerosol optical properties retrieved from Aerosol Robotic Network (AERONET) sun and sky radiance measurements. *Journal of Geophysical Research*, 105(D8): 9791–9806, April 2000. doi:10.1029/2000JD900040.

Dubovik, O., Holben, B. N., Lapyonok, T., Sinyuk, A., Yang, P., Slutsker, I., and Mishchenko, M. I. Non-spherical aerosol retrieval method employing light scattering by spheroids. *Geophysical Research Letters*, 29(10):1415, 2002a. doi:10.1029/2001GL014506.

Dubovik, O., Herman, M., Holdak, A., Lapyonok, T., Tanré, D., Deuzé, J. L., Ducos, F., Sinyuk, A., and Lopatin, A. Statistically optimized inversion algorithm for enhanced retrieval of aerosol properties from spectral multi-angle polarimetric satellite observations. *Atmospheric Measurement Techniques*, 4:975–1018, 2011. doi:10.5194/amt-4-975-2011.

Dubovik, O. and King, M. D. A flexible inversion algorithm for retrieval of aerosol optical properties from sun and sky radiance measurements. *Journal of Geophysical Research*, 105(D16):20673–20696, August 2000. doi:10.1029/2000JD900282.

Dubovik, O., Holben, B., Eck, T. F., Smirnov, A., Kaufman, Y. J., King, M. D., Tanré, D., and Slutsker, I. Variability of absorption and optical properties of key aerosol types observed in worldwide locations. *Journal of the Atmospheric Sciences*, 59:590–608, February 2002b. doi:10.1175/1520-0469(2002)059%3C0590:VOAAOP%3E2.0.CO;2.

Dubuisson, P., Buriez, J. C., and Fouquart, Y. High spectral resolution solar radiative transfer in absorbing and acattering media: Application to the satellite simulation. *Journal of Quantitative Spectroscopy and Radiative Transfer*, 55(1):103–126, 1996. doi:10.1016/0022-4073(95)00134-4.

Dunion, J. P. and Velden, C. S. The impact of the saharan air layer on atlantic tropical cyclone activity. *Bulletin of the American Meteorological Society*, 85:353–365, March 2004. doi:10.1175/BAMS-85-3-353.

Eck, T. F., Holben, B. N., Sinyuk, A., Pinker, R. T., Goloub, P., Chen, H., Chatenet, B., Li, Z., Singh, R. P., Tripathi, S. N., Reid, J. S., Giles, D. M., Dubovik, O., O'Neill, N. T., Smirnov, A., Wang, P., and Xia, X. Climatological aspects of the optical properties of fine/coarse mode aerosol mixtures. *Journal of Geophysical Research*, 115:D13205, 2010. doi:10.1029/2008JD011115.

El wakil, S. A., Haggag, M. H., and Machali, H. M. Padé approximants for radiative transfer in inhomogeneous medium. *Astrophysics and Space Science*, 91:125–131, 1983. doi:10.1007/BF00650219.

El Wakil, S. A., Haggag, M. H., Machali, H. M., and Saad, E. A. Radiation transfer in dispersive media. *Journal of Physics D: Applied Physics*, 18:1469–1473, 1985. doi:10.1086/149664.

Emde, C., Buehler, S. A., Davis, C., Eriksson, P., Sreerekha, T. R., and Teichmann, C. A polarized discrete ordinate scattering model for simulations of limb and nadir long-wave measurements in 1-D/3-D spherical atmospheres. *Journal of Geophysical Research*, 109:D24207, 2004. doi:10.1029/2004JD005140.

Fischer, J. and Cordes, W. Detection of cloud-top height from backscattered radiances within the oxygen A band. Part 2: Measurements. *Journal of Applied Meteorology*, 30:1260–1267, September 1991. doi:10.1175/1520-0450(1991)030%3C1260:DOCTHF%3E2.0.CO;2.

Fischer, J. and Grassl, H. Detection of cloud-top height from backscattered radiances within the oxygen A band. Part 1: Theoretical study. *Journal of Applied Meteorology*, 30:1245–1259, September 1991. doi:10.1175/1520-0450(1991)030%3C1245:DOCTHF%3E2.0.CO;2.

Flatau, P. J. and Stephens, G. L. On the fundamental solution of the radiative transfer equation. *Journal of Geophysical Research*, 93(D9):11037–11050, September 1988. doi:10.1029/JD093iD09p11037.

Fletcher, R. *Practical methods of optimization; (2nd ed.)*. Wiley-Interscience, New York, NY, USA, 1987. ISBN 0471915475.

Flowerdew, R. J. and Haigh, J. D. Retrieval of aerosol optical thickness over land using the ATSR-2 dual-look satellite radiometer. *Geophysical Research Letters*, 23(4):351–354, February 1996. doi:10.1029/96GL00153.

Frankenberg, C., Hasekamp, O., O'Dell, C., Sanghavi, S., Butz, A., and Worden, J. Aerosol information content analysis of multi-angle high spectral resolution measurements and its benefit for high accuracy greenhouse gas retrievals. *Atmospheric Measurement Techniques*, 5:1809–1821, 2012a. doi:10.5194/amt-5-1809-2012.

Frankenberg, C., O'Dell, C., Guanter, L., and McDuffie, J. Remote sensing of near-infrared chlorophyll fluorescence from space in scattering atmospheres: Implications for its retrieval and interferences with atmospheric CO_2 retrievals. *Atmospheric Measurement Techniques*, 5:2081–2094, 2012b. doi:10.5194/amt-5-2081-2012.

Fu, Q. and Liou, K. N. On the correlated k-distributio method for radiative transfer in nonhomogeneous atmospheres. *Journal of the Atmospheric Sciences*, 49(22):2139–2156, November 1992. doi:10.1175/1520-0469(1992)049%3C2139:OTCDMF%3E2.0.CO;2.

Gabella, M., Sanctis, A. D., and Perona, G. An example of vertical profile of tropospheric aerosol retrieved from radiance imagery measured by the MOS/A and MOS/B spectrometers over the mediterranean sea. In *Geoscience and Remote Sensing Symposium, 1999. IGARSS '99 Proceedings. IEEE 1999 International*, volume 1, pages 622–624. IEEE, 1999a. doi:10.1109/IGARSS.1999.773585.

Gabella, M., Vlatcheslev, and Perona, G. Retrieval of aerosol profile variations from reflected radiation in the oxygen absorption A band. *Applied Optics*, 38(15):3190–3195, May 1999b. doi:10.1364/AO.38.003190.

Gabriel, P., Christi, M. J., and Stephens, G. L. Calculation of Jacobians for inverse radiative transfer: An efficient hybrid method. *Journal of Quantitative Spectroscopy and Radiative Transfer*, 97:209–227, 2006. doi:10.1016/j.jqsrt.2005.05.060.

García, O. E., Díaz, A. M., Expósito, F. J., Díaz, J. P., Dubovik, O., Dubuisson, P., Roger, J. C., Eck, T. F., Sinyuk, A., Derimian, Y., Dutton, E. G., Schafer, J. S., Holben, B. N., and García, C. A. Validation of AERONET estimates of atmospheric solar fluxes and aerosol radiative forcing by ground-based broadband measurements. *Journal of Geophysical Research*, 113:D21207, 2008. doi:10.1029/2008JD010211.

García, O. E., Expósito, F. J., Díaz, J. P., and Díaz, A. M. Radiative forcing under mixed aerosol conditions. *Journal of Geophysical Research*, 116:D01201, 2011. doi:10.1029/2009JD013625.

García, O. E., Díaz, J. P., Expósito, F. J., Díaz, A. M., Dubovik, O., Derimian, Y., Dubuisson, P., and Roger, J.-C. Shortwave radiative forcing and efficiency of key aerosol types using AERONET data. *Atmospheric Chemistry and Physics*, 12:5129–5145, 2012. doi:10.5194/acp-12-5129-2012.

Garcia, R. D. M. and Siewert, C. E. A generalized spherical harmonics solution for radiative transfer models that include polarization effects. *Journal of Quantitative Spectroscopy and Radiative Transfer*, 36(5):401–423, 1986. doi:10.1016/0022-4073(86)90097-X.

Garcia, R. D. M. and Siewert, C. E. The F_N method for radiative transfer models that include polarization effects. *Journal of Quantitative Spectroscopy and Radiative Transfer*, 41(2):117–145, 1989. doi:10.1016/0022-4073(89)90133-7.

Gel'fand, I. M., Minlos, R. A., and Shapiro, Z. Y. *Representations of the Rotation and Lorentz Groups and Their Applications*. The Macmillan Company, New York, 1963.

Geller, M. Line identification in ATMOS solar spectra. In *Laboratory and Astronomical High Resolution Spectra*, volume 81 of *ASP Conference Series*, pages 88–101, 1995.

Geller, M. *A High-Resolution Atlas of the Infrared Spectrum of the Sun and the Earth Atmosphere from Space. Volume 3: Key to Identification of Solar Features*. National Aeronautics and Space Administration (NASA), 1992.

Geogdzhayev, I. V., Mishchenko, M. I., Rossow, W. B., Cairns, B., and Lacis, A. A. Global two-channel AVHRR retrievals of aerosol properties over the ocean for the period of NOAA-9 observations and preliminary retrievals using NOAA-7 and NOAA-11 data. *Journal of the Atmospheric Sciences*, 59:262–278, February 2002. doi:10.1175/1520-0469(2002)059%3C0262:GTCARO%3E2.0.CO;2.

Giles, D. M., Holben, B. N., Eck, T. F., Sinyuk, A., Smirnov, A., Slutsker, I., Dickerson, R. R., Thompson, A. M., and Schafer, J. S. An analysis of AERONET aerosol absorption properties and classifications representative of aerosol source regions. *Journal of Geophysical Research*, 117: D17203, 2012. doi:10.1029/2012JD018127.

Golub, G. H. and Van Loan, C. F. *Matrix Computations*. The Johns Hopkins University Press, Baltimore, Maryland, USA, 1996. ISBN 0801854148.

Goody, R., West, R., Chen, L., and Crisp, D. The correlated-k method for radiation calculations in nonhomogeneous atmospheres. *Journal of Quantitative Spectroscopy and Radiative Transfer*, 42 (6):539–550, 1989. doi:10.1016/0022-4073(89)90044-7.

Grant, I. P. and Hunt, G. E. Discrete space theory of radiative transfer I. Fundamentals. *Proceedings of the Royal Society. Series A: Mathematical and Physical Sciences*, 313:183–197, 1969. doi:10.1098/rspa.1969.0187.

Grechko, Y. I. Measuring the differences in effective paths at two wavelengths in the pressence of reflection of light by clouds. *Izv. Acad. Sci. USSR Atmos. Oceanic Phys.*, 114:479–481, 1978.

Grechko, Y. I., Dianov-klokov, V. F., and Malkov, I. P. Aircraft measurments of photon paths in reflection and transmission of light by clouds in the 0.76 μm oxygen band. *Izv. Acad. Sci. USSR Atmos. Oceanic Phys.*, 9:471–485, 1973.

Hale, G. M. and Querry, M. R. Optical constants of water in the 200-nm to 200-μm wavelength region. *Applied Optics*, 12(3):555–563, March 1973. doi:10.1364/AO.12.000555.

Hanel, R. A. Determination of cloud altitude from a satellite. *Journal of Geophysical Research*, 66 (4):1300, April 1961. doi:10.1029/JZ066i004p01300.

Hansen, J., Sato, M., and Ruedy, R. Radiative forcing and climate response. *Journal of Geophysical Research*, 102(D6):6831–6864, March 1997. doi:10.1029/96JD03436.

Hansen, J., Nazarenko, L., Ruedy, R., Sato, M., Willis, J., Genio, A. D., Koch, D., Lacis, A., Lo, K., Menon, S., Novakov, T., Perlwitz, J., Russell, G., Schmidt, G. A., and Tausnev, N. Earth's energy imbalance: Confirmation and implications. *Science*, 308:1431–1435, June 2005. doi:10.1126/science.1110252.

Hansen, J. E. and Hovenier, J. W. Interpretation of the polarization of venus. *Journal of the Atmospheric Sciences*, 31:1137–1160, May 1974. doi:10.1175/1520-0469(1974)031%3C1137:IOTPOV%3E2.0.CO;2.

Hasekamp, O. P. and Butz, A. Efficient calculation of intensity and polarization spectra in vertically inhomogeneous scattering and absorbing atmospheres. *Journal of Geophysical Research*, 113: D20309, 2008. doi:10.1029/2008JD010379.

Hasekamp, O. P. and Landgraf, J. Retrieval of aerosol properties over the ocean from multi-spectral single-viewing-angle measurements of intensity and polarization: Retrieval approach, information content, and sensitivity study. *Journal of Geophysical Research*, 110:D20207, 2005. doi:10.1029/2005JD006212.

Hasekamp, O. P., Landgraf, J., and van Oss, R. The need of polarization modeling for ozone profile retrieval from backscattered sunlight. *Journal of Geophysical Research*, 107(D23):4692, 2002. doi:10.1029/2002JD002387.

Hasekamp, O. P., Litvinov, P., and Butz, A. Aerosol properties over the ocean from PARASOL multiangle photopolarimetric measurements. *Journal of Geophysical Research*, 116:D14204, 2011. doi:10.1029/2010JD015469.

Haywood, J. M. and Shine, K. P. The effect of anthropogenic sulfate and soot aerosol on the clear sky planetary radiation budget. *Geophysical Research Letters*, 22(5):603–606, March 1995. doi:10.1029/95GL00075.

Haywood, J. M., Ramaswamy, V., and Soden, B. J. Tropospheric aerosol climate forcing in clear-sky satellite observations over the oceans. *Science*, 283:1299–1303, February 1999. doi:10.1126/science.283.5406.1299.

Haywood, J. M., Pelon, J., Formenti, P., Bharmal, N., Brooks, M., Capes, G., Chazette, P., Chou, C., Christopher, S., Coe, H., Cuesta, J., Derimian, Y., Desboeufs, K., Greed, G., Harrison, M., Heese, B., Highwood, E. J., Johnson, B., Mallet, M., Marticorena, B., Marsham, J., Milton, S., Myhre, G., Osborne, S. R., Parker, D. J., Rajot, J. L., Schulz, M., Slingo, A., Tanré, D., , and Tulet, P. Overview of the Dust and Biomass-burning Experiment and African Monsoon Multidisciplinary Analysis special observing period-0. *Journal of Geophysical Research*, 113: D00C17, 2008. doi:10.1029/2008JD010077.

Haywood, J. M. and Boucher, O. Estimates of the direct and indirect radiative forcing due to tropospheric aerosols: A review. *Reviews of Geophysics*, 38(4):513–543, November 2000. doi:10.1029/1999RG000078.

Heidinger, A. and Stephens, G. L. Molecular line absorption in a scattering atmosphere. Part II: Application to remote sensing in the O_2 A band. *Journal of the Atmospheric Sciences*, 57: 1616–1634, May 2000. doi:10.1175/1520-0469(2000)057%3C1615:MLAIAS%3E2.0.CO;2.

Heidinger, A. and Stephens, G. L. Molecular line absorption in a scattering atmosphere. Part III: Pathlength characteristics and effects of spatially heterogeneous clouds. *Journal of the Atmospheric Sciences*, 59(10):1641–1654, May 2002. doi:10.1175/1520-0469(2002)059%3C1641:MLAIAS%3E2.0.CO;2.

Herman, J. R., Bhartia, P. K., Torres, O., Hsu, C., Seftor, C., and Celarier, E. Global distribution of UV-absorbing aerosols from Nimbus 7/TOMS data. *Journal of Geophysical Research*, 102 (D14):16911–16922, July 1997a. doi:10.1029/96JD03680.

Herman, M., Deuzé, J. L., Devaux, C., Goloub, P., Bréon, F. M., and Tanré, D. Remote sensing of aerosols over land surfaces including polarization measurements and application to POLDER measurements. *Journal of Geophysical Research*, 102(D14):17039–17049, July 1997b. doi:10.1029/96JD02109.

Herman, M., Deuzé, J.-L., Marchand, A., Roger, B., and Lallert, P. Aerosol remote sensing from POLDER/ADEOS over the ocean: Improved retrieval using a nonspherical particle model. *Journal of Geophysical Research*, 110:D10S02, 2005. doi:10.1029/2004JD004798.

Higham, N. J. The scaling and squaring method for the matrix exponential revisited. *SIAM Journal on Matrix Analysis and Applications*, 26(4):1179–1193, March 1984. doi:10.1137/04061101X.

Higurashi, A. and Nakajima, T. Development of a two-channel aerosol retrieval algorithm on a global scale using NOAA AVHRR. *Journal of the Atmospheric Sciences*, 56:924–941, April 1999. doi:10.1175/1520-0469(1999)056%3C0924:DOATCA%3E2.0.CO;2.

Holben, B. N., Eck, T. F., Slutsker, I., Tanré, D., Buis, J. P., Setzer, A., Vermote, E., Reagan, J. A., Kaufman, Y. J., Nakajima, T., Lavenu, F., Jankowiak, I., and Smirnov, A. AERONET - a federated instrument network and data archive for aerosol characterization. *Remote Sensing of Environment*, 66:1–16, 1998. doi:10.1016/S0034-4257(98)00031-5.

Holben, B., Vermote, E., Kaufman, Y. J., Tanré, D., and Kalb, V. Aerosol retrieval over land from AVHRR data-application for atmospheric correction. *IEEE Transactions on Geoscience and Remote Sensing*, 30(2):212–222, March 1992. doi:10.1109/36.134072.

Hovenier, J. W. Symmetry relationships for scattering of polarized light in a slab of randomly oriented particles. *Journal of the Atmospheric Sciences*, 26:488–499, May 1969. doi:10.1175/1520-0469(1969)026%3C0488:SRFSOP%3E2.0.CO;2.

Hovenier, J. W., Mee, C. V. D., and Domke, H. *Transfer of Polarized Light in Planetary Atmospheres: Basic Concepts and Practical Methods*. KLUWER ACADEMIC PUBLISHERS, P.O. Box 17, 3300 AA Dordrecht, The Netherlands, 2004. ISBN 1402028555.

Hsu, N. C., Herman, J. R., Bhartia, P. K., Seftor, C. J., Torres, O., Thompson, A. M., Gleason, J., Eck, T. F., and Holben, B. Detection of biomass burning smoke from TOMS measurements. *Geophysical Research Letters*, 23(7):745–748, April 1996. doi:10.1029/96GL00455.

Hsu, N. C., Tsay, S.-C., King, M. D., and Herman, J. R. Aerosol properties over bright-reflecting source regions. *IEEE Transactions on Geoscience and Remote Sensing*, 42(3):557–569, March 2004. doi:10.1109/TGRS.2004.824067.

Hsu, N. C., Tsay, S.-C., King, M. D., and Herman, J. R. Deep blue retrievals of asian aerosol properties during ACE-Asia. *IEEE Transactions on Geoscience and Remote Sensing*, 44(11): 3180–3195, November 2006. doi:10.1109/TGRS.2006.879540.

Hu, R.-M. and Sokhi, R. Light scattering and absorption properties of dust particles retrieved from satellite measurements. *Journal of Quantitative Spectroscopy and Radiative Transfer*, 110: 1698–1705, 2009. doi:10.1016/j.jqsrt.2009.04.004.

Hu, R.-M., Martin, R. V., and Fairlie, T. D. Global retrieval of columnar aerosol single scattering albedo from space-based observations. *Journal of Geophysical Research*, 112:D02204, 2007. doi:10.1029/2005JD006832.

Huang, J., Minnis, P., Yan, H., Yi, Y., Chen, B., Zhang, L., and Ayers, J. K. Dust aerosol effect on semi-arid climate over Northwest China detected from A-Train satellite measurements. *Atmospheric Chemistry and Physics*, 10:6863–6872, 2010. doi:10.5194/acp-10-6863-2010.

Huang, J., Lin, B., Minnis, P., Wang, T., Wang, X., Hu, Y., Yi, Y., and Ayers, J. K. Satellite-based assessment of possible dust aerosols semi-direct effect on cloud water path over East Asia. *Geophysical Research Letters*, 31:L19802, 2006. doi:10.1029/2006GL026561.

Huebert, B. J., Bates, T., Russell, P. B., Shi, G., Kim, Y. J., Kawamura, K., Carmichael, G., and Nakajima, T. An overview of ACE-Asia: Strategies for quantifying the relationships between asian aerosols and their climatic impacts. *Journal of Geophysical Research*, 108(D23):8633, 2003. doi:10.1029/2003JD003550.

Ichoku, C., Remer, L. A., Kaufman, Y. J., Levy, R., Chu, D. A., Tanré, D., and Holben, B. N. MODIS observation of aerosols and estimation of aerosol radiative forcing over southern Africa during SAFARI 2000. *Journal of Geophysical Research*, 108(D13):8499, 2003. doi:10.1029/2002JD002366.

Intergovernmental Panel on Climate Change. *Climate Change 2007 - The Physical Science Basis Contribution of Working Group I to the Fourth Assessment Report of the IPCC*. Cambridge University Press, 32 Avenue of the Americas, New York, NY 10013, USA, 2007a.

Intergovernmental Panel on Climate Change. Climate change 2007: Synthesis report. Technical report, 2007b.

Jacobson, M. Z. Global direct radiative forcing due to multicomponent anthropogenic and natural aerosols. *Journal of Geophysical Research*, 106(D2):1551–1568, January 2001. doi:10.1029/2000JD900514.

Jacobson, M. Z. Control of fossil-fuel particulate black carbon and organic matter, possibly the most effective method of slowing global warming. *Journal of Geophysical Research*, 107(D19): 4410, 2002. doi:10.1029/2001JD001376.

Johnson, B. T., Heese, B., McFarlane, S. A., Chazette, P., Jones, A., and Bellouin, N. Vertical distribution and radiative effects of mineral dust and biomass burning aerosol over west africa during DABEX. *Journal of Geophysical Research*, 113:D00C12, 2008. doi:10.1029/2008JD009848.

Kahn, R., West, R., McDonald, D., Rheingans, B., and Mishchenko, M. I. Sensitivity of multiangle remote sensing observations to aerosol sphericity. *Journal of Geophysical Research*, 102(D14): 16861–16870, July 1997. doi:10.1029/96JD01934.

Kahn, R., Banerjee, P., and McDonald, D. Sensitivity of multiangle imaging to natural mixtures of aerosols over the ocean. *Journal of Geophysical Research*, 106(D16):18219–18238, August 2001. doi:10.1029/2000JD900497.

Kahn, R. A., Ogren, J. A., Ackerman, T. P., Bösenberg, J., Charlson, R. J., Diner, D. J., Holben, B. N., Menzies, R. T., Miller, M. A., and Seinfeld, J. H. Aerosol data sources and their roles within PARAGON. *Bulletin of the American Meteorological Society*, 85(10):1511–1522, October 2004. doi:10.1175/BAMS-85-10-1511.

Kaufman, Y. J., Tanré, D., Remer, L. A., Vermote, E. F., Chu, A., and Holben, B. N. Operational remote sensing of tropospheric aerosol over land from EOS Moderate Resolution Imaging Spectrometer. *Journal of Geophysical Research*, 102(D14):17051–17067, July 1997. doi:10.1029/96JD03988.

Kaufman, Y. J., Martins, J. V., Remer, L. A., Schoeberl, M. R., and Yamasoe, M. A. Satellite retrieval of aerosol absorption over the ocean using sunglint. *Geophysical Research Letters*, 29 (19):1928, 2002. doi:10.1029/2002GL015403.

Kaufman, Y. J. Satellite sensing of aerosol absorption. *Journal of Geophysical Research*, 92(D4): 4307–4317, April 1987. doi:10.1029/JD092iD04p04307.

King, M. D., Kaufman, Y. J., Menzel, W. P., and Tanré, D. Remote sensing of cloud, aerosol, and water vapor properties from the moderate resolution imaging spectrometer (MODIS). *IEEE Transactions on Geoscience and Remote Sensing*, 30(1):2–27, January 1992. doi:10.1109/36.124212.

King, M. D., Kaufman, Y. J., Tanré, D., and Nakajima, T. Remote sensing of tropospheric aerosols from space: Past, present, and future. *Bulletin of the American Meteorological Society*, 80(11): 2229–2259, November 1999. doi:10.1175/1520-0477(1999)080%3C2229:RSOTAF%3E2.0.CO;2.

Kinne, S., Lohmann, U., Feichter, J., Schulz, M., Timmreck, C., Ghan, S., Easter, R., Chin, M., Ginoux, P., Takemura, T., Tegen, I., Koch, D., Herzog, M., Penner, J., Pitari, G., Holben, B., Eck, T., Smirnov, A., Dubovik, O., Slutsker, I., Tanré, D., Torres, O., Mishchenko, M., Geogdzhayev, I., Chu, D. A., and Kaufman, Y. Monthly averages of aerosol properties: A global comparison among models, satellite data, and AERONET ground data. *Journal of Geophysical Research*, 108 (D20):4634, 2003. doi:10.1029/2001JD001253.

Kneizys, F. X., Shettle, E. P., Abreu, L. W., Chetwynd, J. H., Anderson, G. P., Gallery, W. O., Selby, J. E. A., and Clough, S. A. Users guide to LOWTRAN. Technical Report Environmental Research Papers, No. 1010, AFGL-TR-88-0177, Air Force Geophysics Laboratory, Hanscom Air Force Base, Massachusetts 01731, 1988.

Koepke, P. Effective reflectance of oceanic whitecaps. *Applied Optics*, 23(11):1816–1824, June 1984. doi:10.1364/AO.23.001816.

Kokhanovsky, A. A. and Leeuw, G. D., editors. *Satellite Aerosol Remote Sensing over Land*. Springer-Praxis Books. Springer Berlin Heidelberg, 2009.

Kuščer, I. and Ribarič, M. Matrix formalism in the theory of diffusion of light. *Journal of Modern Optics*, 6(1):42–51, January 1959. doi:10.1080/713826264.

Kuze, A., Suto, H., Nakajima, M., and Hamazaki, T. Thermal and near infrared sensor for carbon observation Fourier-transform spectrometer on the Greenhouse Gases Observing Satellite for greenhouse gases monitoring. *Applied Optics*, 48(35):6716–6733, December 2009. doi:10.1364/AO.48.006716.

Lacis, A. A., Chowdhary, J., Mishchenko, M. I., and Cairns, B. Modeling errors in diffuse-sky radiation: Vector vs. scalar treatment. *Geophysical Research Letters*, 25(2):135–138, January 1998. doi:10.1029/97GL03613.

Lacis, A. A. and Hansen, J. E. A parameterization for the absorption of solar radiation in the Earth's atmosphere. *Journal of the Atmospheric Sciences*, 31:118–133, January 1974. doi:10.1175/1520-0469(1974)031%3C0118:APFTAO%3E2.0.CO;2.

Lebsock, M. D., L'Ecuyer, T. S., and Stephens, G. L. Information content of near-infrared spaceborne multiangular polarization measurements for aerosol retrievals. *Journal of Geophysical Research*, 112:D14206, 2007. doi:10.1029/2007JD008535.

Lenoble, J., Herman, M., Deuzé, J. L., Lafrance, B., Santer, R., and Tanré, D. A successive order of scattering code for solving the vector equation of transfer in the Earth's atmosphere with aerosols. *Journal of Quantitative Spectroscopy and Radiative Transfer*, 107:479–507, 2007. doi:10.1016/j.jqsrt.2007.03.010.

Lenoble, J. *Radiative Transfer in Scattering and Absorbing Atmospheres: Standard Computational Procedures*. A. Deepak Publishing, Hampton, Virginia, USA, 1985. ISBN 0937194050.

Levelt, P. F., van den Oord, G. H. J., Dobber, M. R., Mälkki, A., Visser, H., de Vries, J., Stammes, P., Lundell, J. O. V., and Saari, H. The Ozone Monitoring Instrument. *IEEE Transactions on Geoscience and Remote Sensing*, 44(5):1093–1101, May 2006. doi:10.1109/TGRS.2006.872333.

Levy, R. C., Remer, L. A., Mattoo, S., Vermote, E. F., and Kaufman, Y. J. Second-generation operational algorithm: Retrieval of aerosol properties over land from inversion of Moderate Resolution Imaging Spectroradiometer spectral reflectance. *Journal of Geophysical Research*, 112: D13211, 2007. doi:10.1029/2006JD007811.

Li, X., Christopher, S. A., Chou, J., and Welch, R. M. Estimation of shortwave direct radiative forcing of biomass-burning aerosols using new angular models. *Journal of Applied Meteorology and Climatology*, 15:1474–1484, June 2002. doi:10.1175/1520-0450(2001)040%3C2278:EOSDRF%3E2.0.CO;2.

Li, Z. Influence of absorbing aerosols on the inference of solar surface radiation budget and cloud absorption. *Journal of Climate*, 11:5–17, January 1998. doi:10.1175/1520-0442(1998)011%3C0005:IOAAOT%3E2.0.CO;2.

Liou, K. N. *An Introduction to Atmospheric Radiation*. Academic Press, 525 B Street, Suite 1900, San Diego, California 92101-4495, USA, second edition, 2002. ISBN 0124514510.

Liou, K.-N. A numerical experiment on Chandrasekhar's discrete-ordinate method for radiative transfer: Applications to cloudy and hazy atmospheres. *Journal of the Atmospheric Sciences*, 30: 1303–1326, October 1973. doi:10.1175/1520-0469(1973)030%3C1303:ANEOCD%3E2.0.CO;2.

Livingston, W. C. and Wallace, L. An atlas of the solar spectrum in the infrared from 1850 to 9000 cm^{-1} (1.1 to 5.4 μm). Technical Report 91-001, National Solar Observatory, Tucson, Arizona, 1991.

Llewellyn-Jones, D. and Remedios, J. The Advanced Along Track Scanning Radiometer (AATSR) and its predecessors ATSR-1 and ATSR-2: An introduction to the special issue. *Remote Sensing of Environment*, 116:1–3, 2012. doi:10.1016/j.rse.2011.06.002.

Loeb, N. G. and Kato, S. Top-of-atmosphere direct radiative effect of aerosols over the tropical oceans from the Clouds and the Earth's Radiant Energy System (CERES) satellite instrument. *Journal of Climate*, 15:1474–1484, June 2002. doi:10.1175/1520-0442(2002)015%3C1474:TOADRE%3E2.0.CO;2.

Loeb, N. G. and Manalo-Smith, N. Top-of-atmosphere direct radiative effect of aerosols over global oceans from merged CERES and MODIS observations. *Journal of Climate*, 18:3506–3526, September 2005. doi:10.1175/JCLI3504.1.

Loeb, N. G., Loukachine, K., Manalo-Smith, N., and Wielicki, B. A. Angular distribution models for top-of-atmosphere radiative flux estimation from the Clouds and the Earth's Radiant Energy System instrument on the Tropical Rainfall Measuring Mission satellite. Part II: Validation. *Journal of Applied Meteorology*, 42:1748–1769, December 2003a. doi:10.1175/1520-0450(2003)042%3C1748:ADMFTR%3E2.0.CO;2.

Loeb, N. G., Manalo-Smith, N., Kato, S., Miller, W. F., Gupta, S. K., Minnis, P., and Wielicki, B. A. Angular distribution models for top-of-atmosphere radiative flux estimation from the Clouds and the Earth's Radiant Energy System instrument on the Tropical Rainfall Measuring Mission satellite. Part I: Methodology. *Journal of Applied Meteorology*, 42:240–265, February 2003b. doi:10.1175/1520-0450(2003)042%3C0240:ADMFTO%3E2.0.CO;2.

Lohmann, U. and Feichter, J. Global indirect aerosol effects: A review. *Atmospheric Chemistry and Physics*, 5:715–737, 2005. doi:10.5194/acp-5-715-2005.

Martins, J. V., Tanré, D., Remer, L., Kaufman, Y., Mattoo, S., and Levy, R. MODIS cloud screening for remote sensing of aerosols over oceans using spatial variability. *Geophysical Research Letters*, 29(12):1–4, 2002. doi:10.1029/2001GL013252.

Martonchik, J. V. and Diner, D. J. Retrieval of aerosol optical properties from multi-angle satellite imagery. *IEEE Transactions on Geoscience and Remote Sensing*, 30(2):223–230, March 1992. doi:10.1109/36.134073.

Martonchik, J. V., Diner, D. J., Kahn, R. A., Ackerman, T. P., Verstraete, M. M., Pinty, B., and Gordon, H. R. Techniques for the retrieval of aerosol properties over land and ocean using multiangle imaging. *IEEE Transactions on Geoscience and Remote Sensing, Aerosols, Remote Sensing*, 36(4):1212–1227, July 1998. doi:10.1109/36.701027.

McClatchey, R. A., Fenn, R. W., Selby, J. E. A., Volz, F. E., and Garing, J. S. Optical properties of the atmosphere (third edition). Technical Report Environmental Research Papers, No. 411, AFCRL-72-0497, Air Force Cambridge Research Laboratories, Bedford, Massachusetts, USA, 1972.

McGarragh, G. *LMie: A Linearized Mie Scattering Implementation, Version 0.90*, January 2013a. URL `http://reef.atmos.colostate.edu/~gregm/lmie/doc/lmie.pdf`.

McGarragh, G. XRTM: A general purpose linearized plane-parallel radiative transfer model. *Journal of Quantitative Spectroscopy and Radiative Transfer*, 2013b. Submitted.

McGarragh, G. and Gabriel, P. Efficient computation of radiances and for optically thin media by Padé approximants. *Journal of Quantitative Spectroscopy and Radiative Transfer*, 111:1885–1889, 2010. doi:10.1016/j.jqsrt.2010.03.011.

McGarragh, G. and Gabriel, P. A new vector radiative transfer solution using Padé approximants. *Journal of Quantitative Spectroscopy and Radiative Transfer*, 119:12–22, 2013. doi:10.1016/j.jqsrt.2013.01.012.

McGarragh, G. and Stephens, G. L. A multi-sensor concept for retrieving aerosol parameters, Part I: Sensitivity and information content analysis. 2013a. In progress.

McGarragh, G. and Stephens, G. L. A multi-sensor concept for retrieving aerosol parameters, Part II: Retrieval method, results, and validation. 2013b. In progress.

Mie, G. Beiträge zur optik trüber medien, speziell kolloidaler metallösungen. *Annalen der Physik*, 25(4):377–445, 1908.

Miller, R. L. and Tegen, I. Climate response to soil dust aerosols. *Journal of Climate*, 11:3247–3267, December 1998. doi:10.1175/1520-0442(1998)011%3C3247:CRTSDA%3E2.0.CO;2.

Min, Q. and Duan, M. Successive order of scattering model for solving vector radiative transfer in the atmosphere. *Journal of Quantitative Spectroscopy and Radiative Transfer*, 87:243–259, 2004. doi:10.1016/j.jqsrt.2003.12.019.

Min, Q. and Harrison, L. C. Retrieval of atmospheric optical depth profiles from downward-looking high-resolution O_2 A-band measurements: Optically thin conditions. *Journal of the Atmospheric Sciences*, 61:2469–2477, October 2004. doi:10.1175/1520-0469(2004)061%3C2469:ROAODP%3E2.0.CO;2.

Minnis, P., Harrison, E. F., Stowe, L. L., Gibson, G. G., Denn, F. M., Doelling, D. R., and Jr., W. L. S. Radiative climate forcing by the Mount Pinatubo eruption. *Science*, 259:1411–1415, March 1993. doi:10.1126/science.259.5100.1411.

Mishchenko, M. I., Lacis, A. A., and Travis, L. D. Errors induced by the neglect of polarization in radiance calculations for Rayleigh-scattering atmospheres. *Journal of Quantitative Spectroscopy and Radiative Transfer*, 51(3):491–510, 1994. doi:10.1016/0022-4073(94)90149-X.

Mishchenko, M. I. and Travis, L. D. Satellite retrieval of aerosol properties over the ocean using measurements of reflected sunlight: Effect of instrumental errors and aerosol absorption. *Journal of Geophysical Research*, 102(D12):13543–13553, June 1997a. doi:10.1029/97JD01124.

Mishchenko, M. I. and Travis, L. D. Satellite retrieval of aerosol properties over the ocean using polarization as well as intensity of reflected sunlight. *Journal of Geophysical Research*, 102(D14): 16989–17013, July 1997b. doi:10.1029/96JD02425.

Mishchenko, M. I., Geogdzhayev, I. V., Cairns, B., Rossow, W. B., and Lacis, A. E. Aerosol retrievals over the ocean by use of channels 1 and 2 AVHRR data: Sensitivity analysis and preliminary results. *Applied Optics*, 38(36):7325–7341, December 1999. doi:10.1364/AO.38.007325.

Mishchenko, M. I., Travis, L. D., and Lacis, A. A. *Scattering, Absorption, and Emission of Light by Small Particles*. Cambridge University Press, Cambridge, 2002. ISBN 052178252X. URL http://www.giss.nasa.gov/~crmim/publications/book_2.pdf.

Mishchenko, M. I., Cairns, B., Hansen, J. E., Travis, L. E., Burg, R., Kaufman, Y. J., Martins, J. V., and Shettle, E. P. Monitoring of aerosol forcing of climate from space: Analysis of measurement requirements. *Journal of Quantitative Spectroscopy and Radiative Transfer*, 88:149–161, 2004. doi:10.1016/j.jqsrt.2004.03.030.

Mishchenko, M. I., Cairns, B., Kopp, G., Schueler, C. F., Fafaul, B. A., Hansen, J. E., Hooker, R. J., Itchkawich, T., Maring, H. B., and Travis, L. D. Accurate monitoring of terrestrial aerosols and total solar irradiance. *Bulletin of the American Meteorological Society*, 88(5):677–691, May 2007a. doi:10.1175/BAMS-88-5-677.

Mishchenko, M. I., Geogdzhayev, I. V., Cairns, B., Carlson, B. E., Chowdhary, J., Lacis, A. A., Liu, L., Rossow, W. B., and Travis, L. D. Past, present, and future of global aerosol climatologies derived from satellite observations: A perspective. *Journal of Quantitative Spectroscopy and Radiative Transfer*, 106:325–347, 2007b. doi:10.1016/j.jqsrt.2007.01.007.

Mitchell, J. F. B. and Johns, T. C. On modification of global warming by sulfate aerosols. *Journal of Climate*, 10:245–267, February 1997. doi:10.1175/1520-0442(1997)010%3C0245:OMOGWB%3E2.0.CO;2.

Mitchell, J. F. B., Davis, R. A., Ingram, W. J., and Senior, C. A. On surface temperature, greenhouse gases, and aerosols: Models and observations. *Journal of Climate*, 8:2364–2386, October 1995. doi:10.1175/1520-0442(1995)008%3C2364:OSTGGA%3E2.0.CO;2.

Moler, C. and Loan, C. V. Nineteen dubious ways to compute the exponential of a matrix. *SIAM Journal on Numerical Analysis*, 20(4):801–836, October 1978. doi:10.1137/1020098.

Moler, C. and Loan, C. V. Nineteen dubious ways to compute the exponential of a matrix, twenty-five years later. *SIAM Review*, 45(1):3–49, 2003. doi:10.1137/S00361445024180.

Molteni, F., Buizza, R., Palmer, T. N., and Petroliagis, T. The ECMWF ensemble prediction system: Methodology and validation. *Quarterly Journal of the Royal Meteorological Society*, 122: 73–119, 1996. doi:10.1002/qj.49712252905.

Monahan, E. C. and Muircheartaigh, I. O. Optimal power-law description of oceanic whitecap coverage dependence on wind speed. *Journal of Physical Oceanography*, 10:2094–2099, December 1980. doi:10.1175/1520-0485(1980)010%3C2094:OPLDOO%3E2.0.CO;2.

Nadal, F. and Bréon, F.-M. Parameterization of surface polarized reflectance derived from POLDER spaceborne measurements. *IEEE Transactions on Geoscience and Remote Sensing*, 37(3):1709–1718, May 1999. doi:10.1109/36.763292.

Nakajima, T. and Tanaka, M. Matrix formulation for the transfer of solar radiation in a plane-parallel scattering atmosphere. *Journal of Quantitative Spectroscopy and Radiative Transfer*, 35(1):13–21, 1986. doi:10.1016/0022-4073(86)90088-9.

Nakajima, T. and Tanaka, M. Algorithms for radiative intensity calculations in moderately thick atmospheres using a truncation approximation. *Journal of Quantitative Spectroscopy and Radiative Transfer*, 40(1):51–69, 1988. doi:10.1016/0022-4073(88)90031-3.

Natraj, V., Jiang, X., lie Shia, R., Huang, X., Margolis, J. S., and Yung, Y. L. Application of principal component analysis to high spectral resolution radiative transfer: A case study of the O_2 A band. *Journal of Quantitative Spectroscopy and Radiative Transfer*, 95:539–556, 2005. doi:10.1016/j.jqsrt.2004.12.024.

Natraj, V., Spurr, R. J. D., Boesch, H., Jiang, Y., and Yung, Y. L. Evaluation of errors from neglecting polarization in the forward modeling of O_2 A band measurements from space, with relevance to CO_2 column retrieval from polarization-sensitive instruments. *Journal of Quantitative Spectroscopy and Radiative Transfer*, 103:245–259, 2007. doi:10.1016/j.jqsrt.2006.02.073.

O'Brien, D. M. and Mitchell, R. M. Error estimates for retrieval of cloud-top pressure using absorption in the A band of oxygen. *Journal of Applied Meteorology*, 31:1179–1192, October 1992. doi:10.1175/1520-0450(1992)031%3C1179:EEFROC%3E2.0.CO;2.

O'Brien, D. M., Polonsky, I., O'Dell, C., and Carheden, A. Orbiting Carbon Observatory (OCO) algorithm theoretical basis document: The OCO simulator. Technical report, Cooperative Institute for Research in the Atmosphere, Colorado State University, Fort Collins, Colorado, 2009.

O'Dell, C. W., Connor, B., Bosch, H., O'Brien, D., Frankenberg, C., Castano, R., Christi, M., Eldering, D., Fisher, B., Gunson, M., McDufie, J., Miller, C. E., Natraj, V., Oyafuso, F., Polonsky, I., Smyth, M., Taylor, T., Toon, G. C., Wennberg, P. O., and Wunch, D. The ACOS CO_2 retrieval algorithm - Part 1: Description and validation against synthetic observations. *Atmospheric Measurement Techniques*, 5:99–121, 2012. doi:10.5194/amt-5-99-2012.

O'Dell, C. W. Acceleration of multiple-scattering, hyperspectral radiative transfer calculations via low-streams interpolation. *Journal of Geophysical Research*, 115:D10206, 2010. doi:10.1029/2009JD012803.

Ohmura, A., Dutton, E. G., Forgan, B., Fröhlich, C., Gilgen, H., Hegner, H., Heimo, A., König-Langlo, G., McArthur, B., Müller, G., Philipona, R., Pinker, R., Whitlock, C. H., Dehne, K., and Wilda, M. Baseline surface radiation network (BSRN/WCRP): New precision radiometry for climate research. *Bulletin of the American Meteorological Society*, 79(10):2115–2136, October 1998. doi:10.1175/1520-0477(1998)079%3C2115:BSRNBW%3E2.0.CO;2.

Palmer, K. F. and Williams, D. Optical properties of water in the near infrared. *Journal of the Optical Society of America*, 64(8):1107–1110, August 1974. doi:10.1364/JOSA.64.001107.

Parlett, B. N. and Reinsch, C. Balancing a matrix for calculation of eigenvalues and eigenvectors. *Numerische Mathematik*, 13(4):293–304, August 1969. doi:10.1007/BF02165404.

Peck, E. R. and Reeder, K. Dispersion of air. *Journal of the Optical Society of America*, 62(8): 958–962, August 1972. doi:10.1364/JOSA.62.000958.

Penner, J. E., Chuang, C. C., and Grant, K. Climate forcing by carbonaceous and sulfate aerosols. *Climate Dynamics*, 14:839–851, 1998. doi:10.1007/s003820050259.

Penner, J. E., Zhang, S. Y., Chin, M., Chuang, C. C., Feichter, J., Feng, Y., Geogdzhayev, I. V., Ginoux, P., Herzog, M., Higurashi, A., Koch, D., Land, C., Lohmann, U., Mishchenko, M., Nakajima, T., Pitari, G., Soden, B., Tegen, I., and Stowe, L. A comparison of model- and satellite-derived aerosol optical depth and reflectivity. *Journal of the Atmospheric Sciences*, 59: 441–460, February 2002. doi:10.1175/1520-0469(2002)059%3C0441:ACOMAS%3E2.0.CO;2.

Peralta, R. J., Nardell, C., Cairns, B., Russell, E. E., Travis, L. D., Mishchenko, M. I., Fafaul, B. A., and Hooker, R. J. Aerosol Polarimetry Sensor for the Glory Mission. *SPIE*, 6786:1–17, 2007. doi:10.1117/12.783307.

Petrenko, M., Ichoku, C., and Leptoukh, G. Multi-sensor Aerosol Products Sampling System (MAPSS). *Atmospheric Measurement Techniques*, 5:913–926, 2012. doi:10.5194/amtd-5-909-2012.

Petty, G. W. *A First Course in Atmospheric Radiation (2nd Ed.)*. Sundog Publishing, 2006. ISBN 0972903313.

Pfeilsticker, K. First geometrical path length probability density function derivation of the skylight from high-resolution oxygen A-band spectroscopy: 2. Derivation of the Lévy index for the skylight transmitted by midlatitude clouds. *Journal of Geophysical Research*, 104(D4):4101–4116, February 1999. doi:10.1029/1998JD200081.

Pfeilsticker, K., Erle, F., Funk, O., Veitel, H., and Platt, U. First geometrical pathlengths probability density function derivation of the skylight from spectroscopically highly resolving oxygen A-band observations: 1. Measurement technique, atmospheric observations and model calculations. *Journal of Geophysical Research*, 103(D10):11483–11504, May 1998. doi:10.1029/98JD00725.

Phillips, D. L. A technique for the numerical solution of certain integral equations of the first kind. *Journal of Geophysical Research*, 9(1):84–97, January 1962. doi:10.1145/321105.321114.

Pincus, R. and Baker, M. B. Effect of precipitation on the albedo susceptibility of clouds in the marine boundary layer. *Nature*, 372, November 1994. doi:10.1038/372250a0.

Plass, G. N., Kattawar, G., and Catchings, F. E. Matrix operator theory of radiative transfer. 1: Rayleigh scattering. *Applied Optics*, 12(2):314–329, February 1973. doi:10.1364/AO.12.000314.

Rahman, H., Pinty, B., and Verstraete, M. M. Coupled surface-atmosphere reflectance (CSAR) model 2. Semiempirical surface model usable with NOAA advanced very high resolution radiometer data. *Journal of Geophysical Research*, 98(D11):20791–20801, November 1993. doi:10.1029/93JD02072.

Ramanathan, V., Crutzen, P. J., Kiehl, J. T., and Rosenfeld, D. Aerosols, climate, and the hydrological cycle. *Science*, 294:2119–2124, December 2001. doi:10.1126/science.1064034.

Remer, L. A. and Kaufman, Y. J. Aerosol direct radiative effect at the top of the atmosphere over cloud free ocean derived from four years of MODIS data. *Atmospheric Chemistry and Physics*, 6: 237–253, 2006. doi:10.5194/acp-6-237-2006.

Remer, L. A., Kaufman, Y. J., Tanré, D., Mattoo, S., Chu, D. A., Martins, J. V., Li, R.-R., Ichoku, C., Levy, R. C., Kleidman, R. G., Eck, T. F., Vermote, E., and Holben, B. N. The MODIS aerosol algorithm, products, and validation. *Journal of the Atmospheric Sciences*, 62:947–973, April 2005. doi:10.1175/JAS3385.1.

Rodgers, C. D. *Inverse Methods for Atmospheric Sounding: Theory and Practice*. World Scientific Publishing Co. Pte. Ltd., 5 Toh Tuck Link, Singapore 596224, 2004. ISBN 981022740X.

Rosenzweig, C., Karoly, D., Vicarelli, M., Neofotis, P., Wu, Q., Casassa, G., Menzel, A., Root, T. L., Estrella, N., Seguin, B., Tryjanowski, P., Liu, C., Rawlins, S., and Imeson, A. Attributing physical and biological impacts to anthropogenic climate change. *Nature*, 453, May 2008. doi:doi:10.1038/nature06937.

Rothman, L. S., Jacquemart, D., Barbe, A., Benner, D. C., Birk, M., Brown, L. R., Carleer, M. R., Jr., C. C., Chance, K., Coudert, L. H., Dana, V., Devi, V. M., Flaud, J.-M., Gamache, R. R., Goldman, A., Hartmann, J.-M., Jucksl, K. W., Makim, A. G., Mandini, J.-Y., Massie, S. T., Orphal, J., Perrin, A., Rinsland, C. P., et al. The HITRAN 2004 molecular spectroscopic database. *Journal of Quantitative Spectroscopy and Radiative Transfer*, 96:139–204, 2005. doi:10.1016/j.jqsrt.2004.10.008.

Rothman, L., Gordon, I. E., Barbe, A., Benner, D. C., Bernath, P. F., Birk, M., Boudon, V., Brown, L. R., Campargue, A., Champion, J.-P., Chance, K., Coudert, L. H., Dana, V., Devi, V. M., Fally, S., Flaud, J.-M., Gamache, R. R., Goldman, A., Jacquemart, D., Kleiner, I., Lacome, N., Lafferty, W. J., Mandin, J.-Y., Massie, S., Mikhailenko, S. N., Miller, C. E., Moazzen-Ahmadi, N., Naumenko, O. V., Nikitin, A. V., Orphal, J., Perevalov, V. I., Perrin, A., Predoi-Cross, A., Rinsland, C. P., Rotger, M., Simeckova, M., Smith, M. A. H., Sung, K., Tashkun, S. A., Tennyson, J., Toth, R. A., Vandaele, A. C., and Auwera, J. V. The HITRAN 2008 molecular spectroscopic database. *Journal of Quantitative Spectroscopy and Radiative Transfer*, 110:533–572, 2009. doi:10.1016/j.jqsrt.2009.02.013.

Roujean, J.-L., Leroy, M., and Deschamps, P.-Y. A bidirectional reflectance model of the Earth's surface for the correction of remote sensing data. *Journal of Geophysical Research*, 97(D18): 20455–20468, December 1992. doi:10.1029/92JD01411.

Saad, E. A., Wakil, S. A. E., Haggag, M. H., and Machali, H. M. Padé approximant for Chandrasekhar H function. *Journal of Quantitative Spectroscopy and Radiative Transfer*, 30(1):25–30, 1983. doi:10.1016/0022-4073(83)90069-9.

Saad, E. A., Krim, M. S. A., and El-Dimerdash, A. A. Padé approximant calculation for dispersive, isotropic scattering, homogeneous media. *Astrophysics and Space Science*, 149:187–195, 1988. doi:10.1007/BF00639789.

Saiedy, F. On cloud-top determination from Gemini-5. *Journal of the Atmospheric Sciences*, 24: 63–69, January 1967. doi:10.1175/1520-0469(1967)024%3C0063:OCTDFG%3E2.0.CO;2.

Salomonson, V. V., Barnes, W. L., Maymon, P. W., Montgomery, H. E., and Istrow, H. MODIS: Advanced facility instrument for studies of the Earth as a system. *IEEE Transactions on Geoscience and Remote Sensing*, 27(2):145–153, March 1989. doi:10.1109/36.20292.

Satheesh, S. K. and Srinivasan, J. A method to estimate aerosol radiative forcing from spectral optical depths. *Journal of the Atmospheric Sciences*, 63:1082–1092, March 2006. doi:10.1175/JAS3663.1.

Satheesh, S. K., Ramanathan, V., Li-Jones, X., Lobert, J. M., Podgorny, I. A., Prospero, J. M., Holben, B. N., and Loeb, N. G. A model for the natural and anthropogenic aerosols over the tropical Indian Ocean derived from Indian Ocean Experiment data. *Journal of Geophysical Research*, 104(D22):27421–27440, November 1999. doi:10.1029/1999JD900478.

Schulz, F. M., Stamnes, K., and Weng, F. VDISORT: An improved and generalized discrete ordinate method for polarized (vector) radiative transfer. *Journal of Quantitative Spectroscopy and Radiative Transfer*, 61(1):105–122, 1999. doi:10.1016/S0022-4073(97)00215-X.

Schutgens, N. A. J. and Stammes, P. A novel approach to the polarization correction of spaceborne spectrometers. *Journal of Geophysical Research*, 108(D7):4229, 2003. doi:10.1029/2002JD002736.

Seftor, C. J., Hsu, N. C., Herman, J. R., Bhartia, P. K., Torres, O., Rose, W. I., Schneider, D. J., and Krotko, N. Detection of volcanic ash clouds from Nimbus 7/total ozone mapping spectrometer. *Journal of Geophysical Research*, 102(D14):16749–16759, July 1997. doi:10.1029/97JD00925.

Seinfeld, J. H. and Pandis, S. N. *Atmospheric Chemistry and Physics: From Air Pollution to Climate Change*. Wiley-Interscience, New York, 1998. ISBN 0471720186.

Siewert, C. E. On the equation of transfer relevant to the scattering of polarized light. *The Astrophysical Journal*, 245:1080–1086, May 1981. doi:10.1086/158884.

Siewert, C. E. On the phase matrix basic to scattering of polarized light. *Astronomy and Astrophysics*, 109:195–200, 1982.

Siewert, C. E. A concise and accurate solution to Chandrasekher's basic problem in radiative transfer. *Journal of Quantitative Spectroscopy and Radiative Transfer*, 64:109–130, 2000. doi:10.1016/S0022-4073(98)00144-7.

Smirnov, A., Holben, B. N., Eck, T. F., Dubovik, O., and Slutsker, I. Cloud-screening and quality control algorithms for the AERONET database. *Remote Sensing of Environment*, 73:337–349, 2000. doi:10.1016/S0034-4257(00)00109-7.

Spurr, R. J. D. and Christi, M. J. Linearization of the interaction principle: Analytic jacobians in the "Radiant" model. *Journal of Quantitative Spectroscopy and Radiative Transfer*, 103:431–446, 2007. doi:10.1016/j.jqsrt.2006.05.001.

Spurr, R. J. D. A new approach to the retrieval of surface properties from earthshine measurements. *Journal of Quantitative Spectroscopy and Radiative Transfer*, 83:15–46, 2004. doi:10.1016/S0022-4073(02)00283-2.

Spurr, R. J. D. VLIDORT: A linearized pseudo-spherical vector discrete ordinate radiative transfer code for forward model and retrieval studies in multilayer multiple scattering media. *Journal of Quantitative Spectroscopy and Radiative Transfer*, 102:316–342, 2006. doi:10.1016/j.jqsrt.2006.05.005.

Stam, D. M., Haan, J. F. D., Hovenier, J. W., and Stammes, P. Degree of linear polarization of light emerging from the cloudless atmosphere in the oxygen A band. *Journal of Geophysical Research*, 104(D14):16843–16858, July 1999. doi:10.1029/1999JD900159.

Stamnes, K. and Swanson, R. A. A new look at the discrete ordinate method for radiative transfer calculations in anisotropic scattering atmospheres. *Journal of the Atmospheric Sciences*, 38: 387–399, February 1981. doi:10.1175/1520-0469(1981)038%3C0387:ANLATD%3E2.0.CO;2.

Stamnes, K., Tsay, S.-C., and Nakajima, T. Computation of eigenvalues and eigenvectors for the discrete ordinate and matrix operator methods in radiative transfer. *Journal of Quantitative Spectroscopy and Radiative Transfer*, 39(5):415–419, 1988a. doi:10.1016/0022-4073(88)90107-0.

Stamnes, K., Tsay, S.-C., Wiscombe, W., and Jayaweera, K. Numerically stable algorithm for discrete-ordinate-method radiative transfer in multiple scattering and emitting layered media. *Applied Optics*, 27(12):2502–2509, June 1988b. doi:10.1364/AO.27.002502.

Steinfelds, E., Samuel, M. A., McCormick, N. J., and Reid, J. H. Radiative transfer single-scattering albedo estimation with a super-Padé approximation of Chandrasekhar's H-functions. *International Journal of Theoretical Physics*, 36(4):997–1007, 1997. doi:10.1007/BF02435797.

Stephens, G. L. and Heidinger, A. Molecular line absorption in a scattering atmosphere. Part I: Theory. *Journal of the Atmospheric Sciences*, 57:1599–1614, May 2000. doi:10.1175/1520-0469(2000)057%3C1599:MLAIAS%3E2.0.CO;2.

Stephens, G. L., Wood, N. B., and Pakula, L. A. On the radiative effects of dust on tropical convection. *Geophysical Research Letters*, 38:L23112, 2004. doi:10.1029/2004GL021342.

Stowe, L. L. Cloud and aerosol products at NOAA/NESDIS. *Global and Planetary Change*, 4:25–32, 1991. doi:10.1016/0921-8181(91)90066-6.

Stowe, L. L., Ignatov, A. M., and Singh, R. R. Development, validation, and potential enhancements to the second-generation operational aerosol product at the national environmental satellite, data, and information service of the national oceanic and atmospheric administration. *Journal of Geophysical Research*, 102(D14):16923–16934, July 1997. doi:10.1029/96JD02132.

Tanré, D., Kaufman, Y. J., Herman, M., and Mattoo, S. Remote sensing of aerosol properties over the oceans using the MODIS/EOS spectral radiances. *Journal of Geophysical Research*, 102(D14): 16971–16988, July 1997. doi:10.1029/96JD03437.

Tanré, D., Bréon, F. M., Deuzé, J. L., Dubovik, O., Ducos, F., Francois, P., Goloub, P., Herman, M., Lifermann, A., , and Waquet, F. Remote sensing of aerosols by using polarized, directional and spectral measurements within the A-Train: The PARASOL mission. *Atmospheric Measurement Techniques*, 4:1383–1395, 2011. doi:10.5194/amt-4-1383-2011.

Tao, W.-K., Chen, J.-P., Li, Z., Wang, C., and Zhang, C. Impact of aerosols on convective clouds and precipitation. *Reviews of Geophysics*, 50, 2012. doi:10.1029/2011RG000369.

Taylor, J. P., Glew, M. D., Jr., J. A. C., Tahnk, W. R., Platnick, S., Hobbs, P. V., and Ferek, R. J. Effects of aerosols on the radiative properties of clouds. *Journal of the Atmospheric Sciences*, 57: 2656–2670, August 2000. doi:10.1175/1520-0469(2000)057%3C2656:EOAOTR%3E2.0.CO;2.

Taylor, T. E., O'Dell, C. W., O'Brien, D. M., Kikuchi, N., Yokota, T., Nakajima, T. Y., Ishida, H., Crisp, D., and Nakajima, T. Comparison of cloud-screening methods applied to GOSAT near-infrared spectra. *IEEE Transactions on Geoscience and Remote Sensing*, 50(1):75–88, January 2012. doi:10.1109/TGRS.2011.2160270.

Tegen, I., Lacis, A. A., and Fung, I. The influence on climate forcing of mineral aerosols from disturbed soils. *Letters to Nature*, 380:419–422, April 1996. doi:10.1038/380419a0.

Thuillier, G., Hersé, M., Labs, D., Foujols, T., Peetermans, W., Gillotay, D., Simon, P. C., and Mandel, H. The solar spectral irradiance from 200 to 2400 nm as measured by the SOLSPEC spectrometer from the ATLAS and EURECA missions. *Solar Physics*, 214:1–22, 2003. doi:10.1023/A:1024048429145.

Tikhonov, A. On the solution of incorrectly state problems and a method of regularization. *Doklady Akademii Nauk SSSR*, 151:501–504, 1963.

Tilstra, L. G., de Graaf, M., Aben, I., and Stammes, P. In-flight degradation correction of SCIAMACHY UV reflectances and absorbing aerosol index. *Journal of Geophysical Research*, 117:D06209, 2012. doi:10.1029/2011JD016957.

Torres, O., Bhartia, P. K., Herman, J. R., Ahmad, Z., and Gleason, J. Derivation of aerosol properties from satellite measurements of backscattered ultraviolet radiation: Theoretical basis. *Journal of Geophysical Research*, 103(D14):17099–17110, July 1998. doi:10.1029/98JD0090.

Torres, O., Bhartia, P. K., Sinyuk, A., Welton, E. J., and Holben, B. Total Ozone Mapping Spectrometer measurements of aerosol absorption from space: Comparison to SAFARI 2000 ground-based observations. *Journal of Geophysical Research*, 110:D10S18, 2005. doi:10.1029/2004JD004611.

Twomey, S. The influence of pollution on the shortwave albedo of clouds. *Journal of the Atmospheric Sciences*, 34:1149–1152, October 1977. doi:10.1175/1520-0469(1977)034%3C1149:TIOPOT%3E2.0.CO;2.

Veefkind, J. P., de Leeuw, G., and Durkee, P. A. Retrieval of aerosol optical depth over land using two-angle view satellite radiometry during TARFOX. *Geophysical Research Letters*, 25(16): 3135–3138, August 1998. doi:10.1029/98GL02264.

Voronovich, A. G., Gasiewski, A. J., and Weber, B. L. A fast multistream scattering-based jacobian for microwave radiance assimilation. *IEEE Transactions on Geoscience and Remote Sensing*, 42 (8):1749–1761, August 2004. doi:10.1109/TGRS.2004.830637.

Wallace, L., Hinkle, K., and Livingston, W. C. An atlas of the photospheric spectrum from 8900 to 13600 cm^{-1} (7350 to 11230 Å). Technical Report 93-001, National Solar Observatory, Tucson, Arizona, 1993.

Wang, C. A modeling study on the climate impacts of black carbon aerosols. *Journal of Geophysical Research*, 109:D03106, 2004. doi:10.1029/2003JD004084.

Wang, M. and Gordon, H. R. Estimating aerosol optical properties over the oceans with the multiangle imaging spectroadiometer: Some preliminary studies. *Applied Optics*, 33(18):4042–4057, June 1994. doi:10.1364/AO.33.004042.

Wanner, W., Li, X., and Strahler, A. H. On the derivation of kernels for kernel-driven models of bidirectional reflectance. *Journal of Geophysical Research*, 100(D10):21077–21089, October 1995. doi:10.1029/95JD02371.

Waquet, F., Goloub, P., Deuzé, J.-L., Léon, J.-F., Auriol, F., Verwaerde, C., Balois, J.-Y., and Francois, P. Aerosol retrieval over land using a multiband polarimeter and comparison with path radiance method. *Journal of Geophysical Research*, 112:D11214, 2007. doi:10.1029/2006JD008029.

Waquet, F., Cairns, B., Knobelspiesse, K., Chowdhary, J., Travis, L. D., Schmid, B., and Mishchenko, M. I. Polarimetric remote sensing of aerosols over land. *Journal of Geophysical Research*, 114: D01206, 2009. doi:10.1029/2008JD010619.

Ward, R. C. Numerical computation of the matrix exponential with accuracy estimate. *SIAM Journal on Numerical Analysis*, 14(4):600–610, September 1977. doi:10.1137/0714039.

Waterman, P. C. Matrix-exponential description of radiative transfer. *Journal of the Optical Society of America*, 71(4):410–422, April 1981. doi:10.1364/JOSA.71.000410.

Weaver, C. J., Ginoux, P., Hsu, N. C., Chou, M.-D., and Joiner, J. Radiative forcing of Saharan dust: GOCART model simulations compared with ERBE data. *Journal of the Atmospheric Sciences*, 59:736–747, February 2002. doi:10.1175/1520-0469(2002)059%3C0736:RFOSDG%3E2.0.CO;2.

Wells, K. C. *Aerosol Single-Scattering Albedo Retrieval Over North Africa Using Critical Reflectance*. PhD thesis, Colorado State University, 2010.

Wells, K. C., Martins, J. V., Remer, L. A., Kreidenweis, S. M., and Stephens, G. L. Critical reflectance derived from MODIS: Application for the retrieval of aerosol absorption over desert regions. *Journal of Geophysical Research*, 117:D03202, 2012. doi:10.1029/2011JD016891.

Whitlock, C. H., Bartlett, D. S., and Gurganus, E. A. Sea foam reflectance and influence on optimum wavelength for remote sensing of ocean aerosols. *Geophysical Research Letters*, 9(6): 719–722, June 1982. doi:10.1029/GL009i006p00719.

Wielicki, B. A., Barkstrom, B. R., Harrison, E. F., Lee, R. B. III, Smith, G. L., and Cooper, J. E. Clouds and the Earth's Radiant Energy System (CERES): An Earth observing system experiment. *Bulletin of the American Meteorological Society*, 77(5):853–868, May 1996. doi:10.1175/1520-0477(1996)077%3C0853:CATERE%3E2.0.CO;2.

Wiscombe, W. J. On initialization, error and flux conservation in the doubling method. *Journal of Quantitative Spectroscopy and Radiative Transfer*, 16:637–658, 1976. doi:10.1016/0022-4073(76)90056-X.

Wiscombe, W. J. The delta-M method: Rapid yet accurate radiative flux calculations for strongly asymmetric phase functions. *Journal of the Atmospheric Sciences*, 34:1408–1422, September 1977. doi:10.1175/1520-0469(1977)034%3C1408:TDMRYA%3E2.0.CO;2.

Wu, M.-L. C. Remote sensing of cloud-top pressure using reflected solar radiation in the oxygen A-band. *Journal of Climate and Applied Meteorology*, 24:539–546, June 1985. doi:10.1175/1520-0450(1985)024%3C0539:RSOCTP%3E2.0.CO;2.

Xiong, X. and Barnes, W. An overview of MODIS radiometric calibration and characterization. *Advances in Atmospheric Sciences*, 23(1):69–79, 2006. doi:10.1007/s00376-006-0008-3.

Yamamoto, G. Direct absorption of solar radiation by atmospheric water vapor, carbon dioxide and molecular oxygen. *Journal of the Atmospheric Sciences*, 19:182–188, March 1962. doi:10.1175/1520-0469(1962)019%3C0182:DAOSRB%3E2.0.CO;2.

Yu, H., Kaufman, Y. J., Chin, M., Feingold, G., Remer, L. A., Anderson, T. L., Balkanski, Y., Bellouin, N., Boucher, O., Christopher, S., DeCola, P., Kahn, R., Koch, D., Loeb, N., Reddy, M. S., Schulz, M., Takemura, T., and Zhou, M. A review of measurement-based assessments of the aerosol direct radiative effect and forcing. *Atmospheric Chemistry and Physics*, 6:613–666, 2006. doi:10.5194/acp-6-613-2006.

Yu, H., Liu, S. C., and Dickinson, R. E. Radiative effects of aerosols on the evolution of the atmospheric boundary layer. *Journal of Geophysical Research*, 107(D12):4142, 2002. doi:10.1029/2001JD000754.

Yu, H., Chin, M., Winker, D. M., Omar, A. H., Liu, Z., Kittaka, C., and Diehl, T. Global view of aerosol vertical distributions from CALIPSO lidar measurements and GOCART simulations: Regional and seasonal variations. *Journal of Geophysical Research*, 115:D00H30, 2010. doi:10.1029/2009JD013364.

Zhang, J. and Christopher, S. A. Longwave radiative forcing of Saharan dust aerosols estimated from MODIS, MISR, and CERES observations on Terra. *Geophysical Research Letters*, 30(23): 2188, 2003. doi:10.1029/2003GL018479.